DE GRUYTER

COMPLEX ENGINEERING SYSTEMS – MODELING AND OPTIMIZATION

MULTI-OBJECTIVE ANALYSIS AND SMART MANUFACTURING APPLICATIONS

Edited by Satyvir Singh and Mukesh Kumar Awasthi

DE GRUYTER SERIES ON THE APPLICATIONS OF MATHEMATICS IN ENGINEERING AND INFORMATION SCIENCES

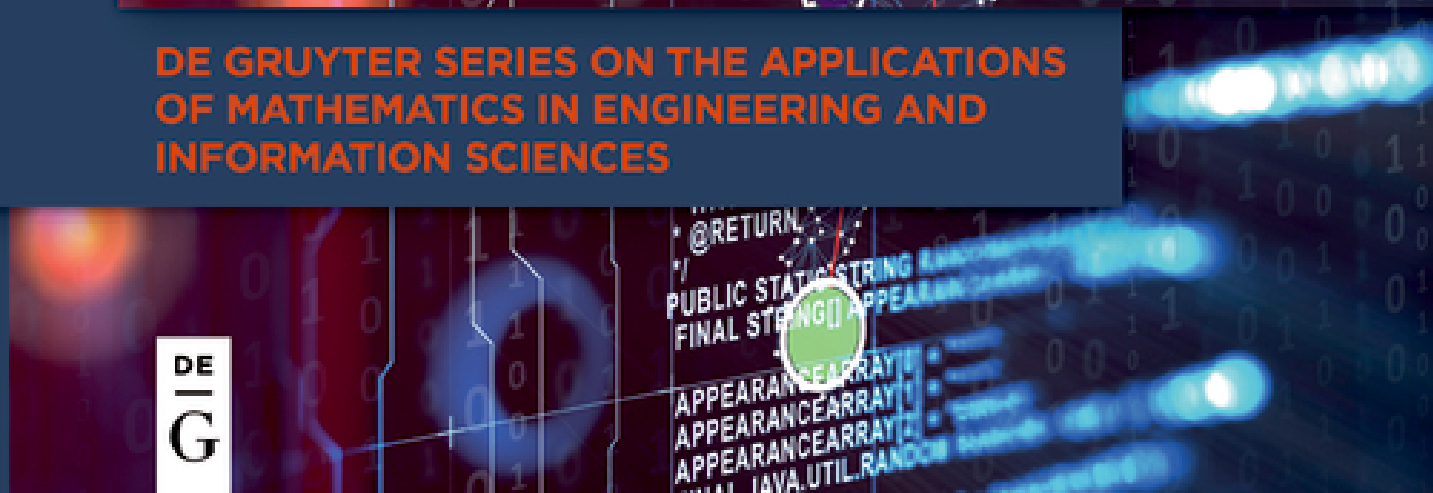

Complex Engineering Systems – Modeling and Optimization

De Gruyter Series on the Applications of Mathematics in Engineering and Information Sciences

Edited by
Mangey Ram

Volume 24

Complex Engineering Systems – Modeling and Optimization

Multi-Objective Analysis and Smart Manufacturing Applications

Edited by
Satyvir Singh and Mukesh Kumar Awasthi

DE GRUYTER

Editors
Dr Satyvir Singh
Institute for Applied and Computational Mathematics
RWTH Aachen University
Schinkelstr. 2
Aachen 52062
Germany
E-mail: singh@acom.rwth-aachen.de

Dr Mukesh Kumar Awasthi
Department of Mathematics
Babasaheb Bhimrao Ambedkar University
Vidya Vihar, Raebareli Road
Lucknow 226025, Uttar Pradesh
India
E-mail: mukeshiitr.kumar@gmail.com

ISBN 978-3-11-172340-2
e-ISBN (PDF) 978-3-11-172346-4
e-ISBN (EPUB) 978-3-11-172359-4
ISSN 2626-5427

Library of Congress Control Number: 2025945719

Bibliographic information published by the Deutsche Nationalbibliothek
The Deutsche Nationalbibliothek lists this publication in the Deutsche Nationalbibliografie; detailed bibliographic data are available on the internet at http://dnb.dnb.de.

© 2026 Walter de Gruyter GmbH, Berlin/Boston, Genthiner Straße 13, 10785 Berlin
Cover image: MF3d/E+/Getty Images
Typesetting: Integra Software Services Pvt. Ltd.
Printing and binding: CPI books GmbH, Leck

www.degruyterbrill.com
Questions about General Product Safety Regulation:
productsafety@degruyterbrill.com

Aim and Scope

This book offers a rigorous and systematic examination of complex engineering systems (CES), integrating foundational theories, advanced modeling techniques, and cutting-edge optimization strategies to bridge the gap between theoretical concepts and practical applications. Designed as a comprehensive reference, it caters to researchers, engineers, and graduate students seeking to analyze, model, and optimize CES across diverse domains, from fluid dynamics and heat transfer to multi-physics interactions and computational intelligence.

The book begins by establishing the fundamentals of CES in **Chapter 1**, introducing their multidisciplinary nature, emergent behaviors, and key principles such as scalability, resilience, and system integration. It underscores the importance of model-based approaches and systems thinking in addressing CES challenges. **Chapter 2** lays the mathematical groundwork, covering differential equations**,** stochastic models, and computational tools for dynamic system analysis, while **Chapter 3** transitions to optimization techniques, including genetic algorithms, dynamic programming, and AI-driven strategies for performance enhancement and cost reduction.

Subsequent chapters delve into specialized methodologies and applications. **Chapter 4** explores multi-physics modeling, emphasizing coupled analyses across structural, thermal, and electromagnetic domains. **Chapter 5** advances numerical methods for fluid dynamics, employing Crank-Nicolson schemes and Shishkin meshes to tackle singular perturbations. **Chapter 6** evaluates weighted residual methods for boundary value problems, comparing techniques like Galerkin and least squares, while **Chapter 7** investigates MHD Stokes flow in microchannels using the boundary element method, with applications in microfluidics.

System optimization and applied engineering solutions take center stage in later chapters. **Chapter 8** analyzes queueing models for resource efficiency, and **Chapter 9** reviews MEMS-based microfluidic pressure sensing for lab-on-a-chip devices. **Chapters 10 and 11** examine nanofluid dynamics, leveraging models like Xue and Cattaneo-Christov to study thermal radiation, MHD effects, and porous media flows. **Chapter 12** presents multiphase flow analysis in cryogenic systems using volume of fluid models, and **Chapter 13** introduces fractional calculus for memory-dependent heat transfer.

The concluding chapters highlight emerging computational and data-driven approaches. **Chapter 14** applies bifurcation theory to manage chaotic dynamics in discretized systems, while **Chapter 15** combines machine learning (artificial neural network) with numerical methods to predict thermodiffusion effects. Finally, **Chapter 16** reviews computational fluid dynamics as a versatile tool for optimizing designs across engineering, biomedical, and environmental systems.

https://doi.org/10.1515/9783111723464-202

By unifying multidisciplinary perspectives – from mathematical modeling and computational simulations to AI-augmented optimization – this book equips readers with the tools and insights needed to solve real-world CES challenges. Featuring case studies, comparative analyses, and hybrid methodologies, it serves as both a reference and an inspiration for advancing research and innovation in complex systems engineering.

Editors
Satyvir Singh
Mukesh Kumar Awasthi

Preface

The complexity and interdisciplinary nature of modern engineering systems have necessitated the development of robust models, advanced simulation techniques, and optimized decision-making frameworks. This book brings together a compendium of contemporary research that addresses these challenges through mathematical, computational, and technological advancements. This volume is a collaborative endeavor by researchers across domains, and it aims to serve as a foundational and reference text for academicians, industry professionals, and students involved in complex system modeling and optimization.

Chapter 1 provides a comprehensive introduction to complex engineering systems (CES), highlighting their systemic behavior, emergent properties, interdependencies, and the need for interdisciplinary approaches to design, integrate, and manage them effectively. It sets the philosophical and practical tone for the rest of the book. **Chapter 2** builds on this foundation by offering a rigorous mathematical framework, covering differential equations, stochastic modeling, and computational tools essential for analyzing dynamic systems under uncertainty.

Optimization remains central to CES, and **Chapter 3** explores a range of classical and modern optimization techniques, including genetic algorithms, dynamic programming, and machine learning methods. These tools are critical in enhancing performance and cost-efficiency in real-world systems. **Chapter 4** introduces multiphysics modeling – a key enabler in capturing interrelated physical phenomena – providing a detailed guide to simulation procedures and coupling strategies for complex domains, such as structural mechanics and fluid dynamics.

Advanced numerical strategies are addressed in **Chapters 5 and 6**. **Chapter 5** presents robust schemes for time-delayed semilinear parabolic problems, often arising in fluid dynamics, whereas **Chapter 6** compares weighted residual methods for boundary value problems, offering both theoretical insight and practical benchmarks. **Chapter 7** introduces a boundary element analysis for magnetohydrodynamic (MHD) Stokes flow in microchannels with surface roughness – crucial for optimizing heat and fluid transport in microscale systems.

The modeling of queuing systems in complex environments is treated in **Chapter 8**, which emphasizes approximation techniques for efficient system performance and cost reduction. **Chapter 9** presents a critical review of pressure sensing mechanisms in microelectromechanical systems-based microfluidic devices, bridging electronics, and biomedical engineering. These insights are particularly valuable in healthcare and lab-on-a-chip applications.

Thermal and fluid transport in advanced materials is explored in **Chapters 10–13**. **Chapter 10** uses the Xue model and the Cattaneo-Christov framework to study trihybrid nanofluids over porous plates, while **Chapter 11** extends the investigation to non-Darcy MHD nanofluid flow with detailed numerical simulations. **Chapter 12** shifts the focus to cryogenic multiphase flow in methane pipelines – crucial for aero-

https://doi.org/10.1515/9783111723464-203

space propulsion systems – employing volume of fluid methods. **Chapter 13** presents fractional calculus and advanced numerical techniques to model anomalous heat transfer, paving the way for more accurate simulations of nonclassical diffusion processes.

Chapter 14 explores chaos control in discrete systems using the Allee effect, bifurcation analysis, and hybrid control methods, demonstrating how ecological modeling concepts can be applied to engineered systems. **Chapter 15** uses machine learning and neural networks to analyze thermodiffusion effects in the Jeffery-Hamel flow, highlighting the power of artificial intelligence in modeling and predictive analytics. The final **Chapter 16** rounds off the book with a broad study of computational fluid dynamics, showcasing its diverse applications in biomedical sciences, astrophysics, and environmental modeling.

Together, the chapters in this book present a multidimensional perspective on the modeling, simulation, and optimization of complex systems. By bringing together mathematical rigor, computational power, and engineering application, this volume seeks to inform, inspire, and enable innovative solutions to modern engineering challenges. We hope this work will contribute meaningfully to ongoing discourse and research in the ever-evolving field of complex systems.

Editors
Satyvir Singh
Mukesh Kumar Awasthi

Acknowledgments

The completion of this book has been made possible through the collective effort and dedication of numerous individuals and institutions. We extend our heartfelt appreciation to all the contributing authors for their scholarly input, rigorous research, and unwavering commitment. Their diverse expertise and deep understanding of complex engineering phenomena have significantly enriched the content of this volume, offering multidisciplinary insights into modeling, simulation, optimization, and computational analysis of engineering systems.

We are profoundly grateful to De Gruyter, Germany, for the opportunity to publish this work. The editorial and production teams have provided outstanding support throughout the publication process. Their professionalism, constructive feedback, and meticulous attention to detail have helped ensure the quality, clarity, and coherence of this book. Their guidance has been instrumental in transforming a diverse collection of ideas into a cohesive and impactful scholarly volume.

Our sincere thanks also go to our families and friends, whose encouragement, patience, and understanding have been a source of constant motivation. Their support during countless hours of coordination, research, editing, and revisions has made this endeavor achievable.

We also acknowledge the broader scientific and engineering communities whose innovations, foundational theories, and ongoing contributions have shaped the evolution of complex systems modeling and optimization. The literature, experimental studies, and computational advances provided by these communities form the backbone of this work.

It is our hope that this book will serve as a valuable reference for students, researchers, and professionals engaged in the study and application of complex engineering systems. We envision it inspiring future research, fostering interdisciplinary collaboration, and contributing meaningfully to the development of intelligent, resilient, and sustainable technological solutions.

Editors
Satyvir Singh
Mukesh Kumar Awasthi

https://doi.org/10.1515/9783111723464-204

Contents

Editors' Biography

Dr Satyvir Singh is currently working as a research associate fellow in the Institute of Applied and Computational Mathematics (ACoM) at RWTH Aachen University, Germany (QS ranking no. 147). He earned his Ph.D. in computational fluid mechanics with thesis entitled "Development of 3D DiscontinuousGalerkin Method for Solving Boltzmann-Type Gas Kinetic Equations for Diatomic and Polyatomic Gases" in the School of Mechanical and Aerospace Engineering at Gyeongsang National University, South Korea (QS ranking nos. 301–350). Subsequently, he worked as a senior research fellow at Research Center for Aircraft Parts Technology, Gyeongsang National University, South Korea, in 2018. After then, he worked as a research fellow in the School of Physical and Mathematical Sciences at the Nanyang Technological University Singapore (QS ranking no. 19) during 2018–2022. He completed his M. Tech. in industrial mathematics and scientific computing at the Indian Institute of Technology, Chennai, India (QS ranking no. 250), as well as M.Sc. in mathematics at CCS University Meerut, India. He has been qualified in two highly competitive Indian examinations – Junior Research Fellowship and National Eligibility Test in Mathematical Sciences (2011) with all India rank no. 38, and Graduate Aptitude Test for Engineering in Mathematics (2012) with all India rank no. 244. For his teaching background, he worked in India as an assistant professor in Galgotias College of Engineering and Technology, Greater Noida, and IMS Engineering College, Ghaziabad, where he taught various mathematics courses (engineering mathematics, calculus, differential equations, linear algebra, discrete mathematics, and numerical analysis) to undergraduate and postgraduate students. He has a vast research area, including computational fluid dynamics, high-order numerical methods, hydrodynamic instability, gas kinetic theory, heat and mass transfer, and computational biology. His commitment to research is reflected in his more than 50 research articles (600+ citations) in reputable journals, including *Physics of Fluids*, *Journal of Computational Physics*, *Computers & Fluids*, *International Journal of Heat and Mass Transfer*, *Physical Review Fluids*, and *Applied Mathematics Computations*. Also, he has published one book. Besides it, he has attended many international conferences and presented his research work in the USA, the UK, Italy, South Korea, Singapore, Germany, Greece, China, Japan, and India. As a Co-PI, he has received the research fund for the project "Mathematical Modelling and High-fidelity Simulations for Brain Tumor Dynamics" by the Deanship of Graduate Studies and Scientific Research Scheme, Jazan University, Saudi Arabia (2024). His ORCID is https://orcid.org/my-orcid?orcid=0000-0001-6669-5296, the Google Scholar web link is https://scholar.google.com/citations?user=sQT89LYAAAAJ&hl=en, and the ResearchGate web page is https://www.researchgate.net/profile/Satyvir-Singh.

Dr Mukesh Kumar Awasthi has done his Ph.D. on the topic "Viscous Correction for the Potential Flow Analysis of Capillary and Kelvin-Helmholtz Instability." He is working as an assistant professor in the Department of Mathematics at Babasaheb Bhimrao Ambedkar University, Lucknow. He is specialized in the mathematical modeling of flow problems. He has taught courses of fluid mechanics, discrete mathematics, partial differential equations, abstract algebra, mathematical methods, and measure theory to postgraduate students. He has acquired excellent knowledge in the mathematical modeling of flow problems, and he can solve these problems analytically as well as numerically. He has a good grasp of the subjects like viscous potential flow, electrohydrodynamics, magnetohydrodynamics, heat, and mass transfer. He has excellent communication skills and leadership qualities. He is self-motivated and responds to suggestions in a more convincing manner. He has qualified National Eligibility Test (NET) conducted on all India level in the year 2008 by the Council of Scientific and Industrial Research (CSIR), and got Junior Research Fellowship (JRF) and Senior Research Fellowship (SRF) for doing research. He has published **135 plus** research publications (journal articles/books/book chapters/conference articles) in Elsevier, Taylor & Francis, Springer, Emerald, World Scientific, and in many other national and international journals and conferences. Also, he has published **18** books. He is also a series editor of *Artificial Intelligence and Machine Learning for Intelligent Engineering Systems* published by the CRC Press

https://doi.org/10.1515/9783111723464-206

(Taylor & Francis, USA). He has attended many symposia, workshops, and conferences in mathematics as well as fluid mechanics. He has got the "Research Awards" consecutively four times from 2013 to 2016 by the University of Petroleum and Energy Studies, Dehradun, India. He has also received the start-up research fund for his project "Nonlinear Study of the Interface in Multilayer Fluid System" from UGC, New Delhi. He is also listed among the **top 2% of influential researchers** in the world, as prepared by the Stanford University based on Scopus data for the years 2022 and 2023. His ORCID is *0000-0002-6706-5226*, Google Scholar web link is https://scholar.google.co.in/citations?user=Dj3ktGAAAAAJ and research gate web link is https://www.researchgate.net/profile/Mukesh-Awasthi-2.

List of Contributors

Atul Kumar Shukla
Department of Mathematics
Ganga Singh College
Chapra 841301, Bihar
India

Mukesh Kumar Awasthi
Department of Mathematics
Babasaheb Bhimrao Ambedkar University
Lucknow, Uttar Pradesh
India

Satyvir Singh
Applied and Computational Mathematics
RWTH Aachen University
Aachen, Germany

Dhananjay Yadav
Department of Mathematical and Physical Sciences
University of Nizwa
Nizwa, Oman

Shikhar Prateek Pandey
USICT, Gautam Buddha University
Greater Noida, Uttar Pradesh
India

Arpit Bhardwaj
USICT, Gautam Buddha University
Greater Noida, Uttar Pradesh
India

A. J. D. Nanthakumar
Department of Automobile Engineering
SRM Institute of Science and Technology
Chennai, Tamil Nadu
India

S. Priyadarshana
Centre for Data Science
ITER, SOA University
Bhubaneswar, Odisha
India

J. Mohapatra
Department of Mathematics
NIT Rourkela
Rourkela, Odisha
India

Anurag Srivastav
Department of Mathematics
Chandigarh University
Chandigarh, Punjab
India

Vishal Chhabra
Pandit Deendayal Energy University
Gandhinagar, Gujarat
India

Chandra Shekhar Nishad
International Institute of Information Technology
Naya Raipur, Chhattisgarh
India

Manoj Sahni
Pandit Deendayal Energy University
Gandhinagar, Gujarat
India

Rachna Khurana
Sharda School of Basic Sciences and Research
Sharda University
Agra, Uttar Pradesh
India

Sangeeta Gupta
A.H. Siddiqi Centre, Sharda University
Greater Noida, Uttar Pradesh
India

Sweta Srivastava
A.H. Siddiqi Centre, Sharda University
Greater Noida, Uttar Pradesh
India

https://doi.org/10.1515/9783111723464-207

Vinay Kumar Jadon
Sharda School of Basic Sciences and Research
Sharda University
Agra, Uttar Pradesh
India

Ankur Saxena
Bharat Institute of Engineering and Technology
Hyderabad, Telangana
India

Mahesh Kumar
Pandit Deendayal Energy University
Gandhinagar, Gujarat
India

Kulwant Singh
Shri Vishwakarma Skill University
Haryana, Punjab
India

Dhaneshwar Mishra
Manipal University Jaipur
Jaipur, Rajasthan
India

Tanya Gupta
Department of Mathematics
IAH, GLA University
Mathura, Uttar Pradesh
India

Shiv Pratap
Division of Mathematics
SBS, Galgotias University
Greater Noida, Uttar Pradesh
India

Padam Singh
Department of Applied Sciences
Galgotias College of Engineering and Technology
Greater Noida, Uttar Pradesh
India

Manoj Kumar
G.B. Pant University of Agriculture and Technology
Pantnagar, Uttarakhand
India

Sham Bansal
Department of Mathematics
Mata Gujri College
Fatehgarh Sahib, Punjab
India

Kanak Raj
Department of Aerospace Engineering
IIEST Shibpur, West Bengal
India

Prince Raj Lawrence Raj
Department of Aerospace Engineering
IIEST Shibpur, West Bengal
India

Dr A. M. Khan
Department of Mathematics
Jodhpur Institute of Engineering and Technology
Jodhpur, Rajasthan
India

Manisha Yadav
Department of Mathematics
Faculty of Applied and Basic Sciences
SGT University
Haryana, Punjab
India

Pradeep Malik
Department of Mathematics
Faculty of Applied and Basic Sciences
SGT University, Haryana
Punjab, India

Ram Prakash Sharma
Department of Mechanical Engineering
NIT Arunachal Pradesh
Jote, Arunachal Pradesh
India

V. Vinay Kumar
Department of Basic and Applied Science
NIT Arunachal Pradesh
Jote, Arunachal Pradesh
India

Jaya Gupta
Department of Mathematics
GNA University
Phagwara, Punjab
India

Geeta Arora
Department of Mathematics
Lovely Professional University
Phagwara, Punjab
India

Shubham Mishra
Department of Mathematics
Lovely Professional University
Phagwara, Punjab
India

Atul Kumar Shukla*, Mukesh Kumar Awasthi, Satyvir Singh,
and Dhananjay Yadav

Chapter 1
Introduction to Complex Engineering Systems

Abstract: The design, integration, and management of large-scale, multifaceted systems made up of interdependent components from various disciplines are the focus of the study of complex engineering systems (CESs). These systems, which include autonomous cars, smart grids, advanced manufacturing platforms, and defense and aerospace infrastructures, display emergent behavior, nonlinear interactions, and dynamic evolution over time. The fundamental ideas of CES, such as system architecture, interoperability, feedback control, and life cycle considerations, are examined in this introductory chapter. The importance of uncertainty in decision-making, model-based design, and systems thinking is emphasized. The difficulties of scalability, resilience, and adaptability are also covered in the chapter, especially in light of organizational, environmental, and technological complexity. The goal of CES research is to create resilient, intelligent, and sustainable systems that can function efficiently by combining interdisciplinary knowledge with cutting-edge computational tools.

Keywords: system of systems (SoS), nonlinearity, emergent behavior, interdependence, modeling and simulation

1.1 Introduction

Systems engineering (SE) has progressed largely in the absence of a codified theoretical foundation, instead of advancing through the accretion of practice-based insights, experiential learning, and heuristic constructs [1, 2]. It emerged as a discipline dedicated to orchestrating equilibrium across heterogeneous subsystems and interdisciplinary domains. In alignment with this foundational objective, a salient trajectory for contemporary SE research is the exploration of systemic holism – interrogating

*__Corresponding author: Atul Kumar Shukla__, Department of Mathematics, Ganga Singh College, Chapra 841301, Bihar, India, e-mail: atulkushukla1993@gmail.com
Mukesh Kumar Awasthi, Department of Mathematics, Babasaheb Bhimrao Ambedkar University, Lucknow, India
Satyvir Singh, Applied and Computational Mathematics, RWTH Aachen University, Schinkelstr. 2, Aachen 52062, Germany
Dhananjay Yadav, Department of Mathematical and Physical Sciences, University of Nizwa, Oman

https://doi.org/10.1515/9783111723464-001

the intrinsic characteristics of a system that are not reducible to its individual constituents, and identifying the mechanisms by which a system manifests capabilities or value exceeding the arithmetic sum of its parts [3]. It is conceivable to envision a foundational science of interrelationships that underlies the principles of SE. Encouragingly, the evolving field of complex systems – often denoted as complexity theory – is beginning to furnish a rigorous theoretical substrate for SE. This nascent framework holds promise not only for elucidating prevailing engineering practices but also for enabling the formal modeling of extant systems, thereby permitting predictive analyses. If mathematical abstractions can reliably anticipate emergent, holistic system behaviors, then system parameters may be methodically adjusted to enhance specific performance attributes – circumventing the inefficiencies and uncertainties associated with empirical, trial-and-error modifications in physical hardware and software implementations. Early identification of critical parameters is essential to prevent costly rework and disruptions in SE projects. As complex systems science rapidly evolves, its shifting insights challenge the notion of fixed "best practices" [4]. Still, staying current with the literature remains vital. This chapter distills key principles from complexity science relevant to engineered systems. While *complex engineered system* (CES) [5] offers a rich theoretical foundation, its abstract nature limits practical application, requiring interpretation beyond the reach of many practitioners.

1.2 Complex Systems' Definition

A complex system is often described as a system composed of many parts that are linked together and have a set number of relationships which are interdependent and dynamic, often not in a straight line. Such interactions result in global patterns, frameworks, and behavior that evolve over time and cannot be easily deduced from individual components; this is called emergence.

Complex systems are often formally defined in system theories and computational modeling as follows:

A collection of agents or elements not only interact in nontrivial ways, most of the time giving rise to some emergent substructure, but whose collective actions do not result to a simple linear sum of the actions of its constituent elements. This definition illustrates the following key features that are important: multiplicity of agents, dependence, nonlinear interactivity, and emergence. These qualities set complex systems apart from merely complicated systems, which are intricate but fundamentally predictable and reducible.

1.3 Key Characteristics of Complex Systems

To make sense of the layers in a complex system (Figure 1.1), one must define and study the parameters that define them. Some of the most salient features of complex systems, as defined by extensive research, are explained further.

1.3.1 Emergence

Emergence is defined as the spontaneous generation of patterns, structures, or behaviors at a macrolevel from the interaction of smaller components at a microlevel. This kind of phenomenon also suggests that the system possesses characteristics and components which are not apparent when examining the parts individually. Such cases are the flocking behavior of birds, the self-organization of cellular structures, or trends in markets in economics. Emergent phenomena often arise without a central control and may result in a stable or metastable configuration that displays a kind of collective intelligence or coordination.

1.3.2 Nonlinearity

Although nonlinearity and a state far from equilibrium are necessary prerequisites for the emergence of complex behavior, they are not sufficient on their own. Complex systems also exhibit other defining characteristics, most notably the presence of numerous interacting components. These components – often simple in nature – interact in nonlinear ways, either locally or globally. Crucially, the architecture of these interactions, including the system's geometry and the topology of its interaction network, significantly influences its behavior. What makes these systems truly complex is their ability to exhibit emergent properties – features that arise not from individual components but from their interactions. This raises a fundamental question: Can the emergence of such properties be understood purely from the coupling of the system's elements? To answer this, we must delve into the dynamics of nonlinear systems with many degrees of freedom. Evidence thus far indicates that global emergent phenomena can indeed arise from local nonlinear interactions

1.3.3 Adaptation and Learning

Many complex systems are adaptive, meaning they have the capacity to learn from their environment and modify their behavior accordingly. This is especially true in biological, social, and artificial systems. Adaptive behavior often emerges from processes such as evolution, learning algorithms, or decision-making protocols.

For example, neural networks in the brain rewire themselves in response to stimuli, and organisms evolve traits that enhance survival under changing environmental conditions.

1.3.4 Decentralized Control

Complex systems require swift control actions in response to localized inputs and disturbances, which naturally leads to the adoption of decentralized information and control architectures. This well-regarded reference work explores systematic approaches for developing control laws under such decentralized constraints. The text opens with a graph-theoretic framework for modeling the structural properties of complex systems and proceeds to examine robust stabilization through decentralized state feedback. Further chapters address key topics such as optimization techniques, output feedback mechanisms, the influence of graph structures on control strategies, overlapping decompositions grounded in the inclusion principle, and methods for enhancing system reliability. Each chapter is supported by detailed notes and references, and the appendix includes a practical collection of efficient graph algorithms.

1.3.5 Hierarchical Organization

This chapter investigates the hierarchical structure of complex networks, which often exhibit weighted, attributed, directed, and dynamic properties. Key contributions include novel algorithms for learning low-dimensional, non-Euclidean representations of nodes in weighted and directed networks, and a framework for analyzing mesoscopic structures in signaling networks to identify potential drug targets. These advancements enhance our understanding of information flow and organization in real-world complex systems.

1.3.6 Sensitivity to Initial Conditions

The notion of sensitive dependence on initial conditions has been famously encapsulated in the metaphor of the “butterfly effect” – the proposition that the infinitesimal disturbance caused by a butterfly’s wingbeat in Brazil could precipitate significant meteorological shifts in Texas. Such systems exhibit extreme sensitivity wherein negligible perturbations in initial parameters can engender vastly divergent trajectories. This phenomenon was first identified by Edward Lorenz in his seminal work on thermal convection [6], from which he astutely deduced the inherent limitations of long-term atmospheric forecasting. The butterfly effect underscores the premise that minuscule alterations in the atmospheric state can cascade through nonlinear interactions and

feedback mechanisms, ultimately manifesting as large-scale climatic variations. Though seemingly implausible, this concept gains credence when considering the intrinsic interconnectivity, nonlinearity, and potential for dynamic signal amplification within complex systems.

1.4 Examples of Complex Systems

Biological Systems:
- **Ecosystems** respond nonlinearly to small changes.
- **Disease spread** depends on network dynamics and feedback.
- **Cellular processes** involve complex signaling and adaptation.

Social Sciences:
- **Social networks** influence rapid information diffusion.
- **Economic systems** show emergent patterns like booms and crashes.
- **Cultural evolution** arises from small, cumulative interactions.

Engineering and Technology:
- **Traffic systems** exhibit large effects from minor disruptions.
- **Swarm robotics** use simple rules for complex coordination.
- **Computer networks** rely on robust internode interactions to avoid cascading failures.

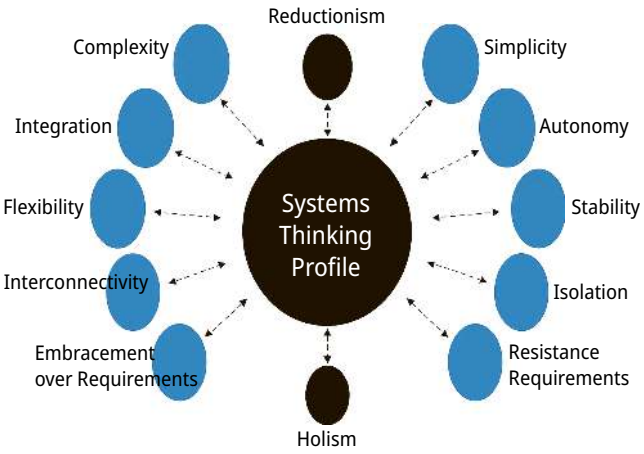

Figure 1.1: Illustration of the hierarchical levels at which systems thinking is applied from micro-level components to macro-level interactions.

1.5 Importance of Modeling and Simulation

Modeling refers to the abstract formulation and conceptual construction of a representative framework that emulates the structural and functional attributes of a real-world system. This surrogate model encapsulates essential system characteristics, enabling analysts to forecast the implications of potential modifications. In essence, modeling constitutes the disciplined endeavor of generating an analog – mathematical, logical, or computational – that mirrors the dynamics and properties of an actual system.

Simulation, on the other hand, entails the dynamic execution of the model across temporal or spatial dimensions to evaluate and interpret system behavior. It serves as an investigative mechanism through which both existing and hypothetical systems can be assessed under varying operational scenarios. In other words, simulation is the methodological deployment of a model to systematically explore, quantify, and predict system performance and response patterns over time.

1.5.1 Safe and Cost-Effective Experimentation

One of the most significant advantages of simulation is the ability to test scenarios in a controlled, risk-free environment. In engineering, simulations allow prototypes to be evaluated under various conditions without the cost and danger of physical testing. For instance, in aerospace engineering, flight simulations help in designing aircraft by assessing aerodynamic performance, control systems, and structural integrity under various stressors.

Similarly, in nuclear power, chemical processing, and transportation, simulations are used to model system behavior under abnormal or emergency conditions, where real-world testing would be dangerous or unethical. This capability is critical for safety analysis and decision support in high-risk industries.

1.5.2 Enhancing Decision-Making and Optimization

System-level trade-off analysis is super important for strategic decision-making, and Modeling and Simulation (M&S) makes this process a lot easier! By using simulations, we can model and analyze optimization issues like scheduling, logistics, and resource allocation to find the best possible solutions. Decision-makers get to evaluate different scenarios, assess risks, and choose the best way to move forward based on what the simulations show.

In supply chain management, simulation models are quite helpful for understanding how delays, inventory policies, or changes in demand can affect overall system performance. This enables companies to proactively adjust their operations instead of just react-

ing to issues. Likewise, in urban planning, traffic flow simulations aid in designing road networks that reduce congestion and enhance the efficiency of public transportation.

1.5.3 Accelerating Innovation and Technological Development

Modeling and simulation play a huge role in speeding up the launch of new technologies by allowing virtual testing and improvements. In product design, computer-aided engineering tools help simulate the mechanics, heat, and fluid dynamics of designs well before any physical prototypes are created. This iterative method boosts innovation and helps cut down development costs.

In the fields of robotics and artificial intelligence (AI), simulation environments provide the opportunity to train and test algorithms across various virtual scenarios. This process leads to the creation of robust systems that can function effectively in real-world situations. Moreover, digital twins – virtual replicas of physical systems – are increasingly utilized in manufacturing and smart infrastructure to continuously monitor and optimize performance in real time.

1.5.4 Educational and Training Value

A pivotal determinant of a nation's prosperous advancement lies in the cultivation of a dynamic and purpose-driven youth. The efficacy of the higher education apparatus manifests conspicuously in the imminent trajectory of national progress. Both the economy and the civil society perpetually demand adept engineers and innovative researchers. Consequently, the evolution of advanced technical education emerges as a critical imperative amid the relentless transformations of the contemporary global landscape. The principal vectors guiding the modernization of higher education encompass the following:

1. Advancement of organizational pedagogical frameworks
2. Formulation and implementation of avant-garde educational technologies and paradigms
3. Systematic monitoring and rigorous evaluation of academic proficiency levels
4. Enhancement of interuniversity collaboration and strategic alliances
5. Promotion of academic mobility for both faculty and students
6. Endorsement of an innovation-centric institutional ethos
7. Expansion of research-intensive and practice-oriented university ecosystems

A further cornerstone in the advancement of higher technical education is the cultivation of engineers adept at navigating intricate and cutting-edge engineering challenges within the dynamic continuum of technological evolution, economic restructuring, and

societal transformation. The nation's trajectory toward innovation-driven growth must be underpinned by the comprehensive preparation of not only engineers grounded in core scientific principles, but also a new cadre of interdisciplinary researchers and versatile professionals attuned to global paradigms and emergent demands.

1.6 The Role of Optimization in Engineering Systems

Escalating market demands compel engineers to conceptualize and engineer products of heightened performance and escalating structural and functional complexity. This intensification necessitates the deployment of intricate simulation frameworks capable of capturing nonlinear dynamical behavior and multifaceted physical interactions. Within such high-fidelity models, analytical expressions for gradients are frequently unattainable or intractable. Consequently, the optimization process must rely on derivative-free methodologies – robust algorithms that circumvent the need for explicit gradient information while navigating complex, multidimensional solution spaces [7].

1.6.1 Concept and Importance

Optimization constitutes a foundational paradigm that underpins analytical reasoning, strategic formulation, and system design across a multitude of disciplines. Whether employed by a data scientist calibrating a machine learning algorithm, an engineer architecting a high-efficiency system, or a business analyst endeavoring to minimize expenditures while maximizing profitability, optimization serves as the quintessential mechanism for deriving the most advantageous outcome within predefined constraints and parameters.

1.6.2 Mathematical and Algorithmic Foundations

Optimization relies on calculus, linear algebra, and numerical analysis. Traditional methods include the following:

- **Linear programming**
- **Nonlinear programming**
- **Dynamic programming**

Advanced metaheuristic algorithms including genetic algorithms, particle swarm optimization, and ant colony optimization are now viable for tackling complex, nonlinear, and large-scale problems, thanks to the power of high-performance computing.

1.6.3 Optimization in Engineering Design

The nation's ability to engineer and deploy complex systems – such as aircraft, automobiles, and space platforms – is nearing a critical threshold. Numerous large-scale programs are afflicted by severe cost overruns and protracted delays due to technical, managerial, and political complications. Boeing's 787 aircraft, for example, was delayed by two years and exceeded its budget by nearly $10 billion. General Motors, after bankruptcy, still reported a $4.3 billion loss in Q4 of 2009, while production costs for the Chevy Volt soared to $40,000 per vehicle – almost double the initial estimate. NASA faces analogous setbacks, with persistent cost inflation and delays in both the International Space Station and Constellation programs, driven as much by political dynamics as technical constraints. These cases exemplify how engineered systems have grown in complexity, exhibiting emergent behaviors that elude existing modeling and optimization tools. Such systems frequently involve poorly quantifiable disciplines – like human behavior – posing a major obstacle to integrative, predictive engineering. In response, National Science Foundation and Defense Advanced Research Projects Agency are launching research initiatives in complex systems design to confront these multidimensional challenges [8–10].

1.6.4 Intelligent and Real-Time Optimization

AI is increasingly recognized for its transformative capacity across sectors such as healthcare, aviation, energy, and transportation. While its applications remain emergent, AI introduces disruptive dynamics into existing innovation and management frameworks, warranting deeper academic investigation. Most current studies treat AI as isolated applications, often neglecting the dynamic, context-dependent nature of its implementation and impact. Complex Products and Systems (CoPS) are evolving into complex intelligent systems as AI becomes embedded, bringing together properties of generativity (adaptive, emergent growth, and scalability) and criticality (safety, security, and regulatory compliance). These characteristics, while seemingly contradictory, are becoming increasingly interdependent. The central focus is on how AI affects engineering management when systems must be both generative and critically robust. Through five managerial dimensions – design goals, system boundaries, system modeling, predictability/emergence, and learning/adaptation – the study analyzes how AI shapes CoPS governance. A case study from the public safety domain illustrates the practical implications of AI adoption in real-world complex system contexts, offering insights into managing trust, safety, and innovation simultaneously [11, 12].

1.6.5 Systems Engineering and Integration

Systems integration challenges persist as a major impediment in the development of CESs. Notably, in 2018, the U.S. Government Accountability Office attributed both cost overruns and schedule delays in NASA's James Webb Space Telescope project to unresolved systems integration complexities. In his seminal work "General Systems Theory", Ludwig von Bertalanffy [13] posits that all systems are governed not only by structural or physical hierarchies but also by functional hierarchies, which represent the sequential flow and organization of system-level processes. In certain configurations, these hierarchies may align – where the physical arrangement of components mirrors the logical sequence of operations.

A compelling example of this dual-hierarchy structure is found in the Patriot Advanced Capability-3 missile system. This CES comprises three core subsystems: the Fire Solution Computer, the Missile Launcher, and the Interceptor Missile. Each subsystem performs a distinct function – computational trajectory analysis and targeting, launch command execution, and threat neutralization. Together, they exemplify both a physical hierarchy of components and a functional hierarchy of operations, illustrating the interdependence and layered complexity inherent in modern engineered defense systems.

1.6.6 Sustainability and Environmental Optimization

Optimization stands as a pivotal instrument in advancing sustainability, functioning as a strategic search paradigm tailored to the specific characteristics and constraints of a given problem. Fundamentally, it entails the determination of optimal parameter values within a feasible solution space, aimed at either minimizing or maximizing the output of a defined system or network. The overarching objective is to identify the most advantageous and feasible outcome while rigorously adhering to problem-specific constraints. Given the escalating intricacy of contemporary scientific and engineering challenges, the application of optimization methodologies has become indispensable. However, the computational intensity and temporal demands of traditional, exact optimization techniques often render them impractical for large-scale, nonlinear, or dynamic problems. Consequently, intelligent optimization algorithms such as those inspired by evolutionary processes, swarm intelligence, and other bioinspired heuristics have emerged as vital alternatives. Nature itself offers a profound reservoir of inspiration, serving as a conceptual framework for the development of artificial metaheuristic strategies capable of resolving complex optimization problems with both computational efficiency and solution accuracy. These biologically inspired algorithms mimic adaptive, self-organizing phenomena, enabling effective navigation through vast and multidimensional search spaces where classical methods fall short.

1.7 Applications in Real-World Scenarios of Complex Engineering Systems

SE is an interdisciplinary paradigm dedicated to the design, synthesis, and coordination of multifaceted components within an unified system architecture. It emphasizes a macroscopic perspective, ensuring that all subsystems function synergistically to fulfill overarching objectives. This field is instrumental in enabling technological innovation and optimizing legacy systems across sectors such as aerospace, information, and communication technologies, infrastructure development, and defense. While industrial engineering similarly seeks to enhance efficiency and productivity, particularly within manufacturing and operational contexts, SE extends its purview further. It addresses the integration of diverse technical domains, ensuring interoperability and coherence across organizational, mechanical, computational, and human subsystems. A fundamental aspect of SE lies in the evaluation and resolution of competing constraints through deliberate trade-offs. It leverages cross-domain expertise to formulate inventive, robust, and purpose-driven solutions – balancing technical feasibility, economic viability, and functional performance to meet complex system requirements.

1.8 Aerospace and Space Systems

1.8.1 Space Telescopes and Satellite Systems

Conventional metrics used to estimate the cost and structural complexity of space telescope systems warrant critical reassessment in light of the volumetric and payload capabilities enabled by the ARES V launch vehicle. The expanded payload capacity significantly alleviates stringent spatial constraints, thereby obviating the need for intricate, deployable configurations previously necessitated by limited launch shroud dimensions. As a result, system architects are no longer compelled to employ complex foldable designs akin to “engineering origami” to accommodate telescopic assemblies within constrained envelopes. This paradigm shift allows for the reallocation of design emphasis – from minimizing mass and volume toward enhancing optical performance, structural robustness, and overall system reliability. The reduced necessity for ultra-lightweight, segmented mirrors and their intricate support mechanisms offers new opportunities for improving mission resilience and scientific return [14].

The nascent era of satellite technology was marked by systems that were markedly rudimentary when juxtaposed with the complex, multifunctional architectures of contemporary orbital platforms. Early satellites, constrained by technological limitations and modest launch capacities, were diminutive in scale and functionally austere – primarily confined to elementary scientific experimentation and rudimentary communication

roles, largely dictated by their operation within low earth orbital regimes. Notably, several pioneering efforts explored the feasibility of passive satellite systems – spaceborne objects devoid of active onboard electronics or propulsion mechanisms. Among the most consequential of these preliminary ventures were Project Diana, which achieved the first successful reflection of radio waves off the lunar surface; Project Echo, a groundbreaking initiative that employed large metallized balloon satellites to facilitate passive signal relay; and Project West Ford, which involved the dispersion of copper dipole needles into orbit to investigate ionospheric-independent radio communication via artificial reflection mediums [15].

1.8.2 Aircraft Systems

This study evaluated the implications of utilizing fuels with relaxed property specifications – specifically in freezing point and thermal stability – in commercial transport aircraft. The analysis explored the effects on system performance, cost, weight, safety, and maintainability. Among three advanced fuel system concepts examined, the most cost-effective, long-term solution involved incorporating insulation and electrically heated elements on the lower surfaces of fuel tanks to accommodate the altered fuel characteristics.

1.9 Defense and Autonomous Weapon Systems

1.9.1 Missile Defense Systems

Recent engineering insights derived from the Missile Defense Agency's ballistic missile defense system (BMDS) underscore the imperative of conducting comprehensive analyses at the system of systems (SoS) level. This includes examining the complex web of interactions among independently developed constituent systems. Within this context, the term "interstitials" refers to the critical domains of interfaces, interoperability, and integration that bind the individual components within the SoS architecture.

BMDS serves as a particularly intricate case study, as many of its foundational elements were retrofitted from legacy programs of record, not originally conceived for holistic integration. While these subsystems generally perform according to their isolated design specifications, their operational metrics often fall short of aligning with overarching SoS-level performance requirements. A central challenge for BMDS lies in achieving interoperability ensuring that discrete components interact cohesively, whether through overt command coordination or subtle data fusion, to realize a consistent, scalable, and resilient national defense capability [16].

1.9.2 Unmanned Aerial Vehicles (UAVs)

In recent years, advancements in miniaturization and weight reduction – combined with enhanced sensor functionalities – have significantly contributed to the growing utility of UAVs. These systems are increasingly employed across a broad spectrum of civil and industrial applications, including atmospheric monitoring, surveillance, aerial photography, and search-and-rescue operations [17]. As the UAV market expands and the diversity of operational scenarios intensifies, there is a corresponding escalation in performance requirements. These include extended flight endurance, improved maneuverability, and greater adaptability to complex and dynamic mission profiles [18].

1.10 Transportation and Smart Mobility

1.10.1 Rail Networks and High-Speed Trains

In recent years, railway networks have garnered increasing attention as a dominant mode for passenger and freight transportation. Notably, high-speed railway networks (HSRNs) have undergone rapid expansion globally, gaining strategic and military importance. Researchers have contributed valuable insights into HSRN planning, operation, and safety. Studies have addressed network design for freight logistics, organizational practices in Japan, fatigue tolerance in railway axles, and high-speed rail development across Japan, South Korea, and Chinese Taiwan.

1.10.2 Autonomous Vehicles and Urban Traffic Systems

Traffic congestion has become an inescapable aspect of urban life, particularly in metropolitan regions, leading to substantial economic losses, travel delays, reduced service quality, and commuter discomfort. Congestion typically arises when transportation demand surpasses system capacity. A sustainable solution lies in equilibrating demand and supply; however, as noted by Morris [20], aligning increased demand with expanded capacity presents significant challenges. Expanding infrastructure through road construction is not only prohibitively expensive but also poses considerable environmental repercussions [19].

1.11 Power and Energy Systems

1.11.1 Smart Grids

This section centers on power electronics, smart grid technologies, and renewable energy systems, which are pivotal in addressing today's pressing energy and environmental concerns. The first electronic revolution began with the invention of the transistor in 1948 by Shockley, Bardeen, and Brattain at Bell Labs. This was followed by the development of the thyristor in 1956, later commercialized by GE in 1958, marking the onset of the modern power electronics era, often termed the second electronic revolution. Subsequent technological progress including integrated circuits, microcomputers, digital signal processors, and field-programmable gate arrays has further revolutionized the field, enabling sophisticated and efficient energy systems.

1.11.2 Nuclear Power Plants

In 2009, global electricity generation reached 20,093.6 TWh, with approximately 14% produced by 438 nuclear power plants (Figure 1.2) and 68% from fossil fuels, jointly accounting for 82% of total output. Both sources face sustainability criticisms of coal for its substantial greenhouse gas emissions and low efficiency, and nuclear for safety risks and waste management challenges. While coal is clearly unsustainable, nuclear energy's sustainability depends on plant design and fuel cycle strategies. This chapter

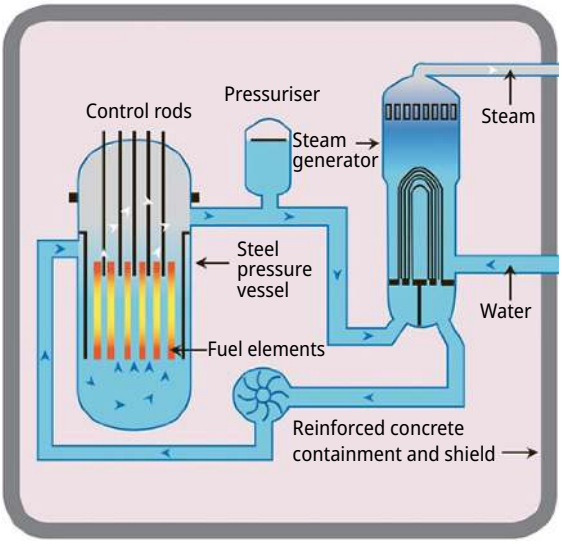

Figure 1.2: Nuclear power plants.

introduces nuclear power principles, explores fuel cycle processes, reviews current and emerging technologies, addresses nuclear waste management, evaluates economic viability, and concludes with a comprehensive sustainability assessment.

1.12 Healthcare and Biomedical Engineering

1.12.1 Robotic Surgery Systems

Robot-assisted surgery is a sophisticated minimally invasive technique wherein surgeons utilize robotic systems to perform complex procedures with heightened precision and control. These systems integrate robotic arms bearing surgical tools, a surgeon-operated console, and a high-definition 3D imaging interface. Unlike conventional open or laparoscopic surgery, robotic surgery fuses human skill with technological augmentation, significantly improving surgical accuracy, visualization, and patient outcomes [20].

1.13 Conclusion

In summary, the study of CESs offers critical insights into the behavior and design of multifaceted systems characterized by nonlinearity, interdependence, and emergent phenomena. Understanding the definition and inherent characteristics of such systems is essential for managing uncertainty, dynamic behavior, and cross-domain interactions. The importance of modeling and simulation cannot be overstated, as these tools provide a virtual environment to analyze, predict, and refine system behavior under diverse operational scenarios – thereby reducing risk and improving design reliability. Additionally, the role of optimization is pivotal in identifying the most efficient and feasible solutions within constrained, multidimensional problem spaces. Intelligent optimization algorithms further enhance the capacity to handle complex, large-scale challenges with computational efficiency. Through a wide array of real-world applications – including smart grids, autonomous systems, transportation networks, and space technologies – the principles and methodologies of complex systems engineering are transforming modern industries. Embracing this interdisciplinary approach equips engineers and researchers to design more robust, adaptive, and sustainable solutions for the increasingly interconnected world.

References

[1] Defoe, J. C. (1993). An identification of pragmatic principles-final report. National Council On Systems Engineering. SE Practice Working Group. Subgroup on Pragmatic Principles.

[2] Rechtin, E. (1992). The art of systems architecting. IEEE Spectrum, 29(10), 66–69.

[3] De Gennes, P. G. (1976). Dynamics of entangled polymer solutions. I. The Rouse model. Macromolecules, 9(4), 587–593.

[4] Sheard, S. A., & Mostashari, A. (2009). Principles of complex systems for systems engineering. Systems Engineering, 12(4), 295–311.

[5] Sheard, S. A., & Mostashari, A. (2009). Principles of complex systems for systems engineering. Systems Engineering, 12(4), 295–311.

[6] Lorenz, E. N. (2017). Deterministic Nonperiodic Flow 1. In Universality in Chaos 2nd edition, pp. 367–378. Routledge.

[7] Sioshansi, R., & Conejo, A. J. (2017). Optimization in engineering. Cham: Springer International Publishing, 120.

[8] Simpson, T. W., & Martins, J. R. (2011). Multidisciplinary design optimization for complex engineered systems: report from a national science foundation workshop. J. Mech. Des. Oct 2011, 133(10): 101002 (10 pages).

[9] Schwartz, L. A., & Busby, J. (2014). The 787 Dreamliner: will it be a dream or nightmare for Boeing Co. Journal of Case Research in Business and Economics, 5(1).

[10] Simpson, T. W., & Martins, J. R. R. A. (2010). The future of multidisciplinary design optimization (MDO): advancing the design of complex engineered systems. National Science Foundation, Arlington, VA, Tech. Rep, 1–20.

[11] Liang, Q., Yu, Y., Wang, P., Chen, D., & Duan, J. (2024 September). An AI Combined with Mathematical Analysis Energy Management System for Active Distribution Network. In 2024 China International Conference on Electricity Distribution (CICED), pp. 1076–1080. IEEE.

[12] Yu, Y. (2023 June). Data-driven Innovation or Innovation-driven Data Generation?. In 2023 IEEE International Conference on Engineering, Technology and Innovation (ICE/ITMC), pp. 1–8. IEEE.

[13] Von Bertalanffy, L., & Sutherland, J. W. (1974). General systems theory: Foundations, developments, applications. IEEE Transactions on Systems, Man and Cybernetics, 6, 592–592.

[14] Pattan, B. (1993). Satellite Systems: Principles and Technologies. Springer Science & Business Media.

[15] Garrett, R. K. Jr, Anderson, S., Baron, N. T., & Moreland, J. D. Jr (2011). Managing the interstitials, a system of systems framework suited for the ballistic missile defense system. . Systems Engineering, 14(1), 87–109.

[16] Chamberlain, P. (2017). Drones and Journalism. Routledge.

[17] Tran, V. P., Santoso, F., Garratt, M. A., & Anavatti, S. G. (2020). Distributed artificial neural networks-based adaptive strictly negative imaginary formation controllers for unmanned aerial vehicles in time-varying environments. IEEE Transactions on Industrial Informatics, 17(6), 3910–3919.

[18] Assaad, R., Dagli, C., & El-Adaway, I. H. (2020). A system-of-systems model to simulate the complex emergent behavior of vehicle traffic on an urban transportation infrastructure network. Procedia Computer Science, 168, 139–146.

[19] Triantis, K., Sarangi, S., Teodorović, D., & Razzolini, L. (2011). Traffic congestion mitigation: combining engineering and economic perspectives. Transportation Planning and Technology, 34(7), 637–645.

[20] Morris, B. (2005). Robotic surgery: applications, limitations, and impact on surgical education. Medscape General Medicine, 7(3), 72.

Atul Kumar Shukla* and Mukesh Kumar Awasthi

Chapter 2
Mathematical Foundations for Modeling Complex Systems

Abstract: Mathematical modeling serves as a vital framework for understanding complex real-world phenomena across engineering, physics, and the life sciences. This study employs a comprehensive toolkit – including differential equations, linear and nonlinear system dynamics, probability and statistics, and computational tools – to develop and analyze dynamic system models. Differential equations form the foundation for representing continuous-time processes, while both linear and nonlinear system dynamics are utilized to capture varying levels of system complexity. Stochastic elements are integrated through probabilistic modeling, enabling the analysis of systems influenced by uncertainty and random behavior. Additionally, computational tools facilitate numerical simulation and visualization, allowing for the validation and refinement of theoretical models. The integration of these methodologies provides a robust platform for interpreting system behavior, predicting future states, and informing practical decision-making in complex environments.

Keywords: modeling, complex systems, differential equations, applications

2.1 Differential Equations and Their Applications

Differential equations are classified as ordinary differential equations (ODEs) or partial differential equations (PDEs) depending on the type of derivatives they contain. If the equation involves only ordinary derivatives with respect to a single independent variable, it is an ODE. If it includes partial derivatives with respect to multiple independent variables, it is a PDE. The order of a differential equation is determined by the highest derivative present in the equation. A solution (or particular solution) to a differential equation of order n is a function that is defined and differentiable up to n times on a domain D. When this function and its derivatives are substituted into the original differential equation, the resulting expression must hold true for every point within the domain D [1].

*__Corresponding author: Atul Kumar Shukla__, Department of Mathematics, Ganga Singh College, Chapra 841301, Bihar, India, e-mail: atulkushukla1993@gmail.com
__Mukesh Kumar Awasthi,__ Department of Mathematics, Babasaheb Bhimrao Ambedkar University, Lucknow, India

https://doi.org/10.1515/9783111723464-002

2.1.1 General Form of an ODE

$$F(x, y, y', \ldots, y^n) = 0 \tag{2.1}$$

2.1.2 Order and Degree

- The order of a differential equation is the order of the highest derivative.
- The degree is the power of the highest-order derivative, assuming the equation is polynomial in derivatives.

2.1.3 First-Order Differential Equations

These are equations involving the first derivative of the unknown function.

2.1.3.1 Separable Equations

A first-order ODE can generally be written in the form $F(x, y, y') = 0$. In principle, algebraic methods can often be used to solve for y' rewriting the equation in the form $y' = G(x, y)$.

If the function $G(x, y)$ can be expressed as the product of a function of x and a function of y, that is, $G(x, y) = M(x)N(y)$, then the differential equation is called separable.

2.1.3.2 Linear Equations

A first-order linear differential equation is an equation that can be written in the following standard form [2, 5]:

$$\frac{dy}{dx} + yP(x) = Q(y) \tag{2.2}$$

Here, $P(x)$ and $Q(y)$ are known functions of x.

2.1.3.3 Exact Equations

An exact differential equation is a first-order differential equation that can be written in the following form:

$$M(x, y)dx + N(x, y)dy = 0 \tag{2.3}$$

It is called **exact** if there exists a function $F(x, y)$ such that:

$$\frac{\partial F}{\partial x} = M(x,y), \quad \frac{\partial F}{\partial y} = N(x,y) \tag{2.4}$$

In other words, the left-hand side of the differential equation is the total differential of some function $F(x,y)$, i.e.,

$$dF = M(x,y)dx + N(x,y)dy \tag{2.5}$$

2.1.4 Second- and Higher-Order Differential Equations

Typically appear in physical systems involving acceleration or curvature.

2.1.4.1 Second-Order Linear ODE

A second-order linear ordinary differential equation is represented as follows:

$$a_o(x)y'' + a_1(x)y' + a_2(x)y = f(x) \tag{2.6}$$

Equation (2.6) is homogeneous if $f(x) = 0$ and called nonhomogeneous if $f(x) \neq 0$.

2.2 Methods of Solution

There are several methods to solve differential equations:

i. Separation of variables
ii. Integrating factors
iii. Method of undetermined coefficients
iv. Variation of parameters
v. Laplace transforms

2.3 Applications of Differential Equations

2.3.1 Physics and Engineering

Newton's Laws of Motion: Second-order ODEs describe the motion of objects.

$$F = ma \Rightarrow F(x) = m\frac{d^2x}{dt^2} \tag{2.7}$$

Electrical Circuits: The behavior of RLC circuits is modeled by second-order linear differential equations.

$$L\frac{d^2q}{dt^2} + R\frac{dq}{dt} + \frac{1}{C_q} = E(t) \tag{2.8}$$

2.3.1.1 Heat Equation (PDE)

The heat equation is a fundamental PDE that describes the distribution of heat (or variation in temperature) in a given region over time. Mathematically, it models how thermal energy diffuses through a medium and is typically written as follows:

$$\frac{\partial u}{\partial t} = \alpha \nabla^2 u \tag{2.9}$$

where $u(x, t)$ represents the temperature at position x and time t, and α is the thermal diffusivity constant. The heat equation is widely used in physics, engineering, and materials science for analyzing heat conduction in solids and plays a key role in understanding diffusion processes more broadly [3, 4].

2.3.2 Population Dynamics

The logistic equation models population growth with carrying capacity:

$$\frac{dP}{dt} = rP\left(1 - \frac{P}{K}\right) \tag{2.10}$$

where P is population, r is the growth rate, and K is the carrying capacity [6].

2.3.3 Economics

Differential equations are used in modeling:

$$\textbf{Growth of investments: } \frac{dA}{dt} = rA$$

$A(t)$ is the value of investment at time t and r is the continuous growth rate.

2.3.3.1 Consumer Behavior

A basic model can describe how consumption $C(t)$ changes over time in response to income $Y(t)$ or price $P(t)$:

$$P(t)\frac{dC}{dt} = \alpha(Y(t) - C(t)) \tag{2.11}$$

Furthermore, differential equations are employed to model the dynamic relationship between supply and demand over time.

2.4 Partial Differential Equations (PDEs)

PDEs are mathematical equations that involve multiple independent variables and partial derivatives of an unknown function. Unlike ODEs, which contain derivatives with respect to a single variable, PDEs are used to describe phenomena that vary with respect to space and time simultaneously. They are fundamental in modeling a wide range of physical and engineering systems, including heat conduction, wave propagation, fluid flow, and electrostatics [7, 8].

The general form of a second-order PDE in two variables x and t is as follows:

$$a(x,t)\frac{\partial^2 u}{\partial x^2} + b(x,t)\frac{\partial^2 u}{\partial x \partial t} + c(x,t)\frac{\partial^2 u}{\partial t^2} + d(x,t)\frac{\partial u}{\partial x} + e(x,t)\frac{\partial u}{\partial t} + f(x,t)u = g(x,t) \tag{2.12}$$

Three classical types of PDEs that frequently arise in applications are as follows:

Heat Equation: Models the distribution of heat over time (Figure 2.1):

$$\frac{\partial q}{\partial t} = \kappa \frac{\partial^2 q}{\partial x^2} \tag{2.13}$$

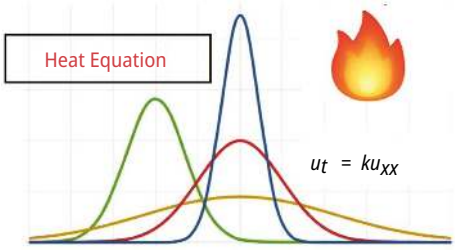

Figure 2.1: Graphical representation of heat equation.

Wave Equation: It describes the propagation of waves such as sound or vibrations:

$$\frac{\partial^2 q}{\partial t^2} = C^2 \frac{\partial^2 q}{\partial x^2} \tag{2.14}$$

Laplace Equation: It represents steady-state solutions in fields such as electrostatics or fluid flow:

$$\nabla^2 q = 0 \tag{2.15}$$

Solving PDEs often requires both analytical techniques (e.g., separation of variables and Fourier transforms) and numerical methods (e.g., finite difference and finite element methods), especially for complex boundary and initial conditions. PDEs form a crucial part of mathematical modeling in science and engineering, enabling precise analysis of dynamic systems in multiple dimensions.

2.5 Applications

Differential equations play a fundamental role in modeling various physical phenomena across scientific and engineering disciplines. In thermal conduction, they are used to describe the distribution of temperature in a given region over time, typically through the heat equation, which is a PDE. In wave propagation, such as sound or light waves, the wave equation models how waves move through different media. In fluid dynamics, differential equations govern the behavior of fluid flow, with the Navier-Stokes equations serving as a cornerstone for understanding velocity, pressure, and turbulence in fluids. Additionally, in the study of electromagnetic fields, Maxwell's equations, a set of coupled PDEs, describe how electric and magnetic fields evolve and interact. These mathematical models are essential for designing and analyzing systems in physics, engineering, and applied mathematics.

2.6 Numerical Methods for Differential Equations

In many cases, exact solutions of differential equations are not possible. Numerical methods provide approximate solutions.

2.6.1 Euler's Method in Differential Equations

Euler's method is a simple and widely used numerical technique for approximating solutions to ODEs when an exact analytical solution is difficult or impossible to obtain. It is particularly useful for first-order initial value problems of the form:

$$\frac{dy}{dx} = f(x,y),\ y(x_o) = y_o \tag{2.16}$$

Euler's method estimates the value of the solution at discrete points by using the tangent (slope) at known points to project the next value. The formula for the method is as follows:

$$y_{n+1} = y_n + h.f(x_n, y_n) \tag{2.17}$$

where h is the step size (interval between points), (x_n, y_n) is the current point, and y_{n+1} is the approximated next value $f(x_n, y_n)$ derivative (slope) at the current point.

2.6.2 Runge-Kutta Methods

Runge-Kutta methods (Figure 2.2) are a family of iterative techniques used to solve ODEs numerically. These methods provide a powerful alternative to simpler approaches such as Euler's method by offering greater accuracy without requiring higher-order derivatives. Named after Carl Runge and Wilhelm Kutta, these techniques are widely used in science and engineering for solving initial value problems. The general idea behind Runge-Kutta methods is to estimate the solution at the next time step by taking a weighted average of several slopes (derivative evaluations) calculated at different points within the current interval. This leads to better stability and accuracy, even with relatively large step sizes [9–13].

The most commonly used version is the fourth-order Runge-Kutta method (RK4), which strikes a balance between computational effort and accuracy. For a first-order ODE $\frac{dy}{dt} = f(t, y)$ with initial condition $y(t_o) = y_o$, the RK4 method computes the next value y_{n+1} as follows:

$$\begin{aligned}
y_1 &= f(t_n, y_n) \\
y_2 &= f\left(t_n + \frac{h}{2}, y_n + \frac{h}{2}k_1\right) \\
y_3 &= f\left(t_n + \frac{h}{2}, y_n + \frac{h}{2}k_2\right) \\
y_4 &= f(t_n + h, y_n + hk_3) \\
y_{n+1} &= y_n + \frac{1}{6}(k_1 + 2k_2 + 2k_3 + k_4)
\end{aligned} \tag{2.18}$$

where h is the step size, and k_1, k_2, k_3, and k_4 are intermediate slope estimates.

Runge-Kutta methods can be extended to higher-order or adaptive forms, such as the Runge-Kutta-Fehlberg or Dormand-Prince methods, which automatically adjust the step size to balance accuracy and computational efficiency. These methods are essential tools in numerical analysis, forming the backbone of many simulation and modeling applications where analytical solutions are not feasible.

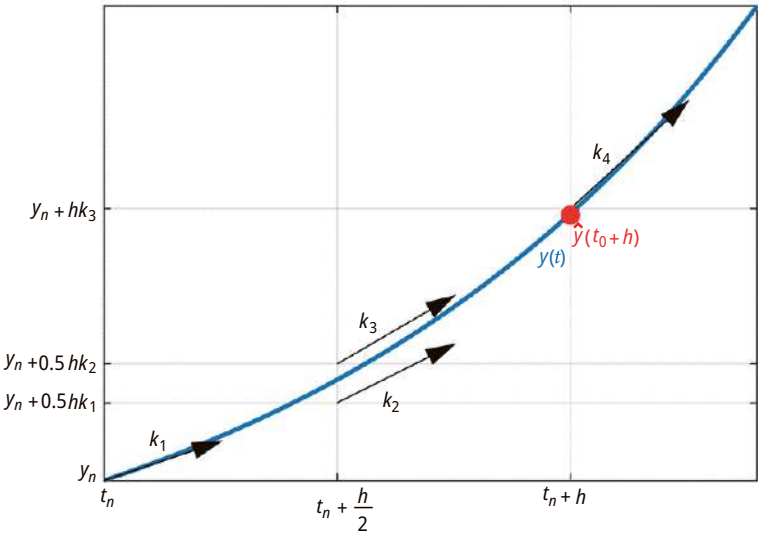

Figure 2.2: Geometrical representation of Runge-Kutta method.

2.6.3 Finite Difference Method (FDM)

The FDM is a numerical technique used to approximate solutions to differential equations, particularly PDEs and ODEs. It works by replacing derivatives with finite difference approximations, allowing the problem to be solved using algebraic equations on a discrete grid of points.

For example, the first derivative of a function $u(x)$ at a point x_i can be approximated by the following equation:

$$\frac{du}{dx} \approx \frac{u(x_i + 1) - u(x_i)}{h} \tag{2.19}$$

where h is the spacing between grid points. Similarly, second derivatives and higher-order terms can be approximated using central, forward, or backward difference schemes.

FDM is widely applied in engineering and science for solving problems involving heat conduction, fluid flow, structural mechanics, and electromagnetic fields. Its simplicity and ease of implementation make it a popular choice, although it may require fine grid resolution and stability analysis for accurate results [14, 15].

2.7 Modern Applications and Interdisciplinary Use

Differential equations have wide-ranging applications across various scientific and engineering fields. In biology, they are essential for modeling phenomena such as the spread of infectious diseases using SIR models, as well as tracking drug concentration in the body over time. In machine learning, differential calculus underpins gradient-based optimization methods, which are fundamental to training algorithms, particularly in deep learning. Climate science relies heavily on complex PDEs to simulate atmospheric dynamics, ocean currents, and long-term climate patterns. Similarly, in control systems, differential equations are central to describing system dynamics and designing feedback mechanisms that ensure stability and performance in engineering applications.

2.8 Linear and Nonlinear System Dynamics

System dynamics is a mathematical modeling approach used to describe the behavior of complex systems over time. It is employed extensively across engineering, physics, economics, biology, and other fields. The classification of systems into linear and nonlinear plays a crucial role in determining the tools and techniques used for analysis, simulation, and control.

2.8.1 Linear System Dynamics

Linear systems are those in which the principle of superposition applies. This means that the output of the system is directly proportional to its input, and the response to a sum of inputs is the sum of the responses to each input individually. Linear system dynamics are governed by linear differential equations, typically of the following form:

$$\begin{aligned} \frac{dx(t)}{dt} &= Ax(t) + Bu(t) \\ \frac{dy(t)}{dt} &= Cx(t) + Du(t) \end{aligned} \tag{2.20}$$

where $x(t)$ represents the state vector, $u(t)$ the input vector, $y(t)$ the output vector, and A, B, C, D are constant matrices that define the system behavior.

The analysis of linear systems is relatively straightforward due to the availability of powerful mathematical tools such as Laplace transforms, Fourier analysis, and matrix algebra. Solutions to linear systems can be explicitly derived, and the stability, controllability, and observability can be systematically assessed using established criteria. Linear models are commonly used in control theory, signal processing, and electrical circuit analysis [17].

2.8.2 Nonlinear System Dynamics

Nonlinear systems, in contrast, do not obey the principle of superposition. Their behavior is governed by nonlinear differential equations, which often take the following general form:

$$\frac{dx(t)}{dt} = f(x(t) + u(t)) \tag{2.21}$$

Here, the function f represents a nonlinear mapping of the state and input variables. Nonlinear systems can exhibit a wide range of complex behaviors, including bifurcations, chaos, limit cycles, and multiple equilibrium points. These features make their analysis significantly more challenging compared to linear systems. Due to their complexity, nonlinear systems are typically analyzed using numerical methods and simulations. Common tools include phase plane analysis, Lyapunov stability theory, perturbation methods, and bifurcation diagrams. Nonlinear models are essential in accurately describing real-world systems such as fluid dynamics, biological processes, climate models, and economic systems [16].

2.8.3 Comparison and Applications

The choice between linear and nonlinear modeling depends on the system's characteristics and the desired accuracy. Linear models are often used for small-signal analysis, where system behavior near an equilibrium point is of interest. They are also preferred in control design due to their mathematical tractability and well-established methods. However, many real-world systems inherently exhibit nonlinear behavior. In such cases, linear approximations may lead to significant errors or fail to capture critical dynamics. Nonlinear modeling becomes indispensable when dealing with large perturbations, time-varying parameters, or systems with inherent nonlinearity. For example, in mechanical systems, small vibrations around equilibrium can be modeled linearly, but large deformations require nonlinear analysis. In electrical engineering, circuits with diodes and transistors are fundamentally nonlinear. In biological systems, feedback mechanisms and enzyme kinetics often result in nonlinear dynamic behavior.

2.8.4 Probability and Statistics in System Modeling

System modeling is a fundamental approach in engineering, science, economics, and many interdisciplinary domains to understand, analyze, and predict the behavior of complex systems. A model can be physical, mathematical, or computational, and aims to replicate the real-world characteristics of a system to forecast its responses under different conditions. Probability and statistics play a crucial role in system modeling

by providing the tools to handle uncertainty, analyze variability, and make informed decisions based on incomplete or noisy data. This essay explores the significance of probability and statistics in the modeling process, highlighting theoretical foundations, applications, and methodologies for integrating probabilistic and statistical techniques into modeling workflows [18].

2.9 Role of Probability in System Modeling

2.9.1 Uncertainty Quantification

Real-world systems are inherently uncertain due to factors such as random disturbances, imperfect knowledge, and incomplete information. Probability theory provides the tools necessary to quantify this uncertainty by defining random variables, probability distributions, and stochastic processes. In the context of system modeling, these probabilistic concepts are essential for representing inputs that are not deterministic, such as fluctuating weather conditions or varying demand. They also play a crucial role in capturing system noise and measurement errors, as well as in characterizing the variability observed in simulation outputs.

2.9.2 Random Variables and Distributions

Random variables are fundamental in probabilistic modeling. Continuous and discrete random variables (e.g., normal, exponential, binomial, and Poisson distributions) are used to describe phenomena such as time between system failures, arrival times in queuing models, and sensor measurement errors. For example, in reliability engineering, the exponential distribution often models the time between failures of electronic components due to its memoryless property. Similarly, in queuing theory, Poisson processes and exponential interarrival times are standard tools [19].

2.9.3 Stochastic Processes

Many dynamic systems evolve randomly over time. Stochastic processes such as Markov chains, Brownian motion, and Poisson processes model temporal randomness. For instance:

- Markov models are used in communication systems to represent channel states.
- Queue models in service systems rely on birth-death processes.
- Stock prices in financial modeling are often modeled using geometric Brownian motion.

2.10 Role of Statistics in System Modeling

2.10.1 Data Collection and Analysis

Statistical methods are vital for collecting, analyzing, and interpreting data. In system modeling, data-driven insights guide model structure, parameter estimation, and validation. Common statistical tools include the following:

- Descriptive statistics (mean, variance, and skewness)
- Inferential statistics (confidence intervals and hypothesis testing)
- Regression analysis and correlation

Through these tools, one can determine whether system behavior has changed over time or whether certain factors significantly affect output variability.

2.10.2 Parameter Estimation

Model parameters often cannot be known a priori and must be estimated from observed data. Statistical estimation techniques such as maximum likelihood estimation and Bayesian inference are used to derive the most probable values for model parameters. For example, in epidemiological modeling, parameters such as transmission rates or recovery rates in SIR models are estimated from infection data using regression or likelihood-based techniques.

2.10.3 Model Validation and Hypothesis Testing

Once a model is built, it must be validated to ensure it accurately represents the system. Statistical tests help assess the goodness-of-fit, compare models, and test assumptions. Techniques such as the chi-squared test, Kolmogorov-Smirnov test, and analysis of variance are commonly employed. Model validation also involves residual analysis, which checks whether the residuals (differences between observed and predicted values) behave randomly and follow expected statistical properties.

2.11 Integrated Approaches: Probabilistic and Statistical Modeling

Modern system modeling increasingly relies on the integration of probability and statistics, especially in fields such as machine learning, control systems, and risk analysis.

2.11.1 Monte Carlo Simulation

Monte Carlo methods use repeated random sampling to approximate complex system behavior. These simulations rely on probabilistic models to estimate system performance, reliability, or uncertainty. Examples include the following:

- Estimating the probability of failure in structural engineering
- Pricing complex financial derivatives in computational finance
- Predicting traffic flow patterns under varying conditions

Monte Carlo simulation is particularly valuable when analytical solutions are intractable or unavailable.

2.11.2 Bayesian Modeling

Bayesian statistics incorporate prior knowledge and observed data to update beliefs about system parameters. Bayesian networks are graphical models representing probabilistic dependencies among variables. They are widely used in the following:

- Fault diagnosis in engineering systems
- Decision support systems in healthcare
- Machine learning for pattern recognition and prediction

Bayesian approaches are advantageous in dynamic systems where data accumulate over time, allowing continuous model refinement.

2.11.3 Statistical Learning and System Identification

In system identification, models are constructed based on input-output data. Techniques such as linear regression, neural networks, support vector machines, and Gaussian processes are employed to learn system behavior statistically. For instance, in robotics, system identification helps determine the dynamics of manipulators. In environmental science, statistical models predict air quality based on meteorological data and pollutant sources.

2.12 Applications Across Domains

2.12.1 Engineering Systems

Probability and statistics are foundational in control systems, signal processing, and telecommunications. Models incorporate noise, uncertainty, and real-time data updates. Techniques such as Kalman filtering and stochastic control optimize performance under uncertainty.

2.12.2 Healthcare and Epidemiology

Statistical models simulate disease spread, evaluate treatment effectiveness, and optimize resource allocation. Probabilistic compartment models (e.g., SEIR) help guide public health policies.

2.12.3 Economics and Finance

Stochastic differential equations and time series models analyze market trends, forecast inflation, and assess investment risks. Probabilistic models underpin modern portfolio theory and derivative pricing.

2.12.4 Environmental Modeling

Climate models, water resource systems, and pollution dispersion are modeled using probabilistic techniques to account for natural variability and long-term uncertainty.

2.13 Challenges and Future Directions

Despite significant advancements, integrating probability and statistics with system modeling continues to face several challenges. One major issue is data quality and availability; inadequate or noisy data can significantly hinder the accuracy of statistical models. Additionally, the computational complexity of probabilistic methods – particularly Bayesian inference and stochastic simulations – can limit their practical application, especially in large-scale systems. Model uncertainty also remains a critical concern, as selecting an appropriate model structure and accounting for potential errors is a complex and ongoing area of research. Moreover, effective system modeling demands interdisciplinary expertise that spans mathematics, statistics, domain-specific knowledge, and

computational proficiency. Looking ahead, emerging trends suggest a growing reliance on probabilistic machine learning, hybrid modeling approaches, and uncertainty-aware artificial intelligence to create more robust, interpretable, and adaptive models capable of handling real-world complexity.

2.14 Computational Tools for Mathematical Modeling

Mathematical modeling is a cornerstone of scientific inquiry and technological innovation, offering a structured framework to understand, predict, and optimize real-world phenomena. From physics and biology to economics and engineering, mathematical models translate complex systems into abstract representations using mathematical language. However, the increasing complexity of modern systems often makes analytical solutions impractical or impossible. This is where computational tools become essential, enabling researchers and practitioners to simulate, analyze, and visualize models efficiently.

Computational tools for mathematical modeling consist of software, programming languages, numerical methods, and simulation environments that facilitate the implementation and exploration of mathematical models. These tools bridge the gap between theoretical formulations and real-world applications by offering powerful platforms for computation, data handling, and visualization. This essay explores the various categories of computational tools, their applications, and their role in advancing modern mathematical modeling [20].

2.15 Categories of Computational Tools

2.15.1 Symbolic Computation Tools

Symbolic computation refers to the processing of mathematical expressions in their symbolic form rather than as numerical values. This approach allows for the exact manipulation of equations, making it particularly valuable for tasks such as solving algebraic equations, performing calculus operations, simplifying complex expressions, and deriving analytical solutions. Several tools are widely used in this domain. Mathematica is a powerful platform that supports both symbolic and numerical computations, excelling in algebraic manipulation, solving differential equations, and visualizing results. Maple is another robust tool, renowned for its strong symbolic engine and its applications in mathematical analysis, code generation, and academic instruction. For those seeking a free, open-source solution, Maxima provides

a comprehensive suite of tools for symbolic computation, including capabilities in calculus, linear algebra, and equation solving.

2.15.2 Numerical Computing Environments

Many mathematical models involve equations that are too complex to be solved analytically, necessitating the use of numerical methods for approximate solutions. Numerical computing environments provide a wide range of libraries and built-in functions to address these challenges, enabling users to perform computations efficiently. MATLAB is one of the most popular tools in this category, extensively used in engineering and applied mathematics for tasks such as matrix operations, numerical integration, optimization, and simulation. GNU Octave serves as a free alternative to MATLAB, offering compatibility with most of its syntax and functions, making it accessible to a broader audience. Scilab is another open-source software designed for numerical computation, particularly useful in areas such as control systems, signal processing, and numerical analysis. These platforms support the creation of custom algorithms and encourage experimentation with various numerical techniques, making them indispensable for both academic research and industrial problem-solving.

2.15.3 Programming Languages for Modeling

General-purpose programming languages with strong mathematical libraries are increasingly used in mathematical modeling, offering flexibility and control over computations.

Examples:

- **Python**: With libraries such as NumPy, SciPy, SymPy, Matplotlib, and pandas, Python has become a dominant language in scientific computing and modeling.
- **R**: Primarily used in statistics, R is excellent for data analysis, regression modeling, and graphical representation.
- **Julia**: Designed for high-performance numerical and scientific computing, Julia is gaining popularity due to its speed and ease of use in mathematical modeling.

2.15.4 Simulation Software

Simulation tools are specialized environments designed to model the behavior of dynamic systems over time. These tools often come with graphical interfaces and predefined modules for specific applications.

Examples:

- **Simulink (with MATLAB)**: A block diagram-based tool for simulating and modeling control systems, mechanical systems, and signal processing.
- **COMSOL Multiphysics**: Used for simulating physical processes such as heat transfer, fluid flow, and electromagnetism using PDEs.
- **AnyLogic**: A platform for agent-based, discrete-event, and system dynamics simulation, particularly useful in logistics and operations research.

2.16 Applications in Various Fields

2.16.1 Engineering

In engineering disciplines, computational modeling is essential for design optimization, structural analysis, and systems control. Tools such as MATLAB/Simulink, ANSYS, and COMSOL allow engineers to build and simulate models for stress analysis, fluid mechanics, thermodynamics, and electrical circuits. For instance, in mechanical engineering, finite element analysis tools are used to predict stress and strain in structures under various loads. In electrical engineering, control systems are modeled using transfer functions and simulated for stability and performance using tools such as Simulink.

2.16.2 Biology and Medicine

Mathematical models in biology are used to understand complex biological systems such as population dynamics, neural activity, and disease spread. Computational tools such as Python (with BioPython), MATLAB, and CellML facilitate the modeling of biochemical pathways, gene regulation networks, and epidemiological models. For example, compartmental models of infectious diseases Susceptible–Infectious–Recovered and Susceptible–Exposed–Infectious–Recovered (SIR and SEIR) are implemented using differential equations and simulated to predict outbreak dynamics, guide public health policies, and assess intervention strategies.

2.16.3 Environmental Science

Environmental modeling involves simulating atmospheric processes, hydrological systems, and climate change effects. Tools such as MATLAB, Python, and specialized software like Soil and Water Assessment Tool and Weather Research and Forecasting Model are commonly used. These models help in evaluating pollutant dispersion, water

resource management, and ecological sustainability. The integration of remote sensing data with computational models enhances prediction accuracy and decision-making.

2.16.4 Economics and Finance

Computational tools are used in economics to model consumer behavior, market dynamics, and financial risks. MATLAB, R, and Python (with libraries such as statsmodels and PyMC) enable econometric modeling, time series forecasting, and Monte Carlo simulations. For example, stochastic differential equations are used to model stock price movements, while agent-based models simulate economic systems involving multiple interacting agents. Optimization algorithms support decision-making in portfolio management and resource allocation.

2.17 Advantages of Computational Tools

Computational tools offer several advantages that enhance the scope and depth of mathematical modeling:

i. **Efficiency**: They drastically reduce the time required to perform complex calculations and simulations.
ii. **Scalability**: Large datasets and high-dimensional models can be handled with ease.
iii. **Visualization**: Graphical outputs and animations aid in interpreting model behavior and communicating results.
iv. **Interactivity**: Many tools support interactive modeling environments, allowing users to modify parameters and observe changes in real time.
v. **Integration**: Tools can often be integrated with databases, web applications, and hardware systems for seamless data flow and control.

2.18 Challenges and Limitations

Despite their powerful capabilities, computational tools also present several challenges. Learning to use advanced platforms such as MATLAB and COMSOL effectively requires a significant investment of time and effort, often involving a steep learning curve. High-fidelity simulations can demand considerable computational resources, including memory and processing power, which may not always be readily available. Additionally, numerical methods used in these tools are inherently approximate, making them prone to rounding errors, discretization issues, and algorithmic instability. Even with precise implementation, models can yield misleading results if they are based on incorrect or oversimplified assumptions. Furthermore, the cost of proprie-

tary software can be prohibitive, with high licensing fees limiting accessibility for students, educators, and smaller institutions.

2.19 Future Directions

With the continuous advancement of computational power and the increasing emphasis on interdisciplinary collaboration, computational tools for mathematical modeling are undergoing rapid evolution. Several emerging trends are shaping the future of this field. Cloud-based modeling is becoming more prominent, with platforms such as Google Colab and MATLAB Online offering remote computing capabilities that enhance collaboration and accessibility. Integration with artificial intelligence and machine learning is also transforming modeling practices, enabling the development of hybrid models that combine physical laws with data-driven insights – particularly impactful in areas such as materials science and bioinformatics. Additionally, open-source ecosystems built around tools such as Python, R, and Julia are flourishing, supported by active communities that contribute extensive libraries and frameworks to diverse modeling needs. The growth of high-performance computing is another significant trend, allowing for the simulation of extraordinarily complex systems, including global climate models and protein folding processes. Finally, interactive and visual modeling tools are becoming increasingly user-friendly, featuring enhanced interactivity and visualization capabilities that make modeling more accessible for teaching, effective communication, and engagement with nonexpert audiences.

2.20 Conclusion

Differential equations, probability and statistics, system dynamics, and computational tools together form the backbone of modern mathematical modeling. Differential equations offer profound insights into dynamic systems and are applied across nearly every scientific field, from physics and biology to economics and artificial intelligence. Probability and statistics complement this by enabling the modeling of uncertainty, randomness, and variability, which are inherent in real-world systems, thereby supporting predictive analytics and adaptive decision-making. Understanding the distinction between linear and nonlinear system dynamics is also essential, as it guides the choice of appropriate modeling strategies – balancing simplicity with the need for realistic representation. At the heart of all these methodologies lie powerful computational tools that allow for the implementation, simulation, and visualization of complex models. These tools, ranging from symbolic solvers to high-performance simulation platforms, have transformed how mathematical modeling is conducted, enabling more accurate insights and faster solutions. As challenges become more intricate and data-rich, the integration of

these mathematical foundations with advanced computational technologies will be indispensable for developing robust, intelligent, and effective models across disciplines.

References

[1] Braun, M. (1993). Differential Equations and Their Applications: An Introduction to Applied Mathematics 4th ed. Springer.
[2] Boyce, W. E., & DiPrima, R. C. (2017). Elementary Differential Equations and Boundary Value Problems 11th ed. Wiley.
[3] Zill, D. G. (2017). A First Course in Differential Equations with Modeling Applications 11th ed. Cengage Learning.
[4] Logan, J. D. (2015). Applied Differential Equations 3rd ed. Springer.
[5] Blanchard, P., Devaney, R. L., & Hall, G. R. (2012). Differential Equations 4th ed. Brooks Cole.
[6] Freedman, H. I. (1980). Deterministic Mathematical Models in Population Ecology. Marcel Dekker.
[7] Evans, L. C. (2010). Partial Differential Equations 2nd ed. American Mathematical Society (Graduate Studies in Mathematics, Vol. 19).
[8] Strauss, W. A. (2007). Partial Differential Equations: An Introduction 2nd ed. Wiley.
[9] Burden, R. L., & Faires, J. D. (2010). Numerical Analysis 9th ed. Brooks/Cole, Cengage Learning.
[10] Süli, E., & Mayers, D. F. (2003). An Introduction to Numerical Analysis. Cambridge University Press.
[11] Kincaid, D., & Cheney, W. (2009). Numerical Analysis: Mathematics of Scientific Computing 3rd ed. American Mathematical Society.
[12] Atkinson, K. E. (1989). An Introduction to Numerical Analysis 2nd ed. Wiley.
[13] Quarteroni, A., Sacco, R., & Saleri, F. (2007). Numerical Mathematics 2nd ed. Springer.
[14] LeVeque, R. J. (2007). Finite Difference Methods for Ordinary and Partial Differential Equations: Steady-State and Time-Dependent Problems. Society for Industrial and Applied Mathematics (SIAM).
[15] Smith, G. D. (1985). Numerical Solution of Partial Differential Equations: Finite Difference Methods 3rd ed. Oxford University Press.
[16] Ogata, K. (2010). Modern Control Engineering 5th ed. Prentice Hall.
[17] Chen, C.-T. (1999). Linear System Theory and Design 3rd ed. Oxford University.
[18] Papoulis, A., & Pillai, S. U. (2002). Probability, Random Variables, and Stochastic Processes 4th ed. McGraw-Hill.
[19] Ross, S. M. (2014). Introduction to Probability Models 11th ed. Academic Press.
[20] Ascher, U. M. & Petzold, L. R. (1998). Computer Methods for Ordinary Differential Equations and Differential-Algebraic Equations. SIAM.

Shikhar Prateek Pandey and Arpit Bhardwaj*

Chapter 3
Optimization Techniques for Engineering Systems

Abstract: The concepts of optimization techniques in engineering systems are examined in this chapter, with a focus on how they can improve system performance, lower costs, and increase efficiency in a variety of fields, including computer science, mechanical, civil, electrical, and medical engineering. At its core, optimization is about getting the best result possible given the constraints, which frequently entails minimizing effort or maximizing benefits. The efficiency of several methods, such as gradient-based approaches, genetic algorithms, dynamic programming, linear and nonlinear programming, and others, in resolving engineering problems is investigated. It is widely used in resource allocation, physical design, machine learning, and control systems, which is essential to decision-making. Despite difficulties with non-convexity and high dimensionality, optimization is still evolving with the help of advancements in artificial intelligence, big data analytics, and real-time decision-making. The historical development of optimization techniques is also covered in this chapter, with a focus on how they first emerged as resource allocation operations research methods during World War II. Optimization strategies are propelling the development of autonomous systems and sustainable solutions through the integration of contemporary smart technology. In order to enable the research community to investigate innovative applications and approaches in engineering optimization, this chapter attempts to offer insights into current trends and future directions.

Keywords: optimization techniques, engineering systems, mathematical programming, decision-making, linear and nonlinear programming, genetic algorithms, machine learning, control systems, AI in optimization

3.1 What Is Optimization in Engineering Systems?

Let's consider yourself in the task of creating an electric car, ensuring passenger safety, minimizing production costs, maximizing battery life, and minimizing impact on the environment. How would you create a balance between these conflicting goals? Which resources and strategies would you employ? This is where optimization helps in the engineering system, which turns difficult problems into achievable

*Corresponding author: **Arpit Bhardwaj**, USICT, Gautam Buddha University, Greater Noida, India
Shikhar Prateek Pandey, USICT, Gautam Buddha University, Greater Noida, India

https://doi.org/10.1515/9783111723464-003

answers by determining the *best feasible results* under certain conditions [1]. The foundation of contemporary engineering is optimization [2]. Whether improving robotic control systems, optimizing energy distribution, or expediting a manufacturing process. We can also say the process of determining the optimal solution to a problem within predetermined parameters is known as optimization [3]. In engineering, it is systematically modifying variables to give the best results.

Now, take an example of a delivery route optimization. Consider a logistics company, FedEx, that delivers thousands of packages per day. To find the most effective routes, optimization algorithms examine factors including delivery windows, traffic patterns, vehicle capacity, and road constraints. By doing this, FedEx ensures to deliver packages on time and also saves the annual cost (Figure 3.1):

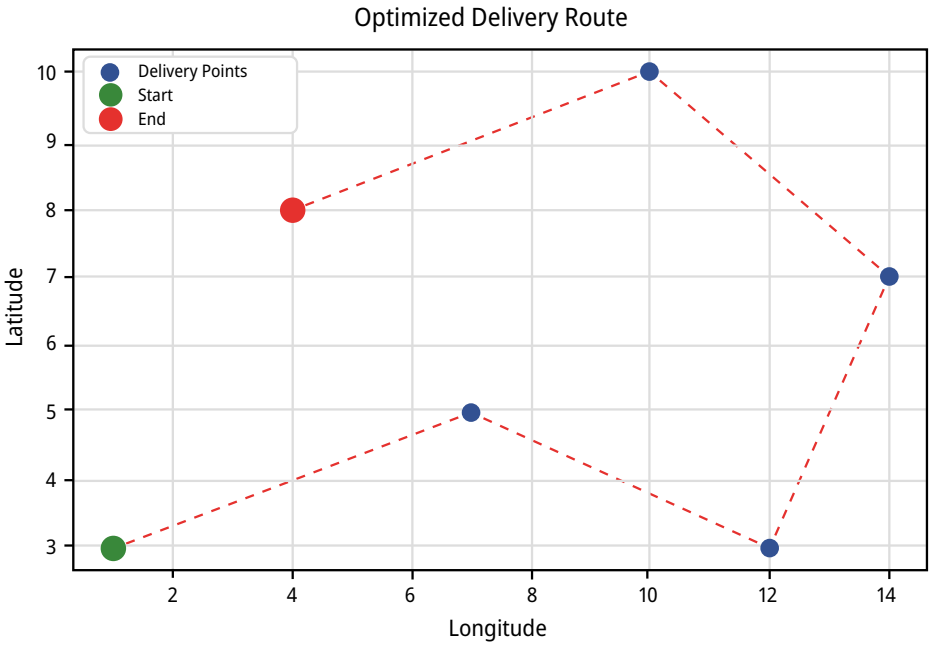

Figure 3.1: Optimized delivery route.

- Delivery locations are indicated with blue dots.
- The best route between sites is shown by dashed red lines.
- The delivery begins with the green dot.
- The final delivery destination is shown by the red dot.

3.1.1 Historical Development of Optimization

The origins of optimization can be traced back to the early work of mathematicians like Newton, Leibniz, and Lagrange. The development of numerical techniques, constrained optimization methods, and calculus all contributed to the field's evolution.

The below-mentioned table lists the important turning points in the evolution of optimization over time (Table 3.1).

Table 3.1: Historical development and significance.

Time period	Key developments	Contributors	Significance
Seventeenth–eighteenth centuries	Development of differential calculus	Newton and Leibniz	Laid foundation for optimization in minimization and maximization problems
Eighteenth century	Calculus of variations	Bernoulli, Euler, Lagrange, and Weierstrass	Addressed functional minimization problems
Nineteenth century	Method of Lagrange multipliers	Lagrange	Introduced constrained optimization
1830s	Steepest descent method	Cauchy	First numerical optimization technique for unconstrained problems
1947	Simplex method for linear programming	George Dantzig	Revolutionized large-scale problem solving
1951	Kuhn-Tucker conditions for nonlinear optimization	Kuhn and Tucker	Established necessary and sufficient optimality conditions
1957	Dynamic programming	Richard Bellman	Solved multistage decision problem
1960	Nonlinear programming advancements	Zoutendijk and Rosen	Improved nonlinear optimization techniques
1960	Geometric programming	Duffin, Zener, and Peterson	Expanded applications in engineering optimization
1960	Integer programming	Gomory	Introduced methods for discrete optimization
1961	Goal programming for multi-objective optimization	Charnes and Cooper	Addressed multiple conflicting objectives

Table 3.1 (continued)

Time period	Key developments	Contributors	Significance
1979	Ellipsoid method for linear programming	Khachian	Demonstrated polynomial-time complexity (limited practical use)
1984	Projective scaling algorithm	Narendra Karmarkar	Improved efficiency of linear programming over simplex method
Twentieth century	Growth of operations research	Various contributors	Advanced mathematical programming and decision-making methodologies

3.2 Statement of an Optimization Problem

An optimization problem is a mathematical formulation where the objective is to find the best possible solution from a set of feasible alternatives under given constraints. The goal is to **maximize or minimize** an objective function while satisfying certain conditions [4]. The general form of an optimization problem can be expressed as [5]:

$$\min/\max f(x)$$

subject to

$$gi(x) \leq 0,\ i = 1,2,\ldots,m$$
$$hj(x) = 0,\ j = 1,2,\ldots,p$$

where $f(x)$ is the **objective function** to be optimized; x represents the **design vector** (decision variables); and $gi(x)$ and $hj(x)$ are **design constraints**, defining feasible solutions.

Here, the **statement of an optimization problem** describes a **constrained optimization problem** because it includes constraints:

– $gi(x) \leq 0$ (inequality constraints)
– $hj(x) = 0$ (equality constraints)

This matches the definition of a constrained optimization problem. If the constraints were absent, it would be classified as an unconstrained optimization problem.

3.3 Key Components of an Optimization Problem

The key components of an optimization problem are shown in Figure 3.2. These components can be defined as follows:

3.3.1 Design Vector

The design vector, $x = (x_1, x_2, \ldots, x_n)$ consists of **decision variables** that define the system. These variables are chosen to achieve optimal performance. The dimensionality of the vector depends on the problem's complexity [6].

3.3.2 Design Constraints

Constraints limit the range of possible solutions. They are classified as:

- **Equality Constraints** ($hj(x) = 0$): These impose strict conditions on the design variables.
- **Inequality Constraints** ($gi(x) \leq 0$): These define permissible boundaries within which solutions must lie.

3.3.3 Constraint Surface

The constraint surface represents the feasible region where all constraints hold. Any point outside this region is infeasible [7], and optimization algorithms must search within or along its boundary.

3.3.4 Objective Function

The objective function, $f(x)$, quantifies system performance. It can be **minimized** (e.g., cost and energy consumption) or **maximized** (e.g., profit and efficiency) [8]. The choice of function depends on the problem's requirements.

3.3.5 Objective Function Surfaces

The objective function defines a surface in the design space. The shape of this surface influences the complexity of the optimization problem. Convex surfaces are easier to solve, whereas non-convex, multi-modal surfaces may require advanced optimization techniques [9].

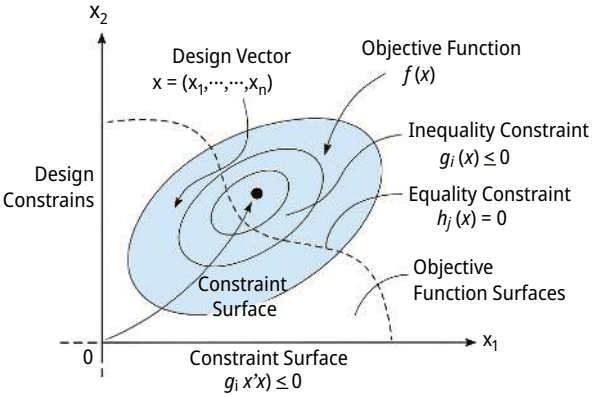

Figure 3.2: Key components of an optimization problem.

3.4 Classification of Optimization problems

Optimization problems are categorized based on various aspects, including constraints, variable types, problem structure, equation characteristics, permissible values, deterministic nature, separability, and the number of objective functions. These classifications help determine the appropriate optimization technique for solving specific problems:

I. Classification based on the existence of constraints
II. Classification based on the nature of the design variables
III. Classification based on the physical structure of the problem
IV. Classification based on the nature of the equations involved
V. Classification based on the permissible values of the design variables
VI. Classification based on the deterministic nature of the variables
VII. Classification based on the separability of the functions
VIII. Classification based on the number of objective functions

3.4.1 Classification Based on the Existence of Constraints

Optimization problems can be divided into **constrained** and **unconstrained** problems:

– **Constrained Optimization Problems (**Figure 3.3**)**: These problems involve limitations or restrictions on the values of design variables, expressed as equality or inequality constraints. Constraints define feasible regions within which the optimization algorithm must find the optimal solution [10].
  – *Example*: In civil engineering, optimizing the design of a bridge involves constraints on material strength, weight limits, and environmental regulations.

  - *Mathematical Formulation*: Minimize $f(X)$ subject to $g_j(X) \leq 0$, $l_j(X) = 0$
- **Unconstrained Optimization Problems**: These problems do not impose any restrictions on the design variables, allowing them to take any value within their defined domain [11].
  - *Example*: Finding the minimum of a quadratic function $f(x) = x^2 + 3x + 5$ without constraints.
  - *Mathematical Formulation*: Minimize $f(X)$.

Feasible and Infeasible Regions in a Constrained Problem

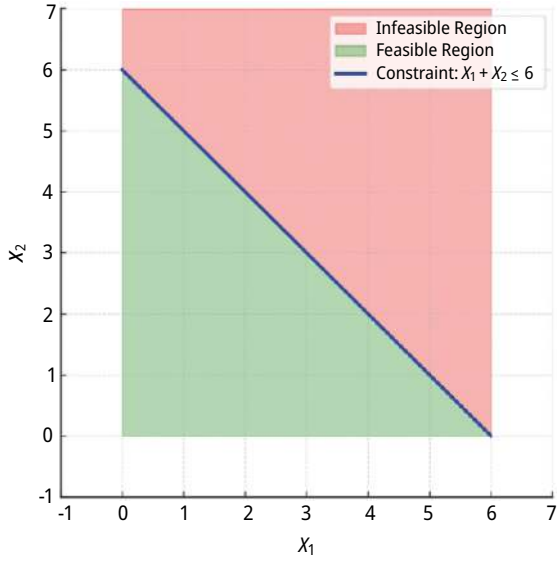

Figure 3.3: Constrained optimization problem.

Here is a 2D graph illustrating feasible and infeasible regions for a constrained optimization problem. The green shaded area represents the feasible region where all constraints hold, while the red shaded area represents the infeasible region. The blue line represents the constraint boundary $x_1 + x_2 \leq 6$.

3.4.2 Classification Based on the Nature of the Design Variables

Optimization problems are classified based on whether the design variables are continuous or discrete (Figure 3.4):

- **Continuous Optimization Problems**: The decision variables can take any value within a given range [12]. These problems typically arise in engineering and physics, where real-valued parameters need optimization:

  - *Example*: Optimizing the temperature settings for an industrial furnace to achieve maximum efficiency.
  - *Mathematical Example*: $x_1, x_2 \in R$.
- **Discrete Optimization Problems**: The decision variables take only discrete values, such as integers or binary values [13]. These problems are common in scheduling, logistics, and combinatorial optimization:
  - *Example*: Assigning workers to shifts, where each worker is either assigned (1) or not assigned (0).
  - *Mathematical Example*: $x_1, x_2 \in \{0,1,2,3, \ldots\}$.

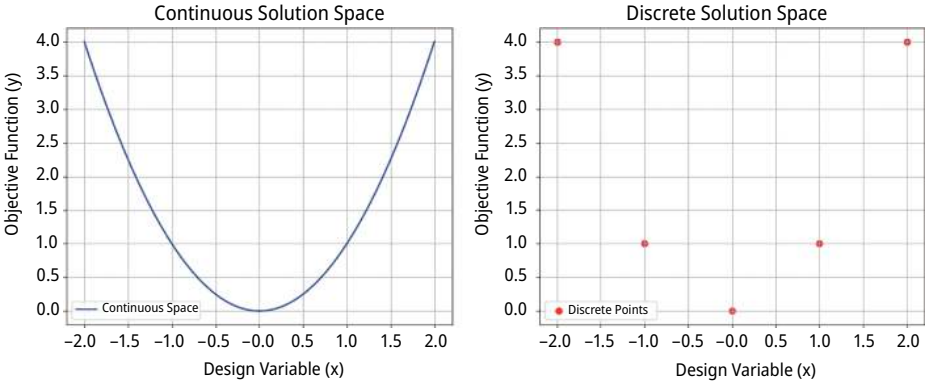

Figure 3.4: Continuous and discrete solution space.

3.4.3 Classification Based on the Physical Structure of the Problem

Optimization problems are often categorized based on the specific domain in which they are applied:

- **Structural Optimization**: Focuses on optimizing the material layout and geometric configuration of structures to maximize strength while minimizing weight or cost [14]:
  - *Example*: Optimizing the shape of a truss bridge to minimize material usage while ensuring durability.
- **Mechanical Optimization**: Deals with optimizing mechanical systems, such as gears, engines, or turbines, for performance and efficiency [15]:
  - *Example*: Reducing the weight of an automobile component while maintaining its structural integrity.

– **Electrical Optimization**: Involves the optimization of electrical circuits, networks, or power systems for efficiency and cost-effectiveness [16]:
  – *Example*: Minimizing power loss in an electrical grid.

3.4.4 Classification Based on the Nature of the Equations Involved (Figure 3.5)

Linear Optimization Problems: The objective function and constraints are linear, meaning that they can be represented as straight lines or planes in a multi-dimensional space. These problems are easier to solve using linear programming (LP) techniques [17]:
– *Example*: Allocating resources in a factory where constraints include available manpower and budget.
– *Mathematical Formulation*: Minimize $f(X) = c_1x_1 + c_2x_2$ subject to $Ax \leq b$.

Nonlinear Optimization Problems: At least one function in the problem is nonlinear, making the solution more complex and requiring iterative numerical methods [18]:
– *Example*: Maximizing profit where the cost varies nonlinearly with production volume.
– *Mathematical Formulation*: Minimize $f(X) = x_1^2 + \sin(x_2)$ subject to $g(x) \leq 0$.

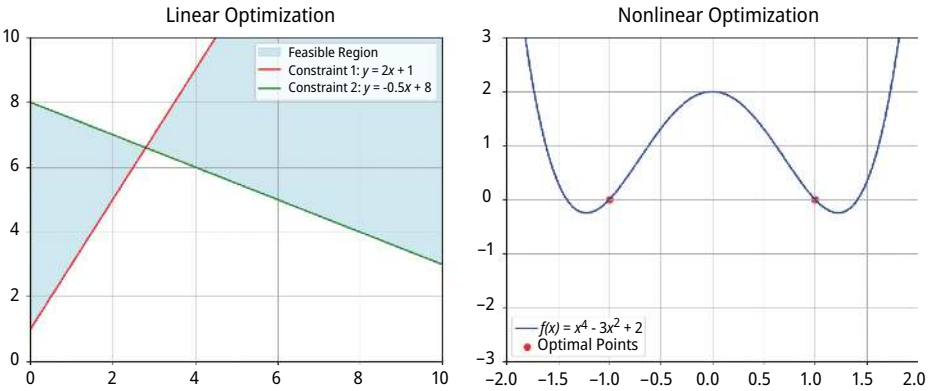

Figure 3.5: Linear and nonlinear optimization.

3.4.5 Classification Based on the Permissible Values of the Design Variables

Optimization problems can be categorized based on the allowable values for the design variables (Figure 3.6). These categories include integer programming (IP) and real-valued programming:

- **IP Problem**: If some or all of the design variables (x_1, x_2, . . ., x_n) are restricted to take only integer (discrete) values [19], the problem is classified as an IP problem.
- **Real-Valued Programming Problem**: If all design variables are allowed to take any continuous real value [6], the optimization problem falls under real-valued programming.

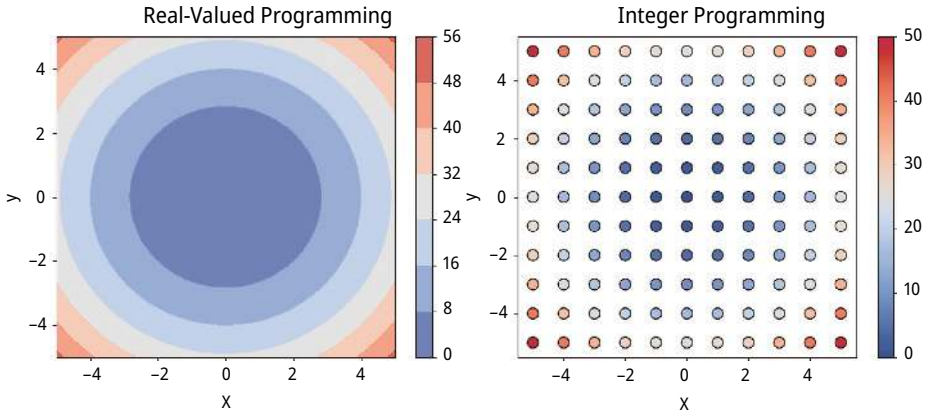

Figure 3.6: Permissible values of the design variables.

Here, this visualization helps in understanding how IP restricts the solution space compared to real-valued programming. The left plot shows **real-valued programming**, where solutions form a continuous space. And the right plot shows **IP**, where only discrete integer values are considered.

3.4.6 Classification Based on the Deterministic Nature of the Variables

- **Deterministic Optimization Problems**: All parameters, constraints, and functions are known with certainty [20]:
  - *Example*: Finding the shortest path in a well-defined road network.
- **Stochastic Optimization Problems**: Some elements, such as variables or constraints, involve randomness or probability distributions [21]:
  - *Example*: Portfolio optimization where stock prices are uncertain.

Here, the decision tree (Figure 3.7) starts with the **optimization problem**, branching into **deterministic** and **stochastic** categories. **Deterministic problems** (e.g., linear and nonlinear programming (NLP)) have fixed, predictable outcomes. **Stochastic problems** (e.g., Monte Carlo and probabilistic models) involve randomness and

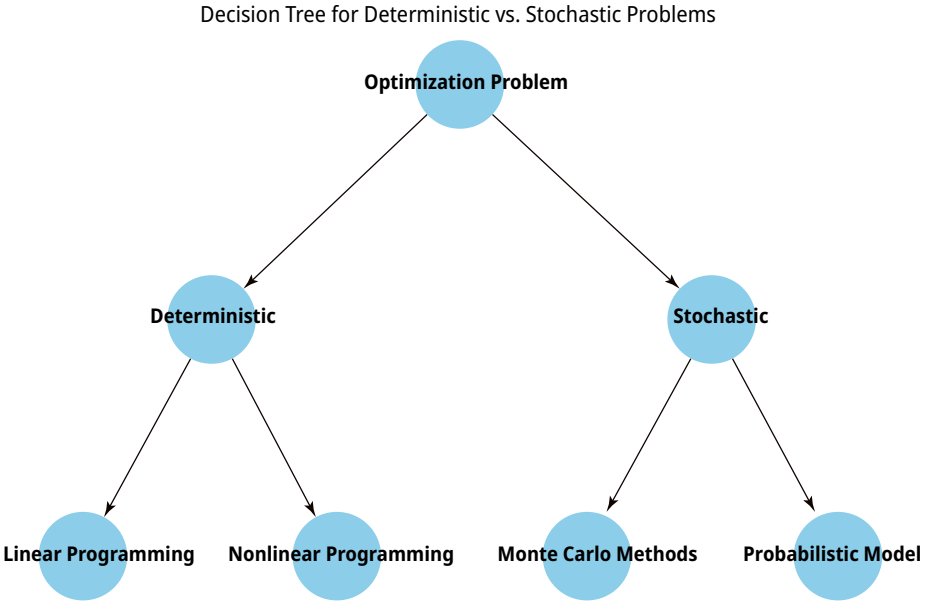

Figure 3.7: Decision tree starts with an optimization problem.

uncertainty. This classification helps in choosing the right optimization approach based on the problem's nature.

3.4.7 Classification Based on the Separability of the Functions

- **Separable Optimization Problems**: The objective function can be divided into independent subproblems that can be optimized separately [22]:
  - *Example*: A logistics company optimizing delivery routes for different cities separately.
- **Non-separable Optimization Problems**: The variables are interdependent, making the problem more complex [23]:
  - *Example*: Network flow optimization in telecommunications, where all variables interact.

Here in the separable problem (Figure 3.8), the surface appears as distinct, smooth sections, showing independent behavior of variables like logistics optimization, where delivery routes for different cities are optimized separately. In the non-separable optimization problem, the surface is interconnected, meaning variables cannot be optimized separately, as seen in network flow optimization, where all nodes in a telecommunications network interact dynamically.

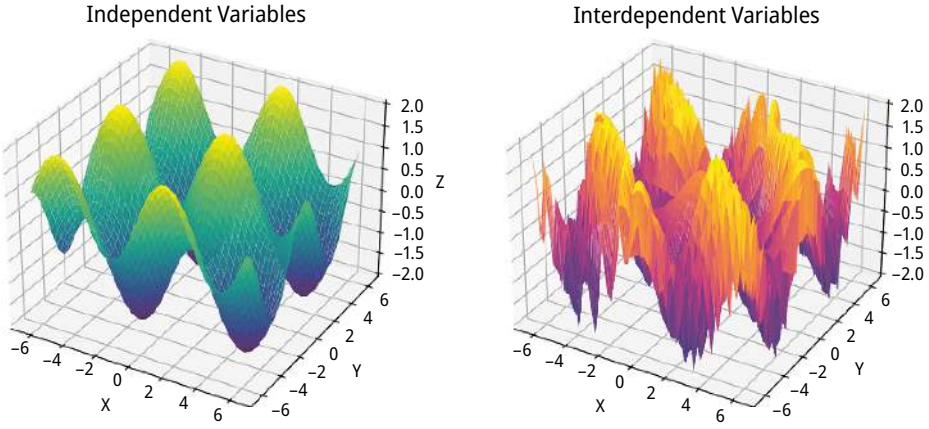

Figure 3.8: Separable problem (independent variables) and non-separable problem (interdependent variables).

3.4.8 Classification Based on the Number of Objective Functions Figure 3.9

- **Single-Objective Optimization Problems**: Focus on optimizing a single criterion while adhering to one or more constraints [24]:
  - *Example*: Minimizing fuel consumption in an aircraft.
- **Multi-objective Optimization Problems**: Aim to optimize multiple conflicting objectives simultaneously, requiring trade-offs [25]:
  - *Example*: Optimizing both cost and environmental impact in a manufacturing process.

Here, the graph plots a **single-objective optimization problem**, showing a function with a clear minimum (optimal point), which represents the best solution for the given criterion (e.g., minimizing fuel consumption).

3.5 Classical Optimization Techniques

Optimization is a fundamental mathematical process used to find the best possible solution under given conditions. **Classical optimization techniques** can be broadly classified into two categories [26]:

Based on mathematical approach, these techniques focus on the **methods** used to optimize a function, depending on the number of variables and constraints involved.

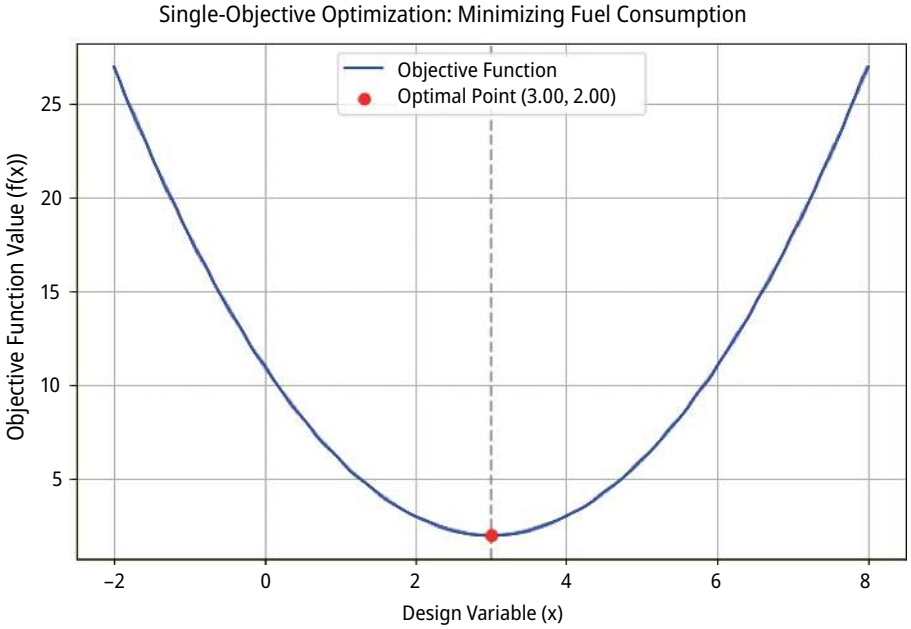

Figure 3.9: Single-objective optimization.

Based on problem structure, these techniques classify optimization problems based on the **nature of the equations, constraints, and variables**, determining how the problem is formulated.

Each category plays a crucial role in solving real-world optimization problems, ranging from simple single-variable functions to complex, multi-objective, and constrained systems. The choice of technique depends on the nature of the problem, whether it involves **linear versus nonlinear** equations, **continuous versus discrete** variables, or **deterministic versus stochastic** models.

Classical optimization techniques based on the **mathematical approach** (Table 3.2) primarily rely on calculus-based and algebraic techniques to find optimal solutions under given constraints. The key categories include **analytical methods**, such as **differential calculus-based optimization**, where derivatives help identify local minima and maxima, and **Lagrange multipliers**, which handle constrained problems by introducing auxiliary variables. For more complex cases, **Kuhn-Tucker conditions** are used to solve inequality-constrained problems, particularly in **NLP**. Additionally, **convex optimization** ensures global optimality when dealing with convex functions. These techniques are commonly used in **engineering design**, **economic modeling**, **supply chain management**, and **machine learning**, where precise mathematical formulations are available. They are particularly effective when the problem is well-defined, differentiable,

and follows smooth constraints, making them suitable for scenarios requiring highly accurate solutions with deterministic conditions.

Table 3.2: Overview of common optimization techniques (mathematical approach).

Category	Description	Example applications
Single-variable optimization	Optimizing a function with only one decision variable	Maximizing revenue based on a single factor
Multivariable optimization (no constraints)	Optimizing a function with multiple variables but no constraints	Finding the best mix of materials in production
Multivariable optimization (equality constraints)	Optimization involving multiple variables with equality constraints	Designing an aircraft wing shape with a fixed surface area
Solution by direct substitution	Replacing one variable with another to simplify the equation	Budget allocation in a project with a fixed total cost
Solution by constrained variation	Optimization by small changes in variables under constraints	Chemical process optimization
Method of Lagrange multipliers	A mathematical approach for constrained optimization	Economics (utility maximization)
Multivariable optimization (inequality constraints)	Optimization with constraints that limit variable ranges	Portfolio optimization with risk constraints
Kuhn-Tucker conditions	Generalized conditions for solving constrained problems	Machine learning (support vector machines)
Convex programming	Optimization of convex functions where local minima are global	Traffic flow optimization in cities

Classical optimization techniques based on the **structure of the problem** (Table 3.3) determine the nature of decision variables, constraints, and objective functions. The key types include **LP** for problems with linear relationships, **NLP** when the objective function or constraints are nonlinear, and **IP** where some or all variables must be integers. Other specialized forms include **quadratic programming (QP)** for quadratic objective functions, **dynamic programming (DP)** for multi-stage decision problems, and **geometric programming (GP)** for problems with specific functional relationships. These techniques are widely used in **logistics**, **manufacturing**, **finance**, **energy management**, and **robotics**, where the problem's structural properties dictate the best optimization method. They are particularly useful when dealing with **real-world constraints**, such as **discrete decision-making, dynamic changes, and interdependent variables**, making them essential for practical applications requiring computational efficiency and adaptability.

Table 3.3: Overview of common optimization techniques (structure of the problem).

Category	Description	Example applications
Linear programming (LP)	Optimization where both objective function and constraints are linear.	Supply chain optimization, resource allocation.
Nonlinear programming (NLP)	Deals with optimization problems where the objective function and/or constraints are nonlinear.	Engineering design, economic modeling.
Integer programming (IP)	Optimization where some or all variables must be integers.	Scheduling, facility location problems.
Mixed-integer programming (MIP)	A combination of integer and continuous variables in the optimization model.	Production planning, robotics path planning.
Quadratic programming (QP)	A special case of NLP where the objective function is quadratic and constraints are linear.	Portfolio optimization in finance.
Convex programming	Optimization of convex functions ensures global optimality.	Image reconstruction, traffic network design.
Geometric programming (GP)	A method dealing with problems having posynomial functions.	Circuit design, mechanical engineering.
Dynamic programming (DP)	Optimization of multi-stage decision problems.	Route planning, inventory control.
Stochastic programming	Optimization under uncertainty where some parameters are probabilistic.	Financial risk management, power grid optimization.
Multi-objective optimization (MOO)	Optimization involving multiple conflicting objectives.	Environmental impact vs. cost in manufacturing.

3.6 Engineering Applications of Optimization

Optimization is a powerful tool in engineering, enabling the development of efficient, cost-effective, and high-performance systems. It plays a crucial role in various engineering disciplines by enhancing designs, improving processes, and ensuring optimal resource utilization. Below are key applications of optimization in different engineering fields:

Structural and Civil Engineering

1. **Design of aerospace structures**: Optimization helps achieve minimum weight while maintaining structural integrity.
2. **Structural design**: Bridges, dams, towers, and chimneys are optimized for minimal material usage and cost while ensuring safety.

3. **Seismic and wind-resistant structures**: Optimization ensures minimal weight and high resilience to natural forces.
4. **Water resource systems**: Optimization maximizes benefits in reservoir management and irrigation planning.

Mechanical and Industrial Engineering

5. **Mechanical component design**: Optimization improves the efficiency of gears, cams, linkages, and machine tools.
6. **Machining processes**: Optimal selection of cutting parameters reduces production costs and increases tool life.
7. **Material handling systems**: Conveyor belts, cranes, and trucks are optimized for minimal cost and high efficiency.
8. **Heat transfer and fluid machinery**: Pumps, turbines, and heat exchangers are optimized for maximum efficiency.
9. **Manufacturing scheduling**: Optimization enhances production planning, control, and inventory management.
10. **Queueing and idle time control**: Reducing wait times in production lines enhances overall efficiency.

Electrical and Electronics Engineering

11. **Electrical machinery design**: Optimization enhances the efficiency of motors, generators, and transformers.
12. **Electrical network optimization**: Ensures optimal power distribution with minimal losses.
13. **Control system design**: Optimal tuning of controllers ensures stability and performance.
14. **Circuit design**: Component selection and layout are optimized for performance and power efficiency.

Chemical and Process Engineering

15. **Chemical plant optimization**: Process parameters are optimized for maximum yield and efficiency.
16. **Pipeline network design**: Optimized layouts reduce costs and improve flow efficiency.
17. **Site selection for industries**: Optimization considers cost, logistics, and environmental factors.

Operations Research and Management

18. **Route optimization**: Used in logistics and transportation for minimal cost and maximum efficiency.
19. **Resource allocation**: Ensures maximum benefit across multiple competing activities.

20. **Maintenance and replacement scheduling**: Optimizes maintenance strategies to reduce downtime and costs.

3.7 Challenges in Optimization

Although optimization is a strong tool that is applied in many different domains, but still there are a number of issues that can affect its accuracy and efficiency. Issues like the curse of dimensionality, non-convexity, computing expense, and constraint handling surface as problems become more complicated (Table 3.4). The procedure is made more difficult by scalability, data unpredictability, and multi-objective choices. Furthermore, some issues cannot be solved analytically and call for iterative or heuristic approaches. Developing effective and useful optimization strategies requires addressing these issues.

Table 3.4: Challenges in optimization.

Challenge	Description	Example
Curse of dimensionality	As the number of variables increases, computational complexity grows exponentially.	High-dimensional machine learning models
Non-convexity	Presence of multiple local optima makes finding the global optimum difficult.	Neural network training and structural optimization
Computational cost	Some optimization algorithms require extensive computational power and time.	Large-scale industrial simulations
Constraint handling	Hard and soft constraints can make optimization complex and infeasible.	Aircraft design with safety and weight constraints
Multi-objective trade-offs	Optimizing multiple conflicting objectives requires careful balancing.	Cost versus efficiency in manufacturing
Uncertainty and stochasticity	Input parameters may have randomness, making deterministic optimization difficult.	Stock market prediction and weather modeling
Convergence issues	Algorithms may get stuck in local optima or take too long to converge.	Gradient-based methods in deep learning
Lack of analytical solutions	Some problems lack closed-form solutions, requiring iterative or heuristic methods.	Complex fluid dynamics models
Data quality and availability	Optimization requires accurate data; noisy or missing data affects results.	Medical diagnosis using AI
Scalability	Algorithms that work well on small problems may not scale efficiently.	Optimization in cloud computing resource allocation

3.8 Conclusion

In engineering, research, economics, and management, optimization is essential because it facilitates effective resource allocation and decision-making. This chapter examined the classification, historical evolution, and range of optimization techniques as well as the technical applications of optimization. Even if traditional optimization methods offer a solid foundation, there are still many obstacles to overcome, including computing complexity, multi-objective trade-offs, and uncertainty in practical issues. Optimization techniques continue to be improved by developments in artificial intelligence, heuristics, and mathematical modelling, which makes them more reliable and suitable for complicated systems. Optimization will continue to be a vital tool for creativity and problem-solving in a variety of industries as technology develops.

References

[1] Pham, D. T. and Karaboga, D. (2011). *Intelligent Optimization Techniques: Genetic Algorithms, Tabu Search, Simulated Annealing and Neural Networks*. http://ci.nii.ac.jp/ncid/BA4534625X

[2] Rao, S. S. (2011). *Engineering Optimization : Theory and Practice*. https://openlibrary.telkomuniversity.ac.id/home/catalog/id/159888/slug/engineering-optimization-theory-and-practice.html

[3] Lam, R. W. and Chen, W. (2019). Process Design Optimization. Cham: Springer, 329–368. https://doi.org/10.1007/978-3-030-24237-4_12.

[4] *Optimization* (pp. 65–75). (2023). https://doi.org/10.1007/978-981-19-2008-0_7

[5] Ghosh, S., Squillante, M. S. and Wollega, E. D. (2019). On Min-Max Optimization Over Large Data Sets. 46(2), 45–47. https://doi.org/10.1145/3305218.3305235.

[6] Arora, J. S. (2025). Optimum Design Problem Formulation. Elsevier BV, 19–76. https://doi.org/10.1016/b978-0-12-818320-5.00002-6.

[7] Tian, Y., Zuniga, A., Zhang, X., Dürholt, J. P., Das, P., Chen, J., Matusik, W. and Konakovic-Lukovic, M. (2024). Boundary Exploration for Bayesian Optimization With Unknown Physical Constraints. arXiv.Org, Abs/2402.07692. https://doi.org/10.48550/arxiv.2402.07692.

[8] King, A. J. and Wallace, S. W. (2024). Modeling the Objective Function. Springer International Publishing, 55–75. https://doi.org/10.1007/978-3-031-54550-4_3.

[9] Serani, A. and Diez, M. (2024). *A Survey on Design-space Dimensionality Reduction Methods for Shape Optimization*. https://doi.org/10.48550/arxiv.2405.13944

[10] Aggarwal, C. C. (2020). Constrained Optimization and Duality. Cham: Springer, 255–297. https://doi.org/10.1007/978-3-030-40344-7_6.

[11] Kaira, K. (2022). Unconstrained Optimization. Apress eBooks, 447–494. https://doi.org/10.1007/978-1-4842-6797-4_9.

[12] Liao, T. (2015). Population-based heuristic algorithms for continuous and mixed discrete-continuous optimization problems. A Quarterly Journal of Operations Research, 13(3), 337–338. https://doi.org/10.1007/S10288-015-0285-8.

[13] Nelson, B. L. (2022). *Discrete-decision-variable Simulation Optimization in Operational Research*. https://doi.org/10.52843/cassyni.gkby95

[14] Andersen, M. E. M., Poulsen, P. N., Olesen, J. F. and Hoang, L. C. (2023). Strength-based material layout optimization of solid reinforced concrete. 276, 106941. https://doi.org/10.1016/j.compstruc.2022.106941.

[15] Wilson, P. R., Clark, S. M. and Scott, C. P. (2024). *Energy Efficiency Optimization In Mechanical Systems: Innovative Approaches In Industrial Applications*. *1*(2), 28–32. https://doi.org/10.61132/ijiime.v1i2.61

[16] Nagarani, S., Arivarasi, A., Ancelin, L., Kumar, R., Sharma, A. and Myilsamy, S. (2024). A Comprehensive Exploration of Mathematical Programming and Optimization Techniques in Electrical and Electronics Engineering. IGI Global, 392–418. https://doi.org/10.4018/979-8-3693-1487-6.ch019.

[17] Peren, F. W. (2024). Linear Optimization. Springer International Publishing, 29–43. https://doi.org/10.1007/978-3-031-47206-0_2.

[18] Peren, F. W. (2024). Nonlinear Optimization: The Nelder-Mead Simplex Search Procedure. Springer International Publishing, 187–199. https://doi.org/10.1007/978-3-031-47206-0_10.

[19] Chandru, V. and Rao, M. R. (2010). *Integer programming*.

[20] Xue, C. (2008). Algorithm for Solving a Class of Optimization Problems. *Science Technology and Engineering*. https://en.cnki.com.cn/Article_en/CJFDTOTAL-KXJS200807029.htm

[21] Diwekar, U. M. (2008). Optimization Under Uncertainty. Boston, MA: Springer, 1–54. https://doi.org/10.1007/978-0-387-76635-5_5.

[22] Van Der Linden, J. J. M., De Weerdt, M. and Demirovi'c, E. (2023). Optimal Decision Trees for Separable Objectives: Pushing the Limits of Dynamic Programming. arXiv.Org, Abs/2305.19706. https://doi.org/10.48550/arXiv.2305.19706.

[23] Sayed, E., Essam, D. and Sarker, R. A. (2012). Dependency Identification technique for large scale optimization problems. Congress on Evolutionary Computation, 1–8. https://doi.org/10.1109/CEC.2012.6256117.

[24] Inghels, D. (2020). Single Objective Optimization. Cham: Springer, 31–58. https://doi.org/10.1007/978-3-030-58422-1_2.

[25] Oswald, S. E. (2023). Solving Multi-objective Traveling Salesman Problem. Synthesis Lectures on Operations Research and Applications, 83–95. https://doi.org/10.1007/978-3-031-35719-0_5.

[26] Jin, Y., Wang, H. and Sun, C. (2021). Classical Optimization Algorithms. Cham: Springer, 41–51. https://doi.org/10.1007/978-3-030-74640-7_2.

A. J. D. Nanthakumar

Chapter 4
Multiphysics Modeling in Engineering

Abstract: Multiphysics modeling and simulation has become a quintessential tool in the present-day science and engineering activities. The multiphysics approach enables the product development engineers in understanding the behavior of complex systems that involve interactions between multiple physical phenomenona. Conventional approaches employing single physics approach are not capable of capturing the interactions that result in inaccurate system behavior prediction. This chapter explores the necessity and significance of multiphysics approach mentioning its capability for deployment in various domains. The study reviewed the procedural steps for modeling and simulation, including mathematical modeling, derivation of the governing equation, arrival of numerical solutions for the governing equation, and the computational implementation of the solution procedure. This chapter reviewed the relevant literature in the domains of multiphysics modeling and simulation. The coupling approaches to be followed for a multiphysics problem is discussed that include direct and sequential coupling approaches. The governing equations in the domains of structural mechanics, fluid dynamics, and electromagnetics are presented. The procedure for multiphysics modeling and simulation is explained that include problem definition, geometry creation and meshing, selection and setting up of appropriate physics, selection of suitable solver, and the execution of simulation. The discussions highlighted the benefits of incorporating multiphysics simulation approach into the engineering design and optimization phase of product development.

Keywords: multiphysics modeling, multiphysics simulation, engineering simulation, physics coupling

4.1 Introduction

The conventional product development process starts from the idea generation stage wherein innovative and cost-effective concepts are being analyzed. The conceived idea is then developed into a concept suitable for practical implementation. A feasibility study is conducted thereon that assesses the technical feasibility, financial requirements, and the market viability. The engineering design process is then carried out over those

A. J. D. Nanthakumar, Department of Automobile Engineering, SRM Institute of Science and Technology, Kattankulathur, Tamil Nadu, India, e-mail: ajd.nanthakumar@gmail.com

https://doi.org/10.1515/9783111723464-004

results in the prototyping of the product. The prototype is then subjected to testing and validation procedure that ensures the satisfaction of performance requirements and ensuring of safety and regulatory norms. The production process of the product is then carried over with necessary quality requirements. The product is then released into the market and successive monitoring and feedback mechanism is implemented for continuous improvement. Such a procedure typically involves a time frame of 3–5 years.

Virtual modeling and simulation techniques accelerate the product development process and reduce costs [6]. Apart from cost measures and time-saving benefits, such modeling and simulation tools transform problem-solving and organizational dynamics, enhancing development performance and fostering innovation. Finite element analysis is essential for shortening product development cycles, lowering costs, and improving quality [40]. As the technology is getting matured, a growing push is being carried over to streamline the process by integrating various simulation techniques. The product development process is in practice an iterative process [17], since the requirements arising from the feedback necessitate revisiting design rationale, and repeating assessments and syntheses.

A model for a system acts as a tool for answering questions related to the system and help in solving problems arising from similar systems [41]. A good model accurately replicates the required aspects of the system it represents. A system can have a number of models but a best model is the simplest of all the perceived models yet complex enough to understand the system and solve problems. Modeling should be undertaken as a goal achievement technique for which the purpose of a model should be known first before creating the model itself. The simulation procedure utilizes a model for analyzing a system, so that, strategies can be derived to solve a synonymous problem and aid in decision-making. The fundamental steps in modeling and simulation procedure can be enumerated as follows:

1. Problem identification: Identify the real-world problem to be solved and understand the parameters involved
2. Mathematical modeling: Representation of a real-world system or process using mathematical expressions, equations, and variables to describe its behavior
3. Derivation of governing equations: Fundamental equations derived from physical laws
4. Solution of governing equations: Solving the governing equations by analytical or numerical procedure
5. Computer modeling: The equations (mathematical models) are translated into a computational framework using tools like programming languages or software to handle complex calculations
6. Simulation: It involves running these computer models to predict the system's response to various scenarios, enabling analysis, optimization, and decision-making without physical experimentation
7. Verification and validation: Verify the model output with reference data and validate the developed model

Figure 4.1 represents the flowchart for modeling and simulation procedure. The mathematical modeling and derivation of governing equation and its solution are combined in one step in the flowchart.

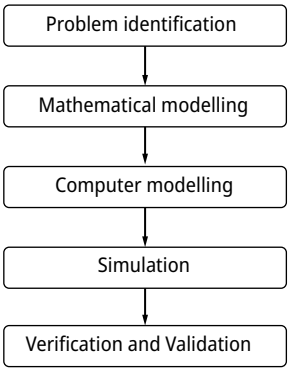

Figure 4.1: Modeling and simulation flowchart.

The process of modeling and simulation explained thereof has been carried over for the physical analysis of engineering systems. Most of the analysis had been in the single physics domain such as fluid flow, heat transfer, structural mechanics or electromagnetics. In such single physics analysis, the physical interactions of the system with other domains are assumed to be negligible and if needed treated as a separate study. This makes the single physics approach relatively simpler and computationally inexpensive. But every system happening in nature or engineered systems are practically multiphysics. In such systems, multiple physical phenomena are interacting and there exist a coupling characteristic among them. Multiphysics analysis has become the order of the day since the interactions between different domains significantly influence behavior, such as in combustion engines (fluid-thermal-chemical interactions) or piezoelectric devices (electro-mechanical interactions). While more computationally demanding, multiphysics analysis provides a comprehensive and realistic understanding of complex systems.

The primary advantages as well as challenges associated with multiphysics simulation arise from the coupling between the different physics fields. Prior to the advent of multiphysics software, the coupling was complex as well as complicated wherein the solution obtained from one physics solution software was passed into another for subsequent simulations. While transferring the file data from one software to the other inadvertent errors propagate during the data exchange with extraordinarily long time requirements. Such disadvantages have been reduced to a considerable extent through the deployment of multiphysics simulation software. The coupling between the multiphysics problems may happen in one of the two following ways:

1. Direct coupling in which a single matrix system of equations based on all of the relevant physics is assembled and then solved. Such a methodology may require high computational power and memory requirements.

2. Sequential coupling in which the solution from the first set of field equations is passed on to the next set of field equations which after being solved is passed on to the next set of field equations and thereon. Such an iterative procedure is repeated till the final solution is obtained.

4.2 Literature Review

4.2.1 Modeling and Simulation

Sinha et al. [39] reviewed state-of-the-art modeling and simulation technologies, evaluating their effectiveness in supporting the design process. It highlighted the need for adaptable modeling languages and seamless tool integration, focusing on multidisciplinary systems combining continuous- and discrete-time phenomena. Magana [28] used the Delphi technique with 37 experts from academia and industry to identify essential modeling and simulation practices for workplace engineering. It explored their relevance and integration into engineering curricula, informing a preliminary learning progression and future research on instructional pathways for modeling proficiency. Carson [10] informed about the discrete event simulation, explaining key concepts like system state, events, and processes, along with major simulation software worldviews. It reviewed the benefits, challenges, and skills required, as well as key steps and project management considerations for conducting valid simulation studies. Bossel [8] presented computer-based models as extensions of traditional mental models, enabling simulations to explore complex scenarios more reliably and efficiently. It provided a comprehensive guide to modeling methods, SIMPAS software, and 50 system models, supporting diverse fields, such as ecology and economics. Modeling and simulation fundamentals provided a comprehensive guide, covering definitions, paradigms, and applications to equip readers as effective developers and users. Computer simulations have traditionally been viewed as extensions of formal mathematical models or as specific cases of empirical experiments. Alvarado [4] argued that simulations are best understood as instruments, offering clearer insights into their role and epistemic value in science and their relationship to other scientific methods and practices. Modeling played a critical role for national governments and the WHO in strategizing COVID-19 mitigation, focusing primarily on epidemiological models to understand disease spread and intervention impacts. However, the pandemic presented diverse challenges requiring tailored models for optimal solutions. Currie [11] identified these challenges and highlighted how simulation modeling could support informed decision-making, serving as a call to action for modelers and a guide for decision-makers.

4.2.2 Single Physics Modeling and Simulation

Rivera [33] summarized the significance of mathematical modeling and computational fluid dynamics (CFD) simulation in optimizing electrochemical reactors for specialized processing, energy conversion, storage, and environmental applications. It highlighted improvements to existing reactors and advanced cell designs, drawing examples from literature and the authors' experience to showcase CFD's role in design, characterization, and scale-up. Ajorloo et al. [2] reviewed thermodynamic modeling in biomass gasification, emphasizing its role in optimizing complex interdependent parameters. It highlighted modeling approaches, such as stoichiometric, nonstoichiometric, and Aspen Plus, alongside modification methods to enhance accuracy, based on a decade of research findings. Conventional Darcy-based models fail to capture shale gas flow due to nanopores (a few to hundreds of nanometers) and non-Darcy processes, such as gas slippage and Knudsen diffusion. Javadpour et al. [23] reviewed these phenomena through theoretical models, molecular simulations, and pore network modeling, addressing the complex gas dynamics in shale reservoirs. The study conducted by Mayur et al. [29] developed a thermodynamic and kinetic modeling framework for lithium-ion batteries within Cantera, introducing a new class for intercalation materials. It demonstrated the framework using a single-particle model in MATLAB, providing supplementary code and parameters to support the modeling community. The Newtonian fluid model has been widely used for simulating cerebral blood flow in intracranial atherosclerotic stenosis using CFD, despite blood being a shear-thinning non-Newtonian fluid. This study conducted by Liu et al. [27] investigated differences in cerebral hemodynamic metrics between CFD models based on Newtonian and non-Newtonian fluid assumptions in patients.

The review conducted by Guo et al. [16] highlighted electrospinning as a versatile nanomaterial preparation method, summarizing its parameters, models, and simulations. Applications in biomedicine, energy, and catalysis were discussed alongside recent advancements, challenges, and future development trends. Al-Obaidi [3] investigated axial pumps, widely used for their high flow and low head, focusing on hydraulic-induced vibrations stemming from pressure pulsations at the impeller inlet. Numerical simulations using the Shear Stress Transport (SST) turbulence model and sliding mesh technique analyzed the impact of blade configurations on flow behaviors. Results, validated against experimental data, revealed the influence of impeller blades on pressure, velocity components, and shear stress across operating conditions, highlighting their critical role in pump performance and vibration characteristics. Aftabi [1] examined the biomechanics of unpowered exoskeleton augmentation for human running gait, focusing on the assistive torque profile of I-RUN. Using OpenSim simulations with a 92-muscle, 29-degrees of freedom lower limb model, optimal stiffness coefficients were identified to reduce metabolic rate, biological hip moments, and major hip muscle forces. The findings also revealed reduced fatigue in 92 muscles and key monoarticular hip muscles at optimal stiffness.

Jaśkiewicz [22] presented a simulation model of an anthropometric dummy in ADAMS for low-velocity crash tests, representing a 50th-percentile male with optimized joint stiffness and damping. It addressed gaps in low-speed crash testing, particularly between 16 and 25 km/h. Simulation results at 20 km/h were validated against experimental data, forming the foundation for a physical dummy model. Jami [21] presented a simulation framework for hybrid transportation systems, integrating human-driven and automated vehicles. A modular approach decomposed human driving tasks, enabling customizable driver behavior representation using expressive parameters from a large dataset. Dense traffic scenarios were simulated to analyze human- and system-specific factors on traffic safety and performance. The study conducted by Prabhaharan et al. [35] focused on improving the crashworthiness of a lightweight passenger car's crash box for better energy absorption (EA) in frontal impacts. Using analytical and finite element methods with Pam-Crash simulations, the study achieved a 97% accuracy and improved EA by 30% and crush force efficiency by 8.8% through design of experiments-based response surface methodology. Hockney [18] explored about particle-based simulation techniques, including Nearest Grid Point (NGP), Cloud-In-Cell (CIC) and Particle-Particle-Particle-Mesh (P3M) algorithms, with applications in astrophysics, semiconductors, and plasma physics, and highlighted predictive modeling as a cost-effective tool for optimizing engineering designs prior to manufacturing. Zhou [45] introduced the particle flow map (PFM) method for efficient incompressible fluid simulation, combining Lagrangian particles and a hybrid solver to enhance accuracy and vorticity preservation. PFM achieved up to 49× faster computation and 41% lower memory usage compared to Neural Flow Maps (NFM).

4.2.3 Multiphysics Modeling and Simulation

Hu et al. [19] conducted a study that utilized a multiphysics coupling simulation model to analyze the performance of the hybrid fluid flow magnetorheological (MR) damper. This approach integrated the interactions between electromagnetic, fluid flow, and mechanical dynamics to accurately predict the damper's behavior. The model helped to assess critical parameters, such as the output damping force and the dynamic adjustable range, providing insights into the damper's response for a given current input and aiding in its optimization for constrained volume applications. Shi et al. [36] used a multiphysics model to analyze fluid flow, heat transfer, and reactions in thermochemical heat storage, identifying low thermal conductivity as a limiting factor. Fin designs (axial, radial, and spiral) improved heat transfer, reducing exothermic times by up to 89.97%, providing insights for reactor optimization. Lanetc et al. [26] developed a hybrid numerical model combining the Hagen-Poiseuille solution and volume of fluid advection for fractures with Darcy multiphysics flow for the coal matrix, incorporating sorption and swelling effects. Validated against analytical solutions, the model was computationally efficient, outperforming parallelized direct numerical simulations, and is applicable to

natural gas production, hydrogen storage, and CO_2 geosequestration. Bera et al. [7] analyzed the multiphysics flow dynamics in nanoporous unconventional gas reservoirs, addressing mechanisms, such as viscous flow, diffusion, adsorption-desorption, stress effects, and capillary forces. It emphasized the need for a combined approach to tackle the complexity of fluid transport and highlighted the significance of each mechanism in accurate modeling. Challenges and prospects in unconventional reservoir modeling were discussed, offering insights and suggestions to advance research in this field.

Gao and Elsworth [14] developed a coupled hydrological-mechanical-chemical-biological [14] developed . . .” multiphysics model to simulate microbial processes in underground hydrogen storage within porous aquifers. It showed microbial clogging and hydrogen consumption significantly impact initial injection/withdrawal cycles and recovery efficiency. Effective stress influenced aquifer permeability throughout, while mineral dissolution/precipitation had negligible effects. Cai et al. [9] reviewed multiscale and multiphysics influences on fluid behavior, modeling efforts for fluid transport, and their implications for enhanced recovery. It also highlighted potential environmentally driven applications, such as greenhouse gas storage and underground energy storage. Plait et al. [31] validated a multiphysics model for a magnetocaloric regenerator operating under active magnetic regeneration cycles. The model, combining a semi-analytical magnetostatic model with magnetocaloric and thermofluidic models, was experimentally compared with a gadolinium-based regenerator. The work analyzed the thermal behavior and inertia during cycles, proposing a time constant for active magnetic refrigeration that aligned with both numerical and experimental results. Wilkins et al. [42] developed a multiphysics module for nonisothermal, multicomponent, multiphase flow in porous media within the open-source MOOSE framework. By coupling it with solid mechanics and geochemistry modules, fully implicit thermo-hydro-mechanical-chemical simulations are achieved. The open-source nature of MOOSE promotes collaborative advancements in porous media research. Mianroodi et al. [30] reviewed advancements in computational modeling of the interplay between chemistry, microstructure, and material behavior, highlighting continuum thermodynamics, phase-field methods, and crystal plasticity for multiphysics microstructure evolution. It discussed the current status of simulation approaches and software tools while providing insights into future research directions. Yan et al. [43] introduced a three-dimensional (3D) thermal-hydro-mechanical (THM) coupling model incorporating rock fracturing, utilizing the combined finite discrete element method (FDEM) for fracture and fragmentation simulation. The model integrated a fracture-pore mixed seepage model, heat transfer mechanisms, and FDEM-based fracture mechanics. Validation examples confirmed its accuracy for THM coupling problems, and simulations demonstrate its ability to capture complex fracture initiation, propagation, and extension under multiphysics effects.

Siddiqui et al. [37] reviewed mathematical models for predicting the performance of photovoltaic systems, including optical, thermal, electrical, structural, and exergo-economic aspects. It highlighted the significance of multiphysics models and discussed the future directions for improving their reliability and practical applications in system

design, evaluation, and optimization. Huang et al. [20] developed a 3D multiphysics model to analyze the electrochemical and fluidic processes in industrial alkaline water electrolysis. The model accounted for structural design effects, including the shunting current effect, and accurately estimated the current–voltage curve with less than 5% error, particularly at high current densities. The study aimed to advance water electrolysis modeling and guide industrial Alkaline Water Electrolysis (AWE) cell design. DualSPHysics [12] is a meshless SPH Navier-Stokes solver initially designed for coastal engineering problems, particularly wave impacts on structures. Since its 2011 release, it has evolved to handle extreme wave events, fluid-driven objects, debris flows, and offshore energy devices, with enhancements, such as Graphical Processing Unit (GPU) computing, coupling with wave models, and integration with Project Chrono and MoorDyn. Recent advancements include multiphase simulations and Newtonian/non-Newtonian modeling, making it a robust tool for free-surface flow and complex engineering applications. Singh et al., [38] highlighted the growing significance of additive manufacturing (AM) due to its ability to produce multiscale features using stock feed materials, which was previously unattainable. It also addressed challenges like undesirable microstructures, dimensional instability, and property control. The review discussed advancements in modeling and simulation for addressing these challenges, particularly in the AM of metals and polymeric nanocomposites.

Donnarumma et al. [13] introduced a multiphysics modeling approach to design an integrated electric propulsion system for ship dynamic positioning. The platform combined models of the shipboard power plant, hydrodynamic forces, and dynamic positioning controller, enabling real-time simulations and control hardware integration. A hardware-in-the-loop configuration was implemented to test controller logic on a physical Programmable Logic Controller (PLC), with results compared and discussed. Kumar et al. [25] modeled and simulated the electrochemical machining process using COMSOL multiphysics to predict material removal and workpiece geometry. It analyzed interactions based on electrochemistry, fluid dynamics, and solid mechanics for various materials, including aluminium and tungsten. The results provided insights into physics and improved process accuracy and optimization. Garcia-Michelena et al. [15] developed a multiphysics numerical model to simulate vacuum induction melting of Inconel 718, integrating magnetic fields, heat transfer, and fluid dynamics. A moving mesh approach captured melt surface oscillations with less than 5% error in temperature predictions. Insights into melt homogenization and crucible insulation effects enhance the process for Ni-based superalloys. Ragusa [32] examined the multiphysics modeling and simulation of nuclear reactors, integrating disciplines, such as neutronics, thermal fluid dynamics, fuel performance, structural mechanics, and chemistry. A pedagogical example introduced the coupled approach, followed by a case study on a core-cavity draining transient in a molten salt reactor, emphasizing its role in safety evaluations.

Kemppainen et al. [24] conducted a study that dealt with the development and operation of direct ammonia fuel cells (DAFCs), highlighting the challenges of slow ammonia oxidation reaction kinetics and the need for advanced anode catalysts. A

one-dimensional model was developed to analyze the interactions between reaction kinetics and transport phenomena, with sensitivity analysis revealing the importance of temperature and humidity for cell performance. Observations, such as the limited effect of increasing catalyst loading, provide insights to guide future research and optimization of DAFCs. Yildirim et al. [44] introduced MPhys, a modular multiphysics simulation library built on the OpenMDAO framework to address challenges in multidisciplinary design optimization (MDO). MPhys enables efficient coupling of models and computation of analytic derivatives for large-scale simulations, supporting rapid development of coupled models for gradient-based MDO. Demonstrated through aerostructural and aeropropulsive design optimization, MPhys has shown versatility in various applications and is expected to accelerate the adoption of MDO in engineering design. Rui et al. [34] developed a multiscale, multiphysics numerical model to quantify rock thermal damage under microwave and laser irradiation, integrating grain-based modeling, COMSOL solutions, and 4D-Lattice Spring Model (LSM) fracture simulation. Results showed that mesostructure and mineral composition dominate rock damage rather than temperature gradients. A calibration method was proposed to reuse muffle furnace data for predicting microwave- and laser-induced rock damages at larger scales. Angelidakis et al. [5] reviewed YADE, an open-source framework for dynamic simulations, which has evolved over 19 years into a versatile multiscale and multiphysics solver. Written in C++ with a Python interface, YADE allows easy implementation of new features, interactive simulation control, and postprocessing. Its growth is driven by a robust core design, rigorous testing, and contributions from diverse fields, such as soil mechanics, physics, and material handling, offering versatility, user-friendliness, and computational efficiency.

A distribution of multiphysics analysis for various applications discussed in the literature review is shown in Figure 4.2.

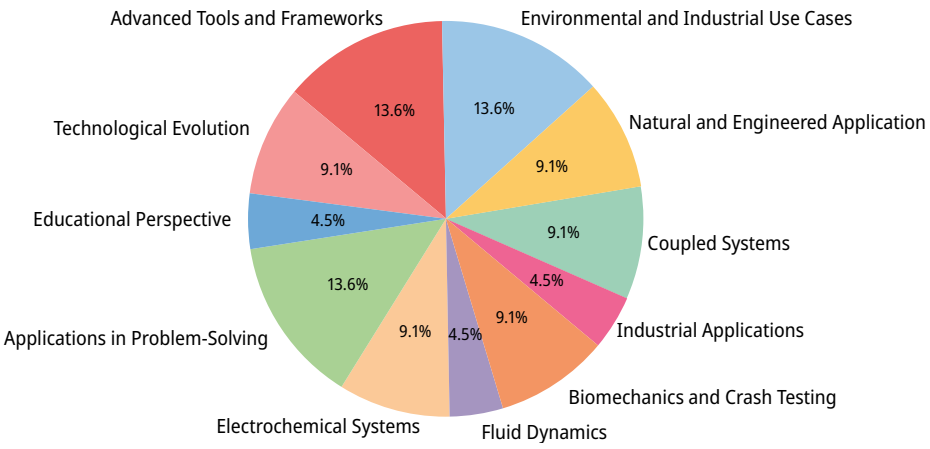

Figure 4.2: Distribution of applications discussed in the literature review.

Multiphysics approach is preferred, due to its ability to consider the interactions among the physical domains where single-physics models often fail to capture these interactions. Ignoring the couplings between the physical domains can lead to deviations in the predicted behavior of the engineering systems. Moreover, multiphysics tools enable the design and optimization of innovative technologies allowing for accurate understanding of performance parameters and enable the development of optimized solutions.

4.3 Physics Modeling and Simulation

4.3.1 Single Physics Modeling and Simulation

Single physics modeling and simulation involves analysis and simulation of engineering systems governed by one primary physical discipline. The governing equations for the related physical discipline is formulated and solved for the computational domain. The most widely concerned domains include structural mechanics, fluid dynamics, thermal analysis, and electromagnetic analyses.

4.3.1.1 Structural Mechanics

The procedure involves defining the structural problem, including the geometry (e.g., beam and plate), load type and application (e.g., point or distributed load), and constraints or supports (e.g., fixed, pinned). For instance, analyzing a beam under a uniform load involves studying bending and stress distribution along its length. The governing equations for structural deformation problems include the equilibrium equation given by:

$$\nabla \cdot \sigma + f = 0 \tag{4.1}$$

where σ is the stress tensor and f is the body force. The constitutive equation is given by

$$\sigma = C : \varepsilon \tag{4.2}$$

where C is the elasticity tensor and ε is the strain tensor. The kinematic equation is given by:

$$\varepsilon = \frac{1}{2}\left(\nabla u + (\nabla u)^T\right) \tag{4.3}$$

where u is the displacement vector. In case of bending problems, the bending equation for a slender beam is given by:

$$EI\frac{d^4w}{dx^4} = q(x) \tag{4.4}$$

where E is Young's modulus, I is the area moment of inertia, w is the deflection, and $q(x)$ is the distributed load per unit length. The materials mechanical properties are given by Young's modulus (E), Poisson's ratio (ν), and density of the material (ρ). The computational domain is then discretized by one of the numerical methods that shall be described later. For most of the numerical methods, the overall equation is the assemblage of the global stiffness matrix and the load vector is given by

$$Ku = F \tag{4.5}$$

The solution of equation (4.5) is then postprocessed for visualizing the required results that include stress distribution contours, deformation values for the structure, etc.

4.3.1.2 Fluid Dynamics

Fluid dynamics focuses on the motion of fluids (liquids and gases) under the influence of forces such as pressure gradients, gravity, and viscous effects. Solving fluid dynamics problems involves applying the principles of conservation of mass, momentum, and energy to predict flow behavior.

In a similar approach, the governing equation that includes the continuity equation is given by

$$\frac{\partial \rho}{\partial t} + \nabla \cdot (\rho u) = 0 \tag{4.6}$$

where u is the velocity vector, ρ is the fluid density, and for incompressible flows, ρ is the constant. The momentum equation derived from the Navier-Stokes equation is given by

$$\rho\left(\frac{\partial u}{\partial t} + u\nabla \cdot u\right) = -\nabla p + \mu\nabla^2 u + \rho g \tag{4.7}$$

where p is the pressure, μ is the dynamic viscosity, and g is the gravitational acceleration. The material properties include the density (ρ) and the viscosity coefficient (μ). The computational domain is discretized by one of the numerical methods and applying the solution techniques. After solving the governing equations in the computational domain, the post processing is carried over for plotting the stream lines and contours for representing the velocity field, plotting the pressure gradients, and further derived quantities, such as the aerodynamic drag, heat transfer rates.

4.3.1.3 Electromagnetic Analysis

Electromagnetics focuses on the behavior of electric and magnetic fields, and primary objective is to solve the fields, potentials, currents under various configurations, and boundary conditions. The governing equations include Maxwell's equations. The Gauss law for electric fields is given by

$$\nabla \cdot E = \frac{\rho}{\varepsilon_0} \tag{4.8}$$

where is E is the electric field, ρ is the charge density, and ε_0 is the permittivity of free space. The Gauss law for magnetism is given by

$$\nabla \cdot B = 0 \tag{4.9}$$

where B is the magnetic flux density. Faraday's law of induction is given by

$$\nabla \times E = -\frac{\partial B}{\partial t} \tag{4.10}$$

The material properties in electromagnetic analysis include material permittivity (ε), material permeability (μ), and conductivity (σ). The computational domain is discretized by one of the numerical methods and solved for plots of electric or magnetic field distribution, contours of potential V and other derived quantities, including capacitance, inductance, etc.

4.3.2 Multiphysics Modeling and Simulation

The systems found in nature as well as systems engineered by man involve multitude of physical phenomenon for achieving an objective. Understanding such systems through a single physical domain analysis is insufficient to predict its behavior. Hence, a multiphysics analysis is quintessential. Multiphysics analysis involves studying the interaction among multiple physical phenomena. The very natural human body study to understand cells, tissues, and organs require a fundamental knowledge of the biological characteristics and chemical behavior of the human body. In engineered systems, for solving complex engineering problems, it is necessary to analyze the interactions between different physical domains, such as fluid flow, heat transfer, structural mechanics, electromagnetism, chemical reactions, etc.

4.3.2.1 Coupling in Multiphysics Simulation

The coupling procedure in multiphysics simulations refers to the interaction and dependence of one physical phenomenon on the other within the proposed computational

framework. The efficiency and accuracy of multiphysics simulations depend upon the implementation of the coupling between the physical phenomena. The coupling can be carried over as weak or strong coupling. In weak coupling, the interaction among the physical domains happens in a sequential manner. The solution obtained from one domain influences the analysis in the other domain. A typical example is the thermal expansion problem, wherein temperature fields calculated in the heat transfer analysis are applied as inputs to a structural analysis. The computational cost is relatively low. In a strong coupling, interactions among various physical domains occur in an iterative manner wherein the data exchange among the domains happen continuously till a converged solution is achieved. For instance, in fluid–structure interaction problems, fluid forces a structure to deform and the deformed structure alters the fluid flow. For such strong couplings, accurate and efficient data exchange between domains with different discretizations, such as meshes, is crucial. Strongly coupled simulations require considerable memory and processing power requiring high-performance computing resources.

4.3.2.2 Procedure for Multiphysics Modeling and Simulation

A) Defining the Problem

The objective for the study is to be defined in the initial stage. A multiphysics modeling and simulation task can be carried out for designing a system, optimizing a system, understanding the physical behavior of a system, predicting the performance of a system for a given set of conditions, improving the efficiency of an existing system, etc. The physical phenomenon involved with the problem under study should be identified. Most of the common multiphysics problems include the physical domain analysis of fluid flow, heat transfer, structural analysis, electromagnetics, chemical reaction engineering, etc. The spatial and the temporal scales for which the multiphysics analysis is to be carried over are fixed based on the objectives. The interactions (coupling) among the domains need to be identified. The governing equations for the corresponding domain need to be identified and utilized for solving. The boundary and initial conditions of the problem under study are then specified. Thus, the problem definition phase ensures that the objectives of the study are fixed; physical processes and their governing equations are formulated.

B) Geometry and Meshing

The geometrical representation of the physical system represents the spatial dimensions of the system and all the spatial features of interest. Such a geometry creation is implemented through computer-aided design of the system. The geometrical representation can be in file formats, such as STEP, IGES, STL, etc. Domain decomposition is the next step in which the geometry is divided into subdomains pertaining to different

physical phenomena. The process of meshing divides the geometry into discrete elements or cells setting the background for numerical solution of the governing equations for the entire domain. Meshes can be structured wherein regular, grid patterned arrangement of elements are present enabling efficient and accurate computation. The main limitation is the generation of meshes for complex geometries. Unstructured meshes consist of irregular arrangement of meshes with tetrahedron like mesh elements. Complex geometries can be meshed using unstructured meshes at the cost of higher computing power requirements. Nowadays, software that are capable of hybrid meshes are available, wherein both structured and unstructured meshes are present in the same domain to balance accuracy and efficiency.

C) Setting Up the Physics for Simulations

In the physics setup step, the material properties are assigned to the system. The material properties are assigned in the corresponding terms in the governing equations for further solving. The most commonly used material properties include the density, Young's modulus, Poisson's ratio, yield strength for the structural analysis, viscosity, compressibility, thermal diffusivity for the fluid domain, thermal conductivity, specific heat, thermal expansion coefficient for the thermal analysis domains, electrical conductivity, permittivity, and permeability for the electromagnetic domain. The boundary and initial conditions for the corresponding physical domain are applied. Most of the widely deployed boundary conditions include inlet velocity, no-slip condition, outlet pressure, ambient pressure, symmetry and periodicity for the fluid dynamics domain, fixed support, displacement, traction load for the structural mechanics domain, temperature constraint, convective heat flux, radiation limits, thermal insulation for the heat transfer domain, electric potential, magnetic flux, and conductivity for the electromagnetic domain.

D) Solver Selection

Solver selection step involves the choosing of specific solvers for each domain. Usually, a control volume-based CFD solver is chosen for fluid flow applications, finite element method-based solvers for structural analysis, and electromagnetic solvers for filed interactions. The solver selection is carried over in tandem with the coupling approach wherein a monolithic approach solves all governing equations simultaneously in a unified system, offering high accuracy and numerical stability but requiring significant computational resources and less flexibility. The partitioned approach solves equations separately for each domain, exchanging data iteratively between solvers. Such an approach is more flexible and scalable, suitable for leveraging domain-specific solvers, but may face numerical instabilities and higher coupling costs. The choice between these approaches depends on the nature of the problem, complexity, computational resources, and software compatibility.

E) Simulation Execution

In simulation execution step, the selected solvers are configured for the required accuracy and stability. The simulation run is then carried over and the interactions between the domains are managed subsequently. A proper simulation setup ensures that simulation is carried over without any errors as well as the simulation output is meaningful and reliable. For steady-state simulations, the time step size is not considered as the solving procedure aims to achieve a steady-state solution rather than a time track solution. For transient simulation problems, a suitable time step size is selected, so that, the dynamics of the system is captured without numerical instabilities. Usually, smaller time steps result in improved accuracy especially for highly dynamic cases, such as shocks in fluid flow, high-frequency vibrations, etc. Larger time steps reduce computational cost but are not suitable for dynamic cases.

4.4 Conclusion

This chapter emphasizes the role of multiphysics modeling and simulation in the present-day engineering problems, as the contextual problems require complex interactions between various physical domains. Such interactions are found to influence the performance characteristics of the system under study. Various single physics approach has been reviewed and when compared with multiphysics approach, the later one is capable of providing an accurate representation of real world problems. Using such an approach aids in improving predictive capabilities of the simulation studies. The work highlighted the two important coupling methodologies associated with multiphysics problem, direct coupling and sequential coupling. The implications of both coupling approaches have been informed. The present-day availability of computational power combined with software capability improvements have rendered multiphysics simulation more accessible wording to effective design, analysis, and optimization of engineered systems. The present-day industrial requirements are varied. The multiphysics approach can be deployed for domains from energy storage to biomedical applications. High-performance computing taking the center stage can be utilized to enhance the curability as well as the scalability of multiphysics approach.

References

[1] Aftabi, H., Nasiri, R., & Ahmadabadi, M. N. (2021). Simulation-based biomechanical assessment of unpowered exoskeletons for running. Scientific Reports, 11(1), 11846.

[2] Ajorloo, M., Ghodrat, M., Scott, J., & Strezov, V. (2022). Recent advances in thermodynamic analysis of biomass gasification: A review on numerical modelling and simulation. Journal of the Energy Institute, 102, 395–419.

[3] Al-Obaidi, A. R. & Alhamid, J. (2024). Analysis of unsteady internal flow characteristics in axial pump with varying number of blades using computational modelling and vibration techniques. Flow Measurement and Instrumentation, 99, 102654.
[4] Alvarado, R. (2022). Computer simulations as scientific instruments. Foundations of Science, 1–23.
[5] Angelidakis, V., Boschi, K., Brzeziński, K., Caulk, R. A., Chareyre, B., Del Valle, C. A., Duriez, J., Gladky, A., Van Der Haven, D. L., Kozicki, J. et al. (2024). Yade-an extensible framework for the interactive simulation of multiscale, multiphase, and multiphysics particulate systems. Computer Physics Communications, 304, 109293.
[6] Becker, M. C., Salvatore, P., & Zirpoli, F. (2005). The impact of virtual simulation tools on problem-solving and new product development organization. Research Policy, 34(9), 1305–1321.
[7] Bera, A., Kumar, S., Foroozesh, J., & Gharavi, A. (2022). Multiphysics gas transport in nanoporous unconventional reservoirs: Challenges of mathematical modelling. Journal of Natural Gas Science and Engineering, 103, 104649.
[8] Bossel, H. (2018). Modeling and Simulation. AK Peters/CRC Press.
[9] Cai, J., Wood, D. A., Hajibeygi, H., & Iglauer, S. (2022). Multiscale and multiphysics influences on fluids in unconventional reservoirs: Modeling and simulation.
[10] Carson, J. S. (2005). Introduction to modeling and simulation. In Proceedings of the Winter Simulation Conference, 2005, IEEE, 8–.
[11] Currie, C. S., Fowler, J. W., Kotiadis, K., Monks, T., Onggo, B. S., Robertson, D. A., & Tako, A. A. (2020). How simulation modelling can help reduce the impact of covid-19. Journal of Simulation, 14(2), 83–97.
[12] Domínguez, J. M., Fourtakas, G., Altomare, C., Canelas, R. B., Tafuni, A., García-Feal, O., Martínez-Estévez, I., Mokos, A., Vacondio, R., Crespo, A. J. et al. (2022). Dualsphysics: From fluid dynamics to multiphysics problems. Computational Particle Mechanics, 9(5), 867–895.
[13] Donnarumma, S., Martelli, M., D'Agostino, F., Kaza, D., & Silvestro, F. (2024). Multiphysics modeling and simulation of integrated electric propulsion system for ship dynamic positioning. IEEE Transactions on Industry Applications.
[14] Gao, Q., Liu, J., & Elsworth, D. (2024). Phenomenal study of microbial impact on hydrogen storage in aquifers: A coupled multiphysics modelling. International Journal of Hydrogen Energy, 79, 883–900.
[15] Garcia-Michelena, P., Ruiz-Reina, E., Herrero-Dorca, N., & Chamorro, X. (2024). Multiphysics modeling and experimental validation of heat and mass transfer for the vacuum induction melting process. Applied Thermal Engineering, 243, 122562.
[16] Guo, Y., Wang, X., Shen, Y., Dong, K., Shen, L., & Alzalab, A. A. A. (2022). Research progress, models and simulation of electrospinning technology: A review. Journal of Materials Science, 1–47.
[17] Heikkinen, T., Johansson, J., & Elgh, F. (2018). Review of cad-model capabilities and restrictions for multidisciplinary use. Computer-Aided Design and Applications, 15(4), 509–519.
[18] Hockney, R. W. & Eastwood, J. W. (2021). Computer Simulation Using Particles. CRC Press.
[19] Hu, G., Ying, S., Qi, H., Yu, L., & Li, G. (2023). Design, analysis and optimization of a hybrid fluid flow magnetorheological damper based on multiphysics coupling model. Mechanical Systems and Signal Processing, 205, 110877.
[20] Huang, D., Xiong, B., Fang, J., Hu, K., Zhong, Z., Ying, Y., Ai, X., & Chen, Z. (2022). A multiphysics model of the compactly-assembled industrial alkaline water electrolysis cell. Applied Energy, 314, 118987.
[21] Jami, A., Razzaghpour, M., Alnuweiri, H., & Fallah, Y. P. (2024). Augmented driver behavior models for high-fidelity simulation study of crash detection algorithms. IET Intelligent Transport Systems, 18(3), 436–449.
[22] Jaśkiewicz, M., Frej, D., Matej, J., & Chaba, R. (2021). Analysis of the head of a simulation crash test dummy with speed motion. Energies, 14(5), 1476.

[23] Javadpour, F., Singh, H., Rabbani, A., Babaei, M., & Enayati, S. (2021). Gas flow models of shale: A review. Energy & Fuels, 35(4), 2999–3010.
[24] Kemppainen, E., Schlatmann, R., & Calnan, S. (2024). Analysis of the effect of operating conditions on the performance of a direct ammonia fuel cell using multiphysics modelling. Journal of the Electrochemical Society, 171(4), 044507.
[25] Kumar, P., Kumar Jain, A., Srivastava, J. P., Kumar, R., Saxena, K. K., Prakash, C., & Buddhi, D. (2024). Multiphysics simulation of the shape prediction and material removal rate in electrochemical machining process. Advances in Materials and Processing Technologies, 10(2), 772–784.
[26] Lanetc, Z., Zhuravljov, A., Armstrong, R. T., & Mostaghimi, P. (2023). Hybrid numerical methods for modelling multi-physics mass transport in coal. International Journal of Heat and Mass Transfer, 214, 124386.
[27] Liu, H., Lan, L., Abrigo, J., Ip, H. L., Soo, Y., Zheng, D., Wong, K. S., Wang, D., Shi, L., Leung, T. W. et al. (2021). Comparison of Newtonian and non-Newtonian fluid models in blood flow simulation in patients with intracranial arterial stenosis. Frontiers in Physiology, 12, 718540.
[28] Magana, A. J. (2017). Modeling and simulation in engineering education: A learning progression. Journal of Professional Issues in Engineering Education and Practice, 143(4), 04017008.
[29] Mayur, M., DeCaluwe, S. C., Kee, B. L., & Bessler, W. G. (2019). Modeling and simulation of the thermodynamics of lithium-ion battery intercalation materials in the open-source software Cantera. Electrochimica Acta, 323, 134797.
[30] Mianroodi, J. R., Shanthraj, P., Liu, C., Vakili, S., Roongta, S., Siboni, N. H., Perchikov, N., Bai, Y., Svendsen, B., Rot Ers, F. et al. (2022). Modeling and simulation of microstructure in metallic systems based on multi-physics approaches. Npj Computational Materials, 8(1), 93.
[31] Plait, A., De Larochelambert, T., Giurgea, S., & Espanet, C. (2022). Experimental validation of a multiphysics modeling for a magnetocaloric bench. Applied Thermal Engineering, 211, 118415.
[32] Ragusa, J. C. (2024). Coupled multiphysics simulations in nuclear reactor design and safety. In Risk-Informed Methods and Applications in Nuclear and Energy Engineering. Elsevier, 91–112.
[33] Rivera, F. F., Pérez, T., Castañeda, L. F., & Nava, J. L. (2021). Mathematical modeling and simulation of electro chemical reactors: A critical review. Chemical Engineering Science, 239, 116622.
[34] Rui, F., Zhao, G.-F., Zhang, Y., Fan, L., & Zhao, X. (2024). Study on the mechanism of rock damage under mi crowave and laser irradiation through multiscale and multiphysics numerical modelling. Rock Mechanics and Rock Engineering, 57(2), 1079–1102.
[35] Prabhaharan S. A., Balaji, G., & Annamalai, K. (2022). Numerical simulation of crashworthiness parameters for design optimization of an automotive crash-box. International Journal for Simulation and Multidisciplinary Design Optimization, 13, 3.
[36] Shi, T., Xu, H., Qi, C., Lei, B., Wu, Y., & Zhao, C. (2021). Multi-physics modeling of thermochemical heat storage with enhance heat transfer. Applied Thermal Engineering, 198, 117508.
[37] Siddiqui, M., Siddiqui, O. K., Alquaity, A. B., Ali, H., Arif, A., & Zubair, S. M. (2022). A comprehensive review on multi-physics modeling of photovoltaic modules. Energy Conversion and Management, 258, 115414.
[38] Singh, P., Singari, R. M., & Mishra, R. (2022). A review of study on modeling and simulation of additive manufac turing processes. Materials Today: Proceedings, 56, 3594–3603.
[39] Sinha, R., Paredis, C. J., Liang, V.-C., & Khosla, P. K. (2001). Modeling and simulation methods for design of engineering systems. Journal of Computing and Information Science in Engineering, 1(1), 84–91.
[40] Somnay, R. & Shih, S. (1999). Product development support with integrated simulation modeling. SAE Transactions, 193–198.
[41] Velten, K., Schmidt, D. M., & Kahlen, K. (2024). Mathematical Modeling and Simulation: Introduction for Scientists and Engineers. John Wiley & Sons.

[42] Wilkins, A., Green, C. P., & Ennis-King, J. (2021). An open-source multiphysics simulation code for coupled problems in porous media. Computers & Geosciences, 154, 104820.
[43] Yan, C., Zhao, Z., Yang, Y., & Zheng, H. (2023). A three-dimensional thermal-hydro-mechanical coupling model for simulation of fracturing driven by multiphysics. Computers and Geotechnics, 155, 105162.
[44] Yildirim, A., Jacobson, K. E., Anibal, J. L., Stanford, B. K., Gray, J. S., Mader, C. A., Martins, J. R., & Kennedy, G. J. (2025). Mphys: A modular multiphysics library for coupled simulation and adjoint derivative computation. Structural and Multidisciplinary Optimization, 68(1), 1–28.
[45] Zhou, J., Chen, D., Deng, M., Deng, Y., Sun, Y., Wang, S., Xiong, S., & Zhu, B. (2024). Eulerian-Lagrangian fluid simulation on particle flow maps. ACM Transactions on Graphics (TOG), 43(4), 1–20.

S. Priyadarshana and J. Mohapatra

Chapter 5
Robust Numerical Methods for Time-Delayed Semilinear Parabolic Problems with a Small Parameter Arising in Fluid Dynamics

Abstract: The work enunciates two robust numerical techniques to solve singularly perturbed semilinear parabolic problems with a large time lag. At first, the semilinearity is treated with the help of Newton's linearization technique. The temporal derivative is handled using the second-order accurate Crank-Nicolson scheme on a uniform mesh. Further, in order to tackle the layer behavior of the solution due to the presence of the perturbation parameter, two-layer rectifying Shishkin-type meshes are used. In combination with the Crank-Nicolson scheme in time, Scheme-I discusses the widely used upwind scheme in the spatial direction, providing a first-order global accuracy. Furthermore, in order to complement the second-order temporal accuracy, a comparatively new difference scheme, namely the monotone hybrid scheme, is discussed in Scheme-II, which is beneficial over many existing schemes in the literature by being a priori and second-order accurate. A comparative study of both schemes is presented with all the necessary existence, uniqueness, and convergence results. Further, the use of the Thomas algorithm makes the proposed schemes computationally more desirable than some existing schemes in the literature.

Keywords: singular perturbation problem, semilinear problem, time delay, Crank-Nicholson scheme, upwind scheme, monotone hybrid scheme

5.1 Introduction

The concept of time-lag is moderately a classical matter of experimentation, tracking back to the contribution of Euler-Bernoulli in the eighteenth century. Other than being a simple mathematical practice, it is persistent in various man-made and natural phenomenon, such as mechatronic motions, process industries, and biology. These lags can capture or predict all the possible after-effects of any elementary system. In biology, it can depict abundant biological events, accounting only for the completion

S. Priyadarshana, Department of Mathematics, National Institute of Technology Warangal Telangana-506004, India, e-mail: sushree@nitw.ac.in
J. Mohapatra, Department of Mathematics, National Institute of Technology, Rourkela 769008, India, e-mail: jugal@nitrkl.ac.in

https://doi.org/10.1515/9783111723464-005

time. It sometimes can represent the time gap amidst the infection of any cell and the formation of new viruses. It can further represent the time span of any biological procedure, like various stages of the life cycle, the life span of the infection period, the gestation and incubation period, the time needed by the body to react toward any medication, or in easier words, it can be the obstructions that happen due to the transport delays [1]. In engineering, time lag usually describes data transmission in communication systems, conduction of energy or material in inter-command systems, and propagation phenomenon [2]. A time lag can happen if any system certainly has a feedback control or, in simpler words, if the system's evolution at a definite time is dependent upon the past history/memory. Typically, these lags are the key reasons to instigate low control performance, oscillations, and instability.

It is evident that the involvement of a time-lag can significantly increase the complexity of any differential equation. An important subclass of the time-delayed differential equations (DDEs) is the time-delayed singularly perturbed parabolic differential equations (SPPDEs) [3, 4], which is the major focus of this work. Along with the time delay, the involvement of a perturbation parameter $0 < \varepsilon \ll 1$ affects the solution to these kinds of problems in larger extent. As the conventional numerical techniques fail to capture this irregular behavior on a uniform mesh, it has gone through generations of experimentation and generalization to formulate some robust fitted mesh methods (FMMs) for the solution of these time-delayed SPPDEs [5, 6]. The numerical solution to a semilinear time delayed SPPDE is discussed in this chapter. Before discussing the problem, some basic notations are put forward as:

Define $G = G \cup \partial G$, where $G = (0,1) \times (0,T]$ and $\partial G = B_d \cup B_l \cup B_r$, with $B_d = [0,1] \times [-\tau, 0]$, $B_l = 0 \times [0,T]$, and $B_r = 1 \times [0,T]$. G_z and G_ζ are the corresponding spatial and temporal domains. SPPDDE of the following form is considered:

$$\begin{cases} L\omega \equiv \left(\omega_\zeta + L_\varepsilon \omega\right)(x,\zeta) \\ \qquad = \left(\omega_\zeta - \varepsilon\omega_{zz} - a(z)\omega_z + b(z)\omega\right)(x,\zeta) = \omega(z,\zeta-\tau) + f(z,\zeta,\omega(z,\zeta)) \text{ in } G \\ \omega|_{B_d} = \phi_d(x,\zeta),\ \omega|_{B_l} = \phi_l(\zeta),\ \omega|_{B_r} = \phi_r(\zeta), \end{cases} \tag{5.1}$$

where $0 < \varepsilon \ll 1$ and $\tau > 0$ are the notions used to denote the perturbation parameter and temporal lag. $T = i\tau$ for $i \in M$ is the terminal time. The used coefficients satisfy $0 < \alpha \le a(z) \le \alpha^*$, $0 < \beta \le b(z) \le \beta^*$ and considered to be sufficiently smooth. As $\varepsilon \to 0$, the solution undergoes a rapid change near $z = 0$ creating a layer of $O(\varepsilon)$.

It has gone through numerous experimentations, generalizations, and extensions over the past few decades to formulate some efficient parameter-uniform numerical schemes based on some locally refined meshes for the afore-mentioned problems. Notably, Kaushik and Sharma in [7] used an upwind-based scheme and later investigated the use of discrete invariant imbedding algorithm. Das and Natesan in [8] used a hybrid scheme (HYB scheme) on the piecewise-uniform Shishkin-mesh (S-mesh) in space and the implicit Euler scheme (IE scheme) on a uniform mesh in time. A first-order

globally accurate scheme over the S-mesh in the spatial direction is discussed by Gowrisankar and Natesan [9]. Govindrao et al. [10], developed a global second-order convergent scheme by using the Crank-Nicolson scheme (C-N scheme) in the time direction along with the HYB scheme discussed in [8]. In [11], a collocation method consisting of cubic B-spline basis functions on an appropriate piecewise-uniform mesh is used to discretize the system of ordinary differential equations obtained by using Rothe's method on an equidistant mesh in the temporal direction. One can also go through [12, 13], where Priyadarshana et al. have solved several time-delayed 1D SPPDEs using some efficient numerical techniques on various S-type meshes. One can go through the references therein for more such works on time-delayed SPPDEs. A thorough survey of the literature proves the infant stage of the numerical experimentation upon semilinear form of the afore mentioned problems.

Our work functions as a bridge to fill this gap in the literature. Two efficient numerical approximations are discussed in this chapter to solve (5.1). The temporal derivative for both schemes is approximated with the second-order accurate C-N scheme. As the formation of layers is independent of the temporal variable, the discretization is done over a uniform mesh in time. Further, two-layer rectifying meshes are used in the spatial domain, in order to capture the layer behavior of the solution that happens because of the perturbation parameter being multiplied with the height order spatial derivative term. The renowned S-mesh and a modified version of Shishkin-type mesh, namely the Bakhvalov–Shishkin mesh (B-S-mesh), are used for spatial discretization. In Scheme-I, the upwind scheme (UP scheme) and in Scheme-II, a monotone hybrid scheme (M.HYB scheme) are used to approximate the spatial derivative terms. The UP scheme is quite established in the literature, providing an almost first-order accuracy when applied over S-mesh. Further, the M.HYB scheme is dependent upon a weighted variable which changes a prescribed monotone scheme from the central difference scheme (CEN scheme) to the mid-point upwind scheme (M.UP scheme) by judging the mesh-widths, which is the intuitive expectation from a hybrid scheme (HYB scheme). The chapter consists of six different sections. In Section 5.2, a detailed discussion on the asymptotic nature of the proposed problem is given, along with some quintessential bounds that are needed for the convergence analysis later. Along with the construction of the layer-resolving meshes, Section 5.4 discusses the details of both the proposed schemes, followed by their respective stability analysis. The detailed convergence analyses of both the proposed schemes are given in Section 5.4. The theoretical outcomes are corroborated in practice with valid numerical tests in Section 5.5, followed by a brief conclusion in Section 5.6.

5.2 Asymptotic Nature of the Analytic Solution

Some necessary estimates and bounds on the solution of (5.1) and its components are discussed in this section, which are quintessential for convergence and stability analyses later. The idea of lower and upper solutions mentioned in [14] can be followed to derive the below-mentioned results:

$$\breve{\omega}_\zeta - \varepsilon\breve{\omega}_{zz}(z,\zeta) - a(z)\breve{\omega}_z(z,\zeta) + b(z)\breve{\omega}_z(z,\zeta) \geq \hat{\omega}_\zeta - \varepsilon\hat{\omega}_{zz}(z,\zeta) - a(z)\hat{\omega}_z(z,\zeta) + b(z)\hat{\omega}_z(z,\zeta),$$

$\breve{\omega}$ and $\hat{\omega}$ signify the lower and upper solutions of (5.1), respectively. Further, for $\omega \in \langle\breve{\omega}, \hat{\omega}\rangle$ the weaker assumption $f_\omega(z,\zeta,\omega) \geq 0$ in G, problem (5.1) has a unique solution.

Lemma 5.2.1: Let $\Theta(z,\zeta), \Psi(z,\zeta)$ are two times differentiable in x, once in t, and satisfy $L\Theta \leq L\Psi$ in G, $\Theta \leq \Psi$ on ∂G, where L is the operator defined in (5.1). Then, $\Theta \leq \Psi$ in $\bar{G}$.

Proof: The lemma will be proved by the method of contradiction. Let, (z^*, ζ^*) be a point in G such that $(\Theta - \Psi)(z^*, \zeta^*) = \max_{(z,\zeta)\in G}(\Theta - \Psi)(z,\zeta)$. In $[0,\tau]$ clearly, $(\Theta - \Psi)''\Big|_{(z^*,\zeta^*)} \leq 0$, $(\Theta - \Psi)'\Big|_{(z^*,\zeta^*)} = 0$, and $(\Theta - \Psi)''\Big|_{(z^*,\zeta^*)} > 0$. In the right-hand side, as $\Theta \leq \Psi$ on ∂G is given, so we have $(\Theta - \Psi)(z^*, \zeta^* - \tau) \geq 0$ for $\omega(z^*, \zeta^* - \tau) \in \partial G$. Again, $f(z^*, \zeta^*, \Theta) - f(z^*, \zeta^*, \Psi) = f_\omega(z^*, \zeta^*, \xi)(\Theta - \Psi)(z^*, \zeta^*) > 0$ as $f_\omega > 0$, taking ξ as an intermediate value between Θ and Ψ. Hence, we get $L(\Theta - \Psi) > 0$, which is a contradiction to our given statement. Hence, $\Theta \leq \Psi$ in $\bar{G}$. A similar proof is given in [15].

5.2.1 The Reduced Problem After Quasilinearization

With an initial approximation, i.e., $\omega^{(0)}(z,\zeta)$ in $f(z,\zeta,\omega)$, the Newton's linearization algorithm is used to treat the semilinearity (5.1). On further rearrangement, we have

$$\begin{cases} L\omega \equiv (\omega_\zeta + L_\varepsilon\omega)(x,\zeta) \\ \quad \cong \omega_\zeta^{(n+1)}(x,\zeta) - \varepsilon\omega_{zz}^{(n+1)}(x,\zeta) - a(z)\omega_z^{(n+1)}(x,\zeta) + B(z,\zeta)\omega^{(n+1)}(x,\zeta) \\ \quad = \omega^{(n+1)}(x,\zeta-\tau) + F(z,\zeta)\cdot \end{cases} \tag{5.2}$$

$B(z,\zeta) = b(z) + \dfrac{\partial f}{\partial\omega}\Big|_{(z,t,\omega^{(n)})}$ and $F(z,\zeta) = f\left(z^*, \zeta^*, \omega^{(n)}\right) - \omega^{(n)}\dfrac{\partial f}{\partial\omega}\Big|_{(z^*,\zeta^*,\omega^{(n)})}$. The initial and boundary conditions are identical as in (5.1). The stopping criterion is as follows:

$$\max_{(z_m,\zeta_k)\in G}\left|W^{(n+1)}(z_m,\zeta_k) - W^{(n)}(z_m,\zeta_k)\right| \leq \mathbf{TOL}\cdot$$

Sufficient smoothness of $\phi_d(z,\zeta), \phi_l(\zeta),$ and $\phi_r(\zeta)$ are considered along with the compatibility conditions at the corners and delayed region as

$$\begin{cases} \dfrac{d\phi_l(0)}{d\zeta} - \varepsilon\dfrac{\partial\phi_d(0,0)}{\partial z^2} - a(0)\dfrac{d\phi_d(0,0)}{d\zeta} + B(0,0)\phi_d(0,0) = \phi_d(0,-\tau) + F(0,0) \\ \dfrac{d\phi_r(0)}{d\zeta} - \varepsilon\dfrac{\partial\phi_d(1,0)}{\partial z^2} - a(1)\dfrac{d\phi_d(1,0)}{d\zeta} + B(1,0)\phi_d(1,0) = \phi_d(1,-\tau) + F(1,0)\cdot \end{cases}$$

Lemma 5.2.2: The following estimates are valid for the solution to (5.2):

$$|\omega(z,\zeta) - \phi_d(z,0)| \le \rho\zeta \text{ and } |\omega(z,\zeta)| \le \rho.$$

Proof: Assume

$$u(z,\zeta) = \begin{cases} |\omega(z,\zeta) - \phi_d(z,0)|, & 0 \le \zeta \le T \\ |\omega(z,\zeta) - \phi_d(z,0)|, & -\tau \le \zeta \le 0\cdot \end{cases}$$

Such that $u(z,\zeta)$ satisfies

$$\begin{cases} \left(\dfrac{\partial}{\partial\zeta} + L_\varepsilon\right)u(z,\zeta) = v(z,\zeta) \\ v(z,\zeta) = \phi_d(z,-\tau) + F(z,\zeta) - \left(\dfrac{\partial}{\partial\zeta} + L_\varepsilon\right)\phi_d(z,0)\cdot \end{cases}$$

and

$$\begin{cases} u|_{B_d} = 0 \\ u|_{B_l} = \phi_l(\zeta) - \phi_d(0,0) \\ u|_{B_r} = \phi_r(\zeta) - \phi_d(1,0)\cdot \end{cases}$$

With arbitrary constants ρ_1 and ρ_2, one can obtain $|u(0,\zeta)| \le \rho_1\zeta$ and $|u(1,\zeta)| \le \rho_2\zeta$, $\zeta \in [0,T]$ with the help of compatibility conditions. Furthermore, setting

$$y(z,\zeta) = \begin{cases} \rho\zeta, & 0 \le \zeta \le T \\ 0, & -\tau \le \zeta \le 0\cdot \end{cases}$$

And for any ε-independent ρ, we get

$$\begin{cases} \left(\dfrac{\partial}{\partial\zeta} + L_\varepsilon\right)y(z,\zeta) = (1 + \rho B(z,\zeta))\zeta \\ y(z,\zeta) = 0 \text{ on } B_d \\ y(0,\zeta) = y(1,\zeta) = \rho\zeta \text{ for } 0 \le \zeta \le T\cdot \end{cases}$$

Now, $\left|\left(\frac{\partial}{\partial\zeta}+L_\varepsilon\right)u(z,\zeta)\right| \le \left(\frac{\partial}{\partial\zeta}+L_\varepsilon\right)y(z,\zeta)$ and $|u(z,\zeta)| \le y(z,\zeta)$ on B_d. As $|u(z,\zeta)| \le y(z,\zeta)$ on $\bar{G}$, one can show $|u(z,\zeta)| \le \rho\zeta$ on $\bar{G}$, using Lemma 5.2.1. The second inequality follows immediately as $\zeta \in [0,T]$.

Theorem 5.2.3: *For $i,j \ge 0$ and $0 \le i+j \le 5$, the solution to* (5.2) *satisfies*

$$\left|\frac{\partial^{i+j}\omega}{\partial z^i \partial\zeta^j}\right| \le \left(1+\varepsilon^{-i\exp(-\beta z/\varepsilon)}\right).$$

Proof: The proof can be done in an analogous approach as mentioned in [8].

5.2.2 Properties of the Solution to the Reduced Problem

As the conventional process fails to conclude the parameter-uniform error estimates, the solution to equation (2.1) is split into its outer and boundary layer components as $\omega(z,\zeta) = r(z,\zeta) + s(z,\zeta)$, so that the error estimates can be calculated component-wise using the truncation error and barrier function approach.The smooth component satisfies:

$$r(z,\zeta) = \sum_{p=0}^{4} \varepsilon^p r_p(z,\zeta),$$

where $r_p(z,\zeta), p = 0,1,2,\ \ldots,\ 4$, satisfy the following time-delayed IBVPs:

$$\begin{cases} -a(z)(r_0)_z(z,\zeta) + B(z,\zeta)r_0(z,\zeta) + (r_0)_\zeta(z,\zeta) = r_0(z,\zeta-\tau) + F(z,\zeta) \text{ in } G \\ r_0|_{B_d} = \phi_d(z,\zeta) \\ r_0|_{B_r} = \phi_r(\zeta) \text{ for } 0 \le \zeta \le T, \end{cases} \tag{5.3}$$

$$\begin{cases} -a(z)\left(r_p\right)_z(z,\zeta) + B(z,\zeta)r_p(z,\zeta) + \left(r_p\right)_\zeta(z,\zeta) = r_p(z,\zeta-\tau) + \left(r_{p-1}\right)_{zz} \text{ in } G \\ r_p|_{B_d} = 0 \\ r_p|_{B_r} = 0, \text{ for } 0 \le \zeta \le T, \text{ for } p = 1,2,3, \end{cases} \tag{5.4}$$

$$\begin{cases} (r_4)_\zeta(z,\zeta) + L_\varepsilon(z,\zeta)r_4(z,\zeta) = r_4(z,\zeta-\tau) + (r_3)_{zz} \text{ in } G \\ r_4|_{B_d} = 0 \\ r_4|_{B_r} = r_4|_{Bl} = 0, \text{ for } 0 \le \zeta \le T\cdot \end{cases} \tag{5.5}$$

So the outer component satisfies

$$\begin{cases} \left(r_\zeta + L_\varepsilon r\right)(z,\zeta) = r(z,\zeta-\tau) + F(z,\zeta) \text{ in } G \\ r|_{B_d} = \phi_d(z,\zeta) \\ r|_{B_l} = \sum_{p=0}^{4} \varepsilon^p (r)_p(0,\zeta) \\ r|_{B_r} = \phi_r(1,\zeta) \text{ for } 0 \le \zeta \le T \cdot \end{cases} \tag{5.6}$$

Now, the layer component satisfies

$$\begin{cases} \left(s_\zeta + L_\varepsilon s\right)(z,\zeta) = s(z,\zeta-\tau) \text{ in } G \\ s|_{B_d} = 0 \\ s|_{B_l} = \omega(0,\zeta) - r(0,\zeta) \text{ for } 0 \le \zeta \le T \\ s|_{B_r} = 0 \text{ for } 0 \le \zeta \le T \cdot \end{cases} \tag{5.7}$$

Theorem 5.2.4: *With enough compatibility at the corners of G, consider* $i,j \ge 0$ *satisfying* $0 \le i+j \le 5$. *Then, r and s satisfy*

$$\left|\frac{\partial^{i+j} r(z,\zeta)}{\partial z^i \partial \zeta^j}\right|_\infty \le \rho\left(1+\varepsilon^{4-i}\right), \left|\left|\frac{\partial^{i+j} s(z,\zeta)}{\partial z^i \partial \zeta^j}\right|\right|_\infty \le \rho\varepsilon^{-i}\exp(-\alpha z/\varepsilon) \cdot$$

Proof: The statement is straightforward for the outer region components with $p = 0,1,2,3$, as (5.3) and (5.4) are ε–independent. Hence, the below-mentioned bounds can be obtained for r_p, $p = 0,1,2,3$:

$$\left|\frac{\partial^{i+j} r(z,\zeta)}{\partial z^i \partial \zeta^j}\right|_\infty \le \rho \cdot$$

Here, (5.5) is in similar form as (5.2). Hence, r_4 satisfies the bounds discussed in Theorem 5.2.3. Further, by accumulating the bounds for the derivatives of r_p, $p = 0,1, \ldots, 4$, one can get

$$\left|\frac{\partial^{i+j} r(z,\zeta)}{\partial z^i \partial \zeta^j}\right|_\infty \le \rho\left(1+\varepsilon^{4-i}\right) \cdot$$

Now, $s(z,\zeta)$ in (5.7) satisfies the bounds of $\omega(z,\zeta)$ in $G_z \times [0,\tau]$. So, following [16] for $G_z \times [0,\tau]$, the bounds for $s(z,\zeta)$ can be obtained as

$$\left|\left|\frac{\partial^{i+j} s(z,\zeta)}{\partial z^i \partial \zeta^j}\right|\right|_\infty \le \rho\varepsilon^{-i}\exp(-\alpha z/\varepsilon) \text{ for } (z,\zeta) \in G_z \times [0,\tau] \cdot \tag{5.8}$$

Extending the ideas to $G_z \times [0,2\tau]$ and taking $i = j = 0$, consider a barrier function $\Psi^{\pm}(z,\zeta) = \rho\exp(-\alpha z/\varepsilon) \pm s(z,\zeta)$. For sufficiently large ρ, we have $\Psi^{\pm} \ge 0$ on $\partial\bar{G}$. Hence,

$$L(\Psi^{\pm})(z,\zeta) = \left[\frac{\partial}{\partial\zeta} - \varepsilon\frac{\partial^2}{\partial z^2} - a(z)\frac{\partial}{\partial z} + B(z,\zeta)\right]\Psi^{\pm}(z,\zeta)$$
$$= \rho\exp(-\alpha z/\varepsilon)\left[\frac{\alpha^2}{\varepsilon} + \frac{a(z)\alpha}{\varepsilon} + B(z,\zeta)\right] \pm L(s(z,\zeta))$$
$$= \rho\exp(-\alpha z/\varepsilon)\left[\frac{\alpha^2}{\varepsilon} + \frac{a(z)\alpha}{\varepsilon} + B(z,\zeta)\right] \pm s(z,\zeta-\tau)\cdot$$

Using (5.8), $a(z) \geq \alpha \geq 0$ and enough large ρ, we have

$$L(\Psi^{\pm})(z,\zeta) \text{ on } G_z \times [0,2\tau].$$

Now, using Lemma 5.2.1, we have $\Psi^{\pm}(z,\zeta) \geq 0$ and consequently $|s(z,\zeta)| \leq \rho\exp(-\alpha z/\varepsilon)$. All other bounds can be obtained by following an identical procedure and the argument in [16].

5.3 Numerical Estimations

A detailed discussion on the approximation of (5.2) through two different numerical schemes is given in this section. Along with the difference schemes, their respective stability analysis is discussed thoroughly.

The entire rectangular domain $\bar{G}$ is decomposed into two sub-domains namely, $G_1 = (0,1)\times[0,\tau]$ and $G_2 = (0,1)\times[\tau,2\tau]$. This decomposition makes the numerical estimation and convergence analysis quite easy and distinguishable. It is noteworthy to mention that the nature of $w(z,\zeta)$ in G_1 depends upon the known conditions in $\partial G^{K.M}$ and therefore can be treated as any SPP without time-lag. The solution and convergence in G_2 is analyzed thoroughly as for any domain $[(i-1)\tau, i\tau]$ with $i > 2$, the discussions will be analogous to G_2.

5.3.1 Temporal Semidiscretization

The temporal variable is approximated through a uniform mesh with step length $\Delta\zeta$. The discretized temporal domain is $\bar{G}_\zeta^K = [-\tau, 2\tau = T]$ such that

$$G_\zeta^{K_1} = \left\{\zeta_{K-K_1} = -\tau + k\Delta\zeta, k = 0,1\ldots K_1, \zeta_{-K_1} = -\tau, \Delta\zeta = \tau/K_1\right\}$$
$$G_\zeta^{K_2} = \left\{\zeta_K = k\Delta\zeta, k = 0,1\ldots K_2, \zeta_{K_2} = T, \Delta\zeta = T/K_2\right\}\cdot$$

The total count of mesh points in $\bar{G}_\zeta^K$ is $K = (K_1 + K_2)$, where K_1 and K_2 are the count of mesh intervals in $[-\tau, 0] = \bar{G}_\zeta^{K_1}$ and $[0, T] = \bar{G}_\zeta^{K_2}$, respectively. The application of the C-N scheme on (5.2) at $(k+1)^{\text{th}}$ is

$$\begin{cases} L^K\hat{\omega} \cong \left(I + \dfrac{\Delta\zeta}{2}L_\varepsilon{}^K\right)\hat{w}^{k+1}(z) \\ \qquad = \dfrac{\Delta\zeta}{2}\left(\hat{w}^{k+1-K_1}(z) + \hat{w}^{k-K_1}(z) + F^{k+1}(z) + F^k(z)\right) + \left(I + \dfrac{\Delta\zeta}{2}L_\varepsilon{}^K\right)\hat{w}^k(z), \\ \hat{\omega}|_{B_d} = \phi_d\left(z, \zeta_{k+1-K_1}\right), \quad k = K_1, K_1+1, \ldots, K \\ \hat{\omega}|_{B_1} = \phi_1(\zeta_{k+1})\hat{\omega}|_{B_r}, \qquad k = K_1, K_1+1, \ldots, K. \end{cases} \tag{5.9}$$

5.3.2 Spatial Discretization

$\mu \geq 0$ is considered to be the transition parameter and M is the total count of spatial mesh intervals. With $\mu_0 \geq 2/\alpha$, the transition parameter is:

$$\mu = \min\left(\frac{1}{2}, \mu_0\varepsilon \ln M\right).$$

Due to singularity in the solution of (5.1), a layer with width $O(\varepsilon)$ $O(\varepsilon)$ is formed near the narrow region of $z = 0$. $\bar{G}_z^M$ is henceforth split into two identical subdomains, namely, [0, μ] $[0, \mu]$ and $[\mu, 1]$ [17, 18]. With $z_0 = 0, z_{M/2} = \mu$ and $z_m = 1$. $\bar{G}_z^M$ is

$$\bar{G}_z^M = \left\{z_0 = 0, z_1, z_2, \ldots, z_{M/2} = \mu, \ldots, z_m = 1\right\}.$$

Let $z_m = mh_m$ with $h_m = z_m - z_{m-1}$. S-mesh [19] is

$$z_m = \begin{cases} m\frac{2\mu}{M} & \text{for} \quad m = 1, 2, \ldots, \frac{M}{2} \\ \mu + \frac{2(1-\mu)}{M}(m - M/2) & \text{for} \quad m = \frac{M}{2} + 1, \ldots, (M-1) \end{cases}$$

and B-S-mesh [20] is

$$z_m = \begin{cases} -\mu_0\varepsilon \ln[1 - (2(1-1/M)(m/M))] & \text{for} \quad m = 1, 2, \ldots, \frac{M}{2} \\ \mu + \frac{2(1-\mu)}{M}(m - M/2) & \text{for} \quad m = \frac{M}{2} + 1, \ldots, (M-1) \end{cases}$$

5.3.2.1 Scheme-I

$G^{K,M}$ is the discretized rectangular domain of discussion with K and M number of mesh intervals in time and space direction, respectively. The fully-discrete form of (5.2) in $G^{K,M}$, using the C-N UP scheme is

$$\begin{cases} L_{\text{up}}^{K,M} W_m^{k+1} = 2D_\zeta^- W_m^{k+1} + L_{\text{up}}^M W_m^{k+1} = \\ W_m^{k+1-K_1} + W_m^{k-K_1} + F_m^{k+1} + F_m^k - L_{\text{up}}^{K,M} W_m^k, \ m = 1, 2, \ldots, (M-1) \\ W_m^{-k} = \phi_d(z_m, -\zeta_k), \ k = 0, 1, \ldots, K_1 \text{ and } m = 1, 2, \ldots, M \\ W_0^{k+1} = \phi_I(\zeta_{k+1}), \ W_m^{k+1} = \phi_r(\zeta_{k+1}), \ k = K_1, K_1+1, \ldots, K, \end{cases} \tag{5.10}$$

where

$$L_{\text{up}}^{K,M} W_m^{k+1} = \left(-\varepsilon D_z^+ D_z^- - a_m D_z^+ + B_m^{k+1} \right) W_m^{k+1}.$$

The used operators are quite standard in the literature; one can follow [5,13] and the references therein for the details. Now, rearranging the terms, we have:

$$\begin{cases} A_{\text{up},m}^- W_{m-1}^{k+1} + A_{\text{up},m}^c W_m^{k+1} + A_{\text{up},m}^+ W_{m+1}^{k+1} \\ = \dfrac{1}{2} \left[W_m^{k+1-K_1} + W_m^{k-K_1} + F_m^{k+1} + F_m^k - L_{\text{up}}^{K,M} W_m^k \right] + \dfrac{W_m^k}{\Delta\zeta}, \ m = 1, 2, \ldots, (M-1) \\ W_m^{-k} = \phi_d(z_m - \zeta_k), k = 0, 1, \ldots, K_1 \text{ and } m = 0, 1, \ldots, M \\ W_0^{k+1} = \phi_I(\zeta_{k+1}), \ W_m^{k+1} = \phi_r(\zeta_{k+1}), \ k = K_1, K_1+1, \ldots, K. \end{cases} \tag{5.11}$$

The coefficients are given by

$$\begin{cases} A_{\text{up},m}^+ = \left[\dfrac{2\varepsilon}{h_m h_{m+1}} + \dfrac{a_m^{k+1}}{h_{m+1}} \right] \\ A_{\text{up},m}^c = \left[\dfrac{2\varepsilon}{h_m h_{m+1}} + \dfrac{a_m^{k+1}}{h_{m+1}} + B_m^{k+1} \right] + \dfrac{1}{\Delta\zeta} \\ A_{\text{up},m}^- = -\dfrac{\varepsilon}{h_m h_m}. \end{cases}$$

5.3.3 Stability Result for Scheme-I

Lemma 5.3.1: *The coefficient matrix A_{up} associated with (5.11) is an M-matrix.*

Proof: The matrix formed in (5.11) is tridiagonal with $A_{\text{up},m}^+ < 0$, $A_{\text{up},m}^c > 0$, $A_{\text{up},m}^- < 0$, and $|A_{\text{up},m}^c| \geq |A_{\text{up},m}^+| + |A_{\text{up},m}^-|$, $m = 1, 2, \ldots, (M-1)$. Hence, proves the claim.

Lemma 5.3.2: *The discrete function $\Theta(z_m, \zeta_k)$ satisfying $\Theta(z_m, \zeta_k) \geq 0$ on $\partial \bar{G}^{K,M}$ and $L_{up}^{K,M} \Theta(z_m, \zeta_k) \leq 0$ on $(z_m, \zeta_k) \in G^{k,M}$ implies $\Theta(z_m, \zeta_k) \geq 0$ at each point $(z_m, \zeta_k) \in \bar{G}^{k,M}$.*

Proof: Let (z_m^*, ζ_k^*) be the index, such that

$$\Theta(z_m^*, \zeta_k^*) = \min_{(z_m, \zeta_k) \in G^{K,M}} \Theta(z_m, \zeta_k) < 0$$

Clearly, $(z_m^*, \zeta_k^*) \notin \partial G^{K,M}$. Again, $\Theta(z_m^*, \zeta_k^*) - \Theta(z_m^*, \zeta_{k-1}^*) < 0$ and $\Theta(z_m^*, \zeta_k^*) - \Theta(z_{m-1}^*, \zeta_{k-1}^*) < 0$. Henceforth, a contradiction arises as $\left(I + \frac{\Delta\zeta}{2} L_{up}^{K,M}\right)\Theta(z_m, \zeta_k) \geq 0$ on $G^{k,M}$. Hence, the proof is complete.

Lemma 5.3.3: *For $m = 0, 1, \ldots, M$ and for fixed time at $(k+1)^{th}$ level, define a mesh function as $\psi(z_m, \zeta_{k+1}) = \psi_m^{k+1} \prod_{k=1}^{m} \left[1 + \frac{ah_k}{\varepsilon}\right]^{-1}$ with $\psi_0^{k+1} = 1$. Then, for $m = 1, 2, \ldots, M$, we have $L_{up}^{K,M} \psi_m^{k+1} \geq \frac{C}{\max(\varepsilon, h_{m+1})} \psi_m^{k+1}$.*

Lemma 5.3.4: *For $m = 1, 2, \ldots, (M-1)$,we have* $\exp(-\alpha z_m/\varepsilon) \leq \prod_{k=1}^{n} \left[1 + \frac{ah_k}{\varepsilon}\right]^{-1}$.

Proof: For any m, $\left[1 + \frac{ah_k}{\varepsilon}\right]^{-1} \geq \exp(-\alpha z_m/\varepsilon)$. So, $\prod_{k=1}^{n} \left[1 + \frac{ah_k}{\varepsilon}\right]^{-1} \geq \prod_{k=1}^{m} \exp(-\alpha h_k/\varepsilon) = \exp(-\alpha z_m/\varepsilon)$.

5.3.3.1 Scheme-II

The complete-discrete form of (5.2) after using the C-N-M.HYB scheme on (5.9) is

$$\begin{cases} L_{\text{up}}^{K,M} W_m^{k+1} = 2D_\zeta^- W_m^{k+1} + L_{\text{up}}^M W_m^{k+1} = \\ W_{v,m-1/2}^{k+1-K_1} + W_{v,m-1/2}^{k-K_1} + F_{v,m-1/2}^{k+1} + F_{v,m-1/2}^{k} - L_{mh}^M W_m^k, \ \ m = 1, 2, \ldots, (M-1) \\ W_m^{-k} = \phi_d(z_m, -\zeta_k), \ k = 0, 1, \ldots, K_1 \ \text{ and } \ m = 1, 2, \ldots, M \\ W_0^{k+1} = \phi_I(\zeta_{k+1}), \ W_m^{k+1} = \phi_r(\zeta_{k+1}), \ k = K_1, K_1+1, \ldots, K, \end{cases} \tag{5.12}$$

where

$$\begin{cases} L_{mh}^M W_m^{k+1} = \dfrac{[QW]_{m+1}^{k+1} - [QW]_m^{k+1}}{h_{v,n}} + (BW)_{v,m-1/2}^{k+1} \\ F_{v,m-1/2}^{k+1} = \dfrac{F_{m-1}^{k+1}(1-v_m) - F_m^{k+1}(1+v_m-v_{m+1}) + F_{m+1}^{k+1}(v_{m+1})}{2}, \\ [QW]_m^{k+1} = \varepsilon D_z^- W_m^{k+1} + v_m a_m W_m^{k+1} + (1-v_m) a_m W_{m-1}^{k+1} \\ h_{v,m} = (1-v_m) h_m v_{m+1} h_{m+1}. \end{cases}$$

$W_{v,m-1/2}^{k+1}$ is derived in a similar way as $F_{v,m-1/2}^{k+1}$. The variable weight $v_m, m = 1, 2, \ldots, (M-1)$, is chosen as mentioned in [16], i.e.,

$$v_m = \begin{cases} 1/2, & \text{if } 1/2 \geq (1-\varepsilon/h_m a_{m-1}) \\ 1, & \text{if } 1/2 < (1-\varepsilon/h_m a_{m-1}), \end{cases}$$

where by fixing $v = 1/2$ and $v = 1$, the scheme reacts as the CEN scheme and the M. UP scheme, respectively. After suitable rearrangement, the below-mentioned form can be obtained:

$$\begin{cases} A^{-}_{mh,m} W^{k+1}_{m-1} + A^{c}_{mh,m} W^{k+1}_{m} + A^{+}_{mh,m} W^{k+1}_{m+1} = \\ W^{k+1-K_1}_{v,m-1/2} + W^{k-K_1}_{v,m-1/2} + F^{k+1}_{v,m-1/2} + F^{k}_{v,m-1/2} - L^{M}_{mh} W^{k}_{m}, \quad m = 1,2,...,(M-1) \\ W^{-k}_{m} = \phi_d(z_m - \zeta_k), k = 0,1,\ldots,K_1 \text{ and } m = 0,1,\ldots,M \\ W^{k+1}_{0} = \phi_I(\zeta_{k+1}), \quad W^{k+1}_{m} = \phi_r(\zeta_{k+1}), \quad k = K_1, K_1+1,\ldots,K. \end{cases} \tag{5.13}$$

The corresponding coefficient matrix is:

$$\begin{cases} A^{+}_{mh,m} = \dfrac{1}{2}\left[\dfrac{-1}{h_{v,n}}\left(\dfrac{\varepsilon}{h_{m+1}} + v_{m+1}a_{m+1}\right) + \dfrac{B^{k+1}_{m+1}}{2} v_{m+1}\right] + \dfrac{1}{\Delta\zeta} v_{m+1} \\ A^{c}_{mh,m} = \dfrac{1}{2}\left[\dfrac{1}{h_{v,n}}\left(\dfrac{\varepsilon}{h_m} + \dfrac{\varepsilon}{h_{m+1}} - (1-v_m-v_{m+1})a_m\right) + \dfrac{B^{k+1}_{m}}{2}(1+v_m-v_{m+1})\right] + \dfrac{1}{\Delta\zeta}(1+v_m-v_{m+1}) \\ A^{-}_{mh,m} = \dfrac{1}{2}\left[\dfrac{-1}{h_{v,n}}\left(\dfrac{\varepsilon}{h_m} - (1-v_m)a_{m-1}\right) + \dfrac{B^{k+1}_{m-1}}{2}(1-v_m)\right] + \dfrac{1}{\Delta\zeta}(1-v_m). \end{cases}$$

5.3.4 Stability Result for Scheme-II

Lemma 5.3.5: Assume that there exists $M_0 > 0$ such that for $M > M_0$

$$\begin{cases} \dfrac{M_0}{\ln M_0} \geq \mu_0 \|a\|_\infty \\ \left(\|B\|_\infty + 2\Delta\zeta^{-1}\right) \leq \alpha M \end{cases}$$

then, we have

$$\begin{cases} A^{-}_{mh,m} < 0, A^{+}_{mh,m} < 0 \quad \text{for } 1 \leq m \leq (M-1) \\ \left|A^{c}_{mh,1}\right| - \left|A^{+}_{mh,1}\right| \geq 0, \quad \left|A^{c}_{mh,m}\right| - \left|A^{-}_{mh,m}\right| - \left|A^{+}_{mh,m}\right| \geq 0, \quad 1 < m < M/2 \\ \left|A^{c}_{mh,M-1}\right| - \left|A^{-}_{mh,M-1}\right| > 0, \quad \left|A^{c}_{mh,m}\right| - \left|A^{-}_{mh,m}\right| - \left|A^{+}_{mh,m}\right| > 0, \quad M/2 < m < (M-1). \end{cases}$$

Proof: The proof is similar to the proof given in [8].

Lemma 5.3.6: With $\Theta(z_m,\zeta_k)\geq 0$ an $(z_m,\zeta_k)\in\partial G^{K,M}$, $\left(I+\frac{\Delta\zeta}{2}L_{mh}^{K,M}\right)\Theta(z_m,\zeta_k)\geq 0$ on $G^{K,M}$ implies $\Theta(z_m,\zeta_k)\geq 0$ on $G^{K,M}$.

Proof: The argument mentioned in Lemma 5.3.2 can be followed to proof the statement.

5.4 Error Estimates

5.4.1 Temporal Error Estimate

Lemma 5.4.1: Let $\left|\frac{\partial^j w}{\partial\zeta^j}\right|\leq\rho,(z,\zeta)\in g,0\leq j\leq 3$. The local truncation error at ζ_{k+1} with respect to (5.9) is $\|e_{k+1}\|_\infty\leq\rho(\Delta\zeta)^3$.

Proof: The semidiscrete equation in (5.9) on $\bar{G_\zeta}^k$ at $(z,\zeta_{k+0.5})$ is

$$\begin{cases} L^K\hat{\omega}(z,\zeta_{k+0.5})\cong(\hat{\omega}_\zeta-\varepsilon\hat{\omega}_{zz}-a(z)\hat{\omega}_z+\mathrm{B}(z,\zeta_{k+0.5})\hat{\omega})(z,\zeta_{k+0.5}) \\ \qquad\qquad =\hat{\omega}(z,\zeta_{k+0.5-K_1})F(z,\zeta_{k+0.5}) \\ \hat{\omega}\Big|_{\beta_d}=\phi_d(z,\zeta_{k+0.5}),\hat{\omega}\Big|_{\beta_l}=\phi_l(\zeta_{k+0.5}),\hat{\omega}\Big|_{\beta_r}=\phi_r(\zeta_{k+0.5})\cdot \end{cases} \tag{5.14}$$

Taylor series expansion around $(z,\zeta_{k+0.5})$ gives

$$\hat{\omega}(z,\zeta_{k+1})=(\hat{\omega}+\frac{\Delta\zeta}{2}\omega_\zeta+\frac{1}{2!}\left(\frac{\Delta\zeta}{2}\right)^2\hat{\omega}_{tt}+\frac{1}{3!}\left(\frac{\Delta\zeta}{2}\right)^3\hat{\omega}_{ttt})(z,\zeta_{k+0.5})+\cdots \tag{5.15}$$

$$\hat{\omega}(z,\zeta_k)=(\hat{\omega}-\frac{\Delta\zeta}{2}\hat{\omega}_\zeta+\frac{1}{2!}\left(\frac{\Delta\zeta}{2}\right)^2\hat{\omega}_{tt}-\frac{1}{3!}\left(\frac{\Delta\zeta}{2}\right)^3\omega_{ttt})(z,\zeta_{k+0.5})+\cdots \tag{5.16}$$

Subtracting (5.16) from (5.15), we have

$$\hat{\omega}_\zeta(z,\zeta_{k+0.5})=\frac{\hat{\omega}(z,\zeta_{k+1})-\hat{\omega}(z,\zeta_k)}{\Delta\zeta}+O(\Delta\zeta)^2\cdot \tag{5.17}$$

Hence,

$$L\hat{\omega}(z,\zeta_{k+0.5})=L\frac{\hat{\omega}(z,\zeta_{k+1})-\hat{\omega}(z,\zeta_k)}{2}+O(\Delta\zeta)^2\cdot \tag{5.18}$$

Clearly, e_m is the solution of

$$\begin{cases} (I+\frac{\Delta\zeta}{2}L_\varepsilon^K)e_k=O(\Delta\zeta)^3 \\ e_k\Big|_{\beta_d}=e_k\Big|_{\beta_l}=e_k\Big|_{\beta_r}=0\cdot \end{cases}$$

The consistency arguments of the C-N scheme is concluded with the maximum principle applied to $(I + (\Delta\zeta/2)L_\varepsilon^K)$.

$\varepsilon_k = \left|\omega(z,\zeta_k) - \hat{\omega}^k(z)\right|$ is considered as the global error corresponding to the semi-discrete scheme (5.9). Clearly, $E_k = e_k + \Re E_{k-1}$, where

$$\Re \equiv \left(I + \frac{\Delta\zeta}{2}L_\varepsilon^K\right)^{-1}\left(I - \frac{\Delta\zeta}{2}L_\varepsilon^K\right)$$

is a transition operator. The afore-mentioned condition is derived such that $\Re E_{k-1}$ is the solution acquired after a single step of the scheme (5.9) with zero values of $F(z,\zeta)$ and considering $\hat{\omega}^k = E_{k-1}$ as the initial data. The resultant recurrence relation is $E_k = \sum_{n=1}^{k} \Re^{k-n} e_n$.

Theorem 5.4.2: Under the hypothesis given in Lemma 5.3.6, the following bound for E_k associated with (5.9) at ζ_k is

$$\sup_{k \le T/\Delta\zeta} \|E_k\|_\infty \le \rho(\Delta\zeta)^2 .$$

Proof: Using the recurrence,

$$\sup_{k \le T/\Delta\zeta} \|E_k\|_\infty = \left\|\sum_{n=1}^{k} \Re^{k-n} e_n\right\|_\infty \le \rho k(\Delta\zeta)^3 = \rho(\zeta/\Delta\zeta)(\Delta\zeta)^3 = \rho(\Delta\zeta)^2 .$$

If the following condition holds:

$$\|\Re^n\|_\infty \le \rho, n = 1, 2, \ldots, k . \tag{5.19}$$

The stability condition mentioned in (5.19) can be proved following [13].

5.4.2 Error Estimate for Scheme-I

Theorem 5.4.3: *The error bound for the UP scheme on G_1^M with the S-mesh is*

$$\left|\hat{W}_m^{k+1} - \hat{\omega}(z_m, \zeta_{k+1})\right| \le \rho M^{-1}(lnM)^2$$

and for the B-S-mesh:

$$\left|\hat{W}_m^{k+1} - \hat{\omega}(z_m, \zeta_{k+1})\right| \le \rho M^{-1} .$$

Proof: For the temporal domain $[0, \tau]$, the right-hand side of (5.11) is ε-independent; as the initial conditions in ∂G are known. Hence, following classical approach of [21], the error bounds can be easily obtained.

Theorem 5.4.4: *With L_{UP}^{M}, the error bound on G_2^M with the S-mesh is*

$$\left|\hat{W}_m^{k+1} - \hat{\omega}(z_{m,}\zeta_{k+1})\right| \le \rho M^{-1}(lnM)^2$$

and for the B-S-mesh:

$$\left|\hat{W}_m^{k+1} - \hat{\omega}(z_m,\zeta_{k+1})\right| \le \rho M^{-1}.$$

Proof: While calculating the error estimate in $[\tau, 2\tau]$, one can observe that the right side is ε-dependent. The regular and boundary layer components of the semidiscrete solution on $G_2^{K,M}$ satisfy

$$\begin{cases} L_\varepsilon \hat{r}(z,\zeta) + \hat{r}_\zeta(z,\zeta) = \hat{r}(z,\zeta-\tau) + F(z,\zeta) \text{ in } G_1 \\ \hat{r}\Big|_{\beta_d} = \omega_\varsigma(z,\zeta), (z,\zeta) \in G_1 \\ \hat{r}\Big|_{\beta_l} = \sum_{p=0}^{4} \varepsilon^p \hat{r}_p(0,\zeta); \\ \hat{r}\big|_{\beta_r} = \phi_r(1,\zeta) \text{ for } \tau \le \zeta \le T \end{cases} \tag{5.20}$$

and

$$\begin{cases} L_\varepsilon \hat{s}(z,\zeta) + \hat{s}_\zeta(z,\zeta) = \hat{s}(z,\zeta-\tau) \text{ in } \mathrm{G}_1 \\ \hat{s}\Big|_{\beta_d} = 0,, (z,\zeta) \in G_1, \\ \hat{s}\Big|_{\beta_l} = \omega(0,\zeta) - \hat{\Re}(0,\zeta), \tau \le \zeta \le \mathrm{T} \\ \hat{s}\big|_{\beta_r} = 0, \text{ for } \tau \le \zeta \le \mathrm{T}. \end{cases} \tag{5.21}$$

The solution in (5.11) is also decomposed into its smooth and boundary layer components, as

$$\hat{W}(z_m,\zeta_{k+1}) = \hat{\Re}(z_m,\zeta_{k+1}) + \hat{\delta}(z_m,\zeta_{k+1}).$$

Satisfying the below-mentioned expressions

$$\begin{cases} L_{up}^{K,M}\hat{\Re}(z_m,\zeta_{k+1}) = \hat{\Re}(z_m,\zeta_{k+1-K_1}) + F(z_m,\zeta_{k+1}) \text{ in } \mathrm{G}_2^{\mathrm{K,M}} \\ \hat{\Re}\Big|_{\beta_d} = \hat{W}_\tau(z_m,\zeta_{k+1}), (z_m,\zeta_{k+1}) \in K_1^{\mathrm{K,M}} \\ \hat{\Re}\Big|_{\beta_l} = \sum_{p=0}^{4} \varepsilon^p \Re_p(z_m,\zeta_{k+1}) \\ \hat{\Re}\big|_{\beta_r} = \phi_r(z_m,\zeta_{k+1}), k = (K_1 + (K_2/2) + 1), \ldots, K. \end{cases} \tag{5.22}$$

and

$$\begin{cases} L_{up}^{K,M}\hat{\delta}(z_m,\zeta_{k+1}) = \hat{S}(z_m,\zeta_{k+1-K_1}) \\ \hat{S}\big|_{\beta_d} = 0 \\ \hat{S}\big|_{\beta_l} = \hat{W}(0,\zeta_{k+1}) - \hat{\Re}(0,\zeta_{k+1}) \\ \hat{S}\big|_{\beta_r} = 0, k = (K_1 + (K_2/2) + 1), \ldots, K, \end{cases} \tag{5.23}$$

respectively. The error in $\bar{G}_2^M$ is

$$\left|(\hat{\omega} - \hat{W})(z_m,\zeta_{k+1})\right| \le \left|(\hat{r} - \hat{\Re})(z_m,\zeta_{k+1})\right| + \left|(\hat{s} - \hat{S})(z_m,\zeta_{k+1})\right|.$$

Error in the smooth component:
For the smooth part of the solution, using (5.20) and (5.22), we have

$$\begin{aligned} \left|L_{\text{up}}^M(\hat{r} - \hat{\Re})(z_m - \zeta_{k+1})\right| &= (\hat{r} - \hat{\Re})(z_m,\zeta_{k+1-K_1}) + \left|L_\varepsilon \hat{r} - L_{\text{up}}^M \hat{\Re}\right| \\ &\le (\hat{W}_\tau - \hat{\omega})(z_m,\zeta_{k+1-K_1}) \\ &\quad + \left|\varepsilon\left(\frac{\partial^2}{\partial z^2} - D_z^+ D_z^-\right)\hat{r}\right| + \left|a((z_m - \zeta_{k+1})\left(\frac{\partial}{\partial z} - D_z^+\right)\hat{r}\right|. \end{aligned}$$

From Taylor's series expansion and Theorem 5.4.3 on the *S*-mesh, we get

$$\begin{aligned} \left|L_{\text{up}}^M(\hat{r} - \hat{\Re})(z_m,\zeta_{k+1})\right| &\le \rho M^{-1}(\ln M)^2 \\ &\quad + \rho\left[\varepsilon(z_{m+1} - z_{m-1})\left\|\frac{\partial^3 \hat{r}}{\partial z^3}\right\|_\infty + (z_{m+1} - z_m)a(z_m,\zeta_{k+1})\left\|\frac{\partial^2 \hat{r}}{\partial z^2}\right\|_\infty\right]. \end{aligned} \tag{5.24}$$

Using Theorem 5.2.4 and Lemma 5.3.1, we get our required bounds for the S-mesh as

$$\left|(\hat{r}(z_m,\zeta_{k+1}) - \hat{\Re}(z_m,\zeta_{k+1}))\right| \le \rho M^{-1}(\ln M)^2 \ . \tag{5.25}$$

As $\eta_m = \dfrac{2(1 - \mu_0 \varepsilon \ln M)}{N} \le \rho M^{-1}$, for the *B*-*S*-mesh, one can get

$$\left|\hat{r}(z_m,\zeta_{k+1}) - \hat{\Re}(z_m,\zeta_{k+1})\right| \le \rho M^{-1} \ . \tag{5.26}$$

Error in the layer component:
The bounds for boundary layer component depend upon μ.

$$\left|L_{\text{up}}^M(\hat{\delta}(z_m,\zeta_{k+1}) - \hat{s}(z_m,\zeta_{k+1}))\right| \le \rho\varepsilon(z_{m+1} - z_{m-1})\left\|\frac{\partial^3 \hat{s}}{\partial z^3}\right\|_\infty + \rho(z_{m+1} - z_m)a(z_m,\zeta_{k+1})\left\|\frac{\partial^2 \hat{s}}{\partial z^2}\right\|_\infty . \tag{5.27}$$

Case 1: For $\mu = \mu_0 \varepsilon \ln M$ and $\mu_0 \varepsilon \ln M < 1/2$, the error outside the layer region i.e., $(\mu, 1]$ will be discussed, first. Using the bounds mentioned in Lemma 5.3.1 for the continuous and Lemma 3.4 for the discrete solution, we have

$$\left|\hat{S}(z_m, \zeta_k) - \hat{s}(z_m, \zeta_{k+1})\right| \le \rho M^{-1} \text{ for } m = (M/2+1), \ldots, M-1. \tag{5.28}$$

In $[0, \mu]$, the Taylor's series expansion and Theorem 5.2.4 are used to get the following inequalities for S-mesh:

$$\left|L_{up}^{M}(\hat{\delta}(z_m, \zeta_{k+1}) - \hat{s}(z_m, \zeta_{k+1}))\right| \le \rho \varepsilon^{-2}(z_{m+1} - z_{m-1}) \text{ for } m = 0, 1, \ldots, M/2.$$

Further, as $\eta_m - \eta_{m-1} = 4\mu/N$ in $[0, \mu]$, one can get

$$\left|L_{up}^{M}(\hat{S}(z_m, \zeta_{k+1}) - \hat{s}(z_m, \zeta_{k+1}))\right| \le \rho \varepsilon^{-2} \mu M^{-1.}$$

Again, $\left|(\hat{S}(z_m, \zeta_{k+1}) - \hat{s}(z_m, \zeta_{k+1}))\right| \le \rho M^{-1}$. Further, the barrier function, $\phi_m = \rho_1 M^{-1} + (\mu - z_m)\rho_2 \varepsilon^{-2} \mu M^{-2}$ is used on $1 \le m \le M/2$, where ρ_1 and ρ_2 are some user chosen constants. $\psi_m^{\pm} = \Upsilon_m \pm (\hat{S} - \hat{s})$ I is the considered mess function for S-mesh. Clearly, $\psi_m^{\pm} \ge 0$ at z_0 and $z_{M/2}$. For preferred ρ, we can also get $L_\varepsilon \psi_m^{\pm} \ge 0$ for $m = 2, \ldots, (M/2-1)$. Hence,

$$\left|(\hat{S}(z_m, \zeta_{k+1}) - \hat{s}(z_m, \zeta_{k+1}))\right| \le \rho_1 M^{-1} + \rho_2 \varepsilon^{-2} \mu M^{-1} \le \rho M^{-1} (\ln M)^2. \tag{5.29}$$

In $[0, \mu]$, the construction of B-S-mesh gives $z_m = -\mu_0 \varepsilon \ln[1 - 2(1 - M^{-1}) m M^{-1}]$. Clearly

$$\eta_m = \mu_0 \varepsilon \left[-\ln(1 - 2(1 - M^{-1}) m M^{-1}) + \ln(1 - 2(1 - M^{-1})(m-1) M^{-1}) \right].$$

Using the above mean value theorem, we get

$$\eta_m = \mu_0 \varepsilon \left[\frac{2(1 - M^{-1}) M^{-1}}{1 - 2(1 - M^{-1})(m-1) M^{-1}}\right] \le \ell M^{-1}.$$

and

$$\exp(-\beta z_{m+1}/\varepsilon) + \exp(-\beta z_{m-1}/\varepsilon) \le \exp(-\beta z_{m+1}/\varepsilon)(1 - \exp(-\beta(z_{m+1} - z_{m-1})/\varepsilon)) \le \rho M^{-1}.$$

Using the above inequalities in (5.27) for $[0, \mu]$, one can get

$$\left|(\hat{S}(z_m, \zeta_{k+1}) - \hat{s}(z_m, \zeta_{k+1}))\right| \le \rho M^{-1}. \tag{5.30}$$

Case 2: if $\mu = 1/2$, i.e., $\mu_0 \varepsilon \ln M \ge 1/2.$, with the S-mesh $(z_{m+1} - z_{m-1}) \le 2M^{-1}$, so we have

$$\left|L_{\text{up}}^{M}(\hat{\delta}(z_m, \zeta_{k+1}) - \hat{s}(z_m, \zeta_{k+1}))\right| \le \rho M^{-1} \left(\varepsilon \left\| \frac{\partial^3 \hat{\delta}}{\partial z^3} \right\|_\infty + \left\| \frac{\partial^2 \hat{\delta}}{\partial z^2} \right\|_\infty \right).$$

Using Theorem 5.2.4 and the fact $2\varepsilon \ln M \ge 1/2$, we reach at

$$\left|L_{\text{up}}^{M}(\hat{S}(z_m,\zeta_k)-\hat{s}(z_m,\zeta_k))\right| \le \rho M^{-1}(\ln M)^2 \cdot$$

Now, use of Lemma 5.3.2 gives

$$\left|(\hat{S}(z_m,\zeta_k)-\hat{s}(z_m,\zeta_k))\right| \le \rho M^{-1}(\ln M)^2 \cdot \tag{5.31}$$

Further using (5.25), (5.28), (5.29), and (5.31), we get

$$\left|(\hat{\omega}(z_m,\zeta_k)-\hat{W}(z_m,\zeta_k))\right| \le \rho M^{-1}(\ln M)^2 \cdot$$

Similarly for the B-S-mesh, a similar approach is followed as mentioned above for mesh region. As,

$\mu_0 \varepsilon \ln M \ge 1/2$, we have $\exp(-\beta z_{m+1}/\varepsilon) + \exp(-\beta z_{m-1}/\varepsilon) \le \ell M^{-1}$ and $\eta_m = 2(1-\mu)M^{-1} \le \ell M^{-1}$. Application of this condition along with Lemma 5.3.2 in (5.27), one can get

$$\left|(\hat{S}(z_m,\zeta_k)-\hat{s}(z_m,\zeta_k))\right| \le \rho M^{-1} \cdot \tag{5.32}$$

Now, using (5.26), (5.28), (5.30), and (5.32), the desired bounds for the B-S-mesh is:

$$\left|(\hat{\omega}(z_m,\zeta_k)-\hat{W}(z_m,\zeta_k))\right| \le \rho M^{-1} \cdot$$

Hence, the proof is complete.

The fully discrete scheme on $G^{K,M} = G_{\zeta}^{K} \times G_{z}^{M}$ becomes

$$\begin{cases} L_{\text{up}}^{K,M} W_m^{k+1} = 2D_{\zeta}^{-} W_m^{k+1} + L_{\text{up}}^{M} W_m^{k+1} = \\ W_m^{k+1-K_1} + W_m^{k-K_1} + F_m^{k+1} + F_m^{k} - L_{\text{up}}^{K,M} W_m^{k},\ m = 1, 2, \ldots, (M-1) \\ W_m^{-k} = \phi_d(z_{m,} - \zeta_k),\ k = 0, 1, \ldots, K_1 \text{ and } m = 0, 1, \ldots, M \\ W_0^{k+1} = \phi_l(\zeta_{k+1}),\ W_m^{k+1} = \phi_r(\zeta_{k+1}),\ k = K_{1,} K_1 + 1, \ldots, K \cdot \end{cases} \tag{5.33}$$

The below-mentioned theorem proves uniform convergence of the fully discrete scheme.

Theorem 5.4.5: *The maximum absolute error using $L_{up}^{K,M}$ on the S-mesh is given by*

$$\max_{(z_m,\zeta_{k+1})\in G^{K,M}} |\omega(z_m,\zeta_k) - W(z_m,\zeta_k)| \le \rho(M^{-1}(\ln M)^2 + \Delta\zeta^2) \cdot$$

and on the B-S-mesh is

$$\max_{(z_m,\zeta_{k+1})\in G^{K,M}} |\omega(z_m,\zeta_k) - W(z_m,\zeta_k)| \le \rho(M^{-1} + \Delta\zeta^2) \cdot$$

Proof: By the use of Theorems 5.4.2, 5.4.3, and 5.4.4, the required error bounds are obtained.

5.4.3 Error Estimate for Scheme-II

Theorem 5.4.6: *The error bound in the spatial direction on using the M.HYB scheme G_1 with the S-mesh is*

$$\left|\hat{W}_m^{k+1} - \hat{\omega}(z_m - \zeta_{k+1})\right| \leq \begin{cases} \rho(M^{-2} + M^{-1}\varepsilon) & \text{for } \frac{\varepsilon}{h_m a_{m-1}} < \frac{1}{2} \\ \rho M^{-2}(\ln M)^2 & \text{for } \frac{\varepsilon}{h_m a_{m-1}} \geq \frac{1}{2} \end{cases}$$

and with the B-S-mesh is

$$\left|\hat{W}_m^{k+1} - \hat{\omega}(z_m, \zeta_{k+1})\right| \leq \rho M^{-2}.$$

Proof: A similar argument given in Scheme-I can be followed using the idea mentioned in [16] to prove the statement.

Theorem 5.4.7: *Error bound for M.HYB-algorithm on G_2 with the S-mesh is*

$$\left|\hat{W}_m^{k+1} - \hat{\omega}(z_m, \zeta_{k+1})\right| \leq \begin{cases} \rho(M^{-2} + M^{-1}\varepsilon) & \text{for } \frac{\varepsilon}{h_m a_{m-1}} < \frac{1}{2} \\ \rho M^{-2}(\ln M)^2 & \text{for } \frac{\varepsilon}{h_m a_{m-1}} \geq \frac{1}{2} \end{cases}$$

and with the B-S-mesh is

$$\left|\hat{W}_m^{k+1} - \hat{\omega}(z_m, \zeta_{k+1})\right| \leq \rho M^{-2}.$$

Proof. The complete-discrete scheme on $g_2^{K,M}$ is

$$\begin{cases} L_{mh}^{K,M} W_m^{k+1} = \\ W_{\vartheta,m-1/2}^{k+1-K_1} + W_{\vartheta,m-1/2}^{k-K_1} + F_{\vartheta,m-1/2}^{k+1} + F_{\vartheta,m-1/2}^{k} - L_{mh}^{M} W_m^k, \quad m = 1, 2, \ldots, (M-1) \\ W|_{\beta d} = W\tau(z_m, \zeta_k),\ (z_m, \zeta_{k+1}) \in G_1^{K,M} \\ W_0^{k+1} = \phi_l(\zeta_{k+1}),\ W_m^{k+1} = \phi_r(\zeta_{k+1}),\ k = K_1, (K_2/2), \ldots, K. \end{cases} \tag{5.34}$$

where

$$\begin{cases} L_{mh}^{K,M} W_m^{k+1} = -\dfrac{[\mathbb{Q}W]_{m+1}^{k+1} - [\mathbb{Q}W]_m^{k+1}}{\hbar_{\vartheta,m}} + (BW)_{v,m-1/2}^{k+1} \\ F_{\vartheta,m-1/2}^{k+1} = \dfrac{F_{m-1}^{k+1}(1-\vartheta_m) - F_m^{k+1}(1+\vartheta_m-\vartheta_{m+1}) + F_{m+1}^{k+1}(\vartheta_{m+1})}{2} \\ [\mathbb{Q}W]_m^{k+1} = \varepsilon D_z^{-1} W_m^{k+1} + \vartheta_m a_m W_m^{k+1} + (1-\vartheta_m) a_{m-1} W_{m-1}^{k+1} \\ \hbar_{\vartheta,m} = (1-\vartheta_m)h_m + \vartheta_{m+1} h_{m+1}. \end{cases}$$

The decomposition of the approximated solution of (5.9) is analogous to the process maintained in the Theorem 5.4.4, where the components satisfy the following IBVPs:

$$\begin{cases} L_\varepsilon \hat{r}(z,\zeta) + \hat{r}_\zeta(z,\zeta) = \hat{r}(z,\zeta-\tau) + F(z,\zeta) \text{ in } G_2 \\ \hat{r}|_{\beta_d} = \omega_\tau(z,\zeta),\ (z,\zeta) \in G_1 \\ \hat{r}|_{\beta_l} = \sum_{p=0}^{4} \varepsilon^p \hat{r}_p(0,\zeta) \\ \hat{r}|_{\beta_r} = \phi_r(1,\zeta) \text{ for } \tau \le \zeta \le T \end{cases} \tag{5.35}$$

and

$$\begin{cases} L_\varepsilon \hat{s}(z,\zeta) + \hat{s}_\zeta(z,\zeta) = \hat{s}(z,\zeta-\tau) \text{ in } G_2 \\ \hat{s}|_{B_d} = 0,\ (z,\zeta) \in G_1 \\ \hat{s}|_{B_l} = \omega(0,\zeta) - \hat{\Re}(0,\zeta),\ \tau \le \zeta \le T \\ \hat{s}|_{B_r} = 0 \text{ for } \tau \le \zeta \le T. \end{cases} \tag{5.36}$$

The corresponding fully discrete forms of (5.35) and (5.36) are

$$\begin{cases} L_{mh}^{K,M} \hat{\Re}(z_m,\zeta_{k+1}) = \hat{\Re}\left(z_m, \zeta_{k+1-K_1}\right) + F(z_m,\zeta_{k+1}) \text{ in } G_2^{K,M} \\ \hat{\Re}|_{B_d} = W_\tau(z_m,\zeta_{k+1}),\ (z_m,\zeta_{k+1}) \in G_1^{K,M} \\ \hat{\Re}|_{B_l} = \sum_{p=0}^{4} \varepsilon^p \Re_p(z_m,\zeta_{k+1}) \\ \hat{\Re}|_{B_r} = \phi_r(z_m,\zeta_{k+1}),\ k = (K_1 + (K_2/2) + 1), \ldots, K. \end{cases} \tag{5.37}$$

and

$$\begin{cases} L_{mh}^{K,M}\hat{S}(z_m,\zeta_{k+1}) = \hat{S}\left(z_m,\zeta_{k+1-K_1}\right) \text{ in } G_2^{K,M} \\ \hat{S}|_{B_d} = 0 \\ \hat{S}|_{B_l} = W(0,\zeta_{k+1}) - \Re(0,\zeta_{k+1}) \\ \hat{S}|_{B_r} = 0,\ k = (K_1 + (K_2/2) + 1),\ \ldots, K\,. \end{cases} \tag{5.38}$$

W_τ and ω_τ are the solutions obtained in $G_1^{K,M}$ and G_1, respectively.

5.4.3.1 Error in the Smooth Component

$$\left|L_{mh}^{M}\left(\hat{r}-\hat{\Re}\right)(z_m,\zeta_{k+1})\right| = \begin{cases} \left(\hat{r}_{m-1/2}^{k+1-K_1} - \hat{\Re}_{m-1/2}^{k+1-K_1}\right) + \left|L_\varepsilon \hat{r}_{m-1/2}^{k+1-K_1} - L_{mh}^{M}\hat{\Re}_{m-1/2}^{k+1-K_1}\right| \text{ for } \frac{\varepsilon}{h_m a_{m-1}} < \frac{1}{2} \\ \left(\hat{r}_{m}^{k+1-K_1} - \hat{\Re}_{m}^{k+1-K_1}\right) + \left|L_\varepsilon \hat{r}_{m}^{k+1-K_1} - L_{mh}^{M}\hat{\Re}_{m}^{k+1-K_1}\right| \text{ for } \frac{\varepsilon}{h_m a_{m-1}} \geq \frac{1}{2}\,. \end{cases}$$

Following the approach of [16], using (5.35) and (5.37), the error for $\frac{\varepsilon}{h_m a_{m-1}} < \frac{1}{2}$ can be followed as

$$\left|L_{mh}^{M}\left(\hat{r}-\hat{\Re}\right)(z_m,\zeta_{k+1})\right| = \left(\omega_\tau^{k+1-K_1} - W_\tau^{k+1-K_1}\right) + \left|L_\varepsilon \hat{r}_{m-1/2}^{k+1-K_1} - L_{mh}^{M}\hat{\Re}_{m-1/2}^{k+1-K_1}\right|$$

The bounds in Theorem 5.4.6 with the Taylor series approximation give:

$$\left|L_{mh}^{M}\left(\hat{r}-\hat{\Re}\right)(z_m,\zeta_{k+1})\right| \leq \rho\left[M^{-1}\left(\varepsilon + M^{-1}\right) + (\varepsilon + h_{m+1})(h_m + h_{m+1})\left\|\frac{\partial^3 \hat{r}}{\partial z^3}\right\|_\infty + h_m^2\left(\left\|\frac{\partial^2 \hat{r}}{\partial z^2}\right\|_\infty + \left\|\frac{\partial \hat{r}}{\partial z}\right\|_\infty\right)\right].$$

Choosing $h_m \leq 2M^{-1},\ h_m + h_{m+1} \leq 4M^{-1},$ we have

$$\left|L_{mh}^{M}\left(\hat{r}-\hat{\Re}\right)(z_m,\zeta_{k+1})\right| \leq \rho M^{-1}\left(\varepsilon + M^{-1}\right).$$

After the application of Lemma 5.3.6, we have

$$\left|\hat{r}(z_m,\zeta_{k+1}) - \hat{\Re}_m^{k+1}\right| \leq \rho M^{-1}\left(\varepsilon + M^{-1}\right). \tag{5.39}$$

In an analogous approach to $\frac{\varepsilon}{h_m a_{m-1}} \geq \frac{1}{2}$, we have

$$\left|L_{mh}^{M}\left(\hat{r}-\hat{\Re}\right)(z_m,\zeta_{k+1})\right| \leq \rho\left[M^{-2}(\ln M)^2+\varepsilon h_m^2\left\|\frac{\partial^4 \hat{r}}{\partial z^4}\right\|_{\infty}+h_m^2\left\|\frac{\partial^3 \hat{r}}{\partial z^3}\right\|_{\infty}\right].$$

The bounds derived in Theorem 5.4.6 gives

$$\left|\hat{r}(z_m,\zeta_{k+1})-\hat{\Re}_m^{k+1}\right| \leq \rho M^{-2}(\ln M)^2. \tag{5.40}$$

5.4.3.2 Error in the Layer Component

$$\left|L_{mh}^{M}\left(\hat{s}-\hat{S}\right)(z_m,\zeta_{k+1})\right| = \begin{cases} \left(\hat{s}_{m-1/2}^{k+1-K_1}-\hat{S}_{m-1/2}^{k+1-K_1}\right)+\left|L_\varepsilon \hat{s}_{m-1/2}^{k+1-K_1}-L_{mh}^{K,M}\hat{S}_{m-1/2}^{k+1-K_1}\right| \text{ for } \frac{\varepsilon}{h_m a_{m-1}} < \frac{1}{2} \\ \left(\hat{s}_{m}^{k+1-K_1}-\hat{S}_{m}^{k+1-K_1}\right)+\left|L_\varepsilon \hat{s}_{m}^{k+1-K_1}-L_{mh}^{K,M}\hat{S}_{m}^{k+1-K_1}\right| \text{ for } \frac{\varepsilon}{h_m a_{m-1}} \geq \frac{1}{2}. \end{cases}$$

Using (4.23) and (4.25), the error can be written as

$$\left|L_{mh}^{M}\left(\hat{s}-\hat{S}\right)(z_m,\zeta_{k+1})\right| = \begin{cases} \left|L_\varepsilon \hat{s}_{m-1/2}^{k+1-K_1}-L_{mh}^{M}\hat{S}_{m-1/2}^{k+1-K_1}\right| & \text{for} \quad \frac{\varepsilon}{h_m a_{m-1}} < \frac{1}{2} \\ \left|L_\varepsilon \hat{s}_{m}^{k+1-K_1}-L_{mh}^{M}\hat{S}_{m}^{k+1-K_1}\right| & \text{for} \quad \frac{\varepsilon}{h_m a_{m-1}} \geq \frac{1}{2}. \end{cases}$$

At a particular ζ_{k+1}, the above expression represents the truncation error of any two-point BVPs. Further, the approach mentioned in [22] gives

$$\left|L_{mh}^{M}\left(\hat{s}-\hat{S}\right)(z_m,\zeta_{k+1})\right| = \begin{cases} \rho\left(M^{-1}\left(\varepsilon+M^{-1}\right)\right) & \text{for} \quad \frac{\varepsilon}{h_m a_{m-1}} < \frac{1}{2} \\ \rho M^{-2}(\ln M)^2 & \text{for} \quad \frac{\varepsilon}{h_m a_{m-1}} \geq \frac{1}{2}. \end{cases}$$

As the operator satisfies the discrete maximum principle, hence, we have

$$\left|\left(\hat{s}-\hat{S}\right)(z_m,\zeta_{k+1})\right| = \begin{cases} \rho\left(M^{-1}\left(\varepsilon+M^{-1}\right)\right) & \text{for} \quad \frac{\varepsilon}{h_m a_{m-1}} < \frac{1}{2} \\ \rho M^{-2}(\ln M)^2 & \text{for} \quad \frac{\varepsilon}{h_m a_{m-1}} \geq \frac{1}{2}. \end{cases} \tag{5.41}$$

The error bounds for the S-mesh can be concluded from eqs. (5.39), (5.40), and (5.41). Furthermore, an analogous approach as mentioned for Scheme-I, along with the fact that $h_m \leq \rho M^{-1}$, allows the bounds for the B-S mesh to be proved.

Theorem 5.4.8: *Error using (3.4) for (1.1) on $G^{K,M}$ with S-mesh is*

$$\max_{(z_m,\zeta_{k+1})\in G^{K,M}} \left|W_m^{k+1} - \omega(z_m,\zeta_{k+1})\right| \le \begin{cases} \rho\left(\left(M^{-2}+M^{-1}\varepsilon\right)+(\Delta\zeta)^2\right) & \text{for} \quad \frac{\varepsilon}{h_m a_{m-1}} < \frac{1}{2} \\ \rho\left(M^{-2}(\ln M)^2 + (\Delta\zeta)^2\right) & \text{for} \quad \frac{\varepsilon}{h_m a_{m-1}} \ge \frac{1}{2} \end{cases}$$

and with B-S mesh is

$$\max_{(z_m,\zeta_{k+1})\in G^{K,M}} \left|W_m^{k+1} - \omega(z_m,\zeta_{k+1})\right| \le \rho\left(M^{-2} + (\Delta\zeta)^2\right).$$

Proof: The conclusion can be drawn from Theorems 5.4.2, 5.4.6, and 5.4.7.

5.5 Numerical Investigation and Discussion

An exemplifying problem is solved to validate the theoretical findings of this chapter. The errors $\left(\rho^{M,\Delta\zeta}\right)$ and rates of convergence $\Re^{M,\Delta t}$ are computed using the double-mesh principle [5, 12] as

$$\rho^{M,\Delta\zeta} = \max_{(z_m,\zeta_k)\in G} |\omega(z_m,\zeta_k) - W(z_m,\zeta_k)|,\ \Re^{M,\Delta t} = \log_2\left(\frac{\rho^{M,\Delta\zeta}}{\rho^{2M,\Delta\zeta/2}}\right).$$

Example 5.1 *Consider the following time-delayed semilinear SPPDE:*

$$\begin{cases} \left(\omega_\zeta - \varepsilon\omega_{zz} - (4-z)\omega_z + (z+\cos(\pi z)+8)\omega\right)(x,\zeta) \\ = \omega(z,\zeta-1) + 16z^2(1-z)^2\exp(\omega(z,\zeta)), \qquad (z,\zeta)\in(0,1)\times(0,2] \\ \omega(z,\zeta) = 0, \qquad \zeta\in[-\tau,0] \\ \omega(0,\zeta) = 0, \qquad \omega(1,\zeta) = 0, \qquad \zeta\in[1,2]. \end{cases}$$

The time-delay parameter and the **TOL** are chosen to be 1 and 10^{-5}, respectively, while solving Example 5.1. The solution profiles can be observed through the surface plots given in Figure 5.1. A clearly observable layer can be visualized near $z=0$ when ε is comparatively small. A similar nature can be concluded from Figure 5.2a, where the line plots are given for different values of ε at $\zeta=1$. From Figure 5.2b, one can observe that the severity of the layers remains identical in the solution plots at different time levels, claiming that the formation of layers is **independent of time**. The errors and corresponding order of accuracy for **Scheme-I** are tabulated in Table 5.1. Despite using a second-order accurate Crank-Nicolson (C-N) scheme in the temporal direction, one can observe a global first-order accuracy in Scheme-I because of the upwind (UP) scheme applied in space, indicating that the problem is dominated by spatial derivative terms. An analogous result can be concluded from Table 5.2, which tabulates the numerical outcomes through **Scheme-II**. Further, comparing both the

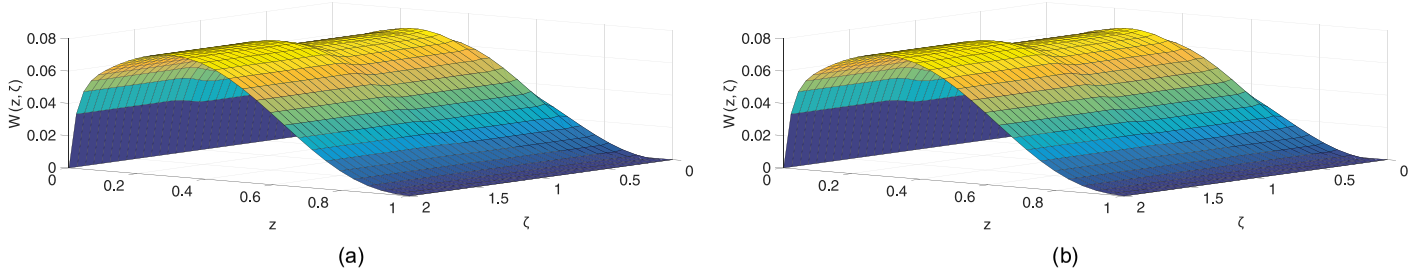

Figure 5.1: Surface plots with different values of ε for Example 5.1.

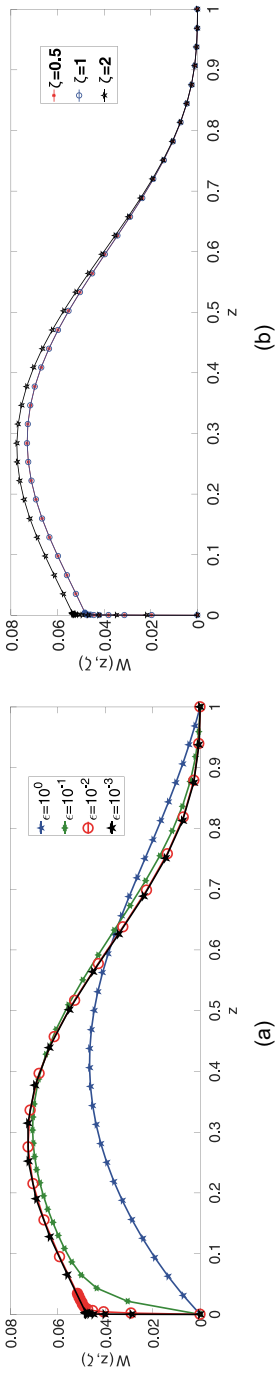

Figure 5.2: Different solution profiles for Example 5.1.

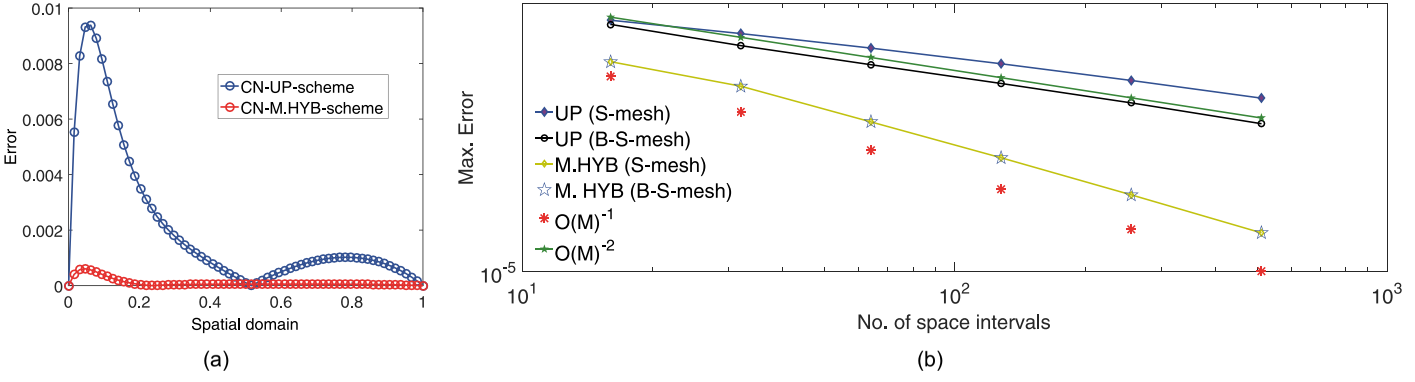

Figure 5.3: Error profiles for Example 5.1.

Table 5.1: Numerical results with Scheme-I for Example 5.1.

ε	Mesh	16	32	64	128	256	512
10^{-3}	S-mesh	5.6238e-2	3.5557e-2	2.1576e-2	1.2557e-2	7.0947e-3	3.8619e-3
		0.6614	0.7207	0.7809	0.8237	0.8774	
	B-S-mesh	4.8685e-2	2.3483e-2	1.2188e-2	6.3967e-3	3.2832e-3	1.6065e-3
		1.0519	0.9461	0.9300	0.9622	1.0312	
10^{-5}	S-mesh	5.6245e-2	3.5568e-2	2.1582e-2	1.2591e-2	7.0964e-3	3.8637e-3
		0.6611	0.7208	0.7774	0.8272	0.8771	
	B-S-mesh	4.8688e-2	2.3479e-2	1.2188e-2	6.3970e-3	3.2832e-3	1.6060e-3
		1.0522	0.9459	0.9299	0.9623	1.0316	
10^{-7}	S-mesh	5.6247e-2	3.5570e-2	2.1585e-2	1.2597e-2	7.0968e-3	3.8641e-3
		0.6611	0.7206	0.7769	0.8278	0.8770	
	B-S-mesh	4.8688e-2	2.3479e-2	1.2188e-2	6.3970e-3	3.2832e-3	1.6056e-3
		1.0522	0.9459	0.9299	0.9623	1.0320	
$10^{-9}$to 10^{-12}	S-mesh	5.6247e-2	3.5570e-2	2.1585e-2	1.2597e-2	7.0968e-3	3.8641e-3
		0.6611	0.7206	0.7769	0.8278	0.8770	
	B-S-mesh	4.8688e-2	2.3479e-2	1.2188e-2	6.3970e-3	3.2832e-3	1.6053e-3
		1.0522	0.9459	0.9299	0.9623	1.0323	

Table 5.2: Numerical results with Scheme-II for Example 5.1.

ε	Mesh	16	32	64	128	256	512
10^{-3}	S-mesh	1.3519e-2	5.8088e-3	1.7027e-3	4.9660e-4	1.3867e-4	3.7570e-5
			1.2187	1.7704	1.7789	1.8404	1.8840
	B-S-mesh	8.1530e-3	2.3956e-3	6.3828e-4	1.6691e-4	4.1729e-5	9.8119e-6
			1.7669	1.9081	1.9351	1.9999	2.0884
10^{-5}	S-mesh	1.3515e-2	5.8211e-3	1.7055e-33	4.9710e-4	1.3887e-4	3.7630e-5
			1.2152	1.7711	1.7785	1.8398	1.8838
	B-S-mesh	8.1592e-3	2.3992e-3	6.4213e-4	1.6860e-4	4.2515e-5	1.0037e-5
			1.7659	1.9016	1.9292	1.9876	2.0826
10^{-7}	S-mesh	1.3515e-2	5.8212e-3	1.7056e-3	4.9716e-4	1.3894e-4	3.7654e-5
			1.2152	1.7711	1.7785	1.8392	1.8836
	B-S-mesh	8.1593e-3	2.3992e-3	6.4217e-4	1.6862e-4	4.2510e-5	1.0029e-5
			1.7659	1.9015	1.9292	1.9879	2.0836

Table 5.2 (continued)

ε	Mesh	16	32	64	128	256	512
10^{-9} to 10^{-12}	S-mesh	1.3515e-2	5.8212e-3	1.7056e-3	4.9716e-4	1.3894e-4	3.7654e-5
			1.2152	1.7711	1.7785	1.8392	1.8836
	B-S-mesh	8.1593e-3	2.3992e-3	6.4217e-4	1.6862e-4	4.2510e-5	1.0029e-5
			1.7659	1.9015	1.9292	1.9879	2.0836

tabular data, one can claim that Scheme-II is more accurate than Scheme-I, as also supported by the theoretical analysis. All the tabular data validates the **efficacy of the B-S mesh** over the **S-mesh**, even for smaller values of $\boldsymbol{\varepsilon}$. The described advantages of the B-S mesh and Scheme-II can also be validated through the error plots provided in Figure 5.3. Furthermore, the decreasing error with respect to increasing mesh points validates the schemes to be **convergent with respect to both space and time**. The preferred schemes can be concluded to be **parameter-uniform**, as after certain values of ε, both the error and accuracy can be seen to become stagnant.

5.6 Conclusion

This chapter highlights two robust numerical techniques to solve singularly perturbed semilinear parabolic problems with a large time lag. The semilinearity is handled using Newton's linearization technique. The temporal derivative is approximated with a second-order accurate Crank-Nicolson scheme on a uniform mesh. Further, two layer-rectifying Shishkin-type meshes are constructed to handle the layer behavior of the solution. In combination with the Crank-Nicolson scheme in time, Scheme-I discusses a first-order globally accurate scheme using the upwind scheme in the spatial direction. Furthermore, a comparatively new difference scheme, namely the monotone hybrid scheme, is discussed in Scheme-II, which is beneficial over many existing schemes, providing second-order accuracy and by being a priori in nature. A comparative study of both schemes is presented with all the necessary existence, uniqueness, and convergence results.

References

[1] Rihan, F. A. (2021). Delay Differential Equations and Applications to Biology. Springer Singapore. https://doi.org/10.1007/978-981-16-0626-7.

[2] Kyrycho, Y. N. and Hogan, S. J. (2010). On the use of delay equations in engineering applications. Journal of Vibration and Control, 16(7–8), 943–960. Doi: 10.1177/1077546309341100.

[3] Priyadarshana, S., Mohapatra, J., and Pattanaik, S. R. (2023). An improved time accurate numeri cal estimation for singularly perturbed semilinear parabolic differential equations with small space shifts and a large time lag. Mathematics and Computers in Simulation, 214, 183–203. https://doi.org/10.1016/j.matcom.2023.07.009.

[4] Mohapatra, J., Govindarao, L., and Priyadarshana, S. (2025). A splitting based higher-order numerical scheme for 2D time-dependent singularly perturbed reaction-diffusion problems. Journal of Supercomputing, 81(203). https://doi.org/10.1007/s11227-024-06479-x.

[5] Priyadarshana, S. and Mohapatra, J. (2024). An efficient numerical approximation for mixed singularly perturbed parabolic problems involving large time-lag. Indian Journal of Pure and Applied Mathematics, 55, 1389––1408. https://doi.org/10.1007/s13226-023-00445-8.

[6] Priyadarshana, S. (2023). Monotone hybrid numerical method for singularly perturbed time-lagged semilinear parabolic problems. National Academy Science Letters, 46, 347–350. https://doi.org/10.1007/s40009-023-01237-8.

[7] Kaushik, A. and Sharma, M. (2012). A robust numerical approach for singularly perturbed time delayed parabolic partial differential equations. Computational Mathematics and Modeling, 23(1), 96–106.

[8] Das, A. and Natesan, S. (2015). Uniformly convergent hybrid numerical scheme for singularly perturbed delay parabolic convection-diffusion problems on Shishkin mesh. Applied Mathematics and Computation, 271, 168–186.

[9] Gowrisankar, S. and Natesan, S. (2017). ε-Uniformly convergent numerical scheme for singularly per turbed delay parabolic partial differential equations. International Journal of Computer Mathematics, 94(5), 902–921.

[10] Govindarao, L. and Mohapatra, J. (2020). Numerical analysis and simulation of delay parabolic partial differential equation involving a small parameter. Engineering Computer, 37(1), 289–312. 22.

[11] Kumar, D. (2021). A parameter-uniform scheme for the parabolic singularly perturbed problem with a delay in time. Numerical Methods for Partial Differential Equations, 37(1), 626–642.

[12] Priyadarshana, S., Mohapatra, J., and Ramos, H. (2024). Robust numerical schemes for time delayed singularly perturbed parabolic problems with discontinuous convection and source terms. Calcolo, 61(1).

[13] Mohapatra, J., Priyadarshana, S., and Reddy, N. R. (2023). Uniformly convergent computational method for singularly perturbed time delayed parabolic differential-difference equations. Engineering Computer, 40(3), 694–717.

[14] Pao, C. V. (1992). Nonlinear Parabolic and Elliptic Equations. Springer Science and Business Media.

[15] Yu-Cheng, Y. and Quan, C. (1991). The numerical solution of a singularly perturbed problem for semilinear parabolic differential equation. Journal of Applied Mathematics and Mechanics, 12(11), 1047–1056.

[16] Das, A., Govindarao, L., and Mohapatra, J. (2022). A second order weighted monotone numerical scheme for time delayed parabolic initial-boundary-value problem involving a small parameter. International Journal of Mathematical Modelling and Numerical Optimisation, 12(3), 233–251.

[17] Ladyˇ Zenskaja, O. A., Solonnikov, V. A., and Ural'ceva, N. N. (1968). Linear and Quasi-linear Equations of Parabolic Type. Vol. 23. Providence: American Mathematical Society.

[18] Shishkin, G. I. and Shishkina, L. P. (2008). Difference Methods for Singular Perturbation Problems. New York: CRC Press.

[19] Miller, J. J. H., O'Riordan, E., and Shishkin, G. I. (1995). On piecewise-uniform meshes for upwind- and central difference operators for solving singularly perturbed problems. The IMA Journal of Numerical Analysis, 15(1), 89–99. https://doi.org/10.1093/imanum/15.1.89.

[20] Arslan, D. (2020). A uniformly convergent numerical study on Bakhvalov-Shishkin mesh for singu larly perturbed problem. Mathematical communications, 11(1), 161––171.

[21] Miller, J. J. H., O'Riordan, E., and Shishkin, E. I. (1996). Fitted Numerical Methods for Singular per Turbation Problems. Singapore: World Scientific.

[22] Stynes, M. and Roos, H. G. (1997). The midpoint-upwind scheme. Applied Numerical Mathematics, 23(3), 361–374.

Anurag Srivastava

Chapter 6
Comparison of Various Weighted Residual Methods up to Three-Step Solution

Abstract: In this chapter, a class of various numerical methods known as weighted residual methods (WRMs) has been discussed which is very useful in solving differential equations arising in physical sciences and engineering. A boundary value problem (BVP) is solved using five WRMs, namely, Galerkin's method, least squares (LS) method, collocation method, subdomain (SD) method, and moment method. Two- and three-step approximate solutions are evaluated and compared with the exact solution of the BVP. Comparison of different WRMs is presented graphically and in the tabular form also. Maximum (L_∞) error and root mean square (RMS) error for each method is also evaluated. It is found that three-step Galerkin's solution is in the good agreement with the exact solution in comparison to other WRMs.

Keywords: Galerkin's method, least squares (LS) method, collocation method, subdomain (SD) method, moment method

6.1 Introduction

Weighted residual methods (WRMs) are a class of techniques used to approximate the solution of differential equations, particularly in engineering and applied mathematics. These methods are widely used in finite element analysis (FEA), computational fluid dynamics (CFD), and numerical solutions of partial differential equations (PDEs). In these methods, the solution is globally approximated as a weighted summation of various linearly independent functions. Differential equations are not directly solved instead an approximate solution satisfying the boundary conditions is assumed, which provides the residual [1]. Galerkin [2] introduced the concept of weighted residuals as a fundamental approach to approximate solutions of differential equations. Galerkin's method is used by several researchers in their work. Bhadauria and Srivastava [3] used Galerkin's method to perform convective stability analysis. Srivastava and Bhadauria [4] developed a five-dimensional Lorenz like nonlinear model using Galerkin's technique. Singh and Gupta [5] developed a numerical simulation of fractional nonlinear Burgers' equation using collocation approach. Singh and Gupta [6] used fourth-order collocation scheme to find the numerical solution of Fisher's equation.

Anurag Srivastava, Department of Mathematics, Chandigarh University, Mohali 140413, Punjab, India

https://doi.org/10.1515/9783111723464-006

Choi [7] used least squares (LS)-weighted residual method for level-set formulation. Lindvall and Scheffel [8] analyzed a novel subdomain (SD) scheme for time-spectral solution of an initial value PDE. Now-a-days, researchers are very much interested to integrate these classical techniques with advanced machine learning algorithms to solve various differential equations arising in engineering, physics, biomedicals, finance, etc. The aim of this chapter is to present a comparison among these WRMs. A detailed mathematical introduction is provided as follows:

Consider a differential equation:

$$u'' + P(x)u' + Q(x)u = 0 \tag{6.1}$$

with boundary conditions $u(a) = u(b) = 0,\ a \le x \le b$.

(Primes denote the derivative with respect to x)

The approximate solutions are obtained in the following manner:

$$u_1(x) = c_1\phi_1(x) \text{ \#one-step solution}$$

$$u_2(x) = c_1\phi_1(x) + c_2\phi_2(x) \text{ \#two-step solution}$$

$$u_n(x) = c_1\phi_1(x) + c_2\phi_2(x) + \cdots + c_n\phi_n(x) \text{ \#}n\text{-step solution}$$

$\phi_1,\ \phi_2, \ldots,\ \phi_n$ are called *base functions*. These base functions are selected in such a way that they satisfy the given boundary conditions and they must be linearly independent.

Some examples of the base functions for the above boundary conditions are:

$\phi_1(x) = (x-a)(x-b)$	$\phi_1(x) = \sin\left\{\pi\left(\frac{x-a}{b-a}\right)\right\}$
$\phi_2(x) = (x-a)^2(x-b)$	$\phi_2(x) = \sin\left\{2\pi\left(\frac{x-a}{b-a}\right)\right\}$
$\phi_3(x) = (x-a)^3(x-b)$	.
.	.
.	$\phi_n(x) = \sin\left\{n\pi\left(\frac{x-a}{b-a}\right)\right\}$
$\phi_n(x) = (x-a)^n(x-b)$	

Note that the selection of base function is not unique.

WRMs are actually a class of different numerical methods developed to obtain an approximate solution of a differential equation, in a domain D, of the form:

$$\mathcal{O}(u(x)) + X(x) = 0 \tag{6.2}$$

where $u(x)$ is the unknown dependent variable, $\mathcal{O}$ is the differential operator, $X(x)$ is the known function.

Steps:

- Select suitable base functions $\phi_i(x)$, satisfying the boundary conditions.
- Construct an approximate solution ($\bar{u}(x) = c_i\phi_i(x)$), which is a linear combination of the selected base functions, where c_is are unknown parameters and $i = 1, 2, \ldots, n$.
- Substitute $\bar{u}(x)$ into eq. (6.2).
- Get residual $R(x)$.
- Force the residual to vanish in some average sense to get an algebraic system in terms of unknown parameters c_i's.
- Solve the algebraic system to get the unknown parameters c_i's.

Note: Since $\bar{u}(x)$ is the approximate solution, it cannot satisfy eq. (6.2) completely and therefore an error (residual $R(x)$) is created. Mathematically:

$$O(\bar{u}(x)) + X(x) = R(x) \neq 0 \tag{6.3}$$

Multiply $R(x)$ by an arbitrary function known as *weight function* $W(x)$ and force the weighted average of the residual to vanish over the domain D:

$$\int_a^b R(x) \cdot W(x)dx = 0 \tag{6.4}$$

The technique of picking different weight functions gives rise to the different WRMs.

6.2 Types of WRM

On the basis of selecting different weight functions, given in Table 6.1, WRMs are generally classified in the following five types:

1. Galerkin's method
2. LS method
3. Collocation method
4. SD method
5. Moment method

Table 6.1: Weight functions of different WRMs.

S. no.	Method	Weight function
1	Galerkin's method	Base functions are the weight functions $W_i(x) = \phi_i(x)$
2	Least squares method	$W_i(x) = \dfrac{\partial R(x)}{\partial c_i}$

Table 6.1 (continued)

S. no.	Method	Weight function
3	Collocation method	The residual is made zero at as many points of the domain as there are unknown parameters. These points of the domain are called *collocation points* $R(x_i) = 0$, where $x_i \in D$ 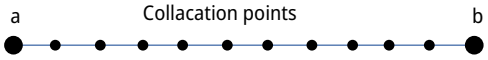
4	Subdomain method	The domain D is divided into as many subdomains as there are unknown parameters. The integral of the residual in each domain is then put to be zero: $\int_{d_i} R(x)dx = 0$ 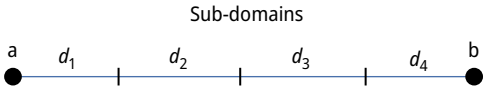
5	Moment method	$W_i(x) = x^i, i \in \mathbb{N}$

6.3 Mathematical Analysis

The following example is taken for the mathematical analysis:

$$\frac{d^2u}{dx^2} - 4\frac{du}{dx} + 4u + x^2 = 0 \tag{6.5}$$

Boundary conditions:

$$u(0) = 0,\ u(2) = 0 \tag{6.6}$$

6.3.1 Exact Solution

Complimentary function = $(A + Bx)e^{2x}$ (A and B are arbitrary constants).

Particular integral = $\frac{1}{(D^2 - 4D + 4)}\left(-x^2\right) = -\frac{1}{4}\left(x^2 + 2x + \frac{3}{2}\right)$. (using binomial theorem).

The complete solution after using the boundary conditions:

$$u(x) = \left[\frac{3}{8} + \frac{1}{16}\left(19e^{-4} - 3\right)x\right]e^{2x} - \frac{1}{4}\left(x^2 + 2x + \frac{3}{2}\right) \tag{6.7}$$

6.3.2 Galerkin's Method (Two-Step Solution)

Let the base functions are: $\phi_1(x) = x(x-2),\ \phi_2(x) = x^2(x-2)$

Approximate solution:

$$\bar{u}(x) = c_1 x(x-2) + c_2 x^2(x-2) \tag{6.8}$$

Putting the approximate solution into eq. (6.5) to get the residue as follows:

$$R_1(x) = 2c_1\left(2x^2 - 8x + 5\right) + c_2\left(4x^3 - 20x^2 + 22x - 4\right) + x^2 \tag{6.9}$$

Now making use of eq. (6.4) with both weight functions:

$$\int_0^2 R_1(x) \cdot x(x-2)dx = 0, \quad \int_0^2 R_1(x) \cdot x^2(x-2)dx = 0$$

On simplification we get: $3c_1 - c_2 = 3,\ 49c_1 + 8c_2 = 28$

On solving the system, we have $c_1 = \frac{52}{73},\ c_2 = -\frac{63}{73}$

Therefore, from eq. (6.8), the approximate solution is as follows:

$$\bar{u}(x) = \frac{52}{73}x(x-2) - \frac{63}{73}x^2(x-2) \tag{6.10}$$

6.3.3 Galerkin's Method (Three-Step Solution)

Approximate solution:

$$\bar{u}(x) = c_1 x(x-2) + c_2 x^2(x-2) + c_3 x^3(x-2) \tag{6.11}$$

Using the similar procedure as used in the two-step solution, we get the following residue and approximate solution:

$$R_2(x) = 2c_1\left(2x^2 - 8x + 5\right) + c_2\left(4x^3 - 20x^2 + 22x - 4\right) + 4c_3\, x\left(x^3 - 6x^2 + 9x - 3\right) + x^2 \tag{6.12}$$

$$\bar{u}(x) = -\frac{353}{691}x(x-2) + \frac{1{,}743}{1{,}382}x^2(x-2) - \frac{3{,}297}{2{,}764}x^3(x-2) \tag{6.13}$$

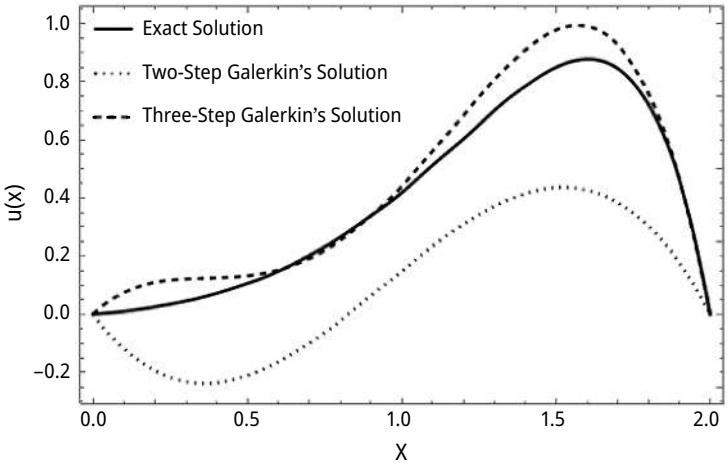

Figure 6.1: Comparison among the two-step Galerkin's solution, three-step Galerkin's solution, and the exact solution.

6.3.4 Least Squares Method (Two-Step Solution)

$$W_1(x) = \frac{\partial R_1(x)}{\partial c_1} = 2\left(2x^2 - 8x + 5\right), \quad W_2(x) = \frac{\partial R_1(x)}{\partial c_2} = \left(4x^3 - 20x^2 + 22x - 4\right)$$

where $R_1(x)$ is defined in eq. (6.9).

Now making use of eq. (6.4) with both of these weight functions:

$$\int_0^2 R_1(x) \cdot 2\left(2x^2 - 8x + 5\right) dx = 0, \quad \int_0^2 R_1(x) \cdot \left(4x^3 - 20x^2 + 22x - 4\right) dx = 0$$

On simplification, we get:

$$87c_1 + 27c_2 = 22, \quad \frac{72}{5}c_1 + \frac{2{,}272}{105}c_2 = 8$$

On solving the system, we have $c_1 = \frac{3{,}413}{19{,}605}, \quad c_2 = \frac{1{,}659}{6{,}535}$

Therefore, from eq. (6.8), the approximate solution is:

$$\bar{u}(x) = \frac{3{,}413}{19{,}605}x(x-2) + \frac{1{,}659}{6{,}535}x^2(x-2) \tag{6.14}$$

6.3.5 Least Squares Method (Three-Step Solution)

$$W_1(x) = \frac{\partial R_2(x)}{\partial c_1} = 2\left(2x^2 - 8x + 5\right),\ W_2(x) = \frac{\partial R_2(x)}{\partial c_2} = \left(4x^3 - 20x^2 + 22x - 4\right),$$

$$W_3(x) = \frac{\partial R_2(x)}{\partial c_3} = 4x\left(x^3 - 6x^2 + 9x - 3\right)$$

where $R_2(x)$ is defined in eq. (6.12).

Now using the similar procedure as used in the two-step LS solution, we get the following approximate solution:

$$\bar{u}(x) = -\frac{178{,}213(x-2)x^3}{777{,}036} + \frac{816{,}991(x-2)x^2}{1{,}942{,}590} + \frac{24{,}217(x-2)x}{224{,}145} \tag{6.15}$$

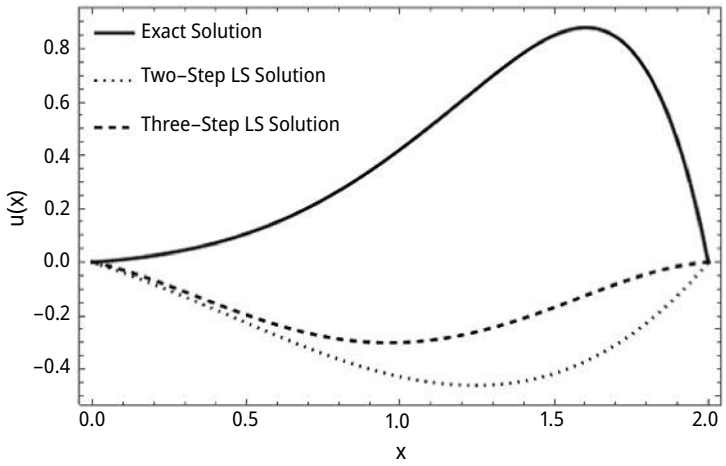

Figure 6.2: Comparison among the two-step LS solution, three-step LS solution, and the exact solution.

6.3.6 Collocation Method (Two-Point)

Consider $x = \frac{2}{3}$ and $x = \frac{4}{3}$ as two collocation points.

Now, using eq. (6.9), $R_1\left(\frac{2}{3}\right) = 0$ and $R_1\left(\frac{4}{3}\right) = 0$ gives:

$$15c_1 + 40c_2 = -6{,}57c_1 + 10c_2 = 24$$

On solving the system, we have $c_1 = \frac{34}{71},\ c_2 = -\frac{117}{355}$

Therefore, from eq. (6.8), the approximate solution is:

$$\bar{u}(x) = \frac{34}{71}x(x-2) - \frac{117}{355}x^2(x-2) \tag{6.16}$$

6.3.7 Collocation Method (Three-Point)

Consider $x = \frac{1}{2}$, $x = 1$, and $x = \frac{3}{2}$ as two collocation points.

Now, using eq. (6.12), $R_2\left(\frac{1}{2}\right) = 0$, $R_2(1) = 0$, and $R_2\left(\frac{3}{2}\right) = 0$ gives:

$$12c_1 + 10c_2 + c_3 = -1,\ -2c_1 + 2c_2 + 4c_3 = -1,\ 20c_1 + 10c_2 - 9c_3 = 9$$

On solving the system, we have $c_1 = -\frac{75}{34}$, $c_2 = \frac{48}{17}$, $c_3 = -\frac{47}{17}$

Therefore, from eq. (6.11), the approximate solution is:

$$\bar{u}(x) = -\frac{75}{34}x(x-2) + \frac{48}{17}x^2(x-2) - \frac{47}{17}x^3(x-2) \tag{6.17}$$

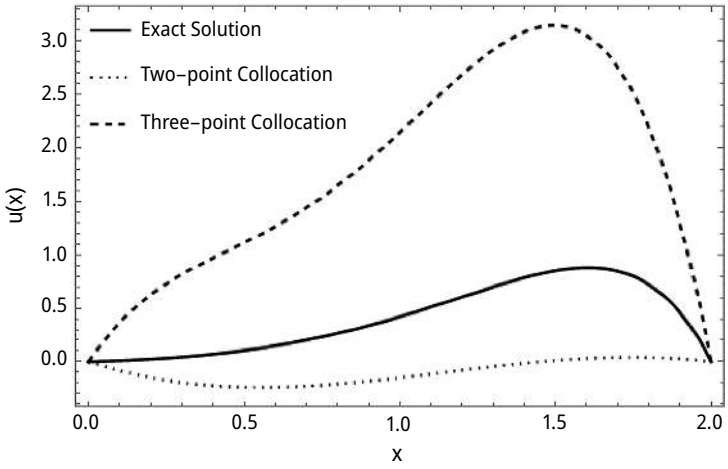

Figure 6.3: Comparison among the two-point collocation solution, three-point collocation solution, and the exact solution.

6.3.8 SD Method (Two-Step Solution)

Dividing the entire domain into two SDs, $0 \le x \le 1$ and $1 \le x \le 2$.

$$\int_0^1 R_1(x)dx = 0 \text{ and } \int_1^2 R_1(x)dx = 0$$

Simplifying, we have $10c_1 + 4c_2 = -1,\ 14c_1 + 8c_2 = 7$

On solving the system, we have $c_1 = -\frac{3}{2}$, $c_2 = \frac{7}{2}$

Therefore, from eq. (6.8), the approximate solution is:

$$\bar{u}(x) = -\frac{3}{2}x(x-2) + \frac{7}{2}x^2(x-2) \tag{6.18}$$

6.3.9 SD Method (Three-Step Solution)

Dividing the entire domain into two SDs, $0 \le x \le \frac{2}{3}$, $\frac{2}{3} \le x \le \frac{4}{3}$, and $\frac{4}{3} \le x \le 2$.

$$\int_0^{2/3} R_2(x)dx = 0, \quad \int_{2/3}^{4/3} R_2(x)dx = 0, \quad \text{and} \quad \int_{4/3}^{2} R_2(x)dx = 0$$

$$\frac{8}{81} + \frac{284}{81}c_1 + \frac{4}{9}c_2 - \frac{232}{1215}c_3 = 0,$$

$$\frac{56}{81} - \frac{100}{81}c_1 + \frac{92}{81}c_2 + \frac{2888}{1215}c_3 = 0,$$

$$\frac{152}{81} - \frac{292}{81}c_1 - \frac{236}{81}c_2 - \frac{712}{1215}c_3 = 0$$

On solving the system, we have $c_1 = -\frac{515}{2{,}357}$, $c_2 = \frac{5{,}193}{4{,}714}$, $c_3 = -\frac{8{,}775}{9{,}428}$

Therefore, from eq. (6.11), the approximate solution is:

$$\bar{u}(x) = -\frac{515}{2{,}357}x(x-2) + \frac{5{,}193}{4{,}714}x^2(x-2) - \frac{8{,}775}{9{,}428}x^3(x-2) \tag{6.19}$$

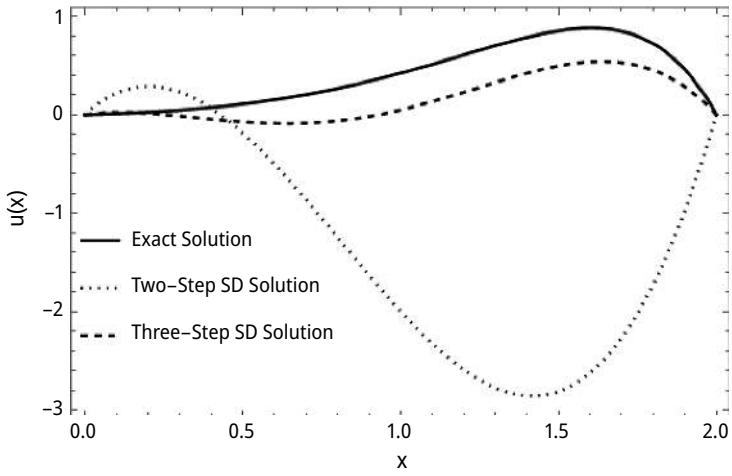

Figure 6.4: Comparison among the two-step subdomain solution, three-step subdomain solution, and the exact solution.

6.3.10 Moment Method (Two-Step Solution)

$$W_1(x) = x, \;\; W_2(x) = x^2$$

Now making use of eq. (6.4) with both the weight functions:

$$\int_0^2 R_1(x) \cdot x \, dx = 0, \quad \int_0^2 R_1(x) \cdot x^2 \, dx = 0$$

On simplification, $\frac{20}{3} c_1 + \frac{56}{15} c_2 = 4, \;\; \frac{176}{15} c_1 + 8c_2 = \frac{32}{5}$

On solving the system, we have $c_1 = \frac{57}{67}, c_2 = -\frac{30}{67}$

Therefore, from eq. (6.8), the approximate solution is:

$$\bar{u}(x) = \frac{57}{67} x(x-2) - \frac{30}{67} x^2(x-2) \tag{6.20}$$

6.3.11 Moment Method (Three-Step Solution)

$$W_1(x) = x, \;\; W_2(x) = x^2, \;\; W_3(x) = x^3$$

$$\int_0^2 R_2(x) \cdot x \, dx = 0, \quad \int_0^2 R_2(x) \cdot x^2 \, dx = 0, \quad \int_0^2 R_2(x) \cdot x^3 \, dx = 0$$

On simplification and solving the obtained system we get the following approximate solution:

$$\bar{u}(x) = -\frac{915}{421} x(x-2) + \frac{3{,}493}{842} x^2(x-2) - \frac{4{,}739}{1{,}684} x^3(x-2) \tag{6.21}$$

6.4 Discussion of the Results

Five different WRMs are used to solve a BVP defined in eqs. (6.5) and (6.6). Both two- and three-step solutions are evaluated. The comparison of results is presented graphically. Entire process of each method is given step-by-step.

Figure 6.1 represents the comparison among the two-step Galerkin's solution, three-step Galerkin's solution with the exact solution. It is observed that the three-step Galerkin's solution is in good agreement with the exact solution. Figure 6.2 represents the comparison among the two-step LS solution, three-step LS solution, and the exact solution. Similarly, in Figures 6.3–6.5, the solutions of collocation method, SD method, and moment method are compared with the exact solution, respectively. Two-step solutions

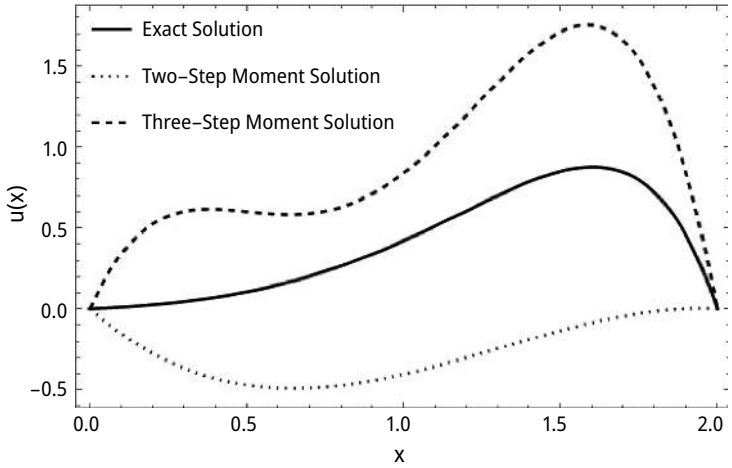

Figure 6.5: Comparison among the two-step moment method solution, three-step moment method solution, and the exact solution.

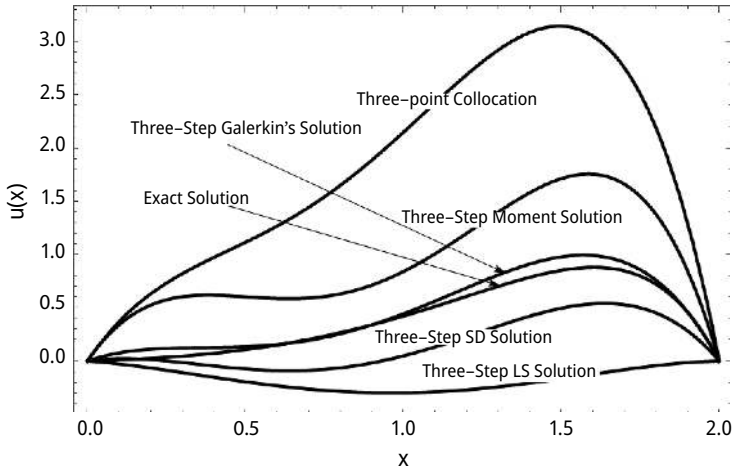

Figure 6.6: Comparison among the solutions of different methods with the exact solution.

Table 6.2: L_∞ error and root mean squared error comparison for three-step solutions of WRM with the exact solution.

Method	$x = 0.0$	0.4	0.8	1.0	1.2	1.6	2.0	L_∞ error	RMS error
Exact solution	0	0.07202	0.26561	0.42116	0.60618	0.87867	0		
Galerkin	0	0.12622	0.25468	0.44248	0.68647	0.9898	0		
Absolute error	0	0.0542	0.01093	0.02132	0.08029	0.11113	0	0.11113	0.05645

Table 6.2 (continued)

Method	$x = 0.0$	0.4	0.8	1.0	1.2	1.6	2.0	L_∞ error	RMS error
Least squares	0	−0.1533	−0.2858	−0.2993	−0.2712	−0.124	0		
Absolute error	0	0.22533	0.55141	0.72042	0.87734	1.00271	0	1.00271	0.61516
Collocation	0	0.97205	1.64781	2.14706	2.68687	3.05016	0		
Absolute error	0	0.90003	1.3822	1.7259	2.08069	2.17149	0	2.17149	1.45130
Subdomain	0	−0.0469	−0.0644	0.04762	0.22735	0.53671	0		
Absolute error	0	0.11887	0.33004	0.37354	0.37883	0.34196	0	0.37883	0.27335
Moment	0	0.61714	0.62945	0.83907	1.1977	1.75363	0		
Absolute error	0	0.54512	0.36384	0.41791	0.59152	0.87496	0	0.87496	0.49564

are very much less accurate than the three-step solutions. In Figure 6.6, the exact solution of the BVP is compared with the solutions of all the five WRMs. It is observed that, although all the solutions converge at the end points, i.e., $x = 0$ and $x = 2$, yet the Galerkin method provides the best approximate solution in comparison to the other WRMs as far as three-step solution is concerned. The error analysis presented in Table 6.2 shows the L_∞ error and the RMS error for the five WRMs under three-step solution.

6.5 Conclusions

The following major conclusions can be drawn:

1. Galerkin's method provides the best approximate solution in comparison to the other WRMs.
2. The increasing order of the RMS error of these methods for three-step solution is as follows:
   Galerkin's method < SD method < moment method < LS method < collocation method
3. The approximate solutions can be made more accurate by increasing the number of steps involved.
4. L_∞ error is always proportional to RMS error.

References

[1] Gupta, R. S. (2015). Elements of Numerical Analysis. Cambridge University Press.

[2] Galerkin, B. G. (1915). Rods and Plates. Series occurring in some problems of elastic equilibrium of rods and plates, Vestn. Inzhen. i Tekh. Petrograd 19, 897–908; Translation 63–18924, Clearinghouse Fed. Sci. Tech. Info.

[3] Bhadauria, B. S. & Srivastava, A. (2022). Combined effect of internal heating and through-flow in a nanofluid saturated porous medium under local thermal nonequilibrium. Journal of Porous Media, 25(2), 75–95. doi; 10.1615/JPorMedia.2021036936.

[4] Srivastava, A. & Bhadauria, B. S. (2023). Heat and mass transfer, and chaotic convection in nanofluids. Journal of Nanofluids, 12(4), 904–918. doi: 10.1166/jon.2023.1967.
[5] Singh, B. K. & Gupta, M. (2024). Trigonometric tension B-spline collocation approximations for time fractional burgers' equation. Journal of Ocean Engineering and Science, 9(5), 508–516. https://doi.org/10.1016/j.joes.2022.03.023.
[6] Singh, B. K. & Gupta, M. (2022). Numerical Solution of Fisher's Equation by using Fourth-Order Collocation Scheme Based on Modified Cubic B-Splines. In Computing and Simulation for Engineers. CRC Press, pp. 209–220.
[7] Choi, H. G. (2012). A least-square weighted residual method for level set formulation. International Journal for Numerical Methods in Fluids, 68(7), 887–904. https://doi.org/10.1002/fld.2585.
[8] Lindvall, K. & Scheffel, J. (2018). A time-spectral method for initial-value problems using a novel spatial subdomain scheme. Cogent Mathematics and Statistics, 5(1), 1529280. https://doi.org/10.1080/25742558.2018.1529280.

Vishal Chhabra, Chandra Shekhar Nishad*, and Manoj Sahni

Chapter 7
Boundary Element Analysis for MHD Stokes Flow Through a Microchannel Exhibiting Surface Roughness

Abstract: This study investigates the two-dimensional, pressure-driven magnetohydrodynamics (MHD) Stokes flow within a rectangular microchannel with surface roughness that is modeled using alternate Navier's slip boundary conditions, maintaining the same phase. The Stokes equations, augmented with the Lorentz force term, are numerically solved using the boundary element method (BEM) based on the stream function and vorticity variables' approach. A very small magnetic Reynolds number is considered to neglect the induced magnetic field equation. We explore the hydrodynamics of the present model by varying assumed dimensionless variables to better understand the dynamics of the Stokes problem. The findings of this study have practical applications in optimizing mixing and heat transfer in microfluidic systems.

Keywords: boundary element method, Hartmann number, surface roughness, slip length, Stokes equations

Nomenclature

L	Characteristic length
U_0	Characteristic velocity
μ	Dynamic viscosity of the fluid
$\widetilde{\boldsymbol{J}}$	Electric current density
$\widetilde{\boldsymbol{B}}$	Magnetic induction vector of the applied uniform magnetic field
$\widetilde{\boldsymbol{F}}$	Lorentz force

Acknowledgment: The author Vishal Chhabra is thankful for the financial support from Pandit Deendayal Energy University, Gujarat, India, in a form of fellowship offered by the institute.

*__Corresponding author: Chandra Shekhar Nishad__, Department of Science, and Mathematics, International Institute of Information Technology, Naya Raipur 493661, Chattisgarh, India, e-mail: chandrashekhar@iiitnr.edu.in
Vishal Chhabra, Department of Mathematics, School of Basic and Applied Sciences, K. R. Mangalam University, Gurugram 122103, Haryana, India, e-mail: vishalchhabra854@gmail.com
Manoj Sahni, Department of Mathematics, School of Technology, Pandit Deendayal Energy University, Gandhinagar 382426, Gujarat, India, e-mail: manojsahani117@gmail.com

https://doi.org/10.1515/9783111723464-007

σ	Electrical conductivity of the fluid
$\widetilde{\boldsymbol{V}}$	Velocity vector of the fluid
ψ	Stream function
$\tilde{P}$	Hydrodynamic pressure
G^L	Free space Green's function for Laplace operator
G^{MH}	Free space Green's function for modified Helmholtz operator
G^C	Free space Green's function for mixed Laplace and modified Helmholtz operators
ω	Vorticity variable
K_0	Modified Bessel function
$d\tilde{P}/d\tilde{X}$	Pressure gradient
Ha	Hartmann number
R_m	Magnetic Reynolds number

7.1 Introduction

Creeping flow, also known as Stokes flow, occurs when fluid motion is primarily influenced by viscous and pressure forces, with negligible inertial force. This low Reynolds limit flow is mathematically modeled using the Stokes equations and it plays a key role in understanding natural phenomena like microorganism swimming [1] along with engineering uses in Micro-Electro-Mechanical Systems (MEMS) [2], paint technologies, flexible fiber dynamics [3], and fluid mixing [4]. Furthermore, Stokes flow appears within microchannels, such as capillaries [5]. In addition to the aforementioned Stokes flow problems, there are multiple problems within the discipline of medical applications [6, 7]. In this way, Stokes flow past a red blood cell was solved by Hadjinicolaou et al. [8] using a combination of the Kelvin inversion method and the idea of semi-separation of the variables of the Stokes operator. Their research significantly contributes to medical testing, such as the erythrocyte sedimentation rate (ESR). Luca and Smith [9] employed the unified transform method, a generalized variant of the conventional Fourier transform, to address the problem of solving the Stokes flow within a convex polygonal domain.

Understanding Stokes flows in confined geometries with Navier's slip and no-penetration boundary conditions is crucial for advancing fluid dynamics research. The concept of the slip boundary condition on an impermeable wall was originally introduced by Navier [10], explaining the relationship between shear stress and the relative movement of fluid layers close to the surface. Later, Helmholtz and Pitrowski [11] expanded on this idea by introducing the concept of slip length to describe the slip behavior occurring near solid surfaces. Furthermore, the inverse proportional relationship between the coefficient of slip and the pressure was studied by Kundt and Warburg [12]. Numerous experiments have been conducted to get insights into the underlying characteristics of slip phenomena occurring over solid surfaces. Following this, it is revealed by Vinogradovand Ivanova [13] that slip velocity might also depend on the normal stress. The concept of slip length involves the introduction of an apparent

surface, referred to as a virtual surface, where the velocity of a fluid may be zero below the actual physical surface. The presence of a substantial slip length is evident in the observed scenario, wherein bubbles become entrapped on a surface exhibiting hydrophobic properties [13–15]. The justification addressed by the investigations [16–19] concerns the implementation of the no-penetration boundary condition at a surface-fluid interface. The theory of such flows has experienced a resurgence in attention due to the emergence of new challenges in microfluidics applications [20].

When slip occurs, the trouble appears in determining its fundamental form. The occurrence of slip is observed by Brenner [21] as a result of variations in the mass density of the fluid adjacent to the wall. Luchini [22] discussed the case of fluid flow near a solid wall exhibiting small-scale roughness or waviness. Additionally, Mele and Tognaccini [23] have developed an appropriate wall boundary condition based on the slip length concept to describe riblets, which are characterized by rough surfaces. However, it is necessary to consider a macroscopic boundary condition that accounts for the slip velocity on a smooth surface, as examined by Zampogna et al. [24]. The determination of whether a slip or a no-slip condition occurs at the interface between an impermeable surface and a fluid is significantly dependent upon the specific characteristics of their interaction. Hydrophobic surfaces exhibit a Navier's slip boundary condition, while hydrophilic surfaces often result in a no-slip condition. In the literature, several investigations have been conducted on the chemical alteration of surfaces to render them either hydrophobic or hydrophilic [25, 26]. Consequently, Kamrin et al. [27] derived the general formula for the effective slip. The slip boundary condition presented by Hendy et al. [28] involves the manipulation of slip length along the primary direction of fluid flow.

The concept of patterned slip was explored by Zhao and Yang [29] in their investigation of electroosmotic flows through microchannels. Afterward, the impact of hydrodynamic slippage on electroosmotic flow through nanochannels was studied by Datta and Choudhary [30]. Following this, Nishad et al. [31] analyzed the steady Stokes flow inside a microchannel, where both walls obeyed the in-phase patterned slip. Their work gives insight into the design principles of microfluidic mixers. The unique characteristics shown by textured superhydrophobic surfaces have drawn significant attention in the field of multidisciplinary study. In light of this, Ageev and Osiptsov [32] applied the boundary integral equation method (BIEM) to demonstrate the decrease in friction within a microchannel including a single superhydrophobic surface. This study gives rise to an insight into understanding the phenomena of some of the realistic biomechanical and medical applications. A numerical solution was obtained by Aissa et al. [33] for the isothermal flow in a microchannel, with a particular focus on the slip regime. The COSMOL algorithm was utilized for this purpose.

The investigation of Stokes flow within a magnetic field across various channel designs is vital, as it relates to a range of practical uses, such as oil filtration and the development of cooling systems [34]. In this regard, the mathematical modeling of magnetohydrodynamics (MHD) Stokes flow was first modified by Chester [35]. Gotoh

[36] studied the behavior of a conducting MHD fluid as it flows past an obstruction. The analysis was performed using the Stokes approximation. Extensive research has been conducted on the phenomenon of unsteady MHD Stokes flow. For instance, Sasikala et al. [37] investigated the characteristics of time-dependent creeping dusty flow within a rectangular porous channel, employing the similarity transformation approach. Celik [38] examined the MHD Stokes flow in a lid-driven cavity, building upon the prior work conducted by Sasikala et al. [37]. However, the author specifically focused on investigating the related Couette flow using the finite difference method (FDM). The work of Çelik [38] was extended by Gurbuz-Caldag and Celik [39] using the same method, with the addition of variation in the inclination of magnetic field.

This study aims to analyze how an inclined magnetic field affects the Stokes flow within a microchannel featuring in-phase slip patterning. The use of patterned slip in the presence of an inclined magnetic field has the potential to promote mixing in microfluidic devices in a manner analogous to patterned topography. The Navier slip boundary condition is used to assess the influence of the slip condition at the microchannel boundary. The analytical solution for this fluid flow problem is not achievable due to the presence of applied slip patterning on the microchannel. Therefore, it is imperative to employ reliable and efficient numerical methodologies to address the above-described fluid flow problem. A variety of numerical approaches may be observed in the existing literature, such as the finite element method (FEM) [40, 41], boundary element method (BEM) [31, 42–44, 45], and FDM [46], among others. Compared to the earlier-discussed numerical methods, the BEM proves to be substantially more advantageous when addressing linear operators [47]. This chapter is structured as follows: Section 7.2 illustrates the mathematical framework for the flow problem. Section 7.3 examines the influence of dimensionless parameters using graphical representations. Section 7.4 provides a short summary of the study.

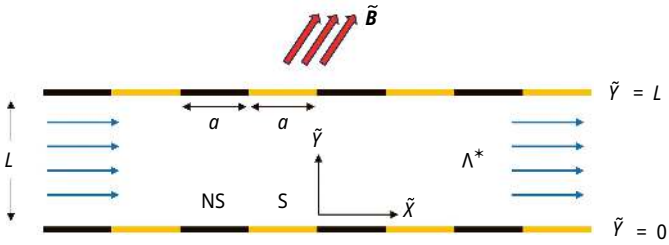

Figure 7.1: Schematic of MHD Stokes flow inside a microchannel exhibiting periodic surface roughness.

7.2 Mathematical Formulation

7.2.1 Dimensional Governing Equations and Assumptions

Assumptions for proposed hydrodynamic model are as follows:

- Two-dimensional $(2D)$, pressure-driven Stokes flow through a horizontal rectangular microchannel is considered.
- The mean width of the channel is L units and mean length of the channel M units.
- The black and golden line segments on the walls of the channel as depicted in Figure 7.1 show the regions that exhibit no-penetration and Navier's slip boundary conditions, respectively.
- The dimensionless periodicity of alternate applied boundary conditions is denoted by a.
- Let $\widetilde{\boldsymbol{J}} = \sigma(\widetilde{\boldsymbol{V}} \times \widetilde{\boldsymbol{B}})$ [48] denote the electric current density, where σ, $\widetilde{\boldsymbol{V}}$, and $\widetilde{\boldsymbol{B}}$ denote the electrical conductivity of the field, the velocity vector, and the magnetic field of uniform strength, respectively. In our study, we assumed that the magnetic field makes an angle (θ) with the vertical axis. The Lorentz force $\widetilde{\boldsymbol{F}} = \widetilde{\boldsymbol{J}} \times \widetilde{\boldsymbol{B}} = -\sigma B_0^2 \cos^2(\theta)\widetilde{\boldsymbol{V}}$ and $\widetilde{\boldsymbol{V}} = (\tilde{U}, \tilde{V})$ are collinear and opposite in the directions, where $B_0 \cos(\theta)$ is the magnitude of the magnetic field in the orthogonal direction of the flow.
- To neglect the effect of the induced magnetic field from the current study, $R_m \ll 1$ is considered.

The steady MHD Stokes flow is mathematically modeled using Stokes equations [49], given by

$$\mu\tilde{\nabla}^2\widetilde{\boldsymbol{V}} - \sigma B_0^2 \cos^2(\theta)\widetilde{\boldsymbol{V}} = \tilde{\nabla}\tilde{P} \tag{7.1}$$

$$\tilde{\nabla}.\widetilde{\boldsymbol{U}} = 0 \tag{7.2}$$

7.2.2 Dimensionless Variables

The dimensionless variables are as follows:

$$\boldsymbol{V} = \frac{\widetilde{\boldsymbol{V}}}{U_0}, X = \frac{\tilde{X}}{L}, \; Y = \frac{\tilde{Y}}{L}, P = \frac{\tilde{P}}{\tilde{P}_0}, \tilde{P}_0 = \frac{\mu U_0}{L}, \tilde{\nabla} = \frac{\nabla}{L}, \tilde{\nabla}^2 = \frac{\nabla^2}{L}, l_s = \frac{b}{L} \tag{7.3}$$

7.2.3 Dimensionless Governing Equations

On utilizing the dimensionless variables stated by eq. (7.3), the X- and Y-components of dimensional governing eqs. (7.1) and (7.2) reduce to:

$$\nabla^2 U - \kappa^2 U = \frac{\partial P}{\partial X} \tag{7.4}$$

$$\nabla^2 V - \kappa^2 V = \frac{\partial P}{\partial Y} \tag{7.5}$$

$$\nabla . \boldsymbol{V} = 0 \tag{7.6}$$

Where $\boldsymbol{V} = (U, V)$, $\kappa^2 = Ha^2 \cos^2(\theta)$, and $Ha = \sqrt{\sigma B_0^2 L^2 / \mu}$ [48].

7.2.4 Stream Function $(\boldsymbol{\psi})$ and Vorticity Variable $(\boldsymbol{\omega})$ Formulation

The stream function (ψ) [50] can be determined with the help of continuity equation:

$$U = \frac{\partial \psi}{\partial Y}, \; V = -\frac{\partial \psi}{\partial X} \tag{7.7}$$

For further solving the dimensionless governing equations (7.4) and (7.5) using stream function expressed by eq. (7.7), the steps are as follows:

$$\begin{aligned}
&\Rightarrow \quad \frac{\partial}{\partial Y}\left(\nabla^2 U - \kappa^2 U = \frac{\partial P}{\partial X}\right) - \frac{\partial}{\partial X}\left(\nabla^2 V - \kappa^2 V = \frac{\partial P}{\partial Y}\right) \\
&\Rightarrow \quad \nabla^2\left(\frac{\partial U}{\partial X} - \frac{\partial V}{\partial Y}\right) - \kappa^2\left(\frac{\partial U}{\partial X} - \frac{\partial V}{\partial Y}\right) = \frac{\partial}{\partial Y}\left(\frac{\partial P}{\partial X}\right) - \frac{\partial}{\partial X}\left(\frac{\partial P}{\partial Y}\right) \\
&\Rightarrow \quad \nabla^2\left[\frac{\partial}{\partial X}\left(\frac{\partial \psi}{\partial Y}\right) - \frac{\partial}{\partial Y}\left(-\frac{\partial \psi}{\partial X}\right)\right] - \kappa^2\left[\frac{\partial}{\partial X}\left(\frac{\partial \psi}{\partial Y}\right) - \frac{\partial}{\partial Y}\left(-\frac{\partial \psi}{\partial X}\right)\right] = 0 \\
&\Rightarrow \quad \nabla^2\left(\nabla^2 - \kappa^2\right)\psi = 0
\end{aligned} \tag{7.8}$$

where $\nabla^2 = \frac{\partial^2}{\partial X^2} + \frac{\partial^2}{\partial Y^2}$ is a harmonic differential operator. The governing equations reduces to:

$$\nabla^2\left(\nabla^2 - \kappa^2\right)\psi = 0 \tag{7.9}$$

$$\nabla . \boldsymbol{V} = 0 \tag{7.10}$$

Introducing vorticity variable (ω), i.e., $\omega = \nabla \times \boldsymbol{V}$, using eq. (7.7), is given by:

$$\omega = \nabla \times \boldsymbol{V} = \nabla \times (U, V) = \frac{\partial V}{\partial X} - \frac{\partial U}{\partial Y} = \frac{\partial}{\partial X}\left(-\frac{\partial \psi}{\partial X}\right) - \frac{\partial}{\partial Y}\left(\frac{\partial \psi}{\partial Y}\right) = -\left(\frac{\partial^2 \psi}{\partial X^2} + \frac{\partial^2 \psi}{\partial Y^2}\right) = -\nabla^2 \psi \tag{7.11}$$

To solve further the boundary value problem stated by eqs. (7.9) and (7.10), we substitute eq. (7.11) into eq. (7.9) to generate a coupled system of Poisson equation (7.12) and modified Helmholtz Eq. (7.13), which are as follows:

$$\nabla^2\psi = -\omega \tag{7.12}$$

$$\left(\nabla^2 - \kappa^2\right)\omega = 0 \tag{7.13}$$

7.2.5 Boundary Conditions

– The no-penetration boundary condition on the top boundary [51] is as follows:

$$U = 0,\ V = 0\ :\ \psi = 1,\ \frac{\partial\psi}{\partial Y} = 0\cdot \tag{7.14}$$

– Navier's slip boundary condition on the upper horizontal surface [52] is as follows:

$$\left(U - B\frac{\partial U}{\partial Y}\right)\Big|_{Y=1} = 0,\ V = 0\ :\ \psi = 1,\ \frac{\partial\psi}{\partial Y} + l_s\omega = 0\cdot \tag{7.15}$$

– The no-penetration boundary condition on the bottom boundary is as follows:

$$U = 0,\ V = 0\ :\ \psi = 0,\ \frac{\partial\psi}{\partial Y} = 0\cdot \tag{7.16}$$

– Navier's slip boundary condition on the lower horizontal surface [52] is as follows:

$$\left(U + B\frac{\partial U}{\partial Y}\right)\Big|_{Y=0} = 0,\ V = 0\ :\ \psi = 0,\ \frac{\partial\psi}{\partial Y} - l_s\omega = 0\cdot \tag{7.17}$$

– At the inlet:

$$U = 6\left(Y - Y^2\right),\ V = 0\ :\ \psi = 3Y^2 - 2Y^3,\ \omega = 12Y - 6\cdot \tag{7.18}$$

– At the outlet:

$$\frac{\partial U}{\partial X} = 0,\ \frac{\partial V}{\partial X} = 0\ :\ \frac{\partial\psi}{\partial X} = 0\ ,\ \frac{\partial\omega}{\partial X} = 0\cdot \tag{7.19}$$

7.2.6 Stream Function and Vorticity Variable-Based Boundary Element Method

Let $\chi\left(\tau_0^*, \eta_0^*\right) \in\ \Lambda^* \cup \partial\Lambda^*$ and $\varphi\left(\tau_1^*, \eta_1^*\right) \in \partial\Lambda^*$ are the integration and field points, respectively. The fundamental solutions of Laplacian operator $G^L = \ln\left(\lambda^*\right)/2\pi,$ modified Helmholtz operator $G^{MH} = -K_0\left(\lambda^*\eta\right)/2\pi,$ and composite operator $G^C = \left(G^{MH} - G^L\right)/\kappa^2,$ where K_0 represents the modified Bessel function of second kind of zeroth order and

$\lambda^* = |\chi - \varphi|$. Implementing Green's second identity to eqs. (7.12) and (7.13) in combination with the fundamental solution leads to boundary integrals at any given field point χ:

$$\Gamma(\chi)\psi(\chi) = \int_{\partial\Lambda^*} \left[\psi(\varphi)\frac{\partial G^L(\chi,\varphi)}{\partial n_\varphi} - G^L(\chi,\varphi)\frac{\partial \psi(\varphi)}{\partial n_\varphi}\right] ds(\varphi) - \int_{\partial\Lambda^*} \left[\omega(\varphi)\frac{\partial G^C(\chi,\varphi)}{\partial n_\varphi} - G^C(\chi,\varphi)\frac{\partial \omega(\varphi)}{\partial n_\varphi}\right] ds(\varphi), \tag{7.20}$$

$$\Gamma(\chi)\omega(\chi) = \int_{\partial\Lambda^*} \left[\omega(\varphi)\frac{\partial G^{MH}(\chi,\varphi)}{\partial n_\varphi} - G^{MH}(\chi,\varphi)\frac{\partial \omega(\varphi)}{\partial n_\varphi}\right] ds(\varphi)\,. \tag{7.21}$$

In eqs. (7.20) and (7.21), $\Gamma(\chi)$ is the free-term coefficient and it is defined as follows:

$$\Gamma(\chi) = \begin{cases} 1, & \text{if } \chi \in \Lambda^* \\ \dfrac{1}{2}, & \text{if } \chi \in \partial\Lambda^* \\ 0, & \text{if } \chi \notin \Lambda^* \cup \partial\Lambda^*\,. \end{cases} \tag{7.22}$$

It is noteworthy to observe that eqs. (7.20) and (7.21) contain integrals with singular kernels, making numerical methods essential for their evaluation, particularly in the context of irregular geometrical configurations. Analytical methods prove inadequate in such cases, as they fail to produce a solution. For numerical computation, the boundary is discretized using straight-line segments, with the assumption that boundary quantities are constant along each line segment. In this light, the computational boundary $\partial\Lambda^*$ is discretized into N_* steady elements (Figure 7.2). The boundary quantities ψ, $\partial\psi/\partial n$, ω, and $\partial\omega/\partial n$ are approximated by piece-wise uniform functions, ψ_j, $\partial\psi_j/\partial n$, ω_j, and $\partial\omega_j/\partial n, j = 1, 2, \ldots, N_*$.

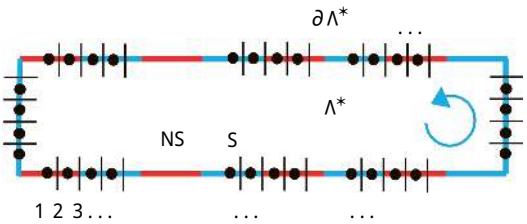

Figure 7.2: Discretization of the computational domain with in-phase fine patterned slip using constant boundary elements.

Using the collocation approach, the discretized forms of eqs. (7.20) and (7.21) are implemented at the midpoints $\chi \equiv \varphi_i, i = 1, 2, \ldots, N_*$ for each element, yielding:

$$\Gamma_i\psi_i = \sum_{j=1}^{N_*}\left[\psi_j \int\limits_{\varphi\in\partial\Lambda_j^*} \frac{\partial G^L(\varphi_i,\varphi)}{\partial n_\varphi} ds(\varphi) - \frac{\partial \psi_j}{\partial n_\varphi} \int\limits_{\varphi\in\partial\Lambda_j^*} G^L(\varphi_i,\varphi) ds(\varphi)\right. \tag{7.23}$$

$$\left. -\omega_j \int\limits_{\varphi\in\partial\Lambda_j^*} \frac{\partial G^C(\varphi_i,\varphi)}{\partial n_\varphi} ds(\varphi) + \frac{\partial \omega_j}{\partial n_\varphi} \int\limits_{\varphi\in\partial\Lambda_j^*} G^C(\varphi_i,\varphi) ds(\varphi)\right],$$

$$\Gamma_i\omega_i = \sum_{j=1}^{N_*}\left[\omega_j \int\limits_{\varphi\in\partial\Lambda_j^*} \frac{\partial G^{MH}(\varphi_i,\varphi)}{\partial n_\varphi} ds(\varphi) - \frac{\partial \omega_j}{\partial n_\varphi} \int\limits_{\varphi\in\partial\Lambda_j^*} G^{MH}(\varphi_i,\varphi) ds(\varphi)\right]. \tag{7.24}$$

Equations (7.23) and (7.24) can be rewritten as follows:

$$A\psi + B\frac{\partial \psi}{\partial n} + C\omega + D\frac{\partial \omega}{\partial n} = 0, \tag{7.25}$$

$$E\omega + F\frac{\partial \omega}{\partial n} = 0. \tag{7.26}$$

where the influence coefficients are given by

$$A_{ij} = \int\limits_{\varphi\in\partial\Lambda_j^*} \frac{\partial G^L(\varphi_i,\varphi)}{\partial n_\tau} ds(\tau) - \Gamma_j\delta_{ij}, \qquad B_{ij} = -\int\limits_{\varphi\in\partial\Lambda_j^*} G^L(\varphi_i,\varphi) ds(\varphi), \tag{7.27}$$

$$C_{ij} = -\int\limits_{\varphi\in\partial\Lambda_j^*} \frac{\partial G^C(\varphi_i,\varphi)}{\partial n_\tau} ds(\varphi), \qquad D_{ij} = \int\limits_{\varphi\in\partial\Lambda_j^*} G^C(\varphi_i,\varphi) ds(\varphi), \tag{7.28}$$

$$E_{ij} = \int\limits_{\varphi\in\partial\Lambda_j^*} \frac{\partial G^{MH}(\varphi_i,\varphi)}{\partial n_\varphi} ds(\varphi) - \Gamma_j\delta_{ij}, \quad F_{ij} = -\int\limits_{\varphi\in\partial\Lambda_j^*} G^{MH}(\varphi_i,\varphi) ds(\varphi). \tag{7.29}$$

In eqs. (7.27)–(7.29), $(A)_{ij} = A_{ij}$, $\psi = (\psi_1, \psi_2, \ldots, \psi_{N_*})^T$ and the term δ_{ij} refers to the Kronecker delta function. To identify the unknown boundary data, eqs. (25) and (26) are resolved with the aid of eqs. (7.14)–(7.19).The present BEM modeling involves discretizing the domain boundary into 220 straight-line elements, with nodes positioned at the midpoints of these elements. It was verified that increasing the number of boundary elements does not produce noticeable changes in the results. A grid of 197 × 197 solution points (N_s) is used for internal domain calculations. The BEM code is implemented using MATLAB®(R2014b) on a computer featuring an Intel®Core™ i5-2400 CPU @ 3.10 GHz processor. The computational time for running the BEM code in MATLAB is 124.8 s for each scenario.

7.2.7 Analysis of Singular Boundary Integrals

When $i \neq j$, the kernels within the integrals lack singularity, making them suitable for evaluation via the numerical Gauss quadrature method. Conversely, when $i = j$, the vector $\boldsymbol{\lambda}$ is associated with the jth element, where $\lambda^* = |\boldsymbol{\lambda}|$ remains tangential to the normal vector $\boldsymbol{n}$. This tangency introduces singularity in the integrals represented by eqs. (7.27)–(7.29). Analytical computation of these integrals is achievable when straight-line elements are employed. The derived influence coefficients A_{jj} and B_{jj} are formulated as follows:

$$A_{jj} = -\Gamma_j, B_{jj} = -\frac{l_j^*}{2\pi}\left(\ln\left(\frac{l_j^*}{2}\right) - 1\right) \tag{7.30}$$

where l_j^* denotes the length of the jth element. The remaining influence coefficients are obtained using the method proposed by Nishad et al. [44] and determined the integrals that appeared in eqs. (7.27)–(7.29), analytically for the case $i = j$. The fundamental solutions, namely, G^L, G^{MH}, and G^C are given by:

$$G^L = \frac{1}{2\pi}\ln\lambda^*, \frac{\partial G^L}{\partial \boldsymbol{n}} = \frac{1}{2\pi}\frac{\partial \lambda^*}{\partial \boldsymbol{n}} = \frac{\boldsymbol{\lambda}.\boldsymbol{n}}{2\pi\lambda^{*2}} \tag{7.31}$$

$$G^{MH} = -\frac{1}{2\pi}K_0(\lambda^*\kappa), \frac{\partial G^{MH}}{\partial \boldsymbol{n}} = \frac{\eta}{2\pi}K_1(\lambda^*\kappa)\frac{\partial \lambda^*}{\partial \boldsymbol{n}} = \frac{\kappa}{2\pi}K_1(\lambda^*\kappa)\frac{\boldsymbol{\lambda}.\boldsymbol{n}}{\lambda^*} \tag{7.32}$$

$$G^C = -\frac{1}{\kappa^2}\left(G^{MH} - G^L\right), \frac{\partial G^C}{\partial \boldsymbol{n}} = \frac{1}{\kappa^2}\left(\frac{\partial G^{MH}}{\partial \boldsymbol{n}} - \frac{\partial G^L}{\partial \boldsymbol{n}}\right) \tag{7.33}$$

when $\lambda^* \to 0$, i.e., the asymptotic behavior of $K_0(\lambda^*\kappa)$ is given by $K_0(\lambda^*\kappa) \approx -\gamma - ln(\lambda^*\kappa) + \ln(2)$, where $\gamma = 0.5772$ is known as Euler's constant. Furthermore, E_{jj} is given by:

$$E_{jj} = -\int_{\varphi \in \partial\Lambda_j^*} \frac{\partial G^{MH}(\varphi_i, \varphi)}{\partial n_\varphi} ds - \Gamma_j = \frac{\kappa}{2\pi}\int_{\varphi \in \partial\Lambda_j^*} K_1(\lambda^*\kappa)\frac{\boldsymbol{\lambda}.\boldsymbol{n}}{\lambda^*} ds - \Gamma_j = -\Gamma_j \tag{7.34}$$

Aforementioned vectors $\boldsymbol{\lambda}$ and $\boldsymbol{n}$ are oriented in a vertical manner relative to each other, resulting in the integral above reducing to zero. Similarly,

$$F_{jj} = -\int_{\varphi \in \partial\Lambda_j^*} G^{MH}\left(\varphi_j, \varphi\right) ds = \frac{1}{2\pi}\int_{-\frac{l_j^*}{2}}^{\frac{l_j^*}{2}} \left(\gamma + \ln\left(\frac{\lambda^*\kappa}{2}\right)\right) d\lambda^* = \frac{l_j^*}{2\pi}\left(\gamma + \ln\left(\frac{l_j^*\kappa}{4}\right) - \frac{2}{\kappa}\right) \tag{7.35}$$

$$C_{jj} = -\int\limits_{\varphi\in\partial\Lambda_j^*} \frac{\partial G^C\left(\varphi_j,\varphi\right)}{\partial n_\varphi} ds = -\frac{1}{\kappa^2}\int\limits_{\varphi\in\partial\Lambda_j^*} \left(\frac{\partial G^{MH}\left(\varphi_j,\varphi\right)}{\partial n_\varphi} - \frac{\partial G^L\left(\varphi_j,\varphi\right)}{\partial n_\varphi}\right) ds = 0 \quad (7.36)$$

$$D_{jj} = \int\limits_{\varphi\in\partial\Lambda_j^*} G^C\left(\varphi_j,\varphi\right) ds = \int\limits_{\varphi\in\partial\Lambda_j^*} \left(G^{MH}\left(\varphi_j,\varphi\right) - G^L\left(\varphi_j,\varphi\right)\right) ds = -\frac{1}{\kappa^2}\left(F_{jj} - B_{jj}\right) \quad (7.37)$$

7.3 Results and Discussion

7.3.1 Validation of Present Boundary Element Code

7.3.1.1 Lid-Driven Cavity Flow Problem

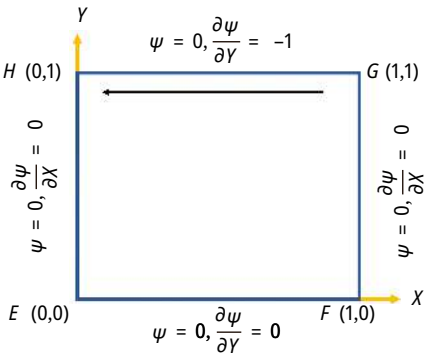

Figure 7.3: Schematic of lid-driven cavity.

We consider pressure-driven Stokes flow passing through within a 2D unit square cavity. The lid of the cavity is assumed to move steadily in the negative X-direction (Figure 7.3). The flow velocity on the boundaries is assumed to be zero.

We have presented a comparative analysis of our results in relation to previous investigations. In this light, we have presented the stream function (ψ) plot against vertical axis (Y) at $X = 0.5$ to compare the present results with existing results [53–55] in Figure 7.4. Furthermore, the comparison of the U versus Y at $X = 0.5$ with existing studies [53, 54, 56], is shown in Figure 7.5. It is apparent from Figures 7.4 and 7.5 that our results are in very good agreement with the existing investigation. This validation indicates that the present BEM code is precise as well as reliable.

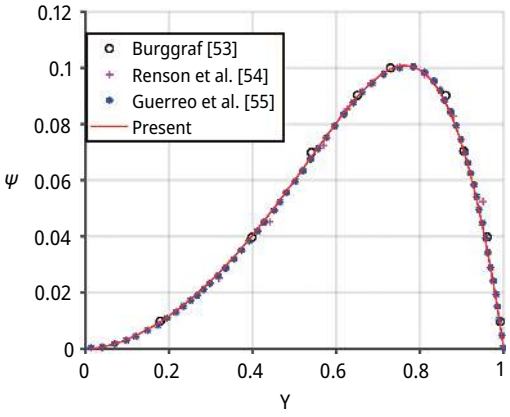

Figure 7.4: Comparison of ψ versus Y at $X = 0.5$ with existing literature [53–55].

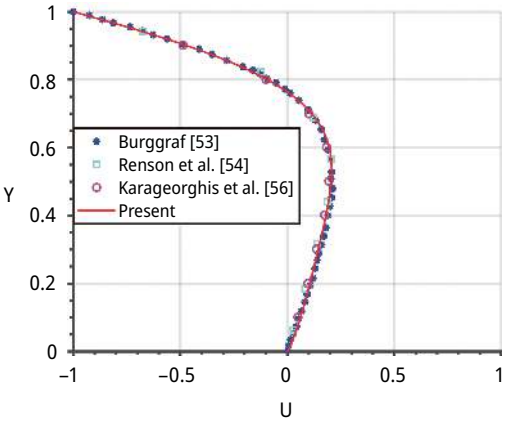

Figure 7.5: Comparison of U versus Y at $X = 0.5$ with existing studies [53, 54, 56].

7.3.1.2 Comparison of BEM Solution with Exact Solution of Stokes Flow Through Rectangular Channel

We assume a steady viscous incompressible Stokes flow passing through a horizontal parallel walled channel bounded by the walls $Y = 0$ and $Y = 1$. The no-penetration boundary conditions $U(0) = 0,\ U(1) = 0$ are applied on top and bottom horizontal boundaries, respectively. The assumed flow through rectangular channel is called plane-Poiseuille flow, whose analytic solution is given by:

$$U(Y) = 6\left(Y - Y^2\right) \tag{7.38}$$

The comparison of computed BEM solution of the above-described Stokes flow with the exact solution is shown in Figure 7.6. We observe that computed BEM solution in a good agreement with compared analytic solution is given by eq. (7.38).This comparison gives the assurance about the precision of the BEM code. This section validates our BEM code, and we continue by analyzing the MHD Stokes flow inside a microchannel exhibiting surface roughness.

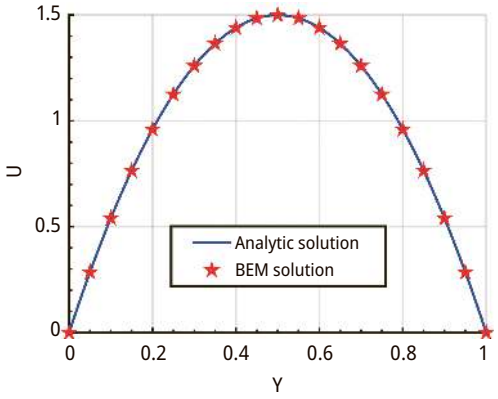

Figure 7.6: Comparison of U versus Y at $X = 0$ determined using boundary element method with the exact solution.

7.3.2 Hydrodynamic Model of MHD Stokes Flow Inside a Microchannel Featuring Wall Roughness

This study focuses on examining the hydrodynamic behavior of the proposed model by exploring factors, such as horizontal velocity (U), pressure gradients, and shear stresses. We assess the effects of varying dimensionless parameters, including the Hartmann number (Ha), the magnetic field inclination angle (θ), and slip length (l_s), while fixing the characteristic length of slip periodicity $a = 0.5$. For the computational purposes, the considered dimension of microchannel is $-5 \le X \le 5, 0 \le Y \le 1$. The vertical cross-section $X = -1.75$ is selected to observe the dynamics of Stokes flow velocity (U) in terms of vertical axis (Y), as this cross-section possesses slip regions on both channel walls. For analyzing the variation of Stokes flow velocity (U) and pressure gradient along horizontal axis, the cross-section $Y = 0.5$ is selected. Additionally, the shear stress distribution along the horizontal axis at the upper surface $(Y = 1)$ is studied comprehensively. Each scenario is evaluated for $l_s = 0.1$ and 1.

7.3.2.1 Effect of Hartmann Number (Ha)

Here, we have discussed the impact of Ha on Stokes flow inside a microchannel with $a = 0.5$. To analyze the hydrodynamics of Stokes flow for varying Ha, we initially present the streamline patterns corresponding to two distinct l_s values at a fixed inclination angle $\theta = 0$. From Figure 7.7, we observed that the contour plots of the streamline show qualitative identical nature for varying Ha with $l_s = 0.1$ and 1, respectively. It is found that for fixed Hartmann number (Ha), The streamlines in the slip regimes are more closer for $l_s = 1$ in comparison to the case when $l_s = 0.1$. During an increase in slip length, the velocity gradient near the wall reduces, resulting in a more equally distributed velocity over the width of the channel. As a result, the flow lines next to the wall are pushed toward the wall due to the higher velocity of the fluid in close contact to the wall.

For knowing more in detail about the hydrodynamics, the U versus Y at $X = -1.7$ (slip regime) with $\theta = 0$ and $a = 0.5$ is presented in Figure 7.8. As the Ha increases, a reduction in U velocity at the center and an increase near the boundaries can be observed in Figure 8.8. The reduction in velocity at the center can be explained by the increase in the Ha parameter, which corresponds to a stronger magnetic field. This decrease in U velocity is caused by the Lorentz force, which induces drag in the Stokes flow. Consequently, the increase in fluid velocity near the walls is due to the constant volumetric flow rate across the channel. Furthermore, for fixed Ha value, the U velocity shows less value at the center and significant values near the boundaries when $l_s = 1$ instead of $l_s = 0.1$ (Figure 7.8). Increasing the slip length (l_s) diminishes the impact of the no-slip boundary effect on the walls, enabling more substantial velocities closer to the walls and due to the constant volumetric flow rate, the velocity at the center decreases. One interesting noteworthy observation from Figure 7.8(a) and (b) is that for $Y = 0.25$ and $Y = 0.75$, the U velocity remains same for varying Ha values corresponding to considered l_s values. This happens due to the existence of the boundary layer formation near the walls of the channel.

Subsequently, for the constant parameters $\theta = 0$, $a = 0.5$, Figure 7.9(a) and (b) shows the U velocity against X-axis at $Y = 0.5$ for varying Ha values with $l_s = 0.1$ and 1, respectively. Here, $a = 0.5$ lead to behave the U velocity like a wave type profile. The U velocity reduces with enhancing Ha values. This behavior again is the consequence of Lorentz force. Furthermore, it is noticed that U velocity shows high values at the regimes that are occupied with no-penetration boundary condition in comparison to the Navier's slip boundary condition. This is due to the principle of mass conservation. Applying the no-penetration boundary condition results in zero velocity at the walls, unlike the slip condition. Due to the fluid's incompressibility, the velocity further from the wall is higher in the no-slip case to maintain a constant mass flow rate. Moreover, corresponding to fixed Hartmann number (Ha), the U velocity decreases at the cross-section that is occupied with slip boundary condition when l_s enhanced from 0.1 to 1 (Figure 7.9). As $l_s = 1$ results in a high boundary velocity, the velocity at

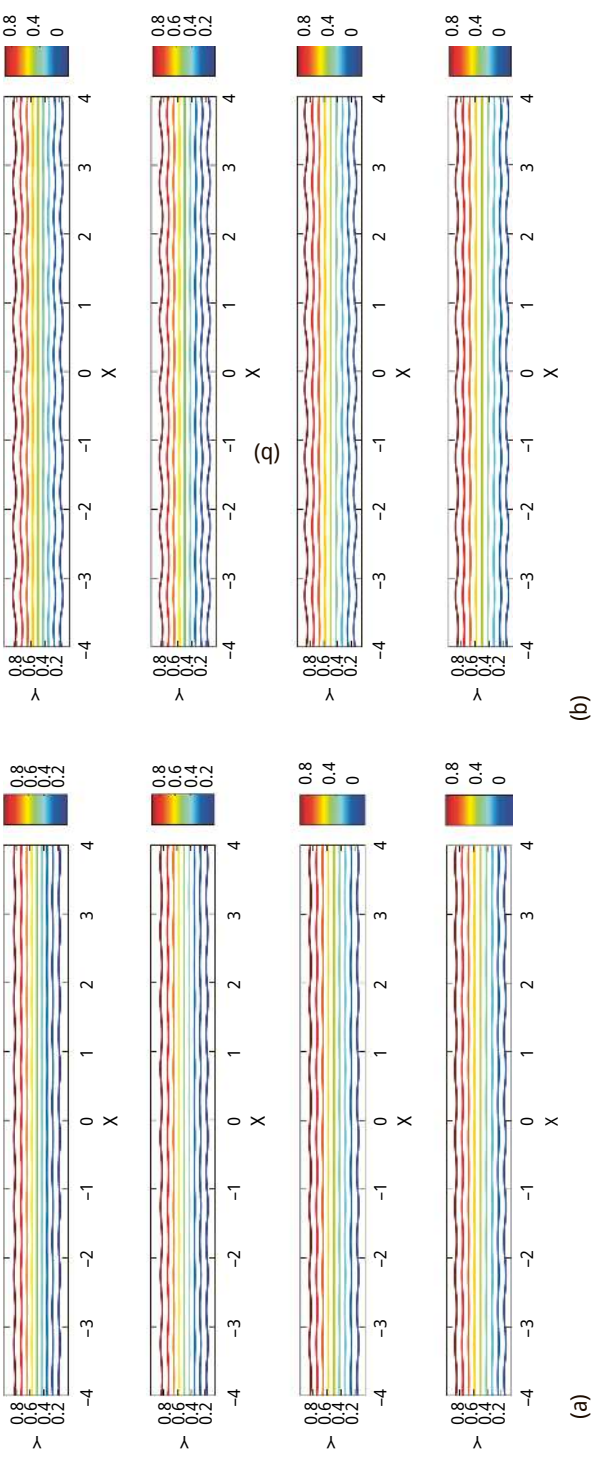

Figure 7.7: Plots of stream function (ψ) for $Ha = 1,\ 4,\ 7$ and 10 with $(a)l_s = 0.1,\ (b)l_s = 1$, and $\alpha = 0.5, \theta = 0$.

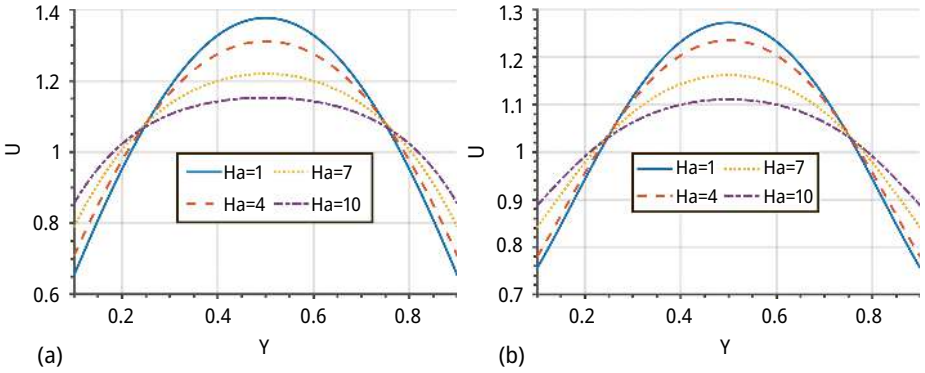

Figure 7.8: *U* versus *Y* at $X = 1.7$ (slip regime) for different *Ha* values with $(a) l_s = 0.1$, $(b) l_s = 1$, and $\theta = 0$, $a = 0.5$.

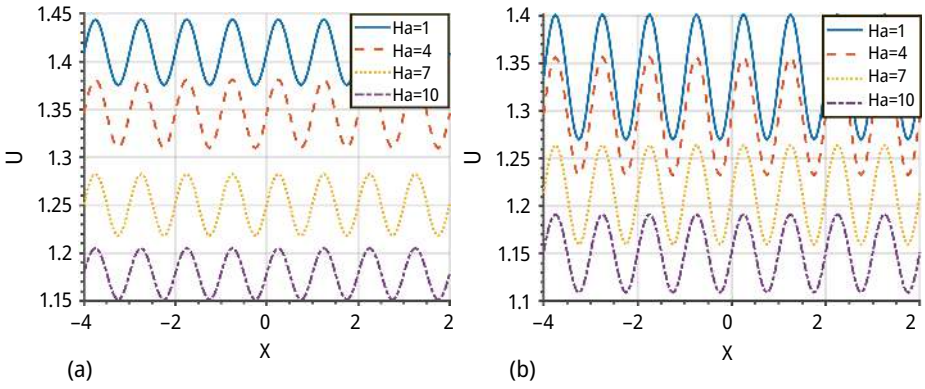

Figure 7.9: *U* versus *X* at $Y = 0.5$ for different *Ha* values with $(a) l_s = 0.1$, and $(b) l_s = 1$, and $\theta = 0$, $a = 0.5$.

the centerline must be lower to satisfy the principle of mass conservation. Whereas, there is no variability in flow velocity (U) at no-slip regimes corresponding to the change in Hartmann number (Ha) when l_s vary from 0.1 to 1 because the no-penetration regimes remain unaffected by the changes in l_s.

Next, the pressure gradient along the *X*-direction at $Y = 0.5$ for varying *Ha* values with distinct slip lengths (l_s) and $\theta = 0$, $a = 0.5$ is illustrated in Figure 7.10. The pressure gradient increases through the entire cross-section with decreasing Hartmann number (Ha) at both the specified regimes, i.e., Navier's slip and no-penetration regimes, respectively. Decreasing the Hartmann number (Ha) results in reducing the strength of the magnetic field, allowing the viscous fluid to flow without resistance, and consequently increasing the pressure gradient. Additionally, it is found that pressure gradient shows the high values at the cross-sections that are occupied with no-penetration boundary condition in comparison with that of Navier's slip boundary condition.

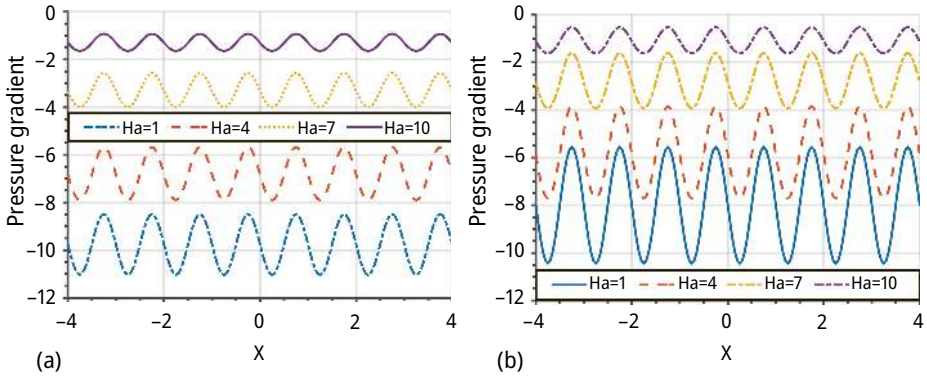

Figure 7.10: Pressure gradient versus X at $Y = 0.5$ for varying Ha values with $(a) l_s = 0.1$, $(b) l_s = 1$, and $\theta = 0$, $a = 0.5$.

Moreover, it can be noticed from Figure 7.10(a) and (b) that pressure gradient gets reduced with enhanced l_s values from 0.1 to 1 corresponding to the fixed Hartmann number (Ha). However, for a fixed Ha, the pressure gradient remains unchanged in the no-penetration regime despite variations in l_s values, as this regime is not influenced by changes in l_s.

We now analyze the behavior of the shear stress distribution of MHD Stokes flow along top boundary $Y = 1$ of the microchannel in terms of X for distinct Ha values with two distinct slip lengths (l_s) with $a = 0.5$ and $\theta = 0$, as shown in Figure 7.11. The shear stress increasing with Ha through the entire cross-section in both the described cases for small and large l_s values, respectively. As the Hartmann number (Ha) increases, the magnetic damping effect strengthens, resulting in higher shear stress. In the slip regimes, the shear stress depends on the Hartmann number when $l_s = 0.1$, but for larger slip lengths $(l_s = 1)$, it becomes independent and approaches zero due to decreased friction at the wall. Furthermore, at the transition points, where the slip regime changes to the no-slip regime and vice versa, the shear stress is higher when $l_s = 1$ compared to $l_s = 0.1$.

7.3.2.2 Influence of Inclination Angle (θ) of Magnetic Field

This section examines how the inclination angle (θ) influences Stokes flow in a microchannel with wall roughness periodicity set to $a = 0.5$. The inclination angle ranges from 0 to $\pi/3$, while the magnetic field strength is fixed at $Ha = 4$. Figure 7.12(a) and (b) presents streamline contour plots for different angles (θ) corresponding to $l_s = 0.1$ and $l_s = 1$, respectively. The streamline patterns exhibit a qualitatively similar trend across the range of inclination angles for each slip length (l_s). Notably, when the slip length is higher $(l_s = 1)$, the streamlines are positioned closer to the microchannel walls compared to the case of lower slip length $(l_s = 0.1)$.

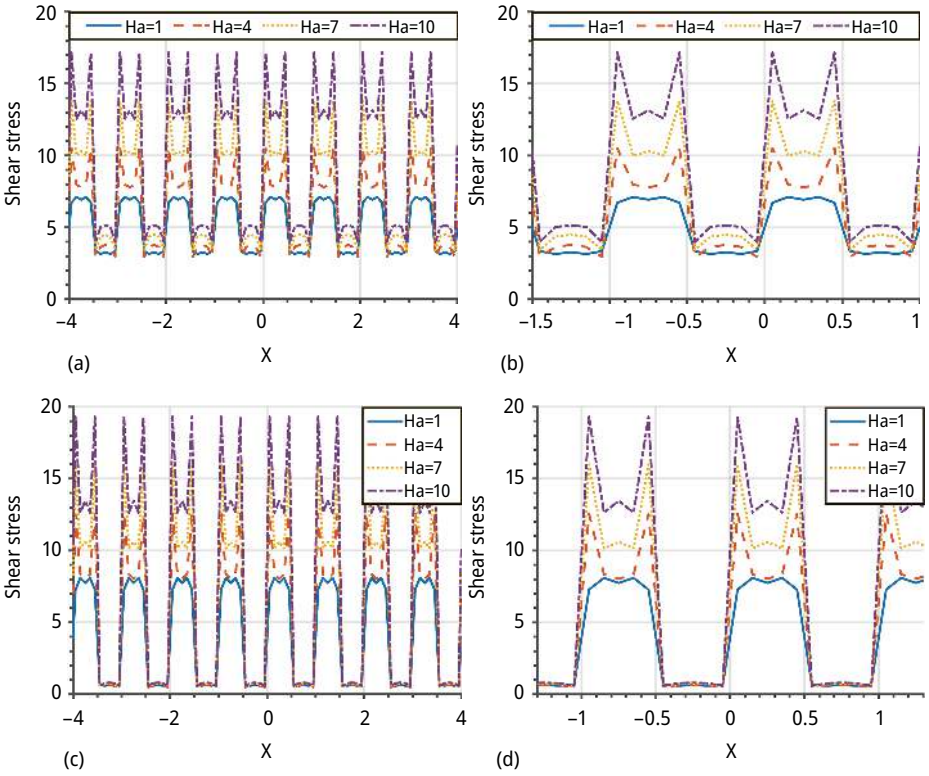

Figure 7.11: Shear stress versus X at $Y = 1$ for varying Ha values with $(a) l_s = 0.1$, $(b) l_s = 0.1$, $(c) l_s = 1$, and $(d) l_s = 1$ and $\theta = 0$, $a = 0.5$.

To understand the hydrodynamics of the considered viscous flow, Figures 7.13 and 7.14 display flow velocity (U) against Y and X at $X = -1.7$ and $Y = 0.5$ for varying θ under different l_s values while keeping $Ha = 4$, and $a = 0.5$ constant. The figures demonstrate that the fluid velocity (U) rises with rising angle (θ). This is because, at $\theta = 0$, the magnetic field acts transversely to the flow direction, causing maximum drag created due to Lorentz force. Additionally, as the inclination angle (θ) increases, the magnetic resistance decreases, allowing the flow velocity to rise. Furthermore, Figure 7.13(a) and (b) indicates drop in U velocity decreases close to walls as angle (θ) increases, which is a consequence of maintaining a constant volumetric flux throughout the microchannel. Furthermore, the fluid velocity (U) reduces with rising slip length (l_s) within the slip regimes at a fixed inclination angle (θ). Larger slip lengths reduce boundary friction, allowing greater slip at the surface and resulting in a lower velocity gradient near the walls and a decreased overall velocity profile. In the no-slip regions, however, the U velocity remains constant regardless of variations in slip length for a fixed magnetic field inclination angle.

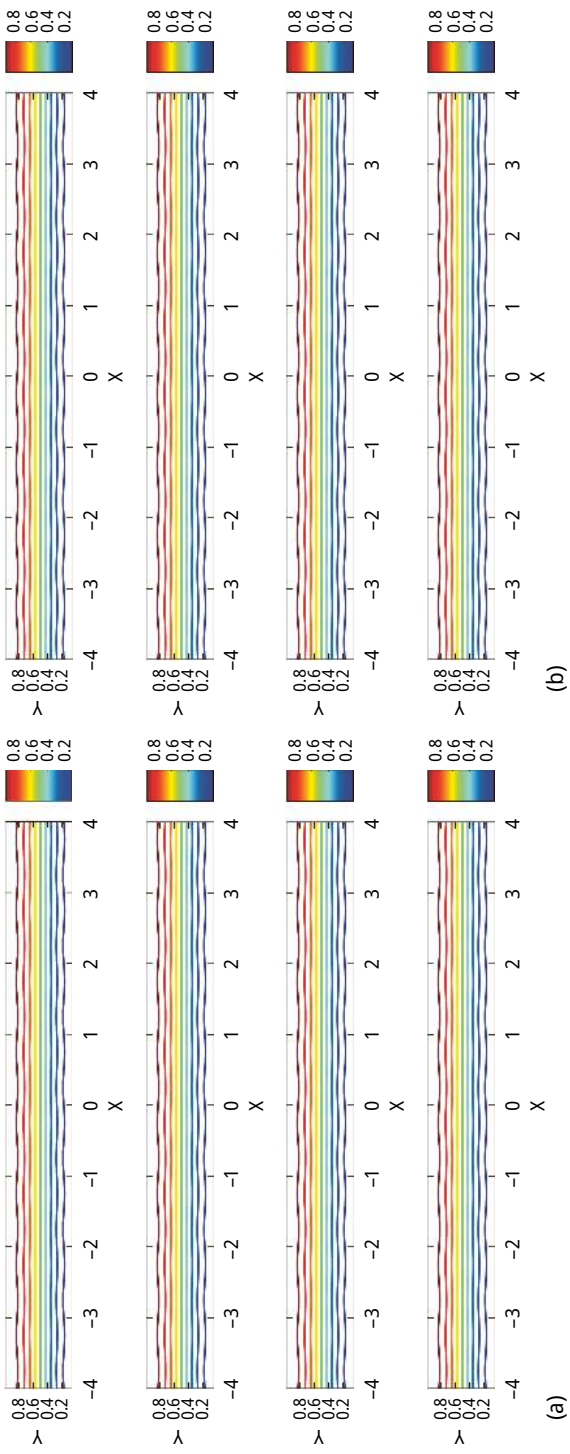

Figure 7.12: Plots of stream function (ψ) for $\theta = 0, \pi/6,\ \pi/4$ and $\pi/3$ with (a) $l_s = 0.1$, (b) $l_s = 1$, and $\alpha = 0.5$, $Ha = 4$.

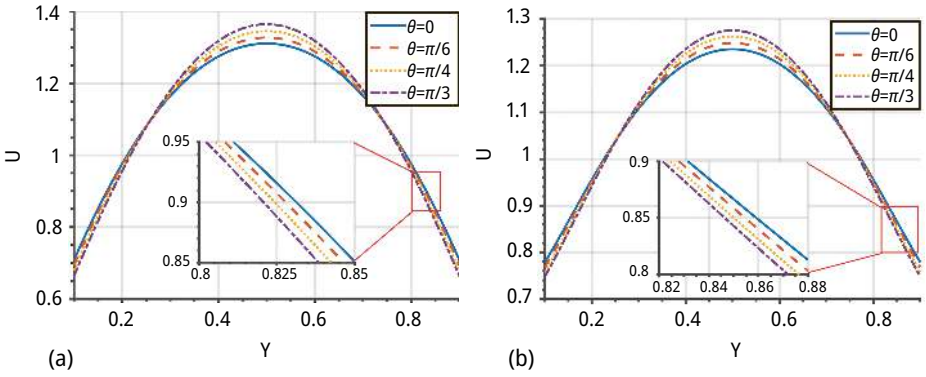

Figure 7.13: U versus Y at $X = 1.7$ for different θ values with $(a)\ l_s = 0.1$, $(b)\ l_s = 1$, and $Ha = 4$, $a = 0.5$.

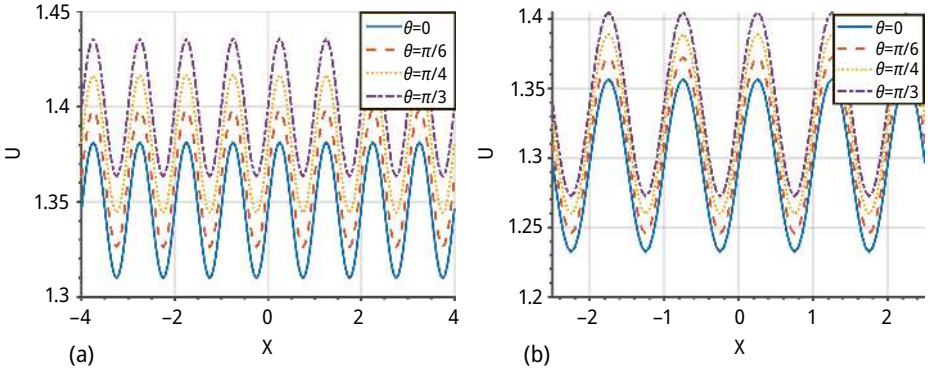

Figure 7.14: U versus X at $Y = 0.5$ for different θ values with $(a) l_s = 0.1$, $(b) l_s = 1$, and $Ha = 4$, $a = 0.5$.

Figure 7.15 displays the pressure gradient along the X-axis at $Y = 0.5$ for different inclination angles (θ) of magnetic field, ranging from 0 to $\pi/3$, with $l_s = 0.1$ and 1, and a constant Hartmann number $Ha = 4$. From this figure, it is evident that an increased inclination angle enhances the pressure gradient due to the reduced influence of the Lorentz force at higher angles, which decreases the fluid's resistance to motion and, consequently, increases the pressure gradient. Furthermore, the pressure gradient is more pronounced in the no-slip regions than in the slip regions for any given inclination angle. Within the slip regimes, it is also observed that as l_s increases, the pressure gradient approaches zero. This behavior occurs because $l_s = 1$ minimizes the frictional resistance at the boundary, allowing the pressure gradient to decrease significantly.

Figure 7.16 depicts the shear stress against X-axis along $Y = 1$ for varying the angle (θ) with two distinct l_s values and $Ha = 4$. The results indicate that the shear stress decreases as the inclination angle increases due to reduced velocity gradients near the walls. Moreover, the shear stress reaches its peak at the transition points, where

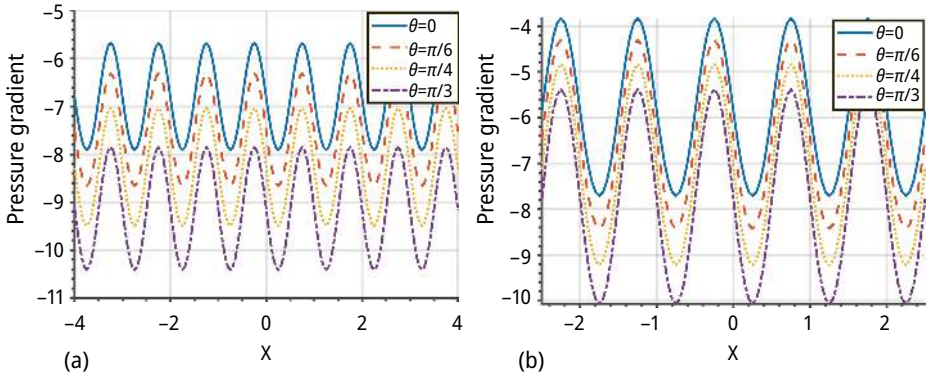

Figure 7.15: Pressure gradient versus X at $Y = 0.5$ for varying θ values with $(a)l_s = 0.1$, $(b)l_s = 1$, and $Ha = 4, a = 0.5$.

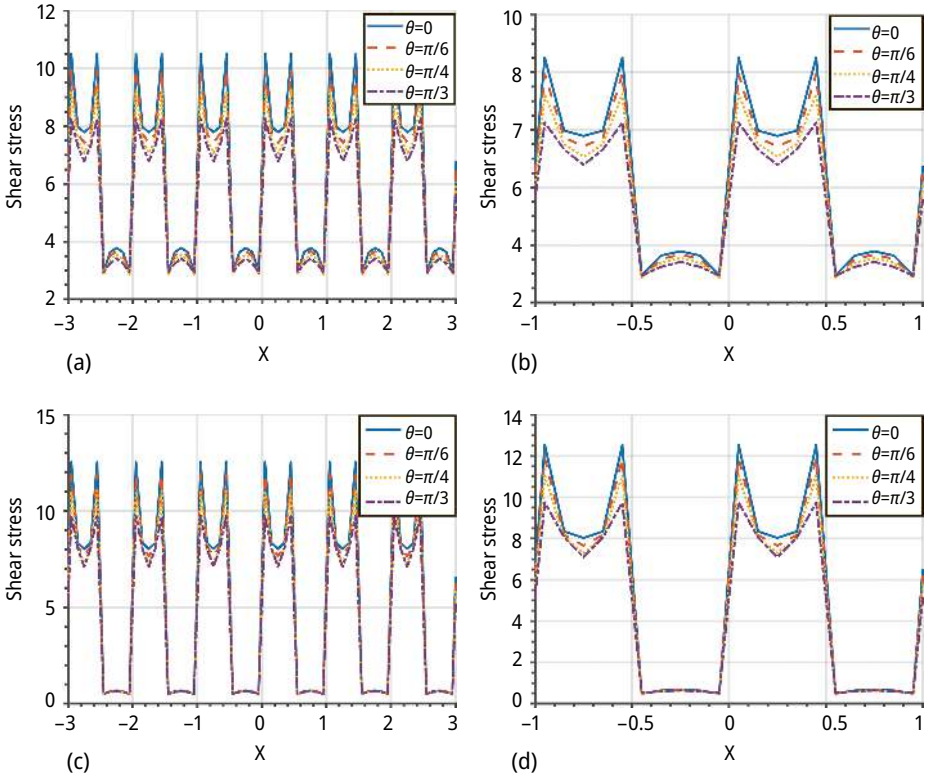

Figure 7.16: Shear stress versus X-axis at $Y = 1$ for varying inclination angle (θ) with $(a)l_s = 0.1$, $(b)l_s = 1$ (zoom-in view), $(c)l_s = 1$, $(d)l_s = 1$ (zoom-in view), and $\theta = 0, a = 0.5$.

Navier's slip and no-penetration conditions overlap, with higher values for a larger slip length $(l_s = 0.1)$ compared to a smaller one $(l_s = 0.1)$. From Figure 7.16(a) and (b), it is also observed that in the slip regions, the shear stress varies with the inclination angle for $l_s = 0.1$, while it remains constant for $l_s = 0.1$. This occurs because smaller slip lengths intensify the boundary effects on the flow, while larger slip lengths reduce these effects, rendering the shear stress invariant to changes in the magnetic field's inclination angle.

7.4 Conclusion

To advance the design of microfluidic and lab-on-a-chip devices, the current hydrodynamic model examines *2D* Stokes flow at a low Reynolds number within a microchannel. The channel features periodic surface roughness on its horizontal walls and is influenced by an externally applied inclined magnetic field. The surface roughness is modeled using Navier's slip boundary condition in an alternating manner. Numerical results obtained using the BEM, as discussed in the previous section, reveal that the dimensionless flow parameters significantly affect the flow dynamics. The key findings of the present investigation are as follows:

- Increasing Hartmann number led to reduce the flow velocity due to the consequence of more counteract force called Lorentz force that opposes the flow.
- Increasing inclination angle of magnetic field gives rise to flow velocity (U) because when angle of magnetic field is non-zero, the flow velocity experiences less drag in contrast to the case when inclination angle of magnetic field is zero.
- Increasing slip length led to reduce the flow velocity (U) at the slip regimes. Using slip conditions and magnetic fields to manipulate Stokes flow in microchannels may be crucial for designing lab-on-a-chip devices for cellular analysis or blood sorting, where precise control over flow is required.
- There exist distinct Y-values for which the flow velocity (U) becomes independent for varying the considered dimensionless flow parameters. The boundary layers' formation in the viscous flow near the boundaries explains this phenomenon.
- Increasing slip length and Hartmann number led to decrease the pressure gradient, while increasing inclination angle of magnetic field increases the pressure gradient.
- Increasing Hartmann number gives rise to shear stress, whereas increasing inclination angle of magnetic field decreases the shear stress. Furthermore, the shear stress becomes independent for increasing the slip lengths at the slip regime and approaches to zero, because at the large slip length, there is no practical resistance to the flow, so that, the shear stress near the walls tends to zero. Apart from this, it is noticed that the shear stress shows significant values at the points where the Navier's slip and no-penetration boundary conditions overlap.

References

[1] Omori, T. & Ishikawa, T. (Dec. 2023). Computational Fluid Dynamics of Swimming Microorganisms. Journal of the Physical Society of Japan, 92(12). doi: 10.7566/JPSJ.92.121002.

[2] Ho, C.-M. & Tai, Y.-C. (Jan. 1998). MICRO-ELECTRO-MECHANICAL-SYSTEMS (MEMS) AND FLUID FLOWS. Annual Review of Fluid Mechanics, 30(1), 579–612. doi: 10.1146/annurev.fluid.30.1.579.

[3] Tornberg, A.-K. & Shelley, M. J. (May 2004). Simulating the dynamics and interactions of flexible fibers in Stokes flows. Journal of Computational Physics, 196(1), 8–40. doi: 10.1016/j.jcp.2003.10.017.

[4] Finn, M. D. & Cox, S. M. (2001). Stokes flow in a mixer with changing geometry. Journal of Engineering Mathematics, 41(1), 75–99. doi: 10.1023/A:1011840630170.

[5] Lima, R., Ishikawa, T., Imai, Y., & Yamaguchi, T. (2012). Blood flow behavior in microchannels: Past, current and future trends. Single and Two-Phase Flows on Chemical and Biomedical Engineering , 513–547. doi: 10.2174/978160805295011201010513.

[6] Setchi, A., Mestel, A. J., Parker, K. H., & Siggers, J. H. (May 2013). Low-Reynolds-number flow through two-dimensional shunts. Journal of Fluid Mechanics, 723, 21–39. doi: 10.1017/jfm.2013.99.

[7] Civit, J., De la Portilla, F., Sevillano, J. L., & Civit, A. (2017). Modelling side to side intestinal anastomosis. Biomedical Engineering Letters, 7(3), 267–271. doi: 10.1007/s13534-017-0032-5.

[8] Hadjinicolaou, M., Kamvyssas, G., & Protopapas, E. (2015). Stokes flow applied to the sedimentation of a red blood cell. Quarterly of Applied Mathematics, 73(3), 511–523. doi: 10.1090/qam/1390.

[9] Luca, E. & Llewellyn Smith, S. G. (2018). Stokes flow through a two-dimensional channel with a linear expansion. Quarterly Journal of Mechanics and Applied Mathematics, 71(4). doi: 10.1093/qjmam/hby013.

[10] Claude, C., Navier, L., & Darve, C. (1823). Memoire sur Memoire sur les les lois du lois du mouvement mouvement des des fluides fluides. Mem. Acad. Sci Inst. Fr, 6, 389–440. [Online]. Available https://www.researchgate.net/publication/246803279_Memoire_sur_les_lois_mouvement_des_fluides.

[11] Helmholtz, H. & Piotrowski, G. (1860). Uber friction tropfbarer fluid's. Proceedings Impact Academic Science, 40, 607–658.

[12] Kundt, A. & Warburg, E. (1875). Ueber Reibung und Wärmeleitung verdünnter Gase. Annalen der Physik Und Chemie, 232(10), 177–211. doi: 10.1002/andp.18752321002.

[13] Vinogradov, G. V. & Ivanova, L. I. (1968). Wall slippage and elastic turbulence of polymers in the rubbery state. Rheologica Acta, 7(3), 243–254. doi: 10.1007/BF01985785.

[14] J. C. Maxwell (Dec. 1879). VII. On stresses in rarified gases arising from inequalities of temperature. Philosophical Transactions of the Royal Society of London, 170, 231–256. doi: 10.1098/rstl.1879.0067.

[15] Mooney, M. (1931). Explicit Formulas for Slip and Fluidity. Journal of Rheology (N. Y. N. Y), 2(2), 210–222. doi: 10.1122/1.2116364.

[16] Zhu, Y. & Granick, S. (2001). Rate-Dependent Slip of Newtonian Liquid at Smooth Surfaces. Physical Review Letters, 87(9), 1–4. doi: 10.1103/PhysRevLett.87.096105.

[17] Zhu, Y. & Granick, S. (2002). Limits of the Hydrodynamic No-Slip Boundary Condition. Physical Review Letters, 88(10), 4. doi: 10.1103/PhysRevLett.88.106102.

[18] Raviv, U., Giasson, S., Frey, J., & Klein, J. (2002). Viscosity of ultra-thin water films confined between hydrophobic or hydrophilic surfaces. Journal of Physics. Condensed Matter, 14(40), 9275–9283. doi: 10.1088/0953-8984/14/40/317.

[19] Cottin-Bizonne, C., Jurine, S., Baudry, J., Crassous, J., Restagno, F., & Charlaix, É. (2002). Nanorheology: An investigation of the boundary condition at hydrophobic and hydrophilic interfaces. European Physical Journal E, 9(1), 47–53. doi: 10.1140/epje/i2001-10112-9.

[20] Lauga, E., Brenner, M., & Stone, H. (2007). Microfluidics: The No-Slip Boundary Condition. In Springer Handbook of Experimental Fluid Mechanics. Berlin, Heidelberg: Springer Berlin Heidelberg, 1219–1240. doi: 10.1007/978-3-540-30299-5_19.

[21] Brenner, H. (2011). Beyond the no-slip boundary condition. Phys Rev E – Stat Nonlinear, Soft Matter Phys, 84(4). doi: 10.1103/PhysRevE.84.046309.
[22] Luchini, P. (2013). Linearized no-slip boundary conditions at a rough surface. Journal of Fluid Mechanics, 737, 349–367. doi: 10.1017/jfm.2013.574.
[23] Mele, B. & Tognaccini, R. (2018). Slip length-based boundary condition for modeling drag reduction devices. AIAA Journal, 56(9), 3478–3490. doi: 10.2514/1.J056589.
[24] Zampogna, G. A., Magnaudet, J., & Bottaro, A. (Jan. 2019). Generalized slip condition over rough surfaces. Journal of Fluid Mechanics, 858, 407–436. doi: 10.1017/jfm.2018.780.
[25] Hu, S., Ren, X., Bachman, M., Sims, C. E., Li, G. P., & Allbritton, N. (2002). Surface modification of poly(dimethylsiloxane) microfluidic devices by ultraviolet polymer grafting. Analytical Chemistry, 74(16), 4117–4123. doi: 10.1021/ac025700w.
[26] Choi, C. H. & Kim, C. J. (2006). Large slip of aqueous liquid flow over a nanoengineered superhydrophobic surface. Physical Review Letters, 96(6). doi: 10.1103/PhysRevLett.96.066001.
[27] Kamrin, K., Bazant, M. Z., & Stone, H. A. (2010). Effective slip boundary conditions for arbitrary periodic surfaces: The surface mobility tensor. Journal of Fluid Mechanics, 658, 409–437. doi: 10.1017/S0022112010001801.
[28] Hendy, S. C., Jasperse, M., & Burnell, J. (2005). Effect of patterned slip on micro- and nanofluidic flows. Phys Rev E – Stat Nonlinear, Soft Matter Phys, 72(1), 1–8. doi: 10.1103/PhysRevE.72.016303.
[29] Zhao, C. & Yang, C. (2012). Electro-osmotic flows in a microchannel with patterned hydrodynamic slip walls. Electrophoresis, 33(6), 899–905. doi: 10.1002/elps.201100564.
[30] Datta, S. & Choudhary, J. N. (2013). Effect of hydrodynamic slippage on electro-osmotic flow in zeta potential patterned nanochannels. Fluid Dynamics Research, 45(5). doi: 10.1088/0169-5983/45/5/055502.
[31] Nishad, C. S., Chandra, A., & Sekhar, G. P. R. (2016). Flows in slip-patterned micro-channels using boundary element methods. Engineering Analysis with Boundary Elements, 73, 95–102. doi: 10.1016/j.enganabound.2016.09.006.
[32] Ageev, A. I. & Osiptsov, A. N. (2019). Stokes Flow in a Microchannel with Superhydrophobic Walls. Fluid Dynamics, 54(2), 205–217. doi: 10.1134/S0015462819020010.
[33] Aissa, A. et al. (2020). Pressure-driven gas flows in micro channels with a slip boundary: A numerical investigation. Fluid Dynamics and Materials Processing, 16(2), 147–159. doi: 10.32604/fdmp.2020.04073.
[34] Delhi Babu, R. & Ganesh, S. (2018). The effects of steady magneto hydrodynamic flow between two parallel porous plates with an angular velocity. Journal of Advanced Research in Dynamical and Control Systems, 10(3), 1362–1367.
[35] Chester, W. (Dec. 1957). The effect of a magnetic field on Stokes flow in a conducting fluid. Journal of Fluid Mechanics, 3(3), 304–308. doi: 10.1017/S0022112057000671.
[36] Gotoh, K. (1960). Stokes Flow of an Electrically Conducting Fluid in a Uniform Magnetic Field. Journal of the Physical Society of Japan, 15(4), 696–705. doi: 10.1143/JPSJ.15.696.
[37] Sasikala, R., Govindarajan, A., & Gayathri, R. (2018). Unsteady stokes flow of dusty fluid between two parallel plates through porous medium in the presence of magnetic field. Journal of Physics Conference Series, 1000(1). doi: 10.1088/1742-6596/1000/1/012151.
[38] Çelik, E. (2021). Effect of the Hartmann Number on MHD Stokes Flow in a Lid-Driven Cavity. Magnetohydrodynamics, 57(4), 423–435. doi: 10.22364/mhd.57.4.1.
[39] Gürbüz, M. & Çelik, E. (2022). Stokes flow in lid-driven cavity under inclined magnetiQc field. Archives of Mechanics, 74(6), 549–564. doi: 10.24423/aom.4013.
[40] Taylor, C. & Hood, P. (1973). A numerical solution of the Navier-Stokes equations using the finite element technique. Comput Fluids, 1(1), 73–100. doi: 10.1016/0045-7930(73)90027-3.

[41] Sandström, C., Larsson, F., Runesson, K., & Johansson, H. (2013). A two-scale finite element formulation of Stokes flow in porous media. Computer Methods in Applied Mechanics and Engineering, 261–262, 96–104. doi: 10.1016/j.cma.2013.03.025.

[42] Nishad, C. S., Karmakar, T., Chandra, A., & Raja Sekhar, G. P. (2018). A non-primitive boundary integral formulation for modeling flow through composite porous channel. Engineering Analysis with Boundary Elements, 109(October), 94–105. 2019, doi: 10.1016/j.enganabound.2019.03.044.

[43] Katsikadelis, J. T. (2016). The Boundary Element Method for Engineers and Scientists: Theory and Applications Second Edition. doi: 10.1016/C2014-0-01297-X.

[44] Nishad, C. S., Chandra, A., & Raja Sekhar, G. P. (2017). Stokes Flow Inside Topographically Patterned Microchannel Using Boundary Element Method. International Journal of Chemical Reactor Engineering, 15(5), 1–17. doi: 10.1515/ijcre-2017-0057.

[45] Chhabra, V., Nishad, C. S., & Sahni, M. (2024). Boundary Element Method for Viscous Flow through Out-phase Slip-patterned Microchannel under the Influence of Inclined Magnetic Field. Chemical Product and Process Modeling. doi: 10.1515/cppm-2024-0065.

[46] Li, M., Tang, T., & Fornberg, B. (1995). A compact fourth-order finite difference scheme for the steady incompressible Navier-Stokes equations. International Journal of Numerical Methods in Fluids, 20(10), 1137–1151. doi: 10.1002/fld.1650201003.

[47] Chhabra, V., Nishad, C. S., & Sahni, M. (2023). Effect of Magnetic Field on Viscous Flow through Composite Porous Channel using Boundary Element Method. Journal of Applied and Computational Mechanics, 9(4), 1016–1035. doi: 10.22055/jacm.2023.43024.4006.

[48] Chhabra, V., Nishad, C. S., & Sahni, M. (Jun. 2024). Effect of magnetic field on viscous flow through porous wavy channel using boundary element method. ZAMM – Journal of Applied Mathematics and Mechanics / Zeitschrift Für Angewandte Mathematik Und Mechanik, 104(6). doi: 10.1002/zamm.202300416.

[49] Chhabra, V., Nishad, C. S., Vijay, K. G., & Sahni, M. (Dec. 2024). Stokes flow past an array of circular cylinders through slip-patterned microchannel using boundary element method. Engineering Analysis with Boundary Elements, 169, 105925. doi: 10.1016/j.enganabound.2024.105925.

[50] Tezduyar, T. E., Liou, J., & Ganjoo, D. K. (1990). Incompressible flow computations based on the vorticity-stream function and velocity-pressure formulations. Computers & Structures, 35(4), 445–472. doi: 10.1016/0045-7949(90)90069-E.

[51] Chhabra, V., Nishad, C. S., Vijay, K. G., & Sahni, M. (Feb. 2025). Stokes flow past circular cylinders in an out-phase slip patterned microchannel using boundary element method. ZAMM – Journal of Applied Mathematics and Mechanics / Zeitschrift Für Angewandte Mathematik Und Mechanik, 105 (2). doi: 10.1002/zamm.202400685.

[52] Chhabra, V., Nishad, C. S., Sahni, M., & Chaurasiya, V. K. (2024). Effect of Magnetic Field and Hydrodynamic Slippage on Electro-osmotic Brinkman Flow through Patterned Zeta Potential Microchannel. Vol. 148, 1, Springer Netherlands. doi: 10.1007/s10665-024-10391-x.

[53] Burggraf, O. R. (1966). Analytical and numerical studies of the structure of steady separated flows. Journal of Fluid Mechanics, 24(1), 113–151. doi: 10.1017/S0022112066000545.

[54] Campion-Renson, A. & Crochet, M. J. (1978). On the stream function-vorticity finite element solutions of Navier-Stokes equations. International Journal for Numerical Methods in Engineering, 12(12), 1809–1818. doi: 10.1002/nme.1620121204.

[55] Guerrero, J. S. P. & Cotta, R. M. (1992). Integral transform solution for the lid-driven cavity flow problem in streamfunction-only formulation. International Journal of Numerical Methods in Fluids, 15(4), 399–409. doi: 10.1002/fld.1650150403.

[56] Karageorghis, A. & Fairweather, G. (Oct. 1989). The simple layer potential method of fundamental solutions for certain biharmonic problems. International Journal of Numerical Methods in Fluids, 9(10), 1221–1234. doi: 10.1002/fld.1650091005.

Rachna Khurana, Sangeeta Gupta, Sweta Srivastava,
and Vinay Kumar Jadon

Chapter 8
A Study of Approximation Techniques Used to Solve Queueing Models Arise in Optimizing Complex Engineering Systems

Abstract: Queueing theory provides efficient tools for modeling and analyzing the complicated structures for optimum utilization of resources. The mathematical models we develop to describe real-world situations are essentially idealized constructs and it is important not to become overly attached to them if we are truly seeking practical solutions. In recent years, methods for determining approximate or bounding behavior for queues have quickly emerged to address real-world scenarios. As approximation methods are computationally efficient, they provide computational convenience for practitioner. Moreover, simple expressions derived using approximation methods provide insight to practitioner in evaluating alternative operating design, in resource allocation, or in optimization, and are acceptable over crude exact mathematical models. This chapter reviews several widely used approximation techniques, including transform approximation, discrete approximation, fluid approximation, diffusion process approximation, heavy traffic approximation, as well as the application of numerical and simulation-based approaches. Case studies from various engineering domains illustrate how these approximation techniques can be effectively applied to improve system performance, minimize delays, and reduce costs.

Keywords: transform approximation, discrete approximation, fluid approximation, diffusion process approximation, heavy traffic approximation, simulation

Acknowledgments: The authors wish to express their sincere gratitude to all those who contributed to the completion of this study. They extend their appreciation to their mentors, colleagues, and researchers in the field of queueing theory and optimization for their valuable insights and constructive contributions.

Rachna Khurana, Sharda School of Basic Sciences and Research, Sharda University, Agra, India, e-mail: rachnaakshaj@gmail.com
Sangeeta Gupta, The A.H. Siddiqi Centre for Advanced Research in Applied Mathematics and Physics, Sharda University, Greater Noida, India, e-mail: sangeeta.gupta@sharda.ac.in
Sweta Srivastava, The A.H. Siddiqi Centre for Advanced Research in Applied Mathematics and Physics, Sharda University, Greater Noida, India, e-mail: sweta.srivastava@sharda.ac.in
Vinay Kumar Jadon, Sharda School of Basic Sciences and Research, Sharda University, Agra, Uttar Pradesh, India, e-mail: dr.vinayjadon@gmail.com

https://doi.org/10.1515/9783111723464-008

8.1 Introduction

Congestion situations arising out in the networks of telecommunications, computer, transportation, and production, not only affect the quality of the service, but also wastes a lot of precious resources. Therefore, it is essential to study queues and find optimum solutions. Fortunately, queues are not problems without solutions and queueing theory provides efficient tools for modeling and analyzing queueing problems.

The importance of queueing theory lies not only in its applicability to real-life problems with its computationally tractable procedures but also in elegance and completeness of the underlying stochastic models and mathematics. But we encounter the fact that the real-life queueing problems rarely follow the assumptions of mathematical construction. On the contrary, queueing theory is rather complicated and exact findings are difficult to obtain. Furthermore, sometimes in the simpler systems where exact results can be found, their form is sometimes so complex, that it renders them ineffectual for practical applications. In such situations, applying approximation method, we can have alternative solutions. A variety of approximation approaches have been developed over time to solve queueing model difficulties.

Kobayashi [18] simplified queueing models by introducing vector-valued Wiener process under some suitable boundary conditions. He found approximate answer to the joint distribution of length of general network queues. Bhat and Shalaby [1] suggested that approximation methods are more suitable in some of the complex queueing model cases. He also notified that more than one approximation technique can be used to obtain the complete solution. His paper was characterized with emphasize on validation of the approximate results. Protopapas [2] analyzed computer systems using finite queueing approximation techniques. He proposed approximate results of response time of M/G/1/N and GI/G/1/N queues for their application in realistic models. Kaufman [3] pointed the reduced approximation technique for priority queues. He focused upon the condition of this technique and figure out its accuracy and applicability. Ibe et al. [19] developed the approximation method for evaluating parameters for a class of queueing system that does not need enumeration of state space and linear equations. He also presented validation of the results by approximation methods over exact solution. Ackroyd [4] developed approximate recursion formula for the probability of delays and the mean delays of nth arrival of G/G/1 queues. Yang and Lipsky [5] discovered that the approximations of queueing models can be done with the differential coefficients and probability density function. He also verified the accuracy of approximations by detailed example. Dallery [6] analyzed approximately open queueing network with general time distribution. He derived performance parameters of an open queue model through its equivalent closed queueing network and compared the results with the classical aggregation technique. Whitt [17] found congestion measures of queueing models approximately based on first two moments. He provided the solution for complicated irregular flow systems for which analytic solution is not available. To find the approximation of delay probability of M/G/s queue

model where “s” is very small, Kimura [7] mentioned asymptotic properties of delay probabilities with mean waiting time. Glynn [8] highlighted positive features of using diffusion approximations for queueing models. Harris and Marchal [9] estimated probability distribution using Laplace transform approximation. He involved phase-type Coxian distribution or hyperexponential distribution for the situations where exact solution is inadequate to apply. Kurasugia and Kino [10] obtained performance measures by applying extended flow equivalent method in two-layered queueing model with limited capacity. Shortle et al. [11] suggested algorithm for steady-state probabilities for M/G/1 queues by approximating Laplace transform. MoghimiHadji and Aydin [12] analyzed performance measures of GI/M/1 queueing system utilizing first three moments of arrival distributions. Sani and Daman [13] studied the queueing systems with heavy traffic of customers and suggested the favorable conditions of diffusion approximations. Deepak [14] tried to cover up gap between theoretical queueing models and realistic situations by simulation. Dai and Yanhua [15] examined a queueing network characterizes with ON/OFF sourced and suggested explicit solution for heavy traffic situation using fractional Brownian motion. Here, we aim to give a summary of various methods and talk about their relative advantages and limitations.

8.2 Approximation Techniques for Queueing Models

8.2.1 Transform Approximation

In engineering systems, particularly when optimizing complex systems, such as communication networks, manufacturing lines, data centers, and cloud computing, queueing models are critical in understanding and improving performance, such as throughput, waiting times, and resource utilization. However, when these systems become highly complex or involve heavy-tailed distributions, exact solutions for queueing models are often difficult to obtain. This is where transform approximation techniques are used to simplify and solve queueing models efficiently.

This technique transforms difficult-to-analyze models into forms that are more manageable or approximate solutions. Here, we shall discuss some common transform approximation techniques that can be applied to solve queueing models to optimize complex engineering systems.

8.2.1.1 Laplace Transform Approximation

The Laplace transform is commonly used to convert time-domain functions (e.g., waiting times, service times, or arrival rates) into the complex frequency domain. This transform helps to simplify the differential equations or probability distribution functions associated

with queueing systems. A difficulty with analyzing queues with this distribution is that arrival and service distributions are heavy tailed (e.g., internet-type queues) and in general does not have closed form Laplace transform. The proposed transform by Harris and Marchal [9] overcomes this by numerically approximating the transform. The basic idea is to approximate the Laplace transform of the service time $B^*(S) = \int_0^\infty e^{-sx} dF(x)$ with a finite sum:

$$B^*(S) \approx \hat{B}^*(S) \equiv \frac{1}{N} \sum_{i=1}^{N} e^{-sx_i}$$

where the points x_i are evenly spaced quantities of cumulative distribution function F. In particular, instead of choosing evenly spaced quantities, arbitrary selection of quantities can be allowed, i.e.,

1. Choose a set of N quantities t_i, where all t_i lies between 0 and 1
2. Find x_i such that $F(x_i) = t_i$
3. For each point x_i, assigning the probability $P_i = \frac{t_{i+1} - t_{i-1}}{2}$, $i = 2, 3, \ldots, N-1$

$$P_1 = \frac{t_1 + t_2}{2}, \; P_N = 1 - \frac{t_{N-1} - t_N}{2}$$

   The idea is to assign x_i, half of the probability between the points to the left and right of x_i. The second equation gives a slight expectation at the boundaries where the leftover probability near 0 and infinity must be counted.
4. Then, approximate Laplace transform of the service time with $\hat{B}^*(S) \equiv \sum_{i=1}^{N} p_i e^{-sx_i}$ The advantage of the general method is that x_i points can be picked (or equidistance quintile's y_i), which are further out in the tail of the distribution.

8.2.1.1.1 Application

– Well-known formula for analyzing the waiting time of an M/G/I queue

$$W_q^*(S) = \int_0^\infty e^{-st} P\left(W_q \le t\right) \, dt = \frac{(1-\rho)s}{s - \lambda(1 - B^*(S))}$$

where $B^*(S)$ is the Laplace transform of the service time, ρ is the offered load, and λ is the arrival rate. Generally, one plugs in the Laplace transform of the service times, then inverts $W_q^*(S)$ to get the waiting time distribution. When the service time distribution of Pareto or Weibull or lognormal, $B^*(S)$ does not exist in the closed form, then this approximation for $B^*(S)$ can be used. Then, $W_q^*(S)$ must be inverted numerically, which accomplished using Fourier method.

Hence, transform approximation method has significant potential in analyzing complicated queueing system involving heavy-tailed distribution.

8.2.1.2 Fourier Transform and Frequency-Domain Approximations

The Fourier transform is another powerful tool used to analyze systems in the frequency domain particularly in signal processing and network traffic analysis. It allows engineers to assess the frequency components of queueing behavior, such as cyclic variations in traffic patterns. Optimization can be achieved by adjusting network protocols, buffer sizes, or scheduling algorithms based on these frequency-domain characteristics. In queueing theory, the Fourier transform helps to approximate the spectral properties of traffic flows (such as burstiness) and their impact on system performance.

8.2.1.2.1 Application

- Traffic Modeling: In communication networks (such as packet-switching systems), queueing models often involve analyzing bursty traffic that exhibits long-range dependence or self-similarity. The Fourier transform is applied to study the power spectral density of traffic. The approximation of the traffic spectrum helps in understanding how bursty or irregular traffic patterns impact network congestion and delays.
- **Approximation of System Performance**: The Fourier series expansion or Fourier transform can approximate complex signals or arrival processes, especially in non-Markovian queueing models where the arrivals might follow heavy-tailed distributions.

8.2.1.3 Z-Transform in Discrete-Time Queueing Models

The Z-transform is used for modeling and analyzing discrete-time queueing systems, which are commonly found in digital systems, telecommunications, and data processing systems. It is especially useful when analyzing systems where the events occur in discrete time intervals, such as packet arrivals in a network or task execution in computer systems. Performance metrics, such as queue lengths and waiting times, can be approximated and optimized using the Z-transform to model systems under high traffic or bursty arrival processes. By adjusting buffer sizes and service rates based on the Z-domain approximation, system performance can be improved, minimizing delays, and packet losses.

8.2.1.3.1 Application

- **M/G/1 Queueing Systems in Discrete Time**: In cases where the system operates in discrete time (e.g., batch arrivals in data systems), the Z-transform is applied to transform the time-domain difference equations into the Z-domain for easier

analysis. This approach allows engineers to study system stability, utilization, and throughput in systems with heavy traffic.
– Finite-Buffer Systems: In systems with finite buffers like those found in telecommunications or data centers, Z-transform is used to approximate the probability of overflow or queue length when the system is under heavy load.

8.2.2 Discrete Approximation

Discrete approximation is an effort for establishing exact results of the approximation of original models in place of finding approximate answers original models. For establishing discrete approximation results in G/G/1 queue purposefully first equation of motion are distorted and then reformulated in a way that allows the equations of the system to get solve. The key approach is to change the distribution of input [$A(t)$ and $B(x)$], so that, the elementary recurrence relation allows for a direct analytic solution of the distribution of waiting time:

$$w_{n+1} = \max[O, w_n + u_n]$$

$$u_n = x_n - t_{n+1}$$

where X_n is the amount of service that nth customer demands, t_{n+1} is the time interval between the arrival of nth demand and (n+1)th demand.

The equation can be applied iteratively when the interarrival and services time are both discrete random variables and occurs at instant k_τ ($k = 0, 1, 2, \ldots$). Here, τ represents basic time unit. To solve this kind of linear difference equations, Z-transform approach can be used.

But when random variables are continuous, then for the discrete approximation, it is desired to consider continuous distribution as a finite number of discontinuities, then discrete approximation is applied to equate original distribution's moments as possible, starting with the first moment and going upward.

8.2.2.1 Application

– Discrete approximations of queueing models are crucial for analyzing and optimizing systems in discrete time intervals. Using tools like Markov chains, discrete event simulation, and performance analysis, engineers can model and predict the behavior of queues in real-world systems, such as computer networks, manufacturing lines, and service systems. These models help optimize resource allocation, minimize delays, and improve system efficiency.

8.2.3 The Fluid Approximation

The fluid approximation of a queueing model is an analytical technique that simplifies the analysis of complex discrete-event queueing systems by approximating them with continuous systems. This method is especially useful in systems with a large number of customers or entities, where exact solutions for discrete models may be too complex or computationally expensive to obtain. Queueing theory is primarily fixated on pleasant outcome, even in the initial bounds and inequalities only equilibrium conditions have to be applied. In fluid approximation, queueing models are considered as continuous flow of arrivals instead of discrete customer flow.

For every queueing model, the size of customers and the unfinished services both as the time function are stochastic processes with discontinuities. If the system is in heavy traffic state, then it is justifiable to substitute these discontinuities by regular continuous time functions. In fluid approximation, the discontinuities magnitude must be small compared to average value of these functions and this approximation deals with a case of small relative increments.

In the basic stochastic processes, the arrival and departure processes of queues are defined as follows:

$\alpha(t)$ represents the number of arrival in (o, t)

$\delta(t)$ represents the number of departure in (o, t)

A step-wise increasing process in fluid approximation is depicted in Figure 8.1.

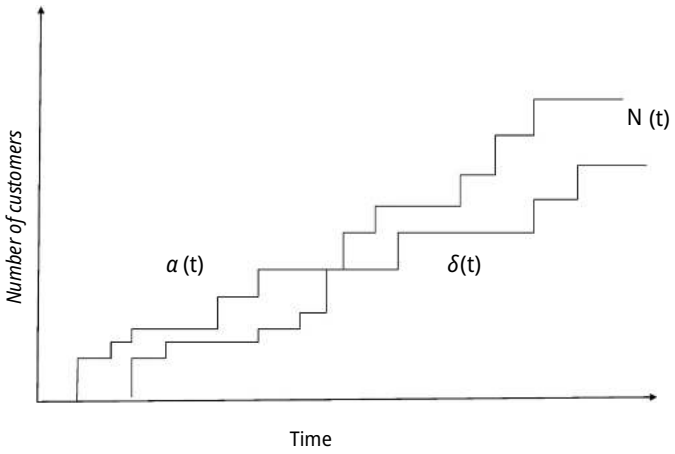

Figure 8.1: Stochastic process in fluid approximation.

At any instant of time, the number of customers present in the system is $N(t) = \alpha(t) - \delta(t)$, $[N(0) = 0]$. When $\alpha(t)$ gets large compared to 1, then its expected only small percentage deviations from its average value $E[\alpha(t)]$ is approximately equivalent to $\bar{\alpha}(t)$. Applying law of large numbers, we have $\lim_{n\to\infty} \frac{\alpha(t) - \alpha^{-}(t)}{\bar{\alpha}(t)} = 0$ with probability 1.

This indicates that approximation of the first order to the stochastic process is to replace it with its mean value as a function of time. Therefore, if one assumes that $N(0) = 0$, the fluid approximation proposes that at time t, the number of customers in the system should be given by

$$N(t) = \bar{\alpha}(t) - \bar{\delta}(t)$$

8.2.3.1 Application

The fluid approximation is a powerful tool for simplifying the analysis of complex queueing systems, particularly in large-scale or continuous systems. By approximating discrete processes as continuous flows, it allows for the use of differential equations to model system dynamics, making the analysis more tractable and providing valuable insights into system performance. However, the method may not be suitable for small or highly variable systems where discrete-event models are more appropriate

8.2.4 Diffusion Process Approximation

A diffusion process is a type of continuous stochastic process that describes how the system evolves over time. The most common diffusion process used in queueing theory is the Brownian motion or Wiener process, which is characterized by continuous paths and has increments that are normally distributed.

The idea is that to scale the parameters of a queueing system (like the arrival rate and service rate), the system can be approximated as a continuous process that is easier to analyze than discrete models.

In the diffusion process, approximation is improved by permitting arrival process $\alpha(t)$ and departure process $\delta(t)$ to have deviations about mean, by allowing the variances $\sigma^2_{\alpha(t)}$ and $\sigma^2_{\delta(t)}$ for the arrival and departure processes, respectively. The fluctuations about the mean of process are represented by normal (Gaussian) distribution, because probability that $\alpha(t) \geq n$ is similar to the customer C_n reach at time τ_n that is at or prior to t, i.e.,

$$P[\alpha(t) \geq n] = P[\tau_n \leq t]$$

The time of arrival C_n is just the summation of n interarrival times, i.e., $\tau_n = t_1 + t_2 + \cdots + t_n$, where τ_0 *is* assumed to be zero for G/G/1, the set $\{t_i\}$ is assumed as an independent identically distributed (IID) set of random variables. As the time t and the number n increase, τ_n becomes the summation of a large number of random variables that are independent and identically distributed. So, central limit theorem can be applied to model the random variable τ_n and random process $\alpha(t)$ as Gaussian

functions. This normality assumption of $\alpha(t)$ {and of $\delta(t)$} is the foundation of diffusion approximation.

Diffusion approximation conceals the discreteness of the arrival and departure processes like a normal random process. However, when $N(t)$ is significantly greater than 1, this approximation is useful.

The diffusion equation (partial differential equations) for probability distribution function of $N(t)$ is referred as follows:

$$-\frac{\partial f}{\partial t} = m(x,t)\frac{\partial F}{\partial x} + \frac{1}{2}\sigma^2(x,t)\frac{\partial^2 F}{\partial x^2}$$

and

$$\frac{\partial f}{\partial t} = -\frac{\partial}{\partial w}[m(w,t)f] + \frac{\partial^2}{\partial w^2}\left[\sigma^2(w,t)f\right]$$

where

1. $F = F\ (x,t;y,\tau) \triangleq P[x(\tau) \le y | x(t) = x]\ f$ or $t < \tau$
   That is, the probability that the diffusion process has a value less than or equal to $\le y$ at τ, when at time t, it had the value x. This (time-dependent) transition probability follows Chapman-Kolmogorov equation: $F(x,t;y,\tau) = \int_{-\infty}^{\infty} F(w,u;y,\tau) d_w F(x,t;w,u)$ where $t < u < \tau$.
2. f is defined as $f(x,t;y,\tau) \triangleq \frac{\partial F\ (x,t;y,\tau)}{\partial y}$.
   This density f also satisfies the Chapman-Kolmogorov equations:
   i.e., $f(x,t;y,\tau) \int_{-\infty}^{\infty} f(w,u;y,\tau) f(x,t;w,u) dw$, where $t < u < \tau$.
3. $m(x,t) \triangleq \frac{\partial M(x,t;\tau)}{\partial \tau}|_{\tau=t'}$ $\sigma^2(x,t) \triangleq \frac{\partial V(x,t;\tau)}{\partial \tau}|_{\tau=t}$
   $M(x,t;\ \tau)$ (conditional mean) $\triangleq E[x(\tau)|X(t) = x]$
   $\sigma^2\ (x,t;\tau)$ (conditional variance) $\triangleq E\left[\{x(\tau) - M(x,t;\ \tau)\}^2 | X(t) = x\right]$

8.2.4.1 Application

In queueing theory, the diffusion process serves as a powerful approximation tool, particularly in large or heavy traffic systems. By treating the system's behavior as a continuous process, we can leverage powerful mathematical tools to analyze and understand the system's performance more efficiently.

8.2.5 The Rush-Hour Approximation

The rush-hour approximation is a concept used in queueing theory to describe the behavior of queueing systems during periods of high traffic, such as rush hours. This approximation is often applied to model systems under heavy load where the arrival rates are high and the system is under stress, leading to long waiting times, queue

buildup, and high utilization. It is a simplification that helps to analyze systems during peak demand times.

When $\rho < 1$, an equilibrium distribution exists but most interesting queueing systems are not stationary. Rush-hour approximation is the study of quasi-stationary situation where queueing behavior lies in the categories of extreme cases. It is assumed particularly that infinitely small mean and variance are function of only *t*, but not of *w*, then Fokker-Planck equation is given as follows:

$$\frac{\partial f}{\partial t} = -m(t)\frac{\partial f}{\partial w} + \frac{\sigma^2(t)}{2}\frac{\partial^2 f}{\partial w^2} \text{ where } m(w,\ t) = m(t)$$

and $\sigma^2(w,t) = \sigma^2(t)$ has been taken. If suppose $m(t) < 0$ (i.e., departure rate can sustain arrival rate) and let deviations in this very small mean is slow in comparison to $[\sigma(t)/m(t)]^2$ the relaxation time of system, then waiting times and queues are likely to have this slow variance, so that, for a small number of relaxation times, the system will look stationary, such situation is referred as quasi-stationary. For the unfinished work, quasi-stationary distribution is given as follows:

$$F(w,t) = 1 - e^{2m(t)w/\sigma^2(t)};\ w \geq 0 \tag{8.1}$$

This is the previous equilibrium solution's natural extension.

$$m(t)\ \left[\frac{\lambda(t)}{\mu(t)}\right] - 1,\ \sigma^2(t) = \lambda(t)\bar{x}^2(t)$$

The second moment of the service time distribution at any time *t* is shown by $\bar{x}^2(t)$. If no notable changes in the waiting time occur, quasi-stationary result will hold. Hence, quasi-stationary becomes:

$$\frac{\left|\frac{d\bar{U}(t)}{dt}\right|(\text{relaxation time})}{\bar{U}(t)} \ll 1 \tag{8.2}$$

where $\bar{U}(t)$ is the average work not finished at time *t*. From eq. (8.1):

$$\overline{U}(t) = -\frac{\sigma^2(t)}{2m(t)}$$

Hence, condition becomes $\left|2\sigma(t)\frac{d\sigma(t)}{dt} - \frac{\sigma^2(t)}{m(t)}\frac{dm(t)}{dt}\right|[m^2(t)]^{-1} \ll 1$

The most interesting observation is when $\rho(t)$ is near to 1 [i.e., $m(t)$ near to zero], then first term is generally insignificant in comparison to other, the condition thus becomes $\frac{\sigma^2(t)}{[1-\rho(t)]^3}\left|\frac{d\rho(t)}{dt}\right| \leq 1$.

Hence, if the time variations are small and slow, quasi-stationary solution will closely approximate the waiting time distribution in the situation $\rho(t) < 1$, but as ρ approaches and subsequently may exceed 1, real waiting time cannot increase as quickly

as quasi-stationary solution would indicate and for stable queueing models, mostly the delays arise because of the stochastic effects of fluctuations in the arrival and service patterns. In this case, fluid approximation plays an important role.

This gives good understanding of behavior of the waiting time at extremes of $\rho(t)$.

8.2.4.1 Application

The rush-hour approximation provides a practical framework for analyzing queueing systems under high demand or peak conditions. It focuses on simplifying the analysis by assuming the system is heavily loaded, allowing for approximations of key metrics like queue length, waiting time, and system utilization. These approximations help system designers and operators optimize performance during critical periods of demand, ensuring efficient resource allocation and minimizing delays during peak times.

8.2.6 Heavy Traffic Approximation

This approximation simplifies the mathematical treatment of complex queueing models by focusing on the behavior of the system when it is under stress, i.e., when the system is almost at capacity. It indicates some interesting limit results and inequalities for G/G/I model in which traffic intensity is just barely less than 1 ($1 - \in < \rho < 1$).

For establishing limit results $v(t)$ and $W(n)$, which are, respectively, virtual wait a customer would undergo if customer arrives at time t and actual waiting time of the nth customer are used to construct random sequences, which are then shown to stochastically converge. Convergence theorems are then applied to obtain approximate distribution of the actual and virtual waits in queue of a customer and their averages.

For the $G/G/1$ model, the difference of the nth service and interarrival times is $U^{(n)} = S^{(n)} - T^{(n)}$. The nth partial sum of $\{U^{(n)}\}$ in $P^n = \sum_{i=0}^{n-1} U^{(n)}$.

Let the mean and variance of the IID $\{U^{(n)}\}$ be $-\alpha$ and β^2, respectively. Then the expectation of $P^{(n)}$ is $-n\alpha$ and variance $n\beta^2$. In heavy traffic case, α should be small. Using central limit theorem for IID random variables, to sequence $\{P^{(n)}\}$

$$Y_n \equiv \frac{P^{(n)} + n\alpha}{\sqrt{n\beta}} \to N(0,1)$$

Using asymptotic normality of Y_n, Laplace transform of $W_q^{(n)}$ for large n, it is given approximately by $W_q^*(S) = \left(1 + \beta^2 S/2\alpha\right)^{-1}$ when α/β is small.

Therefore, it can be deduced that line decay is negative exponential with mean.

$$\frac{\beta^2 S}{2\alpha} = \frac{-1}{2}\ \frac{\text{Var}\,U}{E(U)} = \frac{1}{2}\ \frac{\text{Var}\,[\text{service times}]\ +\ \text{Var}\,[\text{interarrival times}]}{\frac{1}{\mu} - \frac{1}{\lambda}}$$

This provides an approximation for the waiting time distribution around large waiting periods for $\rho \cong 1$:

$$W_q^H = -\frac{1}{2}\ \frac{\text{Var}\,(U)}{E(U)}$$

$$\Rightarrow W_q^H = \frac{1}{2}\ \frac{\text{Var}\,[\text{service times}]\ +\ \text{Var}\,[\text{interarrival times}]}{\frac{1}{\mu} - \frac{1}{\lambda}}$$

8.2.6.1 Application

The heavy traffic approximation is a powerful tool in queueing theory that simplifies the analysis of systems under peak load conditions. By approximating the system's behavior using diffusion processes, heavy traffic approximations help estimate key performance metrics like waiting time, queue length, and system utilization when the system is operating near its capacity. This method is widely used in practical applications, such as telecommunications, transportation, call centers, and manufacturing, where understanding system behavior during high-demand periods is critical for optimization and resource allocation.

8.2.7 Simulation Techniques

Simulation plays a crucial role in approximating queueing theory models, particularly when analytical solutions are impractical (Figure 8.2). It provides a powerful approach to study complex queueing systems where real-world constraints, such as variable arrival patterns, multiple service stages, and priority-based scheduling make mathematical modeling difficult. By simulating queueing systems, it becomes possible to estimate key performance metrics, such as average waiting time, queue length, system utilization, and customer loss probability.

One of the primary advantages of simulation is its ability to handle complexity. Unlike analytical methods that require simplifying assumptions, simulation can incorporate realistic elements, such as time-dependent arrivals, nonexponential service distributions, and customer behaviors like balking and reneging. This flexibility allows for a more accurate representation of actual systems. Another key benefit is that simulation does not require closed-form solutions. Many queueing problems, especially those involving networks of queues or varying service disciplines, have no explicit mathematical solution. Simulation provides a viable alternative by generating approximate results through computational techniques. It also enables sensitivity

analysis, where parameters such as arrival rates, service times, or the number of servers can be adjusted to observe their impact on system performance.

Visualization and experimentation are additional strengths of simulation. Modern simulation tools offer graphical representations of queueing systems, making it easier to identify bottlenecks, inefficiencies and potential improvements. Businesses and organizations can use simulation to test different operational strategies – such as adding more service stations or changing queue management policies – before implementing costly changes in real-world settings. Furthermore, simulation is a cost-effective decision-making tool. Instead of conducting expensive real-world experiments, businesses can use simulation to predict system behavior under various conditions. This helps in optimizing resource allocation, reducing waiting times, and improving overall service efficiency.

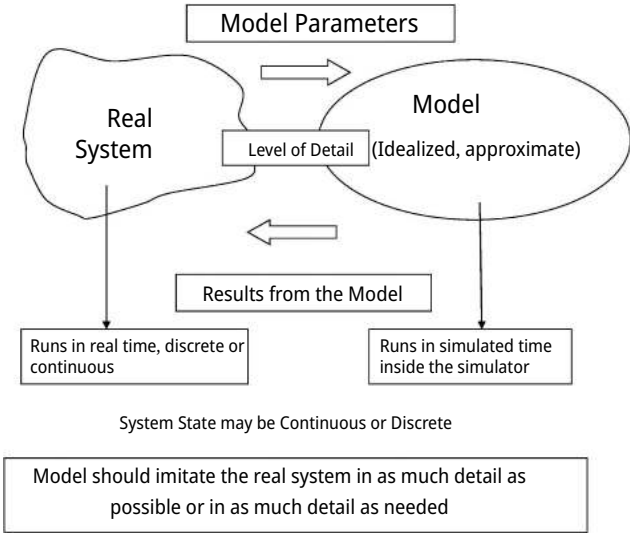

Figure 8.2: Simulation model of real system.
(Copyright2002 [16])

Finally, simulation can integrate real-world data to enhance accuracy. By incorporating empirical data, it ensures that the model reflects actual system dynamics rather than relying solely on theoretical assumptions. This makes it a valuable tool for validating queueing models and making informed operational decision.

8.3 Conclusion

In this chapter, we explored various approximation techniques used to analyze and solve queueing models that arise in optimizing complex engineering systems. The study highlights the importance of selecting the right approximation method based on the system characteristics and performance metrics of interest. While approximations introduced some level of error are invaluable in decision-making, optimization, and real-time system analysis, particularly in telecommunications, manufacturing, healthcare, and computing networks.

Future research should focus on improving the accuracy and efficiency of approximation techniques, incorporating machine learning and hybrid modeling approaches for better adaptability in dynamic environments. Overall, approximation methods remain a cornerstone in queueing theory, enabling engineers to design and optimize complex systems effectively.

References

[1] Bhat, U. N. & Shalaby, M. (June 1979). Approximation techniques in the solution of queueing problems. Naval Research Logistics Quarterly, 26(2), 311–326.
[2] Protopapas, D. A. (May 4–7, 1981). Finite queueing approximation techniques for analysis of computer systems. AFIPS '81: Proceedings of National Computer Conference, 423–429.
[3] Kaufman, J. S. (August 1984). Approximation methods for networks of queues with priorities. Performance Evaluation, 4(3), 183–198.
[4] Ackroyd, M. H. (July 1986). Approximate characterisation of nonstationary discrete time G/G/1 systems. Performance Evaluation, 6(2), 117–123.
[5] Yang, H. & Lipsky, L. (1989). The approximation of density functions for use in queueing theory. Conference Proceedings., IEEE International Conference on Systems, Man and Cybernetics.
[6] Dallery, Y. (1990). Approximate analysis of general open queuing networks with restricted capacity. Performance Evaluation, 11(3), 209–222.
[7] Kimura, T. (November–December 1995). Approximations for the delay probability in the *M*/*G*/*s* queue. Mathematical and Computer Modelling, 22(10–12), 157–165.
[8] Glynn, P. W. (1998). Strong approximations in Queueing Theory. Asymptotic Methods in Probability and Statistics, A Volume in Honour of Miklós Csörgo, 135–150.
[9] Harris, C. M. & Marchal, W. G. (1998). Distribution estimation using Laplace transforms. INFORMS Journal on Computing, Vol. 10(4), 448–458.
[10] Kurasugia, T. & Kino, I. Approximation methods for two-layer queueing models. Performance Evaluation, 36–37, 55–70,1999.
[11] Shortle, J. F., Brill, P. H., Fischer, M. J., Gross, D., & Masi, D. M. B. (2004). An algorithm to compute the waiting time distribution for the M/G/1 queue. INFORMS Journal on Computing,16(2). 152–161.
[12] MoghimiHadji, E. & Aydin, I. (July 3–6, 2012) Approximation to performance measures in queuing systems. In Proceeding of International Conference on Industrial Engineering and Operations Management Istanbul, Turkey, 1536–1541.
[13] Sani, S. & Daman, O. A. (October 2014). Mathematical modeling in heavy traffic queuing. American Journal of Operations Research, 4(6), 340–350.

[14] Deepak,. (Nov-Dec, 2022). A practical study of queueing theory algorithms an simulations. International Journal of Enhanced Research in Educational Development, 10(6), 476–481.
[15] Dai, H. & Yanhua, W. (2024). A queueing model with ON/OFF sources: Approximation and stationarity. Stochastic Models, 4(3), 433–463.
[16] Bose, S. K. (2002). An Introduction to Queueing Systems. New York: Springer-Verlag.
[17] Whitt, W. (1993). Approximations for the GI/G/m queue. Production and Operations Research, 2(2), 114–161.
[18] Kobayashi, H. (1974). Application of the diffusion approximation to queueing networks I: Equilibrium queue distributions. Journal Of The ACM, 21(2), 316–328.
[19] Ibe, O. C. & Maruyama, K. 1985 An approximation method for a class of queueing systems. Performance Evaluation, 5(1), 15–27.

Ankur Saxena, Mahesh Kumar, Kulwant Singh,
and Dhaneshwar Mishra

Chapter 9
Influence of Fluid Pressure in MEMS-Based Microfluidic Device Application: A Review

Abstract: Efficient pressure-sensing mechanism in microfluidic devices has great importance for fluidic analysis in the microchannel. Precise fluid pressure analysis in a microfluidic channel can also give information about forces in a microchannel, which could be further used to indirectly examine particle expected trajectories in various phenomena, such as acoustophoresis, dielectrophoresis, microstructure filtration, and other healthcare application. Currently, pressure-sensing and fluidic velocity inputs in the microchannel are accomplished using a syringe pump, which adds an extra cost and increases the size of the setup. Integrating pressure-sensing mechanisms in microfluidic devices is very much appreciable to overcome this problem and adds an extra feature for superior analysis. This review focused on various strategies and possible solutions for effective pressure-sensing methodology for appropriate application of microfluidic devices. The comparative study was carried out based on parameters, such as fluid pressure, aspect ratio (AR) of microchannel, flow rate, and material of the microfluidic channel. This chapter focused on possible fluid pressure-sensing mechanisms that could be employed along with microfluidic devices for further analysis of microentities for fluidic application.

Keywords: microfluidic, pressure sensor, microchannel, laminar flow, flow rate

9.1 Introduction

Microfluidics has been heavily researched in the healthcare industry in the last few years. Microfluidics in the last decade has been highly involved in various applications, such as biomedical, optical sensors, thermal sensors, flexible sensors, touch

Ankur Saxena, Department of Electronics and Communication Engineering, Bharat Institute of Engineering and Technology, Hyderabad 501510, Telangana, India, e-mail: ankur_saxena6481@yahoo.com
Mahesh Kumar, Department of Information and Communication Technology, Pandit Deendayal Energy University, Gandhinagar 382007, Gujarat, India
Kulwant Singh, Skill Faculty of Engineering and Technology, Shri Vishwakarma Skill University, Palwal 121102, Haryana, India
Dhaneshwar Mishra, Department of Mechanical Engineering, Manipal University Jaipur, Jaipur 303007, Rajasthan, India; Multiscale Simulation Research Center (MSRC), Manipal University Jaipur, Jaipur 303007, Rajasthan, India

https://doi.org/10.1515/9783111723464-009

screens, and medical devices. The designed microfluidic systems consist of the width and height of the device between 100 nm and 100 μm [1]. Microfluidic applications are extensively handled in the territory of bio-MEMS (microelectromechanical system) [2], microreactors [3], pressure sensors [4], and microfuel cells [5]. Microchannel and sensors are essential components of the microfluidics system to evaluate fluid mechanical characteristics [6]. The parameter of microfluidic varies with surface roughness of the channel, which can be expressed as a friction factor or friction coefficient. The size, shape, and material of the microchannel affect the characteristics of microfluidic flow. Researchers analyzed microchannel designs and examined the characteristics of channels for Newtonian and non-Newtonian fluid flow with a high surface area to volume ratio [7]. The researcher performed experiments to observe microfluidic characteristics, including viscosity, pressure at the inlet of a microchannel, fluid pressure, flow rate, and force. The Navier-Stokes equation is used to investigate the characteristics of laminar fluid flow in a microchannel. Mechanical properties of fluids, such as fluid velocity and pressure in a microchannel, fluctuate throughout its length. Fluid flow in the microchannel exerts some pressure through the wall of the microchannel. The wall pressure amount depends on the fluidic nature, such as laminar fluid flow, creeping flow, or turbulent fluid flow in the channel. The laminar fluid pressure value becomes more stable due to no more extended travel in layers and no mixing across the microchannel. At the same time, the creeping and turbulent flow speed is very high, and multilayer mixing with unstable speed or velocity. To understand the properties of laminar microfluidic pressure in a microchannel, the designed process requires implementing an innovation or precise methodology to monitor fluid pressure inside the microchannel and control the fluid velocity.

The literature includes the methodology of laminar microfluidic pressure-sensing mechanisms for the development of microfluidic device applications to control fluid pressure by controlling other parameters of the fluid. The size of the microchannel is in micrometers and laminar fluid flows in a microchannel at a low fluid rate [7, 8]. The fluid pressure control in the microchannel is a crucial component for the detection of fluid velocity and other relevant parameters of fluid in a channel [9]. The literature study shows numerous mechanisms have been developed for the measurement of the pressure inside or across a microfluidic channel, such as piezoelectric[10], piezoresistive[11], capacitive[12], and optical pressure sensors. The advancement of microfluidics research is extensively increasing; researchers try to integrate a microfluidic chip or lab-on-a-chip in a microchannel but problems detect integration in the microfluidic chip. The problem was the size of the MEMS pressure sensor in millimeter while the microchannel size was in micrometer, so that, it was challenging for researchers to integrate a pressure sensor within a microchannel. The researcher gives several techniques to overcome such a type of problem and measure microfluidic pressure. The researcher investigated and designed an integrated gas pressure sensor

or a layer of pressure-sensitive paint () in a microchannel. In this research, monitoring gaseous-liquid molecules with PSP is fascinating and provides an excellent overall pressure profile [13]. The chip-level market is experiencing significant growth in technology, and the demand for flexible and advanced devices in the biomedical industry is rising quickly. The market for microfluidic pressure sensors has grown as a result of its involvement in flexible and wearable applications [14]. The flexible pressure sensor utilized flexible material or conductive material, carbon nanotubes (CNTs), silicon nanowires, and certain liquids as well as nonviscous Galinstan indium material to measure the pressure of the fluid. The polydimethylsiloxane (PDMS)-based flexible microchannel was implanted in a vein to prevent tissue injury and was created for pacemaker heartbeat control devices [15].

Considering the above facts, this chapter aims to project an exhaustive review of the recent developments in microfluidic pressure-sensing mechanisms with the support of the literature focusing on geometrical parameters of device and sensing physics. This chapter is categorized into two broad pressure-sensing mechanisms: an analytical technique for pressure measurement and physics applied for fluid pressure sensing. This chapter discussed geometrical parameters of microchannel with its mechanical properties and analyzed the involved in detection of fluid properties. This chapter compared the experimental and simulation results from various research articles to understand the microfluidic pressure-sensing process and also figured out the deviation in amount of measure parameters. Figure 9.1 shows the classification of the microfluidic pressure-sensing mechanism with its applications.

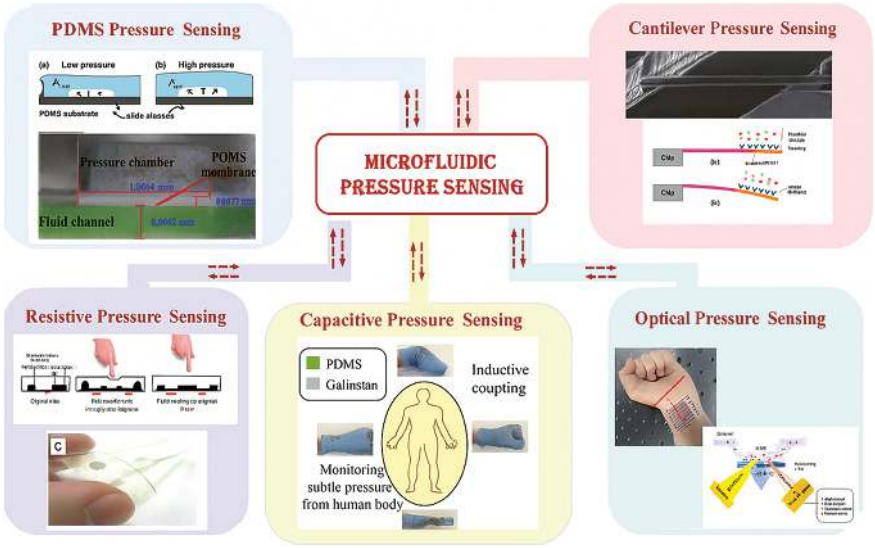

Figure 9.1: Classification of microfluidic pressure-sensing mechanism.

9.2 Pressure-Sensing Role in Microfluidic Device

The fluid pressure sensing and controlling in the microchannel are main features for microfluidic device. The sensing of microfluidic pressure drops in a microchannel is quite different from a macroscale theory. It is difficult to measure microfluidic pressure directly through any instrument. The microfluidic device has a component, i.e., microchannel where the fluid (laminar or creeping) is flowing. The microchannel is a component of a microfluidic device that is utilized in the application of biological sensors, microreactors, chemical sensors, or any microfluidic sensor. The microchannel has various shapes for different types of application and the size of microchannel is in micrometer to millimeter. The measurement of fluid pressure in a microchannel has some steps that first determine the fluid flow pattern inside a microchannel. Generally, fluidic pressure with large amounts can be measured with gauges because it was the simplest approach, but it was incompatible with measuring microfluidic pressure due to the small size of the channel. The researcher has challenge of designing a microfluidic pressure sensor to measure a sensible amount of fluid pressure variation in a microchannel. The technology by growing with years and researcher developed microfluidic sensor that converts physical energy or quantity energy into required energy or signal with the help of a microfluidic system [16] that measures the microfluid pressure. The researchers discovered different types of morphology to measure microfluidic pressure in microchannel, such as the capacitive method [17], piezoresistive method [18], optical-sensing layer [19], deformation layer [20], and electrical resistivity method [21]. These techniques are widely used to monitor microfluidic pressure value and other relevant parameters of fluid that can impact fluid flow in a microchannel. Transformation of technology gives a new direction of methodology and implements the deformation material-sensing process. MEMS and NEMS (nanoelectromechanical system) technology-based microfluidic devices come into focus with large-area applications in biomedical devices. MEMS-based microfluidic pressure sensors have several advantages, such as low cost, lightweight, low power consumption, and high accuracy through the MEMS device becomes easier and smaller in size. Integrated MEMS microfluidic pressure sensors also optimized properties of fluid-like sensitivity, temperature-dependent, linearity, and accuracy for the microfluidic device. The above study shows the importance of the fluidic pressure profile in the main microchannel and branch microchannel. Controlling the fluid pressure in the microchannel is challenging for researchers and they try to control the fluid pressure, then such types of techniques are implemented in a wide range of healthcare applications. This chapter has discussed an analysis of microfluidic flow affected by the structural elements of the microchannel that includes the pressure-sensing mechanism review along with methods to regulate fluid pressure in the microchannel. Additionally, a brief introduction of several microfluidic pressure-sensing techniques with both simulation and experimentation results was utilized for fluidic pressure measurement [22].

9.3 Operating and Design Parameters for Pressure Sensing in Microfluidic Device

9.3.1 Aspect Ratio of Microchannel

An aspect ratio (AR) is a property of a microchannel that affects microfluidic pressure in the channel. AR value depends on the dimension or size and shape of any object, here the author discussed the importance of AR for various structures of microchannel geometry and the effect of AR on pressure in microchannel. Mostly, microchannel design structures are rectangular, so that, the AR is defined in terms of height-to-width ratio. It becomes more challenging for a design engineer to design a stable structure with a stable AR. Microfluidic application requires an AR to be minimum, and to establish minimum requirements of AR for microchannel, the author suggests that the width and height range between approximately 30–100 and 0.1–0.5 μm, respectively [23]. The researcher investigated the relationship between microchannel length and AR and it was found that the amount of AR increased with the reduction in the length of the microchannel. Similar to this, a correlation was established between AR and pressure drop. It was concluded that for a high value of the AR, the pressure value becomes low, and for a low value of the AR, the pressure value becomes high. It was found that in microfluidics application, AR value is required to be low, so that the fluid flows smoothly in the microchannel without any restriction [24].

9.3.2 Friction Coefficient of Microchannel Surface

The friction coefficient in microfluidics is quite different from the macroscale theory of fluid dynamics, as friction coefficients define the fluid flow resistance. Peng et al. give a theory for microfluidics friction coefficient in microchannel by comparing macroscale theory. The author numerically investigates pressure driven in microchannel where electrical double layer (EDL) affects or influences the friction coefficient. Fluidic pressure was investigated in rectangular microchannel using the Poisson-Boltzmann and modified Navier-Stokes equations. The friction coefficient was calculated by electrokinetic theory and compared with EDL macroscale theory. Friction coefficients significantly change for the low electrolyte concentration at high electric potential. The friction coefficient is related to hydraulic diameter and found in the microchannel friction coefficient of liquid higher for low value of hydraulic diameter [25]. The friction factor is also calculated by roughness of microchannel or grooves available in microchannel that generate resistance for smooth fluid flow. Rawool et al. designed and examined numerical simulations of a 3D-serpentine microchannel for the effect of roughness with obstacles present in a microchannel. The study investigated fluid flow friction property where research

explained value of friction factor is increased in a nonlinear fashion with increment in the height of obstruction. An author also observed various shapes of obstruction and found that trapezoidal geometry gives minimum friction factor in comparison to rectangular and triangular obstructions. The research focused on the roughness pitch of the microchannel that affects fluid pressure, if the obstruction roughness pitch is increased, then the pressure drop value becomes decreased. The fluid properties vary with surface roughness and obstacles present in the microchannel at any position [26]. When fluid flows in the microchannel, the fluid flow resistance (increased friction factor) increases, whereas the fluid flow rate decreases. Surface roughness is directly related to friction factor, and fluid friction factor is analyzed using Reynolds number. The obstacles in microchannel are defined in terms of grooves, which can be of any shape, such as regular or irregular. The fluid characteristics for regular-shaped grooves, such as triangular, rectangle, or circular, present in microchannel and simulated at fluid flow rate are shown in Figure 9.2. The blue zone shows the minimum fluid velocity rate, whereas the red zone shows the maximum fluid velocity rate. It concluded that the friction coefficient is an important operating design factor for the fluid flow in the microchannel at various aspects. In the research that includes microfluidics and microchannels, there is friction factor is physical parameters determination plays an important role.

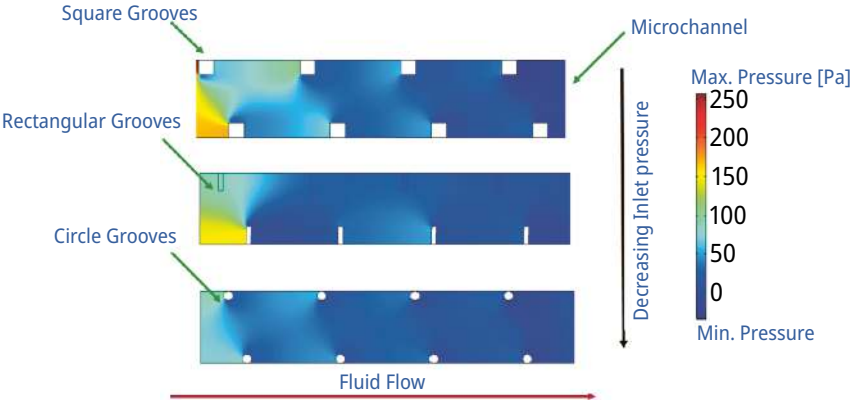

Figure 9.2: COMSOL-simulated schematic representation of microchannel with square grooves, rectangular grooves or obstacles, and circular grooves. The inlet pressure level is shown by the bar spectrum.

9.3.3 Reynolds Number of Microchannels

Reynolds number is dimensionless; it is used to predict fluid flow patterns in various conditions. According to Reynolds number, fluid flow is divided into two categories. If Reynolds number is low, then the fluid flow type is laminar, while for high Reynolds

number, it is creeping flow or turbulent flow. Reynolds number is a ratio of inertia to viscous force concerning the velocity of fluid. The low value of Reynolds number signifies viscous force that is dominant due to this fluid motion being precise, smooth, and constant, whereas the high value of Reynolds number signifies the inertial force that is dominant due to these producing eddies, vortices, and instability of fluid. Reynolds number is defined as follows:

$$\mathrm{Re} = \frac{\boldsymbol{\rho UD}}{\boldsymbol{\mu}} \tag{9.1}$$

Reynolds number describes the characteristics of fluid density, velocity, and viscosity concerning the length of the microchannel. Newtonian fluid is viscous stress that shows linear behavior concerning fluid velocity. The Newtonian fluid flows and non-Newtonian fluid flows do not obey Newton's law. The microfluidic flow in the microchannel is divided into two categories – laminar flow and creeping flow.

9.3.3.1 Laminar Flow

An identical orderly flow representing fluid flow is laminar or when fluid particles move in smooth layers, sliding over particles in adjacent laminar without mixing with them, as shown in Figure 9.3(a). The steady laminar fluid flow in the microchannel required static pressure, strictly axial, low Knudsen number, no slip at the wall, incompressible Newtonian fluid, constant viscosity, and negligible energy dissipation. Bahrami et al. designed a microchannel for measuring a pressure fully developed of incompressible laminar fluid flow. The study focused on geometrical parameters of cross-section and compared models with the experimental data of various researchers. The investigation of pressure drops in the microchannel is done for various shapes of the channel. The research found that all microchannels give maximum deviation in pressure except the equilateral triangular microchannel [27]. Another study investigates the laminar behavior for viscosity or viscous flow in microchannel. The rate of laminar fluid flow is very low and the fluid pattern is straight in parallel stream with no mixing or overturning of motion layers. Between infinite parallel plates, the laminar flow offers an accurate solution for an incompressible constant viscous fluid. Gamrat et al. [28] examined the three different approaches for the influence of laminar due to the roughness in a microchannel. This chapter compared the investigated results experimentally and numerically for various types of roughness in microchannels. The three- (3D) and one-dimensional structures developed a variety of roughness in the microchannel that was investigated numerically and experimentally. The result found that the laminar flow in the microchannel is independent of the height of roughness in the microchannel [28]. In another experiment, Jiang et al. explored microscale cooling techniques for more efficient heat dissipation in microchannels. Jiang

calculated a value that affects the laminar fluid flow in the microchannel. The steady laminar flow in duct friction pressure loss is given by:

$$\Delta P = \mathbf{F}\frac{\boldsymbol{L}\boldsymbol{\rho}\boldsymbol{v}^2}{\boldsymbol{d}2} \tag{9.2}$$

where **F** is the Darcy friction factor, $\boldsymbol{L}$ and $\boldsymbol{d}$ are the length and hydraulic diameter of duct, respectively, P is the fluid density, and $\boldsymbol{v}$ is the mean velocity of ducts. The Darcy function of Reynolds number of the flow at relative surface roughness of the duct is defined as follows:

$$F = \frac{8\ \boldsymbol{\tau}_w}{\boldsymbol{\rho}\boldsymbol{v}^2} = F\left(\mathrm{Re}, \frac{\boldsymbol{\varepsilon}}{\boldsymbol{d}}\right) \tag{9.3}$$

where $\boldsymbol{\tau}_w$ is the shear stress along the wall and ε is the wall roughness height.

This chapter investigated friction factor value in circular and noncircular microchannels and found that reducing the surface roughness cooled down the heat characteristics. Reynolds number is the main component influencing laminar flow, however, several experiments also investigated the surface roughness and duct friction factors that affected the fluid flow [29]. Hrnjak and Tu [30] studied fully developed liquid and vapor flow through a rectangular microchannel with a hydraulic diameter that ranges from 69.5 to 304.7 μm and they reported their findings. Water flow via several geometries of microchannel cross-sections, including triangular, trapezoidal, and rectangular, has been widely studied and used in numerous applications. The researchers selected microchannel diameters ranging from 8 to 42 μm [31]. A study was conducted using five microchannels with an AR of 0.13–0.76. The author presumes a cross-section channel because the channel is planned with a fully developed flow. The laminar fluid flow in the microchannel is affected by various factors of microchannel geometry and fluidic properties, so that, it is important to control the laminar fluid flow in the microchannel for significant result.

9.3.3.2 Creeping Flow

Stokes flow is also known as creeping flow, a fluid motion in which advection inertial force is small compared to viscous force. Creeping flow may occur in any fluid that has Reynolds number Re≪1 [32]. The creeping flow around moving bodies creating fluid resistance against a motion is known as drag. The steady incompressible creeping flow is given by the following Navier-Stokes equation:

$$\mathrm{H}\delta^2 v = \Delta\ p^* \tag{9.4}$$

$$\Delta.V = 0 \tag{9.5}$$

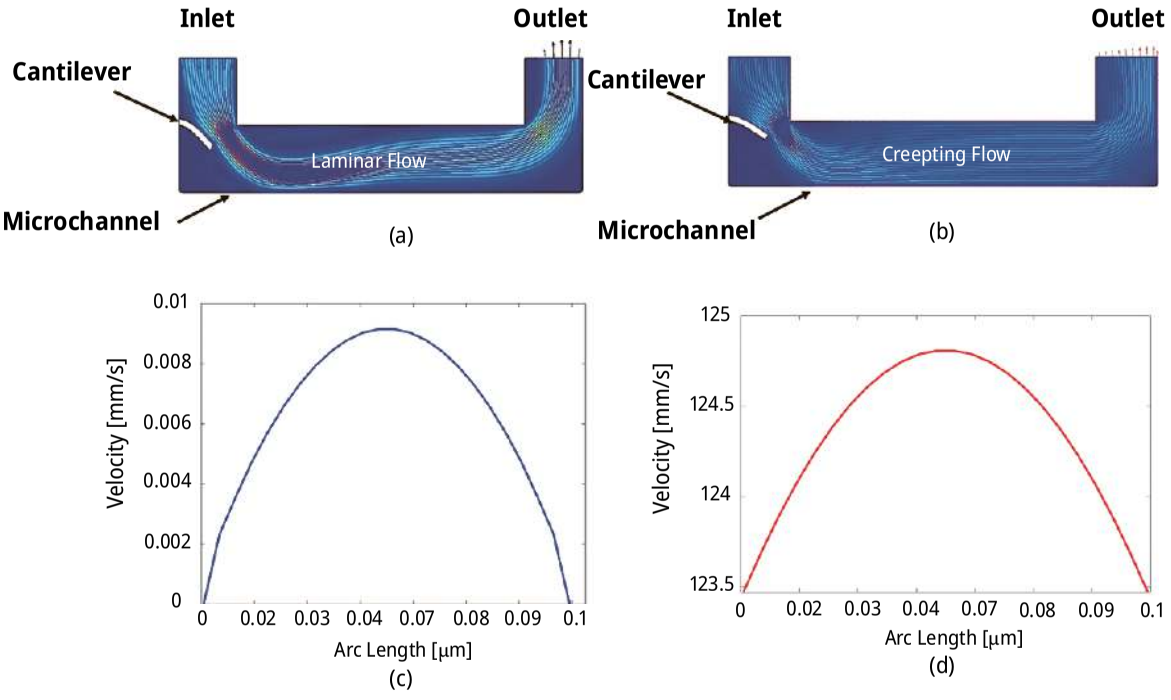

Figure 9.3: COMSOL simulates two different fluid flows across a microchannel and represents a 2D pattern of fluid and velocity profile. (a) Laminar fluid flows across a microchannel. (b) Creeping flow pattern across a microchannel. (c) Velocity profile of laminar fluid flow along with arc length. (d) Velocity profile of creeping fluid flow along with arc length is very high compared to laminar fluid flow.

$$P^{*} = p + \rho_0 \Phi - \text{effective pressure} \tag{9.6}$$

Researchers design and investigate a microchannel with integrating micropillars, which compares mass transfer coefficient, thermal conductance, and surface area to volume ratio with micropillar microchannel. Such types of device applications are used in microheater, microreactor, micropumping, and microfilter.

Stagger micropillars are provided the same porosity as a square micropillar at a lower pressure drop in a creeping flow study using a designed array of micropillar cylinders integrated on a rectangular microchannel [33]. The Navier-Stokes equation is transformed into the Stokes equation for creeping flow due to the tiny channel size's reduction in Reynolds number flow in a system. Through various experiments across a microchannel, the author determined the velocities of fluid and pressure drop in a microchannel. The Navier-Stokes equation, which computed velocity and pressure for several channels, was used to build the 3D orthogonal curvilinear model. The pressure exponential depends on the contraction parameter k, as the expansion-contraction parameter grew, the pressure drops increased [34]. The investigation of creeping flow in a microchannel with a micropost in an aligned and staggered arrangement was explored and simulated. As illustrated in Figure 9.3(b), an investigation discovered slip velocity as Reynolds number or cavity fraction increased. You may compute flow means velocity, slip means velocity, and friction means velocity using Reynolds' number [35].

9.3.4 Fluid Viscosity

The viscosity represents the internal resistance of molecules in fluid flow. An internal resistance increases as the viscosity of fluid increases and the rate of fluid becomes slow, fluid that has no internal resistance is known as inviscid fluid. The viscosity of the fluid influences the fluid's velocity profile, and the behavior of the viscosity can be observed in a variety of fluidic applications, including biological [36], optical [37], flexible wearable sensors [38], and paper-based microfluidics [39]. Figure 9.4(a) shows the microfluidic flow in a microchannel with a low- to high-viscosity pattern. Figure 9.4(b) shows the pressure of fluid increases with increasing in the amount of viscosity. The biological application examined the study of viscous blood to evaluate the fluid's viscosity, which is often measured using a capillary viscometer to calculate the flow rate [40].

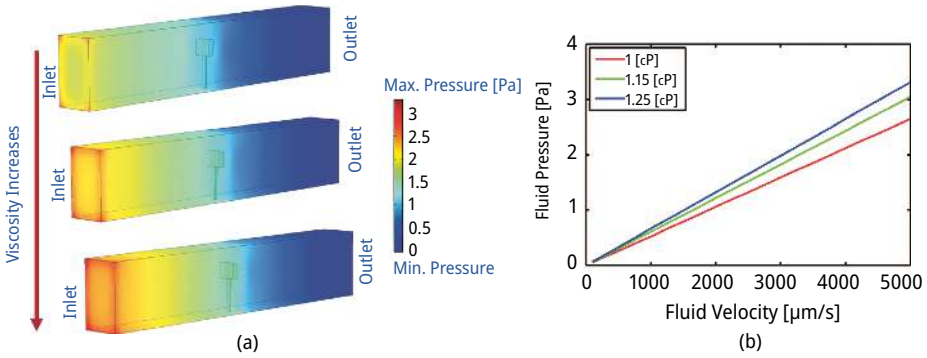

Figure 9.4: Fluid flow in the channel at three different viscosity levels. (a) Viscosity from top to down continuously increases in the microchannel, the pressure level also increasing at the inlet. (b) The graph between fluid velocity and inlet pressure at different viscosity levels.

9.4 Pressure-Sensing Mechanism for Microfluidic Application

The microfluidic pressure-sensing mechanism in a microchannel is broadly classified into two parts based on fluidic parameters, structural parameters variation, and physics applied for pressure sensing:

I. Analytical method of microfluidic pressure-sensing mechanism
II. Physics applied for pressure-sensing mechanism

9.4.1 Analytical Method of Microfluidic Pressure-Sensing Mechanism

Pressure-sensing methods in microfluidics are extensively implemented in biomedical, drug delivery, and chemical testing applications. Laminar fluid has steady flow in a microchannel and the characteristics of laminar flow depend on the structural characteristics of the microchannel, such as AR, Reynolds number, fluid viscosity, and friction factor of a surface that has changed with the flow of fluid. Batchelor investigated liquid's characteristics in a microchannel and discovered that fluid flow is directly correlated with Reynolds number that is used to forecast fluid flow patterns. Using Reynolds number of fluid flow, it is given as follows:

$$\mathrm{Re} = L v \rho / \mu \tag{9.7}$$

where L is the length of connected boundaries, ρ is the density of fluid, v is the microfluidic velocity, and μ is the viscosity of fluid.

Reynolds number defines inertia and viscosity of fluid motion. Low Reynolds number states that if the laminar flow is highly resisted in motion, it shows that high viscosity and low inertia exist. Laminar fluid flow in microchannel built a relationship between Reynolds number with inertia force, surface pressure, mass, force, and viscous force using the Navier-Stokes equation:

$$\frac{dv}{dt} = J - \frac{1}{\rho}\frac{\partial p}{\partial j} + \mu\nabla^2 v \tag{9.8}$$

Jiang et al. [42] developed the circular and noncircular microchannels, and expressed equations for steady laminar fluid flow. The Navier-Stokes equation developed for fluid through such types of microchannel is given as follows:

$$\Delta P = \lambda \frac{l}{d}\frac{\rho v^2}{2} \tag{9.9}$$

$$f = \frac{64}{\mathrm{Re}} \tag{9.10}$$

where Re is Reynolds number, v is the flow velocity, d is the diameter of the channel, l is the length of the channel, ΔP is the pressure difference, and P is the fluid density.

Laminar fluid flow in a microchannel requires a low Reynolds number, but the range or the value of Reynolds number has not been given. It calculated the change in pressure based on the diameter and the length of the channel. The researcher analyzed the laminar friction constant in a rectangular microchannel for a low Reynolds number (Re < 100). Papautsky et al. [43] studied fluid flow at microchannel dimension range with the width of 150–600 μm and the height of 22.71–26.35 μm, the friction constant increased with 20% approximate from the theoretical prediction of the Navier-Stokes equation. Wilding et al. researched on fluid dynamics of biological fluid and cell suspension in a straight glass microchannel. The researcher analyzed at least 1 ml of fluid flow through the channel to analyze the fluid characteristics. The author designed a straight microchannel with the size of 20–40 μm using photolithographic fabrication, which shows the characteristics of biological fluid flow. Wilding et al. [44] studied various aspects of fluid, such as distilled water, serum, RBC in saline, plasma, and WBC in saline. Wilding et al. [44] also discussed fluid characteristics for biological or healthcare application. Zhang et al. designed a stainless steel microchannel for exploring the law of heat and mass transfer and also discussed about reducing the size of the microchannel and increasing the surface roughness. Poiseuille's number and Nusselt's number of the fluid are used to investigate the surface roughness. Both numbers have a significant relation to Reynolds number [45]:

$$\mathrm{Po} = f_{\mathrm{re}} \tag{9.11}$$

where f_{re} is the frictional coefficient resistance.

The pressure drops of fluid in the microchannel sense through differential pressure, which ranges from 0 to 500 kPa. The research observed that a rough surface in 3D morphology by Scanning Electron Microscope (SEM) and an array of micropost-filled reactors produces high resistance to inflow of fluid. Pressure is dependent on the N number of microposts and the ratio of each post to the half-space between two neighboring posts. The comparison of various research studies on microchannel dimension, structure, and material used for microchannel formation is shown in Table 9.1.

9.4.1.1 Effect of Friction Coefficient in Fluid Flow and Pressure Measurement

The fundamental concept of friction factor in microchannel has been conducted by several researchers during the analysis of fluid pressure in microchannel. The deviation in fluid pressure is mainly due to the conjunction of inlet and outlet fluid pressure. To understand such types of problem at inlet and outlet, Sung et al. designed a microchannel with a manifold geometry structure for the uniform fluid distribution and it also determined accurate friction factor value theoretically and experimentally. Park and Punch [46] in their experimental research work determined the heat transfer coefficient and friction factor. The pressure drops in a microchannel caused by the friction are as follows:

$$C = \frac{\left(\frac{\Delta P}{L}\right) D_h}{2\rho V^2} \tag{9.12}$$

In the experimental study, Reynolds number decreased from 800 to 200 and the friction factor increased from 0.05 to 0.3. When Reynolds number is 200, the maximum fluidic pressure drops in a microchannel is 45.8 kPa. Several studies in various experimental and theoretical segments have been conducted to determine the validity of the friction factor, which is based entirely on drop fluid movement in a microchannel. Steinke et al. gave a concept for the conventional flow of single-phase liquid in a microchannel using Stoke's theorem and Poiseuille's flow. They introduced two categories of friction factor, namely, Darcy and Fanning factors. Both the friction factors determined experimentally and theoretically and the fanning friction factor defines the ratio of shear stress to flow energy per unit volume [47].The shape of the microchannel affects friction factor and pressure drop. Gunnasegaran et al. analyzed different shapes of microchannels, such as triangular, trapezoidal, and rectangular. The friction factor is directly related to the geometric ratio of the microchannel, as the geometric ratio of the microchannel increased, the friction factor also increased. The author analyzed fluid flow resistance in a microchannel and found that the friction factor continuously increased with increment of Poiseuille's number; the effect of this flow resistance is also increased. The fluid flow resistance develops heat in the microchannel, so that, it needs a coolant material or a change in geometry of the microchannel to reduce the

heating effect of the fluid [48]. Another experiment by Wang et al. showed the heat transfer rate in the rough surface of the microchannel and found that the heat rate is very high. To control the heat sink, cooling structure microfluidic technology has been widely used for enhancing thermal conductivity of the fluid. Researchers examined the ribbed microchannel and found that the presence of ribs increased the surface friction, in which the consequences increased the pressure loss. The ribbed microchannel represents various types of characteristics of fluid versus heat transfer rate. Wang et al. [49] compared the experimental data of a smooth channel friction factor that is 0.63– 6.67 times higher than a triangular ribbed microchannel.

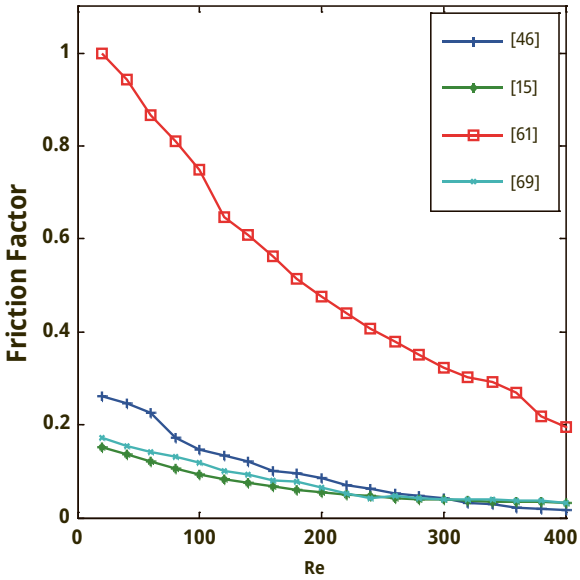

Figure 9.5: Relationship between friction factor and Reynolds number in microchannel.

- The friction factor value increases as Reynolds number decreases due to the low fluid rate and compact geometry of microchannel.
- Friction factor value is very low due to the low hydraulic diameter of the microchannel.
- Friction factor values become low due to the length-to-width ratio of the microchannel.
- Friction factor values get decreased due to the rough surface of the microchannel and pressure loss across the channel.

The ribbed microchannel was suitable for below 600 Reynolds number and Figure 9.5 shows the comparison of friction factor variation concerning Reynolds number in the microchannel. The friction factor value is very high with decreasing Reynolds number.

The friction factor high value represents low viscous fluid across the microchannel and the effect of fluid inside a microchannel. The relationship of pressure with Reynolds number was found, i.e., at a low Reynolds number, friction factor value was very high, and at a high Reynolds number, friction factor became low, so that, it was concluded that at a low friction factor, the amount of fluid pressure was decreased.

The researcher analyzed the effect of friction in microfluidic channel in the form of friction factor. This chapter reviews the pressure drop in microchannel with various amounts of friction factor. The pressure drop can be calculated using the Darcy-Weisbach equation, and this approach is directly dependent on flow in microchannel, shapes, and size of the channel. The Darcy-Weisbach equation for calculating the pressure drop ΔP in a microchannel is given by:

$$\Delta P = f.\frac{L}{D_h}\frac{\rho v^2}{2} \tag{9.13}$$

where ΔP is the pressure drop, f is the friction factor, L is the length of the microchannel, D_h is the hydraulic diameter of the microchannel, ρ is density of the fluid, and v is the average velocity of the fluid.

The hydraulic diameter is defined as follows:

$$D_h = \frac{4A}{P} \tag{9.14}$$

where A is the cross-section area of the channel and P is the wetted perimeter of channel.

The microfluidic application involved often rectangular microchannel, so that, eq. (9.14) becomes:

$$D_h = \frac{4(WH)}{W+H} \tag{9.15}$$

The friction factor is related to Reynolds number, as in the microchannel laminar fluid flow where required Re < 2,300. The researcher calculated the friction factor using Poiseuille's law for low Reynolds number as given by the following empirical formula:

$$f = \frac{24}{\mathrm{Re}}\left(1 - 1.3553\frac{H}{W} + 1.9467\left(\frac{H}{W}\right)^2 - 1.7012\left(\frac{H}{W}\right)^3 + 0.9564\left(\frac{H}{W}\right)^4 - 02537\left(\frac{H}{W}\right)^5\right) \tag{9.16}$$

While for the high AR (W≫H), eq. (9.16) is represented by:

$$f = \frac{24}{\mathrm{Re}} \tag{9.17}$$

Friction factor is directly related to Reynolds number value, if the minimum value of Reynolds number "1" is selected, then the friction factor value will be "24," whereas if the maximum value of Reynolds number "2,300" is selected, then the friction factor value will be "0.0104." The friction value provides the accurate measurement of microfluidic pressure inside the channel.

9.4.1.2 Pressure Measurement Variation in an Aspect Ratio of Microchannel

The AR is a height-to-width ratio for a rectangular microchannel. The AR is directly influenced by different types of shapes of a geometric ratio for the measurement of fluidic pressure. The numerical investigation was done for fluid water flow in various shapes of microchannel and analysis of pressure drop in microchannel with friction factor at different ranges of Reynolds number. Gunnasegaran et al. studied three types of microchannel shapes: rectangular, triangular, and trapezoidal. The AR effect in Poiseuille's number and friction factor for various shapes of microchannel. The researcher investigated the AR of the rectangular and triangular channels, and found that for rectangular microchannel, AR decreased with the increased fluid flow resistance continuously, while for trapezoidal microchannel, AR increased with the increased fluid flow resistance. The heat transfer characteristics or heat sinks of microchannel depend on the AR. Raghuraman et al.'s study investigates the thermal performance of the fluid in the microchannel at different values of AR. The study involves the pressure of the fluid, Poiseuille's number, friction factor, thermal resistance, and temperature at the outlet for various Reynolds numbers. Pressure drops in microchannel analysis at three ARs (i.e., 20, 30, and 46.66) and finds pressure drops, various characteristics with increasing mass flow rate, maximum pressure drop 9 kPa achieved at 819 mg/s for AR = 46.66 [50]. Duryodhan et al. provided a new approach for fluidic pressure drop measurement concerning AR. The researcher discussed the importance of diverging converging microchannels in microfluidic applications. In the experimental method, researchers determined the AR effect on a diverging and converging angle in a 3D-simulated microchannel and also analyzed the fluid characteristics of the diverging-converging angle. They found that pressure drop is independent of the variation of divergence angle at different ARs, but when the AR is larger and the angle is more than 10°, pressure drops deviate from its constant value. Similarly, the converging angle also did not affect the pressure of the fluid till the AR is less than 0.45 [51].

This chapter also included mathematical analysis of fluid pressure in microchannel and the calculation of pressure amount with relation between ARs. The microfluidic channel often involves the Hagen-Poiseuille equation for laminar flow in microchannels. For rectangular microchannels, the pressure drop ΔP can be expressed as a function of the AR, channel dimensions, and fluid properties. The AR is defined as the ratio of channel's width W to its height H (AR = W/H). The Hagen-Poiseuille equation

for laminar flow in microchannels, where pressure drop ΔP along the length of the microchannel L can be used the following equation:

$$\Delta P = \frac{12\mu QL}{WH^3\left(1 - \frac{192H}{H\pi^3 W}\tanh\left(\frac{\pi W}{2H}\right)\right)} \tag{9.18}$$

where ΔP is the pressure drop, μ is the dynamic viscosity of the fluid, Q is the volumetric flow rate, L is the length of the microchannel, W is the width of the microchannel, and H is the height of the microchannel.

The AR values of the effect on fluid pressure inside the microchannel, i.e., AR $\gg$1, it refers to the height H of the microchannel that is less significant compared to the width W of the microchannel. The microfluidic pressure drop can be calculated by:

$$\Delta P = \frac{12\mu QL}{WH^3} \tag{9.19}$$

The AR is given as follows:

$$\mathrm{AR} = \frac{W}{H} \tag{9.20}$$

Then, width of the microchannel can be expressed as follows:

$$W = \mathrm{AR}.H \tag{9.21}$$

Then, pressure drop can be expressed from eqs. (9.20) and (9.21), the simplified form of eq. (19) is given as follows:

$$\Delta P = \frac{12\mu QL}{\mathrm{AR}H^4} \tag{9.22}$$

The pressure drop for the high AR can be calculated when AR $\gg$1, while for the low AR ratio, the original HagenPoiseuille equation should be used. For the low AR, the height of the microchannel is greater than its width. The low AR is suitable for high hydraulic resistance and low flow rates in microfluidic applications. The low AR range, i.e., $0.1 < \mathrm{AR} < 1$, is suitable for chemical sensing or mixing application, and other healthcare applications. The moderate AR range, i.e., $1 < \mathrm{AR} < 5$, is suitable for microfluidic application, such as bioanalytical assays and cell culture. In the high AR, the height of the microchannel is lower than its width. The high AR is suitable for low hydraulic resistance and high flow rates in microfluidic network. The AR range, i.e., $5 < \mathrm{AR} < 20$, is suitable for lab-on-a-chip application and microfluidic cooling system.

9.4.1.3 Impact Analysis of Low Reynolds Number and Viscosity on Pressure of Fluid

The above-mentioned analysis is based on AR, friction factor, and Poiseuille's number to the measurement of pressure drop or change in pressure. As discussed earlier, Reynolds number is categorized into two parts: low Reynolds number and high Reynolds number. The microchannel size varies from micrometer to millimeter, and Reynolds number is used to identify the fluid flow pattern inside the microchannel, which has great importance for researchers. Zhang et al. designed a rectangular microchannel where Deionized Water (DI) and kerosene fluid flow inside the microchannel and measured the velocity or the distributed velocity inside the microchannel. The average velocity of fluid flow in a microchannel is 1 μm/s. The researchers developed a linear relationship between average velocity and pressure drop at low Reynolds numbers, which range from 10.5 to 10.2. The researcher also investigated the flow resistance values for the fluids, such as DI water and kerosene under Reynolds number, i.e., (10 to 5) < R < (10 to 2) [52]. Another method or experimental result obtained by Salah et al. helps to understand Reynolds number impact on fluid pressure in a microchannel. The author simulated the fluid dynamics properties of the microchannel while keeping the height constant. Salah et al.'s numerical investigation applies to the two-dimensional microchannel structure and the effect on fluid when channel height

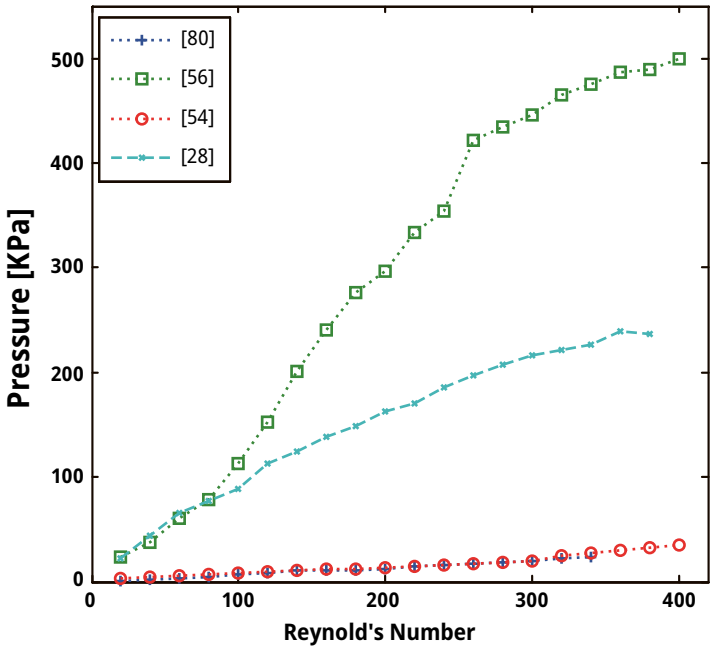

Figure 9.6: Graphical representation of microfluidic pressure at different low Reynolds numbers across microchannel.

varies from 50 to 4.58 μm and Reynolds number varies from 0.4 to 1,600, but found that there is no scaling effect for small height variation:

- Reynolds number value increases as the pressure value also increases due to high fluid rate.
- Pressure value increases due to the high fluid rate and low AR.
- Pressure drops increase due to the increase in mass flow rate of hot fluid.
- Pressure values decrease due to the length of the microchannel is very high.

The numerical investigation determined a pressure of 0.25–8 MPa with no effect on the viscosity of water. The hydraulic diameter decreases the effect on increasing fluid viscosity, but the shear stress-induced heating increases the temperature of fluid that reduces the liquid viscosity. Fluid mechanics was sufficient to explain the theory of liquid flow in microchannel and flow resistance. There is a very high significant effect seen through electrokinetic phenomena at the microscale. There is a new terminology for microfluids, i.e., electroviscous phenomena, electroviscous effect depending on electric streaming current and electric streaming potential. The direction of the pressure driven was the opposite of electric streaming potential. The streamlined current reduced the pressure inflow and produced high flow resistance. The fluid mechanics theory explains if the inflow of fluid is with high resistance, then the viscosity of fluid is also high [53]. Fluid mechanics theory by Ren et al. with its experimental explanation found that laminar flow for the same Reynolds number, high flow resistance, and high viscosity depend on the ion's concentration and height of the channel. Figure 9.6 shows the behavior of fluid pressure concerning Reynolds number, and found that as Reynolds number increases, the fluidic pressure value also increases. The experimentally determined $dp = dx$, "Re" relationships were compared with the predictions of a theoretical electroviscous flow model, and a good agreement was found for pure water, 10^{-4} M KCL & 10^{-4} M $AlCl_3$ (M is represent in molarity) [54].

9.4.1.4 Effect of Poiseuille's Number on Pressure Measurement in a Microchannel

Poiseuille's number is determined by the researcher with several experiments and gives various classical theories for square and rectangular microchannels. The main focus of stability is the Poiseuille number because inside the microchannel, friction factor is high due to this effect and the Poiseuille number became unstable. John et al. researched on stability of Poiseuille's number in microchannels. For this purpose, they designed microchannels using silicon, polymethylmethacrylate (PMMA), stainless steel, and copper, where laminar fluid flows across four square microchannels.

Each channel had a different length and the pressure drop across each channel was different. Reynolds number was kept fixed for fluid flow; the author found that Poiseuille's number has a maximum deviation of 9.46 from its actual value calculated for the largest channel. Figure 9.7 shows that the Poiseuille number with lower value

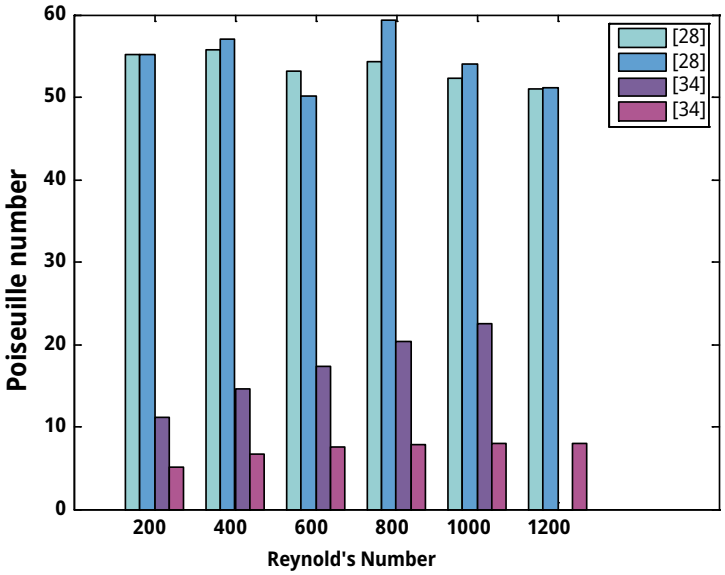

Figure 9.7: Graphical representation of the Poiseuille number variation with Reynold's numberacross microchannels.

observed the result analysis with lower pressure drop, as Reynolds number with lower value attained high temperature with lower viscosity of the fluid [55].

In microfluidics, the Poiseuille number (Po) is a dimensionless number used to describe the pressure drop in a channel due to viscous forces. It is particularly useful when dealing with pressure-driven flow in microchannels. The Poiseuille number is related to the friction factor and Reynold's number. The Poiseuille number (Po) is defined for different channel geometries. For a rectangular channel, it is given by:

$$\mathrm{Po} = \frac{f\mathrm{Re}}{2} \tag{9.23}$$

The HagenPoiseuille equation describes the pressure drop (ΔP) in a microchannel for the laminar flow:

$$\Delta P = \frac{\mathrm{Po}\mu QL}{D_h^2} \tag{9.24}$$

The microfluidic pressure amount for high ARs (i.e., AR≫1) and wide channel, the Poiseuille number approaches a minimum value. If AR ≈ 10, Po is approximately 56.91. For low ARs (i.e., AR ≈ 0.1) and narrow channel, the Poiseuille number can be as high as approximately 96.

Table 9.1: Comparison of analytical pressure-sensing mechanisms and its parameters.

Microchannel dimension (μm)	Hydraulic diameter (μm) (Dh)	Microchannel shape	Fluid velocity	Fluid pressure (Pa)	Re	Fluid	Techniques involved for pressure measurement	References
2,500 × 60 × 25.4	8–42	Circular Trapezoidal Triangular	0.1–0.9 μL/s	30–85 kPa	–	DI Water	Measurement of pressure at different shapes of microchannel	[42]
W: 65–315 *H* : 4,500	106–307	Rectangular	50–200 mLl/min	30 kPa	200–1,500	DI Water	Pressure measurement at different hydraulic diameter range It also identifies heat transfer in channel	[46]
W [R]: 180–380 *W* [T]: 460–390 *W* [T_a]: 460–390 *L*: 10k *H*: 460–360	D_h 259–385 D_h 148–238 D_h 229–370	Rectangular Trapezoidal Triangular	–	200–5,500	100–1,000	Water	Numerical investigation of pressure drop, Poiseuille's number, and friction factor effect through the variation in aspect ratio	[48]
L: 45 mm	279 and 45 mm	Circular	–	–	304–2,997	DI Water	Pressure drops and flow rates are measure in microchannel, various types of Reynolds effect on fluid flow and pressure	[56]
W: 150 *L*: 31k *H* : 7k	387 & 327	Rectangular	100–1,000 mg/s	1,000–10,000	50–350	Water	CFD analysis for friction factor and pressure drop calculation at different height-to-width ratios in microchannel	[50]
W: 100 – 2,552 *H*: 50–450	–	Noncircular microchannel	4.53–6.70 ml/min	204–649	130–280	Water	Pressure drop measurement diverging and converging 2°–14° with aspect ratio 0.05–0.58	[51]

(continued)

Table 9.1 (continued)

Microchannel dimension (μm)	Hydraulic diameter (μm) (Dh)	Microchannel shape	Fluid velocity	Fluid pressure (Pa)	Re	Fluid	Techniques involved for pressure measurement	References
W: 2–11	5 – 17.4	Rectangular	0.001–1 mm/s	Wa – 0–120 Kr –0 = 110	0.1–10	DI Water Kerosene	Fabricated the microchannel at different widths and analysis of two fluids	[57]
H: 4 – 50	15	Rectangular	0–1 m/s	0.25–8 Mpa	0.4–1,600	DI Water	Numerical investigation of low Reynolds number with wide range of microchannel height	[53]
W : 300–500	200–500	Circular	50–7,500 ml/h	–	20–120	DI Water ethylene glycol	Pressure drop analysis on the variation of Poiseuille's number	[54]

9.4.2 Physics Applied for Pressure-Sensing Mechanism

9.4.2.1 Pressure-Sensing Deformation of PDMS

Measurement of fluidic pressure in a microchannel through PDMS deformation method is applied. PDMS structure is highly flexible and yields fluid flow in a microchannel with a flow rate of 15–1,550 μl/min in the laminar region. A microchannel shape becomes shallow at high pressure and it is challenged by researchers that reduce large deformation at high pressure with high stiffness of PDMS[58]. Soft lithography microfabrication made of PDMS is used to design lab-on-a-chip devices, which is the most demanding and flexible material, and also it is low cost, easily available, biocompatible, and has transparent features. Kim et al. give experimental results on the PDMS fabrication method that improved the PDMS material properties without including a foreign material. To enhance the PDMS properties, the mixer ratio (5:1) of the PDMS curing agent has been increased. The deformation of PDMS resistance increased by 860%, this mixer ratio provides good hindrance properties compared to the 10:1 mixer ratio of PDMS. The research study gives a method to increase the stiffness of PDMS material and modifies the ratio of mixing with thermal treatment of PDMS. The curing agent could improve the stiffness by up to 50%, it provides better channel deformation under fluidic pressure [59]. Another method to detect cell deformation measures the pressure inside a microchannel, but if the result is contaminated, then a syringe pump of fixed flow rate is used that controls the fluid flow on volume per unit of time. However, the pump is also not able to control the accurate flow of fluid inside the microchannel. Thus, microfluidic device application is required to control the fluid pressure inside the microchannel or to improve the sensing mechanism more accurately [60]. Such types of problems are removed by designing on-chip pressure sensors to measure the direct pressure inside a microchannel. The author designed a sensing chamber that is connected to a microchannel and PDMS material is used for sensing the pressure of fluid inside a microchannel. The deformation of PDMS compares the result of pressure with its experimental and theoretical studies. Positive pressure or negative pressure is applied on the microchannel, PDMS chamber is deformed into a convex shape or deforms back into a concave shape. A sensing layer senses the pressure of the fluid through various colors and fluid intensity. PDMS microchannel included a sensing chamber which is filled with colored fluid. The colored fluid flows inside and outside of the sensing chamber, which helps to analyze the chamber pressure of the fluid at different intensities. The colored fluid shows various pressure levels of the deformed sensing chamber and the pressure applied between 50 and 100 kPa in sensing chambers, which shows 0.024 and 0.048 displacements, respectively. Figure 9.8 shows the PDMS microfluidic pressure-sensing mechanism, which is an integrated-on chip of microchannel, which specifies the mechanism of fluid from inlet to outlet. Another method targeted the fluid flow property in a microchannel, researchers focused on low fluid flow rate and compared the

steady-state flow rate to quasi-stable flow rate. The PDMS microchannel swelling is detected when fluid is in contact with obstacles. The author studies quasi-steady flow and steady-state flow under low flow rates. The fluid flow at different microfluidic channels, i.e., 15 and 100 μm, compares its theoretical study model. The researcher analyzed the different obstacles placed in microchannels and found the relation between fluid flows with pressure for different microchannels [61]. The rectangular channel required a low AR that produced bulging in the channel under pressure. Figure 9.8 shows the schematic structure of the fluid pressure-sensing mechanism for the integrated PDMS microcantilever. Figure 9.9 shows a fabricated microchannel of the fluid particle flow in the images and the deformation of the PDMS microchannel. Figure 9.9(a) shows the particle imaging velocimetry (PIV) image of particle flow in the microchannel [62]. Figure 9.10 shows the graph between fluid pressure and flow rate in the channel. The graphs also represent the pressure level at different conditions and amount, but clearly define the pressure amount increases as the flow rate amount increases. Table 9.1 shows the comparative study of various researcher-designed PDMS-based microfluidic pressure sensors. Table 9.2 shows the comparison of the observer effect and dimension utilized for design microfluidic pressure sensor.

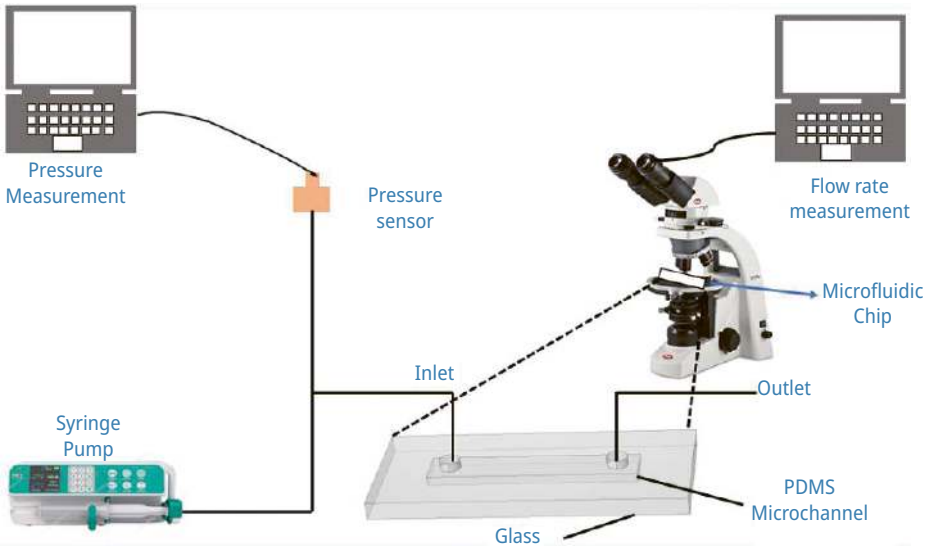

Figure 9.8: Microfluidic pressure-sensing mechanism process with PDMS cantilever deformation with microfluidic chip to monitor the fluid pressure inside the microchannel.

The above review of the research paper on the PDMS microfluidic pressure-sensing mechanism has found some challenges in design and fabrication. The review also found the gap and future work required in PDMS-based microfluidic pressure-sensing mechanisms. The challenges in the PDMS pressure-sensing mechanism are shown

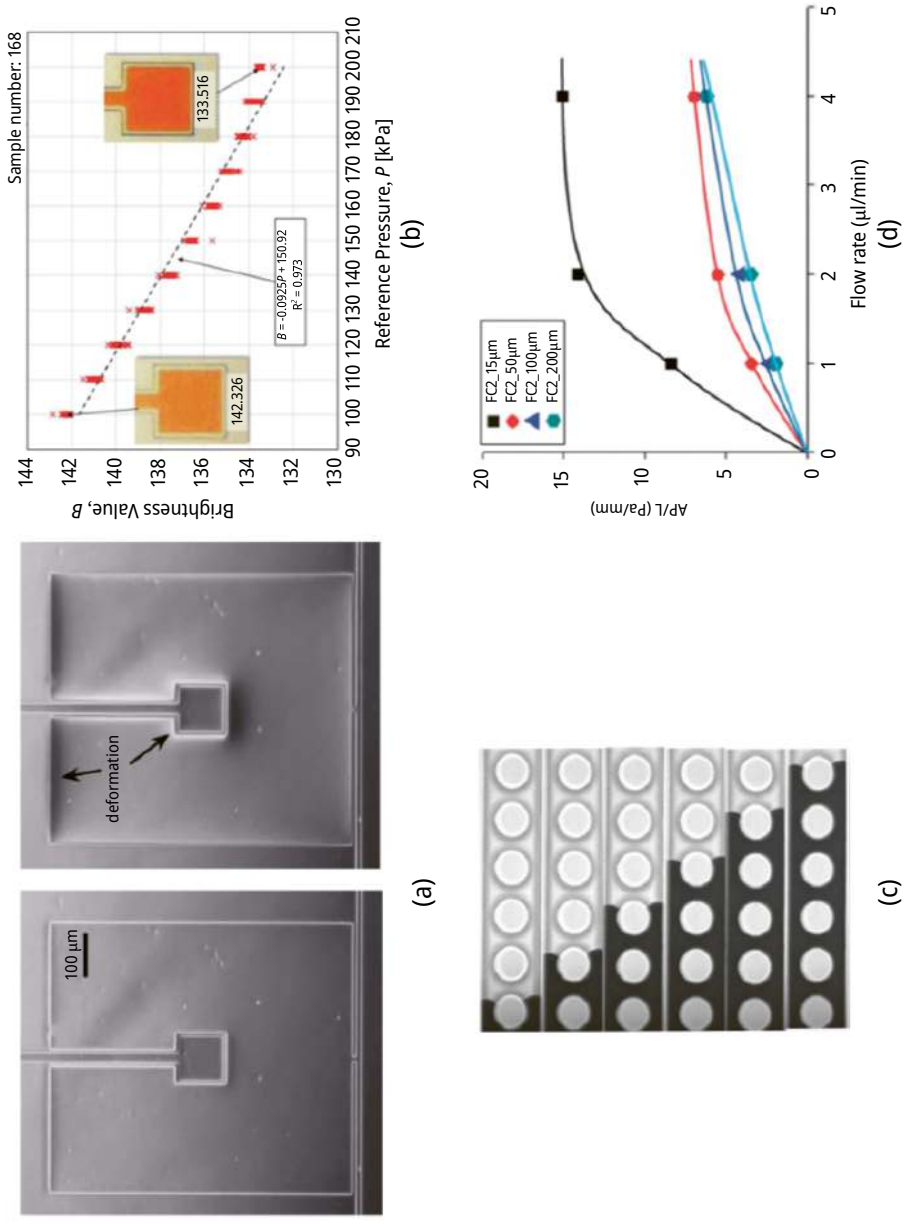

Figure 9.9: Fabricated PDMS microchannel for measurement of fluid pressure (a) Undeformed PDMS and deformed PDMS [61]. (b) The graph of brightness with reference pressure. (c) Obstacles present in microchannel and effect on fluid flow is recorded [60]. (d) The graph shows different heights of channel with pressure-level analysis.

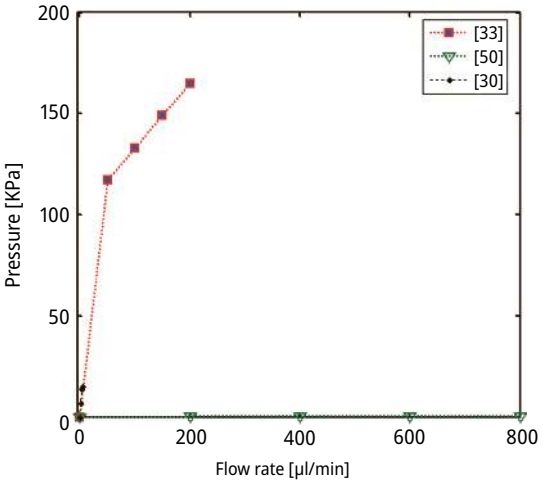

Figure 9.10: Graphical presentation of the performance of fluidic pressure effect with flow rate of fluid in microchannel.

in Table 9.2, and advancement or future work for better device-making is shown in Table 9.3.

Table 9.2: Comparison of PDMS pressure-sensing mechanisms and its parameters.

Pressure-sensing technique	Mechanism	Dimensions	Materials	Optimized parameters	References
PDMS-based pressure sensing	Deformation of channel and sense the pressure through the bright of color fluid	Deformation chamber (W − 700 µm; H − 3.5 µm; L − 600 µm)	PDMS DI water Red-colored fluid	Pressure design electrical free Phase contrast used to see deformation of PDMS channel Pressure increases brightness of color fluid decreases Measure pressure at 3.05 kPa	[60]
	Deformation of channel analysis and the pressure on thermally aged at 200 C for some days	W − 400 µm, H − 40 µm, L − 50 µm	Su-8 negative photoresist acetone and propanol for cleaning Si wafer PDMS channel (10:1 or 5:1)	Channel deformation is very small, changes at lowest flow rate when compared to highest flow rate, 200 µL/min and achieved 167 kPa at the highest flow rate	[59]

Table 9.2 (continued)

Pressure-sensing technique	Mechanism	Dimensions	Materials	Optimized parameters	References
	Channel deformation identified through fluorescence intensity variation	*W* – 243 µm, *H* – 1.5–200 µm, *L* – 9.14–10. 1 µm	Water-based food dye, liquid solution is used PDMS for microchannel	Analysis of friction factor and Reynolds number effect on microchannel height Analysis of PDMS bulging High height is achieved by lower bulging effect	[61]
	PDMS bulging compared numerically predicated values with the experimentally predicated value	Microchannel (*H* – 15 and 100 µm, *W* – 243 µm)	PDMS Liquid food dye	PDMS bulging measured at various fluid velocities PDMS bulging observed at different fluid pressures PDMS bulging observed at different heights of microchannel	[63]
	Fabricated PDMS microfluidic phantoms for Newtonian fluid	Microchannel (*L* – 30 mm, *W* – 15 mm, *H* – 5 mm) Diameter – 510 µm	Blood PDMS	Observed the deformation of microchannel for non-Newtonian fluid Effect of fluid flow rate on fluid pressure in microchannel Pressure measured up to 700 Pa	[64]

Pressure sensing using the deformation of PDMS in microfluidics relies on material's mechanical properties. When pressure is applied to a PDMS structure, it deforms, and this deformation can be measured and related back to the applied pressure. When a pressure P is applied to a PDMS membrane or microchannel, the resulting deformation (strain) can be measured. The relationship between the applied pressure and the deformation can be derived using the material properties of PDMS, such as its Young's modulus E. For a thin PDMS membrane under uniform pressure, the deformation can be approximated using linear elasticity theory. The equation that relates the applied pressure P to the deflection δ at the center of a circular membrane of radius a and thickness h is given by:

$$P = \frac{3E\delta h^3}{4a^4} \tag{9.25}$$

For a rectangular PDMS microchannel with length L, width W, and thickness h, the relationship can be more complex and may require numerical methods or empirical correlations. However, for small deflections, the pressure-deflection relationship can be approximated by:

$$P = \frac{E\delta h^3}{\propto L^4} \tag{9.26}$$

9.4.2.2 Optical Pressure-Sensing Method

Surface pressure measurement is an important method in microfluidics; traditional surface pressure measurement requires an instrument with several taps of pressure drilled into the model, as the model is a high time-consuming process. It was very difficult to drill at thin edges and sharp corners where the pressure is calculated, so to reduce the bulkiness and cost of the model. PSP coating is used in the model; PSP is an optical method to measure the surface pressure without including any instrument. Now surface is coated with paint fluorescent or luminophores molecules that emit a light of longer wavelength than excitation wavelength due to the internal transition before excitation. Some luminophores were in addition to normal deactivation through thermal collision also deactivated through collision with oxygen molecules. As relative contents of oxygen are constant in the air, the oxygen-quenching effect indicates the air pressure above the surface. Hence, the lower the pressure, the less emitted light, and the researcher found that the pressure is proportional to the inverse of emitted light intensity. The first experimental method was developed as a pressure sensor with PSP coating in 1980 [65]. PSP technique measures continuous pressure measurement on the global surface and this method is nonintrusiveness, which means that there are no probes required, and provides qualitative and quantitative pressure profiles [66]. Since luminance decreased continuously by increasing pressure or increased by decreasing pressure. The intensity of light depends on the pressure profile [67]. Thus, the PSP method measures the pressure of fluid interaction of molecules or atoms inside a microchannel. The molecules emit light, and the photodetector collects light and transfers it to image-processing equipment. A PSP is also known as a molecular sensor or temperature-sensitive paint. It can be used to measure temperature or pressure inside the microchannel. A researcher measures fluidic pressure inside a microchannel and found a relationship between molecule behavior and Knudsen number with an explanatory Monte-Carlo simulation method. They found that the pressure on the curvature surface of the microchannel and entrance of the microchannel is a very impactful study for healthcare devices. The result found that the Knudsen number value increases, the pressure drop at curvature of microchannel

decreases due to the rarefaction effect. They also found that the entrance length of the microchannel should be 60% of the hydraulic diameter of the microchannel and Reynolds number is 0.007. Figure 9.12(a) shows two types of microchannel fabricated coating. Channel "A" of PSP layer is coated with PdTFPP while channel "B" is coated with PtTFPP. The two different types of coating distribute the pressure in the microchannel differently along the length of the channel [68].Another method to measure local pressure in microchannel is the deformable diffraction grating. In this experiment, the pressure measurement is done by the change of optical behavior of grating. For the analysis of the optical behavior of grating, PDMS material is used, which is a transparent elastomer, to measure the pressure of fluid change in the intensity of diffracted beams. The local pressure is measured in two methods: the first method observed chromatic variation of the grating using white light for illumination and another method measured the intensity of the diffracted beam using monochromatic light. In both the experiments, pressure range examined 0–80 kPa at a flow rate of air with a range of 0–0.3 cc/min (Hosokawa & Maeda, n.d.) [69]. Matsuda et al. came up with an experiment to analyze the thermos fluid phenomena for microfluidic devices by design and fabrication of pressure-sensitive molecule film (PSMF). Figure 9.11 shows the experimental setup for the optical microfluidic pressure-sensing microchannel and sensor. The optical microfluidic pressure-sensing mechanism process is used by various researchers and they analyze the fluid pressure experimentally through simulation. Figure 9.10 shows the optical fluidic process where the pressure of the fluid is analyzed through the intensity of luminous particles and a relation between intensity and fluidic pressure. The result found that as the intensity of particles increases, the pressure value also increases. The working of PSMF and PSP is almost similar, but PSP is too thick for microfluidic devices and does not have sufficient spatial resolution for the measurement of pressure. In this

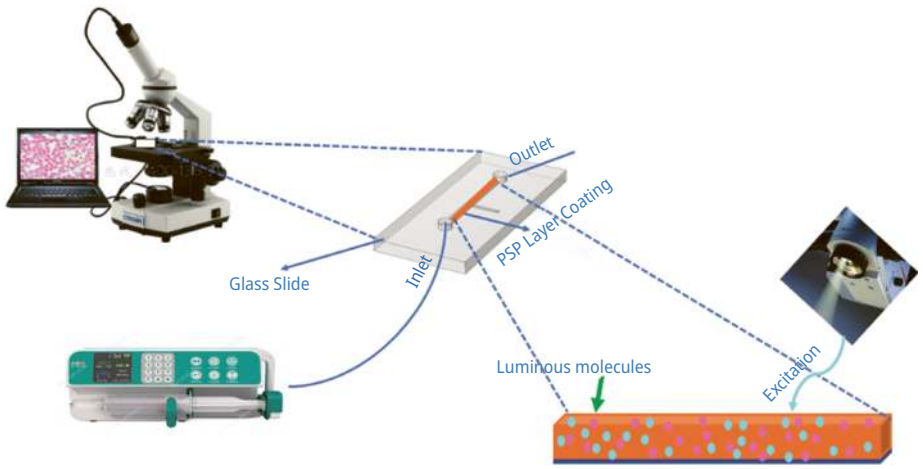

Figure 9.11: Optical microfluidic pressure-sensing mechanism across microchannels with light source targets a microchannel, excitation particle collision with surface particles.

study, an author designed a molecular thin film sensor (PSMF), which is composed of Pd (II) octaethylporphyrin (PdOEP) and Pd (II) mesoporphyrin IX (PdMP).

To fabricate this, composition adopted the LangmuirBlodgett (LB) method for the development of highly sensitive PSMF. In the experiment, the pressure sensitivity of two layers is higher than six and 20 layers PSMF, due to oxygen molecules quenching at the outermost layer only. They also introduced arachidic acid (AA) , which is an organic solvent that controls the intermolecular spacing of luminescent molecule. Figure 9.12(a) fabricates optical pressures sensing microfluidic device for two microchannels, A and B. Microchannels A and B with PSP sensors are coated with PdTFPP and PtTFPP materials, respectively [68]. Figure 9.12(b) shows the graph of pressure along the length of microchannel for PdTFPP and PtTFPP coating. Figure 9.12(c) shows the on-chip integration sensor design where pressure sensing is achieved by a luminescent sensor layer inside of an air-filled cavity. Figure 9.12(d) shows the effect of luminous intensity concerning pressure analysis. The pressure measurement ranges from millibar to several bars, and also trapped the temperature of liquid and oxygen molecule contents of the fluid. Figure 9.12 (e) shows an AFM image of PSMF and PDMS to optimize the roughness of the surface [71]. The range of pressure measurement in Pascal, if measuring the pressure of pores in a microchannel, then PSP is not able to detect pressure because the pores exist in kPa–MPa [72]. The fluid pressure behavior in a microchannel with flow rate is represented by a graph in Figure 9.13. Table 9.3 shows the comparative analysis of various researches in optical microfluidic pressure-sensing mechanisms.

The above review of a research paper on the optical microfluidic pressure-sensing mechanism has found some challenges for design and fabrication. The review also found the gap and future work required in optical-based microfluidic pressure-sensing mechanisms. Optical-based microfluidic pressure sensing typically involves measuring the deflection or deformation of a microfluidic structure, such as a PDMS membrane, when subjected to pressure. The deflection can be monitored using various optical methods, such as interferometry, optical microscopy, or laser displacement sensors. Here is a general approach using an optical measurement of the deflection to calculate the pressure. For a circular membrane under uniform pressure, the relationship between the applied pressure P and the central deflection δ is given by:

$$P = \frac{3E\delta h^3}{4a^4} \tag{9.27}$$

For a rectangular membrane, the relationship can be more complex and often requires numerical solutions or empirical formulas. For small deflections, an approximation can be:

$$P = \frac{E\delta h^3}{\propto L^4} \tag{9.28}$$

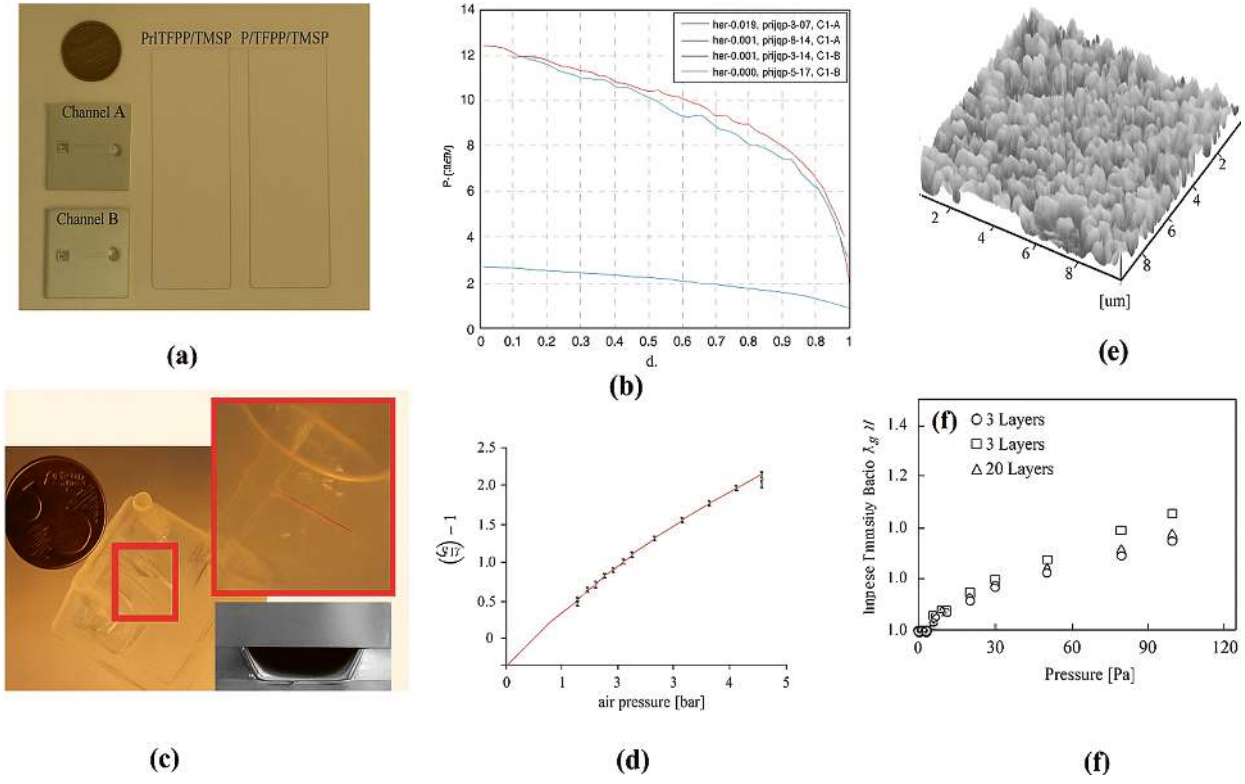

Figure 9.12: Fabricate optical pressure-sensing microfluidic device. (a) Microchannels A and B with PSP sensors PdTFPP and PtTFPP coated on glass slides [68]. (b) The graph of pressure along the length of microchannel for PdTFPP and PtTFPP coatings. (c) Photograph of a pressure sensor chip in relation to 5-cent coin with enlarged detail view of the sealed side channel with integrated sensor layer, and SEM picture of a channel cross section [70]. (d) The graph between optical luminous intensity and pressure. (e) AFM image of the substrate rough PSMF [71]. (f) The graph for 12, 6, and 20 layers of coating to provide smoothness of surface and analysis of the pressure level.

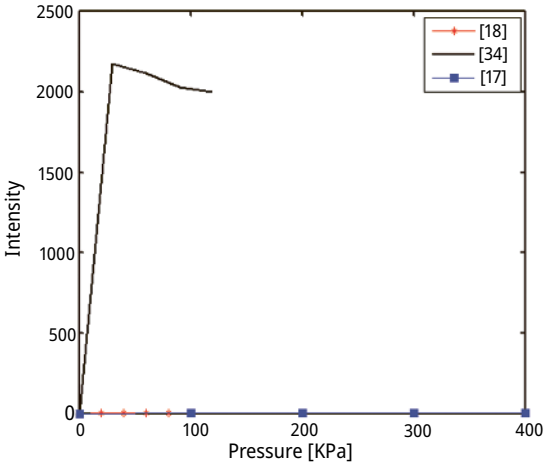

Figure 9.13: Graph between fluid pressure and particle intensity in channel.

Table 9.3: Comparison of optical pressure-sensing mechanisms and its parameters.

Pressure-sensing technique	Mechanism	Dimensions	Materials	Optimized parameters	References
Optical-based pressure sensing	Fluidic pressure sense inside the microfluidic channel through oxygen-sensitive luminescent sensor layer	*W* – 170 µm *H* – 27 µm	Polystyrene, HF, NAOH, toluene-3, sodium silicate, PDMS	Optical on-chip pressure sensor Calculate flow rate at 1–3 µl/min and pressure at 9 mbar	[70]
	Pressure identifies through deformation diffraction grating	*W* – 200 µm and *D* –20 µm Rectangular grooves 5 µm wide and 2 µm deep	PDMS chip and glass plate used for microfluidic channel Su-8 negative photoresist fluorocarbon layer polymerized	Pressure, 0–80 kPa Flow rate, 0–3.3 cc/min Deformation behavior of PDMS diffraction grating analysis	[69]
	Pressure measurement through the PSP method inside the microchannel	Microchannel (*L* – 19 mm, *W* – 235 µm)	PSP PtTFPP/1-trimethysilypropyne (TMSP) Pt(II)meso-tetra (pentafluorophenyl) porphine (PtTFPP)	Pressure measure inside of microchannel and outside of microchannel. Relation between pressure and Knudsen number Pressure measured maximum 12 psi	[63]

9.4.2.3 Resistance-Based Pressure Sensing

The researcher examined several types of simulation and experiments for the measurement of microfluidic pressure, sometimes a sensor was integrated into the microfluidic system but the problem is found during the fabrication of unreliable interfacing; assembly of components is difficult and complex. The author found a new way or approach, i.e., piezoresistive sensor designed to monitor microlevel strain, which is integrated into a microfluidic system using a soft lithography process. Figure 9.14 shows the schematic structure of resistance-based fluid pressure-sensing mechanism for the detection of fluid pressure and its properties. Zhou et al designed a piezoresistive pressure sensor that is flexible and stretchable, which converts mechanical displacement into electrical displacement or signal, and such type of pressure sensor is known as a liquid-based metal pressure sensor.

This thin film-based flexible piezoresistive pressure sensor detects displacement due to high strain and stretching of the film. The author has found that wrinkles on a thin metal film show a minimum change in resistance or as strain increases continuously, resistance also increases in nonlinear trends. Pressure increased the deformed membrane of the piezoresistive sensor due to the change in the resistance. They concluded the linear relationship of the sensor and pressure at the flow rate of fluid at 6–200 μl/min [11]. Another method is designed for a highly stable metal liquid with piezoresistive pressure sensor for the measurement of microfluidic pressure. A liquid thin film sensor is designed using Galinstan material for the detection of DI water fluid pressure. Thin film sensor also measures the viscosity for Newtonian and non-Newtonian fluids, Galinstan material sensitivity was higher than other piezoresistive materials [73].The principle of this experiment is the Wheatstone bridge, where an unknown resistance value of Galinstan material is calculated in terms of voltage when fluid pressure is applied on the Galinstan element. Pressure in a microchannel was sensed by Galinstan liquid metal film up to 12 kPa. The linearity of pressure decreased with the increase in fluidic pressure.

The researchers investigated metal thin film resistors used in the form of Wheatstone bridge with one-resistance Galinstan material. This unknown resistance value was determined and pressure showed a relation with it. Another experimental investigation was done by Inoue et al. for the measurement of microfluidic pressure inside the channel. They designed an inline micropressure sensor that measures the inside pressure in a microfluidic tube. The surface of the microfluidic tube is integrated with the graphene sheet and pressure inside the microfluidic tube expands it, which affects deformed graphene.

The deformation was measured in terms of the electrical resistance of graphene, resistance is directly proportional to strain; graphene strain measures the pressure inside a microchannel, and 85 kPa pressure is measured with a change in resistance of 3.8 Ohms. The electrical resistance behavior on the cross-section area of the membrane shows that as the pressure increased in microchannel, the Wheatstone bridge becomes unbalanced and the unbalanced behavior measured through an electric

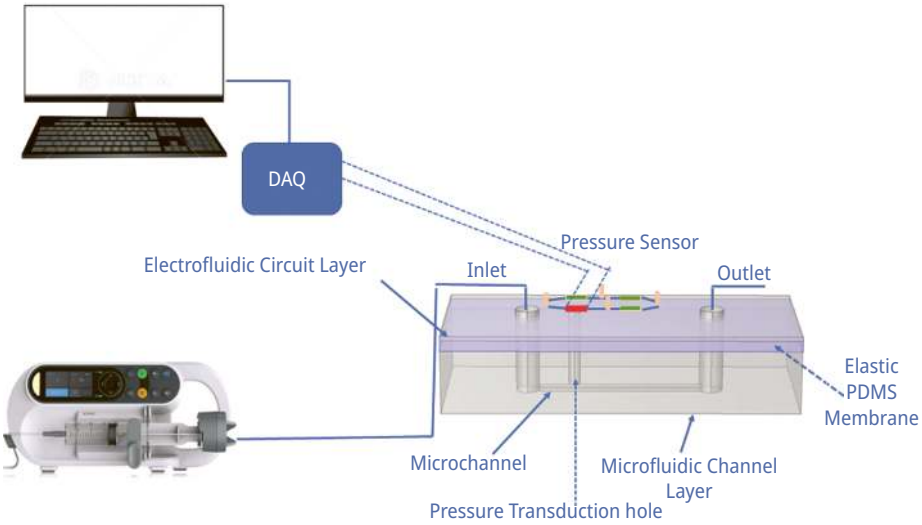

Figure 9.14: Microfluidic pressure sensor with bridge structure for the analysis of pressure through Wheatstone bridge method.

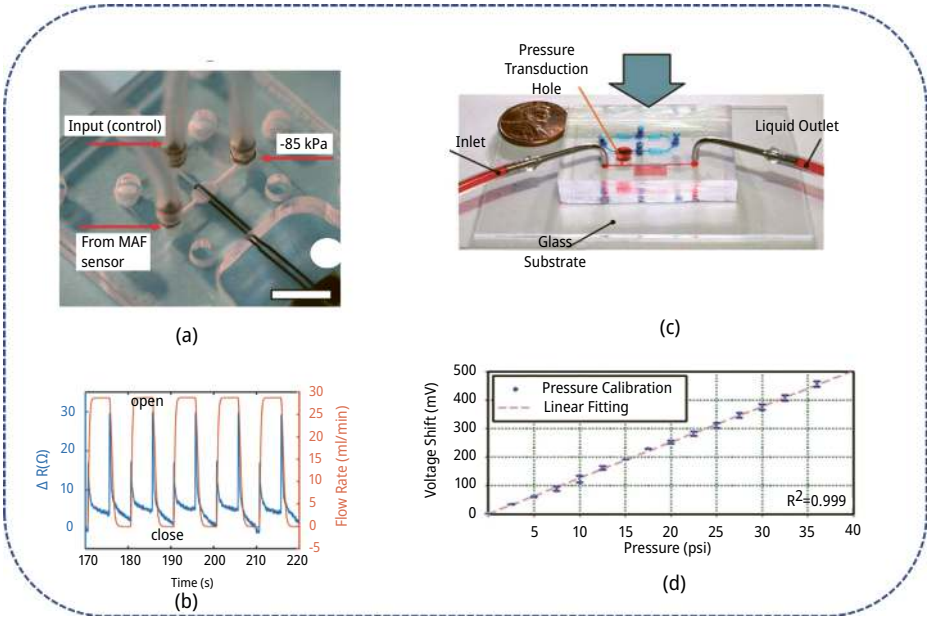

Figure 9.15: Fabricated resistance-based pressure-sensing microfluidic device. (a) Sensor integrated into an elastomeric membrane valve to control the reagent flow. (b) The graph between flow rate and resistance to analyze the pressure by valve open and closed [11]. (c) Model microfluidic pressure sensor with bridge structure, a device filled with blue dyes. (d) Pressure calibration with respect to voltage at terminal of bridge [73].

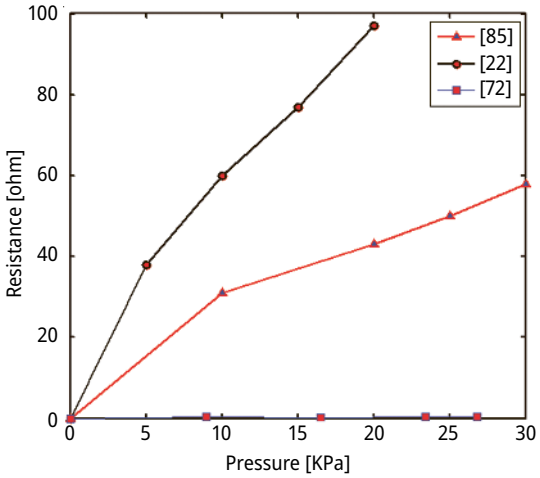

Figure 9.16: Relationship between fluidic pressure in microchannel analysis through the resistance and developed a relationship between resistance and pressure.

Table 9.4: Comparison of resistance-based pressure-sensing mechanisms and its parameters.

Pressure-sensing technique	Mechanism	Dimensions	Materials	Optimized parameters	References
Resistance-based pressure sensing	Thin film paper-based pressure sensor design liquid metal-based sensor form Wheatstone bridge	Channel width – 20 µm and height – 100 µm PDMS membrane, 15 µm thickness	Su-8 – negative photoresist PDMS 10:1 Galinstan liquid metal-based resistor	Calibration of pressure ranges from 0 to 230 kPa. Calculation of shear rate for fluid samples Viscosity for Newtonian and non-Newtonian fluids	[73]
	Piezoresistive sensor integrate to measure pressure, sensitivity by soft lithography	W – 50 µm H – 150 µm L – 241.7 mm	PDMS substrate Polystyrene sheet Polymer layer Metal layer	Reynolds number < 40, electrical resistance increases due to deformation. Fluid flow rate, 1–200 µl/min	[74]

Table 9.4 (continued)

Pressure-sensing technique	Mechanism	Dimensions	Materials	Optimized parameters	References
	Diaphragm cavity used as pressure sensor through lithography process	Pressure-sensing diaphragm layer 7– 50 μm thick active cavity	SU-8 PMMA Pyrex glass	Linear variation pressure vs. resistance Reynolds number becomes high inside the channel, which gives high pressure	[75]
	Pressure sensor design with electrofluidic circuit filled with ionic liquid in microchannel. Wheatstone-based mechanism used to measure pressure for nitrogen gas and various filled Gases	Dimensions are not specified	PDMS Ionic liquid Nitrogen gas	Thermal stability Linear characteristic of pressure in microchannel. Pressure measure, 0.1–4 psi at 0–100 μl/min	[76]
	Inline pressure sensor designed with integrated microfluidic tube and graphene sheet. Pressure of fluid is monitored in channel with change in graphene sheet resistance	PDMS tube diameter (inner − 3 mm, outer − 4 mm)	PDMS Graphene Polypropylene tube Parylene C film Copper foil	Pressure measure, 0–18 kPa with change in resistance	[77]

meter or voltmeter [77]. Figure 9.14 shows the fabricated resistance-based sensor with electrical characteristics and measures pressure concerning the resistance. Figure 9.15(a) shows a different application of resistance-based mechanism, such as an integrated piezoresistive sensor to measure fluid flow pressure through a valve switch with on and off options. Figure 9.15(b) shows whether the valve opens or closes at increased baseline resistance. Figure 9.15(c) shows the Wheatstone bridge structure and the pressure filled with blue inks. The fluid pressure concerning the terminal voltage of the Wheatstone bridge is shown in Figure 9.15(d). Figure 9.16 shows the fluid behavior analysis studied by various researchers and developed a relationship between resistance and pressure. The graphs show as the amount of resistance increases, pressure value also increases. Table 9.4 shows the comparative analysis of various researches

in resistance microfluidic pressure-sensing mechanisms. In the above review of the research paper, the resistance-based microfluidic pressure-sensing mechanism has found some challenges for design and fabrication. The review also found the gap and future work required in resistance-based microfluidic pressure-sensing mechanisms.

Resistance-based microfluidic pressure sensing often involves using the fluidic resistance of the microchannel to determine the pressure drop. The relationship between pressure drops, flow rate, and fluidic resistance is given by Ohm's law for fluid flow, which is similar to electrical circuits. For the laminar flow in a microchannel, the pressure drop (ΔP) can be related to the flow rate (Q) and the fluidic resistance (R):

$$\Delta P = Q.R \tag{9.28}$$

The fluidic resistance depends on the geometry of the microchannel and the viscosity of the fluid. For different channel geometries, the resistance can be calculated, such as for a circular microchannel with radius r and length L:

$$R = \frac{8\mu L}{\pi r^4} \tag{9.29}$$

Similarly for a rectangular microchannel with width W, height H, and length L:

$$R = \frac{12\mu L}{WH^3\left(1 - \frac{192H}{H\pi^3 W}\tanh\left(\frac{\pi W}{2H}\right)\right.} \tag{9.30}$$

For high AR, the resistance is given by:

$$R \approx \frac{12\mu L}{WH^3} \tag{9.31}$$

The pressure drop in microchannel in resistance-based method can be calculated in this way.

9.4.2.4 Capacitive Pressure Sensing

A capacitive pressure sensor is an approach that follows the principle of an electric sensor. The capacitive pressure sensor extensively demands in application of biological sensors, microfluidic sensors, flexible sensors, and chemical sensing. Yoon et al. designed a microfluidic capacitive sensor with liquid metal electrodes and CNT/PDMS to sense the pressure and temperature. The study aims to detect human motion and such types of sensors implemented on wearable electronics, artificial skins, and soft electronics. In this study, the author detects changes in pressure, temperature variation, and lateral movement. The CNT/PDMS composite serves as a dielectric layer, while the ionic liquid is used for pressure sensing. The CPC layer lies between two

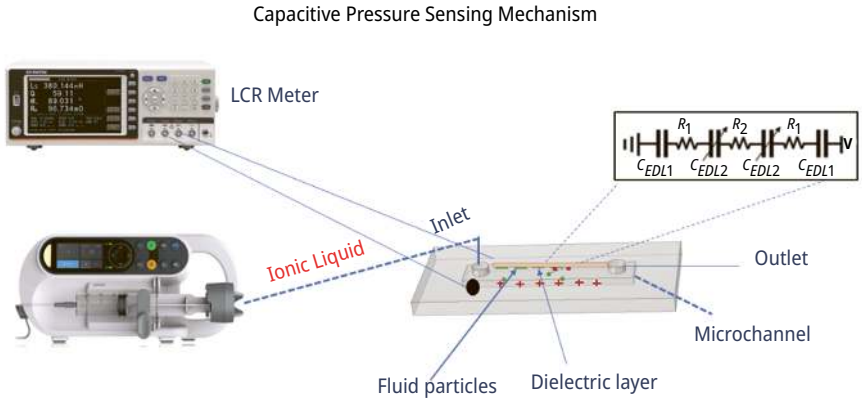

Figure 9.17: Schematic diagram of a capacitive microfluidic pressure-sensing mechanism.

ionic liquid layers when ionic liquid is injected into the microchannel ionic layer contact with the CPC layer and forms an EDL structure at an interfacial layer with electric potential. An AC voltage was applied at 1 V with the frequency of 1 kHz and its large capacitance value variation was achieved. The variation in capacitance value depends on the concentration of CNT, which directly affects variation in the measurement of pressure. Yoon et al. designed a capacitive sensor for human biomedical applications, so that, it is necessary to measure the temperature and sensitivity of the device. They found that temperature sensitivity is 3.46% C-1 at 6% wt. The concentration of CNT is applicable for wearable applications, flexible robotics, and electronics skin [78]. Further experiments in advancement were done by Zhou et al. to design a liquid metal-based capacitive pressure design to measure the pressure inside the microchannel. In this experiment, pressure of the fluid is detected by the sensor when the value of capacitance changes with the movement of immiscible liquids in the microchannel. The variation in capacitance is monitored by an L-Inductance, C-Capacitance, R-Resistance (LCR) meter and device fabricated for testing or monitoring blood pressure.

The design consists of two channels for the measurement of fluidic profile, i.e., short detection channel and target channel. The pair of liquid metal electrodes is fixed at both sides of the detection channel. The two types of layers are functional and shield layers. The electrodes are designed in U shape to make inlet and outlet. They found a relationship between capacitance and dielectric; the reference fluid used is oil and the experimental fluid used is DI water. As a dielectric constant, the value is high in comparison to oil, and then capacitance values of DI are high with the corresponding length. The capacitance range is very high and has fast response time when using a liquid metal-based capacitive sensor [81]. Figure 9.17 shows the sensing mechanism process of capacitive microchannel in liquid metal electrodes placed with fluids. The process utilizes blood pressure measurements for animals or humans. The process of capacitive electrodes used electrical signals to determine the fluidic pressure

that is referred by various researchers. Figure 9.18 shows a graph that helps to understand the capacitance and pressure in microchannel. The graphs also shows that if the capacitance amount increases, the pressure amount also increases, so that, it is concluded that the capacitive microfluidic pressure sensor capacitance value is high for a fluidic pressure profile. Table 9.5 shows a capacitive comparison study of microfluidic pressure-sensing methods in microchannel and its parameters.

Table 9.5: Comparative analysis of capacitive microfluidic pressure-sensing mechanism.

Pressure-sensing technique	Mechanism	Dimensions	Materials	Optimized parameters	References
Capacitive-based pressure sensing	Pressure measurement through capacitive electrode integrated in microchannel	*W* – 100 µm *H* – µm *L* – 2 mm	Polymer parylene acetone	Capacitive electrode distance variation changes in pressure value	[79]
	Soft microsensor formed using two channels, short detection and target channel Deformation of target channel detected	*W* – 100 µm	PDMS substrate Silicon wafer Liquid metal electrode – gain20.5Sn13.5	Pulse pressure testing with respect to capacitance Temperature effect test at 33–43 °C Capacitance ratio change with change in width of channel	[80]
	Developing liquid metal-based pressure sensor. The measuring of the capacitance between these two liquid metal electrodes. The movement of the interface can be detected Pressure change can be detected as well	NA	PDMS Silicon wafer Gain20.5Sn13.5	The researcher measures pressure of 80–230 mmHg Developed a relation between capacitance and pressure Capacitance measured at different temperatures	[81]

Table 9.5 (continued)

Pressure-sensing technique	Mechanism	Dimensions	Materials	Optimized parameters	References
	Developing flexible microfluidic capacitive pressure sensor	NA	Polyurethane sponge Ionic liquid 1-butyl -3-methylimidazolium Polyethylene terephthalate indium tin oxide	Observed the sensitive microfluidic capacitive pressure sensor Compared sensitivity with the other capacitive pressure sensors	[82]

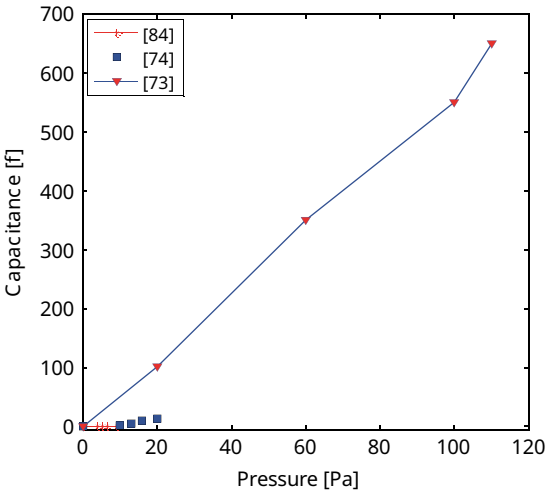

Figure 9.18: The relationship between fluidic pressure in microchannel analysis through the capacitance and developed a relation between capacitance and pressure.

The above review of the research paper on the capacitance-based microfluidic pressure-sensing mechanism has found some challenges for design and fabrication. The review also found the gap and future work required in capacitance-based microfluidic pressure-sensing mechanisms. Tables 9.7 and 9.8 help to understand the challenges in the capacitance microfluidic pressure-sensing mechanism and the advancement or future work for better microfluidic device designing, respectively.

Capacitive-based microfluidic pressure sensing relies on measuring the change in capacitance due to the deformation of a flexible membrane under pressure. This deformation changes the distance between the electrodes in the capacitor, which in turn changes the capacitance. The change in capacitance can be related back to the applied pressure.

For a circular membrane under uniform pressure P, the central deflection δ can be approximated by:

$$P = \frac{3E\delta h^3}{4a^4} \tag{9.32}$$

Deflection (δ) in terms of capacitance;

$$\delta = d_0 - \frac{\in A}{C} \tag{9.33}$$

Substitute δ into the pressure, eq. (9.32) becomes:

$$P = = \frac{3E\left(d_0 - \frac{\in A}{C}\right) h^3}{4a^4} \tag{9.34}$$

Equation (9.34) can be used to calculate the applied pressure P with the measured capacitance C, initial distance d_0, membrane properties E and h, and membrane radius a.

9.4.2.5 Cantilever-Based Pressure-Sensing Mechanism

A cantilever is a structure in which one end is fixed and another end is free for movement as the top of the microcantilever is free to move [83, 84]. Microcantilever structures are using a wide range of applications in microfluidics. The cantilever's free-end movement shows the displacement characteristics concerning force, which is applied by any fluid, electrostatic, magnetostatic, or mechanical [85, 86]. Figure 9.18 shows the process of measurement of fluid pressure inside the microchannel while integrating a microcantilever.

The review paper discusses cantilever deflection in the microscale that replaces optical fluorescence detection and eliminates complex chemicals with a chip-based structure. The material serves in a microfluidic channel, Sounart et al. from Sandia National Laboratories designed an in situ cantilever for a microfluidic channel and the measured fluid flow rate in Figure 9.19 shows the electrostatic actuation process applied on cantilever for the measurement of viscosity and flow rate of fluid. The Si wafer worked as a cantilever membrane and microfluidic channel glass material. The size of the cantilever was 1 mm long and 500 μm wide. DI water fluid flowed across the channel and cantilever [87]. Another experiment by Noeth et al. fabricated a cantilever in SU-8 with integrated holes. The 3.7 μm thick cantilever with holes inserted into a microfluidic channel with the dimensions of the width of 300 μm and a length

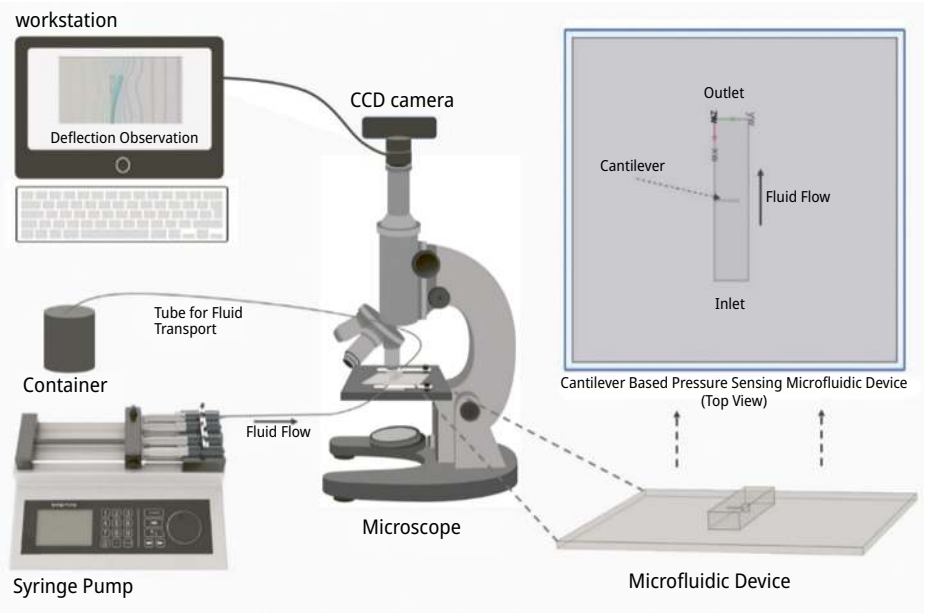

Figure 9.19: Schematic representation of a process of cantilever microfluidic pressure sensing to measure the fluid pressure.

of 400 μm. The perforation in the microcantilever increases the stiffness of the material and deflection of the microcantilever. The observation of microcantilever deflection at the fluid flow rate is 1–5 Nl/min [88]. Nezhad et al. in their experiment design shows the fabricated and simulated microcantilever in a microchannel to control the fluid flow rate. PDMS microcantilever integrated across a SU-8 microchannel without adding any electric field, which detects the fluid pressure through the microcantilever. Such a device is applicable for the biomedical application in cell sorting/separation, drug detection, and diagnosis of disease. The future of integrated microcantilevers across microchannels is extensively used in the field of healthcare applications due to their low cost and the living cells are less sensitive [89]. Figure 9.20 shows a microscopic image of a fabricated and integrated microcantilever in microchannel, the various types of microcantilever are fabricated as shown in Figure 9.20.

Figure 9.20(a) shows the fabricated PDMS microcantilever and Figure 9.20(b) shows the deflection of the microcantilever when force is applied on the top surface. Figure 9.20(c) shows the microfluidic channel and Figure 9.20(d) shows the angular deflection concerning flow rate. The various types of structures of the cantilever can be designed for providing better displacement, and also add holes on the cantilever to provide better flexibility when fluid flows across the channel. The whole dimension takes different types and found cantilever characteristics concerning the fluid. The deflection of the cantilever was directly proportional to microfluidic pressure. The sensitivity of the

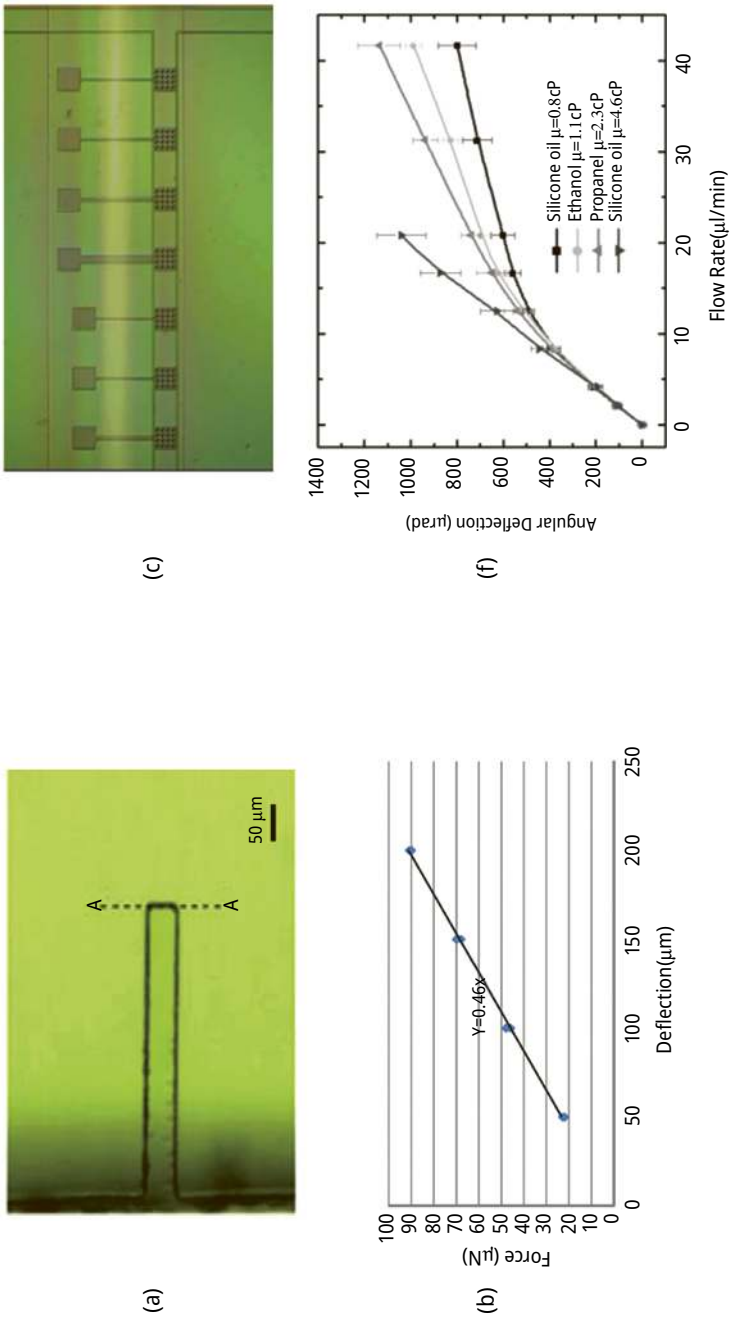

Figure 9.20: Microscope image of integrated microfluidic microcantilever across fluidic microchannel. (a) PDMS microcantilever. (b) Graph between force applied on microcantilever and deflection of cantilever. (c) Fluidic microchannel. (d) Angular deflection of cantilever with respect to the flow rate of fluid.

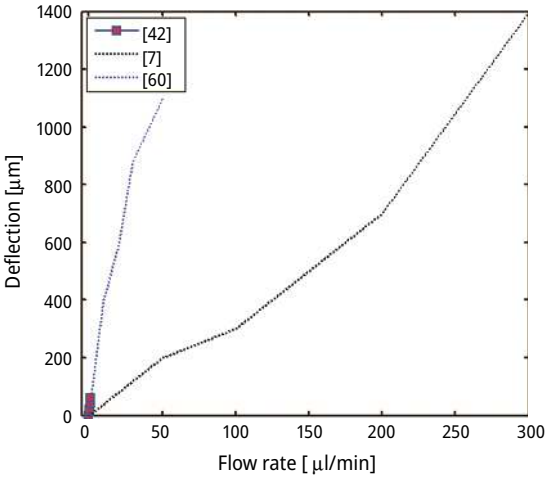

Figure 9.21: The relationship between microcantilever deflection and flow rate of the fluid in the channel.

cantilever varied with changes in hole size, the distance between holes, and the shape of the holes [90, 91]. Figure 9.21 shows the behavior of the fluid in the channel and fluid characteristics are defined by developing a relation between microcantilever deflection and flow rate. Table 9.6 shows a cantilever comparison study of pressure-sensing methods in microchannel and its parameters.

Table 9.6: Comparison of cantilever pressure-sensing mechanisms and its parameters.

Pressure-sensing technique	Mechanism	Dimensions	Materials	Observer effect	References
Cantilever-based pressure sensing	Cantilever sensor design with integrated microchannel	Cantilever (*W* – 340 µm *L* – 370 µm) Microchannel (*W* – 600 µm *L* – 1 mm) Quadratic holes integration (5–20 µm)	SU-8 cantilever Sin-cantilever PDMS channel	SU-8 sensor Five type UV lithographic process serve Sin three lithographic process serve Sin gives more deflection than SU-8 Perforation reduces the resistance fluid flow result gives lower bending for higher porosity Sensitivity decreases with increasing porosity	[91]

Table 9.6 (continued)

Pressure-sensing technique	Mechanism	Dimensions	Materials	Observer effect	References
	Piezoresistive cantilever design at bottom wall of microchannel for measurement of cellular characteristics	Cantilever (*W* – 30 μm *L* – 30 μm *H* – 0.3 μm) Microchannel height, 20 μm	Microchannel – PDMS Cantilever-Si	Microchannel and cantilever aligned using microscopy Photolithography's process of fabrication of microchannel Photolithography mask cantilever	[74]
	HAR piezoresistive cantilever flow sensor	Cantilever (*W* – 3 mm width thickness, 0.5 – 1 mm AR 20) Microfluidic channel (150 μm width and 90 μm depth)	Graphene ink Cantilever of PDMS Silver nanoparticle ink	Airflow testing Waterflow testing Sensitivity of sensor 5.8k ώm/s	[89]
	Experimental and numerical investigation of a cantilever-based optofluidic flow sensor The principle of the sensor is the fringe shift of the Fabry--Pérot (FP) spectrum due to a changing flow rate	Microchannel (*H* – 2 mm, *W* – 1.3 mm, *L* – 1 cm)	Polymethylmethacrylate (PMMA) CO_2 Polydimethylsiloxane (PDMS)	Developing the relation between flow rate and deflection of cantilever Observed the intensity of fluid and developed relation between wavelength and intensity	[90]

The above review of the research paper on the cantilever-based microfluidic pressure-sensing mechanism has found some challenges for design and fabrication. The review also found the gap and future work required in cantilever-based microfluidic pressure-sensing mechanisms. Tables 9.7 and 9.8 show the challenges in the cantilever microfluidic pressure-sensing mechanism and advancement or future work for better microfluidic device design, respectively. Cantilever-based microfluidic pressure sensing involves in measuring the deflection of a cantilever due to the applied pressure in a microfluidic channel. The deflection of the cantilever can be related to the applied pressure through principles of beam theory and mechanics. The deflection δ of a cantilever beam subjected to a uniform pressure P can be described using beam theory. For a rectangular cantilever beam, the maximum deflection at the free end is given by:

$$\delta = \frac{PL^4}{8EI} \tag{9.35}$$

The moment of inertia for a rectangular cross-section is given by:

$$I = \frac{bh^3}{12} \tag{9.36}$$

To relate the deflection δ to the applied pressure P, combining the equation:

$$P = \frac{2Eb\delta\, h^3}{3L^4} \tag{9.37}$$

$$P = \frac{2Eb\delta\, h^3}{3L^4}$$

Equation (9.37) represents to determine the applied microfluidic pressure from the measured deflection of the cantilever.

9.5 Conclusion

They summarize the pressure-sensing mechanism with various technical approaches and the review paper discussed the importance of microfluidics pressure-sensing mechanisms in various applications in industries. The chapter discussed various analytical methods for the control of fluid, monitoring devices, understanding the characteristics of fluids, detection and analysis capabilities, as well as safety for microfluidic devices. These microfluidic pressure-sensing mechanisms enable researchers to explore a wide range of applications and enhance the performance of microfluidics devices in various areas, including healthcare, chemical, biotechnology, and the environment. The chapter discussed a critical aspect of the microfluidic device and the ability to control the pressure, and sensed it accurately within the microfluidic channel. The

first phase of the chapter discussed the impact of the general parameters of microchannel in microfluidics pressure sensing and detection. The AR of the channel refers to the width ratio of the microchannel. The AR amount affects the fluid flow resistance, velocity profile, and pressure drop. As the AR amount increases, the flow resistance also increases due to the increase in the height of the channel. The effect of this higher-pressure drop achieved along the microchannel to maintain higher pressure drop that required high velocity at the inlet. Another parameter is the friction of the microchannel; the friction coefficient of a microchannel in microfluidics refers to the measure of the resistance of fluid flow produced by the interaction between the fluid and microchannel walls. The friction coefficient along the channel shows different behavior, as higher friction coefficients correspond to an increase in the amount of resistance to flow, resulting achieved higher pressure drops. Similarly, lower friction coefficients lead to lower pressure drops. The friction coefficient affects the pressure distribution within the microchannel. In microchannels with higher friction coefficients, the pressure tends to decrease along the channel length due to energy losses caused by wall-fluid interactions. This pressure drop can be nonuniform, with greater pressure losses occurring near the channel entrance or areas of higher friction.

Understanding the pressure distribution is crucial for designing microfluidic systems that require specific pressure profiles for optimal performance. The friction coefficient is related to Reynolds number that defines the flow type in microchannel. Reynolds number influences the pressure drop along the microchannel. In laminar flow, the pressure drop is directly proportional to the flow rate and viscosity of the fluid, according to the HagenPoiseuille equation. Reynolds number influences the velocity profile of the fluid within the microchannel. In laminar flow, the velocity profile is typically parabolic, with the maximum velocity occurring at the channel center and gradually decreasing toward the channel walls. Thus, the first phase reviews microchannel and fluid parameters' effect on microfluidics, and the second phase reviews about different pressure-sensing physics applied in microchannel. The second phase discusses about five types of microfluidic pressure-sensing mechanisms with their challenges and future advancement required. The review paper discusses various techniques for pressure-sensing mechanisms and analysis of microfluidic channels with their parameters. The chapter discussed low Reynolds number laminar flow in microchannel impact on pressure. As the low Reynolds value increases, the pressure in the channel is also increased. AR in microchannel defines the width-to-height ratio and found that most of the channel serves as rectangular but cross-section area can be different due to this fluid sense of high or low pressure. If the cross-section is triangular, then the pressure measurement achieved is high, the height of the grooves provides more friction inflow of the fluid, so that, it is necessary for smooth flow of the fluid and its required groove height should be small. Now, interacting microchannel with pressure-sensing techniques for microfluidics application, various researchers investigate and design such type of a sensor that is in micro size and material property to serve to sense the pressure of fluid flow. Five types of sensing mechanisms are

discussed in this chapter and found that the most demanding approaches are cantilever sensing and optical-based sensing mechanisms. The authors design a sensing layer in a microfluidic chip for the measurement of pressure or sense of pressure, and an optical approach is used to determine the pressure. The integrated microcantilever with microchannel senses pressure without adding or inserting a piezoresistive sensor or piezoelectric sensor. The syringe pump and optical device are used to measure the reading with online monitoring. The integration of a microcantilever in a microchannel and measurement of fluid properties with cantilever deflection without adding any type of piezoresistive sensor, using an optical device to measure displacement in microcantilever tip is highly demanding for living cell detection in biological application. Microfluidic device has a lot of scope for disease diagnosis; most of the technologies come with an individual device for the diagnosis of any disease and the integration of multiple devices with virtuous approach helps to design a microfluidic device for healthcare application.

References

[1] Convery, N. & Gadegaard, N., (Mar. 2019). 30 years of microfluidics. Micro and Nano Engineering, 2, 76–91. doi, 10.1016/j.mne.2019.01.003.

[2] Ashraf, M. W., Tayyaba, S., & Afzulpurkar, N., (Jun. 2011). Micro Electromechanical Systems (MEMS) based microfluidic devices for biomedical applications. International Journal of Molecular Sciences, 12(6), 3648–3704. doi, 10.3390/ijms12063648.

[3] Šalić, A., Tušek, A., & Zelić, B., (Jul. 2012). Application of microreactors in medicine and biomedicine. J Appl Biomed, 10(3), 137–153. doi, 10.2478/v10136-012-0011-1.

[4] Menzel, F., Cotton, J., Klein, T., Maurer, A., Ziegler, T., & Neumaier, J. M., (2023). FOMSy: 3D-printed flexible open-source microfluidic system and flow synthesis of PET-tracer. J Flow Chem, Mar, doi, 10.1007/s41981-023-00267-z.

[5] Parkhey, P. & Sahu, R., (Jan. 2021). Microfluidic microbial fuel cells: Recent advancements and future prospects. International Journal of Hydrogen Energy, 46(4), 3105–3123. doi, 10.1016/j.ijhydene.2020.07.019.

[6] Tamayol, A. & Bahrami, M., (Nov. 2010). Laminar flow in microchannels with noncircular cross-section. Journal of Fluids Engineering, 132(11), doi, 10.1115/1.4001973.

[7] Koo, J. & Kleinstreuer, C., (Sep. 2003). Liquid flow in microchannels: Experimental observations and computational analyses of microfluidics effects. Journal of Micromechanics & Microengineering, 13(5), 568–579. doi, 10.1088/0960-1317/13/5/307.

[8] Papautsky, I., Ameel, T., & Frazier, A. B., (Nov. 2001). A review of laminar single-phase flow in microchannels. Micro-Electro-Mechanical Systems (MEMS), 495–503. American Society of Mechanical Engineers. doi, 10.1115/IMECE2001/MEMS-23872.

[9] Yang, Y.-F. et al.. (Jul. 2023). A high-sensitivity flexible PDMS@rGO-based pressure sensor with ultra-wide working range based on bioinspired gradient hierarchical structure with coplanar electrodes. Composites Science and Technology, 240, 110078. doi, 10.1016/j.compscitech.2023.110078.

[10] Cekas, E., Janusas, G., Guobiene, A., Palevicius, A., Vilkauskas, A., & PonelyteUrbaite, S., (Nov. 2018). Design of controllable novel piezoelectric components for microfluidic applications. Sensors, 18(11), 4049. doi, 10.3390/s18114049.

[11] Li, Y. et al.. (Jul. 2024). A Novel Implantable Piezoresistive Microsensor for Intraocular Pressure Measurement. ACS Sens, doi, 10.1021/acssensors.4c00705.
[12] Isgor, P. K., Marcali, M., Keser, M., & Elbuken, C., (Apr. 2015). Microfluidic droplet content detection using integrated capacitive sensors. Sens Actuators, B: Chem, 210, 669–675. doi, 10.1016/j.snb.2015.01.018.
[13] Gregory, J. W., Asai, K., Kameda, M., Liu, T., & Sullivan, J. P., (2008). A review of pressure-sensitive paint for high-speed and unsteady aerodynamics. Proc Inst Mech Eng G J AerospEng, 222(2), 249–290. doi, 10.1243/09544100JAERO243.
[14] Ramachandran, B. & Liao, Y.-C., (Sep. 2022). Microfluidic wearable electrochemical sweat sensors for health monitoring. Biomicrofluidics, 16(5), 051501. doi, 10.1063/5.0116648.
[15] Tayyaba, S., Ashraf, M. W., Ahmad, Z., Wang, N., Afzal, M. J., & Afzulpurkar, N., (Dec. 2020). Fabrication and analysis of Polydimethylsiloxane (PDMS) microchannels for biomedical application. Processes, 9(1), 57. doi, 10.3390/pr9010057.
[16] Antony, R., Nandagopal, M. S. G., Sreekumar, N., & Selvaraju, N., (2014). Detection Principles and Development of Microfluidic Sensors in the Last Decade. Springer Verlag, doi, 10.1007/s00542-014-2165-0.
[17] Wang, X., Shangguan, P., Huang, P., & Hou, D., (Mar. 2023). Microfluidic channel-based soft electrodes and their application in capacitive pressure sensing. Journal of Visualized Experiments, (193), doi, 10.3791/65175.
[18] Jeon, B., Jeong, B., & Park, Y.-L., (Apr. 2022). Hybrid mechanism of electromagnetic and piezoresistive sensing using a soft microfluidic coil. IEEE Robot Autom Lett, 7(2), 4638–4645. doi, 10.1109/LRA.2022.3152310.
[19] Hampson, S. M., Rowe, W., Christie, S. D. R., & Platt, M., (Mar. 2018). 3D printed microfluidic device with integrated optical sensing for particle analysis. Sens Actuators, B: Chem, 256, 1030–1037. doi, 10.1016/j.snb.2017.10.041.
[20] Inglis, D. W., (Jun. 2010). A method for reducing pressure-induced deformation in silicone microfluidics. Biomicrofluidics, 4(2), 026504. doi, 10.1063/1.3431715.
[21] Kartalov, E. P., Maltezos, G., Anderson, W. F., Taylor, C. R., & Scherer, A., (Oct. 2007). Electrical microfluidic pressure gauge for elastomer microelectromechanical systems. Journal of Applied Physics, 102(8), 084909. doi, 10.1063/1.2801008.
[22] Chu, Y. F., Lin, C. B., & Chen, C. S., (Aug. 2017). Pressure measurement in a microchannel. Microsystem Technologies, 23(8), 3711–3718. doi, 10.1007/s00542-016-3195-6.
[23] Rapp, B. E., (2017). Fluids. Microfluidics: Modelling, Mechanics and Mathematics, 243–263. Elsevier. doi, 10.1016/B978-1-4557-3141-1.50009-5.
[24] Stone, H. A. & Kim, S., (Jun. 2001). Microfluidics: Basic issues, applications, and challenges. AIChE Journal, 47(6), 1250–1254. doi, 10.1002/aic.690470602.
[25] Zhang, P., Zuo, C., & Liu, X., (2010). Study on friction coefficient of liquid flow through a rectangular microchannel with electrokinetic effects. Proceedings – 2010 International Conference on Digital Manufacturing and Automation, ICDMA, 485–489. 2010, doi, 10.1109/ICDMA.2010.78.
[26] Rawool, A. S., Mitra, S. K., & Kandlikar, S. G., (May 2006). Numerical simulation of flow through microchannels with designed roughness. MicrofluidNanofluidics, 2(3), 215–221. doi, 10.1007/s10404-005-0064-5.
[27] Kundu, P. K., Cohen, I. M., & Dowling, D. R., (2016). Laminar Flow. Fluid Mechanics, 409–467. Elsevier. doi, 10.1016/B978-0-12-405935-1.00009-5.
[28] Gamrat, G., Favre-Marinet, M., Person, S. L., Bavière, R., & Ayela, F., (Jan. 2008). An experimental study and modelling of roughness effects on laminar flow in microchannels. J Fluid Mech, 594, 399–423. doi, 10.1017/S0022112007009111.

[29] Jiang, X. N., Zhou, Z. Y., Huang, X. Y., & Liu, C. Y., (Oct, 1997) Laminar flow through microchannels used for microscale cooling systems. Proceedings of the 1997 1st Electronic Packaging Technology Conference (Cat. No.97TH8307), 119–122. IEEE. doi, 10.1109/EPTC.1997.723897.
[30] Hrnjak, P. & Tu, X., (Feb. 2007). Single phase pressure drop in microchannels. International Journal of Heat and Fluid Flow, 28(1), 2–14. doi, 10.1016/j.ijheatfluidflow.2006.05.005.
[31] ZHANG, Y., GU, X.-J., Barber, R. W., & Emerson, D. R., (Dec. 2005). Influence of the electric double layer on induced pressure fields and development lengths in electro-osmotic flows. Modern Physics Letters B, 19(28n29), 1655–1658. doi, 10.1142/S0217984905010141.
[32] Barta, E. & Weihs, D., (Mar. 2006). Creeping flow around a finite row of slender bodies in close proximity. J Fluid Mech, 551(1), 1. doi, 10.1017/S0022112005008268.
[33] Tamayol, A., Gunda, N. S. K., Akbari, M., Mitra, S. K., & Bahrami, M., (Jul. 2012). Creeping flow through microchannels with integrated Micro-Pillars. ASME 2012 10th International Conference on Nanochannels, Microchannels, and Minichannels, 411–417. American Society of Mechanical Engineers. doi, 10.1115/ICNMM2012-73199.
[34] Lepchev, D. & Weihs, D., (Jul. 2010). Low Reynolds Number Flow in Spiral Microchannels. Journal of Fluids Engineering, 132(7), doi, 10.1115/1.4001860.
[35] Kharati-Koopaee, M. & Rezaee, M., (Jul. 2017). Investigation of turbulent flow through microchannels consisting of different micropost arrangements. EngComput (Swansea), 34(5), 1367–1392. doi, 10.1108/EC-02-2016-0069.
[36] Vyawahare, S., Griffiths, A. D., & Merten, C. A., (Oct. 2010). Miniaturization and parallelization of biological and chemical assays in microfluidic devices. Chemistry & Biology, 17(10), 1052–1065. doi, 10.1016/j.chembiol.2010.09.007.
[37] Galambos, P. & Forster, F., (Nov. 1998). An optical micro-fluidic viscometer. Micro-Electro-Mechanical Systems (MEMS), 187–191. American Society of Mechanical Engineers. doi, 10.1115/IMECE1998-1241.
[38] Araci, I. E. et al.. (2019). Flow stabilization in wearable microfluidic sensors enables noise suppression. Lab Chip, 19(22), 3899–3908. doi, 10.1039/C9LC00842J.
[39] Jang, I., Berg, K. E., & Henry, C. S., (Sep. 2020). Viscosity measurements utilizing a fast-flow microfluidic paper-based device. Sens Actuators, B: Chem, 319, 128240. doi, 10.1016/j.snb.2020.128240.
[40] Yeom, E., Kang, Y. J., & Lee, S. J., (May 2014). Changes in velocity profile according to blood viscosity in a microchannel. Biomicrofluidics, 8(3), doi, 10.1063/1.4883275.
[41] Batchelor, G. K., (Jul. 1967). Low Reynolds number flow. by Sir G Eoffrey T Aylor . 16 mm, sound, colour. 33 min. $250.00. J Fluid Mech, 29(1), 204–207. doi, 10.1017/S0022112067230725.
[42] Jiang, X. N., Zhou, Z. Y., Yao, J., Li, Y., & Ye, X. Y., "MICRO-FLUID F4OW IN MICROCHANNEL."
[43] Papautsky', I., Gale, B. K., Mohanty', S., Ameelc, T. A., & Frazier, A. B., "Effects of rectangular microchannel aspect ratio on laminar friction constant." [Online]. Available: http://proceedings.spiedigitallibrary.org/
[44] Wilding, P., Pfahier, J., Bau, H. H., Zemel, J. N., & Krlcka, L. J., "Manipulation and Flow of Biological Fluids in Straight Channels Micromachined in Silicon," 1994.
[45] Zhang, X., Zhao, T., Wu, S., & Yao, F., (2019). Experimental study on liquid flow and heat transfer in rough microchannels. Advances in Condensed Matter Physics, 2019, doi, 10.1155/2019/1974952.
[46] Park, H. S. & Punch, J., (Aug. 2008). Friction factor and heat transfer in multiple microchannels with uniform flow distribution. International Journal Heat Mass Transfer, 51(17–18), 4535–4543. doi, 10.1016/j.ijheatmasstransfer.2008.02.009.
[47] Steinke, M. E. & Kandlikar, S. G., "SINGLE-PHASE LIQUID FRICTION FACTORS IN MICROCHANNELS." [Online]. Available: http://www.asme.org/about-asme/terms-of-use
[48] Gunnasegaran, P., Mohammed, H., & Shuaib, N. H., (Dec. 2009). Pressure drop and friction factor for different shapes of microchannels. 2009 3rd International Conference on Energy and Environment (ICEE), 418–426. IEEE. doi, 10.1109/ICEENVIRON.2009.5398611.

[49] Wang, G. L., Yang, D. W., Wang, Y., Niu, D., Zhao, X. L., & Ding, G. F., (Apr. 2015). Heat transfer and friction characteristics of the microfluidic heat sink with variously-shaped ribs for chip cooling. Sensors (Switzerland), 15(4), 9547–9562. doi, 10.3390/s150409547.

[50] Raghuraman, D. R. S., Thundilkaruppa Raj, R., Nagarajan, P. K., & Rao, B. V. A., (Mar. 2017). Influence of aspect ratio on the thermal performance of rectangular shaped micro channel heat sink using CFD code. Alexandria Engineering Journal, 56(1), 43–54. doi, 10.1016/j.aej.2016.08.033.

[51] Duryodhan, V. S., Singh, S. G., & Agrawal, A., (Jun. 2017). Effect of cross aspect ratio on flow in diverging and converging microchannels. Journal of Fluids Engineering, Transactions of the ASME, 139(6), doi, 10.1115/1.4035945.

[52] Zhang, X. et al.. (Aug. 2016). Characteristics of liquid flow in microchannels at very low Reynolds numbers. Chemical Engineering & Technology, 39(8), 1425–1430. doi, 10.1002/ceat.201500743.

[53] Salah, S. A. S., Filali, E. G., & Djellouli, S., (Aug. 2017). Numerical investigation of Reynolds number and scaling effects in micro-channels flows. Journal of Hydrodynamics, 29(4), 647–658. doi, 10.1016/S1001-6058(16)60777-1.

[54] Ren, L., Li, D., & Qu, W., (Jan. 2001). Electro-viscous effects on liquid flow in microchannels. J of Colloid and Interface Sci, 233(1), 12–22. doi, 10.1006/jcis.2000.7262.

[55] John, T. J., Mathew, B., & Hegab, H., (Jan. 2009). “Experimental Analysis of Poiseuille Number in Square Microchannels,” in Volume 9: Heat Transfer, Fluid Flows, and Thermal Systems. Parts, A., B. & Asmedc, C. 315–321. doi, 10.1115/IMECE2009-11810.

[56] Nadeem Khan, M., Islam, M., & Hasan, M. M., (2011). Experimental approach to study friction factor and temperature profiles of fluid flow in circular microchannels. Journal of Mechanical Engineering Research, 3(6), 209–217. [Online]. Available, http://www.academicjournals.org/jmer

[57] Zhang, X. et al. (Aug. 2016). Characteristics of liquid flow in microchannels at very low Reynolds numbers. Chemical Engineering & Technology, 39(8), 1425–1430. doi, 10.1002/ceat.201500743.

[58] Sollier, E., Murray, C., Maoddi, P., & Di Carlo, D., (2011). Rapid Prototyping Polymers for Microfluidic Devices and High Pressure Injections. Royal Society of Chemistry, 21. Nov, 10.1039/c1lc20514e.

[59] Kim, M., Huang, Y., Choi, K., & Hidrovo, C. H., (Jul. 2014). The improved resistance of PDMS to pressure-induced deformation and chemical solvent swelling for microfluidic devices. Microelectronic Engineering, 124, 66–75. doi, 10.1016/j.mee.2014.04.041.

[60] Tsai, C.-H. D., Nakamura, T., & Kaneko, M., (Sep. 2015). An on-chip, electricity-free and single-layer pressure sensor for microfluidic applications. 2015 IEEE/RSJ International Conference on Intelligent Robots and Systems (IROS), 165–170. IEEE. doi, 10.1109/IROS.2015.7353369.

[61] Kang, C., Roh, C., & Overfelt, R. A., (2014). Pressure-driven deformation with soft polydimethylsiloxane (PDMS) by a regular syringe pump: Challenge to the classical fluid dynamics by comparison of experimental and theoretical results. RSC Advances, 4(7), 3102–3112. doi, 10.1039/c3ra46708b.

[62] Raj, A., Suthanthiraraj, P. P. A., & Sen, A. K., (Nov. 2018). Pressure-driven flow through PDMS-based flexible microchannels and their applications in microfluidics. MicrofluidNanofluidics, 22(11), 128. doi, 10.1007/s10404-018-2150-5.

[63] Roh, C., Lee, J., & Kang, C., (Jun. 2016). The deformation of polydimethylsiloxane (PDMS) microfluidic channels filled with embedded circular obstacles under certain circumstances. Molecules, 21(6), doi, 10.3390/molecules21060798.

[64] Raj, K. M., Chakraborty, J., Dasgupta, S., & Chakraborty, S., (May 2018). Flow-induced deformation in a microchannel with a non-Newtonian fluid. Biomicrofluidics, 12(3), doi, 10.1063/1.5036632.

[65] Kim, D.-S., Jeong, Y.-J., Lee, B.-K., Shanmugasundaram, A., & Lee, D.-W., (Mar. 2017). Piezoresistive sensor-integrated PDMS cantilever: A new class of device for measuring the drug-induced changes in the mechanical activity of cardiomyocytes. Sens Actuators, B: Chem, 240, 566–572. doi, 10.1016/j.snb.2016.08.167.

[66] (2005). Pressure and Temperature Sensitive Paints. Berlin/Heidelberg, Springer-Verlag, doi, 10.1007/b137841.
[67] Cutler, A., (Mar. 2013). Aerodynamic Measurements: From Physical Principles to Turnkey Instrumentation. AIAA Journal, 51(3), 758–758. doi, 10.2514/1.J052027.
[68] Huang, C., Gregory, J. W., & Sullivan, J. P., (Aug. 2007). Microchannel pressure measurements using molecular sensors. Journal of Microelectromechanical Systems, 16(4), 777–785. doi, 10.1109/JMEMS.2007.892914.
[69] Hosokawa, K. & Maeda, R., (Jan. 2001) In-line pressure monitoring for microfluidic devices using a deformable diffraction grating. Technical Digest. MEMS 2001. 14th IEEE International Conference on Micro Electro Mechanical Systems (Cat. No.01CH37090), 174–177. IEEE. doi, 10.1109/MEMSYS.2001.906508.
[70] Hoera, C., Kiontke, A., Pahl, M., & Belder, D., (Feb. 2018). A chip-integrated optical microfluidic pressure sensor. Sens Actuators, B: Chem, 255, 2407–2415. doi, 10.1016/j.snb.2017.08.195.
[71] Matsuda, Y., Mori, H., Niimi, T., Uenishi, H., & Hirako, M., (Apr. 2007). Development of pressure sensitive molecular film applicable to pressure measurement for high Knudsen number flows. Experiments in Fluids, 42(4), 543–550. doi, 10.1007/s00348-007-0259-5.
[72] Zarikos, I. M., Hassanizadeh, S. M., Van Oosterhout, L. M., & Van Oordt, W., (Mar. 2018). Manufacturing a micro-model with integrated fibre optic pressure sensors. Transport in Porous Media, 122(no 1), 221–234. doi, 10.1007/s11242-018-1000-y.
[73] Zhou, Y. et al.. (2021). High-resolution integrated piezoresistive sensors for microfluidic monitoring. Lab Chip, 21(1), 83–92. doi, 10.1039/D0LC01046D.
[74] Jung, T. & Yang, S., (May 2015). Highly stable liquid metal-based pressure sensor integrated with a microfluidic channel. Sensors (Switzerland), 15(5), 11823–11835. doi, 10.3390/s150511823.
[75] Ko', H. S., Liu2, C. W., Liu2and, C. G., & Gaul', C., "Micro Fluidic System by Integrating Pressure Sensor Arrays with a Micro-Channel."
[76] Wu, C. Y., Liao, W. H., & Tung, Y. C., (May 2011). Integrated ionic liquid-based electrofluidic circuits for pressure sensing within polydimethylsiloxane microfluidic systems. Lab Chip, 11(10), 1740–1746. doi, 10.1039/c0lc00620c.
[77] Inoue, N. & Onoe, H., (Jan. 2018). Graphene-based inline pressure sensor integrated with microfluidic elastic tube. Journal of Micromechanics & Microengineering, 28(1), doi, 10.1088/1361-6439/aa9810.
[78] Yoon, S. G. & Chang, S. T., (2017). Microfluidic capacitive sensors with ionic liquid electrodes and CNT/PDMS nanocomposites for simultaneous sensing of pressure and temperature. J Mater Chem C Mater, 5(8), 1910–1919. doi, 10.1039/c6tc03994d.
[79] Eskandarisani, M., Aliverdinia, M., Malakshah, V. M., Mirhosseini, S., & Zand, M. M., (May 2024). Microstructured porous capacitive bio-pressure sensor using droplet-based microfluidics. J Med Signals Sens, 14(5), doi, 10.4103/jmss.jmss_24_23.
[80] Yang, X., Wang, Y., & Qing, X., (Jul. 2018). A flexible capacitive pressure sensor based on ionic liquid. Sensors (Switzerland), 18(7), doi, 10.3390/s18072395.
[81] Zhou, X. et al.. (Mar. 2019). A liquid metal based capacitive soft pressure microsensor. Lab Chip, 19(5), 807–814. doi, 10.1039/c8lc01357h.
[82] Yang, X., Wang, Y., Sun, H., & Qing, X., (Jan. 2019). A flexible ionic liquid-polyurethane sponge capacitive pressure sensor. Sens Actuators A Phys, 285, 67–72. doi, 10.1016/j.sna.2018.10.041.
[83] Saxena, A., & Agrawal, V. K. (2017). Comparative study of Cantilever RF MEMS switch. *Materials Today: Proceedings*, 4(9), 10328–10331.
[84] Saxena, A., Kumar, M., & Singh, K., (May 2024). Comparative examine of fluid pressure within microchannel through integrated cantilevers for microfluidic applications. Materials Today: Proceedings, doi, 10.1016/j.matpr.2024.04.101.

[85] Saxena, A., Kumar, M., Mishra, D., & Singh, K., (May 2024). Optimization of Newtonian fluid pressure in microcantilever integrated flexible microfluidic channel for healthcare application. Biomedical Physics & Engineering Express, 10(3), 035015. doi, 10.1088/2057-1976/ad3187.

[86] Saxena, A., Kumar, M., Mishra, D., & Singh, K., (May 2023). An efficient microfluidic pressure sensing structure optimization using microcantilever integration. PhysScr, 98(5), 055006. doi, 10.1088/1402-4896/acc7d8.

[87] Sounart, T. L., Matzke, C. M., Okandan, M., Ashby, C. L., & Michalske, T. A., "SANDIA REPORT MEMS in microfluidic channels," 2004. [Online]. Available: http://www.doe.gov/bridge

[88] Noeth, N., Keller, S. S., & Boisen, A., (Jan. 2014). Integrated cantilever-based flow sensors with tunable sensitivity for in-line monitoring of flow fluctuations in microfluidic systems. Sensors (Switzerland), 14(1), 229–244. doi, 10.3390/s140100229.

[89] Nezhad, A. S., Ghanbari, M., Agudelo, C. G., Packirisamy, M., Bhat, R. B., & Geitmann, A., (2013). PDMS microcantilever-based flow sensor integration for lab-on-a-chip. IEEE Sensors Journal [Internet], 13(2), 601–609. doi, 10.1109/JSEN.2012.2223667.

[90] Cheri, M. S., Latifi, H., Sadeghi, J., Moghaddam, M. S., Shahraki, H., & Hajghassem, H., (Dec. 2013). Real-time measurement of flow rate in microfluidic devices using a cantilever-based optofluidic sensor. Analyst, 139(2), 431–438. doi, 10.1039/c3an01588b.

[91] Takahashi, H., Dung, N. M., Matsumoto, K., & Shimoyama, I., (May 2012). Differential pressure sensor using a piezoresistive cantilever. Journal of Micromechanics & Microengineering, 22(5), doi, 10.1088/0960-1317/22/5/055015.

Tanya Gupta, Shiv Pratap, Padam Singh*, and Manoj Kumar

Chapter 10
The Xue Model-Based Quadratic Convective Flow Analysis of Radiative Trihybrid Nanofluid over Porous Plate Using Cattaneo-Christov Model

Abstract: This chapter discusses the flow of trihybrid nanofluid (THNF) across a permeable plate, considering nonlinear thermal radiation and nonlinear convection. The Cattaneo-Christov heat flux model is utilized for heat transfer (HT) phenomena. The Xue model is used to find the thermal conductivity of TNHF. The set of partial differential equations is transmuted into ordinary differential equations (ODEs) using the similarity constraints. The ODEs are solved numerically by the BVP4C solver. The analysis of flow parameters on dimensionless velocity and thermal profiles is sketched. The variation in HT and drag coefficient for different parameters is tabulated. The suction parameter and radiation parameter increase the fluid velocity, and the convection parameter, along with the thermal leg factor decrease the energy profile of THNF. The magnetic field and porosity are responsible for an increment in HT and convection, while the slip parameter is responsible for a decrement. The bar graph is also plotted for HT enchantment.

Keywords: trihybrid nanofluid, Xue model, quadratic convection, nonlinear radiation, nonlinear heat source/sink, slip condition

10.1 Introduction

While studying the fluid flow behavior, it is necessary to study the radiation effect due to its applications in different sectors, such as aerospace, combustion systems, atmospheric science, cooling of nuclear reactors, and space fluid dynamics. Josef Stefan

*Corresponding author: **Padam Singh,** Department of Applied Sciences and Humanities, Galgotias College of Engineering and Technology, Greater Noida, Uttar Pradesh, India,
e-mail: tomar.padam@gmail.com
Tanya Gupta, Department of Mathematics, IAH, GLA University, Mathura, India,
e-mail: tanya.gupta@gla.ac.in
Shiv Pratap, Division of Mathematics, SBS Galgotias University, Greater Noida 203201, Uttar Pradesh, India, e-mail: shivpratapsinghmathdu7@gmail.com
Manoj Kumar, G. B. Pant University of Agriculture and Technology, Pantnagar, Uttarakhand, India,
e-mail: mnj_kumar2004@yahoo.com

https://doi.org/10.1515/9783111723464-010

and Ludwig Boltzmann gave the foundation for radiation heat transfer (HT) analysis. They introduced the Stefan-Boltzmann law to describe the relation between thermal radiation and absolute temperature. Later, many researchers conducted their studies on thermal radiation, such as Siddheshwar and Mahabaleshwar [1], who analyzed the radiation effect on the viscoelastic liquid flow along a stretching sheet. Mukhopadhyay and Layek [2] conducted a study on the HT of fluid across a porous stretching sheet in the presence of thermal radiation. Kumar et al. [3] applied the finite element method to analyze the HT of nanofluid flow over an infinite vertical plate in the presence of radiation. They concluded an enhancement in velocity and temperature profile by the radiation parameter. Recently, a study was done by Bejawada and Nandeppanavar [4], in which they analyzed the flow of micropolar fluid in the presence of radiation over a moving plate. They observed a rise in skin friction with the radiation parameter. Sreedevi et al. [5] analyzed the effect of radiation on nanofluid flow with the aid of natural convection inside a differentially heated square chamber. They revealed a rise in the convection HT due to radiation from the hot to the cold wall. Allouche et al. [6] studied the HT attributes of an HNF inside an eccentric annular space under the effect of thermal radiation. They disclosed the influence of radiation on convective HT for low and high Rayleigh numbers. More literature on the effect of radiation can be seen in the works of Mahabaleshwar et al. [7], Alzahrani et al. [8], Saad et al. [9], Karthik et al. [10].

An understanding of magnetohydrodynamics (MHD) is crucial when examining the influence of electrically conductive fluids in the presence of a magnetic field. It has applications in various domains, such as nuclear reactors, power generation, plasma propulsion systems, and many other engineering systems. MHD has the ability to control and manipulate conducting fluid in the presence of magnetic field. Due to this property, it has applications in power generation, metal processing, hypersonic aircraft, biomedical and many more. A lot of work has been done in the vicinity of MHD. In the first light, Alfven [11] introduced the concept of MHD waves and discussed the development of combined electromagnetic-hydrodynamic waves. Ishak et al. [12] presented the solution to the MHD flow problem over a stretching cylinder and described the effect of the magnetic parameter. They disclosed the suppression in velocity and the increment in the temperature field due to the magnetic field. They also disclosed that the drag is increased due to the magnetic field. Das et al. [13] explained the mass transmission effect on convective MHD flow over a vertical plate that is embedded in porous media. They also concluded that there is a decrease in the velocity profile under the influence of the magnetic field. Gul et al. [14] analyzed the HT in a vertical channel. They assumed the MHD flow with the aid of mixed convection and made a comparison between magnetic and nonmagnetic nanoparticles. Ellahi et al. [15] considered the MHD and slip effect on the boundary layer flow over a moving plate. They concluded that the MHD factor results in a rise in temperature. In their study, they also analyzed entropy generation and discussed the Bejan number. Reddy et al. [16] studied the heat generation/absorption effect on the MHD flow over a

stretching cylinder. They concluded that the magnetic parameter resulted in an increase in thermal gradient and a decrease in the velocity profile. Some recent literature on the MHD can be seen in the works of Akbar et al. [17], Mirzaei et al. [18], Li et al. [19], Reddy et al. [20], Adel et al. [21], Reddy and Mangamma [22].

The porous stretching sheet has gained a lot of interest from researchers due to its vast domain of applications. It includes polymer extrusion in which flow can be controlled through pores present on the sheet. The HT study of porous sheets can help in understanding the speed optimization process, cooling rates and much more. In the biomedical field, the porous stretching sheet plays a crucial role in improving the efficiency of drug delivery systems by controlling the release of medicine in the blood or designing artificial organs. Many researchers have analyzed porous stretching sheets and discussed it for different scenarios. Hayat et al. [23] analyzed the HT of MHD flow over a porous stretching sheet. This study was conducted with the aid of slip conditions. Swain et al. [24] visualized the Joule heating effect on the MHD flow over a porous stretching sheet. They discussed the effect of the porous parameter under the Joule heating effect and concluded that a rise in porosity results in an elevated velocity. A study of thermo-diffusion and HT flow over a porous sheet was conducted by Khan et al. [25]. They analyzed the boundary layer flow of nanofluid with the aid of a convective boundary. Khan et al. [26] explored the dual solution of the stagnation point unsteady flow of Casson fluid over a porous sheet. They imposed slip mechanisms and mixed convection on their model. The examination of micropolar fluid flow across a sheet in the presence of viscous dissipation and thermal radiation was done by Kausar et al. [27]. They concluded a rise in the boundary layer along with an increase in porosity. Recently, Akbar et al. [28] simulated the hybrid nanofluid (HNF) flow over a porous sheet with an artificial neural network approach. Their findings include the rise in temperature with an increase in porosity. More work related to porous stretching sheets can be seen in the literature works of Warke et al. [29], Babu et al. [30], Dharmaiah et al. [31], Nabwey and Mahdy [32], Khattak et al. [33].

In the present scenario, the nanoparticles play a crucial role in optimizing the HT properties of the fluid. They have a vast area of applications depending on the nanoparticles chosen. For instance, TiO_2 is used as a nanoparticle in various domains, such as biomedical, water purification, antimicrobial coatings, energy systems, and aerospace. In biomedical, it is used as a carrier of therapeutic agents that respond to magnetic fields for accurate targeting. In water purification, it behaves as a photocatalyst, helping in wastewater treatment. These particles are used in antiviral sprays and air purification systems. These particles can be used as boosters for thermal systems to enhance heat retention and many more. Similarly, Al_2O_3 and single-wall carbon nanotubes (SWCNT) have a wide range of applications. Al_2O_3 is used in heat exchangers to increase thermal conductivity, in biomedical imaging as a contrast agent for accurate diagnostics, in the lubrication process to decrease friction, in the purification process to remove contaminants or organic pollutants, and in storage systems to make them more reliable. SWCNTs are significantly effective nanoparticles. It enhances the thermal

performance of cooling systems and heat exchangers due to its high thermal conductivity. These particles are used for photothermal therapy and bioimaging. Under a magnetic field, these particles are capable of enhancing the fluid control in MHD systems. Overall, these nanoparticles are very useful across a wide range of applications. Some work related to these nanoparticles can be seen in the literature works of Kim et al. [34], Chun Chen et al. [35], Soni and Thomas [36], Manigandan et al. [37], Javadipour et al. [38], Trandabat et al. [39], Khashan et al. [40].

After carefully reviewing the recently published study on trihybrid nanofluid (TNHF) flow over a plate, the authors identified the following gap to fill in the study. The chapter describes the flow of tetrahydrofuran (THF) over a plate of porous medium. The study outcome is the following:

- How is the thermal conductivity of fluid affected by different shapes of nanoparticles?
- What is the importance of C-C HT instead of HT of using classical Fourier's law?
- In many physical phenomena, nonlinearity appears. How does the nonlinear convection affect the fluid velocity and temperature?
- What is the impact of nonlinear radiation on the attendance of irregular heat sources?

10.2 Assumptions and Model Descriptions

The flow description is shown in Figure 10.1, where we consider the 2D laminar, incompressible, and viscous trihybrid nanofluid flow over a permeable plate. The magnetic field of strength B_0 is applied to the plate in the normal direction of flow. The flow is designed in the x-direction. T_w is the temperature at the wall and U_w is the free stream velocity of the fluid. The heat induced by the friction of the adjacent layer and due to the magnetic field is considered. Furthermore, the consequences of irregular heat source/sink, nonlinear radiation, and convection are considered. For the HT analysis, the Cattaneo-Christov model is employed.

10.2.1 Model Equations

Equation of Continuity

$$u_x + v_y = 0 \tag{10.1}$$

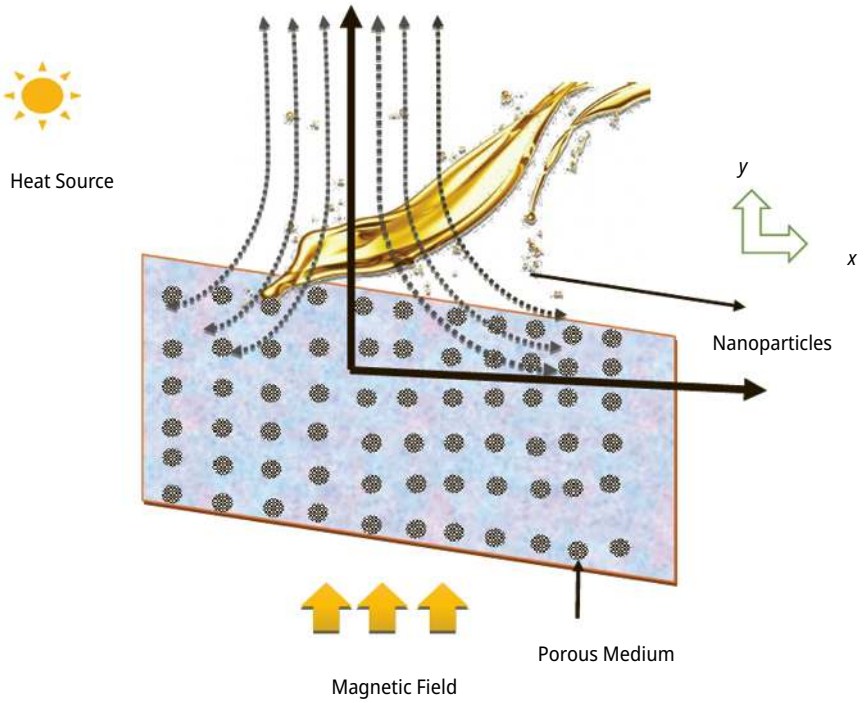

Figure 10.1: Visualization of flow geometry.

Momentum Equation

$$\rho_{tf}(\tilde{u}\tilde{u}_x+\tilde{v}\tilde{u}_y)=\mu_{tf}\tilde{u}_{yy}-\sigma_{tf}B_0^2\tilde{u}-\mu_{tf}\frac{\tilde{u}}{k_p}+g\cos\beta\left[(\rho\beta_0)_{tf}\left(\tilde{T}-\tilde{T}_\infty\right)+(\rho\beta_1)_{tf}\left(\tilde{T}-\tilde{T}_\infty\right)^2\right] \tag{10.2}$$

Energy Equation

$$(\rho C_p)_{tf}\left(\left[\tilde{u}\tilde{T}_x+\tilde{v}\tilde{T}_y\right]+\tau_0\left[\left(\tilde{u}\tilde{u}_x+\tilde{v}\tilde{u}_y\right)\tilde{T}_x+\left(\tilde{u}\tilde{v}_x+\tilde{v}\tilde{v}_y\right)\tilde{T}_y+2\tilde{u}\tilde{v}\tilde{T}_{xy}+\tilde{u}^2\tilde{T}_{xx}+\tilde{v}^2\tilde{T}_{yy}\right]\right)$$
$$=\kappa_{tf}\tilde{T}_{yy}+\sigma_{tf}B_0^2\tilde{u}^2+\frac{16\sigma^*}{3k^*}\frac{\partial}{\partial y}\left(\tilde{T}^3\tilde{T}_y\right)+\mu_{tf}\left(\tilde{u}_y\right)^2+\kappa_{tf}\frac{\tilde{U}_w\left(\tilde{T}_w-\tilde{T}_\infty\right)}{x\upsilon_{tf}}\left(A^*f'(\eta)+B^*\frac{\tilde{T}-\tilde{T}_\infty}{\tilde{T}_w-\tilde{T}_\infty}\right) \tag{10.3}$$

Boundary Conditions

$$\begin{bmatrix} \tilde{u}(x) = \tilde{U}_w + L^*\tilde{u}_y,\ \tilde{v}(x) = \tilde{v}_0, k_{tf}\tilde{T}_y(x) = h_f\left(\tilde{T}_w - \tilde{T}\right)\ y = 0 \\ \tilde{u}(x) \mapsto 0, \qquad \tilde{T}(x) \mapsto \tilde{T}_\infty \qquad\qquad y \mapsto \infty \end{bmatrix} \tag{10.4}$$

where μ_{tf}, ρ_{tf}, σ_{tf}, β_0, β_1, and k show the dynamic viscosity, density, electrical conductivity, thermal expansion coefficient, and thermal conductivity of trihybrid nanofluid, respectively. $K_p{}^*$ is the strength of porous media, A^*, B^* is the irregular source/sink coefficient, L^* is the slip length, τ_0 is the thermal lag time factor, and the subscript *tf* stands for THNF.

The Rosseland equation is employed to evaluate the heat flow of radiation, which is given as follows:

$$q_r = -\frac{4\sigma^*}{3k^*}\frac{\partial \tilde{T}^4}{\partial y} \tag{10.5}$$

10.2.2 Similarity Constraints

The appropriate constraints that convert the coupled PDEs into nonlinear ordinary differential equations (ODEs) are described by the following equation:

$$\xi = y\sqrt{\frac{a}{\upsilon_f}},\ \tilde{u} = axf'(\xi),\ \tilde{v} = -\sqrt{a\upsilon_f}f(\xi),\ \theta(\xi) = \frac{\tilde{T} - \tilde{T}_\infty}{\tilde{T}_w - \tilde{T}_\infty}, \tag{10.6}$$

10.3 Converted Equations

Equation (10.1) is identically satisfied by using the similarity variable defined in eq. (10.6), and eqs. (10.2) and (10.3) along with the boundary assumption (10.4) are transformed as follows:

$$f''' = \frac{\varepsilon_2}{\varepsilon_1}\left[f'^2 - ff'' + \frac{\varepsilon_3}{\varepsilon_2}Mf' + \frac{\varepsilon_1}{\varepsilon_2}\lambda f' - \frac{\varepsilon_4}{\varepsilon_2}\frac{\mathrm{Cos}\beta\ Gr\ \theta}{\mathrm{Re}_x^2}(1 + \varepsilon_4\omega\theta)\right] \tag{10.7}$$

$$- \Pr\varepsilon_5 f\theta' + \Pr\tau\varepsilon_5\left(ff'\theta + f^2\theta''\right) + \varepsilon_6\theta'' + MEc\Pr\varepsilon_3 f'^2$$
$$+ Rd\left[3\{1 + \theta(\theta_w - 1)\}^2(\theta_w - 1)\theta'^2 + \{1 + \theta(\theta_w - 1)\}^3\theta''\right] + \varepsilon_1 Ec\Pr f''^2 + \frac{\varepsilon_2\varepsilon_6}{\varepsilon_1}\left(A^*f' + B^*\theta\right) \tag{10.8}$$

$\varepsilon_1 = \frac{\mu_{tf}}{\mu_f}$, $\varepsilon_2 = \frac{\rho_{tf}}{\rho_f}$, $\varepsilon_3 = \frac{\sigma_{tf}}{\sigma_f}$, $\varepsilon_4 = \frac{(\rho\beta)_{tf}}{(\rho\beta)_f}$, $\varepsilon_5 = \frac{(\rho C_p)_{tf}}{(\rho C_p)_f}$, $\varepsilon_6 = \frac{\kappa_{tf}}{\kappa_f}$, are the thermophysical parameters, $\chi = \frac{Gr}{\mathrm{Re}_x^2}$ mixed convection parameter, $M = \frac{\sigma_f B_0^2}{\rho_f a}$ magnetic parameter, $Ec = \frac{(U_W)^2}{(T_W - T\infty)Cp}$ dissipation parameter, $Rd = \frac{16\sigma^* T_\infty^3}{3k^* \kappa_f}$ radiation parameter, porosity factor is described as $\lambda = \frac{\nu_f}{a k_p}$, $\omega = \beta_f\left(\tilde{T}_w - \tilde{T}_\infty\right)$ nonlinear convection factor, $Pr = \frac{\nu_f (\rho C_p)_f}{\kappa_f}$ Prandtl number, $L = L^* \sqrt{\frac{a}{\nu_f}}$ defines the jump factor, $Re = \frac{U_W x}{\nu_f}$ is local Reynold's number, and $Bi = \frac{h_f}{a_f}\sqrt{\frac{\nu_f}{a}}$ describes the Biot number.

10.4 Numerical Technique

Using the numerical solver known as the BVP4C solver, the changed ODEs (10.7) and (10.8), subject to boundary conditions (10.9), are solved. In this approach, firstly, the set of ODEs is transformed to a set of first-order equations, and this is done by using these variables:

$$f = t_1^*,\ f' = t_2^*,\ f'' = t_3^*,\ \theta = t_4^*,\ \theta' = t_5^* \tag{10.9}$$

Using eq. (10.9), eqs. (10.7) and (10.8) are rewritten in the following form:

$$tt = \frac{\varepsilon_2}{\varepsilon_1}\left[t^{*2} - tt + \frac{\varepsilon_3}{\varepsilon_2} Mf' + \frac{\varepsilon_1}{\varepsilon_2}\alpha f' - \frac{\varepsilon_4}{\varepsilon_2}\frac{\cos\beta Gr}{\mathrm{Re}_x^2}(1 + \varepsilon_4\Omega)\right] \tag{10.10}$$

$$tt_2 = (Pr\varepsilon_5 t_1^* t_5^*) - ((Pr\tau\varepsilon_5 t_1^* t_2^* t_4^*) - M*Ec*Pr*t_2^{*2} -$$

$$Rd\left(3(1 + t_4^* * (\theta_w - 1)) * (1 + t_4^* * (\theta_w - 1)^2 * t_5^{*2}\right) -$$

$$\frac{\varepsilon_1 * Ec * \mathrm{Pr} * t_4^{*3} - \left(\frac{\varepsilon_2\varepsilon_6}{\varepsilon_1}\right)(A^* * t_2^* + B^* * t_4^*)}{\left(-Pr * \varepsilon_5 * \tau * t_1^{*2}\right) + \varepsilon_6 + Rd\left(1 + t_4^* + (1 + t_4^* * (\theta_w - 1)^3\right)} \tag{10.11}$$

The graphical code validation is done by a previously published study. The study shows good agreement (see Table 10.1). The three nanoparticles are taken from 10% of the volume fraction, and the base fluid is kerosene oil. Table 10.2 shows the thermophysical attributes for finding the value.

Table 10.1: Comparison of the values of Nusselt's number for the various values of magnetic field (M) and the remaining parameters are $Pr = 21,\ \lambda = \omega = Rd = \tau = S = Bi = L = \chi = 0$.

M	Shaiq et al. [41]	Present result
0.5	1.2247	1.22479
1	1.4142	1.41423
1.5	1.5811	1.58115
2	1.7321	1.73206

Table 10.2: Thermophysical correlation of properties of ternary hybrid nanofluid [19, 39].

Density	$\frac{\rho_{\text{Thnf}}}{\rho_f} = (1-\delta_1)\left[(1-\delta_2)\left\{(1-\delta_3)+\delta_3\frac{\rho_3}{\rho_f}\right\}+\delta_2\frac{\rho_2}{\rho_f}\right]+\delta_1\frac{\delta_1}{\rho_f}$
Thermal expansion	$\frac{(\rho\beta)_{\text{Thnf}}}{(\rho\beta)_f} = \delta_{\text{TiO}_2}\frac{(\rho\beta)_{\text{TiO}_2}}{(\rho\beta)_f}+(1-\delta_{\text{TiO}_2})\left[(1-\delta_{\text{SiO}_2})\left\{(1-\delta_{\text{MoS}_2})+\delta_{\text{MoS}_2}\frac{(\rho\beta)_{\text{MoS}_2}}{(\rho\beta)_f}\right\}+\delta_{\text{SiO}_2}\frac{(\rho\beta)_{\text{SiO}_2}}{(\rho\beta)_f}\right]$
Heat capacitance	$\frac{(\rho C_p)_{\text{Thnf}}}{(\rho C_p)_f} = \delta_1\frac{(\rho C_p)_{\text{TiO}_2}}{(\rho C_p)_f}+(1-\delta_1)\left[(1-\delta_2)\left\{(1-\delta_3)+\delta_3\frac{(\rho C_p)_{\text{MoS}_2}}{(\rho C_p)_f}\right\}+\delta_2\frac{(\rho C_p)_{\text{SiO}_2}}{(\rho C_p)_f}\right]$
Electrical conductivity	$\frac{\sigma_{Tf}}{\sigma_{hf}} = \left[1+\frac{3(\alpha_1-1)\varphi_3}{(\alpha_1+2)-(\alpha_1-1)\varphi_2}\right],\ \frac{\sigma_{hf}}{\sigma_{nf}} = \left[1+\frac{3(\alpha_2-1)\varphi_2}{(\alpha_2+2)-(\alpha_2-1)\varphi_2}\right]$ $\frac{\sigma_{nf}}{\sigma_f} = \left[1+\frac{3(\alpha_3-1)\varphi_1}{(\alpha_3+2)-(\alpha_3-1)\varphi_1}\right],$ where $\alpha_1 = \frac{\sigma_3}{\sigma_{hf}},\ \alpha_2 = \frac{\sigma_2}{\sigma_{nf}},\ \alpha_3 = \frac{\sigma_1}{\sigma_f}$
Dynamic viscosity	$\frac{\mu_{tf}}{\mu_f} = \frac{1}{(1-\delta_1)^{2.5}(1-\delta_2)^{2.5}(1-\delta_3)^{2.5}}$
Thermal conductivity	$\frac{k_{nf}}{k_f} = \frac{1-\delta_1+2\delta_1\left(\frac{k_3}{k_3-k_f}\right)\ln\frac{k_3+k_f}{2k_f}}{1-\delta_1+2\delta_1\left(\frac{k_f}{k_3-k_f}\right)\ln\frac{k_3+k_f}{2k_f}}$ $\frac{k_{hf}}{k_{nf}} = \frac{1-\delta_2+2\delta_2\left(\frac{k_2}{k_2-k_{nf}}\right)\ln\frac{k_2+k_{nf}}{2k_{nf}}}{1-\delta_1+2\delta_2\left(\frac{k_{nf}}{k_2-k_{nf}}\right)\ln\frac{k_2+k_{nf}}{2k_{nf}}}$ $\frac{k_{tf}}{k_{hf}} = \frac{1-\delta_3+2\delta_3\left(\frac{k_1}{k_1-k_{hf}}\right)\ln\frac{k_1+k_{hf}}{2k_{hf}}}{1-\delta_3+2\delta_3\left(\frac{k_{hf}}{k_1-k_{hf}}\right)\ln\frac{k_1+k_{hf}}{2k_{hf}}}$

10.5 Results and Discussion

This section demonstrates the physical interference of outcomes following the successful computation of this problem using numerical methods. Table 10.2 contains the physical characteristics of THF. Table 10.3 presents the numerical analysis of lagged neural network (LNN) and local sensitivity function (LSF) for certain approximations.

The consequence of the magnetic parameter (M) on the temperature and velocity fields is shown in Figures 10.2 and 10.3. The velocity boundary layer thickness decreases as the M increases because the stream velocity component $f'(\eta)$ decreases. The externally applied magnetic field greatly impacts the electrically conducting fluid's velocity profile, which slows the fluid flow by applying a strong Lorentz force resistance to its motion. The fluid temperature profile $\theta(\eta)$ rises as the M and fluid resistance do, which causes the thermal boundary layer thickness to grow. By increasing the particle motion and raising the fluid's temperature, the magnetic field increases thermal energy and the thickness of the thermal boundary layer, which reduces heat transmission from the sheet.

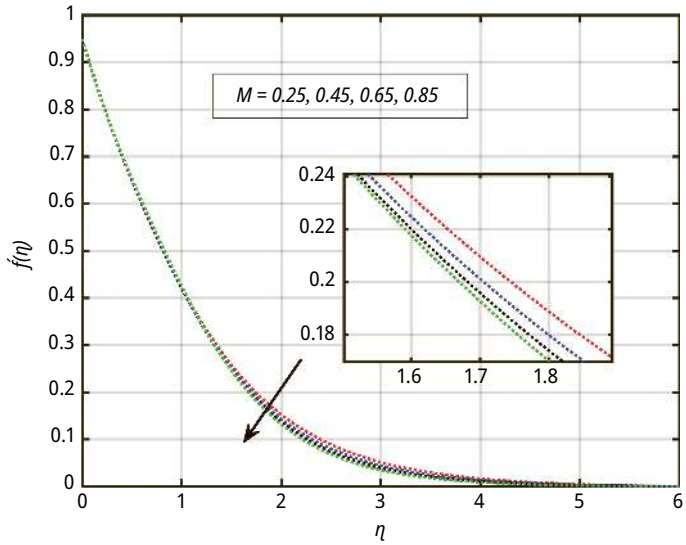

Figure 10.2: The effect of M on velocity profile.

Figures 10.4 and 10.5 exemplify the consequences of altering the porosity parameter (λ) on the thermal and velocity profiles of the nanofluid. A thin boundary layer was observed when the viscosity was increased. Also, it demonstrates that when porosity varies, it results in the growth of the energy profile. Physically, a high-value porosity parameter value enhances the friction force between the liquid layer, thereby reducing flow velocity and enhancing temperature distribution.

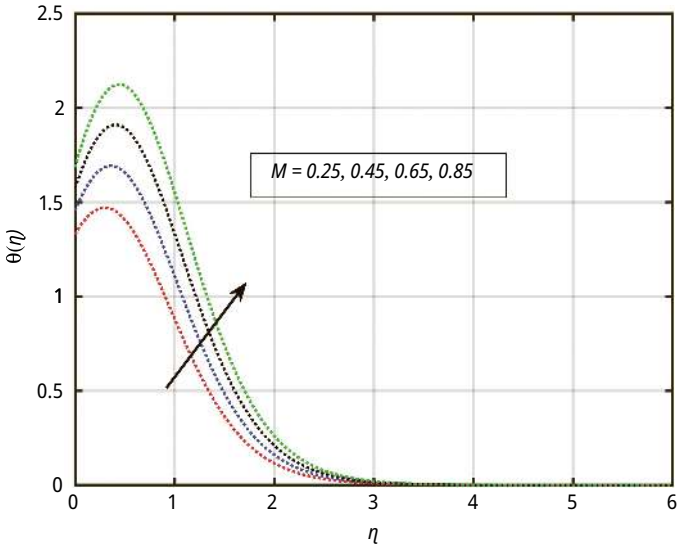

Figure 10.3: The effect of M on thermal profile.

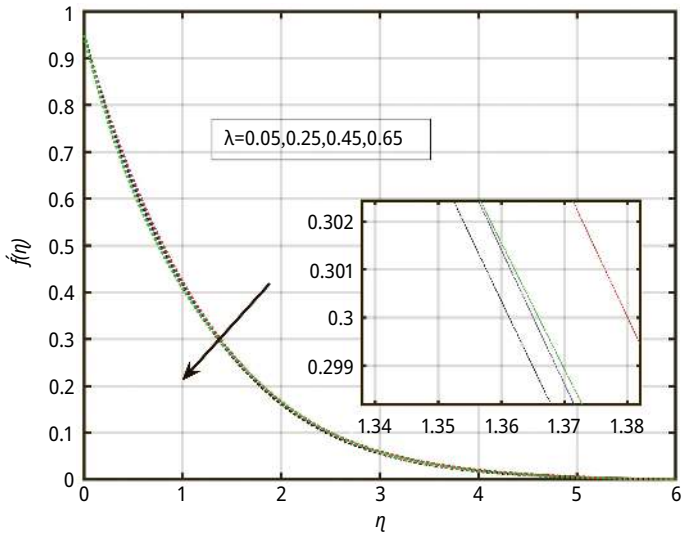

Figure 10.4: The effect of λ on velocity profile.

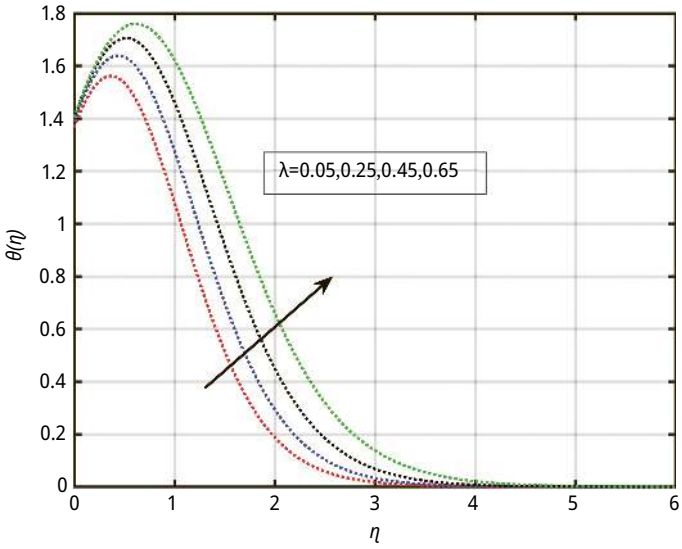

Figure 10.5: The effect of λ on thermal profile.

Figures 10.6 and 10.7 address the influence of the quadratic convection parameter (ω) on dimensionless velocity and thermal profile. The curve of velocity and thermal profiles declines as ω increases. At an elevated value of the quadratic convection parameter, resistance from increased viscosity may oppose the buoyancy force and diminish

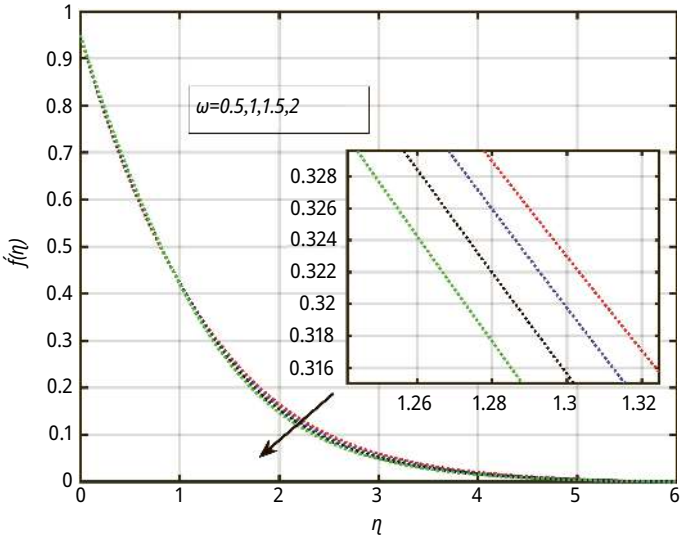

Figure 10.6: The effect of ω on velocity profile.

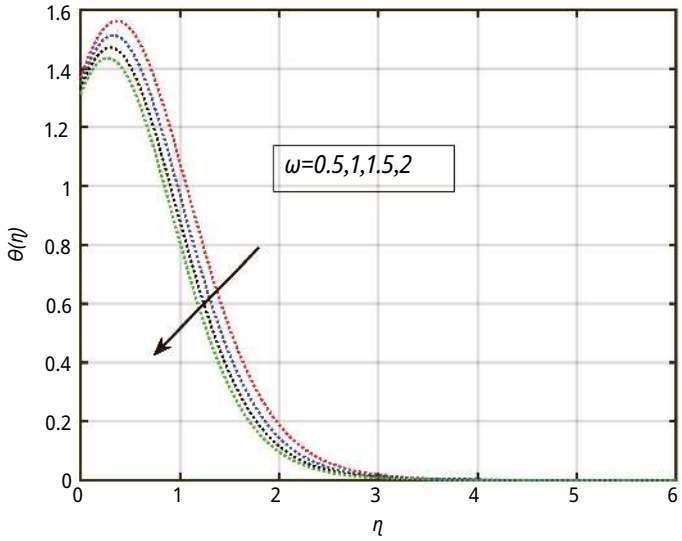

Figure 10.7: The effect of ω on thermal profile.

velocity. An elevated value of the quadratic convection parameter amplifies convection intensity, improving HT, and resulting in a reduced thermal boundary layer.

Figures 10.8 and 10.9 illustrate the impact of modifying the mixed convection parameter (χ) on temperature. In forced convection-dominated flow, the velocity is

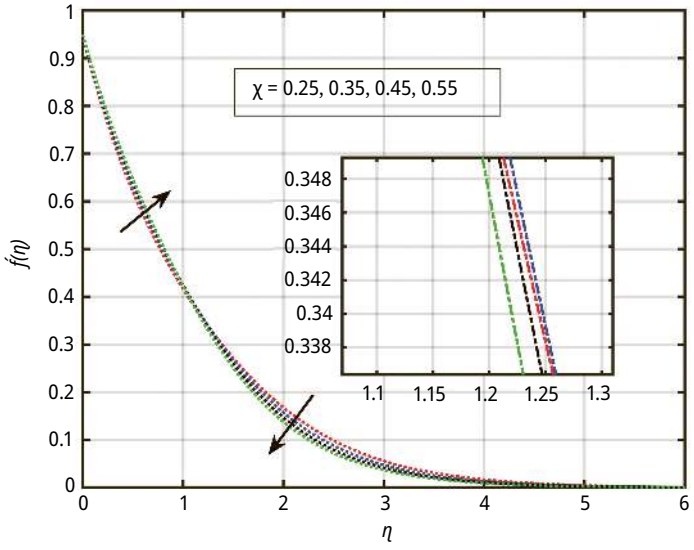

Figure 10.8: The effect of χ on velocity profile.

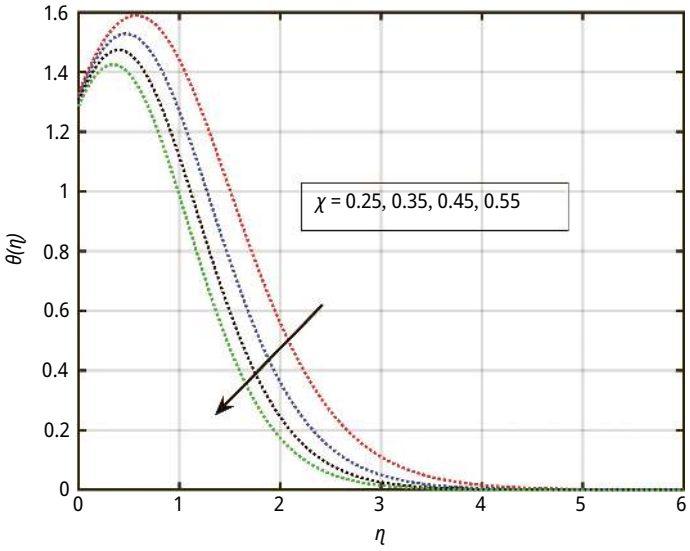

Figure 10.9: The effect of χ on thermal profile.

mostly governed by external flow (Reynold's number). As a rise in (χ) from 0.25 to 0.55, natural convection starts to oppose the external flow, potentially introducing flow resistance. This resistance diminishes the velocity of the fluid. Moreover, the reduced thickness of the thermal boundary layer results in an intensified viscosity effect adjacent to the surface, hence lowering the velocity profile. As forced convection predominantly improves momentum transfer rather than thermal diffusion, heat dissipation becomes more effective, hence lowering the thermal profiles.

Figures 10.10 and 10.11 illustrate how the radiation factor (R_d) affects the temperature and velocity profiles. It demonstrates that a higher magnitude of R_d parameter promotes HT inside the fluid. The positive effect of the nonlinear thermal radiation parameter on the temperature curve of the nanofluid leads to effects. Firstly, it facilitates HT over the boundary layer at all distances, or, in other words, it continuously raises the temperature of the boundary layer. It generates thermal energy in fluid nanoparticles, due to their thermal conductivity, and improves thermal diffusion and transmission throughout the fluid.

The trends of the suction parameter (S) on dimensionless velocity and thermal profiles observed in Figures 10.12 and 10.13. On amplifying the value of S from 0.95 to 1.75, both the velocity and temperature diminish. The momentum transfer toward the surface boosts as suction rises, which reduces velocity by means of more resistance against fluid extraction close to the heated surface and reduces heat retention, therefore affecting the dispersion of temperature. This effect is especially important in trihybrid nanofluids, in which the increased convective cooling caused by suction balances the improved thermal conductivity of nanoparticles. As a result, thermal boundary layer

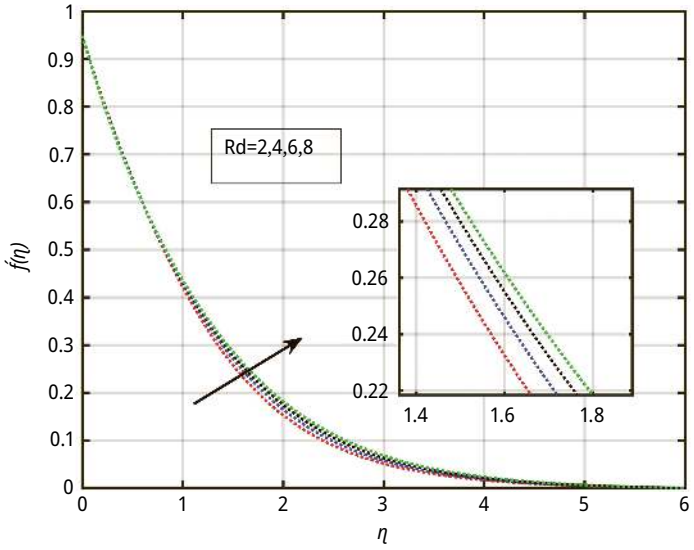

Figure 10.10: The effect of R_d on velocity profile.

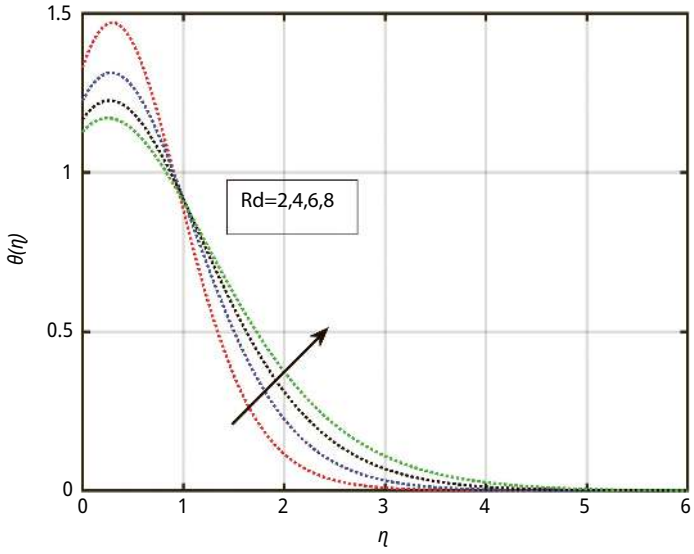

Figure 10.11: The effect of R_d on thermal profile.

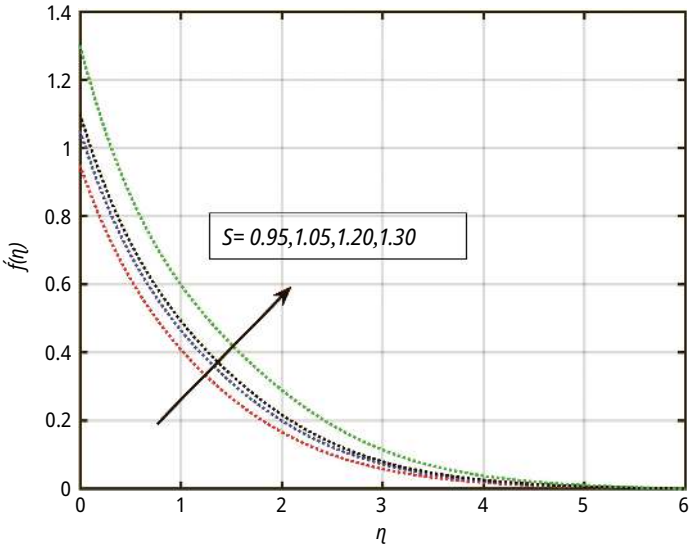

Figure 10.12: The effect of S on velocity profile.

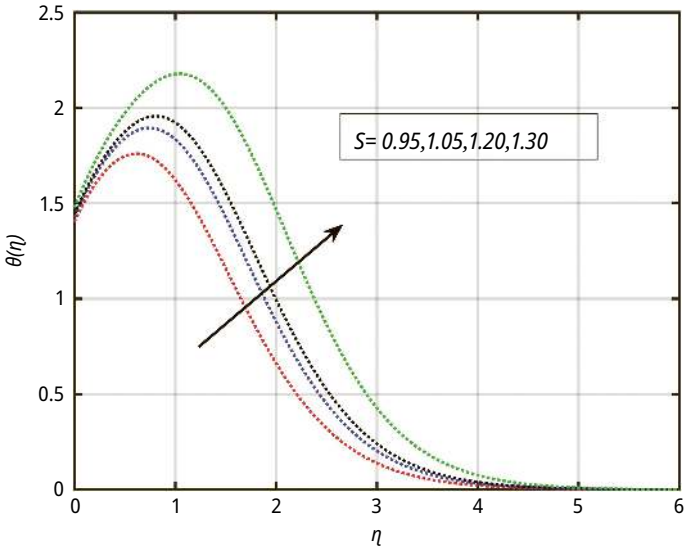

Figure 10.13: The effect of S on thermal profile.

contraction and momentum suppression taken together produce an overall decrease in both velocity and temperature profiles.

Figures 10.14 and 10.15 illustrate the relationship between the Biot number (Bi), the velocity, and the temperature profile. The Biot number positively correlates with both velocity and temperature. Because of increased convection, heat transmission from the wall to the nanofluid improves as Bi boost. This elevates the temperature gradients close to the wall, raising the fluid temperature. The temperature dependency of viscosity in a fluid causes the fluid viscosity to drop as temperature rises. The fluid viscosity decreases, and its thermal expansion increases as the momentum boundary layer becomes more active and the velocity profile increases.

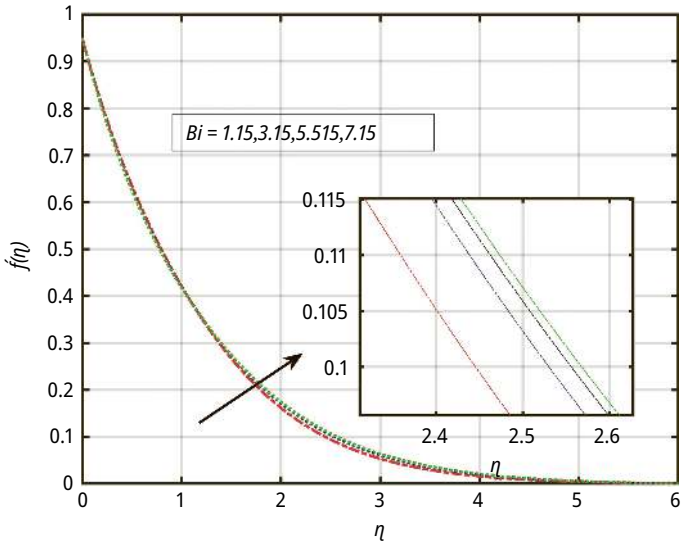

Figure 10.14: The effect of Bi on velocity profile.

Figures 10.16 and 10.17 illustrate the trends of the thermal relaxation parameter on the dimensionless profile. Increasing the value of τ from 0.05 to 0.35 results in a decrease in the heat conduction rate due to the lag in the heat flux reaction. As a result, the temperature distribution in the HNF decreases. In thermal boundary layers, diminished HT decreases thermal diffusion, leading to a smaller boundary layer and reduced fluid velocity adjacent to the surface.

Figures 10.18 and 10.19 exemplify the influence of altering the slip parameter (L) on the thermal and velocity profiles of the nanofluid. The slip provides less resistance to flow, resulting in a velocity increase. Moreover, diminished friction between particles results in a reduced conversion of mechanical energy into heat near the wall, hence altering the temperature gradient.

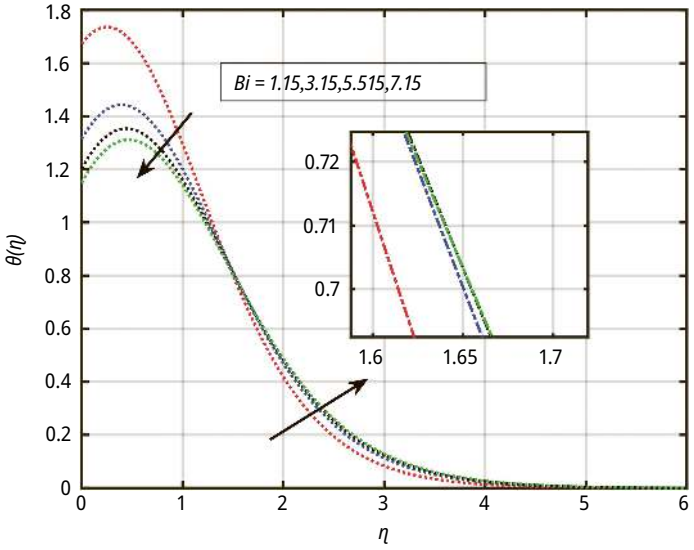

Figure 10.15: The effect of *Bi* on thermal profile.

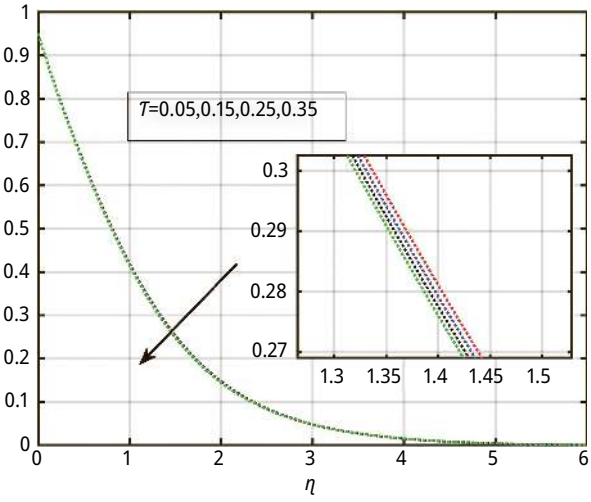

Figure 10.16: The effect of τ on velocity profile.

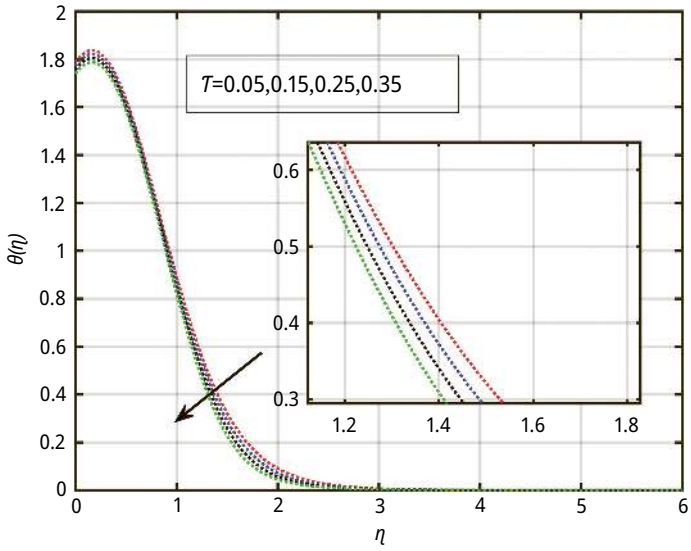

Figure 10.17: The effect of τ on thermal profile.

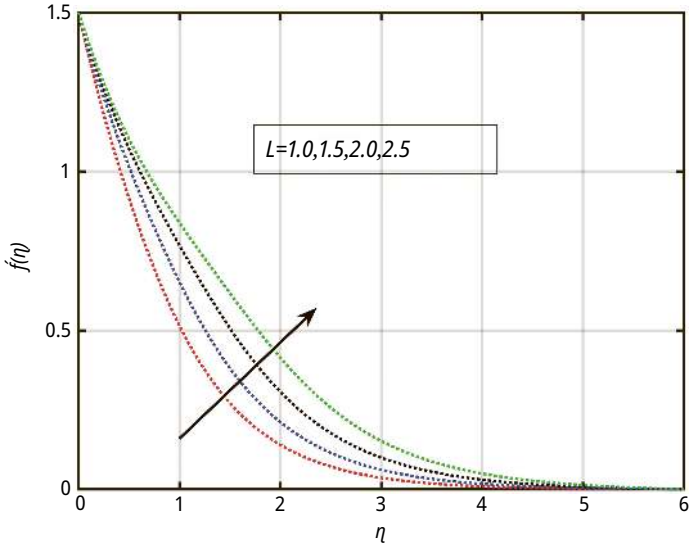

Figure 10.18: The effect of L on velocity profile.

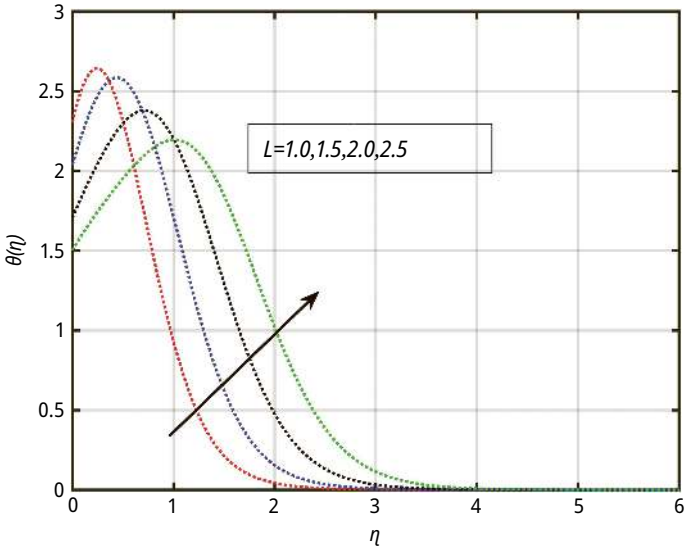

Figure 10.19: The trend of L on thermal profile.

The numerical values of LSF and LNN are tabulated (Table 10.3) for different factors. The HT coefficient is higher for a large magnitude of M. The reduction of LNN is found by the convection parameter. The LSF is positively correlated with M, and negatively correlated with λ. Radiation parameter is positively correlated with the drag and HT coefficient.

Table 10.3: Numerical values of LSF and LNN for trihybrid nanofluid.

M	λ	ω	χ	Rd	S	Bi	LSF	LNN
0.25	0.05	0.5	0.25	2	0.95	1.15	−0.6925	1.7764
0.45							−0.7004	2.4166
0.65							−0.7054	3.0181
0.85							−0.7082	3.5865
	0.25						−0.7163	1.9980
	0.45						−0.7393	2.1834
	0.65						−0.7621	2.3310
		1					−0.6646	1.4805
		1.5					−0.6429	1.2734
		2					−0.6251	1.1169
			0.35				−0.6653	2.0056
			0.45				−0.6428	1.7873
			0.55				−0.6234	1.5944
				4			−0.7085	3.5708
				6			−0.7173	3.8493

Table 10.3 (continued)

M	*λ*	*ω*	*χ*	*Rd*	*S*	*Bi*	LSF	LNN
				8			−0.7230	3.8786
					1.05		−0.7178	2.8678
					1.20		−0.8694	2.8883
					1.30		−0.9303	2.8833
						3.15	−0.9653	2.7291
						5.15	−0.9752	2.8192
						7.15	−0.9797	2.8538

10.6 Conclusion

This chapter addresses the numerical simulation to study the impression of nonlinear convection, nonthermal radiation, Joule heating, and magnetic field for THNF over the plate. To analyze the nonlinear phenomena of HT, the Cattaneo-Christov model is used. The coupled equations are converted into nondimensional equations using the similarity variable. The nonlinear ODEs are solved by the BVP4C solver. The Xue model is used for finding the thermophysical properties of THF. The chapter concludes the following points:

1. The trihybrid is formulated using three different shapes of nanoparticles. The Xue model is responsible for a better thermal conductivity value.
2. The increment in M from 0.25 to 0.85, resulting in a HT rate of 25% and reducing the drag force by 10%.
3. The velocity trace shows a decrement in boosting the values of the quadratic convection parameter, porosity parameter, and thermal relaxation parameter.
4. This comprehensive study was conducted in situations with heat sources and suction.

References

[1] Siddheshwar, P. G., & Mahabaleshwar, U. S. (2005). Effects of radiation and heat source on MHD flow of a viscoelastic liquid and heat transfer over a stretching sheet. International Journal of Non-Linear Mechanics, 40(6), 807–820.

[2] Mukhopadhyay, S., & Layek, G. C. (2008). Effects of thermal radiation and variable fluid viscosity on free convective flow and heat transfer past a porous stretching surface. International Journal of Heat and Mass Transfer, 51(9–10), 2167–2178.

[3] Kumar, M. A., Reddy, Y. D., Rao, V. S., & Goud, B. S. (2021). Thermal radiation impact on MHD heat transfer natural convective nanofluid flow over an impulsively started vertical plate. Case Studies in Thermal Engineering, 24, 100826.

[4] Bejawada, S. G., & Nandeppanavar, M. M. (2023). Effect of thermal radiation on magnetohydrodynamics heat transfer micropolar fluid flow over a vertical moving porous plate. Experimental and Computational Multiphase Flow, 5(2), 149–158.
[5] Sreedevi, P., Reddy, P. S., & Suryanarayana Rao, K. V. (2024). Effect of magnetic field and radiation on heat transfer analysis of nanofluid inside a square cavity filled with silver nanoparticles: Tiwari–Das model. Waves in Random and Complex Media, 34(2), 804–822.
[6] Allouche, B., Djezzar, M., Allouche, S., & Tayebi, T. Natural convection heat transfer in an eccentric annulus filled with hybrid nanofluid under the influence of thermal radiation and heat generation/absorption. Numerical Heat Transfer, Part A: Applications, vol. 2024, 1–21, 2024. https://doi.org/10.1080/10407782.2024.2386607
[7] Mahabaleshwar, U. S., Sneha, K. N., Chan, A., & Zeidan, D. (2022). An effect of MHD fluid flow heat transfer using CNTs with thermal radiation and heat source/sink across a stretching/shrinking sheet. International Communications in Heat and Mass Transfer, 135, 106080.
[8] Alzahrani, H. A., Alsaiari, A., Madhukesh, J. K., Naveen Kumar, R., & Prasanna, B. M. Effect of thermal radiation on heat transfer in plane wall jet flow of Casson nanofluid with suction subject to a slip boundary condition. Waves in Random and Complex Media, 35(1), 1–18, 2022.
[9] Saad, A. A., Martinez, C., & Trice, R. W. (2023). Radiation heat transfer during hypersonic flight: A review of emissivity measurement and enhancement approaches of ultra-high temperature ceramics. International Journal of Ceramic Engineering & Science, 5(2), e10171.
[10] Karthik, K., Jk, M., Kiran, S., Kv, N., Prasannakumara, B. C., & Fehmi, G. Impacts of thermophoretic deposition and thermal radiation on heat and mass transfer analysis of ternary nanofluid flow across a wedge. International Journal of Modelling and Simulation, 45(1) 1–13, 2024.
[11] Alfvén, H. (1942). Existence of electromagnetic-hydrodynamic waves. Nature, 150(3805), 405–406.
[12] Ishak, A., Nazar, R., & Pop, I. (2008). Magnetohydrodynamic (MHD) flow and heat transfer due to a stretching cylinder. Energy Conversion and Management, 49(11), 3265–3269.
[13] Das, S. S., Satapathy, A., Das, J. K., & Panda, J. P. (2009). Mass transfer effects on MHD flow and heat transfer past a vertical porous plate through a porous medium under oscillatory suction and heat source. International Journal of Heat and Mass Transfer, 52(25–26), 5962–5969.
[14] Gul, A., Khan, I., Shafie, S., Khalid, A., & Khan, A. (2015). Heat transfer in MHD mixed convection flow of a ferrofluid along a vertical channel. PloS One, 10(11), e0141213.
[15] Ellahi, R., Alamri, S. Z., Basit, A., & Majeed, A. (2018). Effects of MHD and slip on heat transfer boundary layer flow over a moving plate based on specific entropy generation. Journal of Taibah University for Science, 12(4), 476–482.
[16] Reddy, Y. D., Goud, B. S., Nisar, K. S., Alshahrani, B., Mahmoud, M., & Park, C. (2023). Heat absorption/generation effect on MHD heat transfer fluid flow along a stretching cylinder with a porous medium. Alexandria Engineering Journal, 64, 659–666.
[17] Akbar, A., Ullah, H., Raja, M. A. Z., Nisar, K. S., Islam, S., & Shoaib, M. A design of neural networks to study MHD and heat transfer in two phase model of nano-fluid flow in the presence of thermal radiation. Waves in Random and Complex Media, vol. 2024 1–24, 2022. https://doi.org/10.1080/17455030.2022.2152905
[18] Mirzaei, A., Jalili, P., Afifi, M. D., Jalili, B., & Ganji, D. D. (2023). Convection heat transfer of MHD fluid flow in the circular cavity with various obstacles: Finite element approach. International Journal of Thermofluids, 20, 100522.
[19] Li, S., Faizan, M., Ali, F., Ramasekhar, G., Muhammad, T., Khalifa, H. A. E. W., & Ahmad, Z. (2024). Modelling and analysis of heat transfer in MHD stagnation point flow of Maxwell nanofluid over a porous rotating disk. Alexandria Engineering Journal, 91, 237–248.
[20] Reddy, Y. D., Reddy, N. N., & Goud, B. S. (2024). Suction and double stratification effect on unsteady MHD heat transfer nanofluid flow over a flat surface. Results in Engineering, 23, 102431.

[21] Adel, M., Khader, M. M., & Ahmad, H. (2024). MHD nanofluid flow and heat transfer caused by a stretching sheet that is heated convectively: An approximate solution using ADM. Case Studies in Thermal Engineering, 60, 104683.
[22] Reddy, Y. D., & Mangamma, I. (2024). Significance of radiation and chemical reaction on MHD heat transfer nanofluid flow over a nonlinearly porous stretching sheet with nonuniform heat source. Numerical Heat Transfer, Part A: Applications, 85(18), 2940–2966.
[23] Hayat, T., Qasim, M., & Mesloub, S. (2011). MHD flow and heat transfer over permeable stretching sheet with slip conditions. . International Journal for Numerical Methods in Fluids, 66(8), 963–975.
[24] Swain, B. K., Parida, B. C., Kar, S., & Senapati, N. (2020). Viscous dissipation and joule heating effect on MHD flow and heat transfer past a stretching sheet embedded in a porous medium. Heliyon, 6 (10), 1–8.
[25] Khan, U., Mohyud-Din, S. T., & Bin-Mohsin, B. (2016). Convective heat transfer and thermo-diffusion effects on flow of nanofluid towards a permeable stretching sheet saturated by a porous medium. Aerospace Science and Technology, 50, 196–203.
[26] Khan, M. R., Elkotb, M. A., Matoog, R. T., Alshehri, N. A., & Abdelmohimen, M. A. (2021). Thermal features and heat transfer enhancement of a Casson fluid across a porous stretching/shrinking sheet: Analysis of dual solutions. . Case Studies in Thermal Engineering, 28, 101594.
[27] Kausar, M. S., Hussanan, A., Waqas, M., & Mamat, M. (2022). Boundary layer flow of micropolar nanofluid towards a permeable stretching sheet in the presence of porous medium with thermal radiation and viscous dissipation. Chinese Journal of Physics, 78, 435–452.
[28] Akbar, N. S., Zamir, T., Akram, J., Noor, T., & Muhammad, T. (2024). Simulation of hybrid boiling nano fluid flow with convective boundary conditions through a porous stretching sheet through Levenberg Marquardt artificial neural networks approach. International Journal of Heat and Mass Transfer, 228, 125615.
[29] Warke, A. S., Ramesh, K., Mebarek-Oudina, F., & Abidi, A. Numerical investigation of the stagnation point flow of radiative magnetomicropolar liquid past a heated porous stretching sheet. Journal of Thermal Analysis and Calorimetry, 147, 1–12, 2022. https://doi.org/10.1007/s10973-021-10976-z
[30] Babu, D. H., Tarakaramu, N., Satya Narayana, P. V., Sarojamma, G., & Makinde, O. D. (2021). MHD flow and heat transfer of a Jeffrey fluid over a porous stretching/shrinking sheet with a convective boundary condition. International Journal of Heat & Technology, 39(3), 885–894.
[31] Dharmaiah, G., Mebarek-Oudina, F., Balamurugan, K. S., & Vedavathi, N. (2024). Numerical analysis of the magnetic dipole effect on a radiative ferromagnetic liquid flowing over a porous stretched sheet. Fluid Dyn Mater Process, 20(2), 293–310.
[32] Nabwey, H. A., & Mahdy, A. (2021). Transient flow of micropolar dusty hybrid nanofluid loaded with Fe3O4-Ag nanoparticles through a porous stretching sheet. Results in Physics, 21, 103777.
[33] Khattak, S., Ahmed, M., Abrar, M. N., Uddin, S., Sagheer, M., & Farooq Javeed, M. Numerical simulation of Cattaneo–Christov heat flux model in a porous media past a stretching sheet. Waves in Random and Complex Media, 35(1), 1–20, 2022, 1230–1249.
[34] Kim, J. Y., Lee, K. H., Shin, J., Park, S. H., Kang, J. S., Han, K. S., & Sung, Y. E. (2014). Highly ordered and vertically oriented TiO2/Al2O3 nanotube electrodes for application in dye-sensitized solar cells. Nanotechnology, 25(50), 504003.
[35] Chun Chen, P., Chon Chen, C., & Hsun Chen, S. (2017). A review on production, characterization, and photocatalytic applications of TiO2 nanoparticles and nanotubes. Current Nanoscience, 13(4), 373–393.
[36] Soni, S. K., & Thomas, B. (2020). Influence of TiO2 and MWCNT nanoparticles dispersion on microstructure and mechanical properties of Al6061 matrix hybrid nanocomposites. Materials Research Express, 6(12), 1265f3.

[37] Manigandan, S., Sarweswaran, R., Devi, P. B., Sohret, Y., Kondratiev, A., Venkatesh, S., & Joshua, J. J. (2020). Comparative study of nanoadditives TiO2, CNT, Al2O3, CuO and CeO2 on reduction of diesel engine emission operating on hydrogen fuel blends. Fuel, 262, 116336.

[38] Javadipour, S., Shokuhfar, A., Homayouni, K., Heidary, Z., & Rezaei, F. (2022, December). Investigation into the size distribution of Al2O3-ZnO nanoparticles dispersed in DI water and following the impact of CNTs on the stability, heat transfer, and electricity transfer of Al2O3-ZnO-CNT hybrid nanofluid. In Defect and Diffusion Forum, Vol. 420, pp. 172–192. Trans Tech Publications Ltd.

[39] Trandabat, A. F., Ciobanu, R. C., Schreiner, O. D., Aradoaei, M., & Aradoaei, S. T. (2024). Manufacturing of TiO2, Al2O3 and Y2O3 Ceramic Nanotubes for application as electrodes for printable electrochemical sensors. Crystals, 14(5), 454.

[40] Khashan, K. S., Hadi, A. A., & Hasan, I. F. (2024). Nanosecond laser-supported decoration of titanium oxide nanoparticles on multiwalled carbon nanotubes. Plasmonics, 19(1), 301–310.

Sham Bansal

Chapter 11
Numerical Investigation of Non-Darcy MHD Boundary Layer Nanofluids Flow Over a Nonlinear Stretching Surface

Abstract: This study investigates the influence of ferrous ferric oxide, copper, and silver nanoparticles on a water-based nanofluid's magnetohydrodynamics boundary layer flow via a nonlinear stretched surface contained in a porous media. Employing an appropriate similarity transformation technique, the complex equations governing the flow are transformed into simpler ones, which are then numerically simplified using a finite difference implicit Keller box approach. The investigation considers various factors such as the stretching parameter, magnetic parameter, Eckert number, Soret number, and the volume fraction of nanoparticles, analysing their effects on temperature, velocity, and nanoparticle concentration. The finding shows that a higher nonlinear stretching parameter thins all three boundary layers and strengthens both the heat transfer rate and skin friction coefficient. Conversely, a stronger magnetic field led to thicker temperature and concentration boundary layers due to heat generation by the Lorentz force, and leads to a reduction in the heat transfer rate, while concurrently increasing the coefficient of skin friction. A higher Soret parameter leads to an enhancement in both the fluid's concentration and velocity, but its temperature falls. The fluid's thermal conductivity rises with an increase in the volume fraction. In contrast, the nanofluid's velocity profiles indicate the reverse behavior. The concentration and temperature rise with increasing Eckert number, causing the nanoparticles to disperse away from the wall more quickly, but the nanofluid's velocity reduces. Furthermore, a higher value of the permeability parameter accelerates heat transfer but reduces the skin friction coefficient.

Keywords: nanofluids, magnetohydrodynamics, porous media, Keller-box method

11.1 Introduction

The analysis of nanofluids in the context of magnetohydrodynamics (MHD) boundary layer flow via nonlinear stretched sheet within porous media has garnered significant focus in the past decade due to its crucial role in various engineering applications,

Sham Bansal, Department of Mathematics, Mata Gujri College, Fatehgarh Sahib, Punjab, India, e-mail: shambansal2010@gmail.com

https://doi.org/10.1515/9783111723464-011

including heat exchangers, coatings, and the cooling of electronic devices. This section summarizes key studies and advancements in this multidisciplinary field. Utilizing a comprehensive mathematical model and numerical methods, our research delves into the complex physics governing multifaceted systems. The use of these dynamic models in mathematics is becoming more sophisticated. Scientists in the fields of mathematics, numerical computation, and modeling face exciting challenges in developing numerical or analytical solutions. Numerous scholars have expressed keen interest in modelling nonlinear magnetohydrodynamic fluids in porous media. The Keller box finite difference technique has been utilized in current research.

The intricate interplay between nanofluids, MHD, porous media, and nanoparticle additives has gained significant focus due to their synergistic effect in improving heat transmission and fluid flow across various engineering applications. Nanofluids exhibit enhanced thermal and flow properties in comparison to their base fluids. This enhancement corresponds to the strong thermal conductivity and heating capabilities of nanoparticles, making nanofluids suitable for heat transport applications. Hayat et al. [1] researched the potential effects of a nanofluid on a stretched sheet in a first-order chemical process. Bhargava et al. [2] analyzed the nanofluid's boundary layer flow using an angled stretching sheet and showed that an increase in convection parameter decreases nanoparticle volume fraction. Ferdows et al. [3] researched the flow of a stretched sheet through a viscous nanofluid in the vertical direction through porous media. Chamkha et al. [4] provided valuable insights into optimizing heat transfer processes, contributing significantly to the understanding of nanofluid dynamics. Anusha et al. [5] studied that there was an enhancement in thermal properties with the appearance of various nanoparticles. Hamad [6] studied an exact solution of MHD convection via a stretched sheet using nanofluid flow.

MHD is the area of CFD that explores the behavior of fluids with electrical conductivity. Magnetohydrodynamic fluid analysis has grown into the center of extensive research in recent years for its vast spectrum of technological and commercial applications. The combination of MHD with nanofluids has opened up intriguing possibilities for controlling fluid flow and heat transfer. Sawaya et al. [7] conducted an experimental computation of Hall parameters for electric solutions in a closed loop. The Hall parameter was calculated by means of a theoretical single-dimensional model, and the open-circuit voltage was measured to compute the value. However, it was not considered in these experiments that ion-slip currents were present. Ion rutting effects are typically ignored; thus, ion rutting is often overlooked. Bhatti et al. [8] have given a detailed explanation of the ion slip phenomena. Cai et al. [9] analyzed MHD convection heat transfer via a permeable stretched wedge. Bansal [10] analyzed time-varying MHD blood flow in an inclined, porous, stretching vessel, under slip conditions at the wall. Uddin et al. [11] have discovered that the joint effects of joule heating and axial conduction had a significant impact on Hartmann's thermal input in parallel platforms with diverse wall temperatures. In the case of a breakdown, Hartmann numbers up to 10 were examined by the researchers. The impacts of double diffusion

on MHD fluid flow via a vertical surface are researched by Iranian et al. [12]. Chamkha et al. [13] evaluated the existing models for the physical attributes of nanofluids and specifically highlight studies conducted on MHD convection. By utilizing a Navier-Stokes computer solver, Beg [14] investigated the impact of a Joule heater in MHD channel flow to simulate flow.

Porous media are prevalent in various natural and industrial systems, such as underground aquifers, oil reservoirs, and geothermal systems. It has been extensively studied due to their relevance in practical applications. The Darcian model is the most used model, and it is valid for viscous-dominated flows and utilized in the overwhelming majority of simulations. Bansal [15] explored the stunning nano-fluid boundary layer on a permanently stretched sheet, utilizing the Keller-box technique. Beg et al. [16] explored the impact of Soret and Dufour on the stretched surface in porous medium. Ionized hydromagnetic rotating heat transfer currents utilizing ionized hydromagnetic rotational heat transfer experiments in the effects of conducting and nonconducting walls in a parallel platform channel are examined by Raza et al. [17]. They demonstrated the case of nonconductive walls. If a fixed number and Hall current parameter are assumed, the increase in rotational parameters will decrease the temperature of the channels. They discovered unrelated solutions for hydromagnetic transport in newly identified porous media by expanding the board and including cross-diffusion effects. Kausar et al. [18] discovered the impact on boundary layers with a rise in porosity and volume fraction. The periodic behavior of mixed convection heat transmission surrounding a vertical wedge submerged through a porous media is explored by Chamkha et al. [19]. Their research deepened the understanding of temporal fluctuations in heat transmission characteristics. Bansal et al. [20] utilized the non-Darcy model to illustrate the transportation of nanofluid. By enhancing thermal radiation and conductivity, Vanitha [21] observed a significant boost in heat transfer rate.

The nonlinear stretching sheet, a fundamental concept in fluid dynamics, continues to be a subject of profound scientific interest and practical relevance. This research article embarks on a comprehensive exploration of the intricate phenomena associated with fluid flow via a nonlinear stretched sheet. The nonlinearities introduced by the stretching sheet present unique challenges that demand sophisticated analytical and numerical approaches. Studies establish the profound impact of the nonlinear stretched sheet phenomenon in the applications of the production of polymer sheets, metallurgical processes, and the design of aeronautical surfaces, enhancing our understanding of their efficiency and performance. Hamad and Ferdows [22] investigated the similarity solutions of nanofluid via a nonlinearly stretched sheet. Jakeer et al. [23] studied the influence of hybrid nanoparticles passing through a nonlinear stretched sheet. Bansal et al. [24] explored how boundary layer flow and heat transmission via a nonlinear stretched sheet are affected by thermal wall slip. Alaidrous et al. [25] found that the impact of viscous dissociation on mixed transmission of heat from a surface that increases exponentially may be assessed. Negi et al. [26]

examined how a heat source affected a nanofluid's stagnation point flow through a stretched sheet. Elbashbeshy [27] examined the effects of wall transpiration (suction), with an exponentially continuous extended surface in boundary layer flow. He utilized analysis techniques for exponential sheet models. Because of the physiologically realistic exponential stretch rates and the mathematical examination of similarities, they are often utilized in engineering. Beg et al. [28] carried out an exponentially increasing sheet of heat radiation numerical simulation of boundary layer flow, to better understand the phenomena. The exponential stretching issue is important when it comes to both practical and mathematical considerations. Baron et al. [29] demonstrated that relaxation processes in polymer systems may be described by relaxation functions with extended exponential behavior when applied to actual polymer stretching systems. With the exponential stretching of polymer sheets, it is feasible to overcome the relaxation of elastic strains and create a homogeneous distribution of materials. Uddin et al. [30] suggested using a generalized stretching model for continuous surfaces with a range of arbitrary polynomial speeds, which they termed "super-stretching" and were the most efficient in the context of material processing activities.

A finite difference technique was employed to address non-dimensionalized conservation equations. This approach allowed for a detailed investigation of various thermophysical factors that have a substantial impact on the characteristics of the flux. Abbasbandy et al. [31] researched the flow, heat, and mass transfer features of natural convection. They concluded that boosting the number of couplings reduces the speed. In the realm of mathematical modelling and solving complex physical problems, of partial differential equations (PDEs) into nondimensional, nonlinear ordinary differential equations (ODEs) is a pivotal technique. In this research, we employ a similarity transformation approach to achieve the governing equations, with the resulting system solved by employing the renowned Keller box technique introduced by Keller and Cebeci [32]. This research not only delivers a systematic methodological framework, but also provides valuable perspectives into the applications of the Keller box method, shedding light on its practicality in handling an extensive range of physical problems.

In accordance with a review of existing literature, several studies have detailed the characteristics of a boundary layer formed around a stretching sheet. Despite these individual advancements in nanofluids, MHD, porous media, and nanoparticles, there is a notable research gap in the literature concerning the collective influence of silver (**Ag**), ferrous ferric oxide ($\mathbf{Fe_3O_4}$), and copper (**Cu**) nanofluids in the boundary layer regime via a nonlinear stretched sheet embedded in a porous material. This work intends to impart a crucial understanding of the behavior of such nanofluids in practical engineering applications. The existing body of research has laid the foundation for our investigation, but it is evident that a comprehensive study integrating these aspects is necessary to gain a stronger understanding of the intricate interactions amongst nanofluids, MHD, porous media, and nanoparticles in boundary layer flow scenarios. This study not only bridges an existing research gap but also imparts

instructive insights for engineers and researchers working in the fields of heat exchangers, materials science, and porous media applications. The impacts of various parameters on fluid flow via a nonlinear stretched surface are visually depicted. The current study considers both the physical and engineering implications of porous media.

11.2 Mathematical Formulation

In the ever-evolving landscape of numerical methods for solving the Keller box, the finite difference implicit method stands as a venerable and powerful approach. Its enduring significance lies in its ability to provide accurate solutions to a wide array of differential equations encountered in various scientific and engineering disciplines. Its implicit nature confers numerical stability, making it a robust tool for simulating complex physical processes. It has been applied to problems in heat transfer, fluid flow, chemical engineering, and electromagnetic wave propagation, among others. Ishak et al. [33] implemented Keller's box technique for numerical simulation. Furthermore, focusing on the point-wise numerical algorithm, we unravel the inner workings of this method, offering a deep understanding of its principles and a novel perspective on its applications. The method is equipped with the capability to convert *n*th-order nonlinear PDEs into a system of *n* ODEs of first order, simplifying the numerical solution process. These first-order nonlinear ODEs are then discretized in finite differences and turned into linear algebraic constraints, which are subsequently solved via the block-tridiagonal eliminating approach: Figure 11.1 represents the physical modal of the present research.

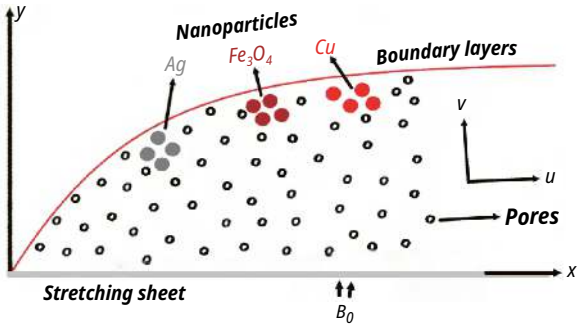

Figure 11.1: Physical model of present research.

$$\frac{\partial u}{\partial x} + \frac{\partial v}{\partial y} = 0 \tag{11.1}$$

$$u\frac{\partial u}{\partial x}+v\frac{\partial u}{\partial y}=\frac{\mu_{nf}}{\rho_{nf}}\frac{\partial^2 u}{\partial y^2}-\frac{\sigma(B(x))^2}{\rho_{nf}}u-\frac{\mu_{nf}}{\rho_{nf}}\frac{1}{K(x)}u \tag{11.2}$$

$$u\frac{\partial T}{\partial x}+v\frac{\partial T}{\partial y}=\alpha_{nf}\frac{\partial^2 T}{\partial y^2}+\frac{\mu_{nf}}{(\rho C_p)_{nf}}\left(\frac{\partial u}{\partial y}\right)^2 \tag{11.3}$$

$$u\frac{\partial C}{\partial x}+v\frac{\partial C}{\partial y}=D_m\frac{\partial^2 C}{\partial y^2}+D_l\frac{\partial^2 T}{\partial y^2} \tag{11.4}$$

$$\left.\begin{array}{c} u=u_w=bx^n,\ v=v_w,\ T=T_w=T_\infty+bx^{2n}\text{ at } y=0 \\ \text{and } u=0, T\to T_\infty \,\&\, C\to C_\infty \text{ as } y\to\infty \end{array}\right\} \tag{11.5}$$

The kinematic viscosity v_f, effective thermal diffusivity α_{nf}, and effective viscosity μ_{nf} for nano-fluids are obtained from [34–36] and are classified as:

$$v_f=\frac{\mu_f}{\rho_f},\ \alpha_{nf}=\frac{\kappa_{nf}}{(\rho C_p)_{nf}},\ \mu_{nf}=\frac{\mu_f}{(1-\phi)^{2.5}},\ (\rho)_{nf}=\left((1-\phi)(\rho)_f+\phi(\rho)_s\right) \tag{11.6}$$

$$(\rho C_p)_{nf}=(1-\phi)(\rho C_p)_f+\phi(\rho C_p)_s \text{ and } \frac{\kappa_{nf}}{\kappa_f}=\frac{\kappa_s+2\kappa_f-2\phi(\kappa_f-\kappa_s)}{\kappa_s+2\kappa_f+2\phi(\kappa_f-\kappa_s)} \tag{11.7}$$

Similarity transformations are described as follows:

$$\left.\begin{array}{c} \eta=yx^{\frac{n-1}{2}}\left(\frac{b(n+1)}{2v_f}\right)^{\frac{1}{2}},\ u=bx^n f'(\eta),\ \xi(\eta)=\frac{C-C_\infty}{C_W-C_\infty} \\ \theta(\eta)=\frac{T-T_\infty}{T_W-T_\infty} \text{ and } v=-x^{\frac{n-1}{2}}\left(\frac{b(n+1)v_f}{2}\right)^{\frac{1}{2}}f(\eta) \end{array}\right\} \tag{11.8}$$

Presenting the stream function $\psi(x,y)$ fulfills the continuity equation (11.1) stated as:

$$u=\frac{\partial\psi}{\partial y} \text{ and } v=-\frac{\partial\psi}{\partial x} \tag{11.9}$$

From eq. (11.2), using eqs. (11.6)–(11.9), we get

$$u\frac{\partial u}{\partial x}=bx^n f'(\eta).bnx^{n-1}f'(\eta)=b^2nx^{2n-1}(f'(\eta))^2,$$

$$v\frac{\partial u}{\partial y}=-x^{\frac{n-1}{2}}\left(\frac{b(n+1)v_f}{2}\right)^{\frac{1}{2}}f(\eta).\ bx^n f''(\eta)\left(\frac{b(n+1)}{2v_f}\right)^{\frac{1}{2}}x^{\frac{n-1}{2}}=-b^2\left(\frac{n+1}{2}\right)x^{2n-1}f(\eta)f''(\eta),$$

$$\frac{\mu_{nf}}{\rho_{nf}}\frac{\partial^2 u}{\partial y^2}=\frac{\mu_f}{(1-\phi)^{2.5}}\times\frac{1}{\rho_f\left(1-\phi+\phi\frac{\rho_s}{\rho_f}\right)}\ b^2x^{2n-1}f'''(\eta)\left(\frac{n+1}{2v_f}\right)=\frac{b^2x^{2n-1}}{\phi_1\phi_2}\left(\frac{n+1}{2}\right)f'''(\eta),$$

$$\frac{\sigma(B(x))^2}{\rho_{nf}}u=\frac{\sigma\left(B_0x^{\frac{n-1}{2}}\right)^2}{\rho_f\phi_2}bxf'(\eta)=\frac{\sigma(B_0)^2}{\rho_f\phi_2}bx^{2n-1}f'(\eta)\ \ and\ \ \frac{\mu_{nf}}{\rho_{nf}}\frac{1}{K_{\mathrm{d}}}u=\nu_f\frac{bx^{2n-1}}{\phi_1\phi_2}\frac{1}{K_{\mathrm{d}}}f'(\eta)$$

Now, putting the above equations into (11.2), we get

$$b^2nx^{2n-1}\left(f'(\eta)\right)^2-b^2\left(\frac{n+1}{2}\right)x^{2n-1}f(\eta)\,f''(\eta)=\frac{b^2}{\phi_1\phi_2}\left(\frac{n+1}{2}\right)x^{2n-1}f'''(\eta)$$

$$-\frac{\sigma(B_0)^2}{\rho_f\phi_2}bx^{2n-1}f'(\eta)-\nu_f\frac{bx^{2n-1}}{\phi_1\phi_2}\frac{1}{K_{\mathrm{d}}}f'(\eta)$$

$$\Rightarrow\ f'''(\eta)-\phi_1\phi_2\left[\frac{2n}{n+1}\left(f'(\eta)\right)^2-f(\eta)\,f''(\eta)\ \right]-\frac{2}{n+1}(\phi_1M-\mathrm{K})f'(\eta)=0 \tag{11.10}$$

Similarly, eqs. (11.3) and (11.4) using eqs. (11.6)–(11.9) can be written as:

$$\theta''(\eta)-Pr\lambda_n^{-1}\phi_3\left\{\frac{4n}{n+1}f'(\eta)\theta(\eta)-f(\eta)\theta'(\eta)-E_C\phi_1^{-1}\phi_3^{-1}\left(f''(\eta)\right)^2\right\}=0 \tag{11.11}$$

$$\xi''(\eta)-Sc\left(\frac{4n}{n+1}\ \xi(\eta)f'(\eta)-f(\eta)\xi'(\eta)\right)+Sr\ \theta''(\eta)=0 \tag{11.12}$$

where the parameters are

$$\left.\begin{aligned}&S_r=\frac{(T-T_\infty)D_l}{(C-C_\infty)D_m},\ Pr=\frac{\nu_f}{\alpha_f},\ \lambda_n^{-1}=\frac{\kappa_f}{\kappa_{nf}},\ \left(\rho C_p\right)_f=\frac{\kappa_f}{\alpha_f},\ Sc=\frac{\nu_f}{D_m},\\&K=\frac{\nu_f}{b\ K_d},\ M=\frac{\sigma B_0^2}{b\rho_f},\ E_C=\frac{x^2b^2}{(T-T_\infty)\left(C_p\right)_f},\ \phi_1=\frac{1}{(1-\phi)^{2.5}},\\&\phi_2=(1-\phi)+\phi\frac{\rho_s}{\rho_f}\ \text{and}\ \phi_3=(1-\phi)+\phi\frac{\left(\rho C_p\right)_s}{\left(\rho C_p\right)_f}\end{aligned}\right\} \tag{11.13}$$

Leveraging eq. (11.8), we can derive the boundary constraints displayed in eq. (11.5)

$$u=u_w=bx^n\Rightarrow bx^nf'(\eta)=bx^n\Rightarrow f'(\eta)=1$$

$$v=v_w\Rightarrow -x^{\frac{n-1}{2}}\left(\frac{b(n+1)\nu_f}{2}\right)^{\frac{1}{2}}f(\eta)=v_w$$

$$\Rightarrow f(\eta)=\frac{-v_w}{x^{\frac{n-1}{2}}\left(\frac{b(n+1)\nu_f}{2}\right)^{\frac{1}{2}}f(\eta)}=S$$

$$T=T_w\Rightarrow T_w-T_\infty=\theta(\eta)(T_w-T_\infty)\Rightarrow\theta(\eta)=1$$

$$\text{and}\ C=C_w\Rightarrow C_w-C_\infty=\xi(\eta)(C_w-C_\infty)\Rightarrow\xi(\eta)=1$$

Therefore, the transformed boundary constraints are

$$\left.\begin{aligned} f(\eta) = S,\ f'(\eta) = \theta(\eta) = \xi(\eta) = 1 \text{ at } \eta = 0, \\ \text{and } f'(\eta),\ \theta(\eta) \text{ and } \xi(\eta) \to 0 \text{ as } \eta \to \infty \end{aligned}\right\} \tag{11.14}$$

11.2.1 Skin Friction Coefficient and Rate of Heat Transfer

The physical parameters for Nu and C_f are expressed as:

$$Nu = \frac{xq_w}{\kappa_f(T_w - T_\infty)} \text{ and } C_f = \frac{\tau_w}{\rho_f\ u_w^2}$$

where $q_w = -\kappa_{nf}\frac{\partial T}{\partial y}$ and $\tau_w = \mu_{nf}\frac{\partial u}{\partial y}$ at $y = 0$ represent the rates of energy and shear stress, respectively.

Eventually, the local Nusselt number and the skin friction coefficient are stated as:

$$f''(0) = \phi_1 C_f \left(\frac{2Re_x}{n+1}\right)^{1/2} \text{ and } -\theta'(0) = \frac{\kappa_f}{\kappa_{nf}} Nu \left(\frac{(n+1)Re_x}{2}\right)^{-1/2}, \text{ where } Re_x = \frac{xu_w}{\nu_f}.$$

11.2.2 Unique Characteristics of Nanoparticles

For nanoparticles, Table 11.1 offers a brief listing of their thermophysical abilities.

Table 11.1: Unique characteristics of nanoparticles.

Physical characteristics	$C_p\,(\mathrm{J/kg\,K})$	$\rho\,(\mathrm{kg/m^3})$	$\kappa\,(\mathrm{W/m\,K})$
Fe_3O_4	670	5,180	9.7
Cu	385	8,933	401
Ag	235	10,500	429
Water (H_2O)	4,179	997.1	0.613

11.3 Results and Discussion

The impact of the nonlinearly stretched sheet on boundary layer flow via porous media under the influence of MHD has been examined in this work. Numerical calculations of nonlinear ODEs (11.10), (11.11), and (11.12) are discretized using the Keller-box finite difference implicit technique, incorporating the boundary conditions (11.14). By making use of graphs and tables combination, a comprehensive analysis of nanoparticles Fe_3O_4, Cu, and Ag in water-based nanofluid have been presented including parameters, such as, suction parameter S, nanoparticles volume fraction ψ, stretching parameter n,

Eckert number *Ec*, Prandtl factor *Pr*, Soret factor *Sr*, and magnetic parameter *M*. The outcomes of the numerical computations are graphically displayed and analyzed in relation to the governing parameter's significance.

11.3.1 Present Research Validation

The validity of research work is the degree for assuring the accuracy and reliability of research findings. Valid research outcomes can be leveraged to provide guidance for practice, contribute meaningfully to knowledge, and provide results that can be extrapolated to other researchers. Validity reduces errors and boosts transparency.

Table 11.2: Results comparison of $-\theta'(0)$ for distinct values of volume fraction ϕ and *Ec* when $M = S = K = 0$, $\Pr = 10$, and $n = 10$.

Ec	ϕ	Ag		Cu	
		Hamad [22]	Present	Hamad [22]	Present
0	0.5	5.57754	5.577539	5.62189	5.621890
0	0.1	5.09104	5.091038	5.17237	5.172369
0.1	0.15	4.31513	4.315130	4.45581	4.455811

Previous studies can be utilized to validate the accuracy of the current study. The current study is reduced to Hamad's model [22], when $M = S = K = 0$, which validates the use of the numerical approach. Comparing $-\theta'(0)$ and $-f'$ (0) for numerous values of ϕ and *Ec* in Tables 11.2 and 11.3 indicates the preciseness of the current research findings.

Table 11.3: Comparison of $-f''(0)$ for distinct values of volume fraction ϕ and *Ec* when $M = S = K = 0$, $\Pr = 10$, and $n = 10$.

ϕ	Ag		Cu	
	Hamad [22]	Present	Hamad [22]	Present
0.05	1.43646	1.436459	1.40049	1.400490
0.1	1.53712	1.537121	1.47769	1.477688
0.15	1.59300	1.593003	1.51794	1.517941
0.2	1.61399	1.613989	1.52880	1.528802

11.3.2 Present Research

Figures 11.2–11.4 show that the stretching parameter affects temperature $\theta(\eta)$, velocity $f'(\eta)$, and nanoparticle concentration $\xi(\eta)$ significantly. An increase in nonlinear

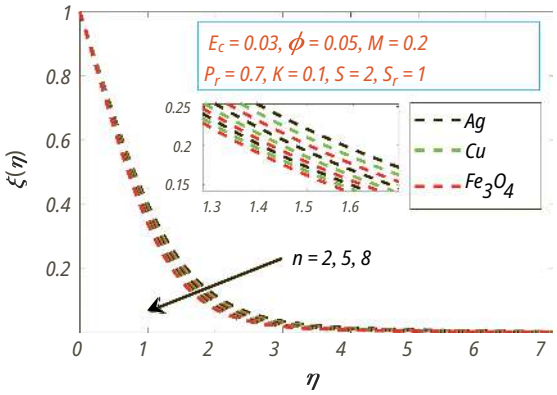

Figure 11.2: Influence of *n* on concentration.

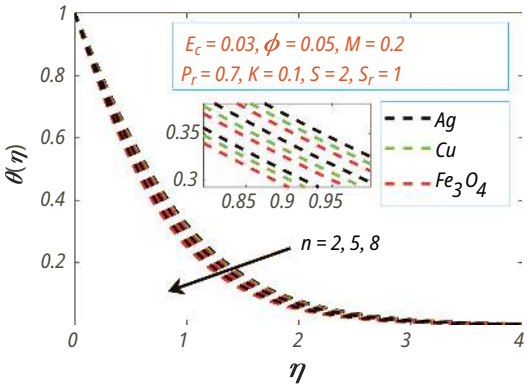

Figure 11.3: Influence of *n* on temperature.

stretching parameter decreases all three boundary layers. The nanoparticle *Ag* has the highest concentration and temperature of the nanofluid, though the maximum velocity is recorded for nanoparticle Fe_3O_4.

Figures 11.5 and 11.6, respectively, illustrate how the magnetic factor M affects the temperature $\theta(\eta)$ and concentration $\xi(\eta)$ of nanoparticles Fe_3O_4, Cu, and Ag in water-based nanofluid. These aforementioned figures demonstrate that rise in the magnetic parameter M causes rise in both concentration and temperature, as heat is developed due to the Lorentz force. The nanoparticles Ag exhibit the maximum concentration and temperature of nanofluid, followed by Cu and Fe_3O_4. On the other side, Figures 11.7 illustrates the reverse impact for velocity $f'(\eta)$, velocity falls as a result of a hike in the retarding body force produced by boosting the magnetic parameter M. In addition, as M rises, the boundary layer's thickness falls. The nanoparticle Fe_3O_4 exhibits the maximum velocity of nanofluid, followed by Cu and Ag.

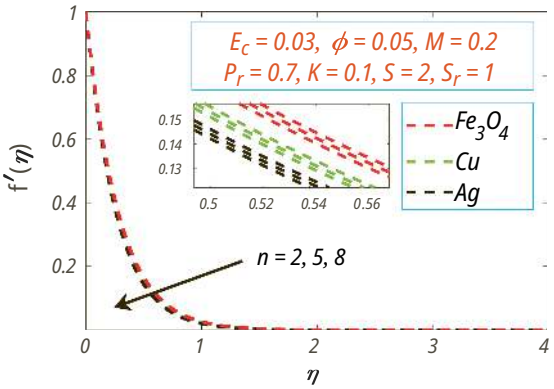

Figure 11.4: Influence of *n* on velocity.

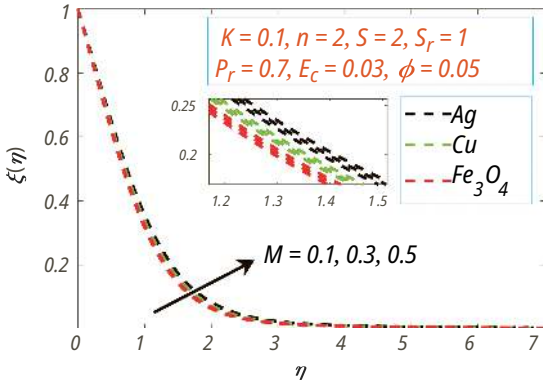

Figure 11.5: Influence of *M* on concentration.

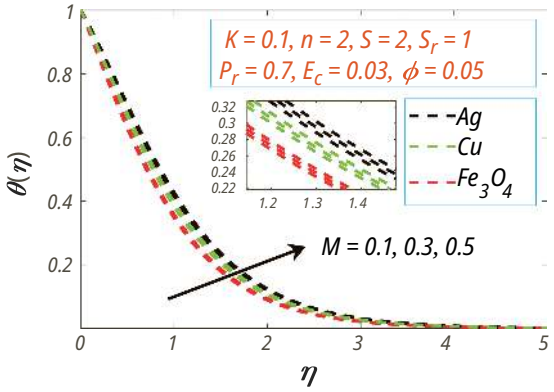

Figure 11.6: Influence of *M* on temperature.

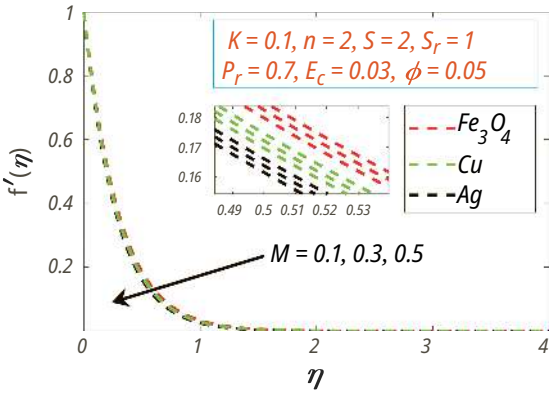

Figure 11.7: Influence of *M* on velocity.

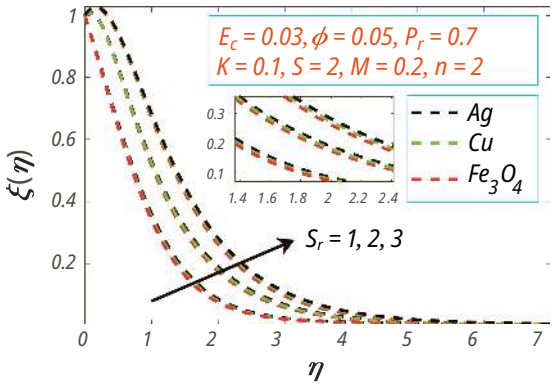

Figure 11.8: Influence of *Sr* on concentration.

The significant influence of the Soret parameter *Sr* on $\xi(\eta)$, $\theta(\eta)$, and $f'(\eta)$ is depicted through Figures 11.8–11.10. The dimensionless Soret factor quantifies the influence of temperature variations on a mixture's concentration gradients. The fluid's particles disperse from hot to cold temperature zones due to the Soret effect. Therefore, a rise in the Soret factor causes the fluid's concentration to rise, but its temperature falls. Consequently, as the Soret number goes up, the thermal boundary layer gets thinner. The particles are also carried by the diffusion process, enhancing the fluid's velocity. Additionally, the Soret factor influences the concentration of different types of nanoparticles in a fluid in varying ways. The Soret coefficient of Ag nanoparticles, for instance, is larger than that of Cu and Fe_3O_4 nanoparticles. The maximum velocity is recorded for nanoparticles Fe_3O_4, followed by Cu and Ag.

The relationship between volume fraction ϕ and concentration $\xi(\eta)$ is depicted in Figure 11.11. The proportion of the fluid's volume that the nanoparticles occupy

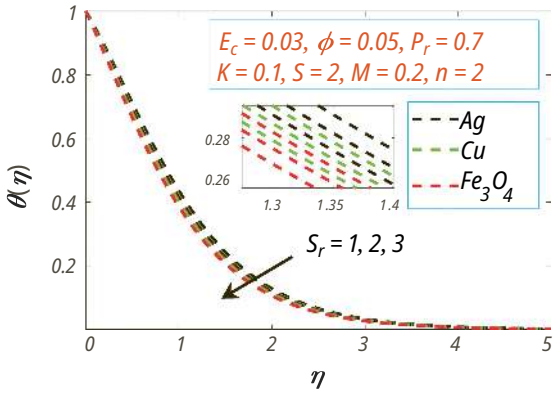

Figure 11.9: Influence of *Sr* on temperature.

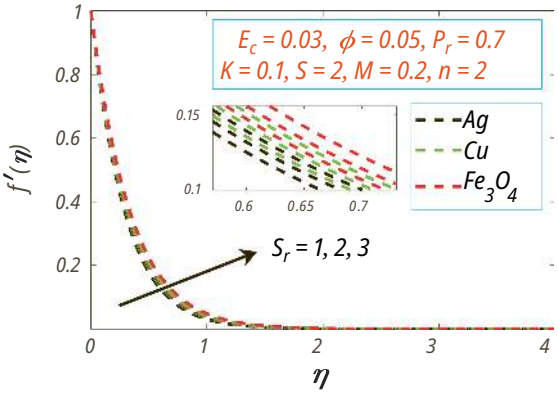

Figure 11.10: Influence of *Sr* on velocity.

is known as the nanoparticles volume fraction ϕ in a given nanofluid. A clear trend emerges from Figure 11.12, boosting the volume percentage of nanoparticles to improves the fluid's thermal conductivity. In contrast, the nanofluid's velocity profiles indicate the reverse behavior, depicted in Figure 11.13. As ϕ rises, the velocity profile diminishes due to the raised viscosity of the nanofluid. However, for concentration $\xi(\eta)$ revealing the nanofluid's dual behavior, for all three nanoparticles, Fe_3O_4, Cu, and Ag, $\xi(\eta)$ falls near $\eta = 0$ and rises at $\eta > 1$.

The impact of *Ec* on $\xi(\eta)$, $\theta(\eta)$, and $f'(\eta)$ distributions for nanofluids containing Fe_3O_4, Cu, and Ag nanoparticles is depicted in Figures 11.14–11.16. The concentration rises with increasing *Ec*. The temperature rises with increasing *Ec* values, causing the nanoparticles to disperse away from the wall more quickly. This occurs because heat is generated through viscous dissipation as it converts motion into thermal energy. Therefore, the *Ec* enhances the level of heat generated in the fluid. Eckert number's

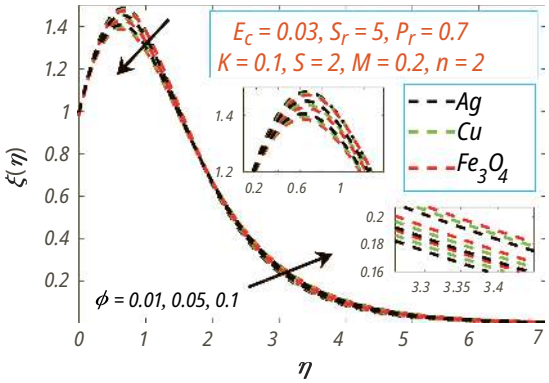

Figure 11.11: Influence of ϕ on concentration.

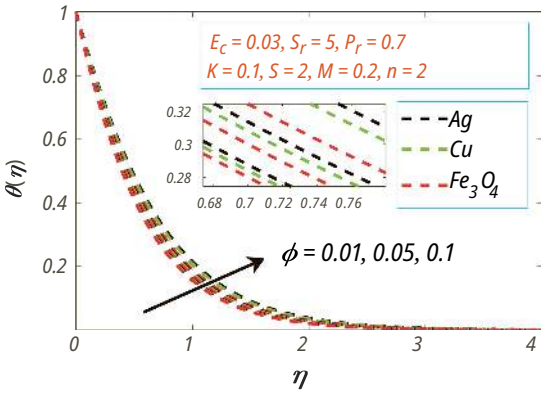

Figure 11.12: Influence of ϕ on temperature.

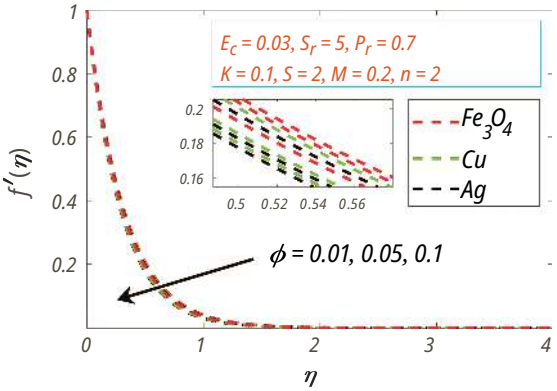

Figure 11.13: Influence of ϕ on velocity.

impact on velocity is dependent upon various parameters, such as flow geometry, fluid characteristics, and boundary conditions. As *Ec* rises, the nanofluid's velocity reduces and velocity of the Ag water falls considerably faster than Fe_3O_4-water nanofluid.

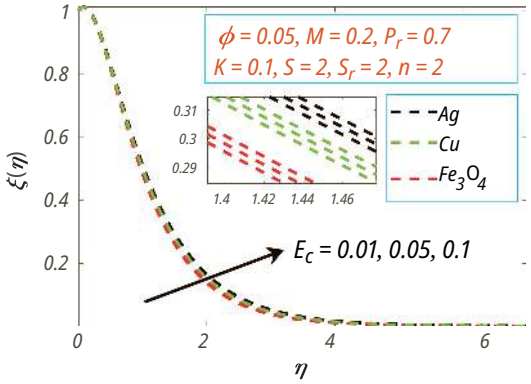

Figure 11.14: Influence of *Ec* on concentration.

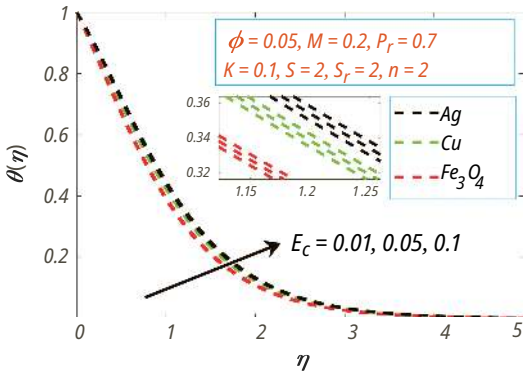

Figure 11.15: Influence of *Ec* on temperature.

Table 11.4 indicates the Computations of $-\theta'(0)$ and $-f''(0)$ for a Cu-water base fluid across various ranges of, K, n, and M, when $Sr = 1$, $Ec = 0.03$, $S = 2$, and $Pr = 0.7$. The data reveal that increasing the volume percentage of nanoparticles causes a simultaneous rise in both $-\theta'(0)$ and $-f''(0)$. Also, raising the magnetic field (M) leads to a lessens the heat transport rate, while concurrently increasing the skin friction. This observation underscores the ability of magnetic factor to impede nanofluid flow and consequently, influence heat transfer processes. Conversely, *a* higher permeability parameter (K) exhibits an opposing effect, where a higher value accelerates heat transfer but reduces the skin friction coefficient. Furthermore, *a* higher nonlinear stretching factor strengthens both $-\theta'(0)$ and $-f''(0)$.

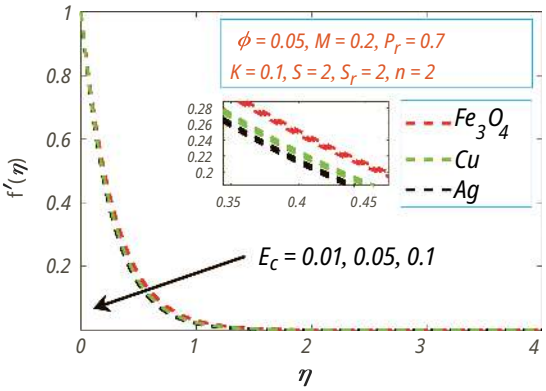

Figure 11.16: Influence of *Ec* on velocity.

Table 11.4: Computations of $-\theta'(0)$ and $-f''(0)$ for a Cu-water base fluid across various ranges of ϕ, K, n, and M, when $Sr = 1$, $Ec = 0.03$, $S = 2$, and $Pr = 0.7$.

ϕ	n	K	$-\theta'(0)$			$-f''(0)$		
			$M = 0.1$	$M = 0.3$	$M = 0.5$	$M = 0.1$	$M = 0.3$	$M = 0.5$
0.01	2	0.1	1.363048	1.316432	1.271410	1.012684	1.124351	1.226786
0.01	2	0.2	1.386901	1.339470	1.293659	0.961212	1.067203	1.164432
0.01	2	0.3	1.411616	1.363339	1.316712	0.936542	1.039813	1.134547
0.01	4	0.1	1.490738	1.439755	1.390516	1.154980	1.282338	1.399167
0.01	6	0.1	1.651064	1.594598	1.540063	1.263173	1.402462	1.529235
0.01	8	0.1	1.805729	1.743974	1.684330	1.345279	1.486609	1.613396
0.02	2	0.1	1.402958	1.354977	1.308637	1.048024	1.165878	1.269598
0.03	2	0.1	1.444037	1.394651	1.346954	1.084495	1.206450	1.312764
0.04	2	0.1	1.486318	1.435486	1.386393	1.117029	1.240231	1.346896

11.4 Conclusion

Present research investigates the impact of Cu, Ag, and Fe_3O_4 nanoparticles on a water-based nanofluid's magnetohydrodynamics boundary layer flow via a nonlinear stretched surface in a porous media. The findings demonstrate that the selection of nanoparticles profoundly influences fluid flow, heat transfer characteristics, and concentration. The research offers significant perspectives on the possible uses of nanofluids across multiple domains. Because nanofluids are substantially more thermally and transport-efficient than base fluids, they are a promising choice for cooling and heat transfer applications. A similarity transformation is utilized to transform PDEs into nondimensional and nonlinear ODEs. These ODEs are subsequently numerically simplified via making use of the finite difference implicit Keller box approach. Multiple factors, such as Soret number *Sr*,

Eckert number *Ec*, magnetic factor *M*, stretching parameter *n*, and nanoparticles volume fraction ϕ, have been examined in relation to temperature $\theta(\eta)$, velocity $f'(\eta)$, and nanoparticles concentration $\xi(\eta)$. A few of the worthy outcomes are:

1. Nonlinear stretching factor significantly alters the concentration, temperature, and velocity profiles of a nanofluid. An increase in the nonlinear stretching parameter, decreases all three boundary layers. The nanoparticles Ag has the highest concentration and temperature of the nanofluid, whereas the maximum velocity is recorded for nanoparticles Fe_3O_4. A higher nonlinear stretching factor strengthens both $-\theta'(0)$ and $-f''(0)$.
2. An enhancement in the magnetic factor *M*, causes a simultaneous rise in both concentration and temperature, as heat is developed due to the Lorentz force. The nanoparticles Ag exhibits the maximum concentration and temperature of nanofluid, but the velocity indicates the reverse behavior of nanofluid. Also, strengthening the magnetic field causes a decline in the heat transmission rate, while concurrently increasing the skin friction.
3. An increase in the *Sr* causes the fluid's concentration and velocity to rise, but its temperature falls. Consequently, as the Soret number goes up, the thermal boundary layer gets thinner. The Soret coefficient of Ag nanoparticles, for instance, is larger than that of Cu and Fe_3O_4 nanoparticles. the maximum velocity is recorded for nanoparticles Fe_3O_4, followed by Cu and Ag.
4. The significant effect of the volume fraction component ϕ on temperature (η), velocity $f'(\eta)$, and nanoparticles concentration $\xi(\eta)$ varies according to the kind of nanofluid. The fluid's temperature rises with a hike in the volume fraction. In contrast, the nanofluid's velocity profiles indicate the reverse behavior. But dual behavior is observed in the concentration, it falls with increasing ϕ near the surface $\eta = 0$, but exhibits reverse behavior for $\eta > 1$. Furthermore, increasing the nanoparticles volume fraction leads to a simultaneous rise in both $-\theta'(0)$ and $-f''(0)$.
5. The concentration and temperature rise with increasing *Ec* values, causing the nanoparticles to disperse away from the wall more quickly. As *Ec* rises, the nanofluid's velocity reduces and compared to the Fe_3O_4-water nanofluid, the velocity of the Ag − water nanofluid falls considerably faster.

Nomenclature

B_0	The uniform magnetic field strength		**Greek Letters**
b	Stretching rate	κ_f	Base fluid thermal conductivity
C	Nanofluid concentration	κ_{nf}	Nanofluid thermal conductivity
C_f	Skin-friction	$\theta(\eta)$	Nondimensional temperature
C_p	Nanoparticle specific heat	β_T	Thermal expansion coefficient

Sc	Schmidt number	σ	Electric conductivity
g	Acceleration due to gravity	η	Nondimensional similarity variable
D_m	Mass diffusivity	κ_s	Nanoparticles thermal conductivity
T	Nanofluid temperature	ρ_f	Base fluid density
Ec	Eckert number	μ_f	Base fluid viscosity
$f(\eta)$	Dimensionless stream function	μ_{nf}	Nanofluid viscosity
$f'(\eta)$	Nondimensional velocity	τ_w	Wall shear stress
$-f''(0)$	Skin friction coefficient	$(\rho C_p)_{nf}$	Nanofluid heat capacitance
C_∞	Concentration of the free stream	α_{nf}	Nanofluid thermal diffusivity
K	Non-dimensional permeability parameter	ϕ	Nanoparticles solid volume fraction
K_d	Dimensional permeability parameter	β_C	Concentration expansion coefficient
v	Velocity component parallel to the y direction	$\xi(\eta)$	Nondimensional concentration
M	Magnetic parameter	ρ_{nf}	Nano fluid density
N	Nonlinearly stretching parameter	λ_n	Ratio of nanofluid's thermal conductivity to base fluid
x,y	Cartesian coordinate axis	$(\rho C_p)_f$	Base fluid heat capacitance
Pr	Prandtl number	v_f	Base fluid kinematic viscosity
u_w	Stretching sheet velocity	$(\rho C_p)_s$	Nanoparticles heat capacitance
q_w	Wall heat flux	$-\xi'(0)$	Local Sherwood number
Re	Reynolds number	$-\theta'(0)$	Local Nusselt number
Re_x	Local Reynolds number	ψ	Stream function
Sr	Soret number	ρ_s	Nanoparticle density
C_w	Concentration of the stretching sheet		**Subscripts**
u	Velocity component parallel to the x direction	nf	Nanofluid
D_l	Mass flux co-efficient	w	Boundary conditions at surface
T_w	Surface temperature	s	Nanoparticles
T_∞	Free stream temperature	f	Base fluid
S	Suction/injection factor	∞	Boundary conditions at free stream
L	Characteristic length		**Superscripts**
Nu	Nusselt number	$'$	Differentiation with respect to η

References

[1] Hayat, T., Ashraf, M., Shehzad, S., and Alsaedi, A. (2015). Mixed Convection Flow of Casson Nanofluid over a Stretching Sheet with Convectively Heated Chemical Reaction and Heated Chemical Reaction and Heat Source/Sink. Journal of Applied Fluid Mechanics, 8(4): 803–813.

[2] Bhargava, R., Pratibha,, and Chandra, H. (2017). Hybrid Numerical Solution of Mixed Convection Boundary Layer Flow of Nanofluid Along an Inclined Plate with Prescribed Surface Fluxes. International Journal of Applied and Computational Mathematics, 3(2909).

[3] Ferdows, M., Shakhaoath Khan, M., Mahmud Alam, M., and Sun, S. (2012). MHD Mixed Convective Boundary Layer Flow of a Nanofluid through a Porous Medium due to an Exponentially Stretching Sheet. Mathematical Problems in Engineering, 2012, 1–21.

[4] Chamkha, A., Yassen, R., Ismael, M., Rashad, A., Salah, T., and Nabwey, H. (2020). MHD free convection of localized heat source/sink in hybrid nanofluid-filled square cavity. Journal of Nanofluids, 9(1): 1–12.

[5] Anusha, T., Mahabaleshwar, U., and Sheikhnejad, Y. (2022). An MHD of Nanofluid Flow Over a Porous Stretching/Shrinking Plate with Mass Transpiration and Brinkman Ratio. Transp. Porous Med, 142, 333–352.

[6] Hamad, M. (2011). Analytical solution of natural convection flow of a nanofluid over a linearly stretching sheet in the presence of magnetic field. Int. Commun. Heat Mass Transfer, 38(4): 487–492.

[7] Sawaya, E., Ghaddar, N., and Chaaban, F. (1993). Evaluation of the Hall parameter of electrolyte solutions in thermosyphonic MHD flow. Int. J. Eng. Sci., 31(7): 1073–1091.

[8] Bhatti, M., Yousif, M., Mishra, S., and Shahid, A. (2019). Simultaneous influence of thermo-diffusion and diffusion-thermo on non-Newtonian hyperbolic tangent magnetized nanofluid with Hall current through a nonlinear stretching surface. Pramana, 93(6): 1–10.

[9] Cai, W., Su, N., and He, X. (2016). MHD convective heat transfer with temperature-dependent viscosity and thermal conductivity: A numerical investigation. Journal of Applied Mathematics and Computing, 52(1): 305–321.

[10] Bansal, S. (2025). Analysis of Unsteady Magnetohydrodynamic Flow of Blood with Slip Conditions in a Permeable Inclined Stretching Vessel. Journal of Neonatal Surgery, 14(6): 553–564.

[11] Uddin, M., Bég, O., and Amin, N. (2014). Hydromagnetic transport phenomena from a stretching or shrinking nonlinear nanomaterial sheet with Navier slip and convective heating: A model for bio-nanomaterials processing. Journal of Magnetism and Magnetic Materials, 368(252–261).

[12] Iranian, D., Karthik, S., and Seethalakshmy, A. (2023). Heat generation effects on Magnetohydrodynamic Powell-Eyring fluid flow along a vertical surface with a Chemical reaction. Forces in Mechanics, 12, 100212.

[13] Chamkha, A., Jena, S., and Mahapatra, S. (2015). MHD convection of nanofluids: A review. Journal of Nanofluids, 4(3): 271–292.

[14] Beg, O. (2012). *Computational Fluid Dynamic (Spectral DTM) Simulation of Hartmann Flow with Joule Heating: Applications in Liquid Metal Processing* [White Paper]. Bradford, UK: GORT Engovation-Aerospace Research.

[15] Bansal, S. (2024). Impacts of Thermophoresis and Brownian Motion on MHD Nanofluid flow over an Inclined Non-Linear Stretching Surface with Chemical Reaction. Nanotechnology Perceptions, 20(3): 379–392.

[16] Bég, O., Bakier, A., and Prasad, V. (2009). Numerical study of free convection magneto-hydrodynamic heat and mass transfer from aa stretching surface to a saturated porous medium with Soret and Dufour effects. Computational Materials Science, 46(1): 57–65.

[17] Raza, J., Farooq, M., Mebarek-Oudina, F., and Mahanthesh, B. (2019). Multiple slip effects on MHD non-Newtonian nanofluid flow over a nonlinear permeable elongated sheet: Numerical and statistical analysis. Multidiscipline Modeling in Materials and Structures, 15(5): 1913–1931.

[18] Kausar, M. S., Hussanan, A., Waqas, M., and Mamat, M. (2022). Boundary layer flow ofmicropolar nanofluid toward a permeable stretching sheet in the presence ofporous medium with thermal radiation and viscous dissipation. Chinese Journal of Physics, 78, 435–452.
[19] Chamkha, A., Nabwey, H., Abdelrahman, Z., and Rashad, A. (2020). Mixed Bioconvective Flow Over a Wedge in Porous Media Drenched with a Nanofluid. Journal of Nanofluids, 9(1): 24–35.
[20] Bansal, S., Pal, J., Bisht, M., and Fartyal, P. (2024). Influence of Nanofluids on Boundary Layer Flow over an Inclined Stretching Sheet in a Porous Media along with Magnetic Field. International Journal of Mathematical, Engineering and Management Science, 9(2): 267–282.
[21] Vanitha, G., Mahabaleshwar, U., Liu, Z., Yang, X., and Sundén, B. (2023). Magnetohydrodynamic Marangoni boundary layer flow of nanoparticles with thermal radiation and heat transfer in a porous sheet. Case Studies in Thermal Engineering, 44, 102815.
[22] Hamad, M. and Ferdows, M. (2012). Similarity solutions to viscous flow and heat transfer of nanofluid over nonlinearly stretching sheet. Appl. Math. Mech.-Engl., 33, 923–930.
[23] Jakeer, S., Reddy, S., Rashad, A., Lakshmi Rupa, M., and Manjula, C. (2023). Nonlinear analysis of Darcy-Forchheimer flow in EMHD ternary hybrid nanofluid (Cu-CNT-Ti/water) with radiation effect. Forces in Mechanics, 10, 100177.
[24] Bansal, S., Kumar, A., Pal, J., Goyal, I., and Negi, A. (2024). Influence of Thermal Wall and Velocity Slips on Non-Darcy MHD Boundary Layer Flow of a Nanofluid over a Non-linear Stretching Sheet. Journal of Physics: Conference Series, 2844, 012018.
[25] Alaidrous, A. and Eid, M. (2020). 3-D electromagnetic radiative non-Newtonian nanofluid flow with Joule heating and higher-order reactions in porous materials. Scientific Reports, 10(1): 1–19.
[26] Negi, A., Kumar, A., Yaseen, M., Rawat, S., and Saini, A. (2023). Effects of heat source on the stagnation point flow of a nanofluid over a stretchable sheet with magnetic field and zero mass flux at the surface. Forces in Mechanics, 11, 100190.
[27] Elbashbeshy, E. (2001). Heat Transfer over an Exponentially Stretching Continuous Surface with Suction. Archives of Mechanics, 53, 643–651.
[28] Bég, O., Hoque, M., Wahiuzzaman, M., Mahmud, M., and Ferdows, M. (2014). Spectral numerical simulation of magneto-physiological laminar Dean flow. Journal of Mechanics in Medicine and Biology, 14(4), *1450047* 1–18.
[29] Baron, A., Szewieczek, D., and Nowosielski, R. (2007). Selected manufacturing techniques of nano-materials. J. Achievements of Materials and Manufacturing Engineering, 20(1): 83–86.
[30] Uddin, M., Yusoff, N., Bég, O., and Ismail, A. (2013). Lie group analysis and numerical solutions for non-Newtonian nanofluid flow in a porous medium with internal heat generation. J. Physica Scripta, 87(2): 025401.
[31] Abbasbandy, S. and Ghehsareh, H. (2012). Solutions of the magnetohydrodynamic flow over a nonlinear stretching sheet and nano boundary layers over stretching surfaces. In.t J. Numerical Methods in Fluids, 70(10): 1324–1340.
[32] Keller, H. and Cebeci, T. (1972). Accurate numerical methods for boundary-layer flows. ii: Two dimensional turbulent flows. AIAA Journal, 10(9): 1193–1199.
[33] Ishak, A., Nazar, R., and Pop, I. (2008). Uniform suction/blowing effect on flow and heat transfer due to a stretching cylinder. Applied Mathematical Modelling, 32(10): 2059–2066.
[34] Brinkman, H. (1952). The viscosity of concentrated suspensions and solutions. The Journal of Chemical Physics, 20(4): 571–581.
[35] Xuan, Y., Li, Q., and Hu, W. (2003). Aggregation structure and thermal conductivity of nanofluids. AIChE Journal, 49, 1038–1043.
[36] Maxwell, J. C. (1954). A Treatise on Electricity and Magnetism. Dover Publications, Inc.

Kanak Raj and Prince Raj Lawrence Raj*

Chapter 12
Multiphase Flow and Heat Transfer Analysis of Liquid Methane in Cryogenic Engine Feed Pipes

Abstract: This study analyzes a comprehensive numerical analysis of the hydrodynamic and thermodynamic characteristics of liquid methane in a vertically positioned cryogenic feed pipe subjected to different inlet velocities and temperatures. A three-dimensional transient volume of fluid (VOF) model integrated with an energy equation is utilized to simulate multiphase flow in the feed pipe system. The calculations account for a constant wall temperature of 500 K, an inlet pressure of 1.5 bar, inlet velocities of 0.5 m/s and 1.0 m/s, and temperatures varying from 95 K to 105 K. The contours of vapor volume fraction indicate transitions in flow regimes from bubble, slug, annular, and dispersed annular flow regimes, which are significantly influenced by thermal and velocity parameters. At lower inlet velocity, increased inlet temperature results in early vaporization and the formation of a high vapor core, promoting a dispersed annular regime near the outlet. At higher inlet velocity, the vaporization is delayed due to reduced residence time, resulting in transitional flow structures. Temperature distributions and bulk mean temperature profiles confirm that higher inlet temperatures enhance thermal penetration, whereas higher velocities suppress wall heat transfer and phase transition. Velocity field analysis shows the development of core-accelerated vapor flow at low velocities and high temperatures, while more symmetric, lower-intensity velocity profiles persist at higher velocities. Probability density functions of vapor fraction validate the corresponding flow regimes at the outlet. The results demonstrate the coupled influence of thermal input and flow residence time on two-phase flow development in cryogenic methane pipelines and offer detailed insight into the underlying physics.

Keywords: two-phase flow, VOF, heat transfer, boiling, computational fluid dynamics (CFD)

*Corresponding author: **Prince Raj Lawrence Raj** Department of Aerospace Engineering and Applied Mechanics, Indian Institute of Engineering Science and Technology, Shibpur, Howrah 711103, West Bengal, India, e-mail: plraj@aero.iiests.ac.in

Kanak Raj, Department of Aerospace Engineering and Applied Mechanics, Indian Institute of Engineering Science and Technology, Shibpur, Howrah 711103, West Bengal, India

https://doi.org/10.1515/9783111723464-012

12.1 Introduction

The space industry has witnessed a significant shift toward cost-effective and commercially driven access to space, largely achieved through reduced launch complexity and advancements in the reusability of launch vehicles [1, 2]. Liquid rocket engines, known for their high specific impulse, have become integral to reusable systems [3, 4]. Various organizations are currently evaluating liquid propellants for use in future deep space missions, including for reusable launch platforms [5–7]. Among these, missions to Mars pose the greatest challenge due to the vast distance from Earth, necessitating high specific impulse propulsion systems. Utilizing propellants derived from Martian atmospheric resources could also benefit return missions, enhancing sustainability and autonomy [8, 9]. Liquid methane has emerged as a promising cryogenic propellant for rocket propulsion, mainly due to its favorable characteristics over conventional fuels. It offers advantages over liquid hydrogen, such as reduced storage complexity, higher density, and a higher boiling point. Compared to kerosene, methane provides a higher specific impulse, lower coking tendency, and superior cooling performance [10]. Furthermore, methane can potentially be extracted from planetary surfaces like Mars through in-situ resource utilization (ISRU), reinforcing its role in long-duration missions [11].

Multiphase flow phenomena are commonly observed in cryogenic systems wherever low-temperature fluids are handled. In cryogenic storage tanks, liquid cryogens are stored below their boiling point, resulting in phase change due to boil-off gas (BOG) formation [12–15]. During propellant transfer to engines via feed pipes, chill-down procedures are critical to establishing stable single-phase flow, preventing combustion instabilities during restart operations [16–18]. Similar multiphase behaviors are also observed in other thermohydraulic systems such as evaporators, nuclear reactors, and chemical process equipment [19–21]. Experimental studies on multiphase flow have progressed significantly with the advent of advanced diagnostics, sensors, and image processing technologies [22–27]. Fang et al. [28] investigated nitrogen boiling in a vertically oriented channel under varying pressure, heat flux, and mass flow conditions, identifying four distinct regimes: bubbly, annular, scattered, and mist. The transition between these regimes directly influenced the heat transfer coefficient and convective heat flux behavior.

Fu et al. [29], using high-speed imaging, visualized nitrogen flow patterns in a vertical mini-tube, reporting flow regimes such as bubbly, slug, churn, and circular flow, and noted that annular flow dominates when vapor quality exceeds 0.15. They also observed that gas velocity significantly affects transition boundaries between regimes. Chill-down performance of cryogenic fluids has been explored by Hartwig et al. [16], who compared LH_2 and LN_2 in terms of temperature evolution and critical heat flux. LH_2 demonstrated faster chill-down due to its lower density and surface tension. Hu et al. [24] studied chill-down in a Pyrex tube using LN_2 and found that increasing mass flow rate reduces critical heat flux while increasing rewetting temperature and

quench front velocity. Additionally, uphill flows prolong the chill-down process, whereas downhill flows exhibit greater heat transfer coefficients and slower front propagation.

Computational studies on cryogenic multiphase flow have also gained attention from researchers due to their cost-efficiency, ability to capture detailed flow physics, and flexibility in analysing a wide range of operating conditions that are often challenging to replicate experimentally [30–37]. Chen et al. [38] formulated a computational model to investigate flow film boiling during chill-down, assessing the effects of wall superheat and mass flux on heat transfer and pressure dynamics. Their findings indicated that the vapor film and liquid layer mostly govern heat transfer at low flow rates, whereas axial convection becomes significant at elevated speeds. Pressure fluctuations were determined to be influenced by wall superheat and flow rate. Agarwal et al. [39] numerically assessed liquid hydrogen flow under both terrestrial and microgravity conditions, noting that annular dominant slug flow regimes are more common in microgravity environments. Jeon et al. [12] utilized the VOF model to simulate heat transfer and phase change in cryogenic cargo systems, observing a sharp increase in cooling rate during the secondary phase of chill-down and accelerated pressure drop in the compression space. Ahammad et al. [40] numerically investigated film boiling of LN_2 and LNG, reporting distinct trends in bubble formation, wall heat flux, and bubble frequency depending on fluid type and temperature.

Despite growing research interest, there remains a lack of comprehensive hydrodynamic and thermodynamic studies of cryogenic propellants above the Leidenfrost temperature. Experimental challenges include difficulty in handling extremely low-temperature fluids, potential measurement errors due to sensor calibration, and heat leakage through feed lines that compromise the accuracy of the results. The present work addresses these gaps by developing a three-dimensional computational model to investigate the two-phase flow behavior of liquid methane in a cryogenic vertical feed line. A conjugate heat transfer model based on the VOF approach, using a simplified Eulerian formulation coupled with the energy equation, is employed. After validation, the model is used to analyze various flow regimes, interfacial structures, probability density function (PDF), velocity profiles, and temperature distributions, providing a deeper understanding of cryogenic methane dynamics essential for thermal regulation and propulsion design in space applications.

12.2 Computational Modeling

This study used a three-dimensional vertical feed pipe model to investigate the multiphase flow and heat transfer properties of liquid methane (LCH_4). The pipe possesses a diameter of 50 mm and a length of 1 m, featuring adiabatic insulation along the wall. Liquid methane enters vertically through the inlet, with the pipe wall maintained

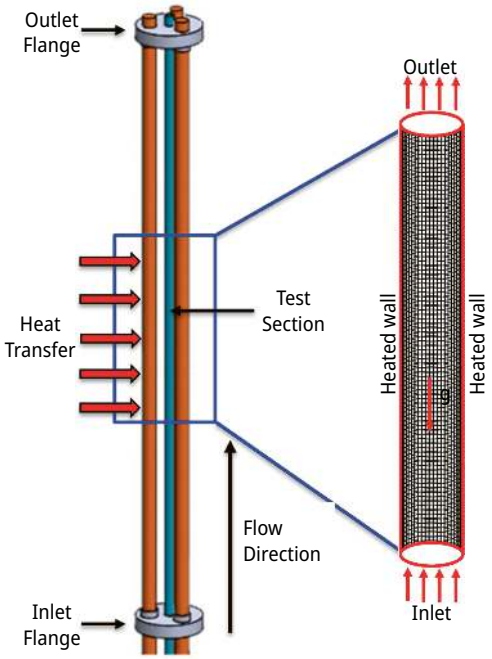

Figure 12.1: Schematic of the methane feed pipe used to investigate the hydrodynamic and thermodynamic characteristics of LCH_4–VCH_4 multiphase flow, along with an enlarged view of the pipe section showing the boundary conditions applied in the present analysis.

at a constant temperature of 500 K and the inlet pressure sustained at 1.5 bar, as illustrated in Figure 12.1. The thermophysical parameters of liquid and vapor methane are sourced from the NIST database [41] and expressed as piecewise polynomial functions of temperature, detailed in Table 12.1.

To accurately resolve multiphase flow behavior, the volume fraction of each phase must be tracked across the entire domain, necessitating the solution of conservation equations for mass, momentum, and phase volume fraction. This increases the number of unknowns in the system. To address this, the study adopts a transient VOF approach, a simplified Eulerian framework [42, 43]. This method solves a single set of governing equations to describe multiple immiscible fluid interfaces and ensures that the sum of phase fractions within a control volume equals one. Known for its interface-capturing capability, the VOF model effectively represents phase interaction phenomena with reliable mass conservation.

The density (ρ) and dynamic viscosity (μ) of the mixture are calculated based on the local phase volume fractions using eqs. (12.1) and (12.2) [39, 44]. Depending on the volume fraction, computational cells are categorized as liquid, vapor, or a mixture of both:

Table 12.1: Properties of methane in both liquid and vapor phases are utilized in the current simulations.

	Liquid methane	Vapor methane
Density (kg/m^3)	$-558.75028 + 44.06114\,T - 0.68466\,T^2 + 0.0046\,T^3 - 1.165 \times 10^{-5}\,T^4$	2.6049
Kinematic viscosity (Pa-s)	$0.00943 - 0.00032\,T + 4.272 \times 10^{-6}\,T^2 - 2.564 * 10^{-8}\,T^3 + 5.827\,10^{-8}\,10^{-11}\,T^4$	4.5034×10^{-8}
Specific heat capacity (J/kg K)	$15{,}523.2487 - 482.2137\,T + 7.122610723\,T^2 - 0.046775447\,T^3 + 1.1655\,10^{-4}\,T^4$	2,259
Thermal conductivity (W/m K)	$-3.04763 + 0.13162\,T - 0.00196\,T^2 + 1.294 * 10^{-5}\,T^3 - 3.205 * 10^{-8}\,T^4$	0.012121
Surface tension (N/m)	0.011950	
Specific latent heat (J/kg)	515,000	
Contact angle (degree)	90	
Boiling temperature (K)	116.66	

$$\rho = \alpha_l \rho_l + (1 - \alpha_l)\rho_v \tag{12.1}$$

$$\mu = \alpha_L \mu_L + (1 - \alpha_L)\mu_V \tag{12.2}$$

If the cell comprises the liquid phase: $\alpha_l = 1$.
If the cell comprises the vapor phase: $\alpha_v = 1$.
If a cell comprises both the two-phase liquid and vapor, then $0 < \alpha_l < 1$.

12.1.1 Continuity Equation

The evaporation-condensation process is governed by the Lee model [45], which describes mass transfer between phases using the vapor transport equation:

$$\frac{\partial \alpha_v}{\partial t} + \nabla \cdot (\alpha_v \vec{v}) = \dot{m}_{lv} \tag{12.3}$$

where α_v is the vapor phase volume fraction and $\dot{m}_{lv}$ is the mass transfer rate due to evaporation or condensation. This model classifies mass transfer direction based on local temperature:

If $T > T_{\text{sat}} + \Delta T$ (superheating), evaporation occurs:

$$\dot{m}_{lv} = r_v (T - T_{\text{sat}}) \tag{12.4}$$

If $T < T_{\text{sat}} - \Delta T$ (subcooling), condensation occurs:

$$\dot{m}_{lv} = r_l(T - T_{\text{sat}}) \tag{12.5}$$

Here, r_v and r_l are empirical coefficients defining the relaxation time for phase change and must be properly calibrated [46]. The resulting source term from phase change is multiplied by the latent heat to calculate the heat transfer effect.

The evolution of the secondary phase (vapor) is determined by a transport equation that maintains the volume fraction:

$$\frac{\partial \alpha_v}{\partial t} + \nabla \cdot (\alpha_v \vec{v}) = \dot{m}_{lv}/\rho_v \tag{12.6}$$

This equation ensures volume conservation of the secondary phase while accounting for the interfacial mass transfer and density of the vapor.

12.1.2 Momentum Equation

The momentum equation, as given in eq. (12.7), incorporates forces due to gravity, pressure gradients, viscous stresses, and surface tension. Surface tension is modeled using the continuous surface force (CSF) model by Brackbill et al. [47]:

$$\frac{\partial(\rho\vec{v})}{\partial t} + \nabla \cdot (\rho\vec{v}\vec{v}) = -\nabla p + \nabla \cdot \tau + \rho\vec{g} + \vec{F}_\sigma \tag{12.7}$$

The surface tension force $\vec{F}_\sigma$ is represented by

$$\vec{F}_\sigma = \sigma k \nabla \alpha \tag{12.8}$$

where σ is surface tension, k is the curvature, and α is the phase volume fraction. Surface tension and curvature are temperature-dependent and defined via:

$$\sigma = f(T) \tag{12.9}$$

$$\rho = \alpha_l \rho_l + \alpha_v \rho_v \tag{12.10}$$

12.1.3 Energy Equation

The energy equation incorporates the mass-averaged internal energy and temperature fields:

$$E = \alpha_l \rho_l h_l + \alpha_v \rho_v h_v \tag{12.11}$$

$$T = \frac{\alpha_l \rho_l T_l + \alpha_v \rho_v T_v}{\alpha_l \rho_l + \alpha_v \rho_v} \tag{12.12}$$

Mixture-specific heat and thermal conductivity are computed as:

$$C_p = \alpha_l C_{p,l} + \alpha_v C_{p,v} \tag{12.13}$$

$$k = \alpha_l k_l + \alpha_v k_v \tag{12.14}$$

Heat transfer due to phase change is modeled using a source term:

$$Q = \dot{m}_{lv} \cdot h_{fg} \tag{12.15}$$

The governing equations are discretized using the control volume method. Pressure-velocity coupling is handled via the semi-implicit method for pressure-linked equations (SIMPLE). A second-order upwind scheme is used for spatial discretization. Turbulence is modeled using the k-ω SST approach for improved accuracy and computational efficiency. A time step of 10^{-6} s is employed to maintain a Courant number below one. Convergence is guaranteed with a residual threshold of 1e-6 for all variables.

12.3 Mesh Independence Study and Validation

A mesh independence analysis was conducted to determine the best mesh size that achieves a balance between computational accuracy and efficiency. Due to the scarcity of experimental data on methane two-phase boiling phenomena, an air–silicone oil mixture at ambient settings was utilized to validate the flow regime through volume fraction plots. Additionally, heat transfer validation was carried out based on the liquid nitrogen cool-down process in a vertical pipe, where wall temperature predictions were compared against experimental results to assess the accuracy of the thermal model.

12.3.1 Mesh Independence Study

An O-grid meshing strategy was applied along the pipe's radial direction to effectively capture the complex interfacial dynamics in multiphase flow, as suggested in previous studies [32, 39, 44, 48]. Figure 12.2(a) illustrates the structured mesh generated along the radial direction, with finer clustering near the wall region to resolve expected steep velocity gradients due to the no-slip boundary condition. Four different mesh densities were evaluated: 40,000, 80,000, 160,000, and 320,000 elements. The test geometry consists of a vertical pipe with a diameter of 50 mm and a length of 1 m. A monitoring plane was positioned at the pipe outlet to track volume fraction over a simulation time of 0 to 3 s for each mesh size. As shown in Figure 12.2(b), the volume fraction profiles for 160,000 and 320,000 element meshes converge after approximately 1 s,

indicating negligible improvement with further refinement. Therefore, the mesh with 160,000 elements was selected for further simulations due to its balance between accuracy and computational cost.

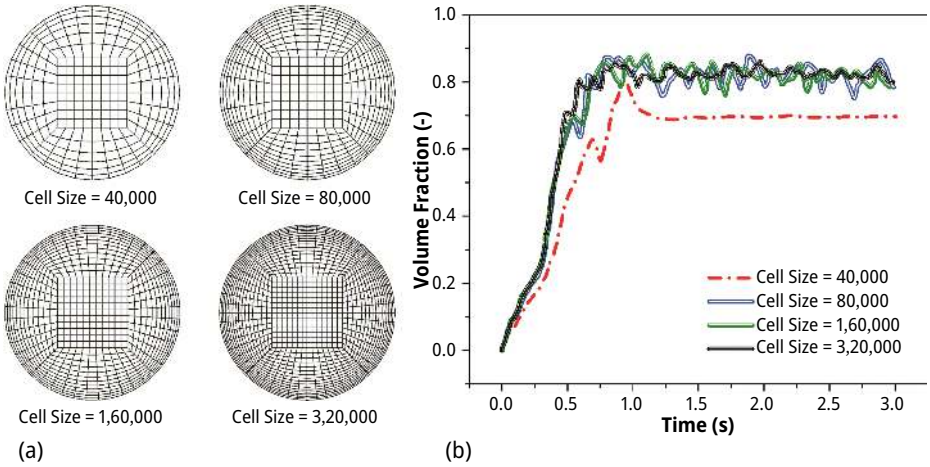

Figure 12.2: (a) Radial mesh distribution for all four mesh configurations; (b) Comparison of volume fraction at the feed pipe output with an inlet velocity of 0.5 m/s and a temperature of 95 K, utilizing four distinct mesh sizes.

12.3.2 Model Validation

The computational model was validated by comparing simulation results with established experimental data. Since studies involving liquid methane are scarce, the model was first validated using data from an air-silicone oil flow system reported by Abdulkadir et al. [48]. The setup and conditions are summarized in Table 12.2, while the thermophysical properties used are provided in Table 12.3. A comparison of vapor volume fraction was made at a plane located 1 m downstream from the inlet. Figure 12.3 demonstrates strong agreement between the numerical and experimental results, confirming the model's capability to accurately predict vapor distribution.

To further validate the model in cryogenic conditions, a second benchmark was conducted using data from Hedayatpour et al. [49] on liquid nitrogen cooldown in a vertical pipe. The experimental configuration and parameters are listed in Table 12.4, and the thermophysical properties of liquid and vapor nitrogen are detailed in Table 12.5. A comparison was made at 90 cm from the inlet, where the wall temperature predictions were matched against the experimental results. As shown in Figure 12.4, the computational model captures the wall temperature distribution qualitatively. The observed underprediction may be attributed to the limitations of the

Table 12.2: Specifications and operating conditions of the reference case used for model validation.

Parameter	Abdulkadir et al. [48]
Working fluid (–)	Air-silicon mixture
Pipe diameter (mm)	67
Length (m)	6
Operating pressure (bar)	1
Ambient temperature (K)	293
Inlet liquid velocity (m)	0.05
Inlet vapor velocity (m)	0.344
Inlet volume fraction of vapor (–)	0.873

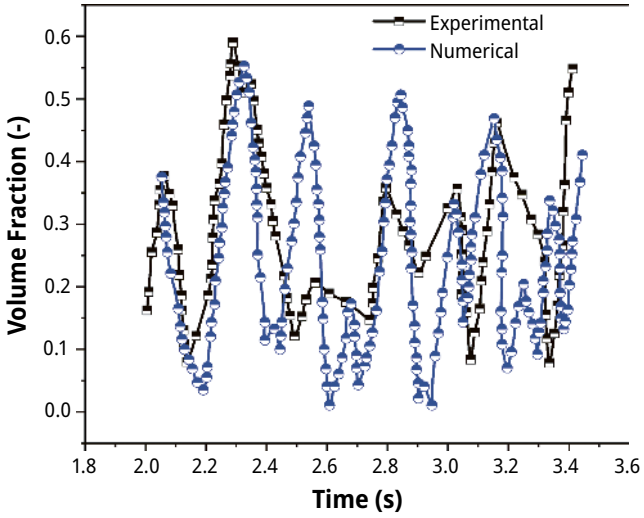

Figure 12.3: Comparison between the computed and experimental volume fraction at 1 m downstream from the inlet for an air-silicone oil mixture, based on the boundary conditions provided in Table 12.2.

Table 12.3: Physical properties of the reference liquid-gas system.

Fluid	Density (kg/m^3)	Viscosity (Pa-s)	Surface tension (N/m)
Air	1.18	0.000018	–
Silicone oil	900	0.0053	0.02

RANS turbulence model, which, due to its time-averaged nature, may not fully resolve all turbulent structures or boundary layer phenomena.

Table 12.4: Specifications and operating conditions of the cryogenic fluid used for validation.

Parameter	Hedayatpour et al. [49]
Fluid (–)	Liquid nitrogen (LN_2)
Outer diameter (mm)	12.7
Inner diameter (mm)	9.5
Pipe length (m)	3.66
Wall temperature (K)	297
Inlet liquid velocity (m)	0.292
Inlet pressure (kN/m^2)	34.5

Table 12.5: Thermophysical properties of the reference liquid–gas system used in the validation study.

Fluid	Density (kg/m^3)	Viscosity (Pa-s)	Thermal conductivity (W/m-K)	Surface tension (N/m)
Liquid nitrogen	806.08	0.00016065	0.14581	0.0089049
Vapor nitrogen	1.138	0.00001663	0.0242	–

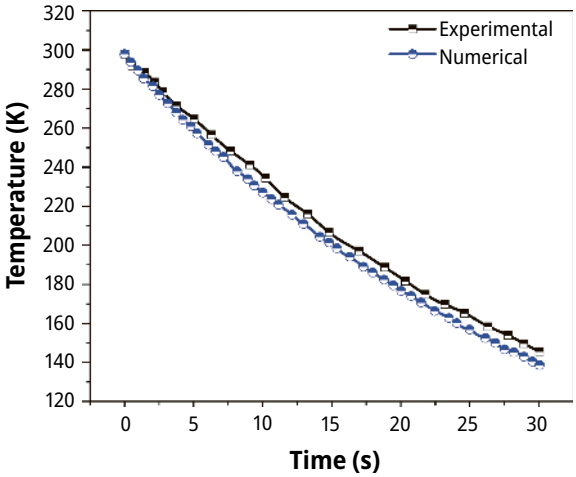

Figure 12.4: Comparison of computed and experimental wall temperatures at 90 cm downstream from the entry for a liquid nitrogen–vapor nitrogen (LN_2–VN_2), utilizing the boundary conditions outlined in Table 12.4.

12.4 Results and Discussion

The multiphase flow characteristics in methane feed pipes are examined utilizing the VOF method under the operational parameters specified in Table 12.6. To comprehend the thermal properties and flow dynamics of liquid methane, the velocity profile as well as velocity magnitude along the pipe radius, bulk mean temperature (T_b), Volume fraction, and probability density function (PDF) are evaluated.

Table 12.6: Flow conditions considered in the present study.

Inlet temperature (K)	Inlet velocity (m/s)	Inlet pressure (Pa)	Wall temperature (K)
95, 100, 105	0.5, 1	1.5×10^5	500

The hydrodynamic characterization process involves identifying the flow regimes in which two-phase flow phenomena occur within the feed pipe. As the flow enters through the inlet, liquid methane is gradually heated by the pipe wall, leading to an increase in its temperature. Once the temperature reaches the saturation point (T_{sat} = 116.66 K), phase transition from liquid to vapor begins. Figure 12.5 depicts the vapor volume fraction contours of methane at 3 s of flow time for different input velocities and temperatures outlined in Table 12.6. The outlines distinctly illustrate the evolution of flow regimes, first with bubble flow, progressing to annular flow, and ultimately culminating in slug flow. The observed multiphase flow patterns may display anomalies due to the gravitational influence integrated into the numerical solver [50].

Figure 12.5(i)–(iii) depicts the vapor volume fraction contours of methane at an inlet velocity of 0.5 m/s at three inlet temperatures: 95 K, 100 K, and 105 K, respectively. In Figure 12.5(i), at an inlet temperature of 95 K, vaporization commences near the wall prior to 0.33 m from the inlet owing to the elevated wall temperature. The radial cross section (a) indicates the initiation of slug flow, characterized by merged vapor structures with a modest vapor volume fraction. Cross section (b), located at 0.66 m, shows the evolution into a fully developed annular flow regime, where the vapor core becomes dominant with a likely liquid film along the wall. At cross section (c), near the pipe outlet (1 m), the vapor occupies nearly the entire cross section, indicating a transition into a dispersed annular flow regime, where entrained liquid droplets may be suspended in the vapor phase.

In Figure 12.5(ii), corresponding to an inlet temperature of 100 K, vaporization begins earlier and becomes more intense due to the reduced superheat requirement. Cross section (a) shows stronger slug flow behavior closer to the inlet than in Figure 12.5(i), while cross sections (b) and (c) demonstrate a quicker transition to annular and dispersed annular flow regimes. The earlier onset and sharper gradients in vapor volume fraction reflect the enhanced phase change at higher initial liquid temperatures. Further, Figure 12.5(iii), at an inlet temperature of 105 K, exhibits the most aggressive phase

transition among the three cases. Cross section (a) shows a well-developed slug flow almost immediately after the inlet, with cross section (b) confirming early annular flow characteristics. Cross section (c) reveals a high vapor volume fraction with minimal visible liquid phase, reinforcing the establishment of a dispersed annular regime. The trend highlights the influence of inlet temperature on accelerating vapor production and shifting flow regime transitions closer to the inlet.

Figure 12.5(iv)–(vi) illustrates the vapor volume fraction contours for the identical inlet temperatures (95 K, 100 K, and 105 K) with an increased inlet velocity of 1.0 m/s. In Figure 12.5(iv), the initiation of vaporization is postponed compared to the 0.5 m/s scenario, owing to the diminished residence time of liquid methane within the pipe. Cross section (a) illustrates minimal vapor adjacent to the wall, indicating bubble movement, whereas cross section (b) depicts the initial phase of slug flow. At cross section (c), the vapor layer becomes more continuous, indicating a transition toward annular flow. However, Figure 12.5(v), at an inlet temperature of 100 K, shows a clear upstream shift in flow regimes. Cross section (a) captures bubble formation earlier than in Figure 12.5(iv), while sections (b) and (c) exhibit stronger slug and annular flow characteristics. The elevated inlet temperature promotes more rapid phase change despite the higher velocity. In Figure 12.5(vi), with an inlet temperature of 105 K, vapor formation begins very close to the inlet. Cross section (a) shows a dense vapor region, while cross section (b) confirms a well-developed slug flow. By cross section (c), the flow is dominated by vapor, marking a fully developed annular regime. The increased inlet temperature compensates for the shorter residence time at 1.0 m/s, resulting in intensified and earlier vapor production.

Figure 12.6 presents the time-dependent variation of the average methane vapor volume fraction at three axial locations: 0.33 m away from the inlet, 0.66 m away from the inlet, and at the outlet (1.0 m) under varying inlet temperatures and a constant inlet velocity of 0.5 m/s. In Figure 12.6(a), for an inlet temperature of 95 K, vapor generation begins gradually due to the higher degree of subcooling. The vapor volume fraction rises steadily and stabilizes near 0.92 at the outlet, indicating that most of the phase transition occurs in the downstream region. At 0.66 m, the vapor content peaks around 0.88, while at 0.33 m, it remains relatively low (~0.60), reflecting limited phase change in the early part of the pipe due to insufficient thermal energy. In Figure 12.6(b), increasing the inlet temperature to 100 K reduces the subcooling, thereby enhancing the rate of phase change. The vapor volume fraction rises more rapidly across all sections. At 0.66 m and 1.0 m, the values exceed 0.85, while at 0.33 m, the vapor content increases to approximately 0.70, indicating that vapor formation begins earlier and progresses more uniformly along the pipe length. In Figure 12.6(c), for an inlet temperature of 105 K, the effect of thermal input is even more prominent. Due to the minimal subcooling, vaporization initiates almost immediately, and the vapor volume fraction exceeds 0.96 at the outlet within the first second. At 0.66 m and 0.33 m, the vapor content also increases significantly, reaching approximately 0.85 and 0.76, respectively. This demonstrates that higher inlet temperatures accelerate the onset and extent of

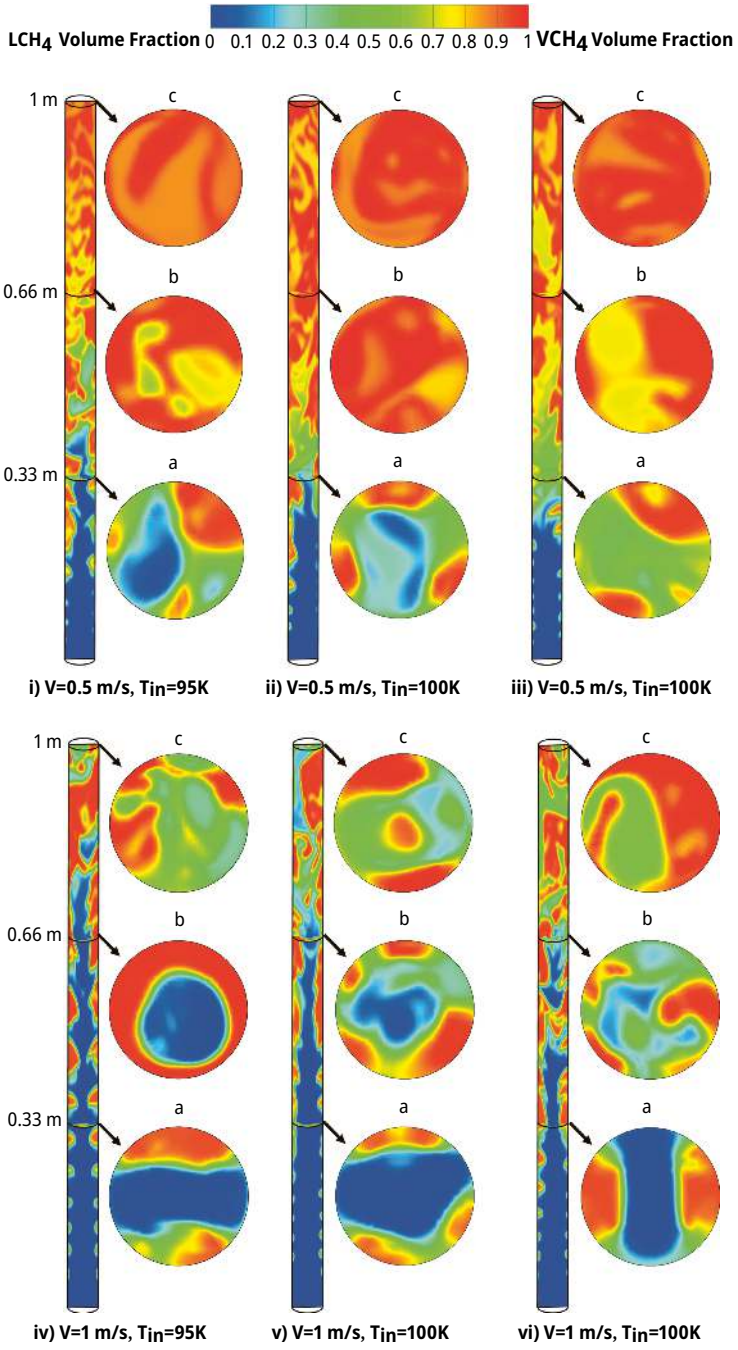

Figure 12.5: Vapor volume fraction contours along the axial midsection and radial direction of the feed pipe at 3 s of flow time for the inlet conditions detailed in Table 12.6.

phase transition, resulting in faster and more homogeneous vapor generation along the entire flow path.

Further, in Figure 12.6(d), with the inlet velocity raised to 1.0 m/s and temperature kept at 95 K, vaporization is delayed, especially near the inlet. The vapor volume fraction at 0.33 m remains low (~0.3), while at 0.66 m and 1.0 m, it stabilizes at ~ 0.7 and ~ 0.81, respectively. This behavior reflects the impact of reduced residence time, which limits early-stage heat absorption and vapor formation. In Figure 12.6(e), corresponding to 100 K and 1.0 m/s, vapor generation improves at the downstream locations. The outlet reaches above 0.85, and 0.66 m increases to 0.77, while at 0.33 m, the increase in vapor volume fraction is only marginal (0.32), indicating that phase change is still delayed in the upstream section despite the higher inlet temperature. In Figure 12.6(f), for an inlet temperature of 105 K and a velocity of 1.0 m/s, vapor formation becomes more effective across all sections. While the vapor fraction at 1.0 m and 0.66 m reaches 0.88 and 0.73, respectively, the increase at 0.33 m remains moderate (0.35). This trend confirms that at higher inlet velocities, the increase in vapor volume fraction near the inlet (0.33 m) is minimal, but noticeable gains are seen at 0.66 m and the outlet with rising temperature, demonstrating that thermal energy input can partially offset the effect of reduced residence time.

Figure 12.7 shows the probability density functions (PDFs) of vapor volume fraction at the outlet of the cryogenic feed pipe for different inlet temperatures (95 K, 100 K, and 105 K) and inlet velocities (0.5 m/s and 1.0 m/s), under heated wall temperature. At the lower inlet velocity of 0.5 m/s, the vapor distribution progressively shifts toward higher volume fractions with increasing inlet temperature. In Figure 12.7(i) (95 K), the PDF is relatively broad, indicating a wider range of vapor content across the outlet cross section, consistent with a developing annular flow regime where vapor is dominant but residual liquid is still present. As the inlet temperature increases to 100 K in Figure 12.7(ii), the distribution becomes more concentrated around the peak, suggesting a stable annular flow with reduced fluctuations in vapor content. In Figure 12.7(iii) (105 K), the PDF becomes sharply skewed and narrowly focused near the upper vapor fraction limit, reflecting a dispersed annular flow in which vapor thoroughly dominates the flow field and liquid exists primarily as entrained droplets.

At the higher inlet velocity of 1.0 m/s, vaporization near the inlet is limited due to reduced residence time, but the outlet still shows a progressive increase in vapor volume fraction with rising inlet temperature. In Figure 12.7(iv) (95 K), the PDF is broad and peaks around 0.85, indicating an incomplete phase transition and the presence of slug or intermittent flow. As the inlet temperature increases to 100 K and 105 K in Figure 12.7(v) and (vi), the peaks shift upward toward 0.90–0.95, while the distributions become slightly narrower. This reflects more consistent vapor formation and the development of a stable annular flow regime. However, the lack of a sharp and narrow peak near unity confirms that the flow does not fully transition into a dispersed annular state. These observations highlight that, while higher temperature enhances vaporization, the elevated velocity

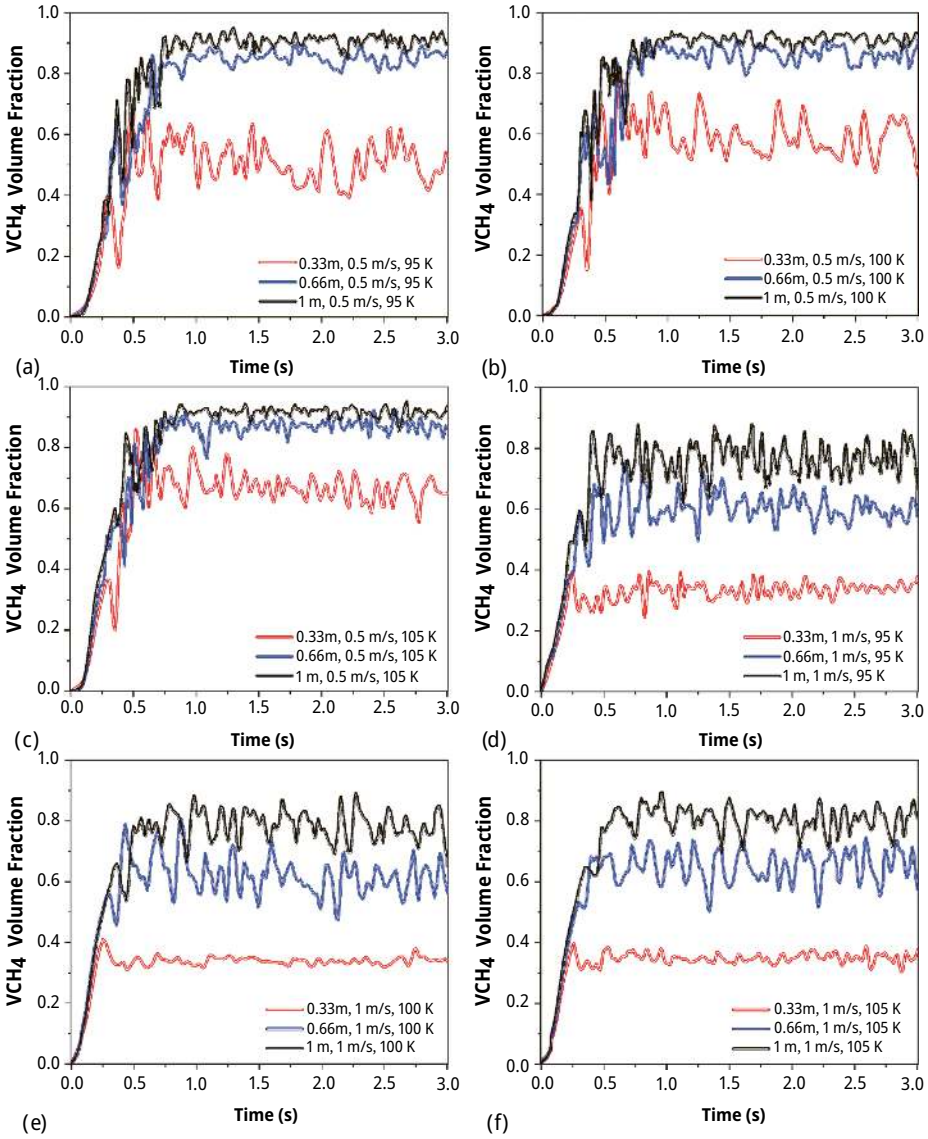

Figure 12.6: Temporal variation of average vapor volume fraction measured at three axial locations: 0.33 m, 0.66 m, and 1.0 m from the inlet for the inlet conditions specified in Table 12.6.

constrains complete phase transition by limiting heat transfer time. Overall, the PDF analysis reveals that inlet temperature is the primary driver of enhanced vaporization, promoting the transition from slug to annular and eventually to dispersed annular flow at lower velocities. In contrast, higher inlet velocities limit phase change near the inlet,

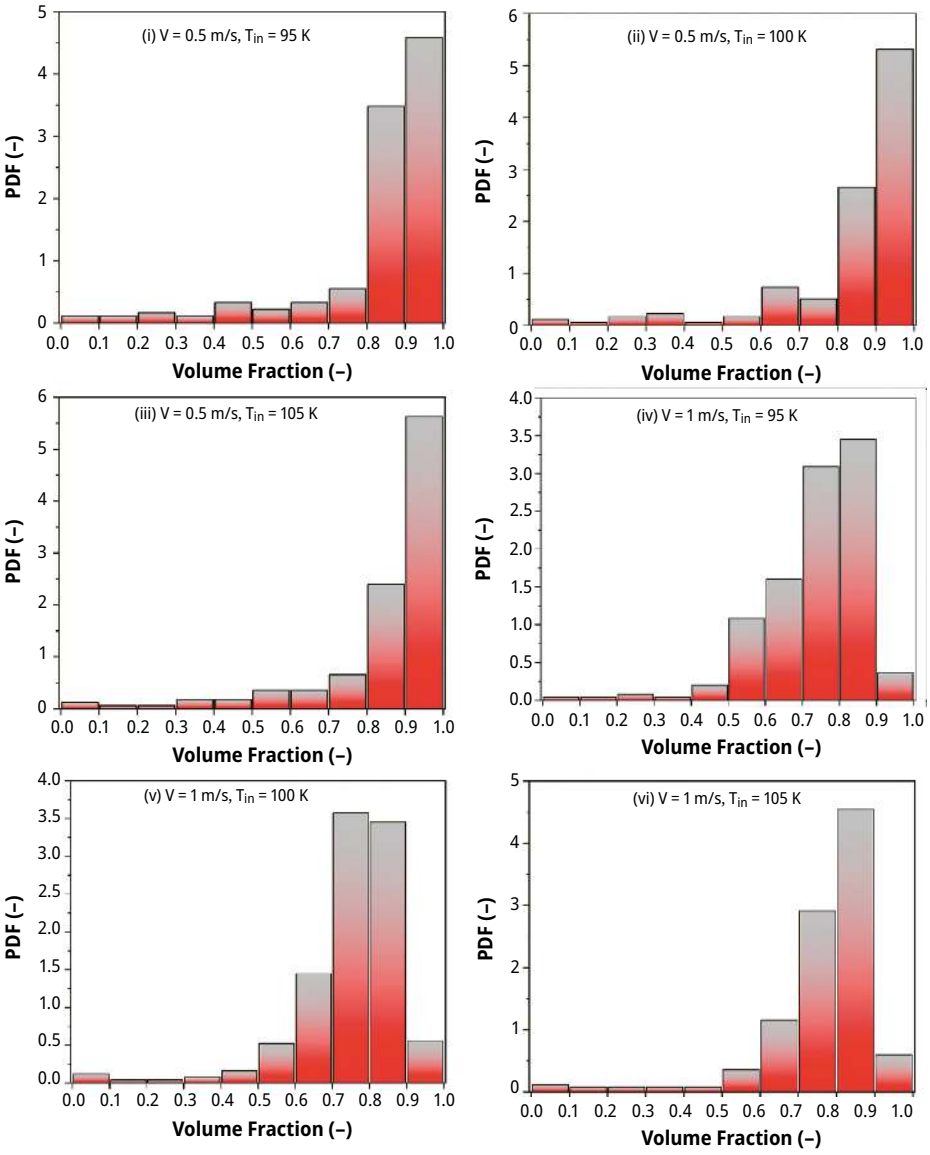

Figure 12.7: Probability density function (PDF) of vapor volume fraction at the outlet monitoring plane for the inlet conditions specified in Table 12.6.

resulting in broader vapor distribution and delayed flow regime transitions, even under elevated thermal conditions.

Figure 12.8 presents the temperature contours along the axial midsection of the cryogenic feed pipe for various inlet temperatures (95 K, 100 K, 105 K) and velocities

(0.5 m/s and 1.0 m/s). These contours provide insight into the heat transfer dynamics and thermal development of the two-phase flow along the pipe length. At the lower inlet velocity of 0.5 m/s, shown in Figure 12.8(i)–(iii), the fluid exhibits higher overall temperature magnitudes along the pipe. In Figure 12.8(i) (95 K), a steep temperature gradient appears near the inlet, indicating strong wall-to-fluid heat transfer and delayed vaporization in the upstream region. As the flow progresses, localized hot zones form due to phase change and latent heat absorption. In Figure 12.8(ii) (100 K), increased thermal penetration leads to elevated temperatures deeper into the pipe, while in Figure 12.8(iii) (105 K), high-temperature regions extend close to the inlet, consistent with accelerated vaporization and the development of annular or dispersed annular flow regimes.

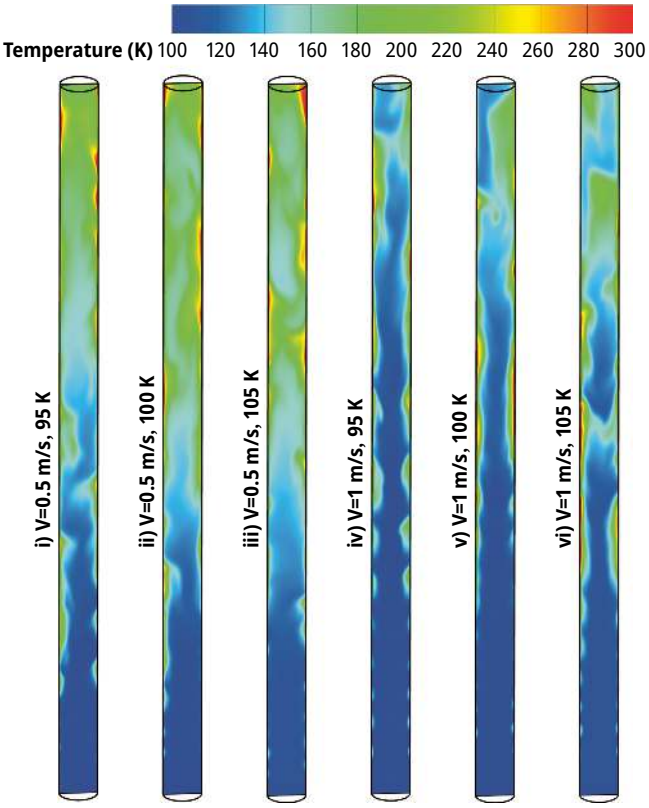

Figure 12.8: Temperature contours along the axial midsection of the feed pipe for the inlet conditions specified in Table 12.6.

In contrast, at the higher inlet velocity of 1.0 m/s (Figure 12.8(iv)–(vi)), the temperature contours show significantly lower magnitudes throughout the domain. This occurs because the increased flow velocity reduces the residence time, limiting the duration

available for heat transfer from the wall to the fluid. In Figure 12.8(iv) (95 K), large portions of the flow remain at low temperature, indicating a delayed and incomplete phase transition. Even at higher inlet temperatures (Figure 12.8(v) and (vi)), while upstream penetration of heat improves slightly, the thermal profile remains less developed than in the 0.5 m/s case. This reflects the inability of the flow to fully utilize the available thermal energy due to its rapid passage through the heated domain. These trends directly correlate with the vapor volume fraction and PDF results. The more intense and widespread heating observed in the 0.5 m/s cases supports the formation of annular and dispersed annular flow regimes, while the limited temperature rise in the 1.0 m/s cases reinforces the presence of transitional or early annular flow at the outlet. The results highlight that flow velocity significantly influences heat transfer efficiency, with lower velocities promoting greater thermal development and more complete phase change in cryogenic two-phase systems.

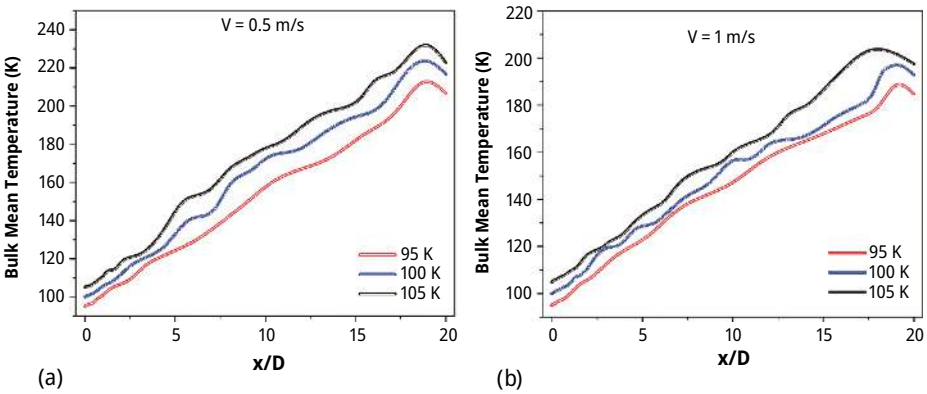

Figure 12.9: Bulk mean temperature distribution along the non-dimensional length of the feed pipe at 3 s for the inlet conditions specified in Table 12.6.

Figure 12.9 illustrates the bulk mean temperature distribution along the nondimensional length (x/D) of the cryogenic feed pipe at 3 s for various inlet temperatures and velocities. In Figure 12.9(a), with an inlet velocity of 0.5 m/s, the bulk mean temperature escalates more rapidly and attains greater values along the pipe length in comparison to Figure 12.9(b). Among the three inlet temperature cases, 105 K consistently exhibits the highest bulk temperatures, followed by 100 K and 95 K, which is attributed to reduced subcooling and an earlier onset of phase transition. The steeper gradient observed toward the outlet indicates intensified vaporization, especially for higher inlet temperatures, where latent heat absorption enhances thermal development. This behavior aligns with the formation of annular and dispersed annular flow regimes as previously identified in the volume fraction and PDF analyzes.

However, in Figure 12.9(b), for the higher inlet velocity of 1.0 m/s, the rise in bulk mean temperature along the pipe is more gradual. The shorter residence time limits the heat transfer from the wall, resulting in lower bulk temperatures throughout the domain. Nevertheless, an increasing trend is still observed with rising inlet temperature, although the spacing between the curves is narrower than in Figure 12.9(a). This reduced thermal separation suggests that the faster-moving fluid has less opportunity to absorb heat, thereby delaying phase transition and limiting the flow's progression into fully developed vapor-dominated regimes. Overall, the results demonstrate that higher inlet temperatures accelerate thermal development and phase transition, while increased inlet velocity diminishes heat transfer efficiency by reducing wall-fluid interaction time.

Figure 12.10 depicts the velocity contours along the axial midsection of the cryogenic feed pipe at 3 s of flow time for two inlet velocities (0.5 m/s and 1.0 m/s) and three inlet temperatures (95 K, 100 K, and 105 K). In the 0.5 m/s cases (Figure 12.10(i)–(iii)), the velocity distribution is more irregular and exhibits greater spatial variation along the pipe length. In Figure 12.10(i) (95 K), localized high-velocity regions appear intermittently along the flow direction, consistent with the formation of slug flow, where alternating vapor slugs and liquid slugs produce velocity fluctuations. As the inlet temperature increases in Figure 12.10(ii) and (iii) (100 K and 105 K), the high-velocity regions become more continuous and elongated, particularly near the centre of the pipe. This shift suggests the development of annular flow, where vapor accelerates through the core and liquid remains confined to a thin wall film. The increasing dominance of the vapor phase at higher temperatures contributes to these higher axial velocities due to its lower density and enhanced expansion.

In the 1.0 m/s cases (Figure 12.10(iv)–(vi)), the velocity contours appear smoother and more aligned along the axial direction, reflecting a more streamlined flow structure. In Figure 12.10(iv) (95 K), velocity magnitudes are generally lower throughout the pipe, with fewer signs of vapor acceleration, consistent with incomplete phase transition. As the inlet temperature increases in Figure 12.10(v) and (vi), axial velocities increase gradually, particularly in the downstream region, indicating enhanced vapor generation. However, the higher inlet velocity results in shorter residence time, which limits heat transfer and delays the onset of fully developed vapor-dominated regimes. Consequently, the high-velocity core observed in the 0.5 m/s cases is less pronounced here, despite higher inlet temperatures. The enhanced core velocity at lower inlet velocity and higher temperature confirms the development of annular and dispersed annular flows, whereas higher velocities suppress this behavior, resulting in transitional or early-stage annular flow structures with lower overall vapor content.

Figure 12.11 shows the radial distribution of velocity magnitude at both the mid-plane and outlet of the cryogenic feed pipe at 3 s, for various inlet velocities and temperatures. Figure 12.11(a) shows a schematic of the cryogenic feed pipe, highlighting the axial locations where the velocity profiles were evaluated: the mid-plane (located at half the pipe length) and the outlet (pipe exit). These two planes were selected to

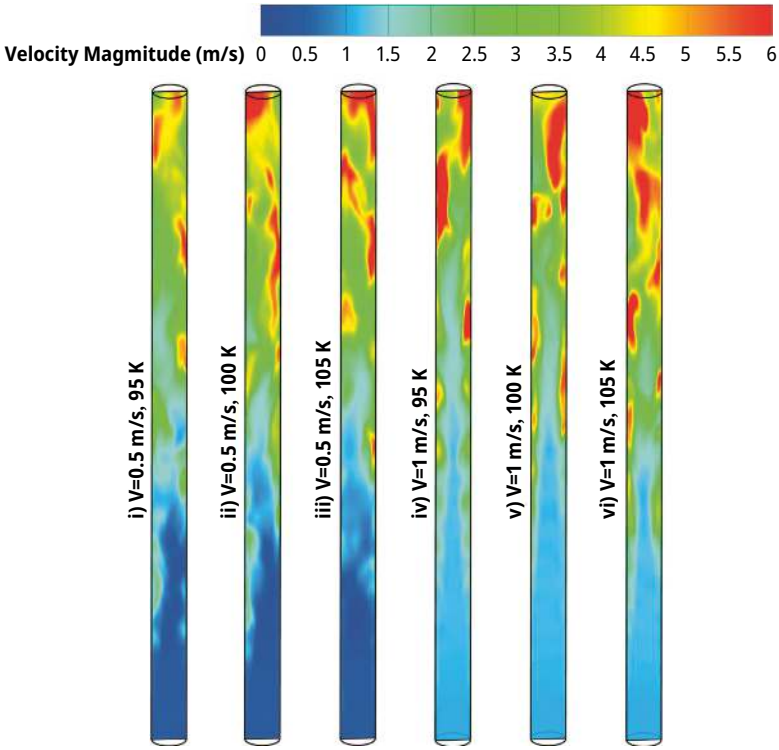

Figure 12.10: Velocity contours along the axial midsection of the feed pipe at 3 s of flow time, for the initial conditions as specified in Table 12.6**.**

capture the velocity development across the flow length, with the mid-plane representing the evolving flow structure during heat transfer and phase change, while the outlet provides insight into the fully developed flow regime. In Figure 12.11(b) (0.5 m/s), the velocity profiles exhibit a marked increase in core velocity with rising inlet temperature. At 95 K, the profiles remain flatter and less symmetric, indicating limited phase transition and potential presence of slug flow with uneven vapor-liquid interfaces. As the inlet temperature increases to 100 K and 105 K, a pronounced velocity peak forms near the centre of the pipe, particularly at the outlet. This central acceleration reflects the formation of a vapor core surrounded by a liquid film, a characteristic of annular flow. The high vapor velocity is driven by the lower density and higher mobility of the vapor phase, which expands as phase change progresses. At 105 K, this effect is most prominent, supporting the onset of a dispersed annular regime at the outlet.

However, in Figure 12.11(c) (1.0 m/s), velocity magnitudes are higher overall due to the increased inlet momentum. However, the velocity profiles are more symmetric and flatter compared to the 0.5 m/s case, especially at 95 K and 100 K. This suggests

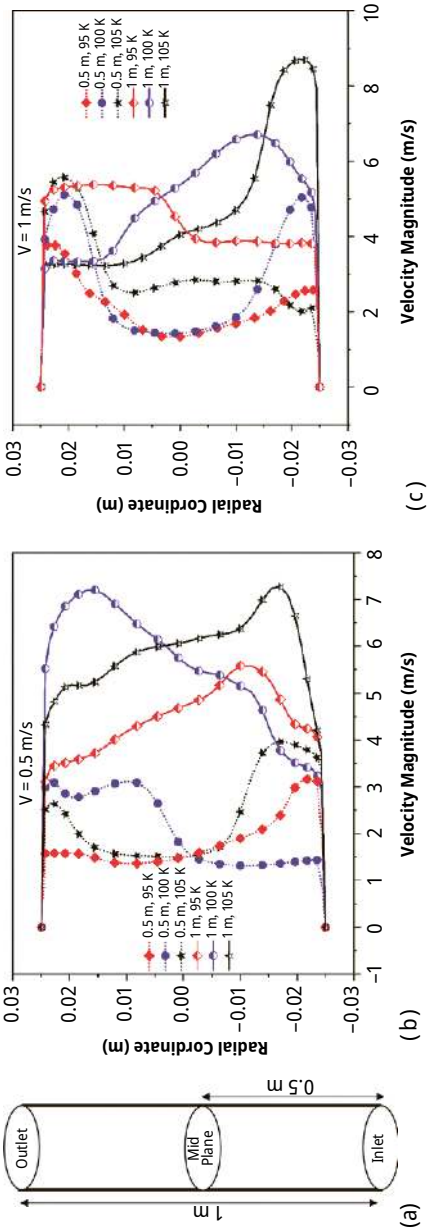

Figure 12.11: Contours of velocity magnitude at the mid-plane and outlet of the pipe after 3 s of flow, under various inlet velocities and temperatures as specified in Table 12.6.

that while the bulk velocity is high, the phase change is less advanced due to reduced residence time, resulting in less vapor core formation and more uniform velocity distributions across the radius. At 105 K, the velocity peak begins to form at the outlet, indicating partial vapor core development, but it is less intense than the 0.5 m/s case. This aligns with the understanding that higher inlet velocity suppresses full development of annular or dispersed annular flow due to insufficient thermal exchange time. Overall, the velocity profiles confirm that higher inlet temperatures promote vapor core acceleration, especially at lower velocities where residence time allows effective phase transition. Conversely, higher velocities limit thermal interaction, leading to more uniform and less structured velocity distributions even at elevated temperatures.

12.5 Conclusion

The present study numerically investigated the multiphase hydrodynamic and thermodynamic behavior of liquid methane in a vertically oriented cryogenic feed pipe using a validated volume of fluid (VOF) model coupled with the energy equation. The analysis focused on the impact of varying inlet velocities and temperatures on phase change characteristics, heat transfer dynamics, and flow regime development. Results indicated that increasing the inlet temperature enhances vapor generation, shifts the onset of vaporization closer to the inlet, and promotes the transition from slug to annular and dispersed annular flow regimes. Conversely, higher inlet velocities reduce the residence time available for wall-fluid heat exchange, delaying phase change and resulting in transitional or early annular flow patterns near the outlet.

Thermal analysis revealed that lower inlet velocities enabled more effective heat transfer, reflected by higher bulk mean temperatures and more developed near-wall temperature gradients. The temperature fields and average vapor volume fraction trends both confirmed that increasing the inlet temperature at a fixed velocity leads to a more uniform and rapid phase transition. At higher velocities, thermal development was suppressed, causing a reduction in vapor generation along the pipe. This was evident from flatter temperature profiles, lower outlet vapor fractions, and reduced near-wall heating. The results emphasize the critical role of flow velocity in controlling the degree of thermal penetration and the location of regime transitions in cryogenic two-phase flows.

Additionally, velocity distribution analysis revealed that annular flow is characterized by a high-velocity vapor core surrounded by a slower-moving liquid film, whereas slug and transitional flows exhibited fluctuating and less organized velocity patterns. At low velocities and high inlet temperatures, a distinct vapor core was observed, accompanied by enhanced axial velocity due to reduced density from thermal expansion. At high velocities, the velocity field remained more symmetric and less developed due to incomplete phase change. These findings provide valuable insights for

the design and optimization of cryogenic feed systems used in space propulsion, rocket engine cooling circuits, and cryogenic fuel storage technologies. Future work may include investigating the effects of pipe inclination, gravitational variation (microgravity conditions), and transient chill-down operations, as well as extending the current model to include real-gas properties and turbulent interface dynamics for improved prediction of unsteady multiphase behavior in advanced cryogenic systems.

References

[1] Jones, H. W. (2018). The recent large reduction in space launch cost. International Conference on Environmental Systems, 81. https://ttu-ir.tdl.org/handle/2346/74082.

[2] Heldens, J. C., Fridh, J., and Östlund, J. (2021). On the characterization of methane in rocket nozzle cooling channels. Acta Astronaut, 186, 337–346. https://doi.org/10.1016/j.actaastro.2021.05.034.

[3] Klepikov, I. A., Katorgin, B. I., and Chvanov, V. K., The new generation of rocket engines, operating by ecologically safe propellant " liquid oxygen and liquefied natural gas(methane)," 1997.

[4] Meyer, M. L., Motil, S. M., Kortes, T. F., Taylor, W. J., and Mcright, P. S., Cryogenic propellant storage and transfer technology demonstration for long duration in-space missions, 2012. http://www.sti.nasa.gov.

[5] Haeseler, D., Mäding, C., Götz, A., Roubinski, V., Khrissanfov, S., and Berejnoy, V. (2002). Testing of LOX-hydrocarbon thrust chambers for future reusable launch vehicles. 38th AIAA/ASME/SAE/ASEE Joint Propulsion Conference and Exhibit, https://doi.org/10.2514/6.2002-3845.

[6] Iannetti, A., Girard, N., Tchou-kien, D., Bonhomme, C., Ravier, N., and Edeline, E. (2017). Prometheus, a Lox/Lch4 reusable rocket engine. 7th European Conference for Aeronautics and Space Sciences, 1–9. https://doi.org/10.13009/EUCASS2017-537.

[7] Baiocco, P. and Bonnal, C. (2016). Technology demonstration for reusable launchers. Acta Astronautica, 120, 43–58. https://doi.org/10.1016/j.actaastro.2015.11.032.

[8] Salerno, L. J. and Kittel, P. (1999). Cryogenics and the human exploration of Mars. Cryogenics (Guildf), 39, 381–388. https://doi.org/10.1016/S0011-2275(99)00043-0.

[9] Rapp, D., Human Missions to Mars, 2016. https://doi.org/10.1007/978-3-319-22249-3.

[10] Burkhardt, H., Sippel, M., Herbertz, A., and Klevanski, J. (2004). Kerosene vs methane: A propellant tradeoff for reusable liquid booster stages. Journal of Spacecraft and Rockets , 41, 762–769. https://doi.org/10.2514/1.2672.

[11] Yung, Y. L., Chen, P., Nealson, K., Atreya, S., Beckett, P., Blank, J. G., Ehlmann, B., Eiler, J., Etiope, G., Ferry, J. G., Forget, F., Gao, P., Hu, R., Kleinböhl, A., Klusman, R., Lefèvre, F., Miller, C., Mischna, M., Mumma, M., Newman, S., Oehler, D., Okumura, M., Oremland, R., Orphan, V., Popa, R., Russell, M., Shen, L., Lollar, B. S., Staehle, R., Stamenković, V., Stolper, D., Templeton, A., Vandaele, A. C., Viscardy, S., Webster, C. R., Wennberg, P. O., Wong, M. L., and Worden, J. (2018). Methane on mars and habitability: Challenges and responses. Astrobiology, 18, 1221–1242. https://doi.org/10.1089/ast.2018.1917.

[12] Jeon, G. M., Park, J. C., and Choi, S. (2021). Multiphase-thermal simulation on BOG/BOR estimation due to phase change in cryogenic liquid storage tanks. Applied Thermal Engineering, 184, 116264. https://doi.org/10.1016/j.applthermaleng.2020.116264.

[13] Ferrín, J. L. and Pérez-Pérez, L. J. (2020). Numerical simulation of natural convection and boil-off in a small size pressurized LNG storage tank. Computers and Chemical Engineering, 138. https://doi.org/10.1016/j.compchemeng.2020.106840.

[14] Ghafri, S. Z. S. A., Swanger, A., Jusko, V., Siahvashi, A., Perez, F., Johns, M. L., and May, E. F. (2022). Modeling of liquid hydrogen boil-off. Energies, 15. https://doi.org/10.3390/en15031149.
[15] Kwak, D.-H., Heo, J.-H., Park, S.-H., Seo, S.-J., and Kim, J.-K. (2018). Energy-efficient design and optimization of boil-off gas (BOG) re-liquefaction process for liquefied natural gas (LNG)-fuelled ship. Energy, 148, 915–929. https://doi.org/10.1016/j.energy.2018.01.154.
[16] Hartwig, J., Hu, H., Styborski, J., and Chung, J. N. (2015). Comparison of cryogenic flow boiling in liquid nitrogen and liquid hydrogen chilldown experiments. International Journal of Heat and Mass Transfer, 88, 662–673. https://doi.org/10.1016/j.ijheatmasstransfer.2015.04.102.
[17] Yuan, K., Ji, Y., and Chung, J. N., Cryogenic chilldown process under low flow rates, 50 (2007) 4011–4022. https://doi.org/10.1016/j.ijheatmasstransfer.2007.01.034.
[18] Yuan, K., Ji, Y., and Chung, J. N. (2009). Numerical modeling of cryogenic chilldown process in terrestrial gravity and microgravity. Journal of Heat and Fluid Flow, 30, 44–53. https://doi.org/10.1016/j.ijheatfluidflow.2008.10.004.
[19] Azzopardi, B. and Hills, J. (2003). Flow Patterns. Transitions and Models for Specific Flow Patterns, 1–77, https://doi.org/10.1007/978-3-7091-2538-0_1.
[20] Jouhara, H., Chauhan, A., Guichet, V., Delpech, B., Abdelkarem, M. A., Olabi, A. G., and Trembley, J. (2023). Low-temperature heat transfer mediums for cryogenic applications. Taiwan Institute of Chemical Engineers, 104709. https://doi.org/10.1016/j.jtice.2023.104709.
[21] Gao, Y., Wang, Z., Li, Y., Ma, E., and Yu, H. (2024). Flow boiling of liquid nitrogen in a horizontal macro-tube at low pressure: Part I – Flow pattern, two-phase flow instability, and pressure drop. Journal of Heat and Fluid Flow, 107, 109335. https://doi.org/10.1016/j.ijheatfluidflow.2024.109335.
[22] Xie, H., Yu, L., Zhou, R., Qiu, L., and Zhang, X. (2017). Preliminary evaluation of cryogenic two-phase flow imaging using electrical capacitance tomography. Cryogenics (Guildf), 86, 97–105. https://doi.org/10.1016/j.cryogenics.2017.07.008.
[23] Sun, D., Qiao, X., Yang, D., and Shen, Q. (2023). Experimental study on a two-stage large cooling capacity stirling cryocooler working below 30 K. Cryogenics (Guildf), 129, 103619. https://doi.org/10.1016/j.cryogenics.2022.103619.
[24] Hu, H., Chung, J. N., and Amber, S. H. (2012). An experimental study on flow patterns and heat transfer characteristics during cryogenic chilldown in a vertical pipe. Cryogenics (Guildf), 52, 268–277. https://doi.org/10.1016/j.cryogenics.2012.01.033.
[25] Kawanami, O., Azuma, H., and Ohta, H. (2007). Effect of gravity on cryogenic boiling heat transfer during tube quenching. International Journal of Heat and Mass Transfer, 50, 3490–3497. https://doi.org/10.1016/j.ijheatmasstransfer.2007.01.025.
[26] Zhang, Z., Jia, L., Dang, C., and Ding, Y. (2024). Experimental study on flow boiling characteristics of R134a inside high-heat-flux microchannels. Journal of Heat and Fluid Flow, 107, 109372. https://doi.org/10.1016/j.ijheatfluidflow.2024.109372.
[27] Voglar, J. (2019). Bubble energy and latent heat flux estimation. Heat Transfer Research, 50, 57–64. https://doi.org/10.1615/HeatTransRes.2018024370.
[28] Fang, X., Sudarchikov, A. M., Chen, Y., Dong, A., and Wang, R. (2016). Experimental investigation of saturated flow boiling heat transfer of nitrogen in a macro-tube. International Journal of Heat and Mass Transfer, 99, 681–690. https://doi.org/10.1016/j.ijheatmasstransfer.2016.03.126.
[29] Fu, X., Qi, S. L., Zhang, P., and Wang, R. Z. (2008). Visualization of flow boiling of liquid nitrogen in a vertical mini-tube. International Journal of Heat and Fluid Flow, 34, 333–351. https://doi.org/10.1016/j.ijmultiphaseflow.2007.10.014.

[30] Ghorai, S. and Nigam, K. D. P. P. (2006). CFD modeling of flow profiles and interfacial phenomena in two-phase flow in pipes. Chemical Engineering and Processing: Process Intensification, 45, 55–65. https://doi.org/10.1016/j.cep.2005.05.006.

[31] Chuang, T. J. and Hibiki, T. (2015). Vertical upward two-phase flow CFD using interfacial area transport equation. Nuclear Energy, 85, 415–427. https://doi.org/10.1016/j.pnucene.2015.07.008.

[32] Chen, J., Zeng, R., Zhang, X., Qiu, L., and Xie, J. (2018). Numerical modeling of flow film boiling in cryogenic chilldown process using the AIAD framework. International Journal of Heat and Mass Transfer, 124, 269–278. https://doi.org/10.1016/j.ijheatmasstransfer.2018.03.087.

[33] Duan, Y., Pan, C., Wang, W., Li, L., and Zhou, Y. (2023). Design and optimization of heat exchanger in coaxial pulse tube cryocooler working above 100 K. Cryogenics (Guildf), 129, 103607. https://doi.org/10.1016/j.cryogenics.2022.103607.

[34] Archipley, C., Barclay, J., Meinhardt, K., Whyatt, G., Thomsen, E., Holladay, J., Cui, J., Anderson, I., and Wolf, S. (2022). Methane liquefaction with an active magnetic regenerative refrigerator. Cryogenics (Guildf), 128, 103588. https://doi.org/10.1016/j.cryogenics.2022.103588.

[35] Liu, Y., Olewski, T., and Véchot, L. N. (2015). Modeling of a cryogenic liquid pool boiling by CFD simulation. Journal of Loss Prevention in the Process Industries, 35, 125–134. https://doi.org/10.1016/j.jlp.2015.04.006.

[36] Zhang, H., Zhi, X., Gu, C., Qi, Y., and Qiu, L. (2022). Numerical analysis of cryogenic LOX-LN2 mass transfer characteristics under different textured surfaces. Cryogenics (Guildf), 125. https://doi.org/10.1016/j.cryogenics.2022.103507.

[37] Raj, K. and Raj, P. R. L. (2025). Hydrodynamic and thermodynamic behavior of liquid Methane in a vertical feed pipe. Journal of Applied Fluid Mechanics, 18, 1266–1284. https://doi.org/10.47176/jafm.18.5.3094.

[38] Chen, J., Zeng, R., Chen, H., and Xie, J. (2020). Effects of wall superheat and mass flux on flow film boiling in cryogenic chilldown process. AIP Advances, 10. https://doi.org/10.1063/1.5135643.

[39] Agarwal, R. and Dondapati, R. S. (2020). Numerical investigation on hydrodynamic characteristics of two-phase flow with liquid hydrogen through cryogenic feed lines at terrestrial and microgravity. Applied Thermal Engineering, 173, 115240. https://doi.org/10.1016/j.applthermaleng.2020.115240.

[40] Ahammad, M., Olewski, T., Véchot, L. N., and Mannan, S. (2016). A CFD based model to predict film boiling heat transfer of cryogenic liquids. Journal of Loss Prevention in the Process Industries, 44, 247–254. https://doi.org/10.1016/j.jlp.2016.09.017.

[41] Linstrom, P. J. and Mallard, W. G. (2001). The NIST chemistry webbook: A chemical data resource on the internet. Journal of Chemical and Engineering Data, 46, 1059–1063.

[42] Raj, K. and Raj, P. R. L. (2025). Investigation of dynamic characteristics of liquid Methane Droplet impact on a heated solid surface. Heat Transfer Research, 56, 49–67. https://doi.org/10.1615/HeatTransRes.2025057349.

[43] Davanipour, M., Javanmardi, H., and Goodarzi, N. (2018). Chaotic self-tuning PID Controller based on fuzzy wavelet neural network model, Iran. Journal of Science and Technology – Transactions of Electrical Engineering, 42, 357–366. https://doi.org/10.1007/s40998-018-0069-1.

[44] Zheng, Y., Chang, H., Chen, J., Chen, H., and Shu, S. (2019). Effect of microgravity on flow boiling heat transfer of liquid hydrogen in transportation pipes. International Journal of Hydrogen Energy, 44, 5543–5550. https://doi.org/10.1016/j.ijhydene.2018.08.047.

[45] Lee, W. H. (2013). A pressure iteration scheme for two-phase flow modeling. Comput. Methods Two-Phase Flow Part. Transp, WORLD SCIENTIFIC, 61–82. https://doi.org/10.1142/9789814460286_0004.

[46] Liu, Z., Li, Y., and Jin, Y. (2016). Pressurization performance and temperature stratification in cryogenic final stage propellant tank. Applied Thermal Engineering, 106, 211–220. https://doi.org/10.1016/j.applthermaleng.2016.05.195.
[47] Brackbill, J. U., Kothe, D. B., and Zemach, C. (1992). A continuum method for modeling surface tension. Journal of Computational Physics, 100, 335–354. https://doi.org/10.1016/0021-9991(92)90240-Y.
[48] Abdulkadir, M., Hernandez-Perez, V., Lo, S., Lowndes, I. S., and Azzopardi, B. J. (2015). Comparison of experimental and Computational Fluid Dynamics (CFD) studies of slug flow in a vertical riser. Experimental Thermal and Fluid Science, 68, 468–483. https://doi.org/10.1016/j.expthermflusci.2015.06.004.
[49] Hedayatpour, A., Antar, B. N., and Kawaji, M. (1993). Cool-down of a vertical line with liquid nitrogen. Journal of Thermophysics and Heat Transfer, 7, 426–434. https://doi.org/10.2514/3.436.
[50] Kharangate, C. R. and Mudawar, I. (2017). Review of computational studies on boiling and condensation. International Journal of Heat and Mass Transfer, 108, 1164–1196. https://doi.org/10.1016/j.ijheatmasstransfer.2016.12.065.

A. M. Khan*

Chapter 13
Advanced Heat Transfer Analysis: Numerical Methods and Fractional Calculus Approaches

Abstract: In many engineering and scientific applications, the study of heat transfer is vital from energy conversion to thermal management systems. The conventional differential equations are usually employed in traditional heat transfer models. In a bid to tackle complicated thermal phenomena, viz., memory effect and dynamic diffusion, a more advanced mathematical framework is needed. The aim of the proposed chapter is to investigate the incorporation of fractional calculus and numerical techniques in heat transfer analysis to provide a more accurate and robust depiction of heat flow in conduction and convection processes. Fractional calculus is an important tool to simulate the history-dependent behavior of systems. The main highlights of the chapter are to investigate the fractional order heat transfer problems using numerous numerical methods, viz., spectral approaches, finite difference methods, finite element methods, and fractional reduced differential transform method. The real-world case studies and benchmarks are used to evaluate proposed methods' accuracy, stability, and computational effectiveness. By employing the theory of fractional calculus and numerical modeling, this chapter gives a strong foundation for dealing with heat transfer cases that supersedes the traditional approaches. These findings are crucial to improve prediction capacities and create novel thermal management techniques.

Keywords: heat transfer analysis, numerical methods, fractional calculus, finite element method (FEM), anomalous diffusion, non-Fourier heat conduction

13.1 Introduction

Since the topic of heat transfer plays a fundamental role in the physical process that governs the transfer of thermal energy between systems. It has numerous applications, including aerospace, energy systems, material processes, and biological systems.

Classical heat transfer models such as Fourier's law of conduction, Stephen-Boltzmann's law of radiation, and Newton's law of cooling provide a theoretical foundation for understanding heat transfer mechanisms. However, these classical models have limitations when applied to complex real-world scenarios, viz. heterogeneous

*Corresponding author: A. M. Khan, Department of Mathematics, Jodhpur Institute of Engineering and Technology, Jodhpur, Rajasthan, India, e-mail: arif.khan@jietjodhpur.ac.in

https://doi.org/10.1515/9783111723464-013

materials, micro- and nanoscale systems, and biological tissues. In recent years, advancements in numerical methods and fractional calculus approaches have significantly improved the ability to model heat transfer phenomena more accurately. Numerical techniques with finite difference method (FDM), boundary element method (BEM), finite element method (FEM), and spectral methods enable the solution of complex heat conduction problems that lack analytical solutions. Fractional calculus that extends classical differentiation and integration to non-integer orders provides accurate real-world simulations, equipped with memory effects and nonlocal interactions of heat transfer processes. This chapter provides a robust mathematical framework to overview advanced heat transfer analysis, focusing on numerical methods and fractional calculus techniques.

The chapter includes classical heat transfer models and their limitations, advanced numerical methods, including finite difference, finite element, finite volume, and spectral techniques.

The chapter emphasizes on the fractional calculus approaches, which address memory effects and nonlocality effects in the heat transfer process. The applications of these advanced methods, ranging from energy systems to biomedical engineering, are also covered by incorporating numerical computation with the fractional differential models. By employing fractional theory, scientists and researchers can develop more accurate simulations of real-world thermal behavior in complex materials, biological tissues, and microstate devices.

This chapter aims to provide a deep understanding of these techniques, offering insights into their applications, advantages, and challenges.

13.1.1 Importance of Heat Transfer Analysis

Since heat transfer analysis is significant in numerous disciplines, influencing the efficiency, safety, and performance of many technologies and natural systems. The key areas include the advanced heat transfer modeling that is important to explore the energy and power generation, thermal power plants, and optimization of heat exchanges, boiler, and cooling systems [1–3].

The chapter also emphasizes on solar energy systems to improve modeling of heat absorption, storage, and dissipation in nuclear reactors. Some important examples are also covered to control advanced thermal management for fuel roads and cool and system spacecraft thermal protections to ensure proper heat dissemination during re-entry. Automatic engines include heat transfer modeling for cooling and combustion systems. An electronics and semiconductor device also incorporates a microprocessor and chips to model heat dissipation to prevent overheating.

MEMS is a microelectromechanical system for accurate thermal behavior prediction at the microscale. Biomedical engineering includes hyperthermia treatment in the form of thermal modeling for cancer therapy. Another application of heat transfer

is found in cryopreservation to optimize heat transfer during freezing of biological tissues. In addition, the advanced material and nanotechnology field includes phase change materials to enhance heat for storage efficiency. The nano-scale heat conduction to understanding ballistic and diffusive thermal transport in nano-materials, given these diverse applications, an advanced heat transfer model incorporating numerical simulations and fractional calculus is significant for accurate and predictive modeling.

13.1.2 Limitation of the Classical Heat Transfer Models

The following are limitations of classical model heat transfer models-

i. Instantaneous heat propagation assumption: The classical model of heat transfer, including numerous examples, viz. Fourier's law of conduction, Newton's law of convection, and Stephen bolts law of radiation are widely used. But having notable limitations, which include the instantaneous heat propagation assumption, that suggest Fourier's law assumes that heat propagates instantaneously, leading to an infinite propagation speed, which contradicts physical reality.
ii. Locally assumptions: Classical model assumes that heat transfer is a purely local process, ignoring long-range interactions observed in heterogeneous and porous materials.
iii. Lack of memory effects: Many real-world material exhibits thermal memories where past temperature states influence present behavior, which classical models cannot capture.
iv. Micro- and nanoskill limitations: It includes that a small scale, heat carriers exhibit, ballistic transport, deviating from diffusion assumptions of Fourier's law.

These limitations have led to the development of numerical techniques and fractional order models that give a more generalized and accurate description of heat transfer modeling.

13.1.3 The Role of Numerical Methods in Heat Transfer Analysis

Due to the complexity of the real-world heat transfer problem, investigations of suitable numerical methods have become essential for solving the governing differential equations. These methods include FDM that approximate derivatives using discrete grade points commonly used for a structure domain. Another important numerical technique is the FEM that uses basis functions and weak formulations to solve partial differential equations suitable for complex geometries, further BEM that reduce the problem dimension for solving boundary integral equations, ideal for semi-infinite

domains. Spectral methods are also effective techniques that expand the solution in terms of orthogonal basis functions, providing high accuracy for smooth problems.

13.1.4 Fractional Calculus: A New Perspective in Heat Transfer

Fractional calculus extends classical differentiation and integration to non-integer orders that facilitate a more generalized and accurate representation of the heat transfer process. The fractional derivative introduces memory effects, unlike classical model fractional order derivatives that capture the influence of past state on present heat conduction behavior. Fractional calculus theory also includes nonlocality in heat transfer that allows modeling of long-range interactions, crucial for heterogeneous and fractal materials. The fractional calculus also improved accuracy in anomalous diffusion, as many physical systems exhibit subdiffusion or superdiffusion, which can be accurately modeled using fractional heat conduction equations. Mathematically, the fractional order heat conduction equation is given as:

$$D_t^{\alpha} T = \alpha \, (-\Delta)^{\beta} T \tag{13.1}$$

where D_t^{α} denotes a fractional time derivative and $(-\Delta)^{\beta}$ is a fractional Laplacian, which allows greater flexibility in modeling memory and nonlocal heat effects.

This chapter is structured as follows: Section 13.2 includes classical heat transfer models and their limitations, Section 13.3 gives numerical methods for heat transfer analysis, Section 13.4 explores fractional calculus approaches in heat transfer, Section 13.5 gives applications and case studies, and finally, Section 13.6 gives a conclusion and future direction. This chapter explores a comprehensive and in-depth analysis of advanced numerical and fractional calculus methods for heat transfer analysis, equipping scientists and researchers with the necessary tools to address complex heat conduction problems.

13.2 Classical Heat Transfer Models and Their Limitations

Heat transfer modeling is an essential process in many engineering and scientific applications, from biological tissues to various energy systems. Fourier's law is a fundamental principle in the classical heat conduction models that have been widely used to depict the heat transfer in solids. Though these models lack in dealing with nonhomogeneous materials, anomalous diffusion, and micro-scale heat transfer process. This section explores the traditional model of heat transfer, its governing equations and deficiencies, leading to the need for advanced numerical methods with fractional calculus approaches.

13.2.1 Fourier's Law and the Classical Heat Conduction Equation

The foundation of the heat transfer process is Fourier's law, which states that heat flux q is directly proportional to the negative temperature gradient ∇T, as given follows:

$$q = -k\nabla T \tag{13.2}$$

Since this law shows the instantaneous heat propagation, means the temperature change at a point is suddenly reflected throughout the material, which seems unrealistic for real-world situations. Here q denotes the heat flux vector (W/m^2) and k is the thermal conductivity (W/mK).

13.2.2 Heat Diffusion Equation (Classical Heat Equation)

The classical heat diffusion equation is given as:

$$\frac{\partial T}{\partial t} = \beta \nabla^2 T \tag{13.3}$$

where β is thermal diffusivity (m^2/s).

Equation (13.3) describes the change of temperature and its evolving in the material with respect to time due to heat flow.

13.2.3 Assumptions in the Classical Heat Equation

A Fourier law and heat equation make many assumptions as mentioned below:

i. Continuum hypothesis: The material is considered as a consistent medium, neglecting atomic-scale effects.
ii. Local equilibrium: Heat flow is treated as a local process without any history-dependent nature.
iii. Constant material properties: Thermal conductivity, density, and heat capacity are assumed constant over time.
iv. Infinite propagation: Speed-contradicting physical reality, it assumes the parabolic nature of equations.

However, the classical heat equation works well in many engineering applications, yet it fails in simulating microscale transfer, heterogeneous materials, and nonlocal effects.

13.2.4 Limitations of the Classical Heat Conduction Model

Despite the successful applications of Fourier's law in heat conduction modeling, it has significant limitations when applied to complex and heat phenomena.

13.2.4.1 Infinite Speed of Heat Propagation (Parabolic Nature)

Predicting an infinite speed of heat flow is a major flaw of Fourier's law. Since the nature of the heat equation is a parabolic PDE, any thermal change at a point instantaneously affects the entire domain. In fact, heat flows at a finite speed, especially in materials like:

i. Low temperature solids: Where quantum effects slow down thermal transport.
ii. Nanoscale systems: Where ballistic heat conduction dominates over diffusive transport.
iii. Biological tissues: Where heat transfer occurs through complex metabolic and transport processes.

13.2.4.2 Nonlocal Heat Transfer Effects

Fourier's law assumes that the heat flux at a point depends only on the local temperature gradient. It is not true in all material cases; in some material, heat flow is affected by the thermal state of distant regions.

This occurs in:

i. Porous and composite materials: Where heat flows through multiple phases, leading to non-uniform conduct pathways.
ii. Fractal and heterogeneous material: Where irregular structure leads to heat transfer patterns that classical models fail to capture.

13.2.4.3 Memory Effects and Non-Fourier Heat Conduction

Many materials exhibit memory effects, meaning that past thermal states influence current heat transfer behavior. For example, in:

i. Polymer and biological tissues: Where heat retention occurs over time.
ii. Super-cooled material and phase change systems: Where latent heat effects dominate.

13.2.5 Alternative Models to Fourier's Law

13.2.5.1 Hyperbolic Heat Conduction Model (Cattaneo-Vernotte Equation)

In order to introduce the component of time delay in heat flux, the Cattaneo-Vernotte equation modifies the Fourier law as given below:

$$\tau_q \frac{\partial q}{\partial t} + q = -k\nabla T \tag{13.4}$$

where τ_q is the relaxation time, representing the time delay in the heat flux response.

This leads to the telegraph mathematical equation given as follows:

$$\frac{\partial^2 T}{\partial t^2} + \frac{1}{\tau_q}\frac{\partial T}{\partial t} - \beta\nabla^2 T = 0 \tag{13.5}$$

13.2.5.2 Ballistic-Diffusive Heat Transfer Models

The ballistic diffusive equation is used for nanoscale heat conduction as follows:

$$\frac{\partial T}{\partial t} + v_g.\nabla T = \beta\,\nabla^2 T \tag{13.6}$$

where v_g is the group velocity of phonons. This model gives a relationship between wave-like ballistic transport and diffusion-dominated conduction.

13.3 Numerical Methods for Heat Transfer Analysis

Numerical methods are unavoidable for the solution of heat transfer problems due to their non-solvability through analytical solutions. The computational methods are essential to obtain approximate solutions when dealing with complex geometries, non-homogeneous materials, and nonlinear boundary conditions [4, 5].

In this section, we explore the numerical techniques used for heat transfer analysis, including the following:

i. Finite difference method (FDM)
ii. Finite element method (FEM)
iii. Boundary element method (BEM)
iv. Finite volume method
v. Spectral methods

13.3.1 Finite Difference Method (FDM)

The FDM is a commonly used numerical approach for solving partial differential equations, viz., the heat equation. The method used a discrete approximation in place of continuous derivatives via a grid-based representation of the solution region.

13.3.1.1 Discretization of the Heat Equation

Following is one-dimensional heat transient equation:

$$\frac{\partial T}{\partial t} = \beta \frac{\partial^2 T}{\partial x^2} \tag{13.7}$$

Using finite difference approximation, the derivatives are replaced as follows:

$$\frac{\partial T}{\partial t} \approx \frac{T_i^{n+1} - T_i^n}{\Delta t} \tag{13.8}$$

Further second-order central difference approximation is given as follows:

$$\frac{\partial^2 T}{\partial x^2} \approx \frac{T_{i+1}^n - 2T_i^n + T_{i-1}^n}{\Delta x^2} \tag{13.9}$$

On using equations (13.13) and (13.14) in equation (13.12) yields

$$\frac{T_i^{n+1} - T_i^n}{\Delta t} = \beta \frac{T_{i+1}^n - 2T_i^n + T_{i-1}^n}{\Delta x^2} \tag{13.10}$$

On rearranging the term, we get an explicit update formula as follows:

$$T_i^{n+1} = T_i^n + \beta \frac{\Delta T}{\Delta x^2} \left(T_{i+1}^n - 2T_i^n + T_{i-1}^n \right) \tag{13.11}$$

13.3.1.2 Explicit Versus Implicit Schemes

The FDM can be categorized into two parts: explicit or implicit, as given below:

The explicit finite difference scheme calculates the temperature at the next time step using known values from the previous step:

$$T_i^{n+1} = T_i^n + r\left(T_{i+1}^n - 2T_i^n + T_{i-1}^n \right) \tag{13.12}$$

where $r = \beta \frac{\Delta T}{\Delta x^2}$ is the coefficient of stability.

This scheme has major disadvantages as mentioned below:

i. Stability requires $r \leq \frac{1}{2}$ (CLF condition).
ii. Require small time steps for accurate solutions.

The implicit scheme modifies stability by solving a system of equations at each time steps:

$$T_i^{n+1} - r\left(T_{i+1}^n - 2T_i^n + T_{i-1}^n\right) = T_i^n \tag{13.13}$$

Easy implementation and computational efficiency are the major advantages of this scheme.

13.3.1.3 Crank-Nicolson Scheme (Semi-implicit Method)

This scheme is a combination of explicit and implicit methods:

$$T_i^{n+1} - \frac{r}{2}\left(T_{i+1}^{n+1} - 2T_i^{n+1} + T_{i-1}^{n+1}\right) = \quad T_i^n + \frac{r}{2}\left(T_{i+1}^n - 2T_i^n + T_{i-1}^n\right) \tag{13.14}$$

This method achieves second-order accuracy in both time and space.

14.3.2 Finite Element Method (FEM)

The FEM is a numerical method that approximates the solution of partial differential equations using a weak formulation and basis functions over finite elements. The method is highly recommended for problems with complex geometries with varying material properties and an anisotropic situation.

14.3.2.1 Weak Formulation

The heat flow equation is given as

$$\frac{\partial T}{\partial t} = \beta \nabla^2 T \tag{13.15}$$

Equation (13.15) can be written in its weak form by multiplying with a test function v and integrating over the domain C:

$$\int_C v \frac{\partial T}{\partial t} dC + \beta \int_C \nabla v . \Delta T dC = 0 \tag{13.16}$$

The above integral allows the equation to be solved numerically by discretizing $T(x, t)$ into basis.

13.3.3 Boundary Element Method (BEM)

The BEM techniques leverage the heat flow problem to reformulate it into a boundary problem integral equation, reducing it to the domain's boundary. It reduces problem dimensionality, efficiently for unbounded domains:

$$cT(P) + \int_{\varphi} kT \frac{\partial G}{\partial n} d\varphi = \int_{\varphi} Gqd\varphi \tag{13.17}$$

where G denotes the fundamental solution of the heat equation.

13.3.4 Finite Volume Method (FVM)

The finite volume method is widely used in computational fluid dynamics for heat transfer problems. It conserves energy across volumes by integrating the heat equation over discrete cells:

$$\int_{\varphi} \frac{\partial T}{\partial t} d\varphi = \int_{\varphi} -k\nabla T.d\varphi \tag{13.18}$$

The method conserves energy exactly at the discrete level, in addition, it is compatible with fluid thermal coupling.

13.3.5 Spectral Methods

Spectral methods approximate the heat equation using global basis functions such as Fourier series or special function polynomials:

$$T(x, t) = \sum_{n=0}^{\infty} b_n(t) \varnothing_n(x) \tag{13.19}$$

13.3.6 Comparison of Numerical Methods

Table 13.1 gives a comparison of different numerical methods based on different parameters, viz. accuracy, computational cost, geometric flexibility, and stability.

Table 13.1: Comparison of numerical methods.

Method	Accuracy	Computational cost	Geometric flexibility	Stability
FDM	Medium	Low	Poor	Explicit unstable and implicit stable
FEM	High	Medium-high	Excellent	Stable
BEM	High	Medium	Good for unbounded problems	Stable
FVM	Medium	Medium	Good	Stable
Spectral	Very high	High	Poor	Stable

The accuracy is very high for spectral method, but gives poor geometric flexibility, whereas the FEM is stable and gives high accuracy and excellent geometric flexibility.

13.4 Fractional Calculus Approaches in Heat Transfer

Fractional calculus is a modified version of a mathematical framework that generalizes differential and integration to non-integer orders. Fractional derivatives and integration describe local and instantaneous changes, and capture history-dependent and nonlocal effects, making them useful for modeling anomalous diffusion and memory effects in heat transfer.

Fractional model extends the heat equation by incorporating nonlocal and memory-based effects.

A fractional integral of order α (where $0 < \alpha \leq 1$) is mathematically expressed as:

$$(I^{\alpha} f)(t) = \frac{1}{\Gamma(\alpha)} \int_0^t (t-s)^{\alpha-1} f(s) ds \tag{13.20}$$

A Riemann-Liouville fractional derivative of order α **(**where $0 < \alpha \leq 1$**)** is mathematically expressed as:

$$(D^{\alpha} f)(t) = \frac{1}{\Gamma(n-\alpha)} \frac{d^n}{dt^n} \int_0^t (t-s)^{n-\alpha-1} f(s) ds \tag{13.21}$$

A Caputo fractional derivative is defined as

$$(D^{\alpha}f)(t) = \frac{1}{\Gamma(n-\alpha)}\int_{0}^{t}(t-s)^{n-\alpha-1}f^{n}(s)ds \tag{13.22}$$

where $n-1<\alpha<n$, $\Gamma(\cdot)$ is the Gamma function, α is the fractional order of differentiation, and T represents temperature as a function of time t.

The Caputo order fractional derivative is preferable in the simulation of real-world modeling as it allows intuitive initial conditions.

The Grunwald-Letnikov fractional derivative is a discrete approach that is widely used in numerical simulations and is given as

$$(D^{\alpha}f)(x) = \lim_{h\to 0}\frac{1}{h^{\alpha}}\sum_{k=0}^{\infty}(-1)^{k}\binom{\alpha}{k}f(x-kh) \tag{13.23}$$

where h is a small step size.

These models better describe the anomalous diffusion in porous and fractal media, memory-dependent heat conduction in biological tissues, and polymers.

13.4.1 Fractional Heat Conduction Models

Fractional-order models generalize the heat equation by incorporating nonlocal and memory effects:

$$D_{t}^{\alpha}T = \beta\,\nabla^{2}\,T \tag{13.24}$$

where D_{t}^{α} denotes fractional order time derivatives, $0<\alpha\leq 1$. Fractional differential generalizes the order of derivatives to an arbitrary order.

13.4.2 Space Fractional Heat Conduction Equation

In heterogeneous or fractal-like media, the Laplace operator ∇^{2} is replaced with fractional Laplacian Δ^{α}, where $1<\alpha\leq 2$:

$$\frac{\partial T}{\partial t} = \beta(-\Delta)^{\alpha}T \tag{13.25}$$

Equation (13.25) is capable of capturing nonlocal spatial interactions common in porous and fractal media. For $\alpha=2$, it reduces to the classical heat equation, if $\alpha<2$, it models super diffusive behavior where heat spreads faster due to long-range dependencies.

13.5 Applications of Fractional Heat Transfer Models

This section explores the important applications of the fractional heat transfer model as given below

a) **Micro- and Nanoscale Heat Transfer**
   Fractional models could capture non-Fourier effects in nanomaterials and semiconductor devices where ballistic transport dominates.
b) **Thermal Analysis of Biological Tissues**
   In bio-heat transfer, the fractional model better describes heat flow in tiny tissues with memory effects, relevant to thermal therapies and hyperthermia treatments.
c) **Heat Transfer in Porous and Fractal Media**
   Material like foams, rocks, and composites exhibits nonlocal thermal interactions, which fractional models accurately capture. It is clear that fractional calculus provides a powerful tool for modeling complex heat transfer phenomena, capturing memory effects and long-range interactions [6–8].

13.6 Applications of Advanced Heat Transfer Analysis

Incorporating numerical methods and fractional calculus has become essential to deal with advanced heat transfer approaches for solving complex thermal problems in various fields, viz, energy systems, biomedical engineering, and advanced materials.

This section deals with key real-world applications where numerical and fractional order models enhance heat transfer analysis and enable innovative solutions.

13.6.1 Micro- and Nanoscale Heat Transfer

The traditional heat transfer models assume that diffusive heat transport does not hold in micro- and nanodevices. At micro- and nanoscales, heat conduction deviates significantly from classical diffusion models due to size effects, ballistic transport, and quantum interaction [9–11].

a) **Ballistic Versus Diffusive Heat Transfer in Nanomaterials**
   In bulk material, heat is conducted via the diffusion of phonons. Ballistic transport means heat carriers travel long paths before scattered, as happens in thin films, nanowires, and quantum dots.

13.6.1.1 Key Numerical Approaches

i. Boltzmann transport equation (BTE): Governs heat conduction at the nanoscale by tracking individual phonon populations.
ii. Monte Carlo methods: Predict the solution of phonon transport via stochastic methods.
iii. Fractional heat conduction models: Incorporate nonlocality and memory effects to simulate complex heat flow.

13.6.1.2 Applications

i. Microprocessor and semiconductor chips: Improved heat dissipation for next-generation processors.
ii. Heat transfer in NEMS/MEMS: Understanding thermal behavior in micro/nanoelectromechanical systems
iii. Thermal management of nanoelectronics: Optimizing cooling solution for graphene and 2D materials.
iv. Thermal management of nanoelectronics: Optimizing cooling solutions for graphene and 2D materials.

13.6.2 Energy and Power Systems

The solar energy, nuclear reactors, and thermal power plants are examples of energy systems that require precise heat analysis for efficiency and safety. Fractional calculus and numerical methods enhance the modeling of thermal energy storage, heat exchangers, and combustion processes.

a) Heat Transfer in Renewable Energy Systems
   i. **Solar thermal collectors:** Modeling radiative and conductive heat transfer in parabolic path and concentrated solar power systems.
   ii. **Geothermal energy systems:** Predicting underground conductive heat transfer in heterogeneous rock formation.
   iii. **Phase change material:** Fractional models equipped to predict the melting and solidification for thermal storage.

b) Advanced Heat Exchangers
   Heat exchangers are significant components in power plants, refrigerator systems, and chemical processes. Computational methods, viz. FEM and CFD optimize their thermal performance.

13.6.3 Biomedical Heat Transfer

Thermal modeling is essential in the field of biomedical engineering, particularly for hyperthermia treatment, crypto therapy, and tissue engineering. Due to the complex vascular network and metabolic heat generation, the biological tissues describe non-Fourier heat conduction.

a) Hyperthermia and Cancer Treatment

Hyperthermia therapy uses localized heating to destroy cancer-based cells. The fractional models can best simulate thermal diffusion and blood perfusion effects, leading to better treatment planning.

Key Numerical Models:

Pennes's Bio-heat Equation: Describes heat transfer in tissues, including blood perfusion effects.

Fractional Bio-heat Model: Improve accuracy in predicting heat distribution in heterogeneous tissues

b) Crypto Preservation of Biological Tissues

Crypto preservation includes freezing cells and organs for long-term storage. Accurate modeling of thermal gradient and ice formation is crucial for preventing tissue damage:

i. Finite element simulation predicts ice numeric nucleation dynamics
ii. Fractional order equation describes non-Fourier cooling effects

13.6.4 Advanced Material and Smart Structures

The development of materials, smart coating, and composite structures needs precise heat transfer modeling in complex materials. Thermal barrier coatings in aerospace is one of the suitable examples that uses following techniques:

i. Finite difference models simulate heat conduction in ceramic coating.
ii. Fractional model predicts long-term thermal fatigue behavior

13.7 Conclusion

This chapter presented an in-depth analysis of advanced heat transfer modeling, focusing on numerical methods and fractional calculus approaches. Classical heat conduction models, particularly the Fourier law, were discussed alongside their limitations in capturing finite thermal propagation speeds, nonlocal interactions, and memory effects. The necessity of advanced numerical methods was established, leading to discussion on finite difference, boundary element, and spectral methods, each tailored for different heat transfer applications. A significant contribution of this

work lies in its integration of fractional calculus in heat transfer analysis. Fractional order models extend classical heat conduction equations by introducing memory and nonlocal effects, making them highly relevant for heterogeneous materials, biological tissues, and micro- and nanoscale thermal systems. The key novel contribution of the work can be seen as bridging classical and fractional heat transfer models, comprehending a numerical solution framework, extension of non-Fourier heat transfer, and an application-oriented approach. By leveraging numerical innovation and fractional calculus, this work paves the way for next-generation heat transfer analysis, ensuring improved efficiency and predictive accuracy in emerging thermal applications

References

[1] Cattaneo, C. (1958). A form of heat conduction equation which eliminates the paradox of instantaneous propagation. Comptes Rendus, 247, 431–433.
[2] Carslaw, H. S. and Jaeger, J. C. (1959). Conduction of Heat in Solids 2nd ed. Oxford University Press.
[3] Crank, J. (1975). The Mathematics of Diffusion 2nd ed. Oxford University Press.
[4] Jaiswal, A. K. (2020). Analytical and Numerical Solutions of Fractional Diffusion Equations. Springer.
[5] Liu, F., Anh, V., and Turner, I. (2004). Numerical solution of the time fractional diffusion equation. Journal of Computational and Applied Mathematics, 166(1), 209–219. doi: https://doi.org/10.1016/j.cam2003.06.006.
[6] Metzler, R. and Klafter, J. (2000). The random walk's guide to anomalous diffusion: A fractional dynamics approach. Physics Reports, 339(1), 1–77. https://doi.org/10.1016/S0370-1573(00)00070-3.
[7] Özisik, M. N. (1993). Heat Conduction 2nd ed. Wiley.
[8] Podlubny, I. (1999). Fractional Differential Equations: An Introduction to Fractional Derivatives, Fractional Differential Equations, Some Methods of Their Solution and Some of Their Applications. Academic Press.
[9] Tzou, D. Y. (1997). Macro- to Microscale Heat Transfer: The Lagging Behavior. Taylor and Francis.
[10] Xu, M. and Zhou, Y. (2018). A numerical method for solving the fractional heat conduction equation. Applied Mathematical Modeling, 62, 350–363. https://doi.org/10.1016/j.apm.2018.05.028.
[11] Yadav, P. and Tomar, S. K. (2021). Computational approaches for fractional heat conduction problems. Mathematical Methods in the Applied Sciences, 44(4), 2730–2752. https://doi.org/10.1002/mma.7047.

Manisha Yadav and Pradeep Malik*

Chapter 14
Controlling the Discretized Complex System's Dynamics with the Allee Effect

Abstract: This chapter examines the stability and dynamical behavior of a modified discrete-time complex system after incorporating the Allee effect. It identifies key bifurcations, namely, Neimark-Sacker and flip, through the application of the center manifold theorem. To control chaotic dynamics, a hybrid control strategy is implemented. Analytical results are validated through numerical simulations.

Keywords: discretized complex system, Allee effect, flip bifurcation, Neimark-Sacker bifurcation, hybrid control technique

14.1 Introduction

Population dynamics plays a key role in biomathematics, focusing on the interactions within ecosystems, such as predation, competition, mutualism, and symbiosis [1]. The foundation of predator-prey theory, established by Volterra [23] [2], has led to the development of various mathematical models to describe how species interact and how populations grow, often based on experimental data. Predator-prey models remain fundamental in both ecology and mathematical biology due to their relevance and complexity [3]. Although the equations may seem simple, they often exhibit highly nonlinear dynamics that are sensitive to initial conditions. These models help explain how ecosystems generate and sustain biomass through competition for resources, adaptation, and survival [12]. Population dynamics models are classified into continuous models, typically used for species with overlapping generations, and discrete models, which are suited for species with distinct breeding seasons or non-overlapping generations. Discrete models, in particular, are valuable in capturing complex behaviors, such as bifurcations and chaos [4–8, 14]. This study investigates a discrete-time predator-prey model using the forward Euler method for discretization [18, 21]. The Allee effect, which describes reduced fitness at low population densities, is integrated into the model to study its impact on population dynamics, including its po-

*Corresponding author: **Pradeep Malik,** Department of Mathematics, Faculty of Applied and Basic Sciences, SGT University, Gurugram 122505, Haryana, India, e-mail: pradeepmaths@gmail.com
Manisha Yadav, Department of Mathematics, Faculty of Applied and Basic Sciences, SGT University, Gurugram 122505, Haryana, India

https://doi.org/10.1515/9783111723464-014

tential to stabilize or destabilize the system [15]. Additionally, control strategies, such as pole-placement and hybrid techniques, are explored to manage chaotic behaviors and ensure ecological stability in systems prone to complex fluctuations [9–11, 13, 16, 17, 20].

14.2 Mathematical Model

Arancibia and Flores [22] studied a modified Leslie-Gower predator-prey model, incorporating the Allee effect on the prey population and alternative food sources for the predator. The model is as follows:

$$\begin{aligned}\frac{dx}{dt} &= rx\left(1-\frac{x}{K}\right)(x-n)-\frac{\beta xy}{x+p}\\ \frac{dy}{dt} &= \alpha y\left(1-\frac{y}{mx+q}\right)\end{aligned} \tag{14.1}$$

Here, every parameter is viewed as positive, i.e., $(r,K,\beta,p,\alpha,m,n,q)\in R_+^8$, $p<K$. Here, n is the strong Allee effect, β is the maximum predation rate per capita, $\frac{\beta x}{x+p}$ is the functional response, p is the population value at which the predation function is half saturation constant, x represents the prey population, and y is the size of population of predator. The parameters r and α represent the intrinsic growth rates for the prey and predator, respectively. m signifies the quality of the prey as a food source for the predator, while K stands for the prey's environmental carrying capacity. By employing the forward Euler scheme with a step size of ϵ, a discrete-time model is derived from system (14.1). As ϵ approaches 1, the dynamics of the $(i+1)$th generation of the prey-predator population must be governed by the following set of equations:

$$\begin{aligned}x_{i+1} &= x_i + rx_i\left(1-\frac{x_i}{K}\right)(x_i-n)-\frac{\beta x_i y_i}{x_i+p}\\ y_{i+1} &= y_i + \alpha y_i\left(1-\frac{y_i}{mx_i+q}\right)\end{aligned} \tag{14.2}$$

with the given initial conditions $x(0)=x_0$ and $y(0)=y_0$. The mapping that can be used to define the discrete time prey-predator model is as follows:

$$F:\begin{pmatrix}x\\ y\end{pmatrix}\rightarrow\begin{pmatrix}x+rx\left(1-\frac{x}{K}\right)(x-n)-\frac{\beta xy}{x+p}\\ y+\alpha y\left(1-\frac{y}{mx+q}\right)\end{pmatrix} \tag{14.3}$$

This chapter focused on analyzing the fixed points of map (14.3) and Section 14.3 studies their existence and dynamical behaviors in the region:

$$\Omega = R_+^2 = (X, Y): X \geq 0, Y \geq 0$$

Then, various bifurcations must be of flip bifurcations and Niemark-Sacker bifurcations, which are discussed in Section 14.4. Chaos control technique is discussed in Section 14.5. Illustrated extensive numerical simulations are carried out for the theoretical results in Section 14.6, and in Section 14.7, concluding remarks are discussed.

14.3 Existence and Stability of Fixed Points

Within this section, an exploration is conducted to ascertain the presence and stability of fixed points within map (14.3):

1. The trivial fixed point is $E_0(0, 0)$.
2. The semitrivial points are $E_{x_1}(K, 0)$ and $E_{x_2}(n, 0)$, where $x_1 = K$ and $x_2 = n$.
3. Another semitrivial point is $E_y(0, q)$.
4. The positive fixed points is $E(x^*, y^*)$, which is the intersection of the nullclines:

$$\begin{aligned} y_1^* &= mx^* + q \text{ and} \\ y_2^* &= \frac{r}{\beta}\left(1 - \frac{x^*}{K}\right)(x^* + p)(x^* - n) \end{aligned} \tag{14.4}$$

The Jacobian matrix of discrete map (14.3) evaluated at an arbitrary fixed point (x^*, y^*) is given by:

$$J(E) = \begin{pmatrix} \frac{r}{K}\left(2rx^*K - rnK - 3x^{*2} + 2nx^{*2}\right) - \frac{p\beta y^*}{(x^* + p)^2} & -\frac{\beta x^*}{(x^* + p)} \\ \frac{-\alpha y^{*2} m}{(mx^* + q)^2} & \alpha - \frac{2\alpha y^*}{mx^* + q} \end{pmatrix}$$

The corresponding characteristic equation is:

$$\lambda^2 - Tr\lambda + Det = 0 \tag{14.5}$$

where,

$$Tr = \frac{r}{k}\left(2rx^*K - rnK - 3x^{*2} + 2nx^{*2}\right) - \frac{p\beta y^*}{(x^* + p)^2} - \frac{2\alpha y^*}{mx^* + q} + \alpha$$

and

$$Det = \left(\frac{r}{k}\left(2rx^*K - rnK - 3x^{*2} + 2nx^{*2}\right) - \frac{p\beta y^*}{(x^* + p)^2}\right)\left(\alpha - \frac{2\alpha y^*}{mx^* + q}\right)$$

$$-\left(\frac{\beta x^*}{(x^*+p)}\right)\left(\frac{\alpha {y^*}^2 m}{(mx^*+q)^2}\right)$$

The behavior of the fixed points can be characterized by considering the following lemma [19]:

Consider a polynomial $\tau(\lambda)=\lambda^2-Tr\lambda+Det$, λ_1 and λ_2 are the eigenvalues. Suppose $\tau(1)>0$, then

1. $|\lambda_1|<1$ and $|\lambda_2|<1$ if and only if $\tau(-1)>0$ and $\tau(0)<1$;
2. $|\lambda_1|<1$ and $|\lambda_2|>1$ (or $|\lambda_1|>1$ and $|\lambda_2|<1$) if and only if $\tau(-1)<0$;
3. $|\lambda_1|>1$ and $|\lambda_2|>1$ if and only if $\tau(-1)>0$ and $\tau(0)>1$;
4. $\lambda_1=-1$ and $\lambda_2\neq 1$ if and only if $\tau(-1)=0$ and $Tr\neq 0,2$; and
5. λ_1 and λ_2 are complex conjugate and $|\lambda_1|=|\lambda_2|$ if and only if $(Tr)^2-4Det<0$ and $\tau(0)=1$.

14.3.1 Dynamical Behavior Around the Trivial Fixed Points

The trivial fixed point E_0 of system (14.3) is characterized by the eigenvalues of its Jacobian matrix: $\lambda_1=-nr^2$ and $\lambda_2=\alpha$.The fixed point E_0 is sink if $|r|<\frac{1}{\sqrt{n}}$ and $|\alpha|<1$, a source when $|r|>\frac{1}{\sqrt{n}}$ and $|\alpha|>1$, a saddle if $|r|<\frac{1}{\sqrt{n}}$ and $|\alpha|>1$ or $|r|>\frac{1}{\sqrt{n}}$ and $|\alpha|<1$ and nonhyperbolic when $r=\frac{1}{\sqrt{n}}$ and $|\alpha|=1$.

14.3.2 Dynamical Behavior Around the Semitrivial Fixed Points

1. The eigenvalues of the Jacobian of map (14.3) are $\lambda_1=r(2rK-n-3K+2n)$ and $\lambda_2=\alpha$ at semitrivial fixed point $E_{(x_1)}(x_1,0)$. $E_{(x_1)}$ is:
   1.1 source if $2rK+2m>\frac{1}{r+n+3K}$ and $|\alpha|>1$;
   1.2 sink when $2rK+2m<\frac{1}{r+n+3K}$ and $|\alpha|<1$;
   1.3 saddle when $2rK+2m<\frac{1}{r+n+3K}$ and $|\lambda|>1$ or $2rK+2m>\frac{1}{r+n+3K}$ and $|\alpha|<1$; and
   1.4 non-hyperbolic if either $2rK+2m=\frac{1}{r+n+3K}$ or $|\alpha|=1$.
2. The eigenvalues are $\lambda_1=\frac{r}{K}\left(2rnK-rnK-n^2\right)$ and $\lambda_2=\alpha$ for the semitrivial fixed point $E_{(x_2)}(x_2,0)$. $E_{(x_2)}$ is:
   2.1 source when $n(rK-n)>\frac{K}{r}$ and $|\alpha|>1$;
   2.2 sink when $n(rK-n)<\frac{K}{r}$ and $|\alpha|<1$;
   2.3 saddle when $n(rK-n)>\frac{K}{r}$ and $|\alpha|<1$ or $n(rK-n)<\frac{K}{r}$ and $|\alpha|>1$; and
   2.4 nonhyperbolic if either $n(rK-n)=\frac{K}{r}$ or $|\alpha|=1$.
3. The eigenvalues of the Jacobian of map (14.3) at semi trivial fixed point $E_y(0,q)$ are $\lambda_1=-r^2n$ and $\lambda_2=0$. $E_y(0,q)$ cannot be a source because λ_2 can never be greater than 1. $E_y(0,q)$ is:

3.1 sink if $n < \frac{1}{r^2}$;
3.2 saddle if $n > \frac{1}{r^2}$; and
3.3 non-hyperbolic if $n = \frac{1}{r^2}$.

14.3.3 Dynamical Behavior at Positive Fixed Point $E(x^*, y^*)$

The characteristic polynomial obtained at the fixed point $E(x^*, y^*)$ is given by

$$\tau(\lambda) = \lambda^2 - \left(\frac{r}{K}A - p\beta B - \alpha\right)\lambda + \left(-\frac{r}{K}A + p\beta B - \beta aC\right)$$

where $A = 2rx^*K - rnK - 3x^{*2} + 2nx^{*2}$; $B = \frac{mx^* + q}{x^* + p^2}$; $C = \frac{x^* m}{x^* + p}$. The dynamical behavior at positive $E(x^*, y^*)$ of map (14.3) is as follows:

Case 1: When $y_1^* = mx^* + q$

1. sink when $\frac{p\beta B - 1}{p\beta B - q\beta} < \alpha < \frac{1}{\beta(pB - q)}$;
2. source when $\alpha > max\left\{\frac{p\beta B - 1}{p\beta B - q\beta}, \frac{1}{\beta(pB - q)}\right\}$;
3. saddle when $\alpha < \frac{p\beta B - 1}{p\beta B - q\beta}$; and
4. nonhyperbolicity arises in the system when any of the following conditions are met:
   (a) $\alpha = \frac{p\beta B - 1}{p\beta B - q\beta}, \alpha \neq \frac{r}{K}A - p\beta B$ and $\alpha \neq \frac{r}{K}A - p\beta B - 2$
   (b) $\left(\frac{r}{K}A - p\beta B - \alpha\right) - 4\left(p\beta B\alpha - \frac{r}{K}A - C\beta\alpha\right) < 0$ and $\alpha = \frac{1 + \frac{r}{K}A}{p\beta B - \beta q}$

Case 2: When $y_2^* = \frac{r}{\beta}\left(1 - \frac{x^*}{K}\right)(x^* - n)(x^* + p)$

1. sink when $\alpha^2 > \frac{M + 1 - \left(1 - \frac{2y_2^*}{mx^*}\right)\alpha}{2My_2^*}$ and

$$2\alpha^2 My_2^* - \alpha\left(M + \frac{\beta x^* y_2 *^2}{(x^* + p)(mx^* + q)^2}\right) < 1;$$

2. source when $\alpha^2 = \frac{M + 1 - \left(1 - \frac{2y_2^*}{mx^*}\right)\alpha}{2My_2^*}$;
3. saddle when $\alpha^2 > \frac{M + 1 - \left(1 - \frac{2y_2^*}{mx^*}\right)\alpha}{2My_2^*}$;

$$2\alpha^2 My_2^* - \alpha\left(M + \frac{\beta x^* y_2 *^2}{(x^* + p)(mx^* + q)^2}\right) > 1; \text{ and}$$

4. the system is considered nonhyperbolic if any of the following conditions hold:

(a) $\alpha^2 = \frac{M+1-\left(1-\frac{2y_2^*}{mx^*}\right)\alpha}{2My_2^*}$, $\alpha \neq M\left(\frac{mx^*+q-2\alpha y_2^*}{mx^*+q}\right)$ and $\alpha \neq 2+M\left(\frac{mx^*+q-2\alpha y_2^*}{mx^*+q}\right)$

(b) $\left(-M+\alpha-\frac{2\alpha y_2^*}{mx^*+q}\right)^2 - 4\left(2\alpha^2 My_2^* - \alpha\left(M+\frac{\beta x^{*2}y_{2*}^2}{(x^*+p)(mx^*+q)^2}\right)\right) < 0$ and

$2\alpha^2 My_2^* - \alpha\left(M+\frac{\beta x^* y_2 *^2}{(x^*+p)(mx^*+q)^2}\right) = 1,$

where $M = -2\alpha 2x^* + r^2 n + \frac{3rx^*}{K} - \frac{2nrx^*}{K} + \frac{p\beta y_2^*}{(x^*+p)^2}$.

14.4 Bifurcation Analysis

In this part, we analyze the way in which map (14.3) behaves when it reaches its equilibrium points, exploring its bifurcation characteristics.

14.4.1 Exploring Bifurcation Around Trivial Point $E_0(0,0)$

Flip bifurcation is observed in map (14.3) when the trivial equilibrium point $E_0(0,0)$ is nonhyperbolic for $r = \frac{1}{\sqrt{n}}$.

14.4.2 Bifurcation Around Equilibrium Point $E_1(K,0)$

Map (14.3) exhibits flip bifurcation when the semitrivial equilibrium point $E_1(K,0)$ is nonhyperbolic for $r = \frac{1}{n-K}$.

At the equilibrium point $E_2(X_n,0)$, map (14.3) exhibits a flip bifurcation when the bifurcation parameter is $r = \frac{1}{n\left(1-\frac{1}{K}\right)}$.

Proof. In similar manner, the equilibrium point E_2 occurs flip bifurcation for the bifurcation parameter $r = \frac{1}{n\left(1-\frac{1}{K}\right)}$. Therefore, we can drop out the process.

The equilibrium point $E_3(0,q)$ of map (14.3) experiences a flip bifurcation as the bifurcation parameter takes the value $n = \frac{1}{r^2}$.

14.4.3 Exploring Bifurcation Around First Positive Fixed Point

In this subsection, the conditions for the emergence of flip bifurcation and Neimark-Sacker bifurcation at the positive fixed point $E_4\left(x^*, y_1^*\right)$ when $y_1^* = mx^* + q$ are determined. (i) Flip bifurcation is observed to occur at $\alpha = \frac{p\beta B}{p\beta B - q\beta}$ and (ii) Neimark-Sacker

bifurcation takes place at $\alpha = \frac{1+\left(\frac{r}{K}\right)A}{p\beta B - \beta q}$ around the positive fixed point $E_4\left(x^*, y_1^*\right)$ in map (14.3).

Proof. (i) By introducing the variables $u = x - x^*$, $v = y - y_1^*$ and $\mu = \alpha - \alpha_1$, the fixed points $E_4\left(x^*, y_1^*\right)$ are shifted to the origin. Expanding the right-hand side of map (14.3), we obtain the following expression:

$$\begin{pmatrix} u \\ v \end{pmatrix} \to \begin{cases} a_{11}u + a_{12}v + a_{13}uv + a_{14}u^2 + a_{15}u^2v + O(|u,v|^4) \\ b_{11}u + b_{12}v + b_{13}\mu + b_{14}v^2 + b_{15}\mu v + b_{16}u^2 + b_{17}\mu u \\ + b_{18}uv + b_{19}uv^2 + O(|u,v|^4) \end{cases} \tag{14.6}$$

where $a_{11} = 1 - x^*r + nr - \frac{y_1^* p\beta}{(x^*+p)^2}$, $a_{12} = -\frac{x^*\beta}{x^*+p}$, $a_{13} = -\frac{(p\beta)}{(x^*+p)^2}$, $a_{14} = \left(-2 + \frac{n}{x^*}\right)r + \frac{y_1^* p\beta}{(x^*+p)^3}$, $a_{15} = \frac{p\beta}{(x^*+p)^3}$, $b_{11} = \frac{a_1 y_1^{*2} m}{(x^*m+q)^2}$, $b_{12} = 1 + a_1 - \frac{2ay_1^*}{x^*m+q}$, $b_{13} = y_1^* - \frac{y_1^*}{x^*m+q}$, $b_{14} = -\frac{a_1}{x^*m+q}$, $b_{15} = 1 - \frac{2}{x^*m+q}$, $b_{16} = -\frac{a_1 y_1^{*2} m^2}{(x^*m+q)^3}$, $b_{17} = \frac{y_1^{*2} m}{(x^*m+q)^2}$

Next, we linearize map (14.6) at the point $(0,0)$ and constructed a matrix that is invertible:

$$T = \begin{pmatrix} \lambda_1 - a_{11} & -a_{11} - 1 & 0 \\ a_{12} & a_{12} & 0 \\ 0 & 0 & 1 \end{pmatrix}.$$

By employing the given transformation, we can rewrite the expression $\begin{pmatrix} u \\ v \\ \mu \end{pmatrix} = T\begin{pmatrix} X \\ Y \\ w \end{pmatrix}$, map (14.6) turns into:

$$\begin{pmatrix} X \\ Y \\ w \end{pmatrix} \to \begin{pmatrix} \lambda_1 - a_{11} & -a_{11} - 1 & 0 \\ a_{12} & a_{12} & 0 \\ 0 & 0 & 1 \end{pmatrix} \begin{pmatrix} X \\ Y \\ w \end{pmatrix} + \begin{pmatrix} F_1(X,Y,w) \\ G_1(X,Y,w) \end{pmatrix}$$

where

$$F_1(X,Y,w) = k_1X^2 + k_2XY + k_3{}^2 + k_4X^2Y + k_5XY^2 + O(|X,Y|^4)$$

$$G_1(X,Y,w) = e_1Y^2 + e_2wY + e_3wX + e_4XY + e_5X^2 + e_6X^3 + e_7Y^3 + O(|X,Y|^4).$$

Here, $k_1 = a_{13}a_{12}(\lambda_1 - a_{11}) + a_{14}(\lambda_1 - a_{11})^2 + a_{15}a_{12}$, $k_2 = -a_{12}a_{13}(1+a_{11}) + a_{14}(1+a_{11})^2 + a_{15}a_{12}$, $k_3 = -a_{12}a_{13}(1+a_{11}) - 2\lambda_1 - a_{11}(1+a_{11}) + 2a_{15}a_{12}$, $k_4 = 4a_{13}a_{12}(\lambda_1 - a_{11})$, $e_1 = b_{14}a_{12} + b_{16}(1+a_{11})^2 - (1+a_{11})a_{12}$, $e_2 = -(b_{17}(1+a_{11}) - b_{15}a_{12})$, $e_3 = (b_{17}(\lambda_1 - a_{11}) + b_{15}a_{12})$, $e_4 = 2b_{14}a_{12} - 2b_{16}(\lambda_1 - a_{11})(1+a_{11}) - b_{18}(1+a_{11})a_{12} + b_{18}(\lambda_1 - a_{11})a_{12}$, $e_5 = b_{14}a_{12} + b_{16}(\lambda_1 - a_{11})^2 + b_{18}(\lambda_1 - a_{11})a_{12}$, $e_6 = b_{19}(\lambda_1 - a_{11})a_{12}^2$.

To investigate the stability of the point $(X, Y) = (0, 0)$ near $w = 0$, we examined the center manifold, which can be described by the following expression:

$$Z^c(0) = \{(X, Y, w) \in R^3 | X = P(Y, w), P(0, 0) = 0, DP(0, 0) = 0\},$$

where X and w are sufficiently small. Let

$$P(Y, w) = P_1 w^2 + P_2 wY + P_3 Y^2 + O(|Y, w|^3). \tag{14.7}$$

Then,

$$\begin{aligned} \kappa(P(Y, w), w) = P(-Y + F_2(P(Y, w), Y, w)) - \lambda_1 P(Y, w) \\ - F_1(P(Y, w), Y, w) = 0. \end{aligned} \tag{14.8}$$

Upon substituting the eq. (14.7) into eq. (14.8) and comparing the coefficients, we can deduce the following outcomes, $P_1 = P_2 = 0$ and $P_3 = \frac{k_2}{1-\lambda_1}$.

The restricted form of map (14.6), when considering the center manifold, is given by the following expression:

$$\begin{aligned} Y \sim \widetilde{G_1}(Y, w) = -Y + e_1 P_3^2 Y^4 + e_2 P_3 Y^3 + e_3 Y^2 \\ + e_5 P_3 Y^4 + e_6 P_3 w Y^2 + e_7 w Y + O|Y, w|^4 \end{aligned}$$

It is evident that $\widetilde{G_1}(0,0) = 0$, $\frac{\partial \widetilde{G_1}}{\partial Y}(0,0) = -1$, $\frac{\partial \widetilde{G_1}}{\partial w}(0,0) = 0$, $\frac{\partial^2 \widetilde{G_1}}{\partial Y^2}(0,0) = 2e_3 \neq 0$, $\frac{\partial^2 \widetilde{G_1}}{\partial Y w}(0,0) =$, $e_7 \neq 0$ and $\frac{\partial^3 G_1}{\partial Y^3}(0,0) = 62P_3 \neq 0$.

Consequently, map (14.3) exhibited flip bifurcation at the fixed point $E(x^*, y_1^*)$ when the bifurcation parameter satisfied the condition $\alpha = \frac{p\beta B}{p\beta B - q\beta}$.

Proof. (ii) Now, we will examine the occurrence of the Neimark-Sacker bifurcation at the fixed point $E(x^*, y_1^*)$ is nonhyperbolic at $\alpha = \frac{1+\frac{r}{K}A}{p\beta B - \beta q}$.

To analyze the Neimark-Sacker bifurcation at the fixed point, we perform a transformation that shifts the coordinates of the fixed point to the origin. This allows to expand the right-hand side of map (14.3) around the origin using a suitable translation $u = x - x_1^*$, $v = y - y_1^*$, and $\alpha = \alpha_1 = \frac{1+\frac{r}{K}A}{p\beta B - \beta q}$. Map (14.3) yields:

$$\begin{pmatrix} u \\ v \end{pmatrix} \to \begin{cases} a_{11}u + a_{12}v + a_{13}uv + a_{14}u^2 + a_{15}u^2 v + O(|u, v|^4) \\ b_{11}u + b_{12}v + b_{13}uv + b_{14}u^2 + b_{15}v^2 + b_{16}u^2 v \\ + b_{17}uv^2 + O(|u, v|^4) \end{cases} \tag{14.9}$$

Replacing α by α_1 and $\mu = 0$, then a_{1i} and b_{1i} are: $a_{11} = r - \frac{2x_1^* r}{K} - \frac{y_1^* p\beta}{(x_1^* + p)^2}$, $a_{12} = -\frac{x_1^* \beta}{x_1^* + p}$, $a_{13} = -\frac{(p\beta)}{(x_1^* + p)^2}$, $a_{14} = -\frac{r}{K} + \frac{y_1^* p\beta}{(x_1^* + p)^3}$, $b_{15} = \frac{(p\beta)}{(x_1^* + p)^3}$, $b_{11} = \frac{\alpha y_1^{*2}}{x_1^{*2} m}$, $b_{12} = 1 + \alpha - \frac{2\alpha y_1^*}{x_1^* m}$, $b_{13} = \frac{2y_1^* \alpha}{x_1^{*2} m}$, $b_{14} = -\frac{\alpha y_1^{*2}}{x_1^{*3} m}$, $b_{15} = \frac{-2y_1^* \alpha}{x_1^{*3} m}$, $b_{16} = -\frac{\alpha}{x_1^{*2} m}$.

Consider the following set of complex eigenvalues derived from the linearization of map (14.9) at $(0, 0)$:

$$\lambda_{1,2} = \frac{m\alpha \pm \iota\sqrt{4n(\alpha) - (m(\alpha))^2}}{2}$$

with $|\lambda_{1,2}| = \sqrt{n(\alpha)}$. In addition, the condition of transversality is considered as follows:

$$\left(\frac{d|\lambda_{1,2}|}{d\alpha}\right)_{\alpha=\alpha_1} = \frac{-1}{2\sqrt{n(\alpha)}} \neq 0$$

Now, it is necessary to validate the nondegeneracy condition $\lambda^j_{1,2} \neq 1$, $j = 1, 2, 3, 4$. This condition can also be stated in an equivalent form $n(\alpha) \neq 0, -1$. Now, assume an invertible matrix:

$$T = \begin{bmatrix} a_{12} & 0 \\ M - a_{11} & -N \end{bmatrix}$$

$$M = \frac{m(\alpha)}{2}, N = \frac{\sqrt{4n(\alpha) - (m(\alpha))^2}}{2}.$$

Map (14.9) becomes:

$$\begin{pmatrix} X \\ Y \end{pmatrix} \to \begin{pmatrix} M & -N \\ N & M \end{pmatrix} \begin{pmatrix} X \\ Y \end{pmatrix} + \begin{pmatrix} F_1(X, Y) \\ G_1(X, Y) \end{pmatrix} \tag{14.10}$$

$$F_1(X, Y) = K_{11}X^2 + K_{12}XY + K_{13}Y^2 + K_{14}X^2Y + K_{15}XY^2 + O(|X, Y|^4) \tag{14.11}$$

$$\begin{aligned} G_1(X, Y) = {} & e_{11}X^2 + e_{12}XY + e_{13}Y^2 + e_{14}X^2Y + e_{15}XY^2 + e_{16}X^3 + e_{17}Y^3 \\ & + O(|X, Y|^4) \end{aligned} \tag{14.12}$$

$K_{11} = a_{12}a_{13}(M - a_{11}) + a_{12}^2 a_{14} + a_{15}(M - a_{11})^2$, $K_{12} = -Na_{12}a_{13} - 2a_{15}N(M - a_{11})$, $K_{13} = a_{15}N^2$, $K_{14} = -2a_{12}a_{16}N(M - a_{11}) - a_{12}^2 a_{17}N$, $K_{15} = a_{16}a_{12}N^2$, $K_{16} = a_{12}a_{16}(M - a_{11})^2 + a_{12}^2 a_{17}(M - a_{11})$ $e_{11} = a_{12}b_{13}(M - a_{11}) + a_{12}^2 b_{14} + b_{15}(M - a_{11})^2$, $e_{12} = -Na_{12}b_{13} - 2b_{15}N(M - a_{11})$, $e_{13} = b_{15}N^2$, $e_{14} = -2a_{12}b_{16}N(M - a_{11}) - a_{12}^2 b_{17}N$, $e_{15} = b_{16}a_{12}N^2$, $e_{16} = a_{12}b_{16}(M - a_{11})^2 + a_{12}^2 b_{17}(M - a_{11})$, and $e_{17} = 0$.

The fact that eq. (14.11) and eq. (14.12) precisely matches the center manifold form is easily recognized, and the nondegeneracy condition for the Neimark-Sacker bifurcation can be expressed by the following equation:

$$\hat{\alpha} = -Re\left(\frac{(1-2\lambda)\bar{\lambda}^2}{1-\lambda}\Psi_{11}\Psi_{20}\right) - \frac{1}{2}\left|\Psi_{11}\right|^2 - \left|\Psi_{02}\right|^2 + Re\left(\bar{\lambda}\Psi_{21}\right) \tag{14.13}$$

where

$$\Psi_{20} = \frac{1}{4}[(K_{11} - K_{13} + e_{12}) + i(e_{11} - e_{13} - K_{12})]_{(0,0)}$$

$$\Psi_{11} = \frac{1}{2}[(K_{11} + K_{13}) + i(e_{11} + e_{13})]_{(0,0)}$$

$$\Psi_{02} = \frac{1}{4}[(K_{11} - K_{13} - e_{12}) + i(e_{11} - e_{13} + K_{12})]_{(0,0)}$$

$$\Psi_{21} = \frac{1}{8}[K_{15} + e_{14} + 3e_{17} + i(3e_{16} + e_{15} - K_4)]_{(0,0)}$$

14.4.4 Bifurcation Investigation Around Another Positive Fixed Point

In this section, the conditions for the emergence of the flip bifurcation and the Neimark-Sacker bifurcation at the positive fixed point $E_4(x^*, y_2^*)$ when $y_2^* = \frac{r}{\beta}\left(1 - \frac{x^*}{K}\right)(x^* + p)(x^* - n)$:

(i) Flip bifurcation occurs at $E_4(x^*, y_2^*)$ when $y_2^* = \frac{r}{\beta}\left(1 - \frac{x^*}{K}\right)(x^* - n)(x^* + p)$ with the bifurcation parameter α and $\alpha^2 = \frac{M + 1 - \left(1 - \frac{2y_2^*}{mx^*}\right)\alpha}{2My_2^*}$, $\alpha \neq M\left(\frac{mx^* + q - 2\alpha y_2^*}{mx^* + q}\right)$ and $\alpha \neq 2 + M\left(\frac{mx^* + q - 2\alpha y_2^*}{mx^* + q}\right)$ and (ii) the Neimark-Sackaer bifurcation at $2\alpha^2 My_2^* - \alpha\left(M + \frac{\beta x^* y_2^{*2}}{(x^* + p)(mx^* + q)^2}\right) = 1$ are determined.

Proof. (i) Let $u = x - x^*$, $v = y - y_2^*$ and $\mu = \alpha - \alpha_1$. By relocating the fixed point $E_4(x^*, y_2^*)$ to the origin and expansion of the right-hand side of map (14.3), gives:

$$\begin{pmatrix} u \\ v \end{pmatrix} \to \begin{cases} a_{11}u + a_{12}v + a_{13}uv + a_{14}u^2 + a_{15}u^2v + O(|u,v|^4) \\ b_{11}u + b_{12}v + b_{13}\mu + b_{14}v^2 + b_{15}\mu v + b_{16}u^2 + b_{17}\mu u \\ + b_{18}uv + b_{19}uv^2 + O(|u,v|^4) \end{cases} \tag{14.14}$$

where, $a_{11} = 1 + \frac{\left(2Kx^* - 3x^{*^2} - Ky_2^* + 2x^*y_2^*\right)r}{K} - \frac{y_2^* p\beta}{(x^* + p)^2}$, $a_{12} = -\frac{x^*\beta}{x^* + p}$,

$a_{13} = -\frac{(p\beta)}{(x^* + p)^2}$, $a_{14} = \frac{\left(K - 3x^* + y_2^*\right)r}{K} + \frac{y_2^* p\beta}{(x^* + p)^3}$, $a_{15} = \frac{(p\beta)}{(x^* + p)^3}$, $b_{11} = \frac{a_1 y_2^{*^2} x^*}{(x^* m + q)^2}$,

$b_{12} = 1 + a_1 - \frac{2a_1 y_2^*}{x^* + q}$, $b_{13} = y_2^* - \frac{y_2^*}{x^* m + q}$, $b_{14} = -\frac{a_1}{x^* m + q}$, $b_{15} = 1 - \frac{2y_2^*}{x^* m + q}$, $b_{16} = -\frac{a_1 y_2^{*^2} m^2}{(x^* m + q)^3}$,

$b_{17} = \frac{y_2^{*^2} m}{(x^* m + q)^2}$.

Next, the linearization of map (14.14) is performed at the point $(0, 0)$, and an invertible matrix is constructed:

$$T = \begin{pmatrix} \lambda_1 - a_{11} & -a_{11} - 1 & 0 \\ a_{12} & a_{12} & 0 \\ 0 & 0 & 1 \end{pmatrix}$$

With the use of the following transformation approach $\begin{pmatrix} u \\ v \\ \mu \end{pmatrix} = T \begin{pmatrix} X \\ Y \\ w \end{pmatrix}$, map (14.6) transformed into:

$$\begin{pmatrix} X \\ Y \\ w \end{pmatrix} \to \begin{pmatrix} \lambda_1 - a_{11} & -a_{11} - 1 & 0 \\ a_{12} & a_{12} & 0 \\ 0 & 0 & 1 \end{pmatrix} \begin{pmatrix} X \\ Y \\ w \end{pmatrix} + \begin{pmatrix} F_1(X, Y, w) \\ G_1(X, Y, w) \end{pmatrix}$$

where

$$F_1(X, Y, w) = k_1 X^2 + k_2 XY + k_3 Y^2 + k_4 X^2 Y + k_5 XY^2 + O(|X, Y|^4)$$

$$G_1(X, Y, w) = e_1 Y^2 + e_2 wY + e_3 wX + e_4 XY + e_5 X^2 + e_6 X^3 + e_7 Y^3 + O(|X, Y|^4)$$

Here, $k_1 = a_{13}a_{12}(\lambda_1 - a_{11}) + a_{14}(\lambda_1 - a_{11})^2 + a_{15}a_{12}$, $k_2 = -a_{12}a_{13}(1 + a_{11}) + a_{14}(1 + a_{11})^2 + a_{15}a_{12}$, $k_3 = -a_{12}a_{13}(1 + a_{11}) - 2\lambda_1 - a_{11}(1 + a_{11}) + 2a_{15}a_{12}$, $k_4 = 4a_{13}a_{12}(\lambda_1 - a_{11})$, $e_1 = b_{14}a_{12} + b_{16}(1 + a_{11})^2 - (1 + a_{11})a_{12}$, $e_2 = -(b_{17}(1 + a_{11}) - b_{15}a_{12})$, $e_3 = (b_{17}(\lambda_1 - a_{11}) + b_{15}a_{12})$, $e_4 = 2b_{14}a_{12} - 2b_{16}(\lambda_1 - a_{11})(1 + a_{11}) - b_{18}(1 + a_{11})a_{12} + b_{18}(\lambda_1 - a_{11})a_{12}$, $e_5 = b_{14}a_{12} + b_{16}(\lambda_1 - a_{11})^2 + b_{18}(\lambda_1 - a_{11})a_{12}$, $e_6 = b_{19}(\lambda_1 - a_{11})a_{12}^2$

In order to analyze the stability of $(X, Y) = (0, 0)$ in the vicinity of $w = 0$, the center manifold is taken into consideration as follows:

$$Z^c(0) = \{(X, Y, w) \in R^3 | X = P(Y, w), P(0, 0) = 0, DP(0, 0) = 0\}$$

where X and w are sufficiently small. Let:

$$P(Y, w) = P_1 w^2 + P_2 wY + P_3 Y^2 + O(|Y, w|^3) \tag{14.15}$$

Then:

$$\begin{aligned} \kappa(P(Y, w), w) = P(-Y + F_2(P(Y, w), Y, w)) - \lambda_1 P(Y, w) \\ - F_1(P(Y, w), Y, w) = 0. \end{aligned} \tag{14.16}$$

By substituting eq. (14.15) into eq. (14.16) and equating the coefficients, we derive the following: $P_1 = P_2 = 0$ and $P_3 = \frac{k_2}{1-\lambda_1}$.

Map (14.6) when limited to the center manifold can be expressed as follows:

$$Y \sim \widetilde{G_1}(Y, w) = -Y + e_1 P_3^2 Y^4 + e_2 P_3 Y^3 + e_3 Y^2 + e_5 P_3 Y^4 + e_6 P_3 w Y^2 + e_7 w Y + O|Y, w|^4$$

It is evident that $\widetilde{G_1}(0, 0) = 0$, $\frac{\partial \widetilde{G_1}}{\partial Y}(0, 0) = -1$, $\frac{\partial \widetilde{G_1}}{\partial w}(0, 0) = 0$, $\frac{\partial^2 \widetilde{G_1}}{\partial Y^2}(0, 0) = 2e_3 \neq 0$, $\frac{\partial^2 \widetilde{G_1}}{\partial Y w}(0, 0) = e_7 \neq 0$ and $\frac{\partial^3 \widetilde{G_1}}{\partial Y^3}(0, 0) = 6e_2 P_3 \neq 0$.

Therefore, map (14.3) occurs flip bifurcation at fixed point $E(x^*, y_2^*)$ for bifurcation parameter α.

Proof. (ii) Next, we analyze the occurrence of the Neimark-Sacker bifurcation at the fixed point $E(x^*, y_2^*)$ is non-hyperbolic at:

$$2\alpha^2 M y_2^* - \alpha\left(M + \frac{\beta x^* y_2^{*2}}{(x^* + p)(mx^* + q)^2}\right) = 1$$

To simplify the analysis, we shift the fixed point $E(x^*, y_2^*)$ to the origin and expand the right-hand side of map (14.3) around the origin using the following translation. $u = x - x^*$, $v = y - y_2^*$ and $\alpha = \alpha_1$ yields:

$$\begin{pmatrix} u \\ v \end{pmatrix} \to \begin{cases} a_{11}u + a_{12}v + a_{13}uv + a_{14}u^2 + a_{15}u^2 v + O(|u, v|^4) \\ b_{11}u + b_{12}v + b_{13}uv + b_{14}u^2 + b_{15}v^2 + b_{16}u^2 v \\ + b_{17}uv^2 + O(|u, v|^4) \end{cases} \tag{14.17}$$

Replacing α by α_1 and $\mu = 0$, then a_{1i} and b_{1i} are: $a_{11} = r - \frac{2x_2^* r}{K} - \frac{y_2^* p\beta}{(x_2^* + p)^2}$, $a_{12} = -\frac{x_2^* \beta}{x_2^* + p}$, $a_{13} = -\frac{(p\beta)}{(x_2^* + p)^2}$, $a_{14} = -\frac{r}{K} + \frac{y_2^* p\beta}{(x_2^* + p)^3}$, $a_{15} - \frac{(p\beta)}{(x_1^* + p)^3}$, $b_{11} = \frac{\alpha y_2^{*2}}{x_2^{*2} m}$, $b_{12} = 1 + \alpha - \frac{2\alpha y_2^*}{x_2^* m}$, $b_{13} = \frac{2y_2^* \alpha}{x_2^{*2} m}$, $b_{14} = -\frac{\alpha y_2^{*2}}{x_2^{*3} m}$, $b_{15} = \frac{-2y_2^* \alpha}{x_2^{*3} m}$, $b_{16} = -\frac{\alpha}{x_1^{*3} + m}$,

A set of complex eigenvalues are examined that are acquired through the linearization of map (14.17) at $(0,0)$:

$$\lambda_{1,2} = \frac{m(\alpha) \pm \iota\sqrt{4n(\alpha) - (m(\alpha))^2}}{2}$$

with $|\lambda_{1,2}| = \sqrt{(\alpha)}$, followed by the transversality condition:

$$\left(\frac{d|\lambda_{1,2}|}{d\alpha}\right)_{\alpha=\alpha_1} = \frac{-1}{2\sqrt{n(\alpha)}} \neq 0$$

It is required to verify nondegeneracy condition $\lambda^j_{1,2} \neq 1,\ j = 1,2,3,4$, which is equivalent to $n(\alpha) \neq 0, -1$. Now, assume an invertible matrix:

$$T = \begin{bmatrix} a_{12} & 0 \\ M - a_{11} & -N \end{bmatrix}$$

$$M = \frac{m(\alpha)}{2},\ M = \frac{\sqrt{4n(\alpha) - (m(\alpha))^2}}{2}$$

So, map (14.17) becomes

$$\begin{pmatrix} X \\ Y \end{pmatrix} \to \begin{pmatrix} M & -N \\ N & M \end{pmatrix}\begin{pmatrix} X \\ Y \end{pmatrix} + \begin{pmatrix} F_1(X,Y) \\ G_1(X,Y) \end{pmatrix} \tag{14.18}$$

$$F_1(X,Y) = K_{11}X^2 + K_{12}XY + K_{13}Y^2 + K_{14}X^2Y + K_{15}XY^2 + O|X,Y|^4) \tag{14.19}$$

$$\begin{aligned} G_1(X,Y) = {} & e_{11}X^2 + e_{12}XY + e_{13}Y^2 + e_{14}X^2Y + e_{15}XY^2 + e_{16}X^3 + e_{17}Y^3 \\ & + O(|X,Y|^4) \end{aligned} \tag{14.20}$$

$K_{11} = a_{12}a_{13}(M - a_{11}) + a_{12}^2a_{14} + a_{15}(M - a_{11})^2,\ \ K_{12} = -Na_{12}a_{13} - 2a_{15}N(M - a_{11},\ \ K_{13} = a_{15}N^2,$
$K_{14} = -2a_{12}a_{16}N(M - a_{11}) - a_{12}^2a_{17}N,\ K_{15} = a_{16}a_{12}N^2,\ K_{16} = a_{12}a_{16}(M - a_{11})^2 + a_{12}^2a_{17}(M - a_{11})$
$e_{11} = a_{12}b_{13}(M - a_{11}) + a_{12}^2b_{14} + b_{15}(M - a_{11})^2,\ \ e_{12} = -Na_{12}b_{13} - 2b_{15}N(M - a_{11}),\ \ e_{13} = b_{15}N^2,$
$e_{15} = b_{16}a_{12}N^2,\ e_{14} = -2a_{12}b_{16}N(M - a_{11}) - a_{12}^2b_{17},\ e_{16} = a_{12}b_{16}(M - a_{11})^2 + a_{12}^2b_{17}(M - a_{11})$
and $e_{17} = 0$.

It is evident that eq. (14.19) and eq. (14.20) takes the exact form of a center manifold. The condition for the Neimark-Sacker bifurcation's nondegeneracy is provided by

$$\hat{\alpha} = -Re\left(\frac{(1-2\lambda)\bar{\lambda}^2}{1-\lambda}\Psi_{11}\Psi_{20}\right) - \frac{1}{2}\left|\Psi_{11}\right|^2 - \left|\Psi_{02}\right|^2 + Re\left(\bar{\lambda}\Psi_{21}\right) \tag{14.21}$$

where

$$\Psi_{20} = \frac{1}{4}[(K_{11} - K_{13} + e_{12}) + i(e_{11} - e_{13} - K_{12})]_{(0,0)}$$

$$\Psi_{11} = \frac{1}{2}[(K_{11} + K_{13}) + i(e_{11} + e_{13})]_{(0,0)}$$

$$\Psi_{02} = \frac{1}{4}[(K_{11} - K_{13} - e_{12}) + i(e_{11} - e_{13} + K_{12})]_{(0,0)}$$

$$\Psi_{21} = \frac{1}{8}[K_{15} + e_{14} + 3e_{17} + i(3e_{16} + e_{15} - K_4)]_{(0,0)}$$

14.5 Chaos Control

In certain cases, inducing or amplifying chaos in a dynamical system may be purposeful, while in others, suppressing it becomes essential due to its disruptive nature. Hybrid control effectively manages chaotic behavior, particularly by stabilizing unstable periodic orbits embedded within a chaotic attractor. This approach integrates state feedback and parameter perturbation techniques [11]. In the present study, hybrid control is applied to the system described by eq. (14.2) to regulate chaos by addressing the influence of both types of bifurcations. The controlled system, which corresponds to eq. (14.2), is given as follows:

$$\begin{aligned} x_{i+1} &= s\left(x_i + rx_i\left(1 - \frac{x_i}{K}\right)(x_i - n) - \frac{\beta x_i y_i}{x_i + p}\right) + (1 - s)x_i \\ y_{i+1} &= s\left(y_i + \alpha y_i\left(1 - \frac{y_i}{mx_i + q}\right)\right) + (1 - s)y_i \end{aligned} \tag{14.22}$$

where $0 < s < 1$. The fixed points of the controlled systems (14.22) and (14.3) are identical. The Jacobian matrix of this controlled system (14.22) is given as follows:

$$J(E^*) = \begin{pmatrix} sr - \dfrac{2rsx}{K} - \beta ys\dfrac{2x + p}{(x + p)^2} & -\dfrac{\beta xs}{(x + p)} \\ \dfrac{\alpha y^2}{(mx^2)} & 1 + \alpha - \dfrac{2y}{mx} \end{pmatrix} \tag{14.23}$$

The trace and determinant of (14.23) are as follows:

$$\tau = \left(-\frac{2rs}{K} - \frac{\beta ys}{(x+p)^2}\right)x - \left(\frac{\beta s}{x+p} + \frac{2}{mx}\right)y + \alpha + 1 + sr$$

$$\Delta = \left(\frac{srK(x+p)^2 - 2rsK(x+p)^2 - \beta ys(x+p) - x\beta ysK}{K(x+p)^2}\right)$$
$$\left(\frac{mx\alpha - 2y + mx}{mx}\right) + \left(\frac{\beta xs}{x+p}\right)\left(\frac{\alpha y^2}{mx^2}\right)$$

Now, system (14.22) is stable if and only if the following condition is satisfied:

$$\left(-\frac{2rs}{K} - \frac{\beta ys}{(x+p)^2}\right)x - \left(\frac{\beta s}{x+p} + \frac{2}{mx}\right)y + \alpha + 1 + sr < 1 + \left(\frac{\beta xs}{x+p}\right)$$
$$\left(\frac{\alpha y^2}{mx^2}\right)\left(\frac{srK(x+p)^2 - 2rsK(x+p)^2 - \beta ys(x+p) - x\beta ysK}{K(x+p)^2}\right)\left(\frac{mx\alpha - 2y + mx}{mx}\right) < 2$$

14.6 Numerical Simulation

This section validates the theoretical analysis and provides examples to support it through specific cases of system (14.3). For the first simulation, the initial conditions

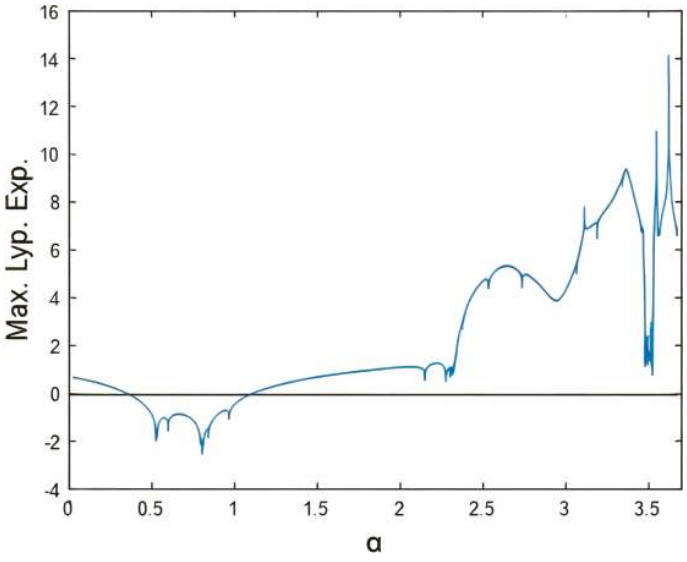

Figure 14.1: Maximum Lyapunov exponent.

$x_0 = 3.1$ and $y_0 = 4.1$ are used, along with the parameters $\alpha \in [2, 2.8]$, K = 4, $n = 0.5$, $\beta = 0.12$, $P = 3$, m = 1, $q = 0.5$, and $r = 0.2$ Figure 14.1 depicts the maximum Lyapunov exponent for system (14.3). The exponent shows a sign change, indicating the transition from periodic to chaotic behavior. This transition occurs as the value of α crosses critical points, which further highlights the system's sensitivity to initial conditions and parameter changes. Figure 14.2 shows the flip bifurcation diagrams of system (14.3) in the (x, α) and (y, α) planes. The unique positive endemic equilibrium point, calculated as $x = 3.50871$ and $y = 4.00871$, loses stability at $\alpha = 2.06123$, marking the transition from a stable state to chaotic behavior as α increases. For Figure 14.3, the initial state $x_0 = 1.8735$ and $y_0 = 2.7444$, with parameters $\alpha \in [1.6, 2.2]$, $K = 3$, $n = 0.5$, $\beta = 0.12$, $p = 1.5$, $m = 1.2$, $q = 0.5$, and $r = 1.1$. This scenario examines the Neimark-Sacker bifurcation with a strong Allee effect. As α varies within the range $[1.6, 2.2]$, closed invariant curves appear, indicating the emergence of quasiperiodic behavior. Figure 14.4 shows the phase portraits of system (14.3) for varying values of α. As α increases, the system transitions from stability to oscillatory dynamics, changing the state accordingly.

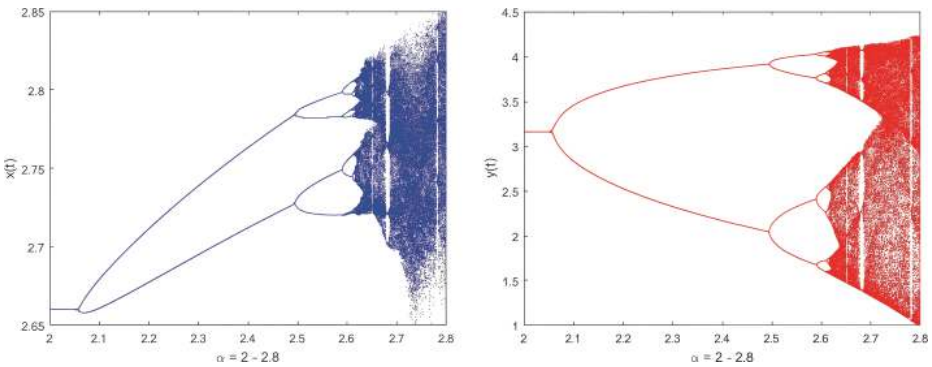

Figure 14.2: Flip bifurcation according to the change of the intrinsic growth rates.

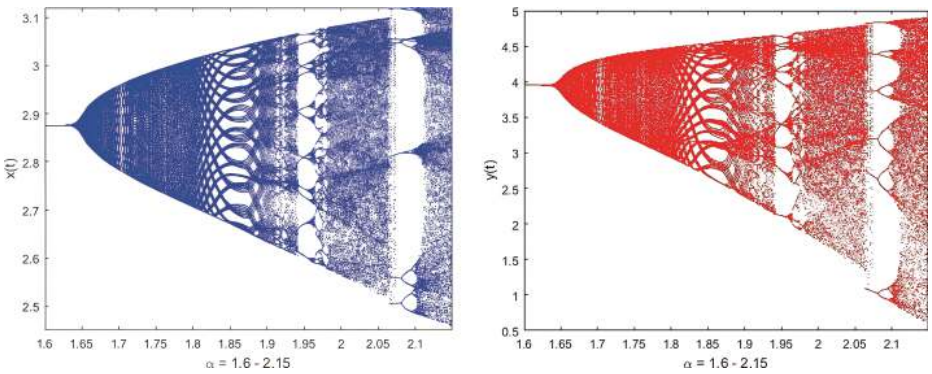

Figure 14.3: N-S bifurcation according to the change of the intrinsic growth rates.

Also, the numerical calculations were performed to stabilize the chaotic behavior within system (14.3). The initial conditions are $x_0 = 3.1$ and $y_0 = 4.1$ for the following set of parameters: $\alpha = 2.7,\ 0 < s < 0.999,\ r = 0.2,\ K = 4,\ n = 0.5,\ \beta = 0.12,\ p = 3,\ m = 1,\ q = 0.5$ with equilibrium points $x = 3.50871$ and $y = 4.00871$. In addition, the plots for $x(t)$ and $y(t)$ of controlled model (14.22) are shown in Figure 14.5 with $s = 0.6$. The stability of the endemic equilibrium point is evident (Figure 14.5).

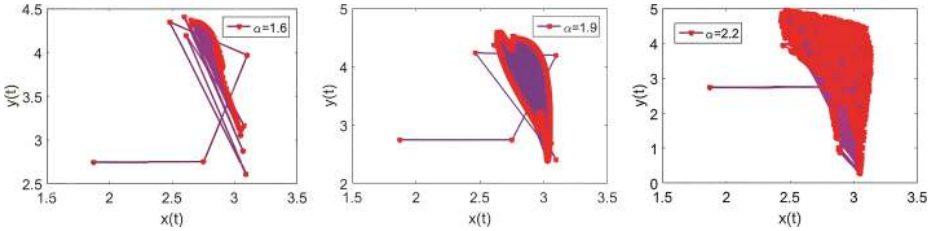

Figure 14.4: Phase portrait for different values of α s.

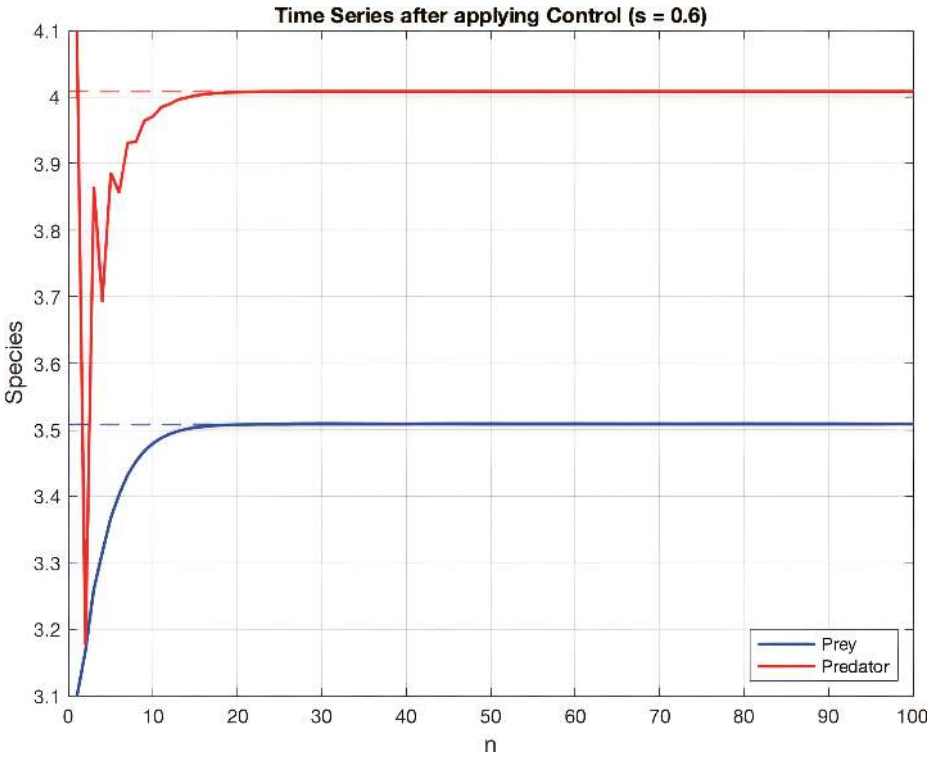

Figure 14.5: Time series of chaos control system.

14.7 Conclusion

This study investigates a modified discrete Leslie-Gower model incorporating the Allee effect on prey. It focuses on equilibrium analysis and stability, exploring the flip and the Neimark-Sacker bifurcations using the center manifold theorem. A hybrid control method is applied to manage chaos, with numerical simulations supporting the theoretical results. The work improves our understanding of predator-prey dynamics and species interactions.

References

[1] Danca, M.; Codreanu, S.; Bako, B. (1997). Detailed analysis of a nonlinear prey-predator model. Journal of Biological Physics, 23, 11–20.
[2] ELabbasy, E. M.; Agiza, H. N.; EL-Metwally, H. A.; Elsadany, A. A. (2012). Chaos and bifurcation of a nonlinear discrete-time prey-predator system. World Journal of Modelling and Simulation, 2, 169–180.
[3] Fan, Y. H.; Li, W. T. (2004). Permanence for a delayed discrete ratio-dependent predator–prey system with Holling type functional response *. Journal of Mathematical Analysis and Applications, 299, 357–374.
[4] Huang, T.; Zhang, H. (2016). Bifurcation, chaos and pattern formation in a space-and time-discrete predator-prey system. Chaos, Solitons & Fractals, 91, 92–107.
[5] Salman, S.; Yousef, A.; Elsadany, A. (2016). Stability, bifurcation analysis and chaos control of a discrete predator-prey system with square root functional response. Chaos, Solitons & Fractals, 93, 20–31.
[6] Banerjee, R.;Das, P.; Mukherjee, D. (2018). Stability and permanence of a discrete-time two-prey one-predator system with Holling type-III functional response. Chaos, Solitons & Fractals, 117, 240–248.
[7] Huang, C.; Liu, S.; Ruan, S.; Xiao, D. (2018). Bifurcations in a discrete predator-prey model with nonmonotonic functional response. Journal of Mathematical Analysis and Applications, 464, 201–230.
[8] Zhao, J.; Yan, Y. (2018). Stability and bifurcation analysis of a discrete predator-prey system with modified Holling-Tanner functional response. Advanced Differential Equations, 2018(402), 1–18.
[9] Rana, S. (2019). Bifurcations and chaos control in a discrete-time predator-prey system of Leslie type. Journal of Applied Analysis and Computation, 9, 31–44.
[10] Santra, P.; Mahapatra, G.; Phaijoo, G. (2020). Bifurcation and chaos of a discrete predator-prey model with Crowley-Martin functional response incorporating proportional prey refuge. Mathematical Problems in Engineering, 202, 5309814, 18 Pages.
[11] Singh, A.; Deolia, P. (2020). Dynamical analysis and chaos control in discrete-time prey-predator model. Communications in Nonlinear Science and Numerical Simulation, 90. Article No: 105313.
[12] Singh, A; Malik, P. (2021). Bifurcation in a modified Lesile-Gower predator-prey discrete model with Michaclis-Menten prey harvesting. Journal of Applied Mathematics and Computing, 67, 1–2.
[13] Elabbasy, E. M; Elsadany, A. A; Zhang, Y. (2014). Bifurcation analysis and chaos in a discrete reduced Lorenz system. Applied Mathematics and Computation, 228, 184–194.
[14] Singh, A.; Elsadany, A. A.; Elsonbaty, A. (2019). Complex dynamics of a discrete fractional-order Leslie-Gower predator-prey model. Mathematical Models and Methods in Applied Sciences , 42, 3992–4007.

[15] AK Gumus, O.;, Ö.; Selvam, G., Maria, A.,Vignesh, D. (2022). The effect of Allee factor on a non-linear delayed population model with harvesting. Journal of Science and Arts, 22(1), 159–176.
[16] Singh A; Gakkhar S. (2015). Controlling chaos in a food chain model. Mathematics and Computer Simulation, 115, 24–36.
[17] Chakraborty, K. (2016). Ecological complexity and feedback control in a prey-predator system with holling type-III functional response. Complexity, 21, 346–360.
[18] AK Gumus, O.;, Ö.; Feckan, M. (2021). Stability, Neimark-Sacker bifurcation and chaos control for a preadtor-prey system with harvesting effect on predator. Miskolc Mathematical Notes, 22(2), 663–679.
[19] George Maria Selvam, A., Janagaraj, R., Mary Jacintha. (2019). Stability, bifurcation, chaos: Discrete prey predator model with step size. International Journal of Innovative Technology and Exploring Engineering, 9(1), 3382–3387.
[20] Yang, L; Liu, Z. Maojm 2000: Controlling hyperchaos. Physical Review Letters, 84(1), 67–70.
[21] George Maria Selvam, A., Janagaraj, R., Vignesh, D. (2021). Discretization and choas control in a fractional order predator-prey harvesting model. Communications Faculty of Sciences University of Ankara-Series A1 Mathematics and Statistics, 70(2), 950–964.
[22] Ibarra, C.; Flores, J. (2021). Dynamics of a modified Leslie-Gower Predator-Prey model with Allee Effect on the Prey and a generalist predator. Mathematics and Computers in Simulation, 188, 1–22.
[23] VOLTERRA, V. (1926) Fluctuations in the Abundance of a Species considered Mathematically1. Nature 118, 558–560.

Ram Prakash Sharma* and V Vinay Kumar

Chapter 15
Machine Learning-Assisted Prediction of Thermo-diffusion and Diffusion-Thermo effects in a Jeffery-Hamel Flow

Abstract: This investigation delves into the core mechanisms governing heat and mass transfer in rotating convergent/divergent channels, with particular emphasis on the influence of Soret and Dufour effects. The results are particularly relevant to fields such as chemical engineering and geoscience, where thermal diffusion plays a crucial role in isotope separation processes – for instance, in differentiating between gas species such as air-N_2 and H_2-He. To tackle the complex nonlinear equations governing the system, the study employs the Runge-Kutta-Fehlberg 45 method, complemented by artificial neural network-based heat transfer analysis. Results show that the classical flow and heat features are considerably altered by the application of sufficient convergent/divergent walls. Moreover increasing Soret numbers enhances the thermal profile whereas, concentration profile retards. The influence of the Dufour effect is evident in its ability to modify heat transfer patterns and concentration distributions across the domain. *Nu* model achieves its most efficient thermal transfer rate at epoch 123, the gradient of 1.648×10^{-4} and *Mu* value of 1×10^{-6}. The model yields its peak *Nu*, indicating efficient heat transfer, at epoch 123 when the gradient is 1.648×10^{-4} and the *Mu* parameter equals 1×10^{-6}.

Keywords: converging/diverging channel, Soret and Dufour effects, heat source/sink, artificial neural network

15.1 Introduction

In various mechanical and industrial applications, fluid flow confined converging/diverging channel plays a crucial role in processes such as polymer molding, forced convection, and cold rolling. The study by Jeffery and Hamel demonstrated that fluid velocity rises in tapered channels, whereas pressure increases in expanding channels.

*Corresponding author: **Ram Prakash Sharma**, Department of Mechanical Engineering, National Institute of Technology Arunachal Pradesh, Jote, Papum Pare 791113, Arunachal Pradesh, India, e-mail: rpsharma@nitap.ac.in https://orcid.org/0000-0002-3359-1316
V. Vinay Kumar, Department of Basic and Applied Science, National Institute of Technology Arunachal Pradesh, Jote Papum Pare 791113, Arunachal Pradesh, India, e-mail: vinyvkv@gmail.com https://orcid.org/0009-0006-1838-4120

https://doi.org/10.1515/9783111723464-015

The principles of fluid dynamics play a pivotal role in aerospace engineering, automotive technology, medical applications, and energy production. Bhaskar et al. [1] focused on evaluating the effects of magnetic fields on liquid stream within a Jeffery-Hamel flow. Shilpa et al. [2] discussed the importance of nanolubricant flow in the context of the Jeffery-Hamel problem, in the presence of a magnetic field. Dinarvand et al. [3] elucidated the role of slip conditions in governing the flow dynamics of nanofluids with biological applications in a Jeffery-Hamel setup. The thermal and mass diffusion mechanisms in hybrid nanofluid flow through converging/diverging channels were explored in the study by Baithalu et al. [4]. Shilpa et al. [5] probed the consequences of heat and mass transfer on a nanolubricant stream via convergent/divergent channels.

Fluid motion involves intricate thermal and mass transfer mechanisms, which are effectively characterized by the Soret and Dufour effects. The Soret effect governs mass migration influenced by thermal variations, while the Dufour effect regulates heat movement due to concentration shifts. These effects are more significant in flows where density differences arise, such as around foreign substances introduced into the fluid. The importance of the Soret and Dufour effect on the Casson liquid stream via a stretchy surface was debriefed by Ramudu et al. [6]. The influence of Soret and Dufour effects on blood flow in a stenosed artery was analyzed by Mishra et al. [7]. The significance of magnetohydrodynamic nanoliquid stream past a wedge was scrutinized by Vinutha et al. [8] with the Soret and Dufour effects. Sharma et al. [9] considered the thermo-diffusion and diffusion-thermoeffect to analyze the thermal and mass transfer phenomena via porous surface. Krishnamoorthy and Prasad [10] discussed the importance of Soret Dufour's effect on thermal transfer phenomena in square cavities.

The role of heat source and sink (N-HSS) is fundamental in practical applications such as semiconductor manufacturing and nuclear power systems. The impact of both spatially dependent and temperature dependent heat sources on thermal behavior has been a key focus in scientific investigations. The study of N-HSS is pivotal for refining heat transfer predictions in complex geometrical frameworks. Shaw et al. [11] deliberated the consequences of non-Newtonian nanoliquid flow via a needle with N-HSS. Sultana et al. [12] deliberated the influence of N-HSS on Maxwell fluid flow via a complex structure with the impact of N-HSS. Gireesha and Anitha [13] analyzed trihybrid nanoliquid flow in a microchannel, considering shape dependency and quadratic thermal radiation effects. The convective behavior of couple stress ternary nanoliquid flow was studied by Gireesha and Anitha [14], highlighting heat transfer, permeability, and N-HSS. Kumar et al. [15] analyzed nanofluid flow in a magneto-radiative slider system with N-HSS, employing RKF-45 and Levenberg-Marquardt algorithm to enhance heat transfer and levitation control performance.

Artificial neural networks (ANNs) represent a major breakthrough in artificial intelligence (AI), adjusting dynamically as they process data. Multilayer perceptron (MLP) networks employ backpropagation, a supervised method leveraging gradient descent, to optimize training accuracy. Backpropagation, initially developed by Paul Werbos and later improved by Rumelhart and Parker, is essential for feedforward

neural networks. The application of ANNs in Newtonian and non-Newtonian fluid dynamics benefits greatly from the stable Levenberg-Marquardt algorithm. Raza et al. [16] used neural networks to study Darcy-Forchheimer flow, revealing parameter impacts on profiles and validating results through error analysis. Panda et al. [17] explored ANN-response surface methodology hybridization to optimize 3D micropolar nanofluid heat transfer. Sharma et al. [18] investigated a ternary nanoliquid stream between parallel plates employing numerical approaches and neural networks. Panda et al. [19] employed a neural network algorithm and regression analysis to enhance heat transfer under slip conditions. Sharma et al. [20] investigated a hybrid nanoliquid stream with a N-HSS to enhance thermal prediction under magnetic and radiative effects using a neural network algorithm.

The surveyed literature indicates that the optimization of heat transfer in viscous flows within rotating convergent/divergent channel remains an underexplored area. To bridge this research gap, this study investigates the impact of Soret and Dufour effects on thermal and mass transfer in convergent/divergent channels through the application of an ANN framework. The key objectives of this research are outlined as follows:

- To analyze the influence of key parameters on the velocity, temperature, and concentration distributions.
- A unique application of an AI-driven deep neural network method is presented for computing solutions to enhance heat transfer rates through regression analysis.

15.2 Mathematical Formulation

The classical Jeffery-Hamel flow problem provides a distinct set of exact solutions to the Navier-Stokes equations. The flow pattern is characterized by streamlines that appear as straight lines radiating from a central point in a two-dimensional space. The problem considers a steady, two-dimensional incompressible viscous flow through a rotating convergent/divergent channel, where the rotational axis is perpendicular to the flow and meets the z-axis, formulated in cylindrical polar coordinates (r, θ, z). The N-HSS is situated at the intake where two plates converge. It is considered that there is 2α angle between the walls. The impact of Soret and Dufour effects is also considered. The velocity $u_\theta = 0$ in z direction, the flow remains unaltered vertically and mainly driven by radial components, solely depending on r and θ. The governing equations are as follows (see [4]):

$$\frac{1}{r}\frac{\partial(ru)}{\partial r} = 0 \tag{15.1}$$

$$u\frac{\partial u}{\partial r} = \upsilon\left[\frac{1}{r}\frac{\partial u}{\partial r} + \frac{\partial^2 u}{\partial r^2} + \frac{1}{r^2}\frac{\partial^2 u}{\partial \theta^2} - \frac{u}{r^2}\right] - \frac{1}{\rho}\frac{\partial p}{\partial r} \tag{15.2}$$

$$-\frac{1}{r}\frac{1}{\rho}\frac{\partial p}{\partial \theta} + \frac{2}{r^2}\upsilon\frac{\partial u}{\partial \theta} - 2\omega u = 0 \tag{15.3}$$

$$u\frac{\partial T}{\partial r} = \frac{k}{\rho C_p}\left[\frac{\partial^2 T}{\partial r^2} + \frac{1}{r}\frac{\partial T}{\partial r} + \frac{1}{r^2}\frac{\partial^2 T}{\partial \theta^2}\right] + \frac{D K_T}{C_p C_s}\left[\frac{\partial^2 C}{\partial r^2} + \frac{1}{r}\frac{\partial C}{\partial r} + \frac{1}{r^2}\frac{\partial^2 C}{\partial \theta^2}\right] \tag{15.4}$$

$$u\frac{\partial C}{\partial r} = D_B\left[\frac{\partial^2 C}{\partial r^2} + \frac{1}{r}\frac{\partial C}{\partial r} + \frac{1}{r^2}\frac{\partial^2 C}{\partial \theta^2}\right] + \frac{D K_T}{T_m}\left[\frac{\partial^2 T}{\partial r^2} + \frac{1}{r}\frac{\partial T}{\partial r} + \frac{1}{r^2}\frac{\partial^2 T}{\partial \theta^2}\right] \tag{15.5}$$

Here, ρ is the density, υ signifies the kinematic viscosity, C_p symbolizes specific heat, D_B depicts mass diffusion coefficient, k_T implies thermal diffusion ratio, T_m denotes mean fluid temperature, and C_s defines concentration susceptibility.

The assumption of symmetry at the midline $(\theta = 0)$ of the channel leads to the following boundary conditions:

$$u = u_c,\ \frac{\partial u}{\partial \theta} = 0,\ \frac{\partial T}{\partial \theta} = 0,\ \frac{\partial C}{\partial \theta} = 0 \tag{15.6}$$

The boundary conditions imposed at the channel walls are as follows $(\theta = \beta)$

$$u = 0,\ T = T_w, C = C_w \tag{15.7}$$

Similarity variables are defined as

$$\begin{gathered} u(r,\theta) = \frac{f(\theta)}{r},\ f(\eta) = \frac{f(\theta)}{u_c},\ \eta = \frac{\theta}{\alpha} \\ \beta(\eta) = \frac{T}{T_w}r^2,\ \phi(\eta) = \frac{C}{C_w}r^2 \end{gathered} \tag{15.8}$$

Upon substituting eq. (15.8) into eqs. (15.1)–(15.5), the continuity eq. (15.1) holds, leading to the following transformed versions of eqs (15.2)–(15.5):

$$f''' + 4\alpha^2 \mathrm{Re} f' + 2\alpha \mathrm{Re}\, ff' - 4R_0\alpha^3 f = 0 \tag{15.9}$$

$$\frac{1}{\mathrm{Pr}}\left[\beta'' + 4\alpha^2\beta\right] + 2\alpha \mathrm{Re}\, f\beta + Du\left[\phi'' + 4\alpha^2\phi\right] = 0 \tag{15.10}$$

$$\frac{1}{Sc}\left[\phi'' + 4\alpha^2\phi\right] + 2\alpha \mathrm{Re}\, f\phi + Sr\left[\beta'' + 4\alpha^2\beta\right] = 0 \tag{15.11}$$

Transformed boundary conditions are

$$\begin{gathered} f'(0) = 0,\ \beta'(0) = 0, \beta'(x)\ f(0) = 1,\ \phi(0) = 0 \\ \beta(1) = 1,\ f(1) = 0,\ \phi(1) = 1 \end{gathered} \tag{15.12}$$

The following are the nondimensional variables:
$R_0 = \frac{\omega r^2}{\upsilon}$ designates rotational parameter, $\mathrm{Re} = \frac{au_c}{\upsilon}$ represent the Reynolds number, $Q = \frac{Q_0 r^2}{k}$ depicts HSS parameter, $Sc = \frac{\upsilon}{D_B}$ represents the Schmidt number, and $Sr = \frac{DK_T T_W}{T_m C_m \upsilon}$ signifies the Soret number, $Du = \frac{DK_T C_W}{C_p C_s \upsilon T_W}$ is the Dufour number.

15.3 Numerical Procedure

By applying a relevant similarity transformation (15.8) and considering the boundary conditions in eqs. (15.6)–(15.7), the coupled nonlinear PDEs (15.2)–(15.5) are converted into their equivalent coupled nonlinear ODEs (15.9)–(15.11), and boundary conditions are transformed into (15.12). The solution approach involves utilizing the RKF-45 method alongside the shooting technique after transforming the equations and boundary conditions into a first-order initial-value problem:

$$f = \Upsilon_1,\ f' = \Upsilon_2,\ f'' = \Upsilon_3,\ \beta = \Upsilon_4,\ \beta' = \Upsilon_5,\ \phi = \Upsilon_6,\ \phi' = \Upsilon_7 \tag{15.13}$$

Eqs. (15.9)–(15.12) are converted as follows:

$$f''' = -4\alpha^2\Upsilon_2 - 2\alpha \mathrm{Re}\Upsilon_1\Upsilon_2 - 4R_0\alpha^3\Upsilon_1 \tag{15.14}$$

$$\beta'' = \frac{-4\alpha^2\Upsilon_4 - 2\alpha\,\mathrm{Pr}\,\mathrm{Re}\Upsilon_1\Upsilon_4 - Du\,\mathrm{Pr}\left[-2\alpha Sr\mathrm{Re}\Upsilon_1\Upsilon_6 - 4Sr\alpha^2\Upsilon_4\right]}{(1 - \mathrm{Pr}\ \ Sr\,Du\,Sc)} \tag{15.15}$$

$$\phi'' = \frac{-4\alpha^2\Upsilon_6 - 2\alpha\,\mathrm{Pr}\,\mathrm{Re}\Upsilon_1\Upsilon_6 - Sr\,Sc\left[-2\alpha Sc\mathrm{Re}\Upsilon_1\Upsilon_4 - 4\,\mathrm{Pr}\ Du\alpha^2\Upsilon_6\right]}{(1 - \mathrm{Pr}\ \ Sr\,Du\,Sc)} \tag{15.16}$$

The boundary constraints are modified accordingly:

$$\begin{aligned} &\Upsilon_1(0) = 1, \Upsilon_2(0) = 0, \Upsilon_4(0) = 0, \Upsilon_6(0) = 0 \\ &\Upsilon_1(1) = 0, \Upsilon_5(1) = 1, \Upsilon_7(1) = 1 \end{aligned} \tag{15.17}$$

15.4 Parametric Analysis with Validation

The current section analyzes the heat transport features for a rotating convergent/divergent model. The impact of diverse parameters, including the Reynolds number, rotational parameter, Schmidt number, bioconvection Lewis number, Soret number, and Dufour number, has been recognized in the current analysis. The numerical results are presented and examined numerically and graphically with tables and figures.

The variations of angle between channels (α) on the $f(\eta)$ are depicted in Figure 15.1(a). The portion of the graph from $\eta = 0$ to $\eta = 1$ represents the superior

part of the channel and $\eta = 0$ to $\eta = -1$ inferior part of the channel. The velocity near the channel's center region is predominant. As we move near the walls of either upper or lower walls, the velocity starts to deteriorate and becomes minimal near the walls; hence, the angle of inclination of the wall becomes far, and their distance increases and leads to the decrease in velocity profile for the divergent channel, but in case of the convergent channel, the angle of inclination decreases.

Figure 15.1(b) demonstrates the contribution of the rotational parameter (R_0) on the $f(\eta)$. The velocity profile of converging channels decreases for increasing values of R_0 while the opposite behavior for diverging channels. Figure 15.1(c) demonstrates the influence of the Reynolds number (Re) on the $f(\eta)$ of converging and diverging channels. A higher Re accelerates fluid velocity increase within a convergent channel while leading to a notable reduction in $f(\eta)$ across a divergent channel. The amplification of Re results in stronger inertial forces, which enhance flow resistance and impede fluid movement along the walls.

Figure 15.2(a) displays the role of the Soret number(Sr) on the $\theta(\eta)$. With the increasing values of *Sr*, thermal profiles increase for both convergent and divergent profiles. The *Sr* characterizes thermal diffusion in fluid mixtures, playing a crucial role in mass and heat transfer processes. Increasing *Sr* results in an upsurge in thermal distribution, demonstrating the heightened influence of thermal diffusion for both converging and diverging channels. Figure 15.2(b) shows the influence of the Dufour number (Du) on the $\theta(\eta)$. The thermal profile strengthens in both converging and diverging channels as the *Du* increases, particularly elevating temperatures in the divergent channel. By defining diffusion-thermoeffects, the Dufour coefficient provides insight into the interdependent relationship between thermal and mass transport processes.

The influence of the Soret number (Sr) for the solutal profile is demonstrated in Figure 15.3(a). Increasing *Sr* enhances species mobility, causing a reduction in concentration levels by preventing localized accumulation. The redistribution of species driven by *Sr* demonstrates its significance in mass transport mechanisms under varying temperature conditions. The variation of Dufour number (Du) for the solutal profile is demonstrated in Figure 15.3(b). A rise in the *Du* results in a decline in the solutal profile, as heat diffusion dominates over mass diffusion. Smaller *Du* results in stronger species accumulation, emphasizing *Du* significance in mass transport regulation. Figure 15.3(c) reports an increase in the Schmidt number (Sc), the solutal profile intensifies in divergent channels but diminishes in convergent channels due to the shifting balance between mass and thermal diffusivity. The present model is validated against the earlier studies of Baithalu et al. [4] for the specific case of $\omega = 0$, $\mathrm{Re} = 100$, $\alpha = 1^0$, $Sr = 0$, $Du = 0$, which is detailed in Table 15.1.

Table 15.1: Validation of the present problem with previously published data.

x	Previous findings [5]	Present findings
0	1.1052668	1.1052668
0.1	1.1042587	1.1042589
0.2	1.1008587	1.1008577
0.3	1.0950765	1.0950766
0.4	1.0866358	1.0866368

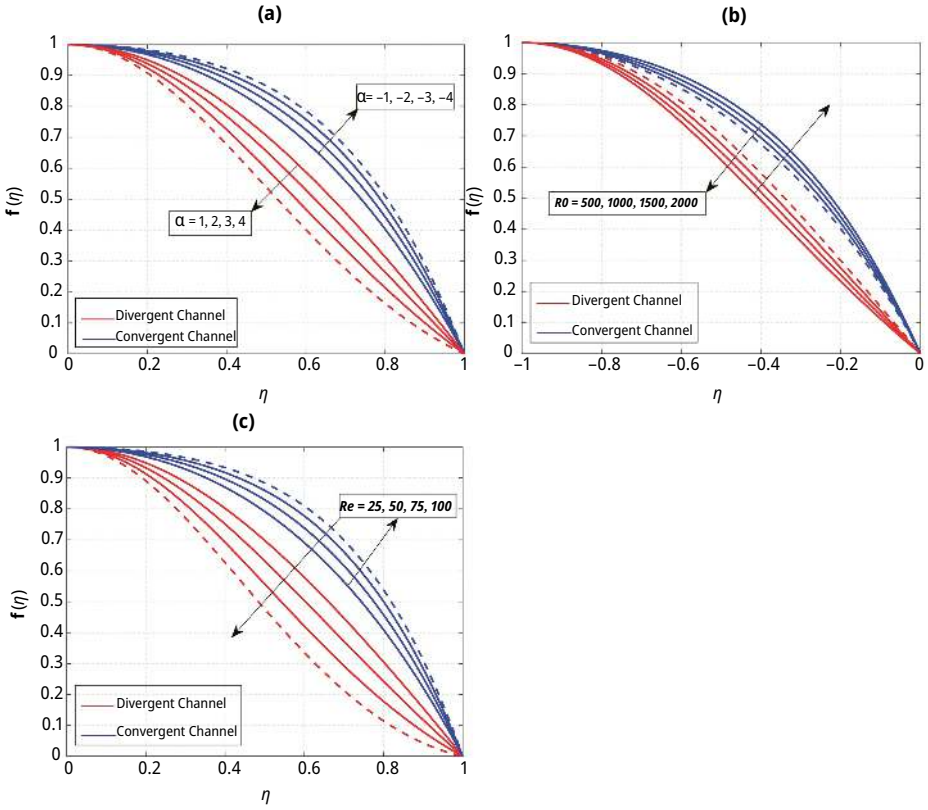

Figure 15.1: Impact of α, R0, Re on f ðηÞ.

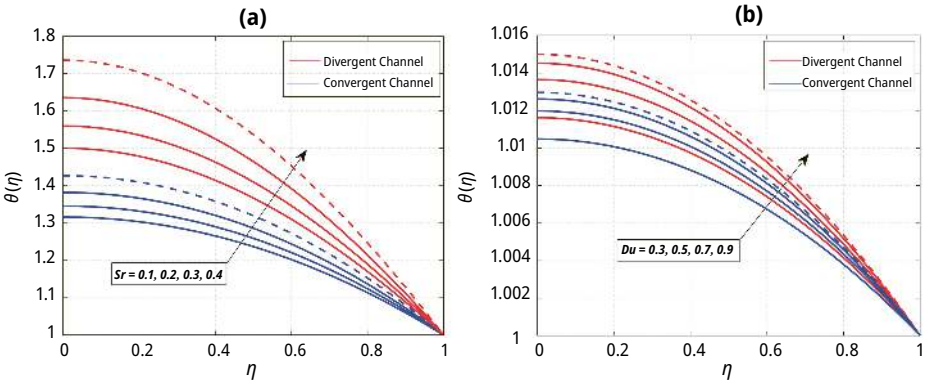

Figure 15.2: Impact of *Sr*, *Du* on $\theta(\eta)$.

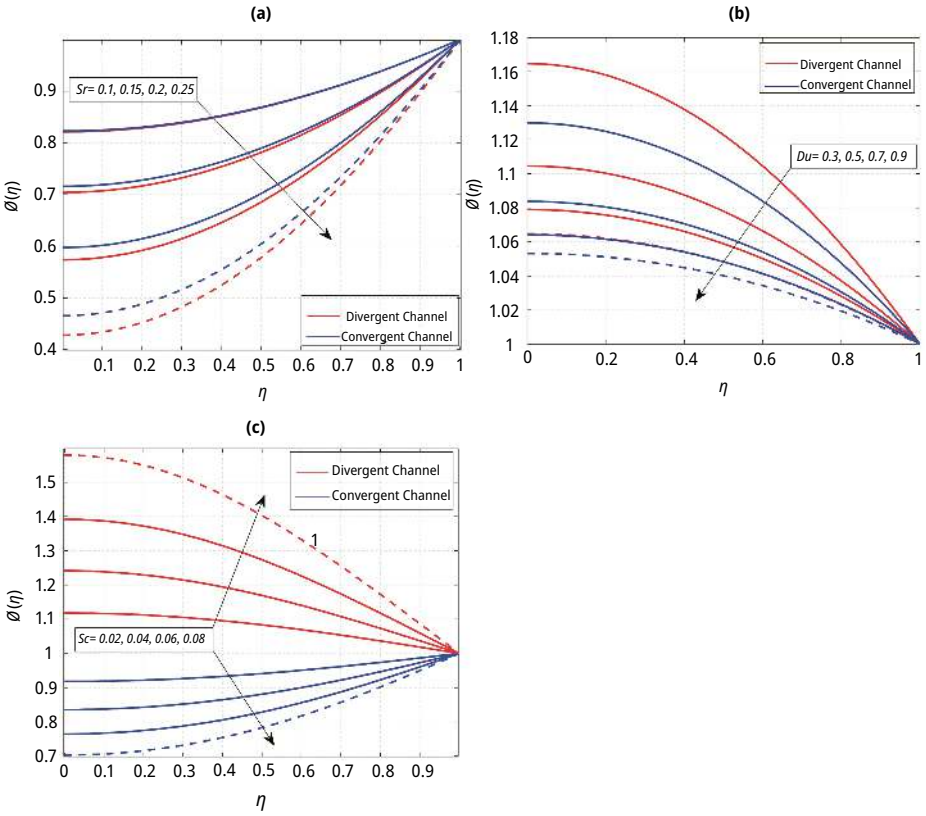

Figure 15.3: Impact of *Sr*, *Du*, *Sc* on $\phi(\eta)$.

15.5 Artificial Neural Network

This section primarily concentrates on the examination of viscous fluid behavior within a converging-diverging channel system. To facilitate accurate heat transfer prediction, the study implements an ANN system targeting the Nusselt number as the output metric. To train the ANN, a dataset of 900 Nusselt number values is employed, systematically split into training, testing, and validation subsets [21–26]. Detailed metrics reflecting the training and validation performance of the ANN model are outlined in Table 15.2. Table 15.3 demonstrates the training progress of the present model.

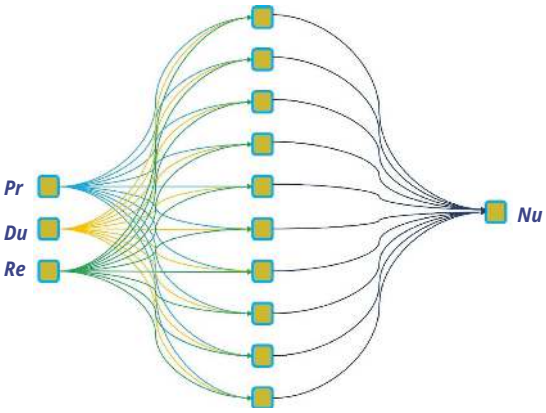

Figure 15.4: Schematic diagram of ANN.

Table 15.2: Analysis of ANN.

	Observation	MSE	R
Training	629	2.1668E-04	0.9996
Validation	135	1.8826E-04	0.9996
Test	135	5.4470E-04	0.9991

Table 15.3: Network training progress.

Unit	Initial value	Stopped value	Target value
Epoch	0	123	1,000
Elapsed time	–	00:00:00	–
Performance	0.217	2.06E–05	0
Gradient	0.578	0.000165	1E–07
Mu	0.001	1E–06	1E+10
Validation checks	0	6	6

To further improve the model's performance, different neuron configurations within the hidden layer were tested, ultimately establishing a network structure that links three input features to a single output through ten hidden neurons, as illustrated in Figure 15.4.

In ANN design, the MLP stands out for its layered structure, integrating inputs, hidden units, and outputs in a sequential flow. To determine predictive robustness, the MLP architecture is assessed via mean squared error (MSE) and the *R*-value, representing statistical reliability. The regression plot in Figure 15.5(a) highlights near-perfect convergence of the correlation coefficient *R*, affirming high model precision.

The gradient descent behavior and *mu* parameter trajectory of the *Nu* model are effectively illustrated in Figure 15.5(b), reflecting training dynamics. At epoch 123, training stabilizes as the *Nu* prediction model achieves a gradient level of 1.648×10^{-4} with a mu coefficient set at 1×10^{-6}. Through the integration of diverse training parameters, the model consistently achieves a coefficient of determination of 0.9995 across all phases, signifying exceptional *Nu* prediction precision.

Figure 15.5(c) illustrates the error distribution from ANN simulations for *Nu* with precision, reflecting variations under multiple influencing parameters. With 20-bin categorization, the ANN error distribution is compared to a zero-error benchmark line, where closeness reflects model precision. A total of 6.1×10^{-4} zero-error points are distinctly marked, while the histogram layout provides a granular view of error trends across conditions.

A clear pattern emerges in Figure 15.5(d), where MSE values for the ANN model begin at higher levels and gradually decline as training progresses. The model's optimal performance is marked by strong alignment with training data and significantly reduced error values. At epoch 117, the *Nu* model reaches its optimal validation state, delivering a remarkably low MSE of 1.8826×10^{-5}, indicative of its robust network configuration.

15.6 Conclusion

The steady, two-dimensional incompressible viscous flow through rotating converging/diverging channels has been studied. The impact of Soret and Dufour effects is also considered. A numerical method RKF-45 is applied to the transformed governing system with the inclusion of various characterizing parameters. Furthermore, the effects have been studied and analyzed by using a deep neural network to optimize the effects of different physical parameters on significant physical quantities.

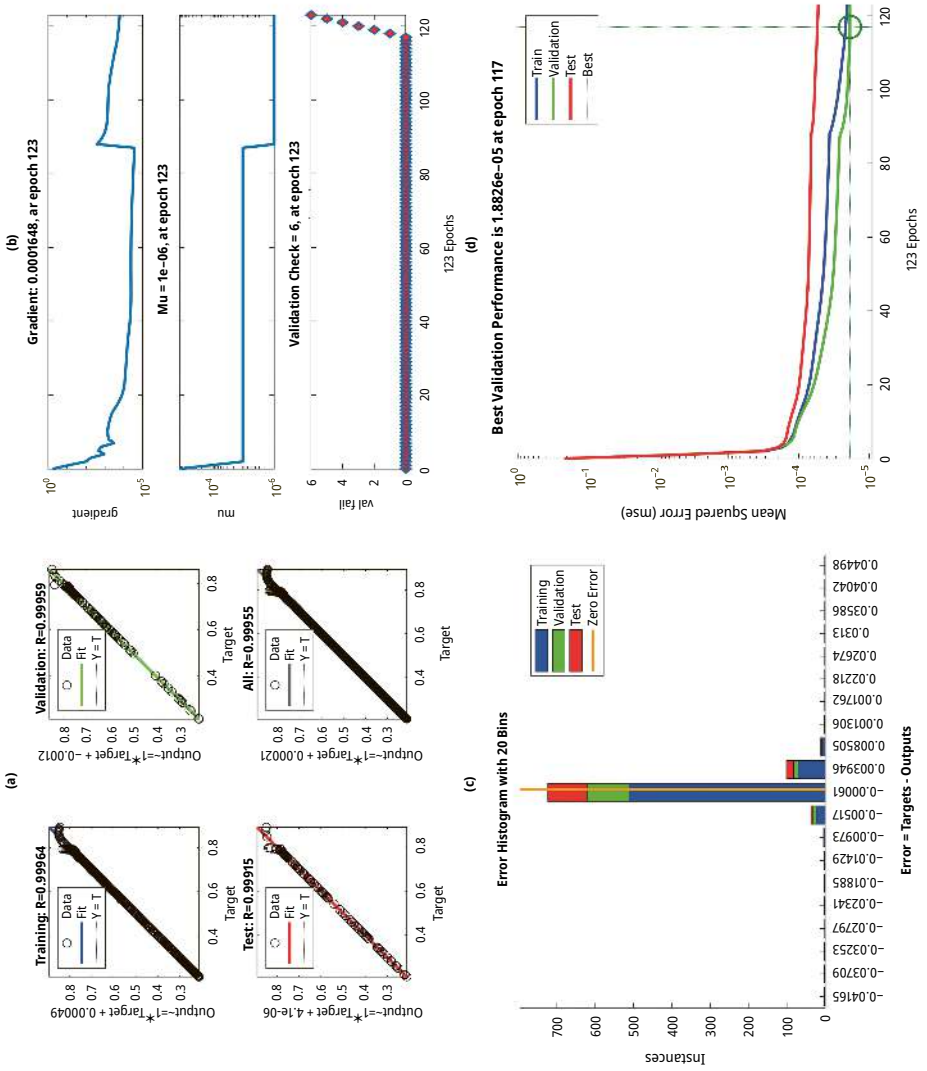

Figure 15.5: Ann plots (a) Regression, (b) Gradient, (c) Histogram, (d) MSE.

The following conclusions can be addressed:

- The comparative analysis demonstrates a strong accord with the previous investigation, thereby validating the methodology's conformity and convergence.
- The rising values of the Soret number raise the thermal profile whereas the opposite for the solutal profile. A rise in the Dufour number enhances the thermal distribution, whereas it leads to a reduction in the solutal concentration profile.
- *Nu* model achieves its most efficient thermal transfer rate at epoch 123, the gradient of 1.648×10^{-4} and *Mu* value of 1×10^{-6}.

References

[1] Bhaskar, K., Sharma, K., & Bhaskar, K. (2022). Cross-diffusion and chemical reaction effects of a MHD nanofluid flow inside a divergent/convergent channel with heat source/sink. Journal of Thermal Analysis and Calorimetry, 148, 573–588.

[2] Shilpa, B., Srilatha, P., Khan, U., kumar, R. N., Ahmed, S. B., & Kumar, R. (2023). Numerical study of thermal and solutal advancements in ZnO–SAE50 nanolubricant flow past a convergent/divergent channel with the effects of thermophoretic particle deposition. Nanoscale Advances, 5, 6647–6658.

[3] Dinarvand, S., Berrehal, H., Pop, I., & Chamkha, A. J. (2022). Blood-based hybrid nanofluid flow through converging/diverging channel with multiple slips effect: A development of Jeffery-Hamel problem. International Journal of Numerical Methods for Heat & Fluid Flow, 33, 1144–1160.

[4] Baithalu, R., Mishra, S. R., & Panda, S. (2024). Heat transfer and flow dynamics of methanol-based CuO and MgO hybrid nanomaterial in convergent and divergent channels: A Jeffery–Hamel flow study. Journal of Thermal Analysis and Calorimetry, 149, 15041–15052.

[5] Shilpa, B., Mann, V. S., Akkur, M., Kedia, A., Kumar, R. N., & Smitha, T. V. (2024). Galerkin finite element analysis on radiative heat transfer in titanium dioxide-polyalphaolefin nanolubricant past a convergent/divergent channel with non-uniform heat source/sink effect. International Journal of Thermofluids, 24, 100918–100918.

[6] Ramudu, A. C. V., Kumar, K. A., Sugunamma, V., & Sandeep, N. (2021). Impact of Soret and Dufour on MHD Casson fluid flow past a stretching surface with convective–diffusive conditions. Journal of Thermal Analysis and Calorimetry, 147, 2653–2663.

[7] Mishra, N. K., Sharma, M., Sharma, B. K., & Khanduri, U. (2023). Soret and Dufour effects on MHD nanofluid flow of blood through a stenosed artery with variable viscosity. International Journal of Modern Physics B, 30, 2350266.

[8] Vinutha, K., Nagaraja, K. V., Sajjan, K., Khan, U., Madhukesh, J. K., Kolli, U. C., & Muhammad, T. (2023). Thermal performance of Fe_3O_4, SWCNT, MWCNT and H_2O based on magnetohydrodynamic nanofluid flow across a wedge with significant impacts of Soret and Dufour. Nanoscale Advances, 5, 5952–5964.

[9] Sharma, R. P., Pattnaik, P. K., Mishra, S. R., & Allipudi, S. R.. (2023). Exploration of diffusion-thermo and thermo-diffusion on the nonlinear radiative heat flow of a conducting fluid over a permeable surface. International Journal of Modern Physics B, 38, 2450301.

[10] Krishnamoorthy, S. & Prasad, V. R. (2024). Heat transfer characteristics of thermo-diffusion (Soret) and diffusion-thermo (Dufour) effects in a square cavity containing a non-Darcy porous medium. Heat Transfer, 53, 1607–1627.

[11] Shaw, S., Nayak, M. K., Dogonchi, A. S., Chamkha, A. J., Elmasry, Y., & Alsulami, R. (2021). Hydrothermal and entropy production analyses of magneto-cross nanoliquid under rectified Fourier viewpoint: A robust approach to industrial applications. Case Studies in Thermal Engineering, 26, 100974.

[12] Sultana, N., Shaw, S., Nayak, M. K., & Mondal, S. (2022). Hydromagnetic slip flow and heat transfer treatment of Maxwell fluid with hybrid nanostructure: Low Prandtl numbers. International Journal of Ambient Energy, 44, 947–957.
[13] Gireesha, B. J. & Anitha, L. (2024). impact of shape dependent ternary hybrid nanoliquid flow through a microchannel with quadratic thermal radiation: Irreversibility analysis. Journal of Applied and Computational Mechanics, 10, 729–741.
[14] Gireesha, B. J. & Anitha, L. (2024). Convective flow of couple stress ternary nanoliquid flow through a permeable microchannel: Irreversibility analysis. International Journal of Modelling and Simulation, 1–18. https://doi.org/10.1080/02286203.2024.2388117
[15] Kumar, V. V., Sharma, R. P., & Kumar, R. N. (2025). The role of time-varying nanofluid flow and particle aggregation on the kinetics of homogeneous and heterogeneous reactions in position-controlled squeezing porous slider. In Proceedings of the Institution of Mechanical Engineers Part N Journal of Nanomaterials Nanoengineering and Nanosystems, https://doi.org/10.1177/23977914251338162.
[16] Raja, M. A. Z., Shoaib, M., Zubair, G., Khan, M. I., Gowda, R. J. P., Prasannakumara, B. C., & Guedri, K. (2022). Intelligent neuro-computing for entropy generated Darcy–Forchheimer mixed convective fluid flow. Mathematics and Computers in Simulation, 201, 193–214.
[17] Panda, S., Ontela, S., Mishra, S. R., & Thumma, T. (2023). Hybridization of artificial neural network and response surface methodology for the optimized heat transfer rate on three-dimensional micropolar nanofluid using Hamilton–Crosser conductivity model through a circular cylinder. Journal of Thermal Analysis and Calorimetry, 148, 9027–9046.
[18] Sharma, R. P., Madhukesh, J. K., Shukla, S., & Prasannakumara, B. C. (2023). Numerical and Levenberg–Marquardt backpropagation neural networks computation of ternary nanofluid flow across parallel plates with Nield boundary conditions. The European Physical Journal Plus, 138, 63 (1–19 pages)
[19] Panda, S., Baag, A. P., Pattnaik, P. K., Baithalu, R., & Mishra, S. R. (2024). Artificial neural network approach to simulate the impact of concentration in optimizing heat transfer rate on water-based hybrid nanofluid under slip conditions: A regression analysis. Numerical Heat Transfer, Part B: Fundamentals, 86(7), 2301–2323.
[20] Sharma, R. P., Barik, B. K., Kumar, V. V., & Sharma, A. (2025). Illustration of low oscillating magnetic field on sodium alginate-based hybrid nanofluid flow between two revolving disks: An artificial neural network-based study. Engineering Applications of Artificial Intelligence, 155, 111101–111101.
[21] Mahboobtosi, M., Ehsani, H., Ganji, A. M., Jalili, P., Mohamed, M. H., Jalili, B., & Ganji, D. D. (2025). AI-driven modeling of bioconvective nanofluid flow: An ANN approach to anisotropic slip and heat transfer in 3D systems. International Communications in Heat and Mass Transfer, 165, 109035.
[22] Kumar, V. V. & Sharma, R. P. (2025). Entropy generation minimization in nuclear reactor cooling via rough rotating disk: A statistical approach, multiscale and multidisciplinary modeling. Experiments and Design, 8, 245.
[23] Alghamdi, W. & Gul, T. (2024). Darcy–Forchheimer hybrid nanofluid flow in a squeezing inclined channel for drug delivery applications by means of artificial neural network. Multidiscipline Modeling in Materials and Structures, 21, 387–404.
[24] Haider, A., Ayub, A., Yuan, Z., Nie, Y., Anwar, M. S., Saidani, T., & Muhammad, T. (2025). Machine learning based modeling of pollutant and heat transfer in ternary nanofluid flow through porous media, Chaos. Solitons & Fractals, 199, 116890.
[25] Sharma, R. P., Praharaj, S., Barik, B. K., Kumar, V. V., Sharma, A., & Mahanta, C. (2024). Neural network-based analysis of thermal and mass transfer in nanofluid flow through a microchannel under pollutant concentration effect, multiscale and multidisciplinary modeling. Experiments and Design, 8, 313.
[26] Sharma, A. & Sharma, R. P. (2025). Utilizing neural networks to illustrate the dynamics of viscous fluid flow over curved surface with homogeneous and heterogeneous reactions. Engineering Applications of Artificial Intelligence, 159, 111629.

Jaya Gupta, Geeta Arora, and Shubham Mishra

Chapter 16
A Comprehensive Study of the Diverse Applicability of Computational Fluid Dynamics to Complex Systems

Abstract: In mechanical engineering, computational fluid dynamics (CFD) employs computer simulation to analyze heat transfer, flow in fluids, and associated phenomena. The widespread adoption of CFD underscores its importance in solving complex problems within modern engineering. CFD excels in both the creation of advanced devices and systems, and the optimization of current equipment via simulation, resulting in enhanced efficiency and reduced operational expenses. By enabling the creation of new and better device and system designs, and allowing for the optimization of current equipment via computational simulations, leads to improved efficiency and lower operating costs. Due to this recent progress in computer science has made high-performance hardware and software readily accessible, consequently increasing the feasibility of research utilizing CFD techniques have become a common tool across a diverse range of disciplines. Beyond these traditional areas, CFD also offers valuable insights in fields like astrophysics, biology, oceanography, oil recovery, architecture, and meteorology. The chapter discloses about the facts and applications of the phenomena in the domain of biomedical field.

Keywords: computational fluid dynamics (CFD), applications, partial differential equations (PDEs), diseases

16.1 Introduction

Computational fluid dynamics (CFD refers to the methodologies that empower computers to perform numerical simulations of how fluids move. The fundamental physical behavior of any fluid is governed by three core principles: (i) conservation of energy, (ii) Newton's second law of motion, and (iii) conservation of mass. The physical aspects of fluid-flow problems, governed by these basic laws, are represented mathe-

Jaya Gupta, Department of Mathematics, Lovely Professional University, Phagwara 144411, Punjab, India
Geeta Arora, Department of Mathematics, Lovely Professional University, Phagwara 144411, Punjab, India, e-mail: geetadma@gmail.com
Shubham Mishra, Department of Mathematics, Lovely Professional University, Phagwara 144411 Punjab India

https://doi.org/10.1515/9783111723464-016

matically through partial differential equations (PDEs) that depict the fluid's behavior throughout the flow domain. Through the application of specific CFD techniques, we can visualize the solutions to fluid-flow problems, the dynamic interaction between solid boundaries and the fluid, and the behavior between adjacent fluid layers. Instead of dealing directly with the differential equations of fluid flow, CFD provides a numerical approach by generating values that are dependent on time and/or spatial location, ultimately yielding a numerical visualization of the entire fluid flow. The strength of CFD lies in its ability to analyze system behavior and facilitate innovative design. Additionally, it efficiently allows for the investigation of performance metrics, leading to benefits like increased profit margins, enhance safety protocols, and other advantageous system features [1–3]. CFD techniques are now commonly employed across a wide spectrum of fields [4–8]. These include engineering applications, such as car design, turbomachinery, ship design, and aircraft manufacturing. Moreover, CFD proves valuable in diverse scientific disciplines like astrophysics, biology, oceanography, oil recovery, architecture, and meteorology. To perform CFD analysis, a multitude of numerical algorithms and software have been developed. Notably, the latest improvements in computer technology allow for the evaluation of numerical simulations for systems exhibiting significant physical and geometric complexities, often utilizing Performance Computing (PC) clusters. While supercomputing power allows for the rapid execution of massive fluid-flow simulations on extremely fine grids, it is inaccurate to view CFD as a completely developed field. Significant open questions remain, particularly concerning heat transfer, combustion modeling, turbulence, and the optimization of solution and discretization techniques. The insufficient research on the interrelation between CFD and other disciplines has created a notable gap, in which this issue intends to fill. The integration of CFD is becoming a standard in the design process for industrial products and systems. CFD finds application in diverse fields, such as electronic and chemical engineering, marine and environmental engineering, vehicle aerodynamics and hydrodynamics, architectural environmental design (both external and internal), power plant design (including turbines), hydrology, meteorology, and biomedical engineering.

By enabling the creation of new and better device and system designs and allowing for the optimization of current equipment via computational simulations, CFD leads to improved efficiency and lower operating costs. While CFD has become well-established in various engineering disciplines, its application in the biomedical domain is still relatively nascent. This lag is largely attributed to the intricate nature of human anatomy and the highly complex behavior of physiological fluids. Recent progress in computer science has made high-performance hardware and software readily accessible, consequently increasing the feasibility of biomedical research utilizing CFD. Medical researchers utilize CFD to gain enhanced insights into the performance of body fluids and physiological systems, thereby informing improvements in biofluid physiology research and the creation of new medical devices. By enabling simulation prior to real-world commitment, CFD allows for informed decision-making in medical

design alterations and can provide valuable direction for developing medical interventions. By analyzing the behavior of moving fluids, CFD helps us understand their influence on diverse processes. In addition, the physical attributes governing fluid motion are typically formulated as fundamental mathematical equations, frequently PDEs referred to as governing equations, which describe the process under consideration. Computer scientists solve these mathematical equations by converting them into code using high-level programming languages. Numerical simulations on high-speed computers are used to study fluid flow through computational programs. The goal of using high-level programming languages is to enable computer scientists to convert these mathematical equations for numerical simulation. The result of this process is numerical solutions, obtained by running programs on high-speed digital computers, which represent the fluid flow.

16.2 Background of CFD

Integrated within the discipline of fluid mechanics, this methodology employs mathematical evaluation and data structure techniques for the analysis and resolution of challenges pertaining to fluid-flow phenomena. The realization of the immense computational power of modern computers has led to a drastic increase in interest in quantified numerical techniques. Within this context, numerical analysis explores the foundational aspects of CFD technology, its operational processes, the importance of boundary conditions, and a review of various software and solvers utilized in the pre- and postprocessing phases of CFD simulations and analysis.

16.2.1 Navier-Stokes equation

Fluid mechanics encompasses the study of all aspects of fluid behavior, from stationary states to dynamic motion. Computer solutions to the equations governing fluid mechanics have significantly attracted the interest of one-third of researchers, with this number continuing to grow **[9]**. By solving the complete Navier-Stokes equations with finite element or finite volume methods, CFD numerically simulates flow fields by approximating hydrodynamic variables like pressure and velocity. To understand the fluid flow under investigation, the continuity equation (governing mass transport) and the momentum equation (describing the flow's momentum field) must be applied simultaneously. The equation involved fluid density, fluid velocity vector, body force and pressure.

16.2.2 Laminar-Turbulent

The nature of flow in a pipe, whether laminar or turbulent, is determined by Reynold's number. Specifically, flow is laminar if this number (based on the pipe's diameter) is less than 2,300 and it is turbulent if it exceeds this value. To model the effects of turbulence within the governing equations, the velocity component u is replaced by its time average, and a corresponding adjustment is made to the kinematic viscosity term. To model turbulence, an effective viscosity is employed, with its formulation derived from various mathematical models, such as the one-equation model, Prandtl mixing length model, k-epsilon, k-omega, RNG k-epsilon, and realizable k-epsilon. Even though blood flow is not perfectly smooth, in most of these models. So, for big blood vessels, it is okay to pretend the flow is completely smooth to get a good enough idea of what is happening, the microvasculature, characterized by the small diameter of capillaries, typically exhibits laminar flow regimes. However, the rheological behavior of blood in capillaries often demonstrates deviations from Newtonian constitutive relations.

16.2.3 Newtonian and Non-Newtonian

Newtonian fluids are characterized by a direct proportionality between viscous stress and local strain rate. For instance, when a fluid moves through a circular tube, stresses are generated due to the interaction of adjacent fluid layers. The non-Newtonian behavior arises from the fact that the fluid velocity is neither consistent across the flow nor exhibits a strictly parabolic distribution. However, within microvessels, the viscosity is not constant but varies as a function of both hematocrit and shear rate, as described by the Quemada rheological relation. Non-Newtonian models offer a more accurate prediction of wall shear stress (WSS) compared to the Newtonian model [10, 11].

16.3 Computational Fluid Dynamic Components

The application of commercial CFD codes is standard practice in CFD. CFD codes are architected using numerical algorithms that take into account the complexities of fluid-flow problems. The design of all CFD codes necessitates the inclusion of three main components to ensure the output is useful: preprocessor, solver, and postprocessor.

In fig 16.1, process of computational fluid dynamics is represented by using a flow diagram.

16.3.1 Preprocessor

The act of preprocessing in CFD involves entering the details of a fluid-flow problem into the software. The process includes the crucial steps of specifying the geometry of the region of interest and then generating the computational grid or mesh. This stage further requires the selection of physical and chemical phenomena for modeling, the definition of fluid properties, and the specification of appropriate boundary conditions at the inlet and outlet of the domain. Solution accuracy in numerical simulations is generally positively correlated with the spatial resolution afforded by a larger number of grid cells. Grid fineness plays a crucial role, impacting both the precision of the solution and the duration of the computational process. A significant amount of time is generally dedicated to this process for example in cardiovascular systems, grid generation information might be obtained from computational imaging tools; however, the limited resolution of these tools and the geometric variations due to the cardiac cycle are significant limitations. The varying viscosity of blood in response to changes in shear rate defines its non-Newtonian nature, illustrating the relationship between these two properties. Thus, the accurate representation of fluid viscosity necessitates the selection of a mathematical model that is appropriate for the specific range of shear rates present in the flow field. The energy conservation law plays a significant role in the foundational understanding of fluid motion. Depending on the specific region being studied, boundary conditions such as blood pressure, blood flow velocity, and temperature are easily accessible through both invasive and noninvasive measurement techniques. A further essential consideration pertains to the temporal variability of these boundary conditions in response to the cardiac cycle, as well as their modulation by the unique hemodynamic environment of the coronary circulation.

16.3.2 Solver

Several numerical solution techniques are available, including finite difference, finite element, finite volume, and spectral methods, among others. While each numerical method possesses a unique algorithmic implementation, the core of the solver's functionality is predicated on the approximation of unknown flow variables by means of elementary functional representations. Discretization is performed by substituting the approximate flow variable representations into the governing PDEs, yielding a system of algebraic equations that is subsequently solved. The computational cost associated with a given numerical solution technique is a function of the available processing capacity of the computing hardware. In the specific domain of cardiovascular system modeling, the finite volume method is a frequently adopted discretization approach.

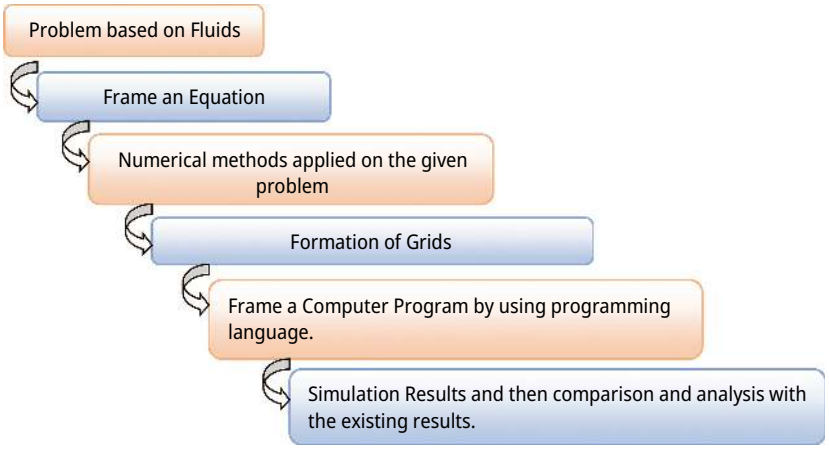

Figure 16.1: A flow diagram to represent the process of computational fluid dynamics.

16.3.3 Postprocessor

The objective of this phase is the graphical representation of the computational output. The field has seen the development of many visualization tools, including features for displaying domain geometry and grids, contour plots, surface plots, vector plots in 2D and 3D, particle tracking, and color postscript outputs. Once this process is complete, the simulation results become readily understandable to the researcher. Color-rendering techniques enable the visualization of changes in key hemodynamic parameters like blood flow profiles, oscillating shear index (OSI), WSS, pressure distribution, and shear rate. Furthermore, a temporal visualization of the cyclic motion can be derived in correlation with the progression of the cardiac cycle [12, 13].

16.4 Applications in the Biomedical System

Using simulation tools, medical researchers have recently been able to better predict the behavior of blood flow in the human circulatory system. The information derived from computational simulations is invaluable and often impossible to obtain experimentally, making it a significant application of CFD in the biomedical field, where it can predict blood flow in abnormal arteries. The application of CFD analysis for the investigation of fluid phenomena within the human vascular system is demonstrating a growing prevalence. The application of computational simulations to model circulatory function offers numerous benefits, notably a reduction in the probability of adverse postoperative events. Additionally, these simulations facilitate the development of enhanced surgical protocols, contribute to a more comprehensive understanding of

underlying biological mechanisms, and enable the design of more efficient and less iatrogenic medical devices, such as ventricular assist devices (VADs). The utility of CFD in medical contexts has expanded beyond the analysis of diseased states to include applications in health maintenance and supportive therapies, such as those employed in sports medicine and rehabilitation programs. By using pictorial representation application of CFD is explained in figure 16.2.

16.4.1 Atherosclerosis: Coronary Artery Disease

Although the development of atherosclerosis is influenced by various body-wide risk factors, its localized occurrence in certain circulatory regions implies that biomechanical factors likely play a role in making those areas prone to lesions. Beyond other established risks, luminal hemodynamic – including flow velocity, pressure changes, and importantly, WSS – have been implicated as potential contributors to coronary atherosclerosis.

Information concerning the spatial arrangement of intraluminal hemodynamic factors within the coronary vascular tree can be obtained through CFD analysis. The initial phase involves the generation of a computational mesh or grid representing the region of interest, derived from extracted coronary angiographic data obtained via computerized tomography (CT). The researchers may employ any three-dimensional volumetric medical imaging datasets. A prerequisite for utilizing digital imaging and communications in medicine (DICOM) files within software designed for the analysis of three-dimensional vector information is their conversion to a compatible file format. All the digitized data, including velocity and pressure information that changed throughout the cardiac cycle (and served as boundary conditions), were selected to be used in the appropriate algebraic solution. And then, the computer proceeds with the mathematical solution process. In order to select suitable viscosity models and governing equations for the non-Newtonian fluid analysis, a crucial discussion involving mechanical engineers and medical scientists about relevant clinical situations must occur at this point. The last stage involves the visualization of results for the user. The processing generates a multitude of representative results, such as visualization of particle paths, pressure and time-averaged WSS, velocity profiles, and the OSI, among others.

The bifurcation of a curved artery, where the outer wall meets the inner wall, is characterized by the formation of low flow velocity regions. The curved outer wall of the left anterior descending coronary artery experiences spatial fluctuations in flow velocity and recirculation, which are caused by variations in flow velocity and shear stress, especially during the deceleration phase of the pulsatile blood flow. The observed hemodynamic patterns imply that the rheological properties of blood may contribute to the atherogenic mechanisms specifically localized at arterial bifurcations and regions of curvature.

Researchers might apply this type of study to models featuring modified coronary artery geometry or to investigate the effects of varying viscosity models. Additionally,

computational models can simulate the outcomes of percutaneous coronary intervention and coronary bypass grafts, aiding in the selection of the best treatment approach. CFD has the potential to provide insights into the biomechanical aspects of how atherosclerosis develops and the problems it can cause [14–16].

16.4.2 Ophthalmology

Ophthalmological research has seen a growing trend in the use of CFD, driven by researchers' commitment to developing retinal mathematical models that closely resemble the actual system to minimize potential inaccuracies. The official website of the American Academy of Ophthalmology presents an article that provides a concise overview of the applications of CFD in the investigation of ophthalmological pathologies. In glaucoma, the optic nerve is damaged because increased pressure within the eye prevents fluid from draining properly. The homeostatic regulation of aqueous humor dynamics, specifically the delicate equilibrium between inflow and outflow in the normotensive human eye, remains a subject of considerable complexity and incomplete understanding, posing numerous unresolved questions [17–19].

16.4.3 Fluid and Air Flow in Lungs

Despite the applicability of the incompressible Navier-Stokes equations for the simulation of low Reynold's number pulmonary airflow, CFD provides a more comprehensive and powerful methodology for predicting the convective and diffusive transport, as well as the depositional patterns, of both gaseous and particulate species throughout the entire respiratory tract. The inherent geometric complexity of the respiratory tract often restricts the applicability of this methodology to relatively localized domains. Despite this limitation, a significant body of research has employed Computational CFD methodologies for the simulation of pulmonary mechanics. This simulation process is contingent upon the generation of a discrete computational mesh from an accurate computer-aided design (CAD) model, derived from magnetic resonance imaging (MRI) and CT datasets. This ultimately enhances the capacity of physicians to develop innovative medical devices and formulate requisite therapeutic interventions [20, 21].

16.4.4 Fontan Circulation

The Fontan circulation, a specific circulatory configuration first documented by Fontan and Baudet, is physiologically defined by the morphological absence of a functional right ventricle, necessitating a distinct hemodynamic profile for systemic blood flow. In the surgical management of single ventricle physiology, a congenital cardiac

anomaly, the geometric correction inherent to the Fontan procedure is primarily directed towards achieving anatomical separation of systemic and pulmonary venous return and the creation of a passive, direct, and unobstructed pathway facilitating systemic venous return to the pulmonary arterial circulation.

Despite its established role as a standard therapeutic approach for functional single ventricle physiology in congenital heart disease, the Fontan procedure is associated with the potential for unfavorable alterations in systemic circulatory hemodynamic. The morphological absence of a right ventricle induces systemic venous hypertension. The fundamental pathophysiological mechanism underlying this is the elevation of central venous pressure, coupled with increased hydrostatic pressure within the superior vena cava (SVC) and inferior vena cava (IVC).

Chronic central venous hypertension, particularly affecting the IVC, results in adverse physiological consequences, including potential hepatic dysfunction and impaired splanchnic microcirculation. The most severe sequelae include protein-losing enteropathy, a syndrome of excessive protein loss via the gastrointestinal tract, and plastic bronchitis, a disorder characterized by the formation of casts in the airways. When the pressure in the big veins near the heart is high, it can mess up the liver in complicated ways. It can also make the body grow new blood vessels in the liver, which can lead to abnormal connections between veins, between lung veins and other vessels, and maybe even between the main artery and the lung artery. Hemodynamically, the superior aspects of the pulmonary arterial vasculature are characterized by hypoperfusion or avascularity, coupled with a systemic compromise of the pulmonary lymphatic drainage pathways. When the heart only has one working pumping chamber, it has to work much harder to push blood through the whole body and the lungs, so the total resistance the heart feels is much higher. The altered hemodynamic state induces compensatory left ventricular hypertrophy, characterized by elevated left ventricular end-diastolic pressure, culminating in a reduction of diastolic compliance. Numerous research initiatives have been launched to attenuate these pathophysiological sequelae [22–25].

CFD simulations, conducted on a physiologically relevant model of Fontan circulation reconstructed from medical imaging modalities, demonstrated a marked increase in volumetric flow rate from the SVC specifically during the inspiratory phase. The augmented SVC flow during inspiration suggests a potential exacerbation of flow impedance in the delivery pathway of deoxygenated systemic venous blood to the pulmonary artery (PA) and the manifestation of increased venous congestion within the IVC during the inspiratory phase of the respiratory cycle relative to expiration. The physiological stressors of orthostasis and inspiration compound the existing challenges of systemic venous return stagnation and impaired physiologic blood-mixing characteristic of Fontan circulation. These observations underscore the potential therapeutic imperative for the implementation of an artificial mechanical circulatory support system in the context of Fontan circulatory decompensation.

16.4.5 Work of the Heart

This serves as an additional demonstration of the diagnostic application of CFD for evaluating myocardial performance. Conventionally, the assessment of cardiac work relies on pressure-volume loop analysis; however, novel indirect diagnostic modalities are emerging for the evaluation of the work of the heart (WOH). A mathematical model for the estimation of cardiac work (WOH) was formulated by employing the modified Windkessel lumped-parameter model in conjunction with constitutive blood viscosity models, utilizing the information encoded within pulse wave propagation between two discrete vascular locations. The human arterial vasculature, an intricate network of conduits, serves to transform the pulsatile ejection of blood from the heart into a continuous flow regime within the capillary beds and the venous return system. The modified Windkessel model, a canonical lumped parameter representation, enables the computational simulation of hemodynamic flow dynamics across the entire circulatory system through its analogy to an electrical circuit.

Within this schematic representation, Qin is defined as the volumetric flow rate ejected from the left ventricle during the systolic phase of the cardiac cycle, while Q1 and Q2 denote the volumetric flow rates perfusing the peripheral and distal vascular beds, respectively. Similarly defined, p1 and p2 denote the hemodynamic pressures recorded at the proximal and distal measurement sites, representing central and peripheral arterial blood pressure values, respectively. Expanding on this, C1 and C2 represent the elasticity or compliance of the vessels at the proximal and distal points, while L signifies the inertia, or resistance to changes in motion, of the blood. (L = 0.017 mmHg s^2/mL). Measuring blood pressure curves at two points in the peripheral arteries allows for the calculation of left ventricular flow rate using mathematical fluid analysis, offering a potential diagnostic tool (brachial and radial arteries). Given the essential role of the blood viscosity model in addressing the increased hemodynamic burden on the heart, subsequent research must prioritize the comparative analysis of different viscosity models against in vivo physiological measurements to ascertain their validity. Nevertheless, this category of investigation may suggest the potential for the development of noninvasive instrumentation for the quantification of cardiac work (WOH) [26–28].

16.4.6 Other Cardiovascular Systems

CFD methodologies are also applied to the study of the physiology and pathologies of the aorta, carotid, and cerebral arteries. There is an increasing trend in the utilization of CFD to elucidate the biomechanical factors associated with carotid stenosis and its biological implications based on geometric risk assessment., or via virtual prototyping methodologies to optimize surgical reconstruction strategies during carotid endarterectomy, frequently in conjunction with MRI data obtained for research purposes. Fur-

thermore, CFD is being implemented to enhance the understanding of hemodynamic flow patterns within abdominal aortic aneurysms and to elucidate the pathogenetic mechanisms underlying the development and progression of aortic dissection. In the context of intracranial cerebrovascular disease, CFD is also applied to the identification of geometric and hemodynamic risk factors associated with cerebral aneurysm rupture and to the optimization of stent design for the endovascular treatment of these aneurysms [29–31].

16.4.7 Thoracic Aorta

The thoracic aorta (TA), defined as the segment encompassing the ascending aorta, the aortic arch, and the descending aorta, gives rise to three major arterial branches from the aortic arch: the brachiocephalic artery (BA), the left common carotid artery (LCA), and the left subclavian artery (LSA), which collectively provide arterial perfusion to the superior aspects of the body. The TA exhibits a highly complex anatomical configuration characterized by significant curvature and a nonplanar helical trajectory of its central lumen. This structural complexity is further compounded by the presence of major arterial branches, a distally tapering luminal diameter, and viscoelastic, distensible arterial walls.

16.4.8 Artificial Organ Design

Artificial organs are bioengineered devices intended for implantation or integration within the human body to functionally replace a nonviable natural organ, thereby facilitating the patient's rehabilitation and return to a normal physiological state and lifestyle The prototype development phase of artificial organs necessitates extensive numerical simulations of hemodynamic performance with optimized geometric parameters to ensure clinical translatability. Computational flow modeling allows for the identification of the size and spatial coordinates of stagnation zones, consequently permitting the quantification of local shear rate magnitudes. Correlation of these parameters with the degree of thrombus formation and hemolysis is essential for establishing the biocompatibility and efficacy of a blood pump. VADs are mechanical circulatory support systems engineered to augment or supplant the function of compromised ventricular chambers. Despite considerable research investment, the numerical analysis of VADs remains limited by the absence of comprehensive computational models, thereby constraining the full exploitation of CFD methodologies in this domain. Implantable VADs are recognized as a promising therapeutic modality in the clinical management of patients with severe heart failure. Chua et al. [35] presented a three-dimensional computational model of the Kyoto-NTN magnetically suspended centrifugal blood pump and provided a comprehensive CFD solution of the internal hemodynamic flow field, encompassing velocity pro-

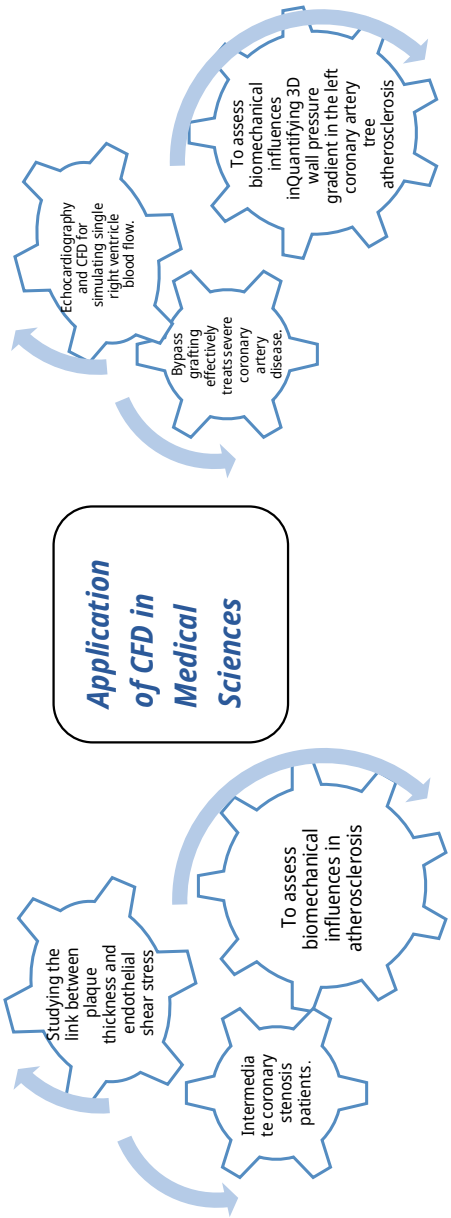

Figure 16.2: A representation to show application of computational fluid dynamics in biomedical.

files, static pressure distributions, and shear stress distributions experienced by the blood. The utility of CFD extends to the performance evaluation of various artificial organs, including the prediction of the in vivo physiological behavior of prosthetic heart valves. As an illustrative example, Claudio Capelli et al. (2017) conducted a comparative analysis of the hemodynamic performance of prosthetic heart valves incorporating different anchoring mechanisms, employing CFD methodologies. Their methodology for the investigation of bioprosthetic aortic valves incorporated a synergistic combination of commercially available experimental and computational modalities. The localization of high shear rate zones, critical for assessing potential blood cell trauma, is enabled by numerical computations, which consequently demand the specification of accurate boundary conditions to ensure the fidelity of the simulation. The application domain of CFD techniques is undergoing consistent expansion to encompass a multitude of additional biomedical applications, including the analysis of vocal tract aerodynamics, the simulation of nasal and paranasal sinus airflow, the investigation of synovial joint lubrication, and the modeling of cerebrospinal fluid dynamics [32–36].

16.5 Advantages and Limitations of Computational Fluid Dynamics

The consideration of CFD presents numerous advantages. Theoretical advancements in computational sciences are primarily directed towards the construction and numerical solution of governing PDEs and the investigation of various approximation methodologies applicable to these equations. CFD serves as a valuable adjunct to experimental and analytical investigations by offering an economically viable means of simulating complex fluid dynamics, with particular applicability to human bodily fluids. CFD offers a distinct advantage over experimental methodologies in geophysical and biological fluid dynamics by enabling the simulation of flow conditions that are not experimentally reproducible, particularly those characterized by extreme spatial dimensions (macro- or microscale), remote spatial domains, or inherent limitations in physical modeling. Moreover, the application of CFD yields a more detailed visual representation and a more comprehensive understanding of fluid dynamic phenomena than is typically obtainable through purely analytical or experimental methodologies.

Notwithstanding its numerous advantages, CFD cannot readily supersede experimental testing as a primary methodology for acquiring design-relevant data. Even though CFD has a lot of good points, scientists have to remember that it has built-in limits. Because the computer makes small mistakes when it is doing the calculations, the answers it gives would not be exactly the same as what really happens. The interpretation of the substantial datasets generated from numerical simulations of unsteady flow is most effectively achieved through the visualization of numerical solutions using vector fields, contour plots, or animated sequences. While aesthetically

appealing, wonderfully bright color visualizations of fluid mechanics within a flow system lack scientific merit if they do not accurately represent quantitative data. Consequently, a rigorous examination of numerical results is a prerequisite to their acceptance. Therefore, it is imperative for CFD practitioners to acquire the skills necessary for the proper analysis and critical evaluation of computed outcomes.

Furthermore, effective outcomes necessitate a collaborative paradigm involving mechanical engineers and medical scientists. Isolated departmental efforts are insufficient; iterative feedback from each discipline at every stage of the research and development process is paramount.

16.6 Conclusion

The inherent flexibility of CFD in adjusting model parameters, such as boundary conditions, is a notable advantage. Given the intricate nature of hemodynamic flow within complex arterial geometries, the synergistic integration of high-resolution simulation techniques with image-based measurement data has demonstrated efficacy as a reliable methodology for realistic arterial blood flow modeling. The inherent limitations associated with the application of CFD simulations are predominantly attributable to the constitutive model assumptions employed during their execution, encompassing parameters, such as geometric representation, fluid viscosity, material distensibility, and imposed flow conditions.

References

[1] Anderson, J. D. & Wendt, J. (1995). Computational Fluid Dynamics. New York, NY: McGraw-Hill.
[2] Andersson, B., Andersson, R., Håkansson, L., Mortensen, M., Sudiyo, R., & Van Wachem, B. (2011). Computational Fluid Dynamics for Engineers. Cambridge, England: Cambridge University Press.
[3] Ferziger, J. H., Perić, M., & Street, R. L. (2002). Computational Methods for Fluid Dynamics. Berlin: Springer.
[4] Chen, Q. (1997). Computational Fluid Dynamics of HVAC: Successes and Failures. Atlanta, GA: American Society of Heating, Refrigerating and Air-Conditioning Engineers, Inc.
[5] Kamyar, A., Saidur, R., & Hasanuzzaman, M. (2012). Application of computational fluid dynamics (CFD) for nanofluids. International Journal of Heat and Mass Transfer, 55(15–16), 4104–4115.
[6] Zakaria, M. S., Ismail, F., Tamagawa, M., Azi, A. F., Wiriadidjaya, S., Basri, A. A. et al. (2018). Computational fluid dynamics study of blood flow in aorta using OpenFOAM. Journal of Advanced Research in Fluid Mechanics and Thermal Sciences, 43, 81–89.
[7] Kozelkov, A. S., Kurulin, V. V., Lashkin, S. V., Shagaliev, R. M., & Yalozo, A. V. (2016). Investigation of supercomputer capabilities for the scalable numerical simulation of computational fluid dynamics problems in industrial applications. Computational Mathematics and Mathematical Physics, 56(8), 1506–1516.

[8] Mader, C. A., Kenway, G. K., Yildirim, A., & Martins, J. R. (2020). ADflow: An open-source computational fluid dynamics solver for aerodynamic and multidisciplinary optimization. Journal of Aerospace Information Systems, 17, 1–20.
[9] Kajishima, T. & Taira, K. (2017). *Computational Fluid Dynamics*: *Incompressible Turbulent Flows*. Springer International Publishing.
[10] Sriram, K., Intaglietta, M., & Tartakovsky, D. M. (2014). Non-Newtonian flow of blood in arterioles: Consequences for wall shear stress measurements. Microcirculation, 21(7), 628–639.
[11] Febina, J., Sikkandar, M. Y., & N M, S. (2018). Wall shear stress estimation of thoracic aortic aneurysm using computational fluid dynamics. Computational and Mathematical Methods in Medicine, 2018, Article ID 7126532, 12.
[12] Wendt, J. Ed. (2009). Computational Fluid Dynamics: An Introduction. Springer International Publishing.
[13] Kajishima, T. & Taira, K. (2017). *Computational Fluid Dynamics*: *Incompressible Turbulent Flows*. Springer International Publishing.
[14] Lee, B. K., Kwon, H. M., Kim, D. S. et al. (1998). Computed numerical analysis of the biomechanical effects on coronary atherogenesis using human hemodynamic and dimensional variables. Yonsei Medical Journal, 39, 166–174.
[15] Qiu, Y. & Tarbell, J. M. (2000). Numerical simulation of pulsatile flow in a compliant curved tube model of a coronary artery. Journal of Biomechanical Engineering, 122, 77–85.
[16] Ramaswamy, S. D., Vigmostad, S. C., Wahle, A. et al. (2004). Fluid dynamic analysis in a human left anterior descending coronary artery with arterial motion. Annals of Biomedical Engineering, 32, 1628–1641.
[17] Fitt, A. D. & Gonzalez, G. (2006). Fluid mechanics of the human eye: Aqueous humour flow in the anterior chamber. Bulletin of Mathematical Biology, 68, 53–71.
[18] Tsaousis, K. (2015). Computational Fluid Dynamics (CFD) in Ophthalmology. American Academy of Ophthalmology Website. [54] Kwon YH, Fingert JH, Kuehn MH, Alward WL, Primary Open-Angle Glaucoma, The New England Journal of Medicine, Vol. 360, 2009, pp.1113–24.
[19] Fuster, V., Badimon, L., Badimon, J., & Chesebro, J. H. (1992). The pathogenesis of coronary artery disease and acute coronary syndromes. New England Journal of Medicine, 326, 242–250.
[20] Nowak, N., Kakade, P. P., & Annapragada, A. V. (2003). Computational fluid dynamics simulation of airflow and aerosol deposition in human lungs. Annals of Biomedical Engineering, 31(4), 374–390.
[21] Geng Tian, P. (2010). Worth longest, development of a CFD boundary condition to model transient vapor absorption in the respiratory airways. Journal of Biomechanical Engineering, 132(5), 051003–051003.
[22] Starnes, S. L., Duncan, B. W., Kneebone, J. M. et al. (2001). Angiogenic proteins in the lungs of children after cavopulmonary anastomosis. Journal of Thoracic and Cardiovascular Surgery, 122(518), –23.
[23] Matthews, I. L., Fredriksen, P. M., Bjørnstad, P. G., Thaulow, E., & Gronn, M. (2006). Reduced pulmonary function in children with the Fontan circulation affects their exercise capacity. Cardiology Young, 16, 261–267.
[24] Gerdes, A., Kunze, J., Pfister, G. et al. (1999). Addition of a small curvature reduces power losses across total cavopulmonary connections. Annals of Thoracic Surgery , 67, 1760–1764.
[25] Myers, C. D., Boyd, J. H., Presson, RG Jr et al. (2006). Neonatal cavopulmonary assist: Pulsatile versus steady-flow pulmonary perfusion. Annals of Thoracic Surgery , 81, 257–263.
[26] Suh, S. H., Kaptan, Y., Roh, H. W. et al. (2011). Estimation of heart work by means of modified Windkessel model and different whole blood viscosity models. In Proceedings of 7th International Conference on Computational Heat and Mass Transfer, *Istanbul.* 344.
[27] Westerhof, N., Lankhaar, J. W., & Westerhof, B. E. (2009). The arterial Windkessel. Medical & Biological Engineering & Computing, 47, 131–141.

[28] Yılmaz, Y. & Gündoğdu, M. Y. (2008). A critical review on blood flow in large arteries: Relevance to blood rheology, viscosity models and physiologic conditions. Korea-Australia Rheology Journal, 20, 197–21.

[29] Frauenfelder, T., Lotfey, M., Boehm, T., & Wildermuth, S. (2006). Computational fl-uid dynamics: Hemodynamic changes in abdominal aortic aneurysm after stent-graft implantation. Cardiovasc Intervent Radiol, *Erratum in*: *Cardiovasc Intervent Radiol 2006; 29*:*724.*, 29, 613–623.

[30] O'Rourke, M. J. & McCullough, J. P. (2008). A comparison of the measured and predicted flowfield in a patient-specific model of an abdominal aortic aneurysm. Proceedings of the Institution of Mechanical Engineers, Part H, 222, 737–750.

[31] Suh, G. Y., Les, A. S., AS, T. et al. (2011). Quantification of particle residence time in abdominal aortic aneurysms using magnetic resonance imaging and computational fluid dynamics. Annals of Biomedical Engineering, 39, 864–883.

[32] Helgeland, A., Mardal, K. A., Haughton, V., & Reif, B. A. (2014). Numerical simulations of the pulsating flow of cerebrospinal fluid flow in the cervical spinal canal of a Chiari patient. Journal of Biomechanics, 47, 1082–1090.

[33] Yiallourou, T. I., Kroger, J. R., Stergiopulos, N., Maintz, D., Martin, B. A., & Bunck, A. C. (2012). Comparison of 4D phase contrast MRI flow measurements to computational fluid dynamics simulations of cerebrospinal fluid motion in the cervical spine. Plos One, 7, e52284.

[34] Sukumar, R., Ahavale, M. M., Makhijani, V. B., & Przekwas, A. J. (1996). Application of computational fluid dynamics techniques to blood pumps. Artificial Organs, 20, 529–533.

[35] Chua, L. P., Song, G., Lim, T. M., & Zhou, T. (2006). Numerical analysis of the inner flow field of a biocentrifugal blood pump. Artificial Organs, 30, 467–477.

[36] Capelli, C., Corsini, C; Biscarini, D; Ruffini, F; Migliavacca, F; Kocher, A; & Rath, C. (2017) Pledget-armed structures affect the haemodynamic performance of biologic aortic valve Substitute: a preliminary experimental and computational study. Cardiovascular Engineering and Technology, 8(1), 17–29.

Index

https://doi.org/10.1515/9783111723464-017

De Gruyter Series on the Applications of Mathematics in Engineering and Information Sciences

Already published in the series

Volume 23
Fuzzy Clustering Algorithms: Symbiotic Relationship Between Mathematics and Similarity Measures
Rakesh Kumar, Geeta Arora
ISBN 978-3-11-149238-4, e-ISBN (PDF) 978-3-11-149427-2,
e-ISBN (EPUB) 978-3-11-149576-7

Volume 22
Metaverse and Digital Twins: Blockchain and Healthcare Technology
Bhupinder Singh, Rishabha Malviya, Christian Kaunert (Eds.)
ISBN 978-3-11-163629-0, e-ISBN (PDF) 978-3-11-164689-3,
e-ISBN (EPUB) 978-3-11-164464-6

Volume 21
Reengineering Cyber Security Process: Quality Management
Mehrdad Sepehri Sharbaf
ISBN 978-3-11-144382-9, e-ISBN (PDF) 978-3-11-144463-5,
e-ISBN (EPUB) 978-3-11-144480-2

Volume 20
Digital Blockchain: Big Data, Artificial Intelligence, and Virtual Reality in Healthcare Ecosystem
Rishabha Malviya, Shristy Verma, Sonali Sundram, Harshil Shah
ISBN 978-3-11-157386-1, e-ISBN (PDF) 978-3-11-157428-8,
e-ISBN (EPUB) 978-3-11-157485-1

Volume 19
Artificial Intelligence for Healthcare: Machine Learning and Diagnostics
Rishabha Malviya, Shivam Rajput, Mukesh Roy, Irfan Ahmad, Saurabh Srivastava
ISBN 978-3-11-154758-9, e-ISBN (PDF) 978-3-11-154972-9,
e-ISBN (EPUB) 978-3-11-154984-2

Volume 18
Operational Perspective of Modeling System Reliability: Research Tools for System Dynamics
Deepti Aggrawal, Adarsh Anand, Yoshinobu Tamura, Mohini Agarwal (Eds.)
ISBN 978-3-11-147540-0, e-ISBN (PDF) 978-3-11-147610-0,
e-ISBN (EPUB) 978-3-11-147713-8

Volume 17
Algorithms: Big Data, Optimization Techniques, Cyber Security
Sushil C. Dimri, Abhay Saxena, Bhuvan Unhelkar and Akshay Kumar (Eds.)
ISBN 978-3-11-122800-6, e-ISBN (PDF) 978-3-11-122915-7,
e-ISBN (EPUB) 978-3-11-122963-8

Volume 16
Distributed Transfer Function Method: One-Dimensional Problems in Engineering
Bingen Yang, Kyoungrae Noh
ISBN 978-3-11-075854-2, e-ISBN (PDF) 978-3-11-075893-1,
e-ISBN (EPUB) 978-3-11-075900-6

Volume 15
Machine Learning for Cyber Security
Malik Preeti, Nautiyal Lata, Ram Mangey (Eds.)
ISBN 978-3-11-076673-8, e-ISBN (PDF) 978-3-11-076674-5,
e-ISBN (EPUB) 978-3-11-076676-9

Volume 14
Multiple Criteria Decision-Making Methods: Applications for Managerial Discretion
Mohini Agarwal, Adarsh Anand, Deepti Aggrawal
ISBN 978-3-11-074356-2, e-ISBN (PDF) 978-3-11-074363-0,
e-ISBN (EPUB) 978-3-11-074374-6

Volume 13
Integral Transforms and Applications
Nita H. Shah, Monika K. Naik
ISBN 978-3-11-079282-9, e-ISBN (PDF) 978-3-11-079285-0,
e-ISBN (EPUB) 978-3-11-079292-8

Volume 12
Noise Filtering for Big Data Analytics
Souvik Bhattacharyya, Koushik Ghosh (Eds.)
ISBN 978-3-11-069709-4, e-ISBN (PDF) 978-3-11-069721-6,
e-ISBN (EPUB) 978-3-11-069726-1

Volume 11
Artificial Intelligence for Signal Processing and Wireless Communication
Abhinav Sharma, Arpit Jain, Ashwini Kumar Arya, Mangey Ram (Eds.)
ISBN 978-3-11-073882-7, e-ISBN (PDF) 978-3-11-073465-2,
e-ISBN (EPUB) 978-3-11-073472-0

Volume 10
Meta-heuristic Optimization Techniques: Applications in Engineering
Anuj Kumar, Sangeeta Pant, Mangey Ram, Om Yadav (Eds.)
ISBN 978-3-11-071617-7, e-ISBN (PDF) 978-3-11-071621-4,
e-ISBN (EPUB) 978-3-11-071625-2

Volume 9
Linear Integer Programming: Theory, Applications, Recent Developments
Elias Munapo, Santosh Kumar
ISBN 978-3-11-070292-7, e-ISBN (PDF) 978-3-11-070302-3
e-ISBN (EPUB) 978-3-11-070311-5

Volume 8
Mathematics for Reliability Engineering: Modern Concepts and Applications
Mangey Ram, Liudong Xing (Eds.)
ISBN 978-3-11-072556-8, e-ISBN (PDF) 978-3-11-072563-6
e-ISBN (EPUB) 978-3-11-072559-9

Volume 7
Mathematical Fluid Mechanics: Advances on Convection Instabilities and Incompressible Fluid Flow
B. Mahanthesh (Ed.)
ISBN 978-3-11-069603-5, e-ISBN (PDF) 978-3-11-069608-0
e-ISBN (EPUB) 978-3-11-069612-7

Volume 6
Distributed Denial of Service Attacks: Concepts, Mathematical and Cryptographic Solutions
Rajeev Singh, Mangey Ram (Eds.)
ISBN 978-3-11-061675-0, e-ISBN (PDF) 978-3-11-061975-1
e-ISBN (EPUB) 978-3-11-061985-0

Volume 5
Systems Reliability Engineering: Modeling and Performance Improvement
Amit Kumar, Mangey Ram (Eds.)
ISBN 978-3-11-060454-2, e-ISBN (PDF) 978-3-11-061737-5
e-ISBN (EPUB) 978-3-11-061754-2

Volume 4
Systems Performance Modeling
Adarsh Anand, Mangey Ram (Eds.)
ISBN 978-3-11-060450-4, e-ISBN (PDF) 978-3-11-061905-8
e-ISBN (EPUB) 978-3-11-060763-5

Volume 3
Computational Intelligence: Theoretical Advances and Advanced Applications
Dinesh C. S. Bisht, Mangey Ram (Eds.)
ISBN 978-3-11-065524-7, e-ISBN (PDF) 978-3-11-067135-3
e-ISBN (EPUB) 978-3-11-066833-9

Volume 2
Supply Chain Sustainability: Modeling and Innovative Research Frameworks
Sachin Kumar Mangla, Mangey Ram (Eds.)
ISBN 978-3-11-062556-1, e-ISBN (PDF) 978-3-11-062859-3,
e-ISBN (EPUB) 978-3-11-062568-4

Volume 1
Soft Computing: Techniques in Engineering Sciences
Mangey Ram, Suraj B. Singh (Eds.)
ISBN 978-3-11-062560-8, e-ISBN (PDF) 978-3-11-062861-6,
e-ISBN (EPUB) 978-3-11-062571-4